Research Project on CO_2 Geological Storage and Groundwater Resources

Water Quality Effects Caused by CO_2 Intrusion into Shallow Groundwater

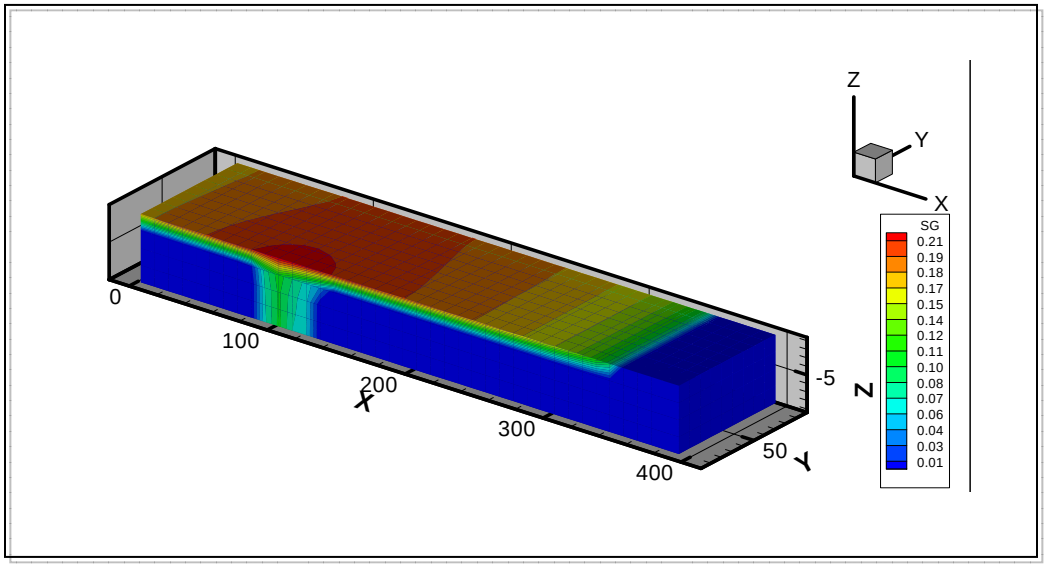

Technical Report, October 2008

Contact: Jens Birkholzer

Earth Sciences Division, Lawrence Berkeley National Laboratory

1 Cyclotron Rd., MS 90-1116; 510-486-7134; jtbirkholzer@lbl.gov

Contributors:

Jens Birkholzer, John Apps, Liange Zheng, Yingqi Zhang, Tianfu Xu, Chin-Fu Tsang

EPA Program Managers: Bruce Kobelski, Anhar Karimjee

Executive Summary

One promising approach to reduce greenhouse gas emissions is injecting CO_2 into suitable geologic formations, typically depleted oil/gas reservoirs or saline formations at depth larger than 800 m. Proper site selection and management of CO_2 storage projects will ensure that the risks to human health and the environment are low. However, a risk remains that CO_2 could migrate from a deep storage formation, e.g. via local high-permeability pathways such as permeable faults or degraded wells, and arrive in shallow groundwater resources. The ingress of CO_2 is by itself not typically a concern to the water quality of an underground source of drinking water (USDW), but it will change the geochemical conditions in the aquifer and will cause secondary effects mainly induced by changes in pH, in particular the mobilization of hazardous inorganic constituents present in the aquifer minerals. Identification and assessment of these potential effects is necessary to analyze risks associated with geologic sequestration of CO_2.

This report describes a systematic evaluation of the possible water quality changes in response to CO_2 intrusion into aquifers currently used as sources of potable water in the United States. Our goal was to develop a general understanding of the potential vulnerability of United States potable groundwater resources in the event of CO_2 leakage. This goal was achieved in two main tasks, the first to develop a comprehensive geochemical model representing typical conditions in many freshwater aquifers (Section 3), the second to conduct a systematic reactive-transport modeling study to quantify the effect of CO_2 intrusion into shallow aquifers (Section 4). Via reactive-transport modeling, the amount of hazardous constituents potentially mobilized by the ingress of CO_2 was determined, the fate and migration of these constituents in the groundwater was predicted, and the likelihood that drinking water standards might be exceeded was evaluated. A variety of scenarios and aquifer conditions was considered in a sensitivity evaluation. The scenarios and conditions simulated in Section 4, in particular those describing the geochemistry and mineralogy of potable aquifers, were selected based on the comprehensive geochemical model developed in Section 3.

An important step in developing the comprehensive geochemical model was the identification of those mineral hosts containing hazardous constituents, which control their equilibrium concentration in potable groundwaters. This step was accomplished through an extensive review of the literature, especially that relating to ore and coal mineralogy, through which plausible mineral hosts containing hazardous constituents, either as essential components or in solid solution, were provisionally identified. The postulated presence of these mineral hosts in aquifer rocks was then examined through a thermodynamic analysis of more than 38,000 potable groundwaters from the USGS NWIS database, using a distribution-of-species code to test for their thermodynamic saturation in solution. Mineral hosts meeting the criterion of thermodynamic saturation were assumed to control the aqueous concentrations of hazardous constituents and any subsequent changes due to the ingress of CO_2. Considering a representative groundwater under reducing conditions (a condition met in the large majority of all evaluated groundwaters), the most likely solubility-controlling mineral host for lead is galena, while arsenic would typically be controlled by the arsenopyrite component as a solid solution in pyrite. Other likely mineral hosts for a reducing groundwater are as follows: barium is likely to be

saturated with respect to barite; cadmium is either in solid solution in sphalerite and/or is present as greenockite or cadmoselite; mercury is likely to be present as cinnabar and possibly as tiemannite, but its presence in solid solution in pyrite, perhaps in minor amounts, cannot be ruled out; antimony is present as the gudmundite component in solid solution in pyrite, and probably as kermesite, especially in neutral to acid conditions; selenium could be present as either clausthalite, tiemannite, or cadmoselite; uranium is present as uraninite and/or coffinite; and zinc is present as sphalerite and/or hemimorphite.

Characterization of thermodynamic controls necessitated the iterative improvement and augmentation of a large supporting thermodynamic database comprising the solubility products of minerals of interest, and of complexes that affect the concentrations of the hazardous constituents in aqueous solution. A comprehensive literature analysis was conducted for this purpose. The resulting thermodynamic data used for geochemical modeling were then tested, and in some instances improved via calibration against field observations from the NWIS database, based on the resulting thermodynamic saturations of the more than 38,000 groundwater samples. In addition, the bulk mineralogy of typical aquifer host rocks had also to be determined, accomplished through review of the scientific literature. The bulk mineralogy was combined with the mineralogy of the previously identified mineral hosts for several hazardous inorganic constituents, with their respective concentrations estimated through an evaluation of natural abundances in soils and sediments. While these abundances are typically very small compared to those of the major minerals (order of 10-7 to >10-4), all hazardous constituents targeted for study occur ubiquitously in soils, sediments, and aquifer rocks, indicating that their potential mobilization in response to CO_2 intrusion can be a widespread one in domestic aquifers.

A preliminary assessment of CO_2-related water quality changes was conducted by calculating the expected equilibrium concentrations of hazardous inorganic constituents as a function of the partial pressure of CO_2. $P(CO_2)$ was varied from 10^{-4} bar to 10 bar, leading to a corresponding pH variation between 8.9 and 5.6. Equilibrium concentrations were determined using a distribution-of-species code, assuming a representative groundwater in reducing conditions and incorporating the thermodynamic controls identified in above-mentioned database evaluation. Results indicate that the concentrations of some of the studied constituents, for example barium, cadmium, antimony, and zinc, are sensitive to changes in $P(CO_2)$, but that only arsenic, and to a lesser extent lead and zinc, have the potential for exceeding their respective maximum contaminant levels (as defined by the U.S. Environmental Protection Agency) at elevated CO_2 concentrations. Therefore, in the systematic reactive-transport modeling study discussed below, primary emphasis was placed on the evaluation of the response and transport of arsenic and lead under intruding CO_2.

The reactive-transport simulator TOUGHREACT was then used to predict the transport of gaseous and dissolved CO_2 within a shallow aquifer, as well as the geochemical changes caused by the presence of CO_2, in particular those changes leading to the mobilization of lead and arsenic and their migration in the groundwater (Section 4). Various sensitivity studies were conducted for different hydrological, geochemical, and mineralogical conditions, (1) to account for a range of conditions found in domestic potable aquifers and their host rocks, and (2) to

evaluate the uncertainty associated with geochemical processes and model parameters. Equilibrium runs were performed prior to modeling CO_2 intrusion to establish the initial chemical composition of the groundwater at equilibrium with the selected mineralogy. This initiation step also establishes equilibrium between mineral solubilities and adsorption sites, essentially "loading up" the latter. Thus, the selection of solubility-controlling minerals for hazardous inorganic constituents not only defined the initial aqueous concentration in the groundwater, but also the amount of contaminants initially sorbed onto clays and iron oxides.

Starting with the equilibrated initial conditions, the impact of CO_2 intrusion was then modeled for a synthetic hydrogeological situation in a representative potable aquifer while considering continuous ingress of CO_2 for a time period of 100 years. CO_2 was assumed to have escaped from a deep geologic sequestration site via a preferential pathway, entering the shallow aquifer locally at a constant rate. A confined aquifer was considered, meaning that excess CO_2 not dissolving into groundwater accumulates at the aquifer top and spreads out laterally, potentially causing widespread pH changes and mobilization of contaminants. (Excess CO_2 in an unconfined aquifer would escape into the vadose zone, causing no further harm to the groundwater quality.) A suite of "representative" aquifer mineralogies was simulated representing a broad range of host rock compositions found throughout the United States.

Our simulation results suggest that CO_2 ingress into a shallow aquifer can lead to significant mobilization of lead and arsenic, contaminating the groundwater near the intrusion location and further downstream. While substantial increases in aqueous concentrations are predicted to occur compared to the initial water composition, the maximum contaminant level for arsenic in groundwater has been exceeded in only a few simulation cases, whereas the maximum contaminant level for lead has not been exceeded at all. Notice that the mobilization of lead and arsenic, from minerals and from adsorption sites, causes only small changes to the initial contaminant mass in the solid phase, even after a time period of 100 years of CO_2 intrusion. Very small amounts of lead and arsenic contained in the aquifer solid phase can provide a long-lasting source of contamination.

As demonstrated in a comprehensive sensitivity study, many conditions and processes impact the severity and spatial distribution of groundwater contamination in response to CO_2 intrusion. Our simulations indicate that adsorption/desorption via surface complexation is arguably the most important process controlling the fate of hazardous constituents mobilized by CO_2 leakage when sorbing minerals are present. In a simulation case without adsorption/desorption taken into account, the resulting long-term contamination of the aquifer is less significant near the region where CO_2 enters, while aqueous concentrations keep increasing with travel distance as acidic water migrates further and more dissolution occurs. The relative importance of dissolution/precipitation versus adsorption/desorption is controlled by many factors, including adsorption parameters and aquifer mineralogy, reaction kinetics, aqueous complexation processes, and mineral solubility constants. For example, the role that adsorption/desorption plays in the mobilization of hazardous constituents depends strongly on the number of adsorption sites. A sensitivity run with lower site density reveals that early increases in aqueous lead and arsenic are much less significant, because desorption is less relevant in mobilizing contaminants.

Moderate to strong sensitivities in the resulting lead and arsenic concentrations have been obtained with respect to other geochemical parameters (such as the solubilities of hazardous-constituent-bearing minerals, the kinetic rates for precipitation and dissolution, and the aqueous complexation constants) and conditions (such as the redox environment, with the simulated behavior in a oxidized aquifer being very different from an aquifer in a reducing environment). Less relevant appears to be the initial volume fraction of trace- element minerals that contain lead and arsenic as essential components. As long as these trace minerals have not been completely dissolved (a very slow process), the contamination of an aquifer via dissolution and/or desorption is fairly independent of the initial mineral volume. With respect to the representative aquifer mineralogies assumed in our study (ranging from almost pure arenites to dolomitic limestone), the most important effects resulted from differences in clay content, which affect the adsorption/desorption behavior, as well as from differences in the presence of carbonate minerals, which can moderate the pH changes caused by CO_2 intrusion.

Sensitivity studies have also been conducted with respect to the assumed flow and CO_2 leakage conditions in the aquifer. It turns out that an increase in the leakage rate does not necessarily lead to increases in the maximum contaminant concentrations in the aquifer. Once the groundwater reaches its solubility limit with respect to CO_2, which occurs at relatively small intrusion rates, there is no further increase in total inorganic carbon and acidity. Consequently, no further mobilization of hazardous constituents occurs once local equilibrium has been achieved. Excess CO_2 remains in the gas phase and rises to the top of the aquifer, thereby bypassing most of the groundwater body. The resulting impact on aqueous contamination is influenced by the general pattern of the CO_2 plume (e.g., the spreading of the plume at the top of the aquifer in the case of a confined aquifer) and the subsequent migration of CO_2-charged and contaminated water further downstream. Similar effects on the dissolution characteristics can be seen when the groundwater flow rate changes, as more or less groundwater undersaturated with respect to CO_2 will flow past the location where CO_2 enters the aquifer.

As stated before, the goal of this study was to better understand, in a global sense, the vulnerability of representative and relevant aquifer types in the case of CO_2 intrusion, thereby providing sound scientific information to regulators and the public. It is understood, however, that even the most comprehensive sensitivity study cannot encompass all possible aquifer conditions and CO_2 intrusion scenarios. Neither can it account for all relevant uncertainties. While the geochemical evaluation conducted in Section 3 was extremely comprehensive, it was also pointed out that several assumptions, approximations, and compromises were necessary in this effort, mostly because of incomplete characterization of important parameters such as dissolution and dissociation constants. We recommend that our study should now be followed up with site-specific model predictions, and that laboratory or field experiments should be performed to test uncertain model assumptions and parameters. Such experiments would involve exposing initially undisturbed groundwater in laboratory samples or in situ in the field to elevated levels of CO_2. We also recommend testing the developed geochemical models using measured data from natural analogue sites, such as those described in Section 5 of this report.

Table of Contents

List of Figures

List of Tables

List of Acronyms and Abbreviations

AA	Atomic Adsorption Spectroscopy
As	Arsenic
ASR	Aquifer Storage and Recovery
Ba	Barium
Cd	Cadmium
EPA	Environmental Protection Agency
ICP-MS	Inductively Coupled Plasma with Mass Spectroscopy
Hg	Mercury
LBNL	Lawrence Berkeley National Laboratory
NAA	Neutron Activation Analysis
NASCENT	Natural Analogs for the Storage of CO_2 in the geological ENvironmenT
NURE	National Uranium Resource Evaluation
MCL	Maximum Contaminant Level
MSW	Municipal Solid Waste
NGS	National Geochemical Survey
NWIS	National Groundwater Information System
Pb	Lead
Sb	Antimony
SDWR	Secondary Drinking Water Regulation
Se	Selenium
SI	Saturation Index
SS	Solid Solution
TIC	Total Inorganic Carbon
TDS	Total Dissolved Solids
USDW	United States Drinking Water
U	Uranium
XPS	X-ray Photo electron Spectroscopy
XAS	X-ray Absorption Spectroscopy

List of Referenced Minerals and Their Chemical Formulas

Name	Formula
Albite-low	$NaAlSi_3O_8$
Akdalaite	$(Al_2O_3)_4 \cdot (H_2O)$
Alstonite	$BaCa(CO_3)_2$
Anglesite	$PbSO_4$
Anhydrite	$CaSO_4$
Ankerite	$Ca(Mg_{0.3}Fe_{0.7})(CO_3)_2$
Antimonselite	Sb_2Se_3
Antimony	Sb
Apatite	$Ca_5(OH)(PO_4)_3$
Arsenic	As
Arsenic Oxide	As_2O_5
Arsenolite	As_2O_3
Arsenopyrite	FeAsS
Barite	BaSO4
Berthierite	$FeSb_2S_4$
Berzelianite	Cu_2Se
Cadmoselite	CdSe
Calcite	$CaCO_3$
Cerussite	$PbCO_3$
Chlorite	$Mg_{2.5}Fe_{2.5}Al_2Si_3O_{10}(OH)_8$
Clinochlore	$Mg_5Al_2Si_3O_{10}(OH)_8$
Cinnabar	HgS
Claudetite II	As_2O_3
Clausthalite	PbSe
Cotunnite	$PbCl_2$
Crandallite	$CaAl_3(PO_4)_2(OH)_5 \cdot (H_2O)$
Dawsonite	$NaAlCO_3(OH)_2$
Dolomite	$CaMg(CO_3)_2$
E-Fe_2O_3	Fe_2O_3
Ferrihydrite	$Fe_{10}O_{14}(OH)_2$
Ferrarisite	$Ca_5(AsO_3OH)_2(AsO_4)_2.9H_2O$

Name	Formula
Ferroselite	$FeSe_2$
FeS,am	FeS
Fieldlerite	$Pb_3(OH)_2Cl_4$
Galena	PbS
Goethite	FeO(OH)
Green Rust	$Fe(II)_4Fe(III)_2(OH)(SO_4).8H_2O$
Greenockite	CdS
Greigite	Fe_3S_4
Gudmundite	FeSbS
Guerinite	$Ca_5(AsO_3OH)_2(AsO_4)_2.9H_2O$
Haidingerite	$Ca(AsO_3OH).H_2O$
Hematite	Fe_2O_3
Hornesite	$Mg_3(AsO_4)_2.8H_2O$
Hydrocerussite	$Pb(OH)_2.(PbCO_3)_2$
Illite	$K_{0.6}Mg_{0.25}Al_{1.8}Al_{0.5}Si_{3.5}O_{10}(OH)_2$
Johnbaumite	$Ca_5(AsO_4)_3(OH)$
Johnbaumite-Pb	$Pb_5(AsO_4)_3(OH)$
K-feldspar	$KAlSi_3O_8$
Kaolinite	$Al_2Si_2O_5(OH)_4$
Kermesite	Sb_2S_2O
Kerogen-OS	$(-CHOH)_{18}(-CHCOOH)_5(-CHCOOCH2CH3)_6(-CHSH)_{10}$
Kullerudite	$NiSe_2$
Lanarkite	$PbO.PbSO_4$
Laurionite	PbClOH
Lead	Pb
Lead Hydroxide	$Pb(OH)_2$
Lepidocrocite	FeO(OH)
Litharge	PbO
Lorretoite	$Pb_7O_6Cl_2$
Mackinawite	FeS
Maghemite	Fe_2O_3
Magnesite	$MgCO_3$
Marcasite	FeS_2

Name	Formula
Massicot	PbO
Matlockite	$PbO.PbCl_2$
Mendipite	$(PbO)_2.PbCl_2$
Meta-cinnabar	HgS
Mimetite	$Pb_5(AsO_4)_3(Cl)$
Naumannite	Ag_2Se
Oligoclase	$CaNa_4Al_6Si_{14}O_{40}$
Opal-CT	SiO_2
Orpiment	As_2S_3
Paralaurionite	PbOHCl
Pararealgar	AsS
Penfieldite	Pb_2OHCl_3
Pharmacolite	$CaHAsO_4.2H_2O$
Pharmacosiderite	$KFe_4(AsO_4)_3(OH)_4.6H_2O$
Picropharmacolite	$Ca4Mg(HAsO_4)_2(AsO_4)_2.11H_2O$
Pitticite	$Fe_2(AsO_4)(SO_4)(OH).6H_2O$
Plumbonacrite	$Pb_{10}O(OH)_6(CO_3)_6$
Pyrite	FeS_2
Pyromorphite	$Pb_5(PO_4)_3(Cl)$
Quartz	SiO2
Realgar	AsS
Schwertmannite	$Fe(III)_{16}O_{16}(OH)_{12}(SO_4)_2.12H_2O$
Scorodite	$FeAsO_4.2H_2O$
Senarmonite	Sb_2O_3
Siderite	$FeCO_3$
Sphalerite	ZnS
Stibnite	Sb_2S_3
Symplesite	$Fe_3(AsO_4)_2.8H_2O$
Smectite-Ca	$Ca_{0.145}Mg_{0.26}Al_{1.77}Si_{3.97}O_{10}(OH)_2$
Smectite-Na	$Na_{0.290}Mg_{0.26}Al_{1.77}Si_{3.97}O_{10}(OH)_2$
Smectite-low-Fe-Mg	$Ca_{0.02}Na_{0.15}K_{0.2}Fe^{++}_{0.29}Fe^{+++}_{0.16}Mg_{0.9}Al_{1.25}Si_{3.75}H2O_2$
Sphalerite	ZnS
Talc	$Mg_3Si_4O_{10}(OH)_2$

Name	Formula
Talmessite	$Ca_2Mg(AsO_4)_2.2H_2O$
Tiemannite	HgSe
Tooeleite	$Fe_6(AsO_3)_4(SO_4)(OH)_4.4H_2O$
Uraninite	UO_2
Valentinite	Sb_2O_3
Weilite	$CaHAsO_4$
Yukonite	$Ca_7Fe_{11}(AsO_4)_9O_{10}.24H_2O$

1. Motivation

Proper site selection and management of CO_2 storage projects will ensure that the risks to human health and the environment are low. However, a risk remains that CO_2 could migrate from a deep storage formation to arrive in shallow groundwater resources. Figure 1.1 shows schematically such a scenario, where a local high-permeability pathway—such as a permeable fault or an open abandoned well—allows for CO_2 to escape from depth and reach a shallow aquifer used for water supply. The buoyant CO_2 will undergo phase transition along this path and will typically reach the shallow strata as a gas, which will partially or completely dissolve into the groundwater. This process is by itself not typically a concern to the water quality of an underground source of drinking water (USDW), but it will change the geochemical conditions in the aquifer and will cause secondary effects, mainly by changes in pH.

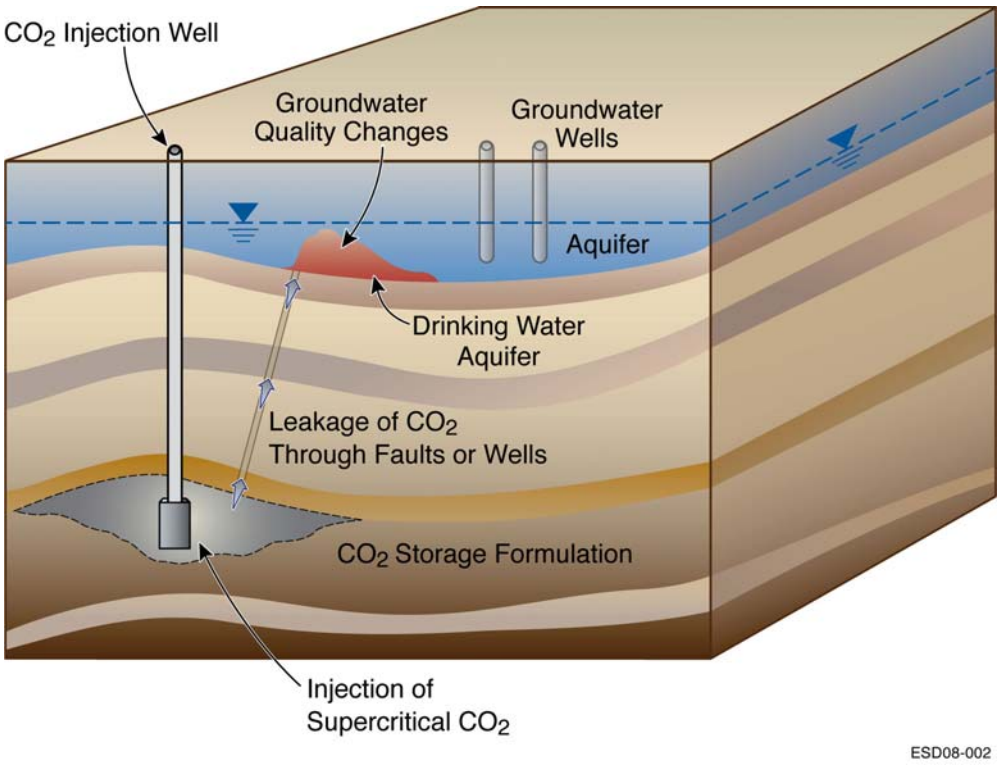

Fig. 1.1. Schematic illustrating potential groundwater quality changes in response to CO_2 leakage from deep storage sites

As CO_2 migrates into a freshwater aquifer and dissolves into the aqueous phase, the total concentration of dissolved carbonate increases and causes a decrease in pH. The higher acidity of the water may lead to enhanced dissolution of many minerals, among these some that may contain hazardous constituents such as lead (Pb) or arsenic (As) as essential components. For example, Pb is an essential component in galena, which is lead sulfide, and As is an essential component in arsenopyrite, which is iron arsenic sulfide. If such minerals are present and dissolve, the increasing concentration of hazardous constituents can cause detrimental effects to groundwater quality, possibly to the extent that maximum allowable levels are exceeded. Another concern related to decreasing pH is the possible mobilization of hazardous constituents on adsorption sites (e.g., clays, iron oxyhydoxides, or sorbed material on sand coats) or ion exchange sites (e.g., smectitic clays). For example, dissolution of iron oxyhydroxides in response to CO_2 injection may have released sorbed toxic metals into the saline water at the Frio Pilot Test site (Kharaka et al., 2006). The problem of mobilizing such hazardous constituents (Pb, As, and others such as barium (Ba), cadmium (Cd), mercury (hg), antimony (Sb), selenium (Se), uranium(U)) in response to CO_2 intrusion is relevant for most freshwater aquifers, because these elements occur—in trace amounts—ubiquitously in soils, sediments, and aquifer rock throughout the world.

To date, the potential geochemical effects of CO_2 intrusion into USDWs, especially those currently exploited as sources of potable water, have not been systematically assessed. Wang and Jaffe (2004) conducted reactive-transport simulations considering the migration of CO_2 into an aquifer with significant volume fraction of galena present as an essential mineral component. Their results suggest strongly increased Pb concentration levels because of galena dissolution, in the case of a poorly buffered aquifer to levels higher than the maximum contaminant level (MCL) for Pb defined by the U.S. Environmental Protection Agency (EPA). It should be noted, however, that the authors intended their study as an illustrative example, to demonstrate the potential effects of CO_2 intrusion on water quality; their simulations do not necessarily represent realistic conditions expected to occur if CO_2 were to penetrate a potable water aquifer. This is because their reactive-transport simulations involved very simplified geochemical systems and were based on extreme mineralogical conditions. Thus, while the simulation results of Wang and

Jaffe (2004) point to a potential concern that needs to be addressed, it is not clear to date how severe and widespread the problem would be in realistic cases.

To adequately analyze the potential vulnerability of our groundwater resources in the event of large-scale deployment of carbon capture and storage, the geochemical consequences of CO_2 migration into current and future potable water sources requires further evaluation. A multiyear research project was initiated in October 2006 to address these issues, the first phase of which is summarized in this annual report. The objective of this first phase is to investigate the water quality changes in response to CO_2 intrusion through development of a geochemical model that describes the complete chemistry of a range of specified shallow aquifer systems. This model is then used in a series of reactive-transport modeling simulations to evaluate transient responses to CO_2 intrusion. The goal is to better understand, in a global sense, the vulnerability of representative and relevant aquifer types in the case of CO_2 intrusion, thereby providing sound scientific information to regulators and the public. It is understood, however, that evaluation of specific sites will require additional simulation analysis considering the site-specific conditions, ideally to be supported by laboratory and field experiments.

2. Work Scope and Research Plan

This report describes a systematic evaluation of the possible water quality changes in response to CO_2 intrusion into aquifers currently used as sources of potable water in the United States. Such waters generally contain total dissolved solids concentrations far less that the maximum permitted 10,000 mg/L permitted in a USDW. Our goal is to develop a principal understanding that would allow us to evaluate which aquifer systems and regions of the United States may be vulnerable in case of CO_2 intrusion. In particular, we need to understand, for a range of relevant aquifer conditions, the potential for hazardous constituents (such as heavy metals or As) to be mobilized by the ingress of CO_2 and the distribution of these constituents in time and space. Ultimately, we need to determine the likelihood for drinking water standards to be exceeded. These issues are addressed by conducting reactive transport simulations for a variety of CO_2-release scenarios and aquifer conditions. A reactive transport model was developed for quantifying the effect of CO_2 intrusion into a shallow aquifer, simulating the multiphase flow of CO_2 and water, and predicting the fate and migration of trace hazardous constituents in the groundwater (Section 4).

As in any numerical simulation study, reliable model predictions can only be achieved when model parameters are both realistic and representative, and when all relevant processes are adequately incorporated. In particular, the reactive transport model needs to (1) account adequately for the complexity in natural geochemical systems, (2) consider the relevant geochemical processes, (3) represent a wide range of geochemical conditions with respect to initial water chemistry and mineralogy, and (4) incorporate variability and uncertainty in relevant hydrogeological and geochemical parameters. To ensure adequate model configuration**,** we have selected the conditions modeled in the reactive transport simulations—e.g., initial abundance and distribution of these hazardous constituents, aquifer mineralogy, initial water chemistry, oxidation state—based on development of a comprehensive geochemical model, which included the rigorous evaluation of more than 38,000 groundwater quality analyses from aquifers throughout the United States, using a version of the EQ3/6 code (Section 3). This geochemical model development allowed us to draw some immediate quantitative conclusions regarding the

potential vulnerability of groundwaters in the United States, for example with respect to the pH or Eh buffering capacity of most samples. The geochemical model also allowed preliminary estimates of the potential concentrations of hazardous constituents in equilibrium with elevated partial pressures of CO_2 following intrusion. However, in order to explore spatial changes in aquifer chemistry under transient conditions following CO_2 intrusion, we employed the reactive transport simulations in which was incorporated a suitable surface complexation model to describe adsorption processes.

Based on the above discussion, the research work as described in this report has two main parts: (1) the development of the aquifer geochemical model detailed in Section 3, and (2) the systematic reactive transport simulations detailed in Section 4. Figure 2.1 depicts the information flow between these two parts. The key information gathered in Part (1), and provided to Part (2), is listed below:

- Review, evaluation, and generation of thermodynamic and solubility data for all relevant minerals and aqueous species, and their incorporation into the reactive transport simulator
- Geochemical evaluation of a large number of water quality analyses with measurable concentrations of hazardous inorganic constituents; determination of chemical potentials and thermodynamic controls for various relevant hazardous constituents; and evaluation of mineral assemblages influencing pH and Eh buffering capacity, as well as background levels of CO_2 concentration
- Review of representative mineralogies for principal aquifers typically exploited for potable water; and classification of these aquifers with respect to expected geochemical behavior; development of selected mineralogies for simulation study (considering major minerals and clays)
- Identification of minor minerals that typically have small volume fraction, but are critical because they contain hazardous chemical constituents such as Pb and/or As; and specification of possible volume fraction ranges for these minor minerals
- Review and evaluation of relevant thermodynamic parameters in support of a surface complexation model to describe adsorption and desorption, and ion exchange processes.

The first step in Part (2) is to set up the reactive transport simulator in a single cell configuration with the above-described inputs, and then run the simulator until a secular equilibrium state is reached. This secular-equilibrium state establishes the initial distribution of the hazardous constituents in the aquifer, which is a necessary prerequisite for reactive transport simulations where the initial state is perturbed following CO_2 intrusion. The initial secular geochemical equilibrium is generated using the same geochemical simulator TOUGHREACT (Xu et al., 2006) employed for the reactive transport simulations (Section 4). The secular equilibrium calculation considers that the substance may be initially distributed (1) in the aqueous phase as ionic, molecular, and complex species (possibly occurring with differing oxidation states), (2) as adsorbed species on the surfaces of the minerals composing the aquifer rock, (3) as species in ion exchange sites, (4) in trace amounts in solid solution, and (5) as discrete minerals in which the substance is an essential component. As a check for the model and its thermodynamic parameters, the simulated initial concentrations of various species in the water are compared back to the range determined in the database evaluation (Section 4.4).

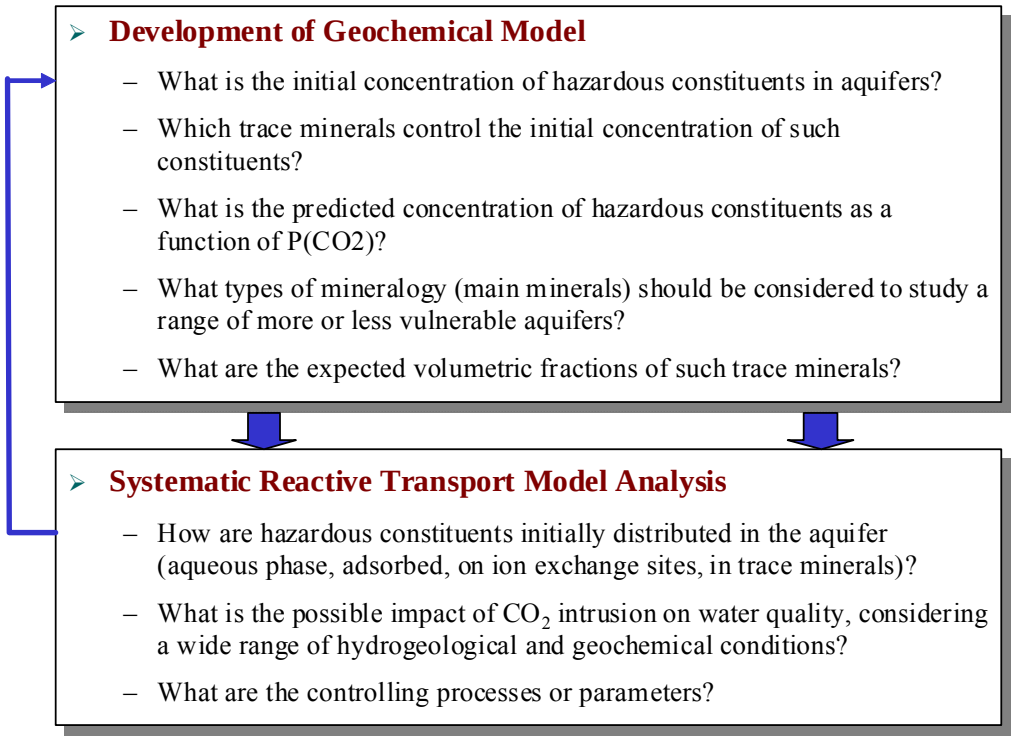

Fig. 2.1. Main research steps and information flow between them

The final step in Part (2) is to conduct the reactive transport simulations for a series of simulation cases. Starting with the specified initial geochemical conditions, these simulations predict the impact of CO_2 intrusion into a fresh-water aquifer and determine the related changes to the host rock mineralogy and water chemistry. Various geochemical sensitivity cases are evaluated to (1) account for the wide range of conditions found in domestic potable aquifers and their host rocks, and (2) to encompass the uncertainty associated with geochemical processes and model parameters. In addition, we have varied certain hydrogeological aquifer conditions (such as the depth of the freshwater resource and the groundwater flow rate), have simulated different CO_2 release scenarios (intrusion rate of CO_2), and have conducted 2D versus 3D modeling to understand the impact of dimensionality. While including a wide range of relevant mineral phases in the reactive transport model, including their potential interactions, we have focused on two major hazardous constituents—Pb and As—when evaluating the detrimental effects of CO_2 intrusion. Based on our modeling results, we can provide a better understanding of the expected vulnerability of relevant domestic aquifer types in the case of CO_2 intrusion. As mentioned before, our broad sensitivity study, intended to provide results for a wide range of representative conditions, is a starting point for an essential next step, to conduct a detailed geochemical evaluation of selected storage sites incorporating the site-specific conditions and parameters.

Note that all geochemical modeling studies conducted in this report assume the intrusion of pure CO_2 into potable drinking water. It is possible, however, that leaking CO_2 may carry organic compounds leached at depth; they may also contain co-injected trace contaminants, such as H_2S. The conditions for this to occur, and the potential ramifications, are explored in future project phases.

We also note that bacterial processes are not explicitly accounted for in our reactive transport modeling. Bacteria take advantage of non-equilibrium states to extract energy from electron transfer reactions where corresponding abiotic reactions, which would otherwise bring the chemical system into redox equilibrium, are kinetically hindered by a large activation energy barrier. The intrusion of CO_2 into potable groundwater aquifers will not materially increase the opportunity for bacteria to extract energy from the system, and potential bacterial mechanisms

that might have some small impact, such as those affecting sulfide mineral dissolution, have not been examined. Instead, we implicitly account for potential bacterial activity through sensitivity studies of the kinetics of redox reactions involving the dissolution respectively of galena and the solid solution of arsenopyrite in pyrite.

In addition to geochemical modeling, we also report on natural and man-made natural analogues providing corroborative information about the potential water quality changes in response to CO_2 intrusion into groundwater (Section 5).

3. Geochemical Model Definition

3.1 Basic Methodology

In this section, a series of steps is described with the goal of developing a geochemical model for use in reactive chemical transport simulations described in Section 4. The fate of inorganic hazardous constituents in the presence of elevated CO_2 levels, such as after intrusion of leaking CO_2 from deep geological storage, ultimately depends on their initial abundance and distribution in the aquifer. Initially, they are distributed (1) in the aqueous phase as ionic, molecular, and complex species, (2) as adsorbed species on the surfaces of the minerals composing the aquifer rock, (3) as species in ion exchange sites (primarily in smectitic clays), and (4) in trace amounts in solid solution in detrital minerals, weathering products, chemical precipitates (e.g., carbonates and sulfates) and diagenetic minerals, and (5) possibly as discrete minerals in which the constituent is an essential component. These initial distributions must be characterized and quantified as a necessary prerequisite for conducting reactive transport simulations evaluating the mobilization of such constituents in the case of CO_2 intrusion. This requirement is met through the compilation of pertinent thermodynamic parameters governing their distribution in the aquifer, e.g., the thermodynamic properties of both the minerals and their dissolved components in aqueous solution, ion exchange coefficients, adsorption coefficients, and coefficients defining solid solutions. Also required are the electrolyte, site complexation, ion exchange, and solid solution models appropriate to the problem at hand.

The steps taken in developing the geochemical model included (1) a comprehensive review of the literature in order to identify mineral hosts controlling the concentrations of hazardous constituents in groundwaters, (2) development of an extensive thermodynamic database for relevant minerals and aqueous species and site complexation constants, (3) rigorous geochemical evaluation of more than 38,000 groundwater quality analyses from potable water aquifers throughout the United States, (4) evaluation of the natural abundances of hazardous constituents in sedimentary formations hosting potable water, and (5) a survey of the sedimentology and

hydrology of the principal potable water aquifers throughout the United States. The key questions addressed are as follows:

1. What minerals might be present that control the aqueous concentrations of hazardous constituents in potable groundwaters?
2. How is the aqueous concentration of each hazardous constituent determined? Is the aquifer water saturated with respect to a particular mineral that contains that constituent as an essential component, or is it in equilibrium with that constituent only as a minor, non-essential component associated with other rock-forming minerals?
3. What would be the mass (or volumetric) fractions of solubility-controlling minerals postulated to be present in the aquifer rocks?
4. What is the framework and matrix mineralogy of typical aquifers exploited for potable water? What types of representative mineral compositions should be considered to study a range of more or less vulnerable aquifers?

Figure 3.1 illustrates schematically the interrelated tasks required to address these questions, and their relationship to tasks performed with the reactive transport model analysis in Section 4. Question (1) is addressed in Section 3.2 through a review of the modes of occurrence for the chosen hazardous constituents in sedimentary rocks, including coal, for which an extensive and highly relevant literature is available. Question (2) is addressed in part through the geochemical evaluation of a large number of groundwater samples from the USGS National Groundwater Information System (NWIS) database (Sections 3.3 and 3.4). The technical objective of the groundwater evaluation is to identify the thermodynamic controls governing the concentrations of hazardous inorganic constituents in potable groundwaters samples taken throughout the United States. Identifying the thermodynamic controls is an indirect way of determining whether (and which) solubility-controlling minerals (i.e., galena possibly controlling the aqueous Pb concentrations) are present in the aquifer from which the sample is recovered. The distribution-of-species code EQ3/6 (Wolery et al., 1993) was used in this study to calculate the saturation indices of minerals containing hazardous constituents as essential components in a selected set of suitable groundwater analyses downloaded from the NWIS database (Section 3.3.1).

The reason for taking this indirect approach is that the mass fractions of the relevant hazardous constituents (i.e., the solubility-controlling phases) in the aquifer host rocks are very low (on the order of 10^{-4} - 10^{-6} or less), and few studies have been conducted that have unequivocally confirmed the presence of their mineral hosts, particularly in potable water aquifers. Direct means of identifying their presence and spatial distribution are only possible with high-resolution imaging techniques or other highly complex methodologies, an effort that is rarely undertaken and certainly not in a systematic manner. Therefore, in this study, we postulate the presence of solubility-controlling phases in the aquifer rocks through geochemical evaluation of groundwater chemical analyses containing specific data for several hazardous inorganic constituents of interest, and corroborated through independent studies reported in the literature (Section 3.4).

Question (3) is addressed by consulting the National Geochemical Survey Database (USGS, 2008) in which the analyzed concentrations of hazardous constituents present in surficial soils and sediments are tabulated (Section 3.3.3). This information was used as a proxy for corresponding concentrations in aquifer host rocks, expressed in mass fraction or volume fraction, and is needed because the thermodynamic analysis described above only identifies which phases may control the concentration of a hazardous constituent in solution, but cannot define the quantities present. (Saturation indices of minerals are intensive thermodynamic variables—i.e., variables that are independent of mass.)

Finally, to answer Question (4), a variety of independent literature sources was used to obtain representative mineralogies for representative aquifer host rocks (Section 3.6). Integration of the bulk mineralogy with the mineralogy characterizing hazardous inorganic constituent mineral hosts, and normalizing to volume fractions, yields input suitable for TOUGHREACT. For the geochemical model to be realistic, further information is also required regarding the rock physical properties such as porosity and specific surface areas.

Once the total mineralogy has been identified and quantified, a geochemical secular equilibrium model is constructed and tested for consistency with groundwater chemical analyses (Section 4.4). The model must have attained a steady-state kinetic or secular equilibrium with respect to the major rock forming primary and secondary minerals, and equilibrium with respect to all

minor and trace minerals that could define the aqueous equilibrium concentration of the hazardous constituents under study. This equilibrium state needs to be established not only with respect to the minerals containing hazardous inorganic constituents as essential components, but also with respect to those constituents on adsorption sites on primary and secondary host rock minerals, on ion exchange sites in clays, and optionally in solid solution in secondary minerals. The geochemical model code needed for this purpose requires a site complexation model with suitable adsorption constants for each inorganic constituent, for the surfaces of each mineral incorporated in the model, an ion-exchange model with suitable ion-exchange coefficients, and a suitable solid-solution model for trace substitution of inorganic substances in specified host minerals. In principle, the distribution of each hazardous constituent between the constituent host minerals can be compared with corresponding field data obtained in answer to Question (1), as a basis for partial model validation. Note that incorporation of all mechanisms for immobilization of hazardous constituents in/on solid phases of the host rock is not always necessary. For example, it was found that Pb^{+2} substitution into ion exchange sites in clays was not a significant sink for Pb in groundwater, when considering the the geochemical model for potable water aquifers generated in this study.

Results from the secular equilibrium geochemical model used in Section 4.4 to generate the simulated aqueous-phase composition at the initial state (prior to CO_2 intrusion) can be compared with the concentration ranges observed in NWIS groundwaters. If the chemical system has been adequately defined, the thermodynamic data used to construct the model are accurate, and (last, but not least) thermodynamic equilibrium is closely approached in the field, then a reasonable agreement should be obtained. The model can therefore be checked for consistency against the known ambient conditions and constitutes a further partial validation of the model.

The final step shown in the flowchart in Figure 3.1 is to conduct the reactive transport simulations predicting the water quality impact in response to CO_2 intrusion from an underlying storage reservoir (Sections 4.5 through 4.10). Starting with the equilibrated initial conditions, the reactive transport model allows for mobilization of relevant hazardous constituents from mineral dissolution as well as from adsorption and ion exchange sites. In such a model, homogeneous

(i.e. within a single phase, most commonly the aqueous phase) and heterogeneous (i.e. between different phases) chemical kinetics, gas-aqueous-phase mass transfer, and aqueous-phase transport play a role. The reactive-transport simulator used in this study, for the reactive transport simulations as well as for conducting secular equilibrium runs, is TOUGHREACT (Xu et al., 2005), described in Section 4.1. The relevant thermodynamic data incorporated into this simulator have been derived from a comprehensive review of the published literature, mostly based on laboratory experiments, some estimated. Extensive revision and augmentation of the thermodynamic data were necessary for the purpose of this study (Section 3.4.2).

Uncertainties associated with the geochemical model remain, primarily because the chemical thermodynamic and kinetic data to model such complex systems, even under ambient conditions, are incomplete or subject to large uncertainties. The physical and chemical response of a potable groundwater aquifer to elevated CO_2 pressures has received only limited study in the laboratory, and then under conditions that are of limited relevance. It is possible that some physical processes and chemical reactions operative in the presence of high pressure CO_2 have not been identified, and therefore the modeling could suffer from unrecognized omissions. Furthermore, the physical characteristics specified for aquifer conditions in this study are generalized, and aquifer host-rock heterogeneity is not taken into account. To remedy the related uncertainties, further laboratory investigations and field characterization are desirable. In the course of this study, uncertainties and knowledge gaps that could affect the findings of this evaluation are identified, and are summarized in Sections 3.7 and 4.10 of this report.

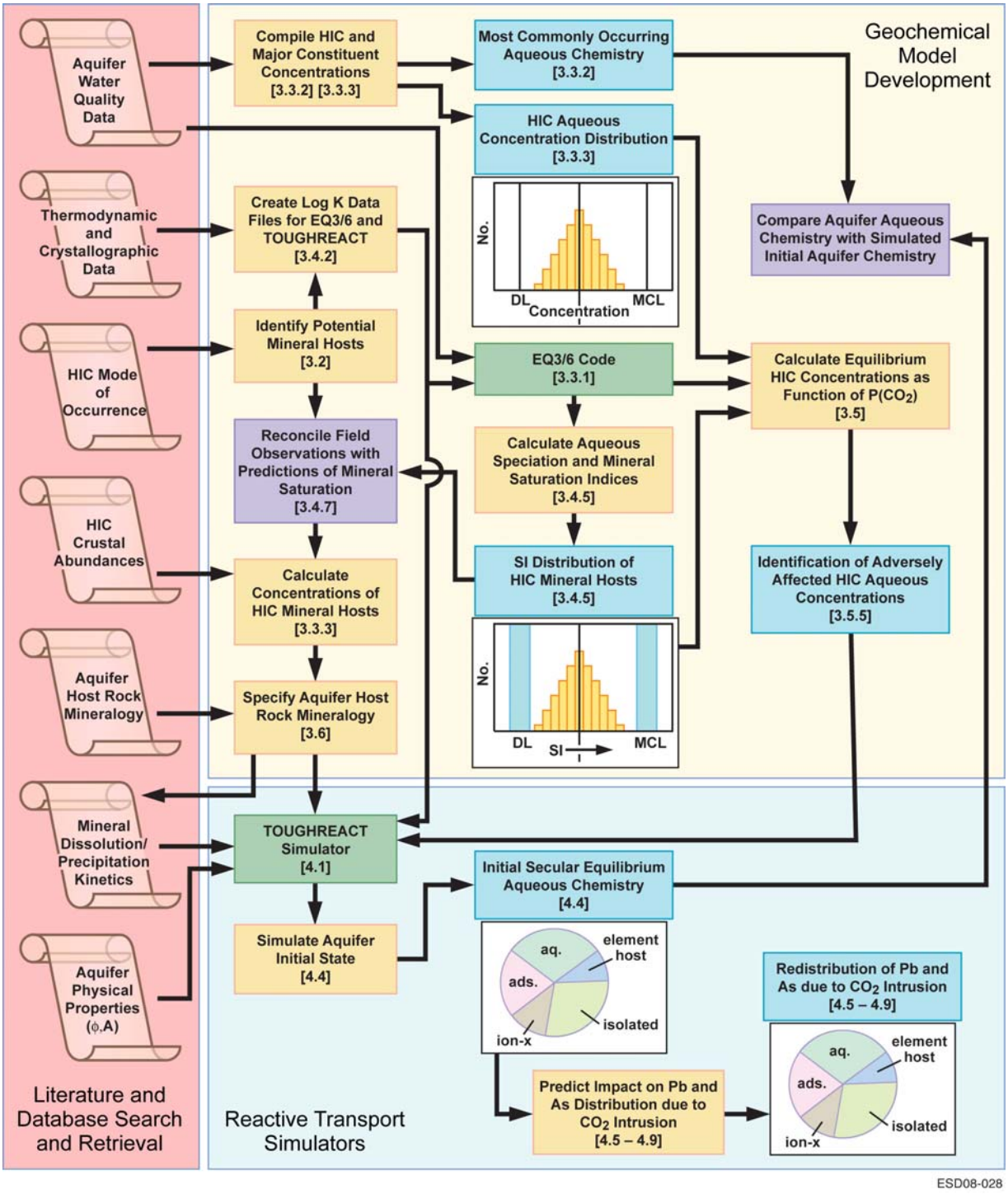

Note: HIC = Hazardous Inorganic Constituent, DL = Detection Limit, MCL = Maximum Contaminant Level

Fig. 3.1. Flow chart describing research steps providing necessary information as input to reactive transport models

3.2 Identification of Mineral Hosts Controlling the Concentration of Hazardous Constituents

A comprehensive review of the literature was conducted to characterize the phase relations expected for relevant hazardous constituents in shallow potable water aquifers, and to identify mineral component(s) best suited as references in the thermodynamic evaluation of water quality data. Emphasis is placed on phase relations expected under reducing conditions, as appears to be the case with the majority of groundwaters for which water quality data are available (Section 3.4.4).

The selection of trace elements was based on their immediate relevance to the study, i.e., considering the work of Wang and Jaffe (2004) regarding lead (Pb) and recognizing a recent study by Focazio et al. (2006), which showed that arsenic (As) and uranium (U) concentrations sometimes exceeded maximum permissible concentrations in domestic wells. Other elements studied include barium (Ba), cadmium (Cd), mercury (Hg), antimony (Sb), selenium (Se), and zinc (Zn). These elements, all of which except Zn are considered potentially hazardous, were selected because their chemical behavior is fairly well known, or can be correlated with other elements whose chemistry is well understood for the conditions of the study. While Zn is not particularly important as a hazardous constituent, its behavior is somewhat similar to Cd, but it is found at higher and more easily detectable concentrations, and can therefore serve as an interpretive tracer.

Most of the selected elements, the exceptions being Ba and U, participate in the formation of chalcogenides, either as a reactive aqueous metal cation or complex in solution (i.e., Cd, Hg, Pb and Zn) or as a co-precipitant that substitutes or proxies for sulfide (S(-II)—i.e., As(-I), Sb(-I?) and Se(-II)). Ba(II) precipitates primarily as a sulfate, sometimes as a carbonate, whereas U in the reduced (IV) state commonly precipitates as the oxide, uraninite (UO_2) and/or as the silicate, coffinite ($USiO_4$), or more rarely as the titanate, brannerite (UTi_2O_6).

Reducing conditions in hydrothermal waters are enhanced through hydrolysis by SO_2, which disproportionates below about 450°C, according to the reaction:

$$4SO_2 + 4H_2O = 7H^+ + 3SO_4^{-2} + HS^-$$

and by hydrolysis of Fe(II) containing minerals, thus:

$$3(FeO)_{ss} + H_2O = Fe_3O_4 + H_2(aq)$$

These reactions contribute to the aqueous precipitation of chalcogenides at temperatures between ≈ 400 and 0°C.

At temperatures above 450°C, the chalcophilic elements, Cd, Hg, Pb and Zn, tend to substitute in their oxide components in rock-forming minerals, except under unusual conditions such as the extreme reduction induced by hydrolysis by the FeO component of mafic minerals. For example, Pb^{+2} together with Al^{+3} tends to participate in coupled substitution for K^+ with Si^{+4} in potash feldspars (Stevenson and Martin, 1986) in a manner similar to that of Ba^{+2}, which is of similar ionic radius (i.e., (Ba,Pb)-$Al_2Si_2O_8$ for K-$AlSi_3O_8$), to preserve charge balance, or partitions as chloride complexes in residual hypersaline brines following solidification of acidic magmas. In contrast, As and Sb in the (V) state are likely to follow phosphate with substitution in apatite or other metamorphic phosphates (Wise and Loh, 1976). Selenium in the (IV) or (VI) states probably mimics S(IV) and S(VI), but further review is required to clarify its behavior at elevated temperatures (see Smith, 1963). The chemistry of U follows similarly with substitution of the oxidized form, U(VI), as in magmatic apatite.

During subaerial weathering, many of the magmatically formed minerals are unstable in the presence of water and decompose, liberating the trace elements in their highest oxidation states. As, S, Sb, and Se tend to form oxy-anionic species, whose salts are soluble, and therefore tend to remain in solution, or are adsorbed on secondary minerals whose surfaces are positively charged, e.g., ferric oxides and oxy-hydroxides. Uranium is also released in its highest oxidation state, as UO_2^{+2}, and Hg as Hg^{+2}. Detrital and secondary products of weathering will undergo further alteration either immediately following shallow burial (authigenesis), or following prolonged

deeper burial, where progressively increasing temperatures lead to further alteration and precipitation of secondary minerals (diagenesis). A critical aspect of both authigenesis and diagenesis is the role that entrapped organic matter plays as an electron donor in facilitating the reduction of As(V), S(VI), Sb(V), Se(IV,VI) and U(VI). Under authigenic conditions, bacteria utilize organic matter in the reduction of these species, together with Fe(III) and Mn(III and IV) to Fe(II) and Mn(II), respectively. Therefore, oxides such as hematite, goethite and ferrihydrite, which initially dominate iron minerals, are partially or completely reduced to secondary iron sulfides under subsurface conditions. Reduction of iron to sulfide is complicated by the formation of metastable sulfide intermediates such as greigite (Fe_3S_4) and mackinawite (FeS). During the formation of metastable precursor iron sulfides or pyrite, Hg, As, Sb and Se are sequestered and incorporated in solid solution, probably in a disordered state. Because the concentration of iron overwhelms the concentrations of these elements, they are substantially partitioned, possibly in metastable equilibrium, into the iron sulfide, the residue being adsorbed onto thiol groups in the organic matter as Hg is believed to behave (Benoit et al., 1999).

With deeper burial and higher temperatures, organic matter undergoes thermolysis and maturation at temperatures between ~75–120°C (Tissot and Welte, 1978), which leads to the destruction of unstable thiol and amino groups on the organic matter, while accelerating the reduction of Fe(III) and Mn(III and IV) and S(VI). Diagenetic recrystallization of metastable iron sulfides to pyrite can lead to significant reduction in the extent of solid solution and expulsion of Hg, As, Sb and Se. Maturation of organic matter also causes the release of previously adsorbed trace metals to the groundwater, potentially assisted through complexation with carboxylates and amines. Increased acidity, due to the release of CO_2 during maturation, also enhances the solubility of trace metals. Finally, increased salinity, either from trapped connate seawater or from the dissolution of evaporites, likewise increases the concentration of Cd, Hg, Pb and Zn through chloride complexing. Thus, several mechanisms are operative that lead to enhanced concentration of trace metals in deep groundwater, which can facilitate their transport to lower temperature regions. In aggregate, these processes can result in supersaturation and secondary precipitation of discrete phases where the affected elements are essential components. Circumstantial evidence in support of this phenomenon is presented below.

Deep burial with temperatures rising to ~300°C can lead to further destruction of primary minerals, with the associated release of trace elements. Secondary pyrite formed under these conditions contains enhanced concentrations of Hg, As, Sb, and Se in solid solution, because the capacity to accept these nonstoichiometric elements in solid solution increases with temperature, and larger quantities become available due to alteration of the primary minerals. With erosional unroofing of deeply buried sediments and falling temperature, retrograde metamorphism takes place, and the initial metastable pyrite solid solution becomes unstable. Supersaturation with respect to secondary minerals containing the trace elements as essential components can then occur. However, it is more likely that ex-solution of secondary phases will occur within pyrite crystals, and therefore, the trace metals will remain sequestered by the pyrite, rather than being released to the groundwater and precipitating as discrete stoichiometric minerals. The scenarios just described are supported by field observations, but many of the mechanisms involved are not well understood, even in a qualitative sense. Nevertheless, a general understanding of the processes involved is essential for understanding how individual hazardous inorganic constituents are likely to behave following the ingress of high-pressure CO_2 into shallow groundwaters.

In the following paragraphs, we speculate on the behavior of each hazardous inorganic constituent and identify mineral component(s) as likely candidates in the thermodynamic evaluation of water quality data presented in Section 3.4. The thermodynamic activity of these components, defined in terms of corresponding mineral saturation indices (SI), can then be used to establish whether they might actually be present as discrete minerals in the aquifer host rocks components (i.e., if $SI \geq 0$). If, however, $SI \leq 0$, then that component is either present in solid solution in another mineral, or some other component is saturated with respect to a discrete mineral. The definition of SI is presented in Section 3.4.1.

Little information is available in the literature concerning the distribution of the hazardous inorganic constituents of interest in shallow aquifer host rocks. However, extensive studies have been undertaken over many years to characterize the distributions of such constituents in the various mineral components of coals—e.g., see Finkelman (1981) and Kolker et al. (2002). The

reason for such an interest is that many trace elements are environmentally hazardous, and potential coal pretreatment processes to minimize their release to the atmosphere following combustion is of more than passing interest. It is obvious that coals differ markedly in composition from a typical shallow aquifer host rock. A typical arenaceous aquifer rarely contains more than 2 wt% of organic matter, in contrast to coal, which in some instances exceeds 95 wt%. Also, the "ash" content of exploitable coal rarely exceeds 30 wt.%, whereas nearly 100 wt.% of an aquifer host rock consists of inorganic material. However, the sustained reducing environment induced by organic matter in coal beds, and the duration of burial, allow sequestration and enrichment of hazardous constituents in discrete mineral hosts, such as chalcogenides, which are more readily identified and characterized in coal than in arenaceous sedimentary rocks. Furthermore, because of the incentive to study the distribution and mode of occurrence of hazardous constituents in coals for environmental reasons, a significant literature selection is available that can be used opportunistically to help define a comparable host mineralogy for hazardous constituents in potable water aquifers. It goes without saying that such an interpretation must be undertaken with full cognizance of the impact that the substantial compositional differences between coal and arenaceous sedimentary rocks have on the distributions of hazardous constituents between the various mineralogical components comprising each material.

The Unites States Geological Survey recently conducted a comprehensive multi-element characterization of selected coals (Kolker et al., 2002). This study is invaluable in providing a qualitative basis for geochemical model development for the present project. Relevant information is summarized in Tables 3.1, 3.2 and 3.3, which show, respectively, the bulk composition and character of three coals, the sequential selective-leaching procedure involved in the separation of the principal components of the coals, and finally, the distribution of the selected inorganic constituents and iron in the three coals, as determined by the sequential selective leaching procedure. The pertinence of these findings in relation to the distributions of individual trace elements in shallow aquifer host rocks is provided in the following discussion.

Table 3.1. Characteristics (in weight percent, dry basis) of coals studied by Kolker et al. (2002)

	Ohio #5, #6, #7 beds	Wyodak, Cordero Mine, Gillette, WY	North Dakota, Falkirk Mine, Underwood, ND
Ash	9.93	8.13	14.64
Pyritic Sulfur	1.42	0.05	0.28
Organic Sulfur	1.24	0.37	0.56
Sulfate Sulfur	0.02	0.01	0.14
Moisture	2.33	25.81	35.88
Rank	Bituminous	Sub-bituminous	Lignite

Table 3.2. Sequential selective leaching procedure to characterize the distribution of trace elements in the constituent components of coal (after Kolker et al., 2002)

#	Procedure	Elements Extracted from:
1	1N ammonium acetate (CH3COONH3)	exchangeable sites, water soluble compounds, some carbonates
2	3N hydrochloric acid (HCl)	carbonates, iron oxides, mono-sulfides, certain chelated organic compounds
3	Conc. hydrofluoric acid (HF; 48 percent)	silicates
4	2N (1:7) nitric acid (HNO3)	disulfides, especially pyrite

The trace-element distributions in the principal components of coal (i.e., ion exchange sites, carbonates, sulfates, silicates, sulfides, and chelating sites in the organic fraction), together with other supporting information (such as the mineralogical composition of the "ash" and assumptions regarding the adsorption characteristics of both inorganic and organic components), can be extrapolated to approximate their distributions in sedimentary rocks of shallow aquifers. Although such a calculation can only be of qualitative value, it is nevertheless a helpful guide for planning similar quantitative evaluations of aquifer host rocks. Furthermore, it can also serve as a check on geochemical models of trace element behavior in aquifer host rocks, which of necessity are based almost entirely on laboratory measurements involving idealized systems.

Table 3.3. Distribution (in %) of iron and selected trace elements in coal (from Kolker et al., 2002)

	Coal Type					
Element	**Ohio 5/6/7**		**Wyodak**		**North Dakota**	
Fe	80 10 10	Pyrite Fe-oxides[1] Silicates	10 75 10	Pyrite Fe-oxides[1] Silicates	10 65 15	Pyrite Fe-oxides[1] Silicates
As	60 25 5 10	Pyrite Arsenates Silicates Organic[2]	15 40 15 30	Pyrite Arsenates Silicates Organic	15 50 15 20	Pyrite Arsenates Silicates organic
Ba	5 90 5	Barite Silicates Organic (5%)	80 5 15	Barite Silicates Organic (5%)[2]	85 15	Barite Silicates
Cd	20 35 40	Sphalerite Pyrite Organic (5%)[2]	70 10 15	Sphalerite Pyrite organic	- - -	ND ND ND
Hg	60 20 10	Pyrite Organic Exchangeable	60 20 20	Pyrite Organic Exchangeable	80 10	Pyrite Organic
Pb	35 40 10 15	Galena Pyrite Silicates Organic	70 10 20	Galena Pyrite Silicates	85 5 10	Galena Pyrite Silicates
Sb	20 60 15	Silicates Organic Pyrite	35 45 15	Silicates Organic Pyrite	40 50 10	Silicates Organic Pyrite
Se	50 50	Pyrite Organic	20 75	Pyrite Organic (5%)[2]	25 70	Pyrite Organic (10%)[2]
U	20 5 70	Silicates HCl Soluble[3] Organic[4]	30 50 15	Silicates HCl Soluble[3] Organic (10%)[2,4]	45 45 15	Silicates HCl Soluble[3] Organic[4]
Zn	30 30 10 30	Sphalerite Pyrite Silicates Organic (5%)[2]	50 25 10 15	Sphalerite Pyrite Silicates Organic	65 5 10 20	Sphalerite Pyrite Silicates Organic

[1] May also include oxidized pyrite and mono-sulfides
[2] Number in parentheses after Organic % indicates percent in exchange sites.
[3] Species unknown, may be associated with organic chelates, and/or with zircon.
[4] Small amounts may be associated with zircon.

Despite the undoubted value of the results regarding the distributions of trace elements in coals, it should be noted that the sequential selective leaching procedure employed in the study introduces artifacts that could misrepresent the true distribution of trace elements in the unmined *in situ* coals. In particular, the low-temperature ashing of the coal, conducted at about 200°C, can lead to the oxidation of redox sensitive elements, such as the presence of As as arsenate indicated in Table 3.3. Even preparation of the coal samples, such as their comminution prior to selective leaching, can result in partial oxidation, if conducted under atmospheric air.

Table 3.4. Molar ratio of trace metals (Me) in relation to As in pyrite compared to their molar abundance ratio in a bulk sample of Ohio 5/6/7 Coal. R^2 denotes correlation.

Trace Element	Molar Ratio (Me:As) in pyrite	R^2	Molar Ratio (Me:As) in bulk coal	Relative Enrichment	Enrichment In Pyrite
As	1.000	1.00	1.000	1.000	18.1[1]
Cd	0.0014	0.71	0.003714	0.377	6.82
Hg	0.0112	0.65	0.003777	2.97	53.8
Pb	0.392	0.73	0.1849	2.12	38.4
Sb	0.0471	0.63	0.6707	0.702	12.7
Se	0.964	0.92	0.0949	10.2	185
Zn	0.0441	0.13	1.352	0.0362	0.66

[1] Ratio of As concentration in pyrite (321 ppm) to hat in coal (17.8 ppm)

Table 3.5. Sequential selective leaching procedure to characterize the distribution of trace elements in marine sediments (after Huerta-Diaz and Morse, 1992)

#	Fraction	Procedure	Elements Extracted from:
1	Reactive	Digestion of a freeze-dried sediment sample for 16 hours with 1M HCI.	Monosulfides, amorphous and crystalline iron, and manganese oxyhydroxides, carbonates, and hydrous aluminosilicates
2	Silicate	Two consecutive leachings with 10M HF for 1 hour and 16 hours, respectively, followed by addition of boric acid to redissolve precipitated fluorides.	Clay minerals
3	Pyrite	Digestion of the silicate fraction residue with concentrated nitric acid for 2 hours.	Pyrite and associated trace metals

Of the extensive suite of trace elements studied, five (As, Cd, Hg, Pb and Zn) are pertinent to the current study. The distributions of these elements and of Fe between the reactive and pyritic fractions (as defined in Table 3.5) are shown in Figure 3.2, which illustrates the depth profiles in organic-rich marsh sediments from Atchafalaya Bay, Mississippi. This sediment contained connate water with a lower salinity (≤5 ‰) than other sedimentary environments studied by the investigators, and is therefore considered to be more relevant to the present evaluation.

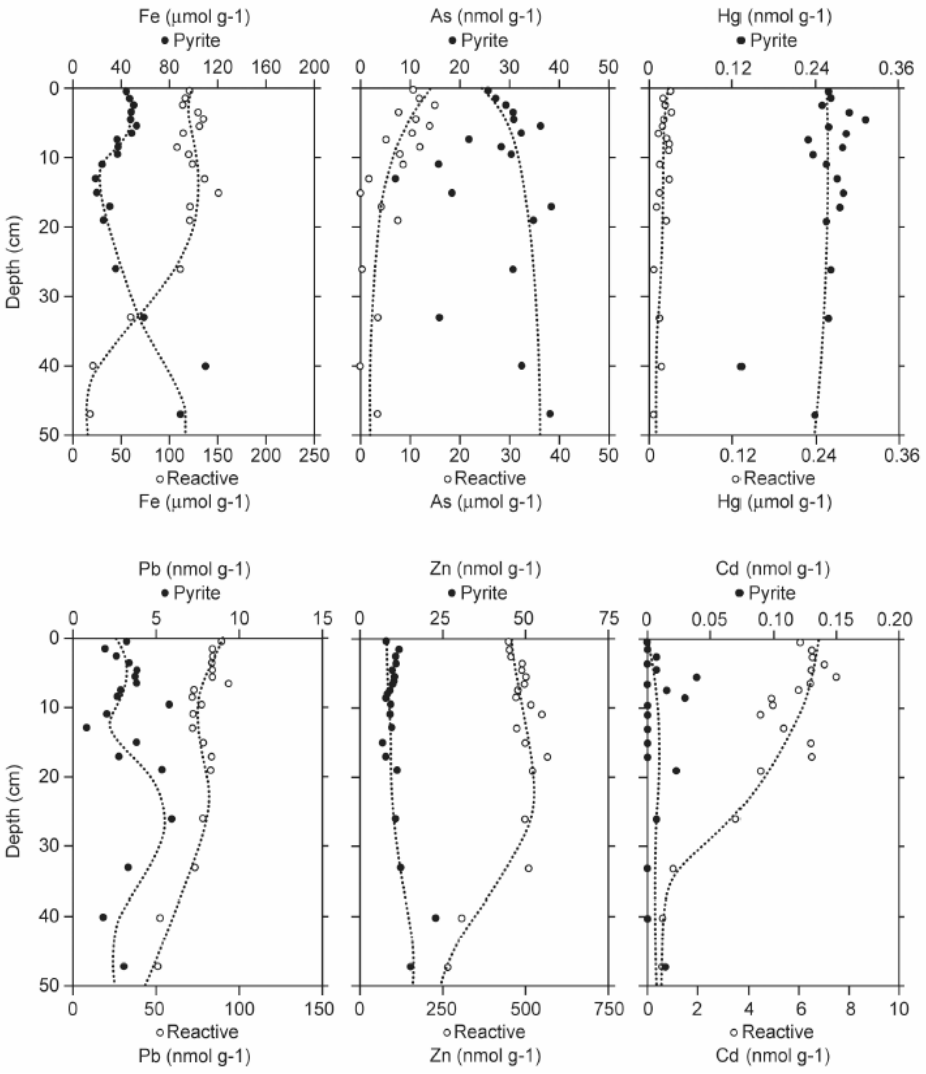

Fig. 3.2. Concentrations (per gram of sediment) of selected trace elements and Fe in the pyritic and reactive fractions of organic-rich marsh sediments from Atchafalaya Bay with depth below the sediment-water interface (after Huerta-Diaz and Morse, 1992). Dashed lines are illustrative only, and included to emphasize trends in the partitioning of trace metals between the reactive and pyritic components.

Of particular interest is the observed partitioning of the trace metals between the reactive and pyritic components as a function of the extent of pyritization. Huerta-Diaz and Morse (1992) examined their behavior in terms of two parameters, the degree of trace-metal pyritization (DTMP):

$$DTMP(\%) = \frac{Pyrite - Me}{Pyrite - Me + \mathrm{Re}\,active - Me} \times 100 \qquad (3.1)$$

and the degree of pyritization (DOP), defined as:

$$DOP(\%) = \frac{Pyrite - Fe}{Pyrite - Fe + \mathrm{Re}\,active - Fe} \times 100 \qquad (3.2)$$

When DTMP is plotted against DOP, a measure of the degree of preferential partitioning of each trace element in pyrite is obtained. This is shown in Figure 3.3 for samples taken from the organic-rich marsh sediments from Atchafalaya Bay, Mississippi.

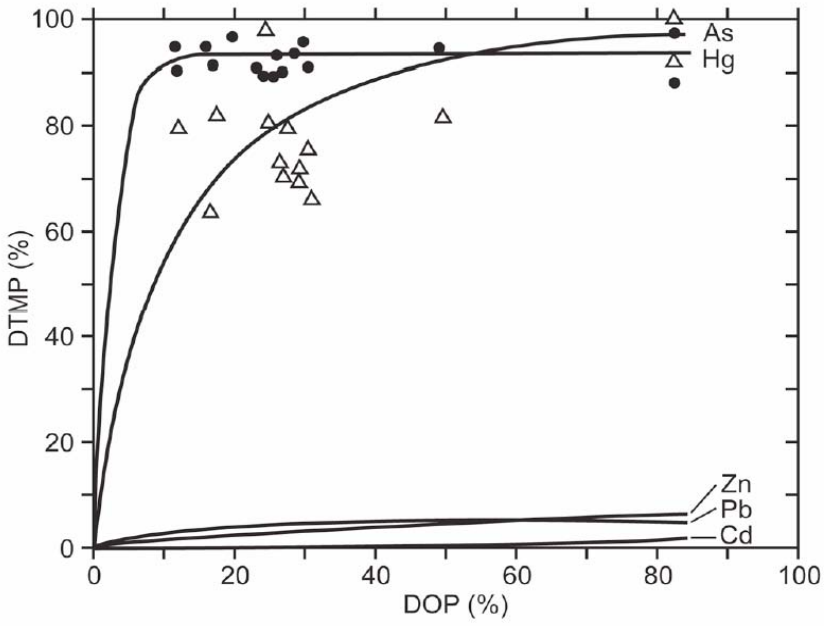

Fig. 3.3. The degree of trace metal pyritization (DTMP) in terms of the degree of pyritization (DOP) for As, Cd, Hg, Pb and Zn in organic-rich marsh sediments from Atchafalaya Bay (after Huerta-Diaz and Morse, 1992).

In the following paragraphs, we make reference to the information taken from Kolker et al. (2002) and from Huerta-Diaz and Morse (1992) in discussions of the likely behavior of each selected hazardous inorganic constituent as it relates to solid solution substitution in pyrite or to the formation of discrete phases forming separately from co-existing pyrite. While reactive transport modeling in Section 4 is applied with a focus on Pb and As, we provide here a summary evaluation of the behavior of several other potentially relevant hazardous inorganic constituents.

Arsenic. An extensive literature testifies to the presence of As substituting for S as As(-I) in authigenic, diagenetic, and hydrothermal pyrite (Blanchard et al., 2006; Reich et al., 2005). The abundance of As in relation to the quantity of sulfide (-II) sulfur in pyrite is generally small (As $\leq$ 0.05), although As substitution in FeS_2 at higher temperatures is more extensive. Reich and Becker (2006) cite concentrations as high as 19 wt% observed in natural pyrite and marcasite samples. These investigators, on the basis of theoretical calculations, show that metastable As substitution in pyrite up to As ~ 0.05 is thermodynamically favored over the corresponding substitution in marcasite, a less stable polymorph of pyrite. At higher mass fractions, a sulfur-rich arsenopyrite (FeAsS), which possesses the marcasite structure, would coexist with the metastable arsenian pyrite.

Saturation with respect to arsenopyrite in the presence of arsenian pyrite in typical low-temperature shallow potable water aquifers is unlikely, since the abundance of As is normally insufficient (see Section 3.4.5.2, Figure 3.34a). Indeed, only one example has been cited in the literature (Utsunomiya et al., 2003). However, Reich and Becker (2006) show that at 300 K, the ultimate state of thermodynamic equilibrium would be a pure end-member pyrite coexisting with sulfur-rich arsenopyrite. This state is not normally achieved in nature. Prolonged annealing of arsenian pyrite leads instead to exsolution of arsenopyrite domains (Fleet et al., 1989; Simon et al., 1999a,b; Palenik et al., 2004) that remain isolated within the pyrite. At low solid-solution concentrations, i.e., As ~ 0.01, unmixing appears to be too sluggish to be observable in field specimens (Savage et al., 2000). Arsenic mobilization will therefore be sensitive only to environmental changes that induce pyrite dissolution, although such changes, when induced by

oxidizing conditions, could be accelerated by the presence of As in pyrite (Blanchard et al., 2007).

The As content in authigenic pyrite as a function of depth in brackish and marine sediments shows that almost all As is sequestered by the pyrite soon after burial (Huerta-Diaz and Morse, 1992), as shown in Figures 3.2 and 3.3. The partitioning of As in coal also supports the belief that As substitutes in autogenously generated pyrite (Finkelman, 1981; Kolker et al., 2002), and that, at most, only about 15% resides in coexisting silicates in coal. A significant concentration of As is, however, associated with organic matter probably complexed with thiol functional groups (Table 3.3). In contrast, the small organic content of arenaceous aquifers, usually less than one percent, would preclude such material being a significant host for As under normal circumstances. Therefore, the contribution of As adsorption on organic material to its overall distribution in aquifer host rocks can be ignored for the purpose of reactive transport modeling described in Section 4.

Barium. The chemistry of barium in groundwaters is relatively simple, because it does not undergo any change in oxidation state in reducing groundwaters, nor does it form any minerals with reduced species of As, S, Sb, and Se. It is present primarily as barite ($BaSO_4$) in sub-bituminous and lignitic coals (Table 3.3). In bituminous coal, it is present dominantly in the silicate component. The concentration of Ba in the latter is about one order of magnitude less than in the other two coals. The reason for its presence in the silicate component suggests the depletion of sulfate through reduction to sulfide. In the absence of sulfate, it can substitute as Ba^{+2} –Al^{+3} for K^{+} - Si^{+4} in potash feldspars, and occupy exchange sites in clays, both occurrences of which have been noted by Finkelman (1981). In coal, Ba can also substitute for Ca in crandallite ($CaAl_3(PO_4)_2(OH)_5$) and can also form the carbonates alstonite ($BaCa(CO_3)_2$) and witherite ($BaCO_3$) (Finkelman, 1981). Because few, if any, potable groundwaters are seriously deficient in SO_4^{-2}, the primary candidate for Ba solubility control is barite, although witherite ($BaCO_3$) and crandallite might also be options in rare sulfate-deficient environments.

Cadmium. Studies of the mineralogy of non-ferrous ore deposits universally recognize that cadmium is sequestered as a solid solution in sphalerite (ZnFeS) (Piatak, 2004), where Cd

concentrations can reach 5 wt%. Cadmium for industrial purposes is recovered primarily during the roasting and acid treatment of sphalerite, the principal zinc ore. In coal, Cd reports in secondary sphalerite in concentrations up to 2-wt% (Gluskoter and Lindahl, 1973; Finkelman, 1981). Indeed, Gluskoter and Lindahl (1973) noted that the Zn:Cd ratio in bulk coal samples was essentially the same as found in the contained sphalerite. Kolker et al. (2002) confirm the strong concentration of Cd in sphalerite, but they noted that significant fractions are also partitioned in pyrite and organic material (Table 3.3). This is partially corroborated by laser ablation ICP-MS (Inductively Coupled Plasma–Mass Spectroscopy) analyses of trace elements in pyrite from Ohio 5/6/7 coal presented in the same report, where Cd shows a modest enrichment over background concentrations (Table 3.4). However, Huerta-Diaz and Morse (1992) show that Cd is essentially excluded from precipitating pyrite in marine and brackish sediments, as illustrated in Figures 3.2 and 3.3.

Experimental investigations by Framson and Leckie (1978) show that neither Fe substitution in greenockite, nor Cd substitution in FeS takes place to any significant extent at 25°C. This behavior is similar to that of Zn, as is noted further below under the discussion for zinc. Given the exclusion of both Cd and Zn from precipitating pyrite, it is reasonable to assume that the CdS component is likely to be incorporated in sphalerite in reducing groundwaters. Experiments by Bostick et al. (2000) also show that Cd^{+2} can oxidize pyrite to elemental sulfur and iron hydroxides with co-precipitation of CdS. This observation is consistent with the experimental findings and thermodynamic predictions by Framson and Leckie (1978) that no ferrous sulfide can precipitate before all excess Cd^{+2} has precipitated from solution, and that Cd would precipitate as CdS in sediments primarily through surface exchange with ferrous monosulfide substrates. Thus, it is possible that the association of Cd with pyrite in coal may have involved redox reactions, leading to physical incorporation of a discrete CdS phase as an impurity. Cd can also substitute for Pb in galena—e.g., see Bethke and Barton (1971)—but the extent of solid solution at 25°C, << 0.005 mol fraction, precludes significant sequestrative competition with sphalerite.

Both Framson and Leckie (1978) and Davies-Colley et al. (1985) infer that Cd precipitates in the form of essentially pure (unspecified) CdS, or greenockite, in shallow marine sediments where high HS- activities are generated through bacterial reduction of sulfate. The latter authors also found that Cd activity appeared to be controlled by a poorly ordered, more soluble form of CdS than greenockite. No reference is made to the possible co-precipitation of Cd with Zn in sphalerite. Further clarification regarding the association of Zn with Cd under authigenic and diagenetic conditions in the field will be required to clarify the relationship.

For the purpose of this study, we assume that Cd is taken up primarily in solid solution in sphalerite. However, as is noted under the following section on selenium, it is possible that Cd could also precipitate as cadmoselite (CdSe) under conditions where sphalerite has been destabilized by a somewhat higher oxidation state, as suggested by the existence of cadmoselite and other ore minerals in calcite veins associated with altered (hematite-stained) amphibolites in Argentina (Paar et al., 2002). However, at the type locality, cadmoselite is reported to coexist with cadmian sphalerite, ferroselite and pyrite (Bur'yanova et al., 1957). The existence of ferroselite suggests an extremely rich selenium environment, and that the cadmoselite is stabilized for that reason rather than being due to the destabilization of sphalerite. Clearly, phase relations in Se-rich assemblages require further study. See also the discussion on zinc, below.

Mercury. During authigenesis, precipitating pyrite sequesters Hg, as is illustrated by field observations of Huerta-Diaz and Morse (1992) involving authigenic pyrite precipitation in brackish water sediments (Figures 3.2 and 3.3), which shows a 50-fold enrichment over background. Similar observations have been made in studies of coal—e.g., Finkelman (1981), Kolker et al. (2002), Diel et al. (2004), Kolker et al. (2006)—where Hg can be enriched in pyrite 50 or more times over background concentrations (Table 3.4). In coals atypically rich in Hg, samples have been found to contain isolated particles of cinnabar (Finkelman, 1981; Brownfield et al., 2005), or finely disseminated particles of tiemannite (HgSe) (Tewalt et al., 2001). Clausthalite (PbSe) also appears to act as a host for Hg in coal, as one sample observed contained 0.54wt% Hg, representing a 10,000 fold enrichment over the background concentration in the coal (Hower and Robertson, 2003). Galena can also act as a host for Hg. Finally, Barbanson et al.

(1985) and Martinez Garcia et al. (1991) describe a variety of sphalerite containing up to 7% substitution of zinc by mercury. This variety has been found in the mines of Argayon, Cotos, Rubios, Tresviso, and Hozarco in Spain. Electrochemical studies (e.g., Giannetti et al., 2006) and spectroscopic studies of Hg adsorption on the pyrite surface (e.g., Ehrhardt et al., 2000), using X-ray photo electron spectroscopy (XPS), and Behra et al. (2001), using XPS and X-ray absorption spectroscopy (XAS)), both affirm that Hg is strongly adsorbed by functional groups on the pyrite surface, which under acid conditions were identified as $\equiv S^{-1}$-Hg-OH or $\equiv S^{-1}$-Hg-Cl. However, it is not clear whether the Hg^{+2} becomes incorporated as a solid solution in the pyrite or concentrates in isolated HgS domains. We take a provisional approach by assuming that Hg enters into solid solution in pyrite in a reducing aquifer, but that substitution in galena or sphalerite, or formation as discrete cinnabar or tiemannite minerals, might be plausible. It is possible that, like As substitution in pyrite, HgS substitution is metastable, and that long-term recrystallization of pyrite leads to its eventual expulsion from the pyrite lattice. Thus, conclusions arrived at through a preliminary literature review must remain tentative, pending further thermodynamic analysis in Section 3.4.5.

Lead. Mineralogical studies of coal suggest that galena is the dominant mineral containing Pb as an essential component (Kolker et al., 2002). However, Finkelman (1981) found that over 50% of coals in the Appalachian Basin and 10% outside the Basin contained PbSe (clausthalite) rather than galena, although it was estimated that at most no more than 50% of the Pb could be present in that form. Kolker et al. (2002) show that Pb does not appear to report in pyrite in significant amounts despite the preponderance of this mineral, except perhaps in bituminous coals from Ohio (Table 3.3). In such coals, Pb is enriched in pyrite by a factor of nearly 40 (Table 3.4). However, Finkelman (1981) suggests that Pb enrichment in pyrite might be due to the presence of impurities such as galena, which may well have been incorporated in a manner similar to that of CdS though redox reactions on the pyrite surface. This supposition is reinforced by the strong correlation displayed between Pb and Sb in pyrite samples from Ohio 5/6/7 coal, where Sb:Pb ~0.13 and R^2 =0.91 and in As bearing pyrite from the Roudny gold deposit of the Bohemian Massif (Zacharias et al., 2004), where Sb:Pb ~1.5 with a correlation coefficient of 0.93 in one generation of pyrite. The latter authors believe that the stoichiometric ratio of Pb to Sb reflects

the possible presence of "crypto-inclusions" of jamesonite ($Pb_4FeSb_6S_{14}$). A similar but somewhat weaker correlation between Pb and Sb ($R^2 = 0.66$) is also observed in arsenian pyrite associated with gold mineralization in neoproterozoic sediments of the Saldania Belt in South Africa (Belcher et al., 2004). Huerta-Diaz and Morse (1992) show that Pb is almost always quantitatively excluded from authigenic pyrite, in conformity with the observed behavior of Cd under the same conditions (Figures 3.2 and 3.3). Thus, we can conclude that galena is the predominant host mineral for Pb except where excess selenium stabilizes clausthalite, and that any association of Pb with pyrite is probably due to the presence of foreign inclusions.

Antimony. Information on the mode of occurrence of antimony is sparse. In principle, it would be expected that Sb would behave somewhat similarly to As. Gudmundite (FeSbS) is an isostructural analogue of arsenopyrite, but occurs infrequently in Sb-rich epigenetic mineralization (Williams-Jones and Normand, 1997). Limited field evidence also indicates that Sb does report in epigenetic arsenian pyrite, although an expected correlation between As and Sb is not always observed (Zacharias et al., 2004). This finding is consistent with the complete lack of a correlation between As and Sb concentrations in a diverse set of pyrite samples associated with coals in the Black Warrior Basin of Northwestern Alabama (Diel et al., 2004). In contrast, a correlation between As and Sb in nine samples of pyrite from Ohio 5/6/7 suggests a sympathetic association ($R^2 = 0.63$), although Sb uptake appears to be less efficient than would be predicted on the basis of the As/Sb ratio in the bulk coal (Table 3.4). A sympathetic correlation between As and Sb ($R^2 = 0.70$) is also observed in arsenian pyrite associated with gold mineralization in Neoproterozoic sediments of the Saldania Belt in South Africa (Belcher et al., 2004). The somewhat less efficient uptake of pyrite from Ohio 5/6/7 may be due to a larger anionic radius of Sb(-I), when substituting for S(-II), or because of the slightly higher stability of Sb(III) compared with As(III) in aqueous solution. The sometimes strong correlation between Pb and Sb in pyrite, noted under the discussion for Pb, above, further suggests that Sb solid solution in pyrite may be restricted, and that Sb is incorporated as nanoparticulate inclusions. The mode of occurrence of Sb in coals (Table 3.5) also indicates that significant fractions of Sb are retained by the organic and silicate components, in agreement with a review of earlier studies by Finkelman (1981).

Therefore, it appears that Sb chemistry differs sufficiently that a correlative chemical behavior with As in pyrite cannot be presumed.

The most commonly observed Sb host mineral under reducing conditions is stibnite (Sb_2S_3). However, Williams-Jones and Normand (1997) point out that stibnite is destabilized in favor of kermesite (Sb_2S_2O) below 150ºC. According to these authors, the vast majority of occurrences of kermesite are of supergene origin. There are several well-documented occurrences of kermesite having been formed through hypogene processes. In the event that pyrite is destabilized, any released Sb is therefore likely to precipitate as stibnite above 150ºC and as kermesite below that temperature, because both possess stability fields extending to more oxidizing conditions than that of pyrite. Stibnite and kermesite also become more stable with decreasing pH and/or H_2S activity (Williams-Jones and Normand, 1997).

The recently discovered, rare antimony analogue of orpiment, antimonselite (Sb_2Se_3) (Chen et al., 1993), has been reported in epithermal deposits associated with galena, sphalerite, and pyrite, marcasite, uraninite, coffinite and organic matter (Min et al., 2000), and with tiemannite, clausthalite, and berzelianite (Cu_2Se) (Vikre, 2005). Antimonselite has also been observed to form a solid solution series with stibnite (Liu et al., 2005). Because the antimonselite stability field also extends to significantly higher redox potentials than pyrite, its formation could result from the liberation of both Sb and Se upon oxidation of the latter. Accordingly, the presence of antimonselite in sedimentary rocks should not be discounted.

In the absence of more definitive information, we tentatively conclude that Sb preferentially substitutes for S in the pyrite lattice in a manner similar to that of As, but that stibnite, kermesite, and antimonselite might also host Sb, especially under less reducing conditions where pyrite is no longer stable.

Selenium. Selenium substitutes for sulfur in the pyrite lattice, and a limited solid solution is observed between pyrite and its selenium metastable isostructural analogue, dzharkenite ($FeSe_2$) (Yakovleva et al., 2003). Limited field evidence from Western phosphatic shales (Ryser et al., 2005) suggests that dzharkenite may form preferentially in the presence of excess Se under

diagenetic conditions. However, the more stable form of $FeSe_2$ is ferroselite, which possesses the marcasite structure. An examination of the behavior of Se in relation to As in pyrite in Ohio bituminous coal shows a remarkable coherence between the two, as shown in Figure 3.4. A stoichiometric ratio close to unity is revealed, with $R^2 = 0.92$ (Table 3.4), despite the ten-fold greater abundance of As. Finkelman (1981) also noted a parallel behavior between As and Se in pyrite from Upper Freeport coal, although in another sample of the same coal, a negative correlation was observed. Whether the correlation in pyrite in coal from Ohio is fortuitous or reflects an underlying energetically favored coupled substitution is not known. However, the mode of occurrence of selenium in coals suggests that excess Se will preferentially co-precipitate with Pb as clausthalite (Finkelman, 1981) or mercury as tiemannite (Tewalt et al., 2001) before saturation with respect to either dzharkenite or ferroselite. Neither dzharkenite nor ferroselite have been observed in coal, an indication that the relative abundance of Se in coal is insufficient to saturate with respect to either of these phases. As noted at the conclusion of Section 3.4.5.1, the coexistence of selenian pyrite with dzharkenite in Western phosphatic shales (Ryser et al., 2005) is probably unusual, since it occurs where the ambient concentration of Se is up to three orders of magnitude higher than the average crustal abundance. In the event that such an association is observed, Se should, depending on availability, preferentially co-precipitate heavy metal selenides such as tiemannite, clausthalite, and cadmoselite, in preference to cinnabar, galena and greenockite or cadmian sphalerite, which is generally consistent with reported field occurrences—e.g., Bur'yanova et al. (1957).

Laboratory studies show an extensive solid solution series between ZnS and ZnSe at temperatures at least as low as 160°C (Wright et al., 1965). Because of the relative abundance of Zn in relation to Se in nature, it is not expected that sufficient excess Se would permit the stabilization of the selenium analogue of sphalerite, stilleite (ZnSe), except where more oxidizing conditions would cause the decomposition of sphalerite in favor of stilleite and zinc carbonates or silicates. Such a mechanism might also explain the occasional occurrence of the selenium analogue of greenockite, cadmoselite (CdSe), in sedimentary strata under reducing conditions despite the potential for Cd sequestration by sphalerite. The thermodynamic analysis (Section 3.4.5.2) likewise suggests that the aqueous concentration of Cd could be controlled by

cadmoselite in preference to greenockite or hawleyite. Unfortunately, the general lack of thermodynamic data and information on the solid solution behavior of Se in FeS_2 polymorphs and of Cd, Hg, Pb and Zn in FeS_2 polymorphs in relation to their monosulfides and monoselenides precludes a quantitative assessment at this time. We will therefore assume that ferroselite (for which thermodynamic data are available) can be treated as a solid solution component in pyrite under reducing groundwater conditions, while monitoring the potential for saturation control by the Cd, Hg, and Pb monoselenides (cadmoselite, tiemannite, and clausthalite) respectively.

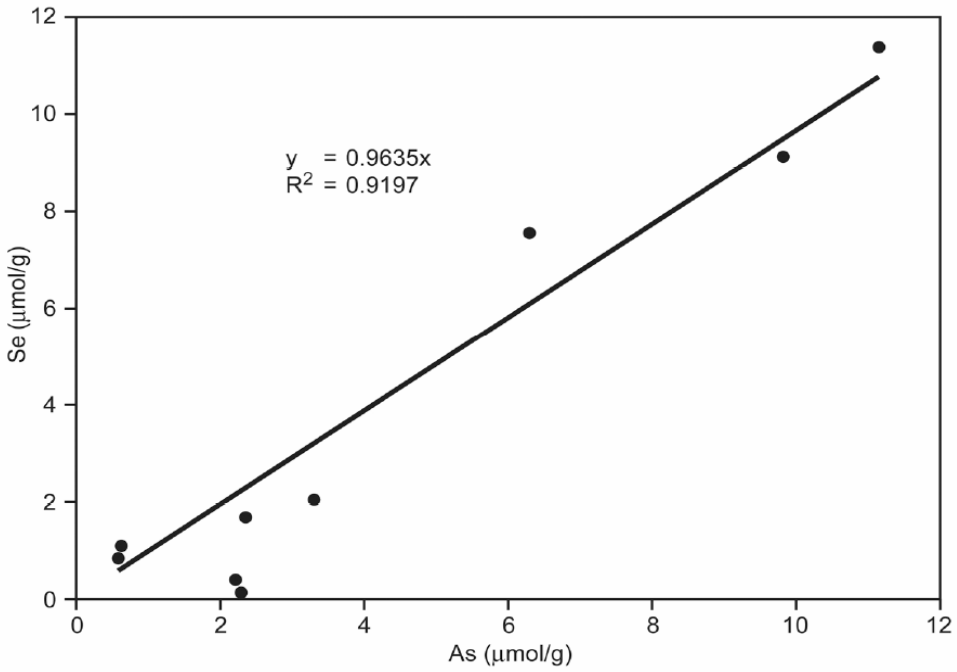

Fig. 3.4. The correlation between the molar concentration of Se and As, determined by laser-ablation ICP-MS, in pyrite from Ohio 5/6/7 bituminous coal (from Kolker et al., 2002)

Uranium. Extensive evidence indicates that U is mobilized in intermediate to acid igneous intrusive and particularly extrusive rocks, under oxic to mildly reducing conditions as the uranyl ion (UO_2^{+2}). The source of UO_2^{+2} is probably apatite, which is a known host for U in igneous rocks. However, uranium in sedimentary rocks is invariably associated with organic matter

(Abdel-Gawad and Kerr, 1961; Szalay, 1964; Mohan et al., 1982; Drew Ilger et al., 1987) or with accessory detrital minerals such as zircon ($ZrSiO_4$). Humic acids within the organic matter sequester UO_2^{+2} through complexation on carboxyl functional groups (R-COOH) (Szalay, 1964; Drew Ilger et al., 1987), primarily as monodentate complexes, i.e.,

$$R\text{-}COOH + UO_2^{+2} = R\text{-}COOUO_2^{+} + H+$$

or

$$R\text{-}COOH + UO_2^{+2} + H_2O = R\text{-}COOUO_2OH + 2H^{+}$$

(e.g., see Nefedov et al., 1998) leading to enrichment factors over contacting groundwaters by a factor as high as 10,000 (Szalay, 1964). Evidence suggests that a significant portion of the U remains adsorbed as metastable UO_2^{+2}. However, field evidence from many sedimentary uranium deposits indicates that some adsorbed UO_2^{+2} is reduced from the (VI) to the (IV) state, through reduction by HS^{-}, resulting from either biogenic or abiogenic activity (Min et al., 2000), e.g.,

$$4UO_2^{+2} + H_2S + 4H_2O = 4UO_2 + SO_4^{-2} + 10H^{+}$$

although direct microbial reduction of U(VI) to U(IV) has also been observed under anaerobic conditions (Suzuki et al., 2005). Autogenous radiolysis of water and/or organic matter—e.g., see Levinson (1977) and Dubessy et al. (1988)—and reduction by reactive hydrogen free radicals (H′) could also be operative, possibly with concomitant oxidation of excess organic material (Min et al., 2000), leading to the formation of uraninite and/or coffinite, thus:

$$UO_2^{+2} + 4H^{\circ} = U^{+4} + 2H_2O$$

$$U^{+4} + 2H_2O = UO_2(\text{uraninite}) + 4H^{+}$$

$$U^{+4} + SiO_2(aq) + 2H_2O = UO_2(\text{coffinite}) + 4H^{+}$$

$$UO_2 + SiO_2(aq) = USiO_4\ (\text{coffinite})$$

Both uraninite (mostly as pitchblende, a poorly ordered and partially oxidized form of uraninite) and coffinite have been reported to occur in association with lignitic, humic, and bitumic material in sedimentary rocks, and in coal beds in a few cases (Drew Ilger et al., 1987), despite significant concentrations of U. When found together, they appear to have been co-generated (Min et al., 2000). Lack of detection of either or both minerals may result from their occurrence in a colloidal or nanoparticular state (Min et al., 2000).

U(IV) has also been reported occasionally in sedimentary rocks as brannerite (UTi_2O_6) (Finkelman and Klemic, 1976; Dutkiewicz et al., 2003), which probably forms through the interaction of dissolved TiO_2 with uraninite, thus:

$$UO_2 + 2TiO_2(aq) = UTi_2O_6 \text{ (brannerite)}$$

The possible presence of brannerite in potable water aquifers should not be discounted, particularly when thermodynamic data is available to calculate its solubility (Helean et al., 2003). However, the very low solubilities of potential sources of $TiO_2(aq)$, such as anatase, rutile or sphene, which are 3–4 orders of magnitude less soluble than the silica polymorphs, precludes rapid formation of this mineral, explaining its normal occurrence primarily in Paleozoic and proterozoic sediments (Finkelman and Klemic, 1976; Dutkiewicz et al., 2003). Uranium is also found in zircon, but because of its extremely low solubility and indefinite persistence in nature, any contained U is essentially isolated from groundwater, and therefore would be of no concern in the present study.

The reported distribution of U in coal, as shown in Table 3.3, is consistent with the previously cited findings regarding its association with organic material. A significant fraction of the U is HCl-soluble, i.e., it is readily desorbed from carboxyl functional groups as UO_2^{+2}, whereas the remainder is present in the silicate fraction (as coffinite?) and in the organic fraction, where its mode of occurrence is uncertain, but probably in the form of organic or mineral colloids. Finkelman (1981) has reviewed an extensive earlier literature on the occurrence of U in coal, and reaches essentially similar conclusions regarding its distribution.

We therefore assume that U is present primarily as uraninite, or as coffinite, in groundwaters under reducing conditions.

Zinc. Both field and experimental evidence uniformly indicate that sphalerite (ZnS) is the predominant host for zinc under reducing conditions. Furthermore, Framson and Leckie (1978), both on experimental and theoretical grounds, argue that Zn is unlikely to substitute in iron sulfides, citing Barton and Toulmin (1966), who found that substitution of Zn^{+2} in pyrrhotite, even at temperatures as high as 850°C, is only 0.006 mol fraction. This argument is further substantiated by field observations. In the sedimentary environment, Zn partitions negligibly into authigenically formed pyrite, as shown in Figures 3.2 and 3.3 (Huerta-Diaz and Morse, 1992). Measurements of Zn concentrations in pyrite from Ohio 5/6/7 coal indicates that Zn is the only trace element that is depleted in pyrite compared with its concentration in bulk coal (Table 3.4). The partitioning of Zn into sphalerite dominates its behavior in coal (Table 3.3). Finkelman (1981), on the basis of a review of the earlier literature and his own mineralogical studies, also concluded that sphalerite is the primary mineral host for Zn. Thus, we can assume that sphalerite controls Zn solubility in groundwaters under reducing conditions.

Summary

In Table 3.6, we summarize the expected occurrences of minerals, which might determine the activities of the selected hazardous inorganic constituents in reducing groundwaters. Where thermodynamic data are available, solubility products for these minerals have been incorporated in the EQ3/6 Data0.dat database, and in the corresponding database in TOUGHREACT, to permit calculation of potential thermodynamic controls of the selected hazardous constituents in groundwaters, respectively under static equilibrium and dynamic conditions.

It should be emphasized that the chemical behavior of the selected hazardous inorganic constituents in groundwaters is affected by many processes, which include the past history of the aquifer, reactive chemical processes involving advective transport from distant sources, segregation due to changing host rocks, oxidation states and salinities, and the current oxidation state of the aquifer at the time of sampling. Because of the complexity of the chemical systems

involved, the preceding review is intended as a preliminary survey, and is subject to future refinement. However, despite this cautionary note, it is believed that the selected suite of minerals presented in Table 3.6 provides a suitable starting point for geochemical modeling thermodynamic controls in Section 3.4.5. The thermodynamic properties of the identified minerals and associated aqueous species of the hazardous constituents (Appendices C, D, and E) were used in compiling solubility product and dissociation constant data, respectively, for incorporation in the EQ3/6 code. The code was then used in evaluating potable groundwater quality analyses to find out whether the identified minerals might be controlling the concentrations of the hazardous constituents in solution. This procedure is described in the next section.

Table 3.6. Potential mineral hosts for hazardous inorganic constituents under reducing conditions

Hazardous Inorganic Constituent	**Potential Mineral Controls**	
	Solid Solution Component	**Discrete Mineral**
As	$(FeAsS)_{py}$	Arsenopyrite (FeAsS)
Ba	-	Barite ($BaSO_4$); Witherite ($BaCO_3$); [Crandallite ($CaAl_3(PO_4)_2(OH)_5$)]
Cd	$(CdS)_{sph}$	Greenockite(CdS); Cadmoselite (CdSe)
Hg	$(HgS)_{py}$	Cinnabar (HgS); Tiemannite (HgSe)
Pb	-	Galena (PbS); Clausthalite (PbSe)
Sb	$(FeSbS)_{py}$	Stibnite (Sb_2S_3); Kermesite (Sb_2S_2O); Antimonselite (Sb_2Se_3); Gudmundite (FeSbS)
Se	$(FeSe_2)_{py}$	Ferroselite ($FeSe_2$); [Dzharkenite ($FeSe_2$)]; Antimonselite (Sb_2Se_3); Cadmoselite (CdSe); Clausthalite (PbSe); Tiemannite (HgSe)
U	-	Uraninite (UO_2); Coffinite ($USiO_4$) [Brannerite (UTi_2O_6)]
Zn	-	Sphalerite (ZnS); Hemimorphite ($Zn_4Si_2O_7(OH)_2 \cdot H_2O$)

Note: py = pyrite, sp = sphalerite

3.3 Evaluation of Potable Groundwater Quality in Relation to Groundwater Model Development

3.3.1 Background

This section describes the geochemical evaluation of a large number of water-quality analyses with measurable concentrations of hazardous inorganic constituents, with the main objective of identifying minerals containing specified hazardous constituents that saturate these waters. Many groundwaters that are recovered for use as drinking water in the United States are analyzed, not only for major dissolved chemical components, but also for trace concentrations of hazardous inorganic (and organic) constituents. Where comprehensive chemical analyses are available, the thermodynamic controls that govern the concentrations of the hazardous inorganic constituents in solution can be identified through comparison of the saturation indices of candidate minerals identified in the previous section. This is accomplished in this study through the use of the distribution-of-species code EQ3/6 (Wolery et al., 1993), which calculates the thermodynamic activities of all dissolved components. The thermodynamic activities of all dissolved components are then used to calculate the saturation indices of minerals that are potentially in equilibrium with the groundwater, including those where the hazardous constituent is an essential component. Other useful information is obtained from the thermodynamic evaluation (e.g., aquifer buffering capacity, redox potential, background levels of CO_2 concentration), which, together with independent information relating to the mineralogical and physical properties of the aquifer host rocks, can be used to support development of a comprehensive geochemical model.

The USGS National Water Information System (NWIS) Database contains approximately a quarter of a million chemical analyses of groundwaters of which a small fraction meets the needs of this project. Data mining of the NWIS was kindly conducted by Jonathon C. Scott, USGS, Oklahoma City, searching the database for all available data on well water specifically used for potable purposes. Search criteria were defined as follows:

1. The groundwaters had to be recovered from wells for drinking water purposes.
2. The chemical analysis had to include at least one of the following elements: As, Ba, Cd, Hg, Pb, Sb, Se, U, Zn.
3. The trace metal analyses had to be accompanied by complete chemical analyses of the water, i.e., pH, Na, K, Mg, Ca, Cl, SO_4, CO_3 or alkalinity, and if possible Fe(II), Fe(III) or Fe(T), Si or SiO_2(aq), Al.
4. Additional information was given that helped define oxidation state, e.g., Eh, dissolved oxygen concentration, or information that would help with the calculation of potential redox pairs such as CH_4/CO_2, H_2S/H_2SO_4, As(III)/As(V), Sb(III)/Sb(V).
5. Electrical conductivity was measured.

In addition, the following supplementary data for each well site was extracted, when available:

1. The geographic coordinate of the well site
2. The geologic formation penetrated
3. The well screen intervals
4. The groundwater temperature
5. Information pertaining to the mineralogy or chemical composition of well core or chips.

Using the above search criteria, data files were extracted from the USGS National Water Quality Information System (NWIS) containing 38,610 water-quality analyses with 703,352 distinct measurements (total) at 22,437 unique data-collection sites nationwide. This large database was uploaded into a data management tool (based on the Matlab software) developed specifically for this study. The following sections describe the analyses conducted and discuss results. Section 3.3.2 shows the concentration histograms of the major chemical constituents of the examined water quality analyses and certain other parameters of interest. Section 3.3.3 shows concentration histograms for the hazardous inorganic constituents selected for study, and illustrates spatial distributions for As, Ba, Pb and U. The raw data presented in Section 3.3.3 are subject to limitations arising from the analytical methods employed in the detection of trace concentrations of hazardous constituents. Discussion of applicable detection limits is given in Section 3.3.4, and the impact of analytical artifacts evident in some of the histograms is discussed in Section 3.3.5.

3.3.2 Concentration of Major Constituents in Potable Groundwater

The downloaded NWIS database of more than 38,000 analyses was first characterized in terms of the distributions of the major constituents contained in all groundwaters, i.e., Na, K, Mg, Ca, Fe(total), HCO_3^-, SO_4, Cl and pH. In addition, analyses of Al, a minor species, with a typical concentration of less than 0.01 mg/L, were also compiled, because of its importance in geochemical modeling. SiO_2(aq) was omitted from the dataset initially downloaded from the NWIS database, but was computed in the following step. The suite of chemical analyses was processed using the EQ3/6 code (see Section 3.4.5) in order to evaluate several additional species that are best represented in a form not readily obtainable from the analytical data, and which are required for comparison with the simulated groundwater composition generated by TOUGHREACT under initial conditions of secular equilibrium. The species included Fe(II), total HCO_3^- and Eh. SiO_2(aq) was set at saturation with respect to opal-CT, which is characteristic of many shallow groundwaters (Abercrombie et al., 1994; Apps, 2004). Total HCO_3^- was calculated from the entered "free" HCO_3^- or alkalinity, see Section 3.4.3 below. The Eh was imposed through an EQ3/6 input specification that both pyrite and goethite are at equilibrium at a given pH. In addition, the calculated concentration of Al was also retrieved from the output for comparison with the analyses of Al in the NWIS samples. The calculated value was based on the assumption that the groundwaters were also in equilibrium with a low Fe, Mg smectite.

The resulting multiple sets of input data were stripped of analyses reporting "greater than", "less than", "zero", "presence verified but not quantified" concentrations, and the remainder, with the exception of pH, were converted to uniform concentration units of mg/L and transformed to a logarithmic scale. The remaining analyses for each constituent were divided into uniform bins, representing incremental concentration ranges on a logarithmic scale, and plotted as histograms. The output parameters from the EQ3/6 species distributions were similarly plotted as histograms. The results are given in Figures 3.5(a)–(m) below, and the appropriate modal value are summarized in Table 3.7.

Note that the analytical methods used for the quantification of major species in solution, with the exception of Al and Fe, are sufficiently sensitive to permit satisfactory measurement of their concentrations. The omission of unquantified analyses therefore has negligible bias on the results, particularly when it is recognized that it is the mode of the distribution that is of interest in this evaluation of the chemical analyses. This condition does not apply, however, to trace element concentrations at or near the limits of detection for the analytical method used, especially with regard to Al and Fe, and to most of the hazardous inorganic constituents identified for study in Section 3.3.3. For these constituents, the omission of unquantified analyses introduces a similarly unquantifiable positive skew to the plotted histograms. No techniques have been identified that would easily correct for this bias. The strategy adopted in this study is to independently develop a geochemical model, and compare the model with field observations as an aid to establishing the degree of bias and acceptability of the field data. It should be noted, however, that a positive bias can be inherently conservative, in that the bias could over-predict ambient concentrations of hazardous constituents in groundwaters in equilibrium with elevated partial pressures of CO_2.

Table 3.7 also includes additional parameters of interest for what is effectively the most commonly encountered or modal groundwater composition among those potable groundwater samples downloaded from the NWIS database. This modal groundwater is just slightly supersaturated with respect to calcite, and displays a relatively elevated $P(CO_2)$ (see Section 3.4.3 for further discussion of $P(CO_2)$ in potable groundwaters). The composition represents of a groundwater of the Ca-Mg bicarbonate type. The "analytical" charge imbalance for this groundwater is excellent, being significantly less than the acceptable value of 5% of total charge. Note, however, that this composite charge imbalance is not representative of the average charge imbalance of the 38,000 groundwater analyses evaluated in this report. As is shown in Section 3.4.3, about two-third of the studied groundwaters meet the 5% charge imbalance criterion for acceptability. The ionic strength is very low as expected, and is a useful benchmark for comparison with other aqueous systems.

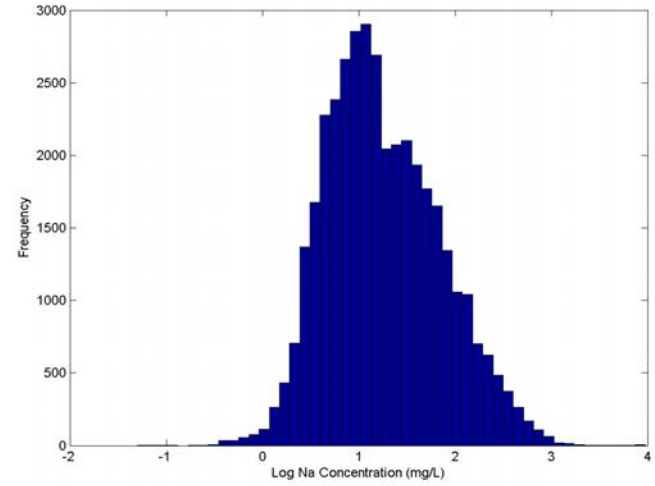

(a)

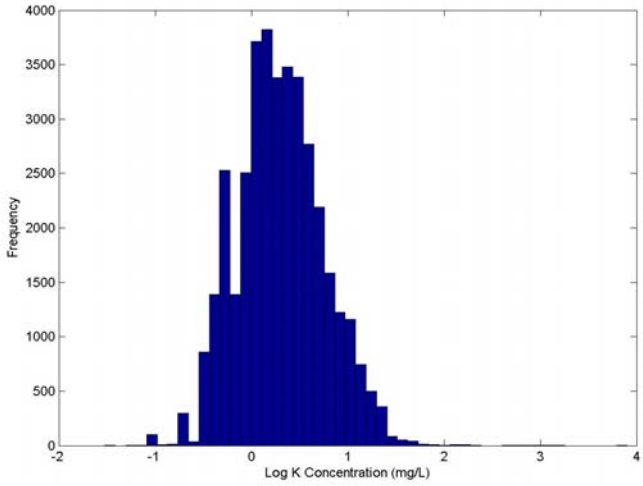

(b)

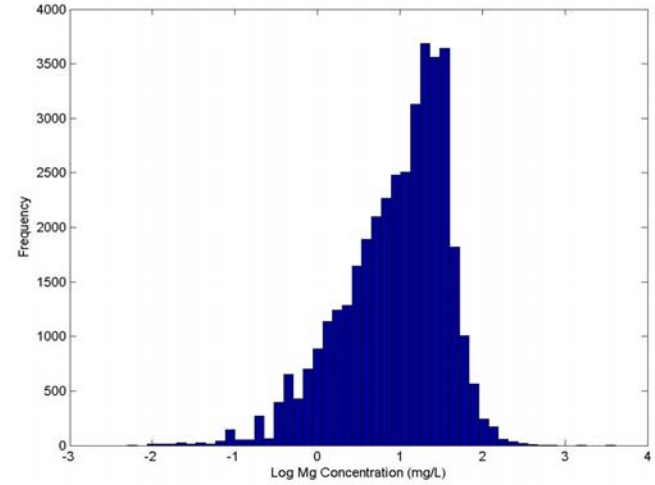

(c)

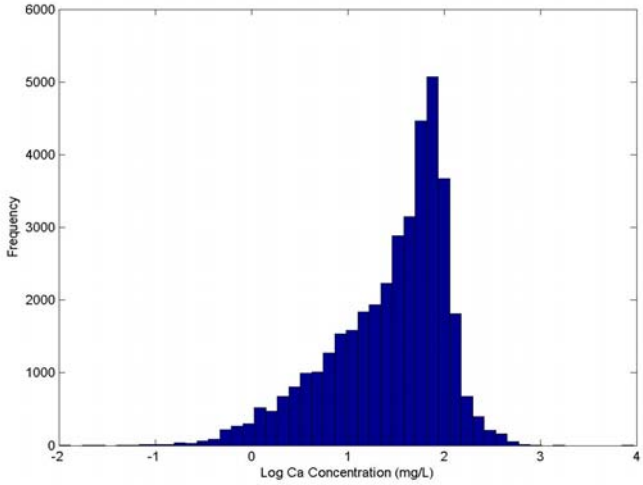

(d)

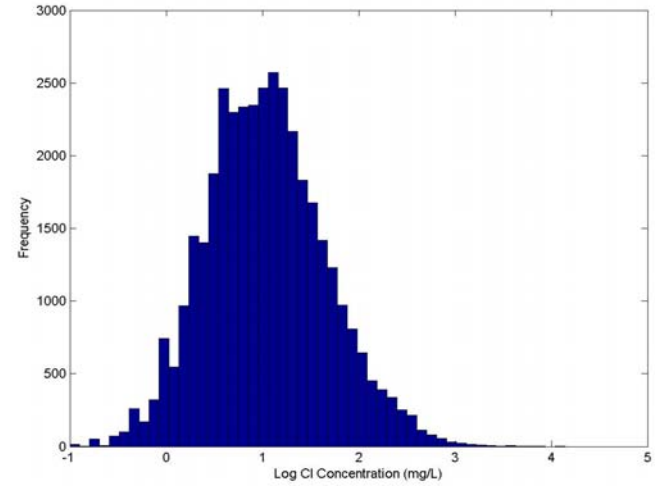

(e)

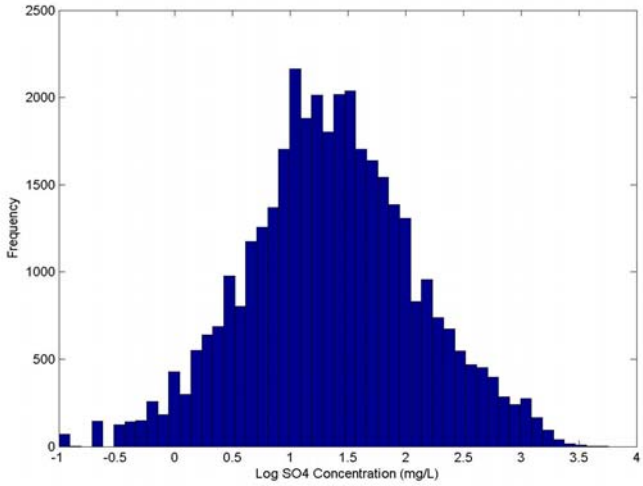

(f)

Fig. 3.5. Part 1

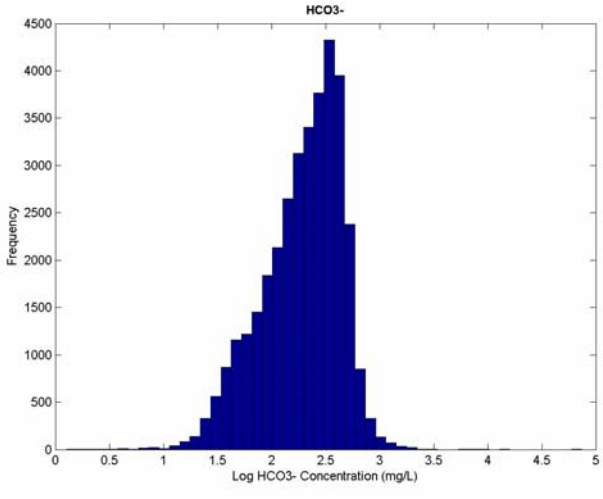

(g)

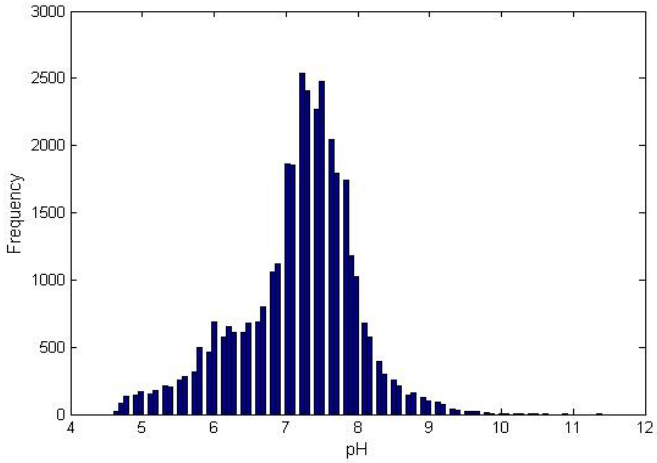

(h)

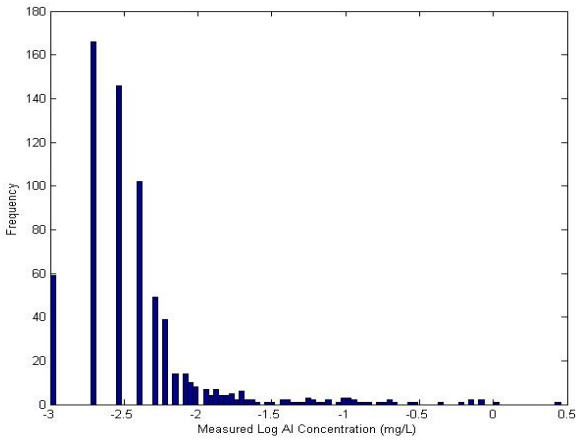

(i)

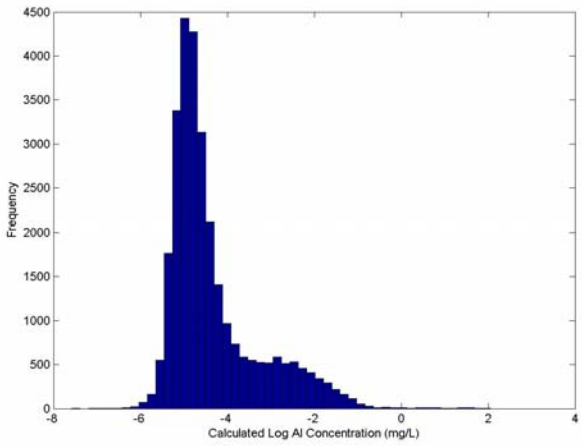

(j)

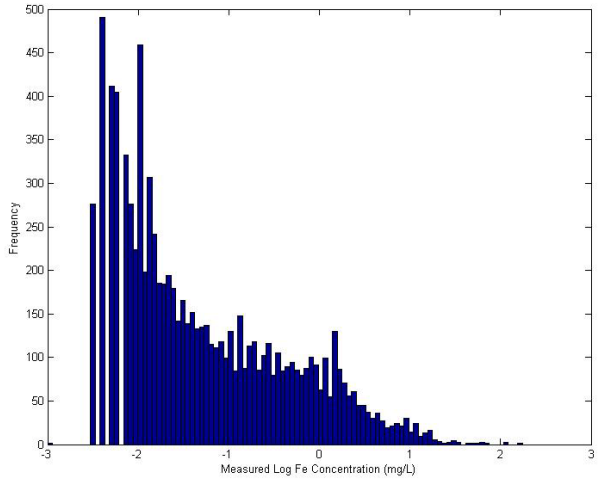

(k)

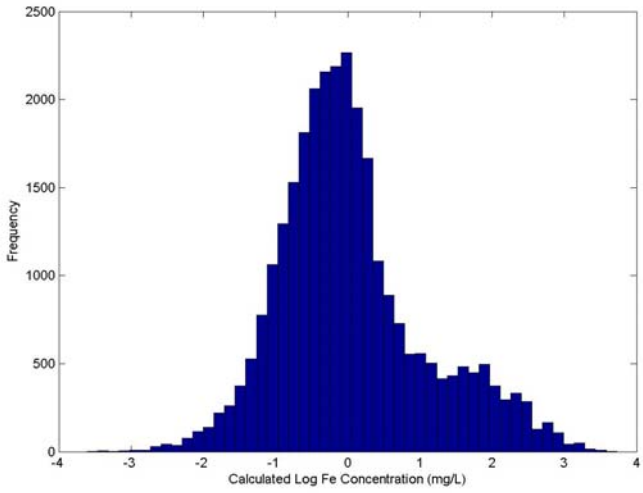

(l)

Fig. 3.5. Part 2

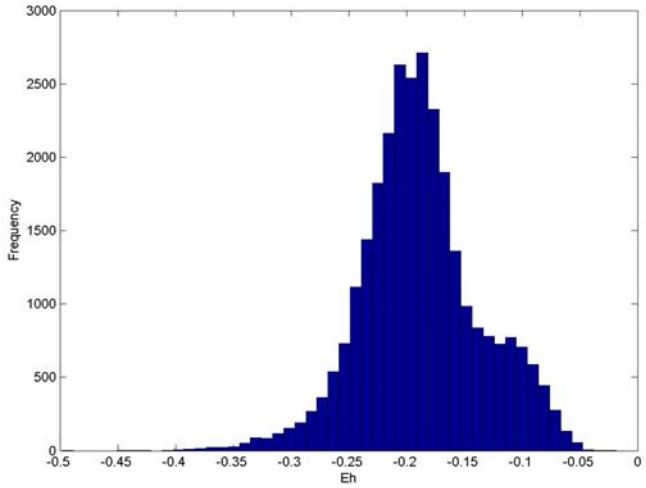

(m)

Fig. 3.5. Histograms showing the concentration distributions of various chemical constituents, as well as pH and calculated Eh in more than 38,000 analyses of potable groundwaters in the United States.

Table 3.7. Values of analytical concentrations of chemical constituents at maximum frequency and associated calculated values of selected species in more than 38,000 potable groundwaters.

Parameter	Unit	Condition	Value
Na	mg/L	measured	12.6
K	mg/L	measured	1.6
Mg	mg/L	measured	20.0
Ca	mg/L	measured	63.1
Fe	mg/L	measured	≈1.3
Fe(total)	mg/L	calculated	1.3
Al	mg/L	measured	≈0.002
Al(total)	mg/L	calculated	0.0002
SiO_2(aq)	mg/L	calculated	75.0
Cl	mg/L	measured	15.8
HCO_3^-	mg/L	calculated	316
SO_4	mg/L	measured	20.0
pH	Log (mol/L)	measured	7.3
Eh	Volt	calculated	-0.18
SI (calcite)	-	calculated	+0.09
$P(CO_2)$	Log (bar)	calculated	-1.86
Ionic Strength	Mol/kg H_2O	calculated	0.0078
Charge Imbalance	% of total charge	calculated	-1.75

The two constituents likely to show the greatest discrepancy between field observation and modeled values are Al and Fe (Figure 3.5i vs. 3.5j for Al, and Figure 3.5k vs. 3.5l for Fe). In the case of Al, only the more recently developed analytical method employing inductively coupled plasma with mass spectroscopy (ICP-MS) is sufficiently sensitive to allow quantitative measurements in groundwaters. Figure 3.5i shows the distribution of analytical concentrations for Al using the PLM43 method (Appendix A), which employs ICP-MS. The detection limit for Al varies when using this method, the most sensitive being 0.001 and 0.002 mg/L. Of all 1,213 analyses reported, 696, or 57%, reported detectable values of Al. This implies that the most common Al concentration lies close to the detection limit at circa 0.002 mg/L. However, even when taking into account all potential Al complexing in groundwaters, especially with respect to silica complexes (Tagirov and Schott, 2001), the calculated concentration is still one order of magnitude less at ≈0.0002 mg/L. The reason for the discrepancy probably lies in the precipitation of a metastable amorphous hydrated Al-Si silicate caused by the dissolution of unstable detrital feldspars (e.g., see Paces, 1978), and which has not yet been incorporated in the geochemical model.

Iron analyses show a very broad range of values in analyzed groundwaters as shown by Figure 3.5k. This range reflects in part the potential variation in oxidation state of groundwaters in relation to the Fe(III)/Fe(II) couple, but also artifacts introduced by exposure of the groundwater sample to air with consequent oxidation and precipitation of Fe(III). As a consequence, the reported analytical concentrations of Fe(T) cannot be considered wholly trustworthy. As is discussed further below (Section 3.4), the evaluation of the concentration distributions of hazardous inorganic constituents strongly suggests that most groundwaters are reducing, which is consistent with redox control by the pyrite/goethite redox buffer, or by other buffers controlling the redox potential within a similar range of values.

3.3.3 Concentrations of Hazardous Inorganic Constituents in Potable Groundwater

The NWIS database was mined for chemical analyses of As, Ba, Cd, Hg, Pb, Sb, Se, U and Zn. Similar to the procedure employed for major constituents, the resulting multiple datasets processed as follows. Analyses reporting ”greater than,” “less than,” “zero,” “presence verified but not quantified” concentrations were deleted, while the remainder were converted to uniform concentration units of mg/L and transformed to a logarithmic scale. (Note: The mg/L unit roughly corresponds to 1,000 ppb for the conditions considered.) The remaining population of analyses for each element was divided into uniform bins, representing incremental concentration ranges on a logarithmic scale, and plotted as histograms. Note that the elimination of unquantified analyses potentially introduces a positive skew to the resulting histogram, as noted in Section 3.3.2, above, which can bear on the ultimate interpretation of the data in terms of the geochemical model developed in Chapter 3. This issue is discussed with respect to certain specific hazardous constituents under their respective sub-headings in Section 3.4.5.

The resulting histograms are given in Figures 3.6(a)–(i). For comparison, the maximum contaminant level (MCL) permitted (U.S. Environmental Protection Agency, 2004) is also plotted, except for Zn. See Table 3.8 for a list of the hazardous elements and respective MCLs in drinking water. (If MCLs are exceeded in more than 10% of tap water samples, water providers need to take corrective actions.) It is evident from Figure 3.6 that, but for a few outliers, for the majority of groundwater samples in the database, most of the elements meet MCL requirements under current conditions. A significant minor percentage of groundwaters containing As and U exceed the MCL for those elements, as noted by Focazio et al. (2006).

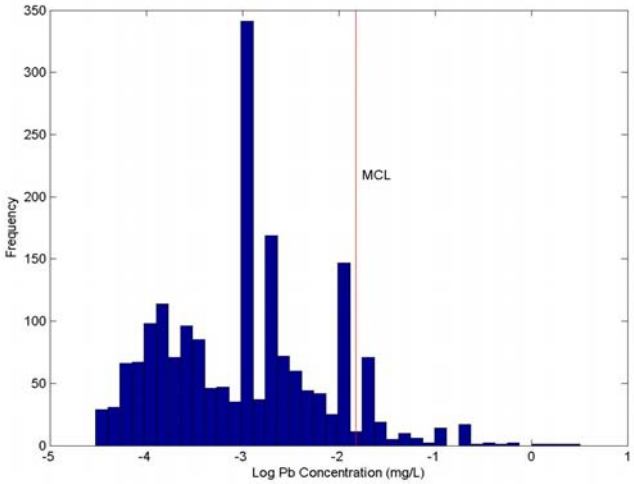

(a) Pb

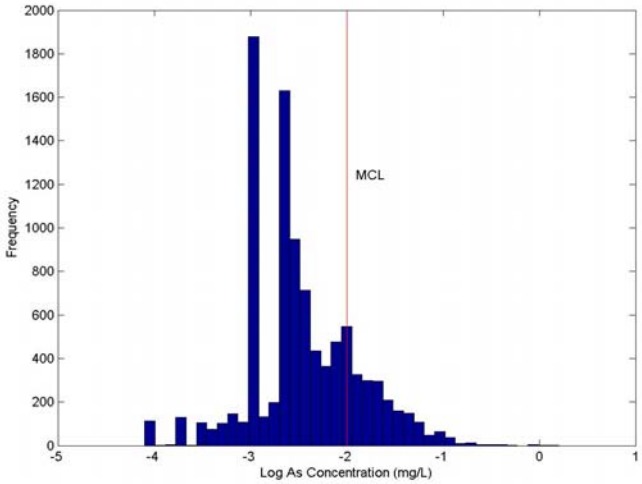

(b) As

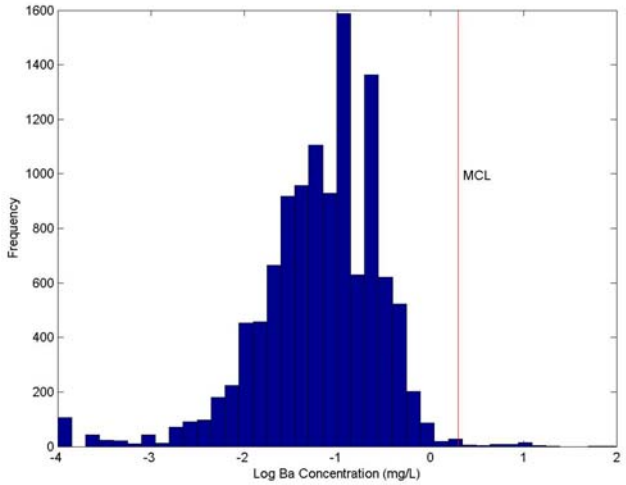

(c) Ba

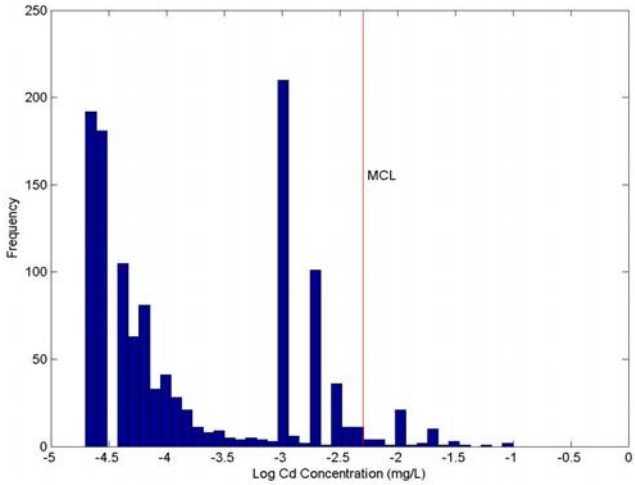

(d) Cd

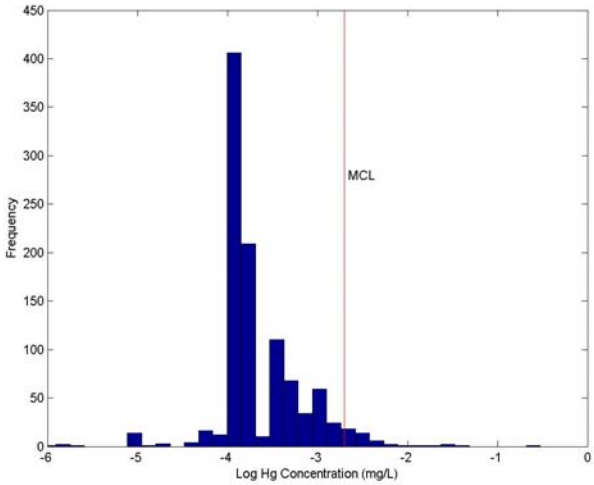

(e) Hg

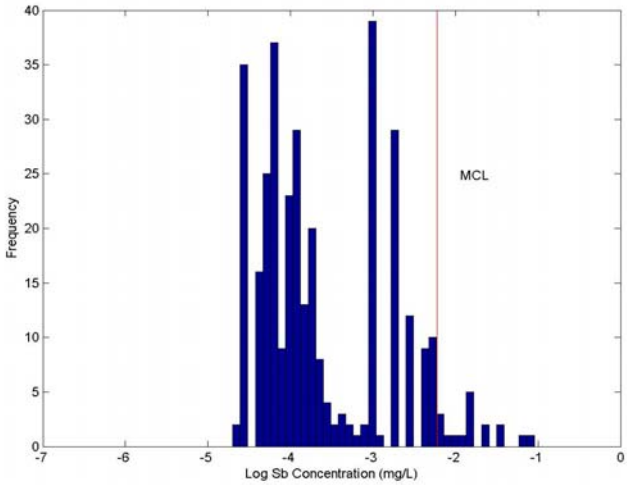

(f) Sb

Fig. 3.6 (Part 1)

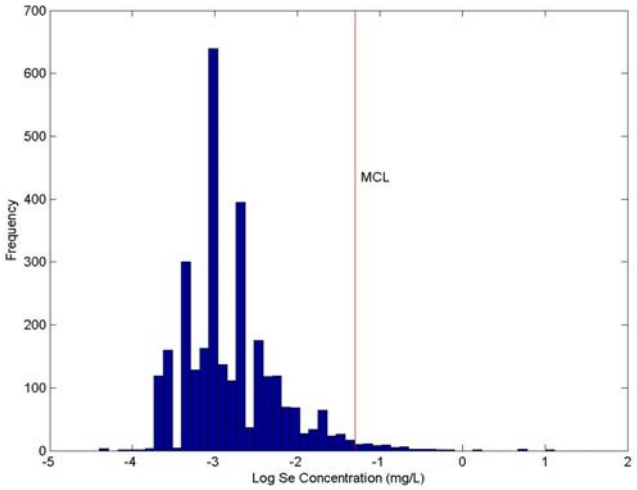

(g) Se

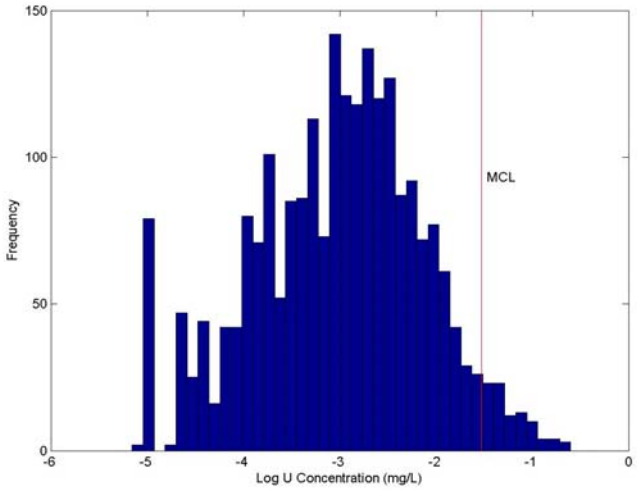

(h) U

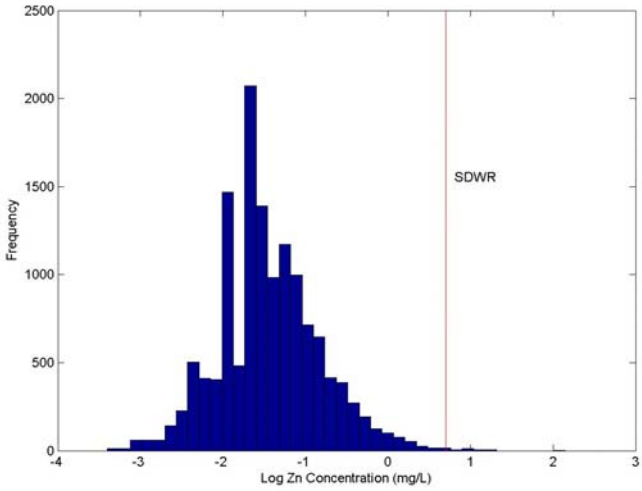

(i) Zn

Fig. 3.6. Histograms showing the concentration distributions of selected hazardous constituents in more than 38,000 analyses of potable groundwaters in the United States. MCL signifies the maximum contaminant level for each constituent. SDWR stands for secondary drinking water regulation.

The histograms reported here are plotted without regard to analytical method or accuracy. All histograms are characterized by isolated bins with anomalously high populations. These bins contain those analyses with "round number" concentrations, such as 0.001 mg/L or 0.002 mg/L, considered to be stemming from analytical artifacts, as discussed in Section 3.3.5.

Table 3.8. Hazardous inorganic constituents with EPA-specified Maximum Contaminant Levels (MCLs)

Contaminant	MCL (in mg/L)	MCL (in ppb)
As, arsenic	0.01	10
Ba, barium	2	2000
Cd, cadmium	0.005	5
Hg, mercury	0.002	2
Pb, lead	0.015	15
Sb, antimony	0.006	6
Se, selenium	0.05	50
U, uranium	0.015	15

The majority of the histograms in Figure 3.6 show concentrations ranging over three to five orders of magnitude. Apart from the analytical artifacts (see Section 3.3.5), the large spread might be attributed to several causes:

1. The element concentration in the aqueous phase may not be controlled by a mineral of which the element is an essential component, meaning a saturation state has not been reached. The aqueous concentration is instead determined by the element concentration in solid solution, on ion exchange sites, or on surface complexation sites, or any distribution between all three.
2. Variations in the bulk chemistry of the system may affect either the total mass of the element in solution, or may impact mass action controls.
3. Different minerals of which the element is an essential component control the concentration in solution.
4. One or more of the components of solubility-controlling minerals may vary naturally over a large range of concentrations, due to, for example, variations in the oxidation state.
5. Large ranges in pH or the presence of complexants may lead to large ranges in saturation concentration of the element in the aqueous phase.
6. Some samples might be contaminated through some form of accidental anthropogenic intervention.

The large aqueous concentration ranges displayed by the selected trace elements highlights the need for a thermodynamic analysis of the data. By calculating the thermodynamic potentials, it is possible to establish which minerals may control the solubility of an element. If such calculations show that no mineral containing that element as an essential component controls solubility, then other minerals may have to be considered, i.e., those minerals which incorporate the element in solid solution, on exchange sites, or on surface complexation sites. The thermodynamic aspects of this problem are discussed further in Section 3.4.5. The lack of saturation control of a hazardous inorganic constituent by a pure mineral of fixed stoichiometry containing that constituent as an essential component could lead to variability in aqueous concentrations that reflects the bulk composition of the aquifer host rocks, as appears to be the case with respect to As under oxidizing conditions (Smedley and Kinniburgh, 2008).

Every stable element in the periodic table, including the hazardous trace elements of interest in this study, possesses a natural crustal abundance (e.g., see Section 3.6, Table 3.17). Geological and geochemical processes can lead to concentration or depletion of certain elements, depending on their chemical properties and the extent and magnitude of the processes involved. No processes, whether natural or artificial, are 100 percent effective in separating and concentrating a given element. Therefore, residues of any element can always be found in all natural materials. As a consequence, all elements targeted for study in this report occur ubiquitously in soils, sediments, and aquifer rocks throughout the world. In the United States, metal concentrations in soils and surficial sediments vary greatly with region, and over ranges of concentration that approach four orders of magnitude. This is illustrated for Pb, As, Ba, and U in distribution maps taken from the USGS National Geochemical Survey database (USGS, 2008) (Figure 3.7).

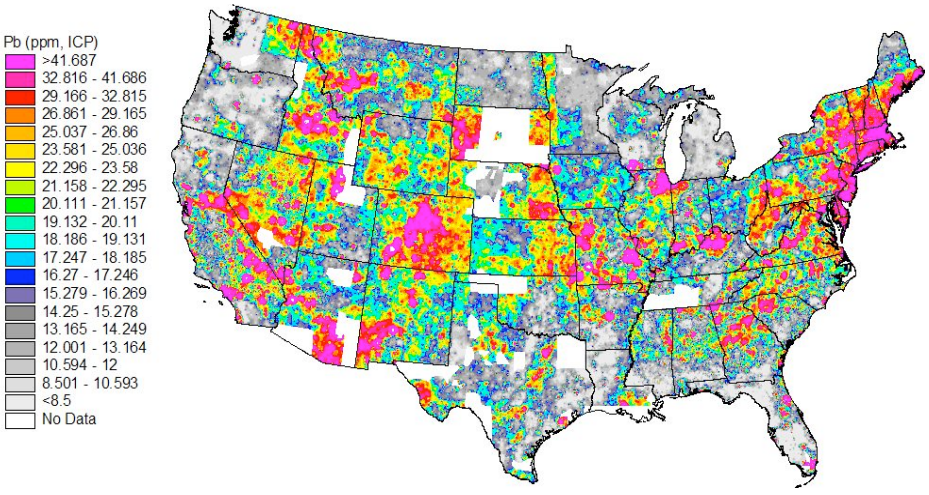

(a)

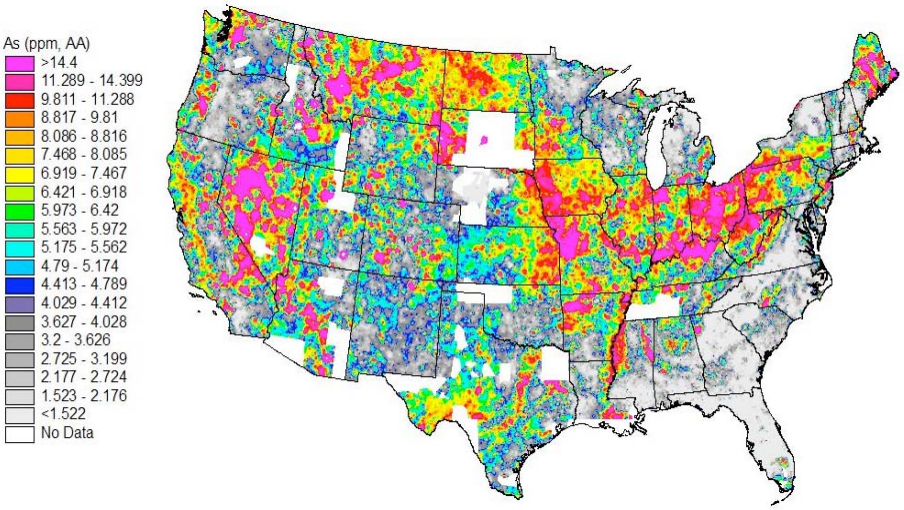

(b)

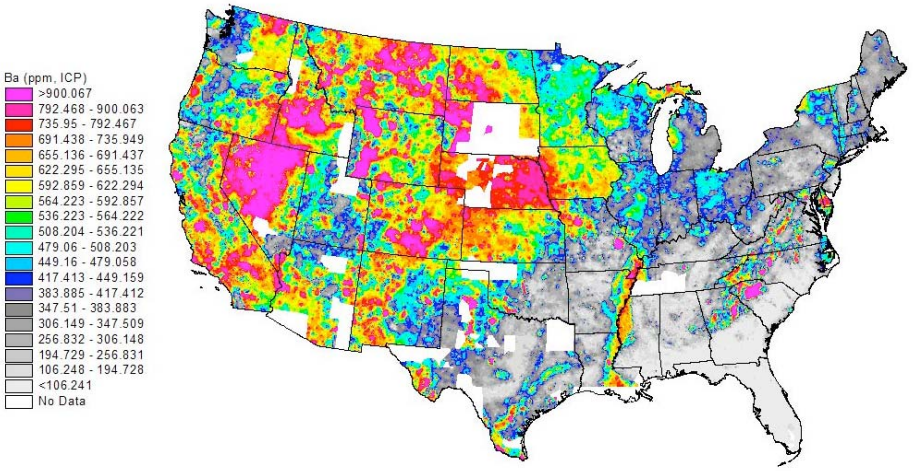

(c)

Fig. 3.7. (Part 1)

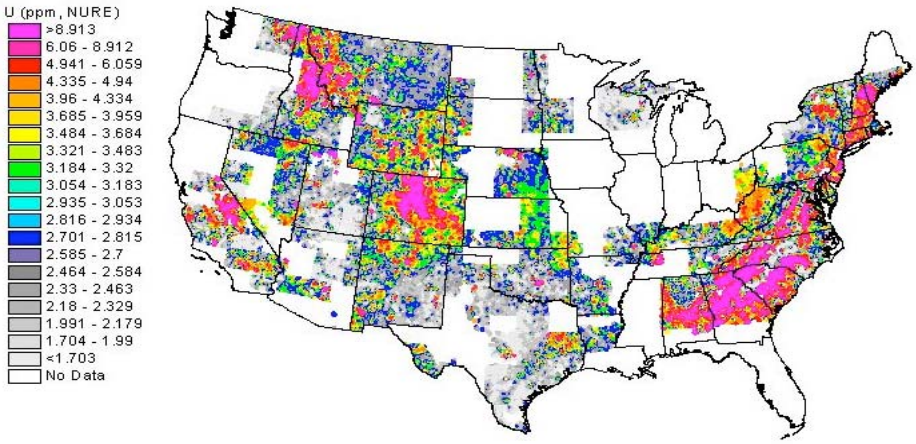

(d)

Fig. 3.7. Spatial distribution of hazardous constituents concentrations in soils and surficial sediments of (a) Pb and (b) As (c) Ba and (d) U in the forty-eight contiguous states, from National Geochemical Survey Database (USGS, 2008).

To check whether the aqueous concentrations might mirror the local natural surficial soil and sediment abundances of these same elements in the aquifer host rocks, they were plotted on a map of the 48 contiguous states, as illustrated in Figures 3.8. The respective aqueous and soil/sediment distributions for each element show a weak correlation, which can be a result of natural and anthrophogenic impacts. We should note that all groundwaters would exhibit small (mostly below MCLs), but non-zero concentrations of hazardous inorganic constituents if measured with sufficiently sensitive analytical techniques, as a corollary of the assertion that these constituents also occur ubiquitously in soils, sediments, and aquifer rocks throughout the United States and elsewhere in the world. Differences between the aqueous and soil/sediment distributions may be caused by sediment transport, climatic variations leading to differing degrees of constituent retention in soils, or localized anthropogenic modifications, such as the environmental dispersion of Pb from vehicular exhausts or battery recycling facilities, river and lake contamination with mercury from chemical plants producing sodium hydroxide, or the application of phosphate fertilizers or gypsum soil amendments containing elevated concentrations of uranium. In each case, elevated surficial concentrations of these elements, and others might be observed in the absence of subsurface aquifer contamination. Modification of aquifer chemistry due to surficial anthropogenic contamination would depend on many factors such as leaching and transport rates, recharge locations, subsurface hydrogeologic conditions, the

chemical properties of the transported elements, and withdrawal rates from potable aquifers. Such complexities can be elucidated only through case-by-case examination of specific aquifers, and not through a generalized review.

Close examination of Figures 3.7 and 3.8 reveals clearly that the weak correlation between aqueous and soil/sediment distributions is in part caused by inconsistencies in sampling density and use of analytical methods. The water quality analyses are sparsely distributed in many parts of the country, while differing analytical methods on solid and aqueous samples were inconsistently applied from state to state and regionally. For example, as pointed out in Appendix B1, the "hot spots" of measurable Pb concentrations in Figure 3.8(a) are clearly correlated to states or regions where large numbers of high-quality analyses (i.e., with low enough detection limits) have been conducted. In contrast, states or regions with no or only few detectable Pb concentrations in Figure 3.8(a) correspond to locations with either no measurements or analyses with insufficient detection limits.

A better correlation appears evident between different hazardous constituents in the aqueous samples than between aqueous and solid samples for a given hazardous constituent. For example, evidence for a "hot spot" of elevated Pb concentrations in the states of Illinois and Iowa is duplicated for As and barium. The origin and occurrence of these observed anomalies has been well documented by Goldhaber et al. (2003).

The distribution of U in Figure 3.8 appears to differ from Pb, As, and Ba. This may reflect the proximity of weathering igneous granitic rocks, which are commonly enriched in U. It is likely that the dissolved species is UO_2^{++}, since minerals containing this cation are relatively soluble, thereby preventing saturation control. The regional variation in metal concentration may also reflect variations in aquifer chemistry rather than lack of saturation control. Only a thermodynamic analysis can help resolve this uncertainty, which points to the need of conducting a distribution-of-species analysis of the selected groundwaters (Section 3.4.5).

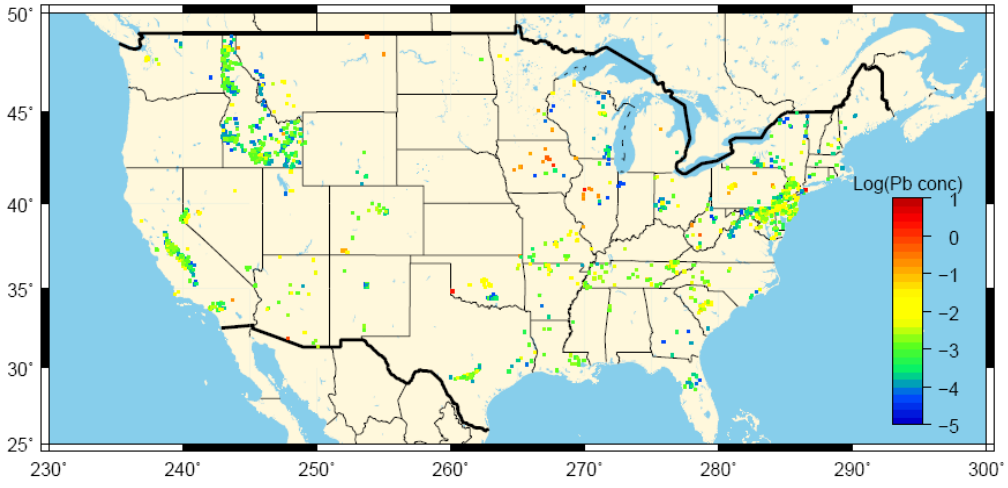

(a)

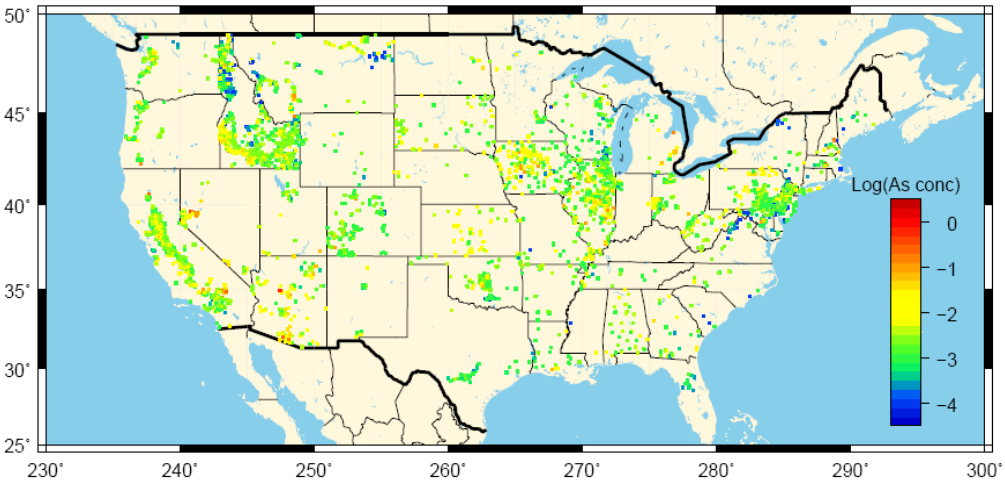

(b)

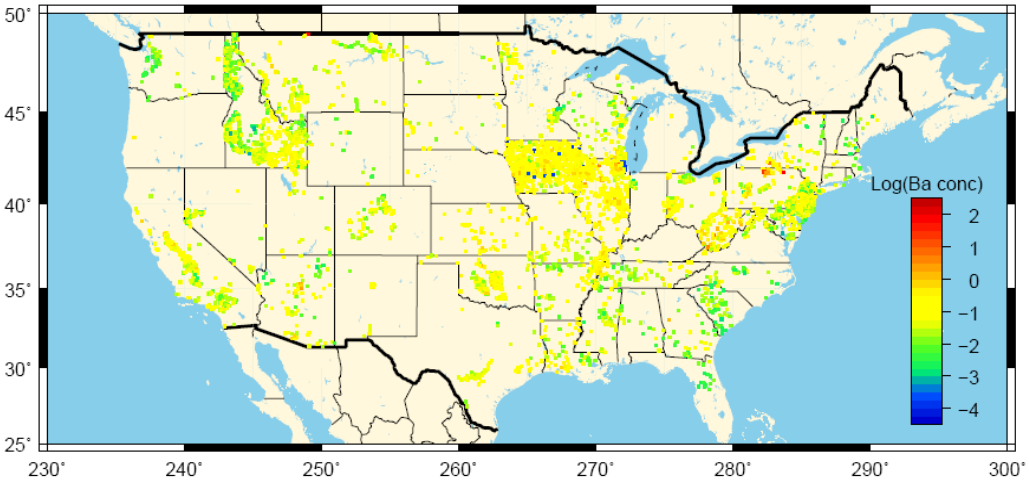

(c)

Fig. 3.8. (Part 1)

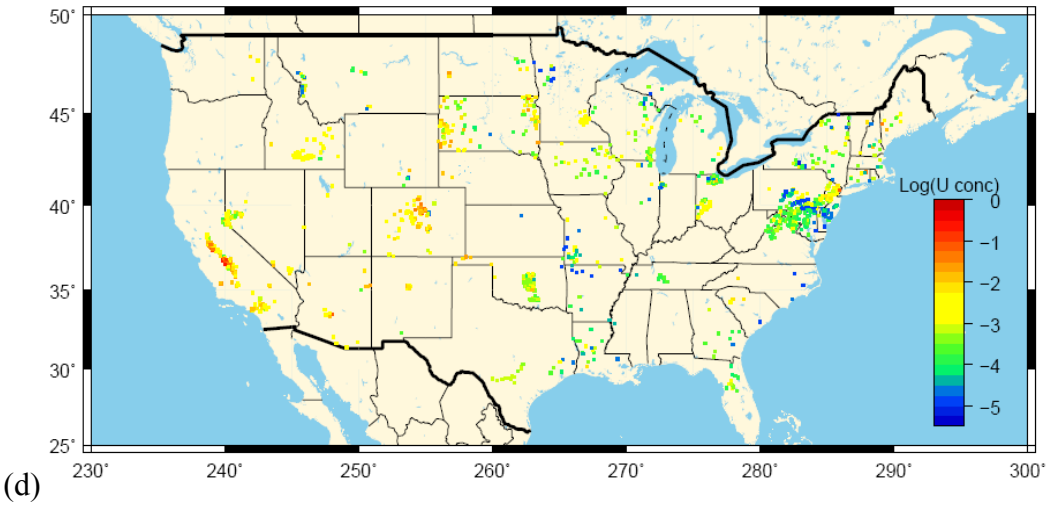

(d)

Fig. 3.8. Spatial distribution of samples with elevated aqueous concentration (Log mg/L) of (a) Pb, (b) As (c) Ba and (d) U in the forty-eight contiguous states. The plotted concentrations were drawn from more than 38,000 groundwater quality analyses downloaded from the National Water Information System Database (NWIS).

3.3.4 Detection Limits of Hazardous Inorganic Constituents in Groundwater

The NWIS database has been compiled over a number of years, during which time newer, more accurate, and more precise analytical methods have supplanted earlier methods. Several of the earlier analytical methods were insufficiently sensitive to provide quantitative measurements of the concentrations of several of the hazardous constituents under investigation in this report. Even the most sensitive methods currently in use are not necessarily sufficiently sensitive in all cases to provide quantitative measurements. Some idea of the limitations of the methods can be gleaned from the percentage of analyses that were successful in providing a quantitative measurement. This percentage also provides a measure of the concentration range expected for a given constituent. For example, if the percentage of measurable values is 50%, we can expect that the most frequent concentration of that constituent is at or near the detection limit. If the value is only 20%, then it can be expected that the most frequent concentration is significantly below the detection limit, although an approximate idea of its value might be estimated from extrapolation of the observed tail providing the upper-bound of the dispersion profile.

In Table 3.9, we have summarized the percentage of samples with measurable concentrations (above the detection limits) compared to all samples taken for the most sensitive analytical methods. For each analytical method, a range of detection limits arises, due to variations in sample quality, background contamination, and other factors that might influence analytical precision and accuracy. A complete tabulation of all analytical methods used, their various detection limits, and the number of analyses recording measurements below and above the limits of detection are given in Appendix A in Tables A1(a)–(i). The different analytical methods are referred to using code names, e.g., PLM43, which refers to metal analyses on unfiltered water conducted with ICP-MS, one of the more sensitive methods in routine use. Descriptions of the analytical methods are provided in Appendix A in Table A2. Table 3.9 suggests that measurable concentrations are frequently observed in the groundwater samples, ranging from as low as 17% of all samples analyzed using PLM47 for Cd to as high as 96%, 97% and 94% of samples analyzed for barium, uranium, and zinc, respectively. These findings are a valuable adjunct in interpreting the thermodynamic analysis of water quality data in Section 3.4.

Table 3.9. Percentage of samples with measurable concentrations of hazardous inorganic constituents in groundwater samples analyzed with the most sensitive analytical method

Contaminant		Analytical Method Code*	Reported Range of Detection Limits (mg/L)	Percentage of Samples above Detection Limit (%)
Arsenic	As	PLM10 PLM40	0.00012 0.0002 – 0.0009	92 87
Barium	Ba	PLM43	0.0002 – 0.001	96
Cadmium	Cd	PLM43 PLM47	0.00004 – 0.001 0.00004 – 0.001	24 17
Mercury	Hg	CV013	0.0001 – 0.001	12
Lead	Pb	PLM43 PLM48	0.0001 – 0.004 0.00006 – 0.001	49 82
Antimony	Sb	PLM43	0.00005 – 0.002	18
Selenium	Se	PLM40	0.0003 – 0.002	58
Uranium	U	FL006 FL007	0.0004 0.00001	69 97
Zinc	Zn	PLM43	0.0006 – 0.010	94

* See Tables A1 and A2 in Appendix A.

3.3.5 Analytical Artifacts Affecting Measurements of Hazardous Inorganic Constituents in Groundwater

The distributions of several of the histograms shown in Figure 3.6 reflect artifacts introduced by the differing accuracy and sensitivity of the analytical methods used, rather than to some underlying chemical control affecting groundwater composition. This issue appears to be most prominent in analyses for Cd, Hg, Sb and Se, as evident by the presence of isolated bins with anomalously high populations, although the effect is also noticeable in the case of As and Pb. The elements Ba, U, and Zn appear to be relatively unaffected, because most analytical methods used over time have been sufficiently sensitive to record quantitative values of concentration.

As noted in the preceding section, the analytical methods used, their various detection limits, and the number of analyses recording measurements below and above the limits of detection, and descriptions of the analytical methods are given in Appendix A. The NWIS database provides the respective detection limits only for those samples with concentrations reported as "less than"; in all other cases, measurable concentrations are reported in the database without further mentioning of the specific detection limit of the analytical method. Using Pb as an example (see Table A1(e)), we have obtained almost 2,000 samples with Pb concentrations analyzed using method PLM43. About 1,000 of these are non-detects, with 700 reporting less than 0.001 mg/L (1 ppb) and 280 reporting less than 0.0001 mg/L (0.1 ppb), indicating that different ICP-MS techniques with different detection limits have been utilized. The other half of about 1,000 samples reports measurable concentrations. The database, however, does not report the specific detection limits for these samples. In Appendix B2, we make a further attempt to evaluate the significance of analytical artifacts for the elements of interest.

An example in which almost all analyses could be artifacts is illustrated by the distribution of Cd analyses. Inspection of Figure 3.6(d) shows that there are essentially two sets of measurements corresponding to log concentration ranges of -4.6 to -3.0 (log mg/L) and -3.0 to -1.0 (log mg/L), respectively. Each set of analyses starts with an initial high frequency, apparently corresponding to the detection limit for most of the analyses, which then falls off with increasing concentration

until a relatively low frequency is recorded approximately one log unit above the detection limit. The question arises whether any of these data, even those provided by the most sensitive methods, can be used to determine thermodynamic controls for Cd. Table A1(c) shows that cadmium has been measured with methods PLM43 or PLM47 in many cases, with detection limits as low as 0.00004 mg/L. In the former method, 24% of the analyses yielded detectable values, whereas the latter yielded 17%. These low levels of detection independently suggest that current analytical methods for Cd may be of marginal utility, and that identification of minerals controlling the solubility of cadmium from the evaluation of groundwater data could be problematic.

We may compare these detection limits to the expected maximum concentration of cadmium in groundwater when in equilibrium with a solubility-controlling mineral. As discussed in Section 3.4.5 below, geochemical calculations using the most current thermodynamic data for greenockite (CdS), which would yield the maximum Cd concentration in solution for a representative reducing potable groundwater, show that the predicted concentration should be about 2×10^{-4} mg/L in the presence of a pyrite/goethite redox couple (see Figure 3.48), or five times the detection limit of the most sensitive analytical methods currently in use. This suggests that the saturation concentration should be detectable, provided that the analytical artifacts described above do not interfere, and that the predicted concentration is correct. However, the uncertainty associated with the predicted concentration is about ± 0.5 log units. Furthermore, Cd^{+2} is likely to substitute as a minor component in either sphalerite (ZnS) or galena, because of its low absolute abundance in crustal rocks, and therefore its concentration in groundwaters could be significantly lower than the predicted saturation concentration of greenockite.

Of particular concern is the adequacy of analytical methods for Pb and As, because the interpretation of thermodynamic controls governing these elements are at the center of the current project for modeling the impact of CO_2 intrusion on ambient concentrations in potable groundwaters. For example, Figures 3.6(a) indicates that similar artifacts are operative for the less sensitive analytical methods measuring Pb, i.e., those with detection limits of 0.001 mg/L and above. The analytical method PLM43, however, for which a detection limit of 0.0001 mg/L

(or 0.1 ppb) is reported in a large number of cases (see Table A1(e)), seems to be of sufficient sensitivity to measure reliable values.

In Figure 3.9, to check this assumption, we have plotted a histogram with measured concentrations using only method PLM43. For reference, the predicted equilibrium log concentration (mg/L) for Pb^{+2} is –4.0 (i.e., 0.0001 mg/L or 0.1 ppb), calculated assuming that galena coexists with pyrite and goethite in a typical reducing groundwater (Figure 3.44) (using the solubility product for galena, $K_{s,}$ based on thermochemical measurements described in Appendix D in Table D1). This concentration is incrementally higher than the lowest detection limit of analytical method PLM48 (0.00006 mg/L), which appears to be situated close to a local maximum in the frequency of Pb concentration values. This would indicate that, indeed, the aqueous concentration of Pb in these samples is likely to be controlled by the presence of galena. This supposition is reinforced by the observation that of the two methods, in 49% of the analyses by PLM43, measurable values of Pb were detected with a detection limit of 0.0001 mg/L, whereas with PLM48, 82% yielded measurable values with a detection limit of 0.00006 mg/L. Unfortunately, reported analyses using the less sensitive method in PLM43 (with a detection limit of 0.001 mg/L) appear to display the same characteristics as those analytical methods for Cd and Hg, showing isolated bins with anomalously high populations. It would therefore be desirable to eliminate from further consideration those reported analyses using the less sensitive method. However, as discussed above, the detection limit for each analysis with measurable concentrations is not reported in the NWIS database, and therefore, the two methods cannot be clearly discriminated.

In the case of As, a similar evaluation to that shown for cadmium or Pb cannot be conducted: as in the majority of potable groundwaters, the concentration of As in solution is determined in reducing groundwaters not by a mineral of fixed stoichiometry, where As is an essential component, but by solid solution substitution of the FeAsS (arsenopyrite) component in pyrite. Consequently, the concentration of As in solution can vary, depending on the local abundance of As in the aquifer host rock and an equilibrium state established between the arsenopyrite solid solution, adsorption sites on host rock mineral surfaces, and the aqueous phase. A

thermodynamic analysis conducted elsewhere in this report (Section 3.4) confirms that no solid phase where As is an essential component controls the concentration of As in the potable groundwaters evaluated in this report The frequency histogram for arsenopyrite saturation indices shows that SI values are negative with a maximum frequency at SI = -3 (see Figure 3.34). Furthermore, no other As minerals were identified that showed higher SI values than those of arsenopyrite. Thus, the evidence is quite convincing that the As concentration in solution is controlled by the binary (metastable) solid solution of the FeAsS component in pyrite in the majority of groundwaters. A comparison can be made between predicted concentrations and those actually measured by developing a thermodynamic model describing the FeS_2-FeAsS binary solid solution, and calculating the metastable equilibrium As concentrations in typical groundwaters from that model. Such an analysis would also require determining the magnitude of the solid solution in pyrite samples from representative potable water aquifers. Absent the current feasibility of such an exercise, it is considered sufficient in this study to estimate the As activity in equilibrium with the arsenopyrite (FeAsS) solid solution component and use this value in subsequent equilibrium and reactive-transport modeling studies.

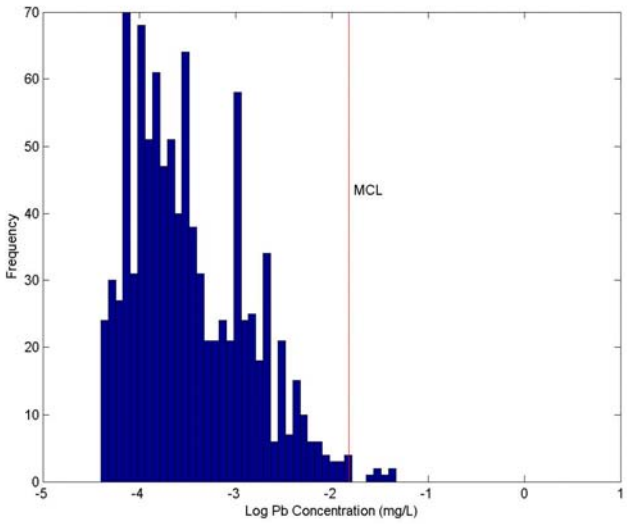

Fig. 3.9. Frequency distribution of Pb analyses in groundwaters using the analytical method PLM43 (ICP-MS). For reference, the predicted equilibrium concentration for Pb^{+2} is 0.0001 mg/L (or -4 in log mg/L), calculated assuming that galena co-exists with pyrite and goethite in a typical reducing groundwater.

Below, we examine the ability of the most sensitive analytical methods to arrive at quantitative As determinations in the potable groundwaters evaluated in this study. The most sensitive analytical methods reported are PLM10 and PLM40, both of which utilize ICP-MS, and which have reported detection limits of 0.00012 and between 0.0002 and 0.0009 mg/L respectively (Appendix A, Table A1(a)). For the former analytical method, the percentage of detectable concentrations out of the total number of determinations is 92%, whereas for the latter, it is 87%, indicating that both methods are sufficiently sensitive for quantitative detection of As in the majority of potable waters studied. Figure 3.10 illustrates the concentration frequency histogram for As using these two analytical methods. It is evident that the maximum concentration frequency occurs at Log As =-2.5 (mg/L), or about 0.003 mg/L, which confirms that PLM10 and PLM40, in particular, are suitable analytical methods.

In conclusion, it can be stated that for several of the inorganic hazardous constituents under investigation, past and even current analytical methods of measuring groundwater concentrations are insufficiently sensitive for the purpose. This is clearly the case for cadmium, possibly also for mercury, antimony, and selenium. Reported values close to the detection limit may be subject to spurious readings, the frequency of which appears to decline in a log-linear manner with increasing concentration (Appendix B2). An explanation for this behavior is at present not known, but may be dependent on the analytical method used. Eliminating the spurious values is not presently feasible, because there is no basis for separating spurious from real values. A partial solution is to eliminate from consideration all analyses obtained using those methods that, on the basis of geochemical considerations, are clearly out of range. This approach gives reasonable results in the cases of Pb and As, for example. Barium, uranium, and zinc are of less concern, as most analytical methods used over time have been sufficiently sensitive to record quantitative values of concentration. Further discussion on the geochemical evaluation of thermodynamic controls in relation to the plausibility of analytical measurements of certain hazardous constituents is given in Section 3.4.

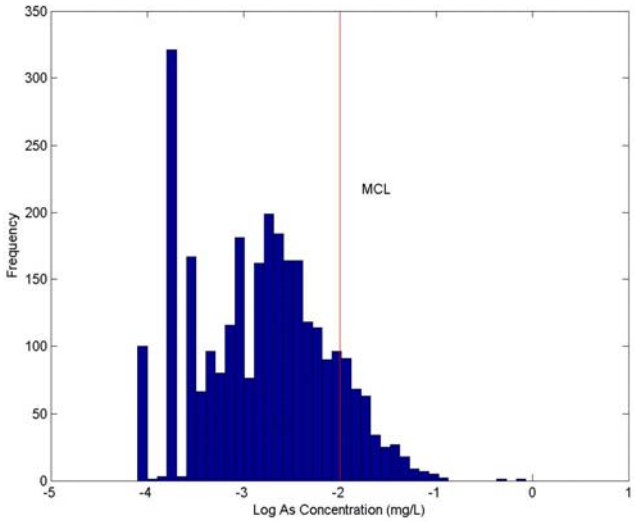

Fig. 3.10. Frequency distribution of As analyses in groundwaters using the analytical methods PLM10 and PLM40 (ICP-MS).

3.4 Thermodynamic Analysis of Potable Groundwater

This section describes the identification of the thermodynamic controls that may influence the concentration and distribution of the selected hazardous inorganic constituents in the groundwater. We start in Section 3.4.1 with a description of the procedure for calculating the saturation indices of selected mineral hosts for hazardous constituents for the large number of groundwater quality analyses available from the NWIS database. Before this procedure can be applied, however, necessary modifications must be made to the thermodynamic database (Section 3.4.2), the integrity of the chemical analyses must be examined by evaluating charge imbalance (Section 3.4.3), and the groundwater redox state must be defined (Section 3.4.4). Results from the thermodynamic analysis are given in Section 3.4.5. Finally, the effect of redox state on the saturation concentration of Cd, Pb, and Zn is examined in Section 3.4.6.

We selected the distribution-of-species code, EQ3/6 V.7.2b (Wolery et al., 1993), to calculate the saturation indices, as well as other parameters of interest such as ion activity ratios, which are related to the chemical potentials of components in the aqueous phase, Eh, charge balance, and the distribution of aqueous complexes in solution. This code has an associated database of

solubility products for solid phases and dissociation constants of aqueous species, data0.ymp.R4. The database was selected primarily because it had undergone several fairly recent revisions, especially with respect to the correction of errors in solubility products for silica polymorphs and rock-forming silicate minerals (Apps, 2004). Nevertheless, we realized that the database contained substantial amounts of obsolete and erroneous data, in some cases because data had been drawn from incompatible secondary data sources that were not checked for internal consistency. Extensive revisions were therefore undertaken in this study to rectify all relevant deficiencies, as further discussed in Section 3.4.2 below.

To conduct thermodynamic analysis of a large number of groundwater data sets (more than 38,000 water-quality analysis for a full set), we developed automated procedures for selecting and entering species concentrations in the input file of EQ3/6. The procedure involves entry of chemical analyses of each constituent in the EQ3 input file. When possible redundancies occurred, preferred analyses were chosen according to a hierarchical set of preferences. EQ3 was then executed, selected parameters were extracted and compiled, and the process was repeated for the next chemical analysis until all or a selected subset of samples was evaluated. If, for some reason, convergence was not obtained, the diagnostics were extracted and recorded for further review. The entire calculation was very rapid; i.e., the complete database of selected groundwater analyses from the National Water Information Database could be processed in a few hours.

3.4.1 Calculation of Activities and Saturation Indices

The saturation state is related to the Gibbs free energy, ΔG_r, associated with the formation of the mineral, thus

$$\Delta G_r = RT \ln \frac{a}{a_0} = RT \ln \Omega \qquad (3.1)$$

where R is the gas constant (units), a and a_0 are, respectively, the mean molar activity of the participating species in the aqueous phase and the mean molar activity of the species in equilibrium with the mineral, and Ω is saturation state, given by:

$$\Omega = \frac{a}{a_o} = \left(\frac{IAP}{K} \right)^{\frac{1}{\upsilon}} \tag{3.2}$$

where IAP is the Ion Activity Product, K is the equilibrium constant, and υ is the number of atoms in the molecular unit. In this study, we follow the usual convention of defining the saturation index, SI, as:

$$S.I. = \log \Omega \tag{3.3}$$

3.4.2 Modification and Augmentation of the Thermodynamic Data Supporting the Codes EQ3/6 and TOUGHREACT

A critical requirement for meaningful interpretation and evaluation of hazardous-inorganic-species behavior in groundwaters is a realistic thermodynamic description of the complete chemical system. The minimum thermochemical parameters needed for such a description include $\Delta G^0_{f,P_r,T_r}$, $S^0_{P_r,T_r}$, $C^0_{P_r}$ and $V^0_{P_r,T_r}$ (these parameters are, respectively, the Gibbs free energy and entropy at the reference pressure and temperature (298.15 K, 1 bar), heat capacity at 1 bar as a function of temperature, and the molar volume at the reference temperature and pressure) for pure solid phases (i.e., minerals), the corresponding partial molal properties of dissolved species, i.e., $\Delta \overline{G}^0_{f,P_r,T_r}$, $\overline{S}^0_{P_r,T_r}$, $\overline{C}^0_{P_r,T_r}$ and $\overline{V}^0_{P_r,T_r}$, and an electrolyte model to describe the thermodynamic activities of the dissolved species in solution as a function of ionic strength.

The distribution-of-species code, EQ3/6, used in this study for thermodynamic analyses, contains a database, Data0.dat, listing solubility products and dissociation constants for minerals and aqueous species. The version of the Data0.dat used in this study was qualified for use under the

U.S. Department of Energy's Yucca Mountain Project, and is not fully suited for the demanding requirements of the current study. Much of the contained information is either irrelevant or has not been revised in the light of more recent data in the published literature. Data of critical importance to interpreting the behavior of the hazardous constituents selected for this study were never incorporated. We have therefore reviewed and, where necessary, revised or augmented the thermodynamic database. For consistency, we have conducted similar modifications to the database employed by TOUGHREACT, the reactive transport simulator utilized in Section 4. Because potable groundwaters are dilute and their ambient temperatures and pressures are relatively close to defined standard state conditions, a number of simplifications and approximations are possible in the derivation of thermodynamic data for this study. When necessary, simple corrections can be made to account for deviations in temperature or ionic strength. The methods used and approximations made in the relevant derivations are discussed at greater length in Appendix C.

Augmentation of the thermodynamic data for solid phases consists of the following steps:

1. Review the literature to find information on the thermodynamic parameters of solid phases of interest, based on calorimetric, thermochemical, phase equilibrium or solubility measurements, and crystallographic data. Where necessary, raw data must be processed to retrieve the needed parameters.
2. Reconcile data to ensure that all thermodynamic data are internally consistent, i.e., are referenced to the same standards.
3. Enter corrected data in the thermodynamic processing code, SUPCRT (Johnson et al., 1992).
4. Generate discrete log solubility product values, logKs, at 0, 25, 60, and 100°C, using SUPCRT.
5. Process the SUPCRT output data in a format suitable for entry of solid phases in the Data0.dat database of EQ3/6.

The processing of thermodynamic data for aqueous species is analogous. However, to maintain consistency with the SUPCRT format for aqueous species, parameters for the HKF (Helgeson-

Kirkham-Flowers) "Equation of State (EoS)" thermodynamic model (Tanger and Helgeson, 1988) were also calculated, where feasible:

1. Review of the literature to find information on the thermodynamic parameters of aqueous species of interest, based on calorimetric, thermochemical, or solubility measurements. Where necessary, reported dissociation constants are processed to retrieve the needed parameters.
2. Reconcile data to ensure internal consistency, i.e., reference data to the same thermodynamic standards.
3. Augment the basic data derived in Step 1 to calculate S, and the C1 and C2 parameters of the HKF EoS. The a1–a4 parameters of the HKF EoS are not needed for the purposes of this study.
4. Enter corrected data in SUPCRT.
5. Generate discrete log dissociation constant values, logKdiss, at 0, 25, 60, and 100°C, using SUPCRT.
6. Process SUPCRT output data in a format suitable for entry in the Data0.dat aqueous species database of EQ3/6.

The entire scope of the thermodynamic data enhancements is indicated in Table 3.10.

It should be noted that the inclusion of certain minerals in the database is made with the understanding that the perturbation of aquifer systems—either resulting from the ingress of oxygenated groundwater, aggressive anaerobic bacterial reduction, or from the intrusion of CO_2, or other anthropogenic perturbations—leads to the precipitation of metastable minerals that are finely crystalline or amorphous and which possess substantial specific surface areas. The large specific surface areas form important reactive adsorption sites that adsorb trace elements, including those hazardous constituents under study. In reactive transport modeling, the precipitation of metastable phases, and concurrent changes in specific surface area and adsorption capacity, can be accounted for using appropriate equations to describe the heterogeneous kinetics.

Table 3.10. Scope of modifications and augmentations to thermodynamic database

Rock forming and accessory minerals • Minerals participating in redox equilibria: – Ferric oxides and oxyhydroxides (ferrihydrite, goethite, lepidocrocite, hematite, ε–Fe2O3, maghemite) – Iron sulfides (pyrite, mackinawite, greigite, amorphous FeS) – Mixed oxide/sulfates (shwertmannite, green-rust) – Silicates containing Fe(II)/Fe(III), e.g. chlorite, smectite, illite • Carbonates (dolomite, ankerite, siderite, magnesite) • Silica polymorphs
Minerals that contain a hazardous constituent as an essential component and are likely to be stable under moderate to strongly reducing groundwater conditions • Arsenopyrite, arsenian pyrite, realgar, orpiment, symplesite (As) • Barite, witherite (Ba) • Greenockite, cadmoselite (Cd) • Cinnabar, tiemannite (Hg) • Galena, clausthalite (Pb) • Stibnite, kermesite, gudmundite, berthierite, antimonselite, (Sb) • Ferroselite, cadmoselite, tiemannite, clausthalite, antimonselite (Se) • Uraninite, coffinite, brannerite (U) • Sphalerite (Zn)
Minerals that contain a hazardous constituent as an essential component and are likely to be stable under oxidizing groundwater conditions • Scorodite, etc. (As). For a complete list, see Appendix C. • Barite, witherite (Ba) • Otavite, (Cd) • Quicksilver, calomel, etc. (Hg). See note. • Carbonates (cerussite, hydrocerussite, plumbonacrite, etc.) (Pb). For complete list, see Appendix C. • Senarmonite, valentinite (Sb). See note. • Other? (Se). See note • Uranophane, boltwoodite, weeksite, soddyite, etc. (U) • Hemimorphite, hydrozincite, smithsonite (Zn)
Aqueous carbonate species for major rock-forming components, e.g., Mg, Ca, Fe(II).
Aqueous carbonate species for Ba, Cd, Hg, Pb, U(IV,VI), Zn
Arsenite (As(III)) and arsenate (As(V)) species and complexes, antimonite (Sb(III)) and antimonate (Sb(VI)) species and complexes; selenite (Se(IV)) and selenate (Se(VI)) species and complexes
Sulfide and selenide complexes of As, Cd, Hg, Pb, Sb, Se, Zn and Fe(II)

Note: Not all potential solubility-controlling minerals have been listed or identified. Some minerals may not have been recognized, or the thermodynamic properties have not been determined. Some minerals may substitute in solid solution as a minor component in a more abundant thermodynamically stable phase under the considered redox conditions. In some cases, thermodynamic data were estimated with varying degrees of precision and confidence, using various estimation techniques as described in Appendices C, D, and E.

A possible complication is the common nonattainment of thermodynamic equilibrium between species participating in redox reactions in the aqueous phase. This problem is well known, and has been investigated previously (Lindberg and Runnells, 1984; Stefansson, 2003). Problems of interpretation in the current study also extend to equilibria involving aqueous species of As (0, III, V); Hg(0, II); Sb (II, IV, VI); Se (II, IV, VI) and U (IV, VI). Furthermore, some of the species in solution form complexes with S(II) (which is also capable of several higher oxidation states, principally IV and VI) and with Fe(II) (which can also be oxidized to Fe(III)). Added complexity arises through the precipitation of phases with components in differing oxidation states, e.g., ferric arsenite (tooeleite), and ferrous arsenate (symplesite). Both EQ3/6 and TOUGHREACT can incorporate nonattainment of homogeneous equilibrium. In both codes, the respective reduced and oxidized forms can be treated as separate nonreacting species. In the case of TOUGHREACT, the kinetics of transformation from oxidized to reduced forms or vice versa can be included in the model.

Finally, it should be recognized that hazardous constituents may co-precipitate to form minerals where two hazardous constituents are present as essential components. Examples are cadmoselite (SCdSe) or mimetite ($Pb_5(AsO_4)_3(Cl)$). A priori evaluation regarding the ranges and pH and Eh conditions where these minerals might be stable is difficult, the easy way out being to incorporate the solubility products of all of these minerals in the thermodynamic database of any model of the groundwater system.

Appendix C provides a detailed discussion of the thermodynamic data for both solid phases and aqueous species that were compiled for this study. The calculations performed to generate both the associated thermodynamic data and the relevant solubility products and dissociation constants are explained. In the discussion of results, it is noted where results are provisional, and how the inclusion of revised or otherwise missing data might impact the current findings.

3.4.3 Evaluating the Integrity of Water Quality Analyses

One of the first tasks in evaluating the groundwater data using EQ3/6 is to evaluate the integrity of the chemical analyses. A rule of thumb for testing the quality of a chemical analysis is to check the charge balance according to the following equation:

$$\frac{\sum cations - \sum anions}{\left|\sum cations\right| + \left|\sum anions\right|} \times 100 \qquad (3.4)$$

The analysis is normally considered acceptable if the charge imbalance is ≤5%. However, the EQ3/6 evaluation demonstrates that imbalances were quite substantial for many of the chemical analyses extracted from the NWIS database. The primary reason is probably the application of analytical data that fail to take into account the effects of CO_2 degassing and possible precipitation of calcium carbonate resulting from inadequate custodial preservation of sample integrity following field sampling and analysis, prior to laboratory determination of alkalinity. Most groundwaters are very dilute, so that the bicarbonate concentration contributes significantly to the charge balance. The bicarbonate concentration is related to the partial pressure of carbon dioxide as follows:

$$HCO_3^- = CO_2(g) + OH^- \qquad K = \frac{\left[P_{CO_2}\right]\left[OH^-\right]}{\left[HCO_3^-\right]} \qquad (3.5)$$

where the brackets [ ] represent activities of the enclosed species. When the equilibrium partial pressure of CO_2 is calculated from chemical analyses of most groundwaters whose integrity is assured, it is found that it is significantly higher than that found in the atmosphere, i.e., Log $P(CO_2)$ varies between –3 and –1 compared with –3.5 for atmospheric conditions (see Figure 3.17, below). Groundwater samples exposed to the atmosphere will therefore tend to degas, which usually leads to a corresponding upward shift in pH, supersaturation with respect to calcium carbonate, and eventual precipitation of calcium carbonate. This can be expressed by the following reaction:

$$2HCO_3^- + Ca^{+2} = CO_2(g) + CaCO_3(s) + H_2O$$

If the pH of a sample is measured in the field before degassing occurs, whereas the water is analyzed for bicarbonate content or alkalinity after degassing, a significant charge imbalance can be expected when calculating the distribution of species in the sample using the reported values for pH and carbonate content. Charge imbalance can furthermore be caused if the resulting supersaturation induces precipitation of calcium carbonate prior to measurement of alkalinity. Less significant charge imbalances may also result from failure to account for the temperature difference between the groundwater and that at which analyses are conducted.

The possible errors introduced as a result of unaccounted-for degassing and precipitation are illustrated in Table 3.11 for a typical groundwater containing a low concentration of dissolved solids, where it is assumed that the groundwater is in equilibrium with respect to calcite before sampling and analysis. In this table, seven changed states of the original sample, given in Column 3, are considered, together with certain assumptions made in interpreting the chemical analyses and their impact on calculated parameters. The "true" groundwater composition is described in Column 3 in terms of the measured analytical parameters (pH, HCO_3^- [alkalinity] and Ca) and the calculated parameters (calcite saturation index SI[calcite), Log P(CO_2) and charge imbalance), all listed in Column 1. The changed states are summarized in Columns 4–10, and are described as follows:

- Column 4. The groundwater is allowed to warm up to normal room conditions, i.e., T = 25ºC, resulting in a minor lowering of pH and slight supersaturation with respect to calcite.
- Column 5. The groundwater is exposed to the atmosphere at 25ºC and allowed to degas CO_2 until Log P(CO_2) = -3.5 (that of the atmosphere). The pH changes by approximately one unit, HCO_3^- falls, and the sample becomes significantly supersaturated with respect to calcite.
- Column 6. The degassed groundwater in Column 5 is allowed to re-equilibrate through precipitation of calcite. Both HCO_3^- and Ca fall substantially, and SI(calcite) returns to zero.
- Column 7. The effect on the calculated parameters is shown by assuming a pH measured at 25ºC in the field (Column 4) and a laboratory alkalinity determination after CO_2 degassing

(Column 5). SI(calcite) increases slightly, Log $P(CO_2)$ is higher than that in the formation (Column 3), and the charge imbalance rises to +6% of the total, a value that would, according to standard criteria, make the overall analysis marginally unacceptable.

- Column 8. The effect of accepting a field alkalinity determination and a laboratory pH after degassing CO_2 is shown. SI(calcite) is strongly supersaturated, and Log $P(CO_2)$ is nearly one log unit lower than the true value in the formation, even though the charge imbalance remains relatively small.

- Column 9. The field pH measurement is accepted together with an alkalinity determination after calcite precipitation, but assuming that Ca was measured on an aliquot acidified in the field prior to sample degassing and precipitation of calcite, as is standard practice. This leads to a relatively modest apparent undersaturation with respect to calcite and slightly lower $P(CO_2)$, but a drastic and normally unacceptable charge imbalance of +27%.

- Column 10. The field pH measurement is accepted together with the alkalinity determination after CO_2 degassing. SI(calcite) and Log $P(CO_2)$ are moderately affected, compared with the true values in the field, and charge imbalance increases by about +6%.

Table 3.11. Errors introduced through inadequate preservation of sample integrity deficiencies.

Parameter	**Unit**	**Ground water with calcite at 10°C**	**Ground water raised to 25°C**	**Degassed to $P(CO_2)$ (atm)**	**Degassed to $P(CO_2)$ (atm) & calcite pptn**	**Field pH; lab HCO_3-**	**Lab pH; degassed to $P(CO_2)$ atm. Fld HCO_3^-**	**Field pH Lab Ca After calcite pptn**	**Field pH HCO_3^- after degas.**
pH	-	7.739	7.611	8.694	8.548	7.611	8.694	7.611	7.611
HCO_3^-	mg/L	227.29	227.29	197.06	114.81	197.81	227.29	114.81	197.06
Ca^{++}	mg/L	37.669	37.669	37.669	6.394	37.669	37.699	37.669	37.669
SI (calcite)	-	0.000	0.093	+1.132	0.000	+0.038	+1.130	-0.184	+0.036
Log $P(CO_2)$	Bar	-2.5	-2.286	-3.5	-3.5	-2.346	-3.372	-2.581	-2.348
Charge imbalance	% of total	0.000	0.000	0.000	0.000	+6.00	-5.73	+27.4	+6.16

Other constituents (mg/L): Na^+, 45.8; K^+, 5.04; Mg^{++}, 2.01; Cl^-, 7.14; SO_4^{-2}, 18.40; SiO_2(aq), 60.97.

A complication arising from low concentrations of dissolved solids typical of potable groundwaters is that the pH may be poorly buffered and subject to effects of contamination and instrumental drift. Thus, both pH measurements and alkalinity (or bicarbonate or carbonate) analyses may be subject to error. Unfortunately, the two parameters are interdependent, and therefore it is not possible to discriminate directly whether they may be erroneous.

Analytical chemists are aware of the fugitive nature of CO_2 and the tendency of pH to drift with time. Therefore, efforts are often made to measure both pH and alkalinity in the field, with additional backup analyses of these parameters (and/or bicarbonate or carbonate) in the laboratory. Because environmental conditions in the field are less well controlled than in the laboratory, field measurements can be less accurate, though more representative of actual conditions prior to sampling. Chemical analyses of groundwaters stored in the NWIS database commonly report both field and laboratory measurements for these parameters, sometimes additionally on filtered or unfiltered samples. Therefore it is necessary to choose those measurements of pH, alkalinity, or bicarbonate/carbonate that are most likely to provide accurate results during subsequent EQ3/6 calculations.

The problem of selecting an appropriate value for alkalinity is further complicated by the multiplicity of different analytical methods used to measure alkalinity, bicarbonate, or total carbonate concentrations over the last decades. The NWIS database contains no less than 20 listed analytical procedures for alkalinity, 12 for HCO_3^- and 17 for CO_3^{-2}. Their persistence in the NWIS database has a long history. Over time, USGS and EPA have attempted to standardize procedures and have supplanted earlier methods with improved techniques (Alexander et al., 1988). However, the legacy of earlier techniques remains embedded in the NWIS database. To guide the choice of analytical methods, we developed a hierarchical 32-step protocol for the selection of HCO_3^- (and CO_3^{-2}) or alkalinity data from the database. All data was transformed to equivalent HCO_3^- (mg/L) for entry in the EQ3 input file.

Earlier versions of the EQ3 code (Wolery, 1983) possessed the option of entering the titration alkalinity directly as an entry in the input file, but this option was subsequently discontinued (Wolery, 1992, p. 21-27). The proposed solution advocated by Wolery (1993) involved the

calculation of the equilibrium concentration of CO_2(aq) in the presence of HCO_3^-, then summing the molar concentration of CO_2(aq) and the incremental titration equivalents of HCO_3^- and CO_3^{-2}, respectively for each analysis, and finally entering the appropriate total concentration of HCO_3^- for each analysis. This solution, however, would have been excessively time consuming. Instead, we opted to transform the measured alkalinity, or titration concentration of HCO_3^-, to HCO_3^- (mg/L), and enter it in the input file as "free" HCO_3^-, i.e., the concentration of that specific species, regardless of the concentrations of other complexes of the HCO_3^- basis species in solution. This automatically accounted for CO_2(aq) and CO_3^{2-} in the final species distribution, but also double counted the concentrations of aqueous complexes with HCO_3^-, such as $NaHCO_3$(aq) or $CaHCO_3^+$. Because the latter complexes represent only a small fraction of total HCO_3^-, the error introduced by this approximation is generally small.

We performed EQ3/6 runs on all 38,597 samples to evaluate the significance of sample degassing. As an additional constraint, we specified that Eh is determined by the coexistence of pyrite and goethite, a reasonable assumption for most anoxic groundwaters. (This assumption is evaluated further in the Section 3.4.5). Out of the total number of samples, 35,069 runs converged, and the initial pH, charge imbalance, P(CO_2) and P(H_2S), as well as calcite, dolomite and siderite (ferrous carbonate) saturation indices, were recorded. The resulting outputs, plotted in the form of histograms of the frequency of occurrence, are of considerable interest, not just for evaluating concerns about charge imbalance, but also with respect to characterizing the average geochemical conditions of most groundwaters.

Figure 3.11 shows the pH range of all groundwaters. The acid "tail" is surprisingly persistent, and may reflect shallow groundwater contamination with organic acids, or relatively high CO_2 partial pressures. The charge imbalance (Fig. 3.12) peaks at a slightly negative value, which would be expected if aqueous complexes of HCO_3^- had been overcounted in the approximation of total HCO_3^- concentration. The positive skew to the histogram has not been investigated, and remains to be explained.

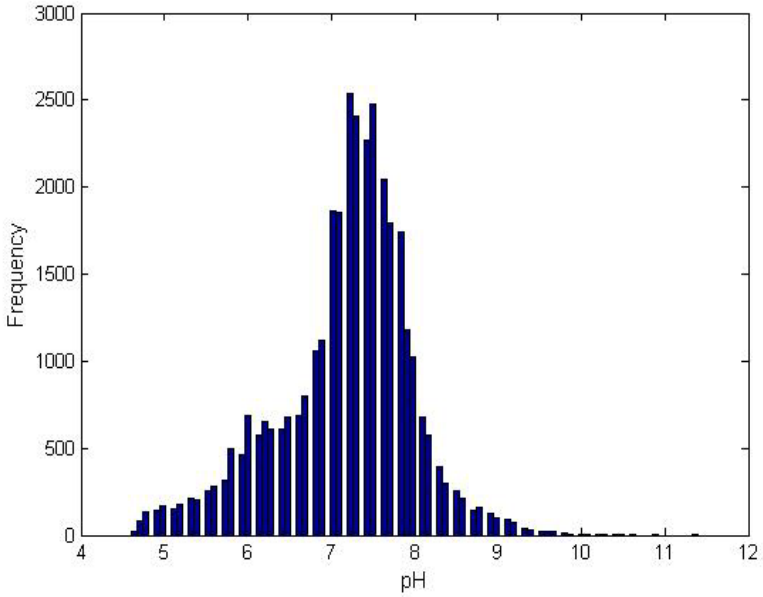

Fig. 3.11. Histogram showing the pH distribution of more than 35,000 groundwater analyses selected from the NWIS Database. No correction for charge imbalance.

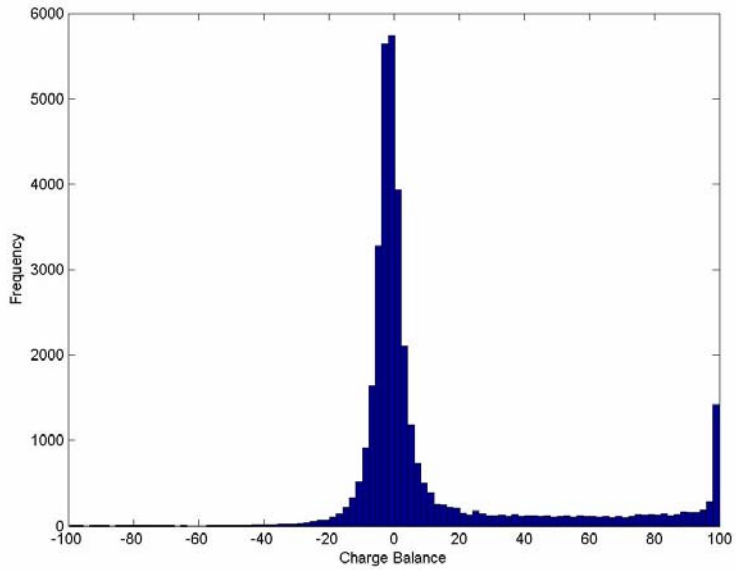

Fig. 3.12. Histogram showing the distribution of percentage charge imbalance of more than 35,000 groundwater analyses selected from the NWIS Database.

The frequency histogram for the calcite saturation index (Fig. 3.13) displays a peak where SI is slightly above zero, indicating supersaturation with respect to calcite. The substantial population

of values approximately centered on SI ~ 0 suggests that the majority of groundwaters are saturated with respect to calcite. The cause of the secondary maximum at SI ~ -3 was not investigated. The pH of a groundwater saturated with respect to calcite is likely to be more strongly buffered and therefore be more resistant to change under increasing partial pressures of CO_2. As a consequence, the concentrations of those hazardous inorganic constituents that are in part determined by ambient pH would be less impacted than would be the case where calcite is absent. It should be noted, however, that if calcite is present only in trace amounts, the ingress of high-pressure CO_2 could lead to the complete dissolution of calcite, and the system would no longer be buffered by its presence.

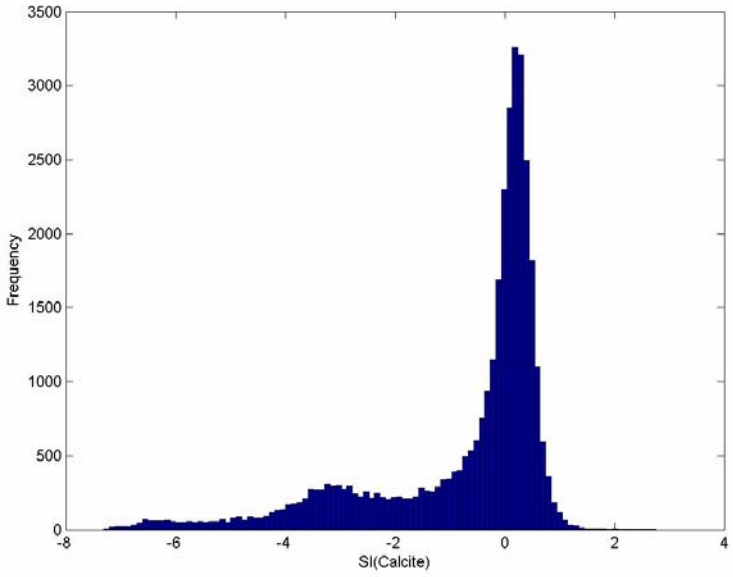

Fig. 3.13. Histogram showing the calculated calcite saturation indices of more than 35,000 groundwater analyses selected from the NWIS Database. No correction for charge imbalance.

Many dolomitic limestones are sources of drinking water in the eastern United States, and it is therefore of interest to examine the state of saturation of all groundwaters with respect to this carbonate. Figure 3.14 shows that almost SI(dolomite) peaks at significantly less than zero, which is consistent with reported occurrences of dedolomitization in shallow groundwaters (Edmunds et al., 1982; Back et al., 1983; Plummer et al., 1990; James et al., 1993; Aravena et al.,

1995; sacks and Tihansky, 1996; Hopkins and Putnam, 2000; Smedley and Edmunds, 2002; Pacheco and Szocs, 2006). Therefore, it is to be expected that groundwaters will not come into thermodynamic equilibrium with those representative host-rock mineralogies containing dolomite, i.e., St Peter Sandstone and Dolomitic Limestone (Section 3.6.3) in TOUGHREACT simulations described in Section 4 of this report, unless complete dedolomitization occurs during the groundwater initialization step.

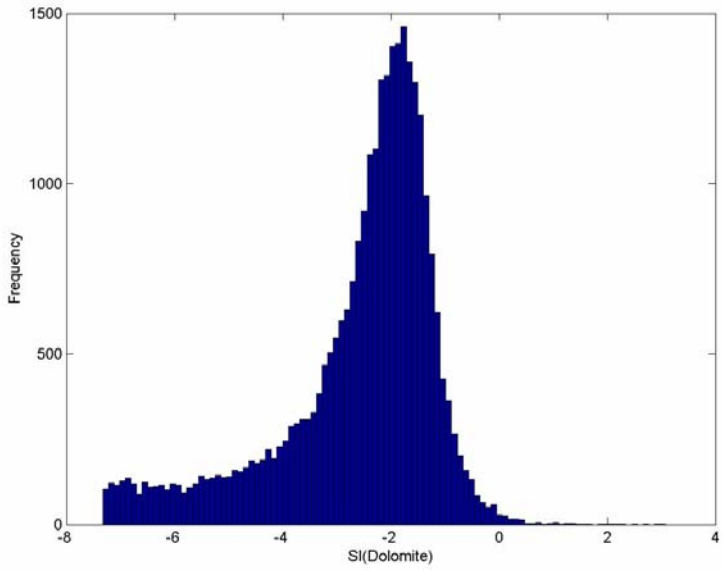

Fig. 3.14. Histogram showing the calculated dolomite saturation indices of more than 35,000 groundwater analyses selected from the NWIS Database. No correction for charge imbalance.

Because several authors cited above have attributed dedolomitization to concomitant dissolution of gypsum ($CaSO_4.2H_2O$) or anhydrite ($CaSO_4$), it is worth checking to establish whether the selected water quality analyses are saturated with respect to calcium sulfate in one form or another. Figure 3.15 illustrates the SI distribution for gypsum. It is clear that few, if any potable groundwaters are saturated with respect to this mineral, and therefore buffering of the sulfate concentration or any influence it might have in defining the redox state via the SO_4^{-2}/HS^- buffer is negligible. Instead, it is more likely that barite may indirectly control SO_4^{-2} activity (Section 3.4.4). It should also be noted that in the calculated equilibrium distribution of species using

EQ3/6, the partial pressure of H_2S is defined though its relation to the activity of SO_4^{-2} in solution, thus:

$$H_2S(g) + 2O_2(g) = 2H^+ + SO_4^{-2}$$

where $O_2(g)$ and H^+ are respectively set by the specified by Eh and pH. See further discussion regarding $P(H_2S)$ below.

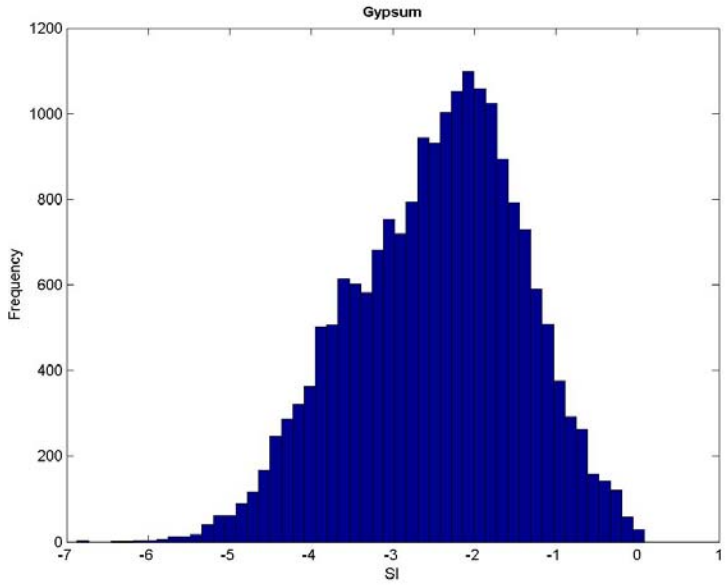

Fig. 3.15. Histogram showing the calculated gypsum saturation indices of more than 35,000 groundwater analyses selected from the NWIS Database. No correction for charge imbalance.

Figure 3.16 indicates that most groundwaters are not saturated with respect to the ferrous carbonate, siderite, which is consistent with relatively infrequent observations of its occurrence in shallow groundwater aquifers. Relaxation of the control of redox state through the co-existence of goethite and pyrite would likely decrease the saturation state even further with respect to siderite saturation. The finding that siderite may not be a common constituent of potable groundwater aquifers has three implications regarding the modeling of hazardous inorganic constituent behavior in potable aquifers being invaded by high-pressure CO_2. First, its inclusion in the model mineralogy of the aquifer host rocks is not critical; second, it need not be

considered as a potential pH buffer; and third, consideration of a system whose redox state is buffered by a siderite/pyrite assemblage can be ignored in modeling general cases.

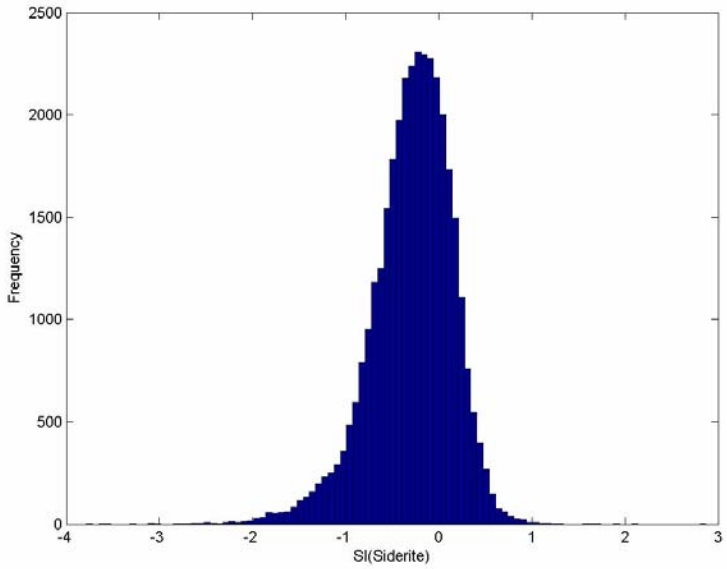

Fig. 3.16. Histogram showing the distribution of calculated siderite saturation indices of more than 35,000 groundwater analyses selected from the NWIS Database. No correction for charge imbalance.

The distribution of partial pressures of CO_2 in Figure 3.17 shows that, in a large majority of groundwaters, they are up to 2.5 orders of magnitude higher than those of the atmosphere (Log $P(CO_2)$ = -3.5), clearly indicating the potential of these groundwaters to degas if exposed to air. Therefore, it is preferable to assume that Log $P(CO_2)$ is buffered at circa –2.0 (the approximate modal value in the more than 35,000 groundwater samples examined), rather than imposing an external Log $P(CO_2)$ = -3.5, as was done by Wang and Jaffe (2004) in their preliminary study of the effect of high-pressure CO_2 intrusion.

Elevated $P(CO_2)$ in the subsurface environment is commonly attributed to the effects of microbial oxidation of organic matter. Indeed, this is most probably the case in shallow subaqueous unconsolidated sediments undergoing active authigenesis. However, elevated $P(CO_2)$ can also result from thermogenesis of organic matter and decarboxylation, or from deeper metasomatic processes, such as translocation of CO_2 to shallower environments occurring

through diffusion/and or advective transport. Furthermore, we conducted test calculations with EQ3 of groundwater saturated with respect to representative diagenetic mineral assemblages including pyrite and goethite, calcite and siderite at 25°C, yielding $P(CO_2)$ levels comparable to those observed without recourse to the external introduction of biogenic CO_2. Therefore it remains an open question whether biogenic CO_2 modifies the diagenetic mineral assemblage, or whether the diagenetic assemblage specifies a $P(CO_2)$ that is elevated with respect to that of the atmosphere, regardless of the presence of organic matter.

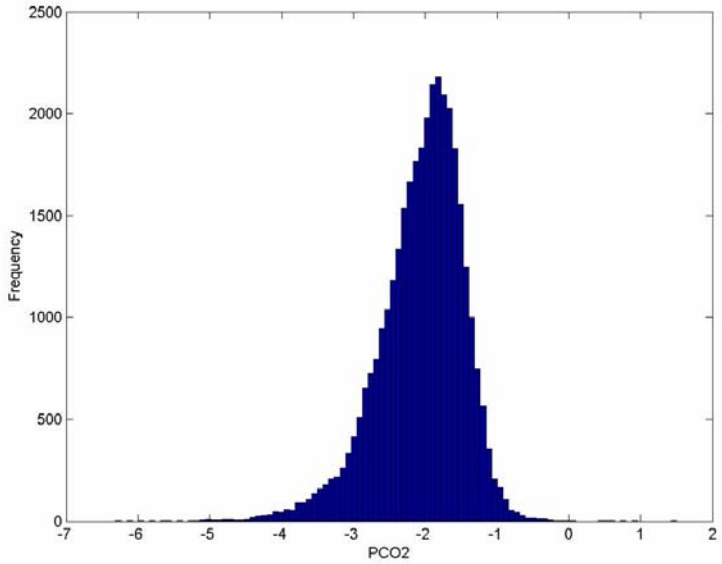

Fig. 3.17. Histogram showing the distribution of calculated Log $P(CO_2)$ of more than 35,000 groundwater analyses selected from the NWIS Database. No correction for charge imbalance.

The $P(H_2S)$ distribution (partial pressure of H_2S) in Figure 3.18 is fictive, in that it is the result of assuming that the coexisting pair of minerals, pyrite and goethite, defines the redox state at a given pH for a given SO_4^{-2} concentration. In reality, the distribution is primarily a reflection of the distribution of SO_4^{-2} in the population of groundwater analyses. However, the calculated range of concentrations is consistent with the fact that only in rare cases would H_2S be detectable in solution, and that most anoxic groundwaters would be free of odor. $P(H_2S)$ is a measure of the hydrogen sulfide activity in solution, and has an important bearing on the extent of sulfide complexing of heavy metals in solution, including Cd, Hg, Pb, and Zn, and under some

circumstances can also affect the behavior of As and Sb. It also defines the activities of these metals with respect to the solubility products of their sulfides. Thus this parameter is an important dependent variable in describing system behavior, just as are pH, Eh and $P(CO_2)$.

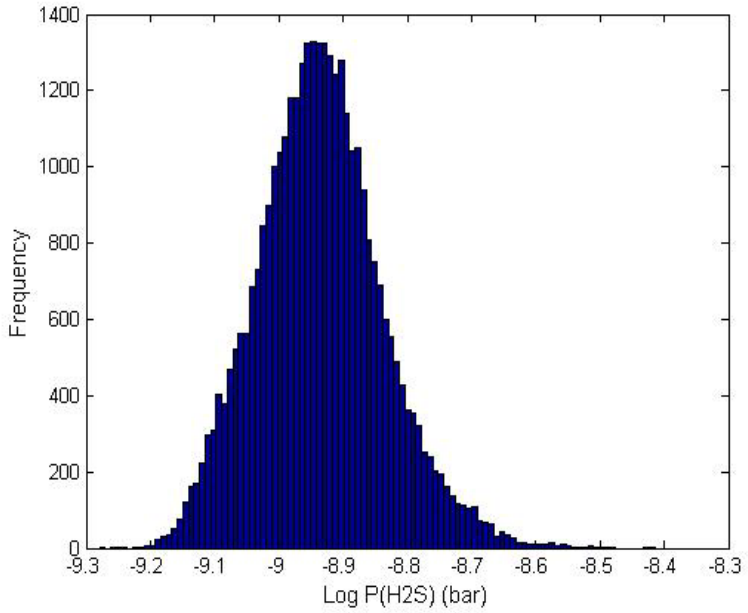

Fig. 3.18. Histogram showing the distribution of calculated Log $P(H_2S)$ distribution of more than 35,000 groundwater analyses selected from the NWIS Database. No correction for charge imbalance.

In recognizing that the above results may in part be distorted by the potential loss of CO_2, we conducted an alternative set of EQ3 runs with adjustment of the concentration of HCO_3^- to eliminate charge imbalance. Figures 3.19 through 3.21 correspond to Figures 3.13, 3.16 and 3.17, but include this correction. Examination of Figure 3.19 shows that by retaining a fixed pH, the saturation index for calcite increases, thereby shifting the SI calcite to higher values. This effect varies with pH, but in aggregate, it leads to a compression of the range and an upscale shift of both primary and secondary maxima, the secondary maximum being more strongly affected.

The histogram for siderite saturation indices (Fig. 3.20) transforms into a nearly symmetrical peak about SI = 0. This result might lead to the conclusion that most groundwaters are saturated with respect to siderite. However, it may also be an artifact arising from the original derivation of the thermodynamic properties of goethite and siderite, which define the solubility product values

incorporated in the EQ3/6 database. Because the $[Fe^{+2}]/[H^{+}]^2$ activity ratio is determined by the redox-controlling pair goethite/pyrite, the SI profile for siderite is actually defined by the corresponding distribution for Log $P(CO_2)$ (Fig. 3.21). Examination of the Log $P(CO_2)$ profile clearly indicates that this parameter has been unduly biased upscale to partial pressures that are unrealistically high for shallow aquifers. Thus, while correction for charge imbalance using HCO_3^- is justified to account for CO_2 degassing, it is inappropriate to apply such a correction in all cases. Unfortunately, there is no simple means by which the correction for charge imbalance may be applied without the inadvertent introduction of other undesired biases.

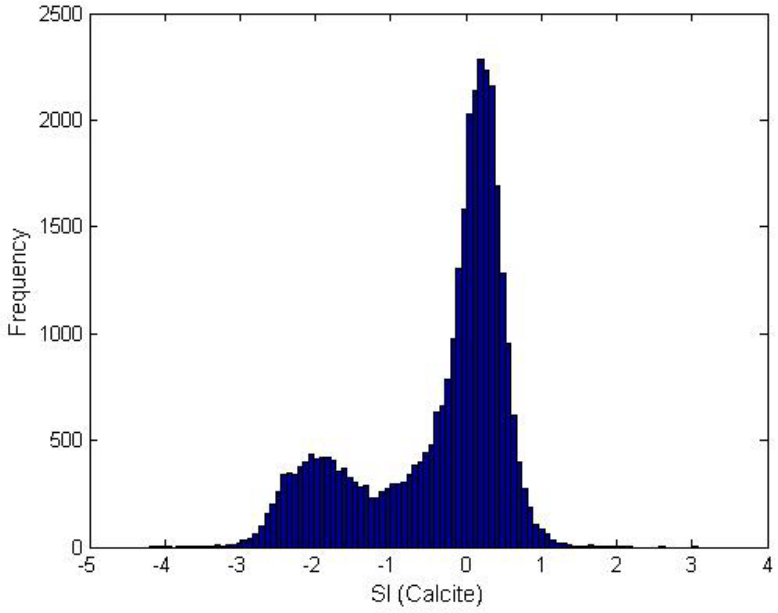

Fig. 3.19. Histogram showing the distribution of calculated calcite saturation indices of more than 35,000 groundwater analyses selected from the NWIS Database. Charge imbalance corrected through adjustment of HCO_3^- concentration.

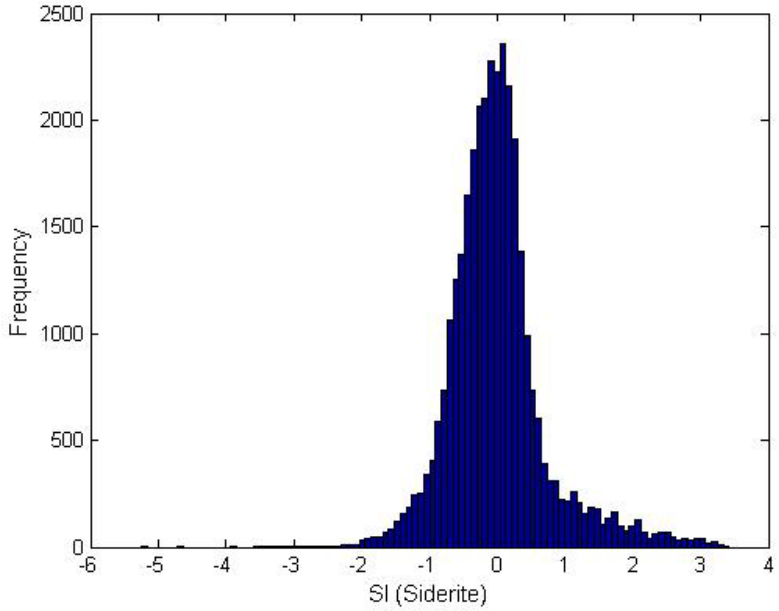

Fig. 3.20. Histogram showing the distribution of calculated siderite saturation indices of more than 35,000 groundwater analyses selected from the NWIS Database. Charge imbalance corrected through adjustment of HCO_3^- concentration.

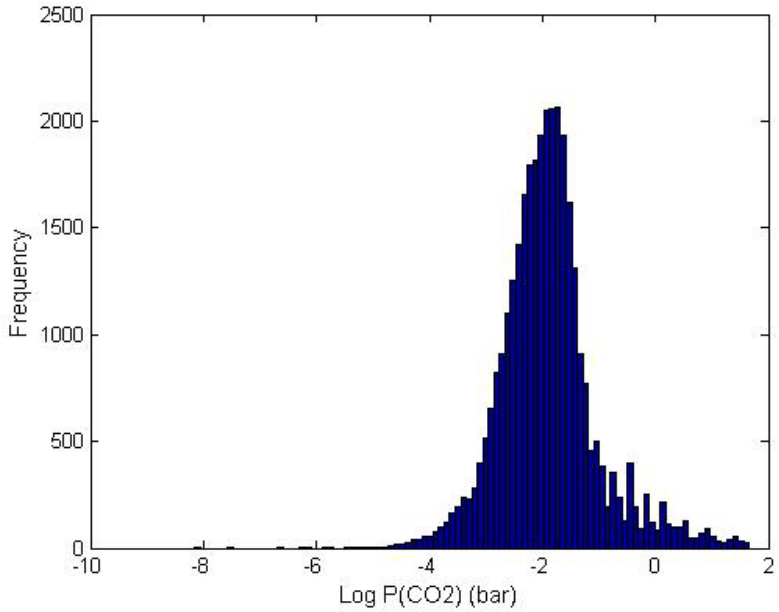

Fig. 3.21. Histogram showing the distribution of calculated Log $P(CO_2)$ of more than 35,000 groundwater analyses selected from the NWIS Database. Charge imbalance corrected through adjustment of HCO_3^- concentration.

The purpose of the foregoing discussion was to evaluate the significance of analytical artifacts primarily associated with inadvertent degassing of groundwater samples prior to alkalinity determinations and associated errors introduced by secondary precipitation of calcium carbonate, and other factors relating to the measurement of pH. By so doing, we hoped to develop a procedure whereby such artifacts might be removed, or at least, mitigated during the subsequent processing of the more than 38,000 groundwater analyses with the EQ3/6 species distribution code. It was not the intent of this analysis to define the parameters required for simulating CO_2 intrusion in a potable water aquifer and its impact on hazardous inorganic constituent concentrations in the aquifer. However, the study raised a number of issues relating to the broader issue of geochemical model validation.

The reference to Figure 3.12 shows that if the criterion for acceptance of a groundwater chemical analysis were a charge imbalance of no more than 5%, then two-thirds of the 35,000 analyses downloaded from the NWIS database and successfully run by EQ3 would be considered acceptable. Table 3.11 shows that errors in the measurement of ambient pH might arise through inappropriate sample handling, even though the sample would pass the charge imbalance screen. Attempts to rectify such by restoring lost CO_2 through charge balancing on HCO_3^- were only partially successful. Thus, it appeared that no simple strategy could be adopted that would account for analytical errors without introducing unwanted biases in the evaluation. The following is a partial list of potential errors affecting the groundwater chemical analyses: (1) permitting degassing of CO_2, (2) permitting precipitation of dissolved constituents, (3) failure to analyze all principal constituents in solution, (4) acidification of a sample containing suspended material, (5) permitting access of oxygen, thereby oxidizing reduced species, (6) inadvertent contamination both before and after sample collection, (7) inadequate calibration of pH electrodes, (8) contamination of sample by reference electrode electrolyte, and (9) interferences and biases associated with individual analytical methods for specific elements.

It became evident that the development of a systematic strategy for correcting chemical analyses containing discrepant measurements would require more time and effort than could be devoted within this study. Furthermore, selecting only those analyses meeting certain criteria might not

necessarily improve the quality of the subsequent evaluation, because analyses might be eliminated that could otherwise contribute significantly to the statistics of small sample populations involving such hazardous constituents as antimony, which is infrequently analyzed in groundwaters. We decided, therefore, to include all analyses regardless of quality. Such a decision is likely to increase the statistical dispersion of calculated saturation indices of minerals controlling the solubilities of hazardous inorganic constituents, but it is unlikely to affect their identification, or to introduce systematic biases, as it is the mode of the distribution that is the critical parameter of interest. It would clearly be interesting to pursue this issue on a broader scale, as it has important implications regarding geochemical model validation and the degree of confidence attached to the results of field studies.

3.4.4 Evaluation of Groundwater Redox State

Estimating the redox potential of groundwaters is critical to interpretation of most hazardous constituents targeted in this study. As noted before, As, Sb, Se, and U can occur in differing oxidation states that are stable in the presence of water. Arsenic, Cd, Hg, Sb, Pb and Zn commonly form insoluble sulfides under reducing conditions, which become unstable under oxidizing conditions, where sulfur is oxidized from the -II to the 0 or the VI state. As, Sb and Se can also form compounds with Fe(II), which is destabilized under oxidizing conditions to the Fe(III) state. Furthermore, some of the hazardous constituents can form compounds with each other, e.g., selenides of As, Cd, Pb or Zn, or arsenates of Pb. Thus, a variety of solubility-controlling minerals can form, depending mainly on both the pH and redox state of the groundwater.

Unfortunately, although the redox state, or Eh, of a groundwater is easily measured using a Pt electrode, this type of measurement is usually subject to large and unpredictable errors (Baas Becking et al., 1960; Lindberg and Runnels, 1984; Fish, 1993; Stefansson, 2003). Furthermore, not all species of an element that can occur in different oxidation states are necessarily in redox equilibrium, as has been observed with respect to As(III)/As(V) (Cherry et al., 1979; Johnston and Singer, 2007), Sb(III)/Sb(V) and Se(II)/(IV)/Se(VI) and S(II)/S(VI) (Sato, 1992). Although

the distribution-of-species code EQ3/6 can account for a lack of homogeneous equilibrium within the aqueous phase, and the transformation of species from one redox state to another can be treated kinetically in TOUGHREACT, such a refinement is beyond the scope of this study and not utilized in the analysis presented here.

Instead of relying on direct Eh measurements, which, as noted above, are of questionable reliability, we use an indirect method to estimate redox state. Equilibration between Fe(II) and Fe(III) occurs relatively rapidly in the aqueous phase (Grundl and Macalady, 1989), and therefore advantage can be taken of measurements of these species in solution to calculate the Eh of solution at a given pH. While the concentration of Fe(III) in solution is usually very low and not normally measured, its concentration and activity can be calculated if equilibrium with a ferric oxide or oxyhydroxide is assumed in the aquifer. This assumption is reasonable, especially under oxidizing conditions. With an increasingly reduced state, more and more of the Fe(III) in the ferric phase would be reduced to Fe(II), which can be incorporated in the octahedral layers of secondary smectites or chlorites. Under even more highly reducing conditions, iron can be sequestered and precipitated as a sulfide, usually as pyrite. Eventually, a state would be reached where all Fe(III) containing minerals are dissolved, and the redox state can no longer be defined by the Fe(II)/Fe(III) activity ratio.

Over 20,000 analyses in the database extracted from the NWIS contain measurable Fe analyses. These provide a basis for calculating the probable Eh of a significant fraction of all samples. As part of the NWIS database search, additional analytical data on redox pairs such as SO_3^{-2}/HS^-, Mn^{+3}/Mn^{+2}, $HCO_3^-/CH_4(aq)$, NO_3^-/NH_4^+, etc., redox measurements, and total dissolved oxygen were also solicited when included in groundwater analyses containing analyses of hazardous inorganic constituents. Such additional information can be used to augment Eh values calculated using Fe analyses and to estimate the state of equilibrium or disequilibrium, but this was not attempted in the present study. Unlike the Fe(III)/Fe(II) couple, the other redox pairs are slow to achieve homogeneous equilibrium, with the possible exception of the Mn(III)/Mn(II) couple,. They are therefore useful in establishing whether authigenic (biogenic) processes are active in a potable groundwater environment, or whether the groundwater has attained a measure of

homogeneous equilibrium. Although of considerable importance (and further study would be merited), this subject was not explored further, owing to the relative paucity of suitable datasets in the groundwater quality analyses downloaded from the NWIS database.

The following approach was taken when using Fe analyses to estimate Eh. It was initially assumed that goethite was present in equilibrium with the groundwater for the given chemical composition and pH. The total measured Fe concentration was then inserted as the Fe^{+2} concentration, and the Eh was computed based on the Fe(III)/Fe(II) ratio. The calculated total iron concentration was then compared with the measured total iron concentration according to the following three criteria, where $Fe(o/p)$ is the calculated total iron concentration and $Fe(i/p)$ is the measured input concentration of total Fe:

(a) If $\frac{Fe(o/p)-Fe(i/p)}{Fe(o/p)}=0$	Leave unchanged, and record Eh.
(b) If $\frac{Fe(o/p)-Fe(i/p)}{Fe(o/p)} \geq 0.05$, but < 0.95	Subtract Fe(i/p) from Fe(o/p) and enter the difference as Fe^{+2}. Re-run and record Eh.
(c) If $\frac{Fe(o/p)-Fe(i/p)}{Fe(o/p)}=1$	Leave unchanged, and record Eh.

Case (a) arises when the calculated output concentration is essentially identical to the input concentration, i.e., when the contribution of Fe(III) to the total Fe concentration is negligible. Case (c) represents the situation when the measured concentration is small in relation to the calculated concentration of Fe(III) in equilibrium with goethite. Case (b) arises when the concentrations of Fe(II) and Fe(III) are approximately equivalent, and the approximations that total iron is predominantly Fe(II), as in Case (a), or predominantly Fe(III), as in Case (b), cannot be applied, and the concentration of Fe(II) must be calculated explicitly. The applicable range where $0.05 \leq \frac{Fe(o/p)-Fe(i/p)}{Fe(o/p)} < 0.95$ is established to ensure stability in the calculations, while also recognizing the analytical uncertainty in the measured Fe concentrations.

An additional specification is that the measured SO_4^{-2} concentration is entered as the "free" concentration, i.e., the total concentration of sulfate species is as analyzed, and sulfide

concentrations are added in to achieve equilibrium with the sulfate at the pH and Eh conditions specified for each run. This adjustment reflects the fact that the analytical procedures usually analyze for sulfate alone rather than total sulfur.

The calculated Eh values were then plotted against pH to produce a typical Eh–pH diagram, as illustrated in Figure 3.22. The plot shows that most of the groundwaters, for which measured Fe analyses are available, fall within a range of moderately to strongly reducing conditions. The upper bound is constrained by the analytical limitations for measuring Fe(total) in solution and falls within the goethite stability field. The lower stability limit is bounded by the decomposition of water and can fall within the stability field of pyrite. Quantitative estimates of Eh are therefore constrained by the sensitivity of analytical methods for measuring dissolved iron. Consequently, a bias might be introduced through this analysis, which must be taken into consideration in interpreting the thermodynamic controls affecting the behavior of hazardous inorganic constituents in groundwater (Section 3.4.5).

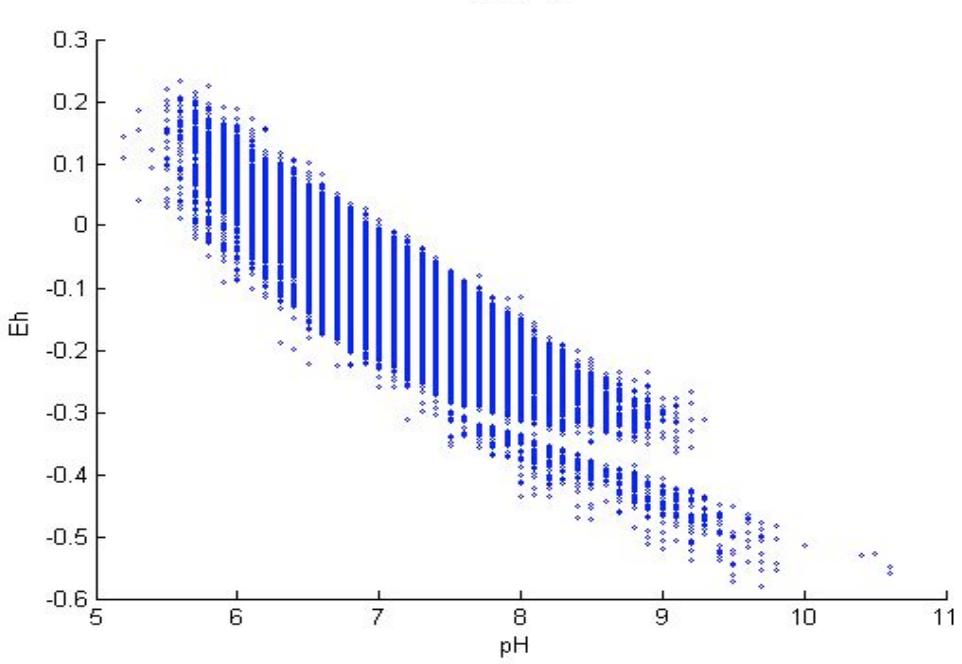

Fig. 3.22. Calculated Eh, based on the distribution of Fe(III) and Fe(II), and the assumption that Fe(III) is in equilibrium with goethite, plotted against measured pH.

3.4.5 Evaluation of Solubility Controls for Hazardous Constituents

A series of five EQ3/6 runs were made in which groundwater analyses extracted from the NWIS database were subject to differing initial constraints. The purpose of these runs was to determine whether concentrations of the selected hazardous inorganic constituents were controlled by certain minerals in the aquifers. A further two runs were conducted on a limited subset of waters containing Pb, analyzed using PLM43 and PLM48 and Cd, analyzed using PLM43 and PLM47. These denote analytical methods employing ICP-MS, which is the most sensitive technique currently available in general use and most likely to yield valid measurements of Pb and Cd concentrations (see Appendix A). A description of the runs is given in Table 3.12. As pointed out before, each run involves an automated procedure with multiple EQ3/6 simulations for a large number of groundwater analyses.

Table 3.12. Input constraints for EQ3/6 species distribution runs conducted on groundwater analyses from the NWIS Database.

Run	Input Constraints
0	Eh defined by goethite saturation and total dissolved iron distributed between Fe(II) and Fe(III). No correction for charge imbalance.
01	Eh defined by goethite saturation and total dissolved iron distributed between Fe(II) and Fe(III). Charge imbalance corrected through adjustment of HCO_3^- concentration.
1	Eh at the measured pH buffered by the pyrite/goethite redox couple. No correction for charge imbalance.
2	Eh at the measured pH buffered by the pyrite/goethite redox couple. Charge imbalance corrected through adjustment of HCO_3^- concentration.
3	Eh at the measured pH buffered by the pyrite/goethite redox couple. Charge imbalance corrected through adjustment of H^+ concentration.
4	Pb analyzed using PLM43 and PLM48 and Cd analyzed using PLM43 and PLM47. Eh defined by goethite saturation and total dissolved iron distributed between Fe(II) and Fe(III). No correction for charge imbalance.
5	Pb analyzed using PLM43 and PLM48 and Cd analyzed using PLM43 and PLM47. Eh at the measured pH buffered by the pyrite/goethite redox couple. No correction for charge imbalance.

The rationale for conducting these different runs is as follows.

1. Considerable uncertainty attends the characterization of the redox state of the analyzed groundwaters. It is surmised that most are anoxic and have equilibrated under reducing conditions. However, a minor fraction of the sampled groundwaters may be oxic, although recognition that those waters stabilized under such conditions can be made only indirectly through examination of their total chemistry.

2. Two alternative approaches are taken to better constrain the oxidation state: (a) The oxidation state can be determined if either the Fe(II) and Fe(III), or total Fe have been analyzed in solution, while it is assumed that the groundwater is saturated with respect to goethite. This assumption is reasonable, but goethite saturation cannot be presumed in all cases. Fe(II)/Fe(III) buffering might be accomplished through the presence of other ferric oxides or oxyhydroxides, which would modify the calculated Eh. Furthermore, acid stabilization of the groundwater for subsequently analyzing Fe(II) in solution must be made prior to exposure to air, to prevent oxidation and precipitation of Fe(III) (Singer and Stumm, 1968, 1970). Unfortunately, not all analyses from the NWIS database report either Fe(II) and Fe(III), or total Fe. Therefore, the entire dataset is not available for evaluation by this method. (b) The redox state is controlled by the pyrite/goethite redox couple in all cases. This constraint would obviously be inapplicable to oxic groundwaters. Furthermore, not all reducing groundwaters are necessarily buffered by the pyrite/goethite couple. Other couples, for example pyrite/magnetite, pyrite/hematite, pyrite/siderite, pyrite/pyrrhotite and pyrite/chlorite, are possible. See Section 3.4.5.1 below.

3. The thermodynamic analyses conducted using EQ3/6 are carried out assuming that homogeneous equilibrium with respect to redox conditions has been established in all cases. However, groundwaters of relatively young age are known not to be in homogeneous equilibrium, as noted in Section 3.4.3, above. As a working hypothesis, it is assumed that most of the groundwaters sampled are in homogeneous equilibrium.

4. The partial oxidation of sulfides can lead to a metastable equilibrium state with respect to native sulfur. For example, the oxidation of galena proceeds according to the following half-cell reaction:

$$PbS = S_{rhombohedral} + Pb^{+2} + 2e^{-}$$

under anoxic conditions where neither hydrogen peroxide (Sato, 1992) nor bacterial populations are available to promote the oxidation of sulfur to sulfate. We assume that the metastable persistence of native sulfur does not occur over the long time frames available for sulfide equilibration in groundwaters, because natural radioactive decay of ubiquitous uranium will induce a low ambient H_2O_2 flux to catalyze sulfur oxidation.

5. The majority of analyses display unacceptably large charge imbalances, i.e., > ±10%. The probable cause is CO_2 loss followed by carbonate precipitation before analysis of alkalinity or bicarbonate concentration, but after pH measurement. A secondary cause could be measurement of pH after analysis of alkalinity or bicarbonate concentration CO_2 degassing. Evaluations presented in Section 3.4.4 indicate that these causes are operative. No simple strategy exists, however, for identifying and correcting for both causes on a case-by-case basis.

6. As noted in Sections 3.3.4 and 3.3.5, the analyses of some hazardous inorganic constituents are suspect, because the analytical methods used are insufficiently sensitive to detect the low concentrations that would equilibrate with host minerals under reducing conditions. Because it is not easily determined whether the groundwater was exposed to reducing conditions, it is generally not possible to state unequivocally whether a particular analysis is invalid. Thus, it was decided to accept all available hazardous inorganic constituent analyses for preliminary evaluation.

7. Given the uncertainties listed above, it was decided that by making a multiplicity of runs testing different hypothetical conditions, and examining the results, it would be possible to determine the most plausible thermodynamic controls affecting the concentrations of the selected hazardous inorganic constituents. The runs are therefore exploratory in nature, and aimed towards narrowing the scope of the problem.

The output histograms of the saturation indices of selected minerals from the series of runs were examined closely. The output of Run 0 is comparable with that of Run 01, and likewise, the output of Run 1 is comparable with those of Runs 2 and 3, meaning that no significant reduction in statistical dispersion has been obtained through charge balancing. Instead, a bias is introduced through either an increase in the calculated value of $P(CO_2)$ as a consequence of charge balancing on HCO3-, or through effects caused by an upward shift in pH through charge balancing on pH. Because these biases could not be justified by independent lines of inquiry and statistical dispersion is not improved, and also because no differences in interpretation are obtained, we decided to omit further discussion of runs 01, 2 and 3. The following discussion of results is therefore restricted to Runs 0 and 1, where charge balancing is ignored. The findings from Runs 4 and 5, which also omit charge balancing, are included in Section 3.4.5, below, where the effect of redox potential on Cd, Pb and Zn aqueous concentrations is considered.

3.4.5.1 Discussion of Results from Run 0

Histograms showing the calculated saturation indices for the minerals expected to control the selected hazardous inorganic constituents under reducing conditions (see Section 3.2), as defined by goethite saturation and the concentration of iron in solution, are illustrated in Figures 3.25 through 3.33 below. However, because the redox potential is defined independently of other minerals assumed to contain Fe in the reduced (II) state, we start a discussion of results by examining how many of the sampled groundwaters might actually have been close to or at saturation with respect to such minerals. In Figure 3.23, we illustrate the histograms of saturation indices for pyrite, magnetite, siderite, and chlorite. The pyrite SI histogram attains a maximum at SI ~ +5, with a broad plateau extending to SI ~ -20. This suggests that some groundwaters are near or at saturation with respect to this mineral. Both the spread in values and the lengthy tail extending to SI ~ -70 are open to several interpretations. The pronounced skew towards negative values suggests a range of oxidation states in the subset of samples for which Fe analyses exist. The sharp cutoff at SI ~ +10 reflects a natural limitation in realistic aqueous concentrations of Fe, but also implies a considerable analytical uncertainty associated with quantitative measurements for SI(pyrite). Another explanation is that the assumed homogeneous equilibrium

with respect to the SO_4^{-2}/HS^- couple is not applicable to many of the groundwater samples, or that some or all of the aqueous Fe(II) oxidized and precipitated prior to analysis. Such questions should be investigated further. Despite the substantial uncertainties associated with this analysis, it is nevertheless plausible to assume that many of the samples had equilibrated with pyrite, the uncertainties all suggesting a higher proportion than is indicated in Figure 3.23a.

The spread in SI values for magnetite (Figure 3.23b) is much more restricted than for pyrite, although a negative skew is again observed. The frequency of SI values peaks at about zero, which is strongly suggestive that a magnetite/goethite or magnetite/hematite buffer might also participate in controlling the oxidation state of many of the groundwaters. In contrast, siderite SI values in Figure 3.23c peak at about -2, indicating that the presence of this mineral is less common, and that the likelihood that it could buffer the oxidation state with either goethite or hematite is small. Note that this figure differs from that of Figure 3.16, which also displays a SI frequency histogram for siderite, because the latter was determined assuming the coexistence of pyrite and goethite and a calculated activity of Fe^{+2}.

Another possible redox buffer involves the coexistence of chlorite with goethite, hematite, magnetite, or possibly pyrite. The stability relations between chlorite and the cited iron-bearing minerals are complicated, because this mineral is a solid solution where Mg^{+2} substitutes for Fe^{+2} in the structure, whose end members are respectively identified by the minerals clinochlore and daphnite. The calculated SI for chlorite, where $Mg^{+2}/(Mg^{+2} + Fe^{+2}) = 0.5$, indicates significant supersaturation with SI ~ 5, as shown in Figure 3.23d. However, the calculations assume saturation with respect to opal-CT, which would supersaturate the groundwater with respect to quartz. Correction for silica saturation to quartz and normalization of the SI to unit Fe stoichiometry results in SI(chlorite) ~ +1, which is reasonably close to saturation, given the potential uncertainties associated with the derivation of the thermodynamic properties for this mineral. It should be noted that the precipitation of Fe in pyrite usually results in depletion of Fe in the chlorite, and shifting of the chlorite composition towards end-member clinochlore.

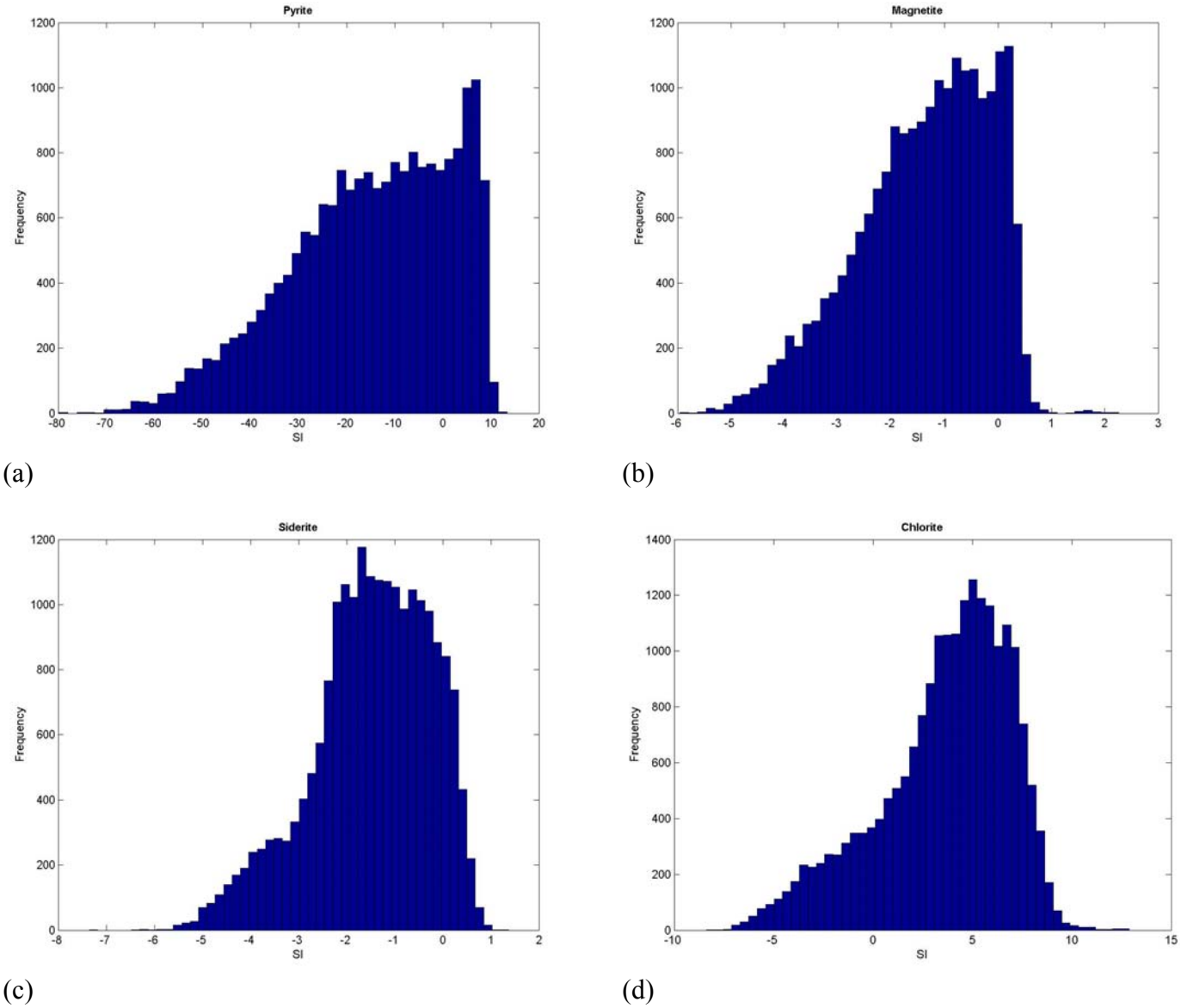

Fig. 3.23. Frequency Distribution of Saturation Indices of (a) Pyrite, (b) Magnetite, (c) Siderite and (d) Chlorite. Saturation Indices are calculated assuming Eh to be defined by Fe(III)/Fe(II) in solution in the presence of goethite, using a selected set of groundwaters from the NWIS.

The calculated SI histogram for clinochlore, Figure 3.24, shows a somewhat similar profile to chlorite, but is shifted to a somewhat lower degree of supersaturation (≈ 3). Allowing for corrections for SIO_2(aq) and possible sympathetic errors in the thermodynamic properties of both clinochlore and chlorite (Appendix C), it is reasonable to suggest that clinochlore might

preferentially coexist with pyrite when the latter occurs in the absence of ferric minerals in potable water aquifers. Further investigation of this association would be warranted.

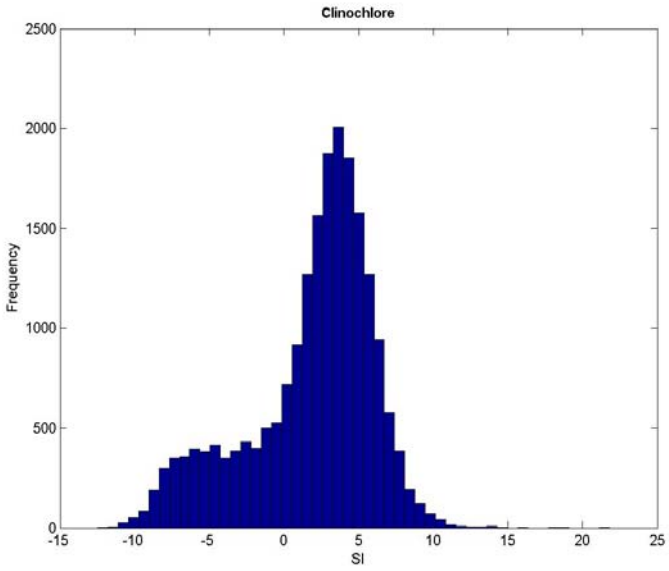

Fig. 3.24. Frequency Distribution of Saturation Indices of Clinochlore. Clinochlore saturation is not significantly affected by variation in Eh.

We now follow with a discussion of the calculated SI frequency histograms of minerals that might control the activities of the hazardous inorganic constituents selected for evaluation. They are given in the alphabetical order of their chemical symbols, i.e., As, Ba, Cd, Hg, Pb, Sb, Se, U and Zn. Candidate minerals have been previously identified in Section 3.2.

Arsenic. Figures 3.25a, b, and c show the histograms of saturation indices for arsenopyrite (FeAsS), scorodite ($FeASO_4.2H_2O$), and symplesite ($Fe(II)_3(AsO_4)_2 \cdot 8H_2O$), respectively. The histogram for arsenopyrite Figure 3.25a displays a bimodal distribution. The smaller peak on the right hand side has a broad maximum at SI ~ 0, suggesting arsenopyrite solid solution in pyrite, as is often observed in the field. The broad distribution of values about SI(max) ~ -50 relates to conditions where As(V) species predominate under oxidation states too high to support the presence of pyrite. The scorodite and symplesite histograms, in contrast, show no evidence that

any groundwaters attain saturation with respect to either mineral. This finding is in conflict with the postulated existence of a scorodite-like phase in groundwaters subject to oxidation, as suggested by Thornberg and Sahai (2004). .

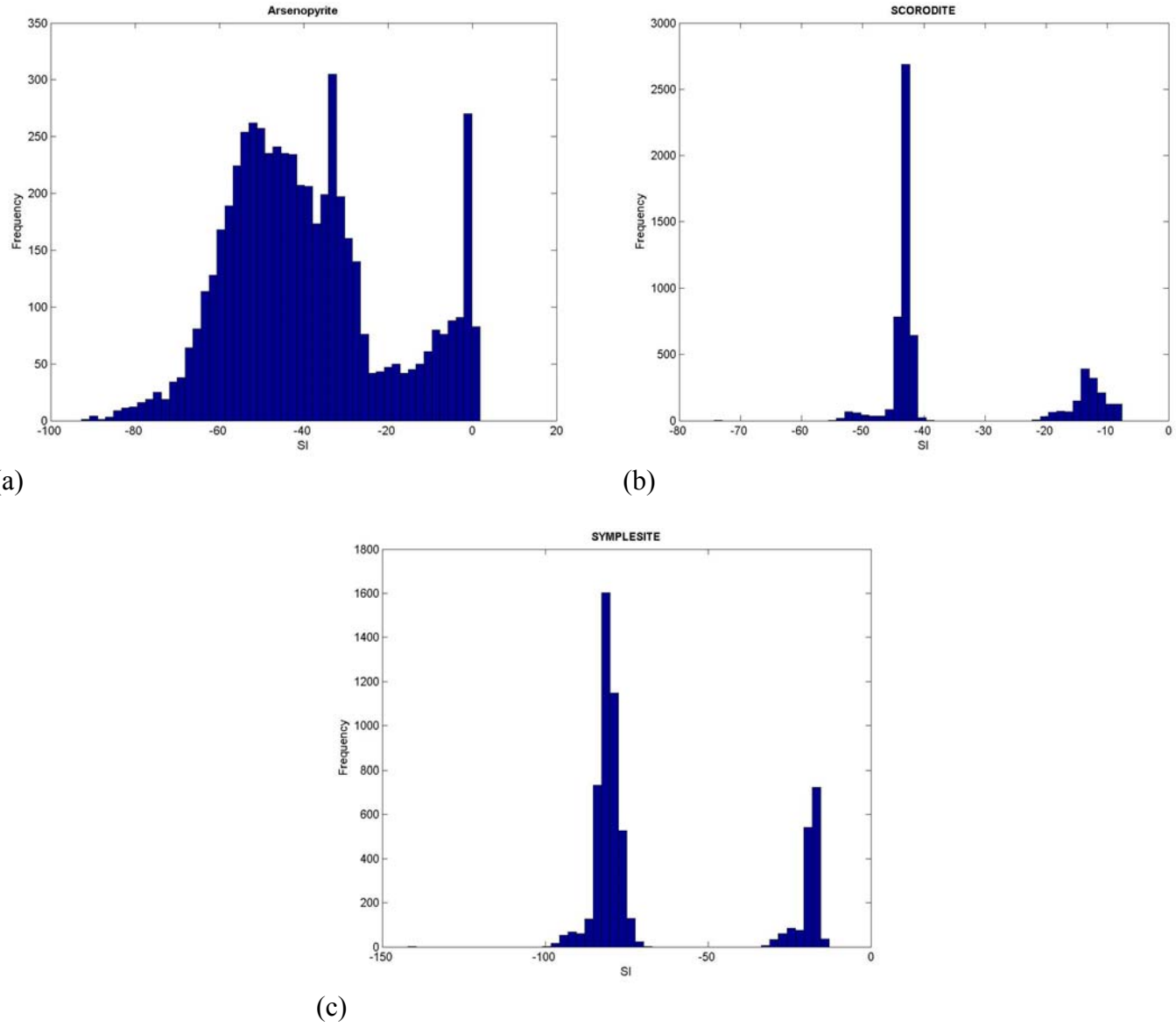

(a) (b)

(c)

Fig. 3.25. Frequency Distribution of Saturation Indices of (a) Arsenopyrite, (b) Scorodite, and (c) Symplesite. The Saturation Indices are calculated using a selected set of groundwaters from the NWIS and assuming Eh to be defined by Fe(III)/Fe(II) in solution.

Barium. Figures 3.26a and b display SI histograms for barite ($BaSO_4$) and witherite ($BaCO_3$). These two minerals are isostructural with the analogous Pb minerals, anglesite ($PbSO_4$) and cerussite ($PbCO_3$), which are compared separately, below. Because barium is present only in one oxidation state in natural groundwaters, solubility control is essentially independent of Eh, unless all sulfate in the system is reduced to sulfide. Such conditions can arise in coal beds where Ba is observed associated with silicates or phosphates, e.g., crandallite ($(Ca, Ba)Al_3(PO_4)_2(OH)_5 \cdot H_2O$) (Finkelman, 1981; Brownfield et al., 2005), or during hydrolysis by diabase, when the presence of witherite is favored. From Figure 3.26a, it is evident that barium solubility is controlled by the presence of barite where SI(max) ~ 0, rather than by witherite, which is undersaturated (SI(max) ≈ -3).

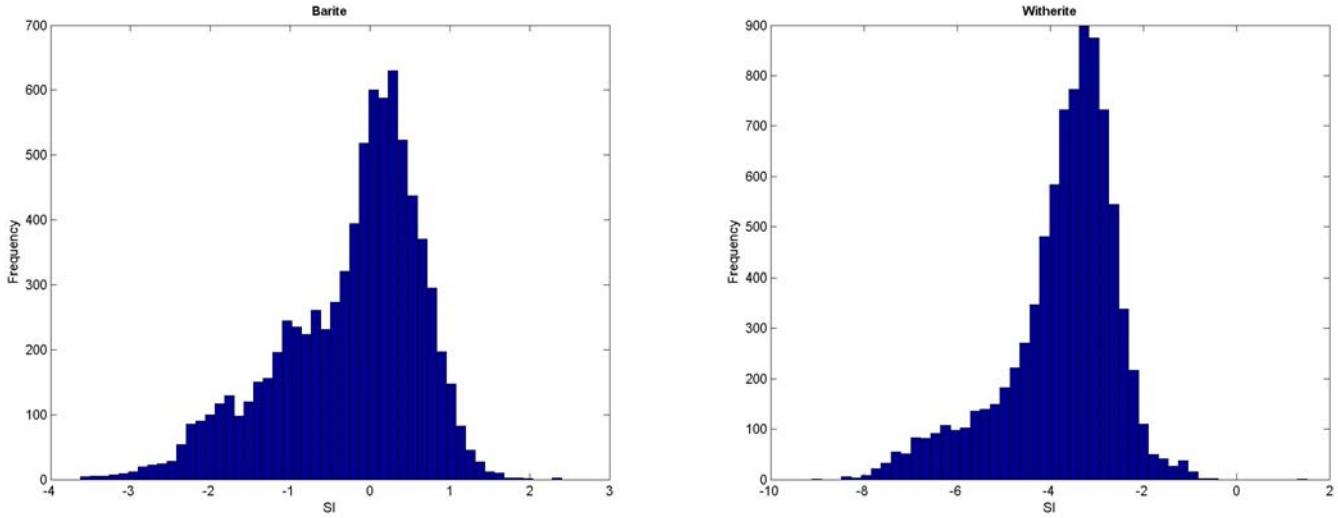

(a) (b)

Fig. 3.26. Frequency Distribution of Saturation Indices of (a) Barite and (b) Witherite. The Saturation Indices are calculated for a selected set of groundwaters from the NWIS. Eh is defined by Fe(III)/Fe(II) in solution, which generally does not significantly affect either barite or witherite saturation.

Cadmium. A broad distribution of SI's for CdS (cadmium sulfide, or greenockite) is illustrated in Figure 3.27a. The peak reflects (a) the dispersion of analytical values in the calculation of SI(CdS), (b) false positive readings due to the application of insufficiently sensitive methods, (c) uncertainty in the calculated solubility product of CdS, and finally (d) uncertainties associated with the identities and thermodynamic properties of Cd sulfide and selenide complexes in solution in the EQ3/6 distribution. The sharp peak distribution at SI ~ 0 strongly suggests that at least some of the samples are saturated with respect to greenockite. However, as noted in Section 3.4.5.2 below, this apparent saturation can be an artifact resulting from the omission of selenide complexing due to the absence of Se analyses in some of the groundwaters for which Cd analyses have been made. Therefore, the possibility that CdS exists only in solid solution with sphalerite cannot be excluded on the basis of the present analysis.

Figure 3.27b illustrates the calculated SI distribution for cadmoselite (CdSe), an example where two separate trace hazardous constituents are essential components of the same mineral. The distribution is much narrower for the selenide than for the corresponding sulfide, because the Se(II) state is stable over a wider range of oxidation potentials defined in this case by Fe(III)/Fe(II). However, it is interesting to note that SI(max) ~ 0, suggesting that this mineral could actually control Cd(II) activity in the majority of potable groundwaters.

The SI histogram for otavite ($CdCO_3$) is given in Figure 3.27c. Otavite is generally believed to be the most stable phase containing Cd as an essential component under oxidizing conditions (Carroll et al., 1998; McGrath et al., 2007). The histogram indicates that almost all groundwaters analyzed for Cd, and passing the screen for Run 0, are undersaturated with respect to this mineral.

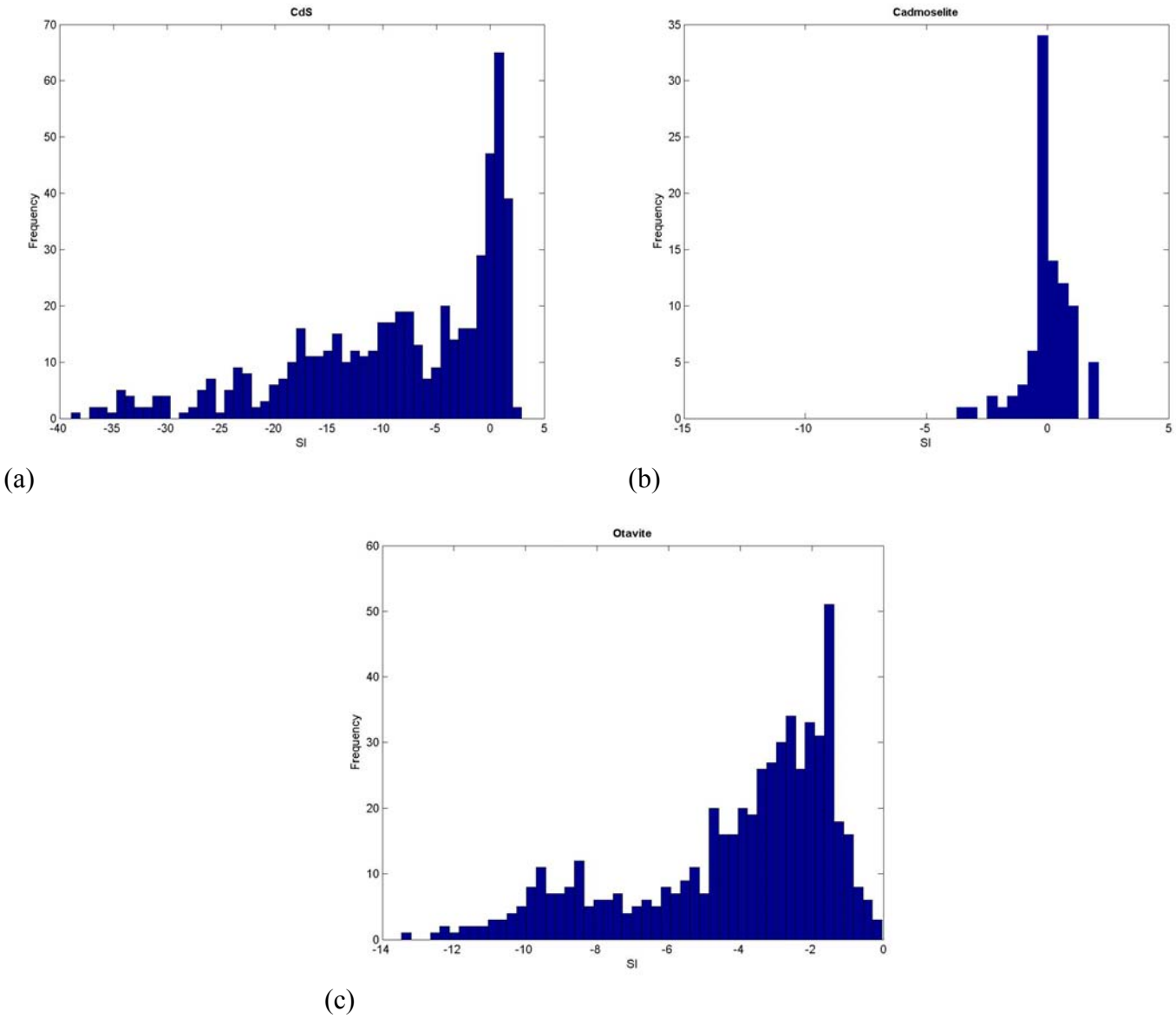

Fig. 3.27. Frequency Distribution of Saturation Indices of (a) CdS (Greenockite), (b) Cadmoselite and (c) Otavite. The Saturation Indices are calculated using a selected set of groundwaters from the NWIS. Eh is defined by Fe(III)/Fe(II) in solution, which generally does not significantly affect otavite saturation.

Mercury. The distribution of SI's for cinnabar, tiemannite (HgSe), and quicksilver are illustrated in Figure 3.28a–c. The distribution for cinnabar is similar to that of CdS, but a significant fraction is supersaturated in those groundwater samples that were analyzed for Hg, with SI(max) being achieved at SI ~ +1. The SI distribution for tiemannite is ill defined, because of the limited number of analyses conducted for both Hg and Se. However, most of the available determinations fall between SI = 0 and –1, suggesting that this phase might form, especially in Se rich environments.

In conformity with observations for CdS regarding interpretations concerning the saturation of this phase in groundwaters, similar arguments can be presented for caution in accepting the corresponding findings for cinnabar and tiemannite. The peaks reflect (a) the dispersion of analytical values in the calculation of SI for cinnabar and tiemannite, (b) false positive readings caused by the application of insufficiently sensitive methods, (c) uncertainty in the calculated solubility products of cinnabar and tiemannite, and finally (d) uncertainty regarding the identities and thermodynamic properties of Hg sulfide and selenide complexes in solution in the EQ3/6 distribution (see Appendices D and E).

The findings presented here are inconsistent with field observations by Benoit et al (2003) on shallow organic-rich sediments, and by Huerta-Diaz and Morse (1992) on shallow marine sediments, who show, respectively, that Hg activity is unsaturated with respect to cinnabar, and that Hg is preferentially incorporated in precipitating pyrite, rather than forming a discrete solid phase where Hg is an essential component. However, both field environments reflect transient authigenic conditions where metastable phases are likely controlling the aqueous solubility of Hg, and where long-term evolution of the system, as postulated by the Ostwald Rule of stages, will lead to recrystallization of pyrite and expulsion of Hg from the lattice involving the formation of metastable phases. Both cinnabar and tiemannite have been observed in coal (Tewalt et al., 2001; Brownfield et al., 2005; Kolker et al., 2006), and it is therefore probable that, given sufficient time, the natural environment evolves and saturation is achieved with respect to either or both minerals in shallow reducing groundwaters.

Also included in Figure 3.28 is the SI histogram for quicksilver, which shows a bimodal distribution. The secondary peak at SI ~ -1 probably reflects the true saturation state of quicksilver under reducing conditions. The supersaturation where SI(max) ~ +9 is indicative of artifacts caused by an erroneously elevated oxidation state calculated from the Fe(III)/Fe(II) ratio. Comparison should be made with the data provided by Run 1, in Section 3.4.5.2 below.

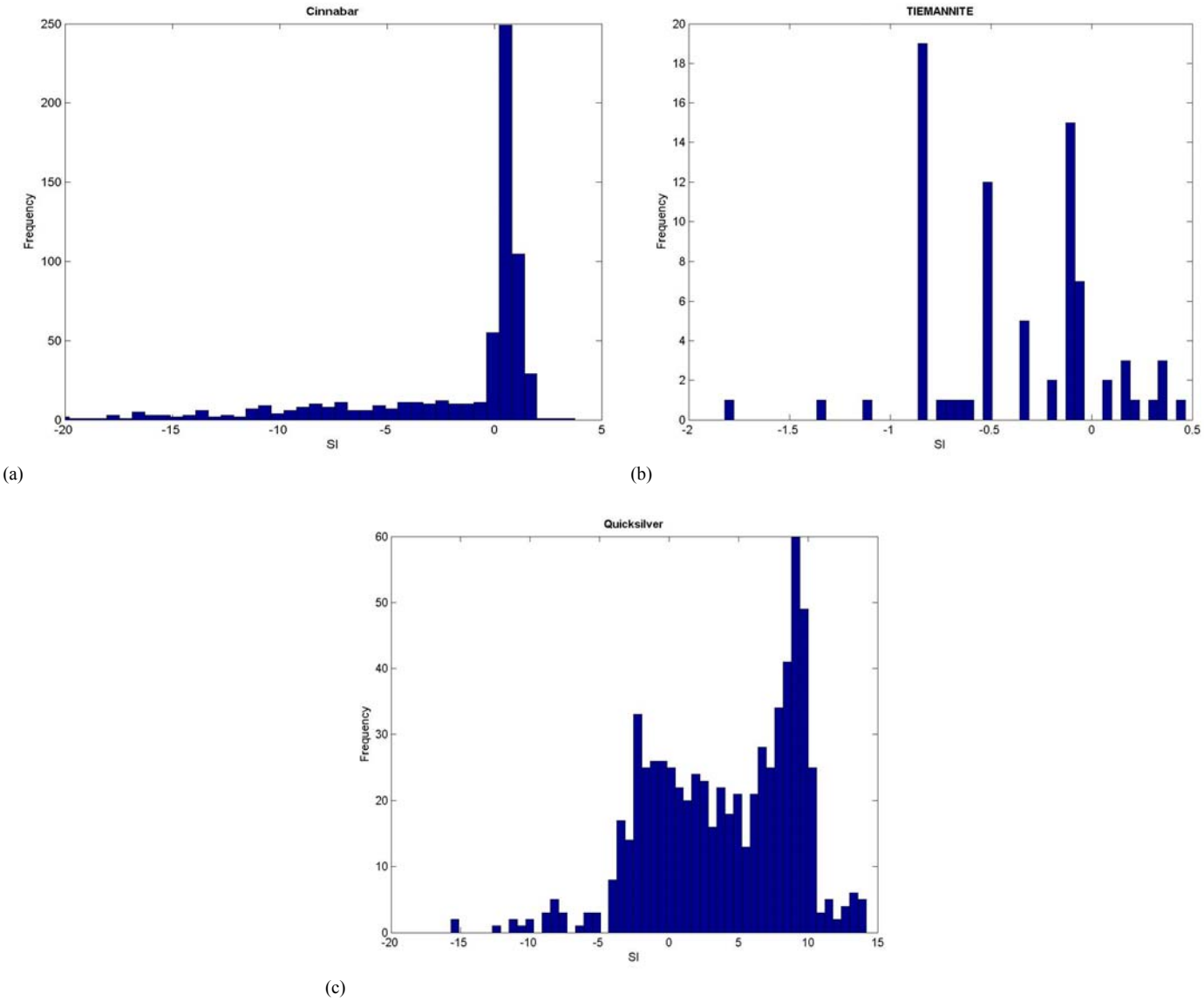

Fig. 3.28. Frequency Distribution of the Saturation Index of (a) Cinnabar, (b) Tiemannite, and (c) Quicksilver. The Saturation Indices are calculated using a selected set of groundwaters from the NWIS and assuming Eh to be defined by Fe(III)/Fe(II) in solution.

Lead. The thermodynamic control of Pb by galena (PbS) was assumed in a recent study to evaluate the impact of elevated $P(CO_2)$ on hazardous inorganic constituent concentrations in groundwaters (Wang and Jaffe, 2005), and provided a motivation for the current project. Therefore, the general behavior of Pb in groundwater, and of galena in particular, deserves special attention. Figures 3.29a through 3.29f illustrate the SI distributions for galena and clausthalite (PbSe), either of which might control the Pb activity in reducing groundwaters, and for five other minerals that might potentially control the Pb activity in oxic aquifers: cerussite ($PbCO_3$), hydrocerussite ($Pb_3(CO_3)_2(OH)_2$), plumbonacrite ($Pb_{10}(CO_3)_6O(OH)_6$), anglesite ($PbSO_4$) and mimetite ($Pb_5(AsO_4)_3Cl$). Another relatively insoluble Pb mineral, pyromorphite ($Pb_5(PO_4)_3Cl$), the phosphate analogue of mimetite, was not examined, because no special effort was made to acquire and evaluate phosphate analyses in the NWIS groundwater quality data.

The distribution of galena SI's suggests that a significant fraction of the groundwaters is saturated with respect to this mineral, as a clearly defined maximum frequency in SI is observed at SI ~ 0 in Figure 3.29a. In common with cadmoselite, clausthalite displays a tight dispersion in SI with SI(max) ~ 0. Also, as noted above, the stability field for Se(II) extends to higher oxidation states at a given pH than does S(II), thereby restricting the broader distribution shown by galena. The SI distribution profile for clausthalite strongly suggests that this phase may coexist with or supplant galena in potable water aquifers. The dominance of clausthalite over galena in Appalachian coal deposits is suggestive that this might be the case.

The findings regarding Pb carbonate minerals, and anglesite and mimetite, indicate that, with the exception of a very small fraction of groundwaters saturated with respect to cerussite, these minerals all show moderate to substantial degrees of undersaturation, and appear to be implausible candidates for control of Pb activity in all groundwaters studied. However, either cerussite or hydrocerussite saturation would be expected, depending on pH, if galena in an aquifer were to be oxidized. Taken together, these observations suggest that most groundwaters are sufficiently reducing to stabilize galena.

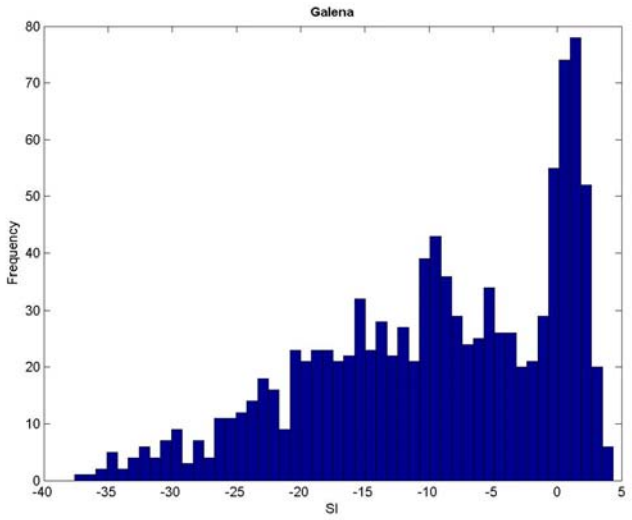

(a)

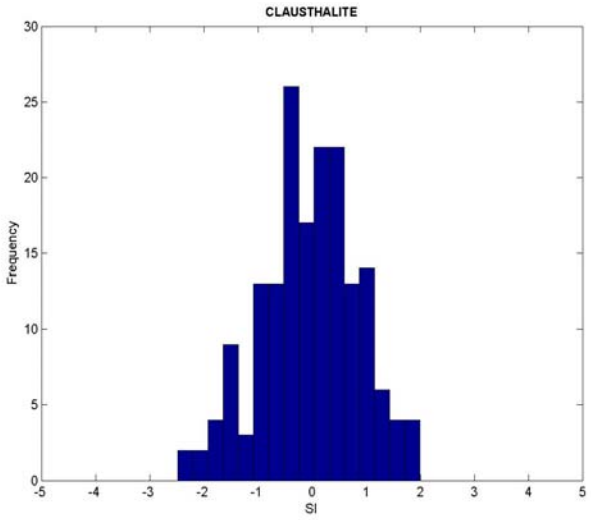

(b)

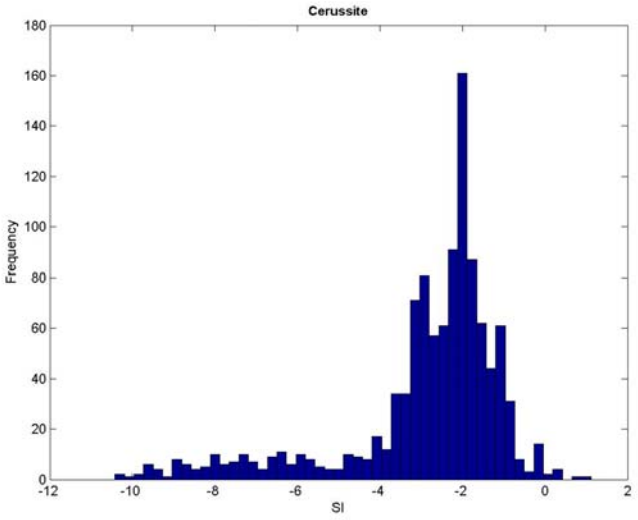

(c)

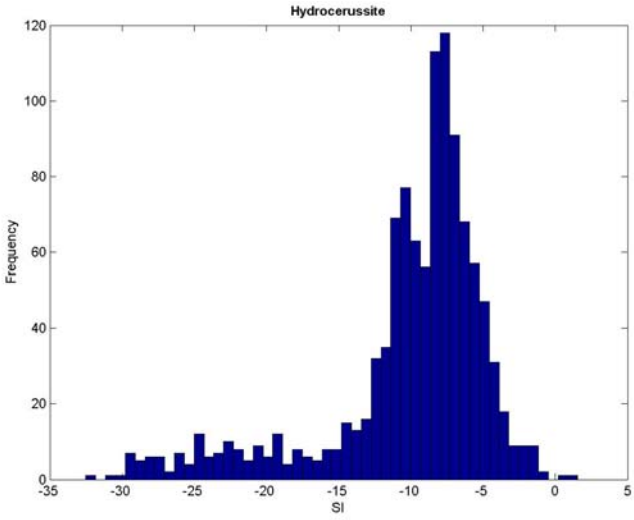

(d)

Fig. 3.29. (Part 1)

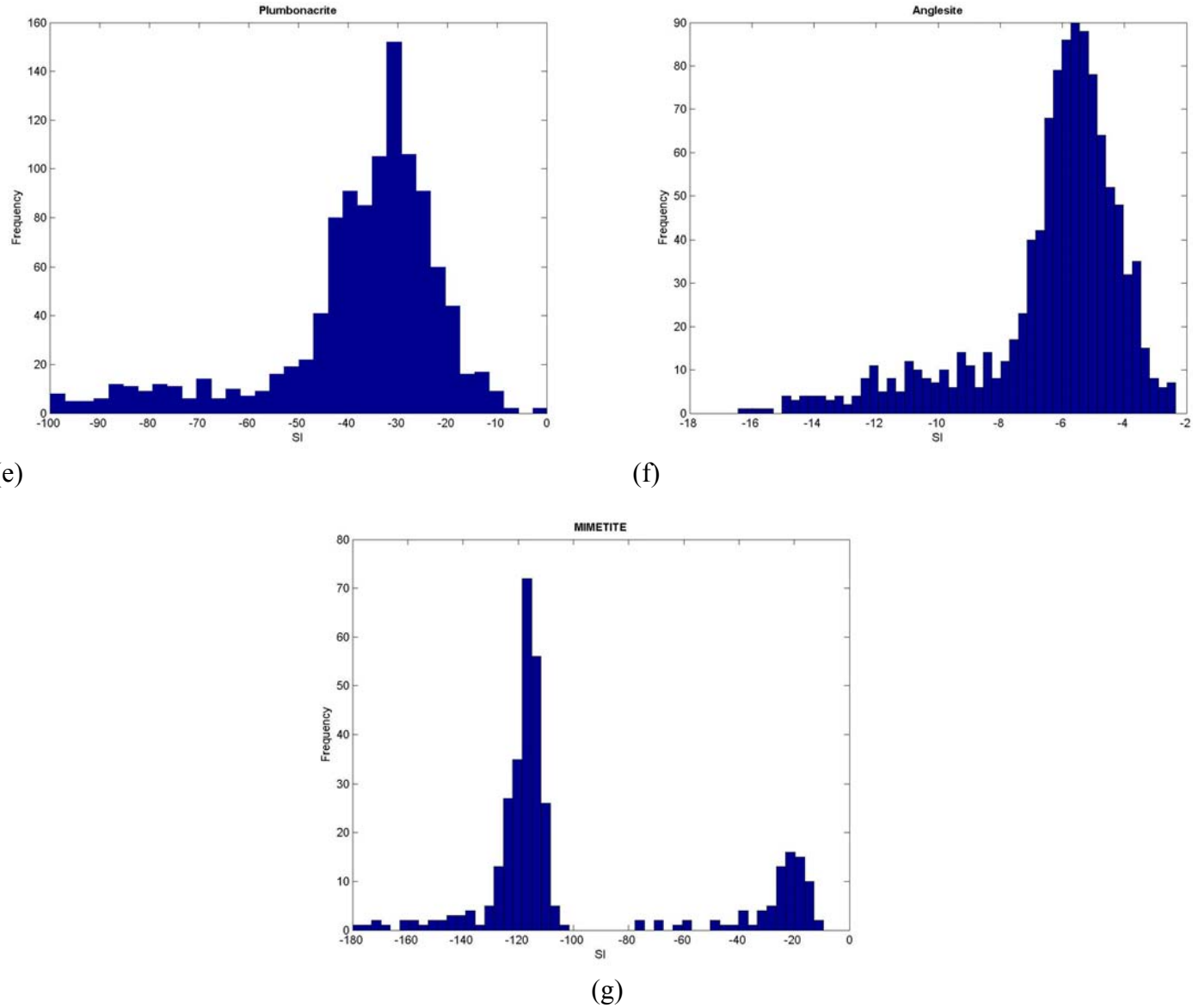

Fig. 3.29. Frequency Distribution of Saturation Indices of (a) Galena, (b) Clausthalite, (c) Cerussite, (d) Hydrocerussite (e) Plumbonacrite (f) Anglesite and (g) Mimetite in a selected set of groundwaters from the NWIS. The Saturation Indices are calculated assuming Eh to be defined by Fe(III)/Fe(II) in solution. Cerussite and anglesite saturations are not significantly affected by variations in Eh.

Finally, it should be mentioned that a significant array of naturally occurring, but obscure Pb silicates formed mainly under epithermal conditions have been described in the literature. Nothing is known of their solubilities or other thermodynamic properties, and thus it is

impossible to state that any one of these minerals might also control Pb activity in groundwaters, where oxidation has destabilized either galena or clausthalite. Although remote, the possibility exists that one of these minerals, as with hemimorphite controlling Zn, might likewise control Pb.

Antimony. Histograms of the saturation indices of selected antimony minerals, which might control the activity of Sb in potable groundwaters, are presented in Figure 3.30a-e. Gudmundite (FeSbS) is the antimony analogue of arsenopyrite and, like its As counterpart, is believed to enter in solid solution in pyrite. Gudmundite, berthierite ($FeSb_2S_4$), and stibnite (Sb_2S_3) are antimony minerals found in epithermal ore deposits of antimony, the latter being the primary and most abundant antimony ore mineral. Antimonselite (Sb_2Se_3), the selenium analogue of stibnite, is rarely observed in nature, but may control Sb activity in potable water aquifers. Kermesite (Sb_2S_2O), or red antimony, is commonly found as a supergene alteration product in antimony ores, but occasionally occurs as a primary mineral (Williams-Jones and Normand, 1997).

Interpretation of Sb activity control by candidate minerals is complicated by uncertainties regarding the validity of some of the Sb analyses in groundwaters, by the sparsity of data, and by uncertainties regarding the validity of the oxidation state defined by Fe(III)/Fe(II) where Fe analyses are of uncertain quality. From the distribution of measured concentrations illustrated by Figure 3.6f, we might infer that meaningful concentrations of Sb in NWIS groundwaters fall between –5 and -3 (in Log mg/L), and that concentrations above this range are artifacts resulting from the application of insufficiently sensitive analytical methods. However, as noted elsewhere, carte blanche rejection of questionable analyses cannot be justified through speculation alone, and therefore all available Sb measurements are used in the present analysis. In the following discussion, we recognize the limitations imposed by both the analytical methods and the sparsity of measurements.

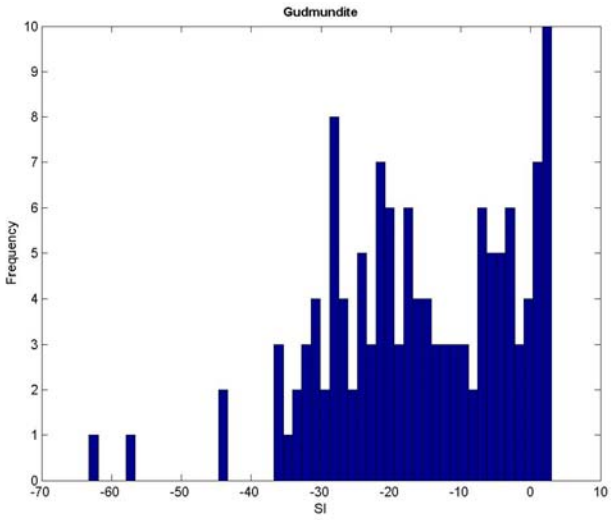

(a)

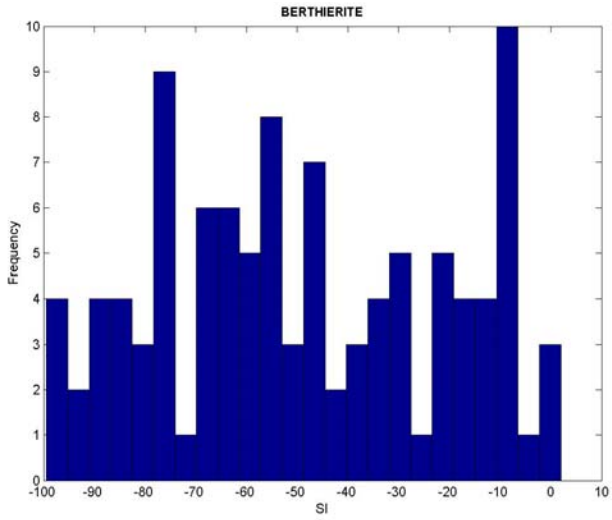

(b)

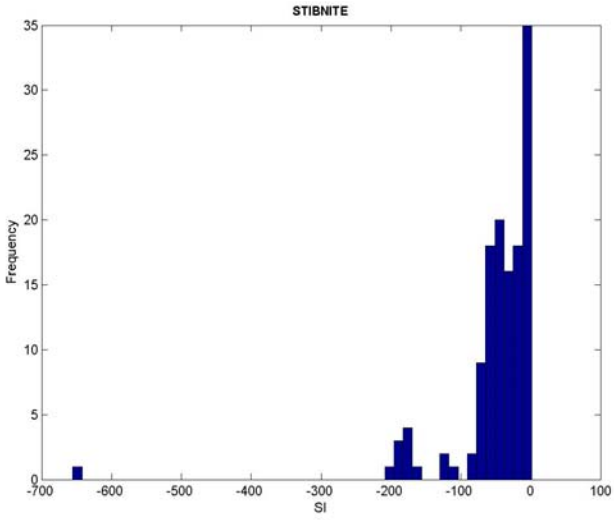

(c)

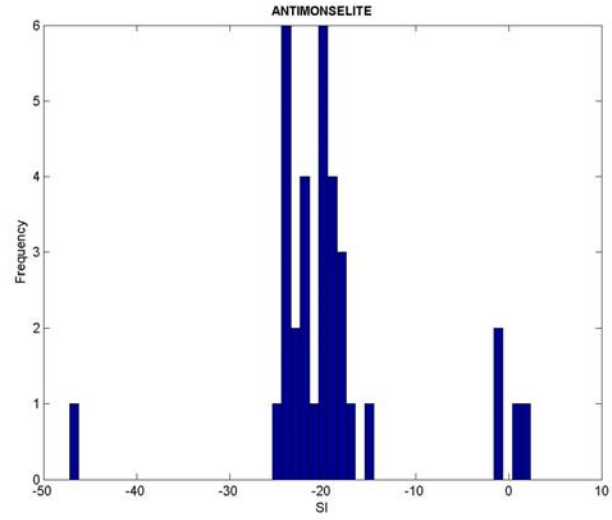

(d)

Fig. 3.30. (Part 1)

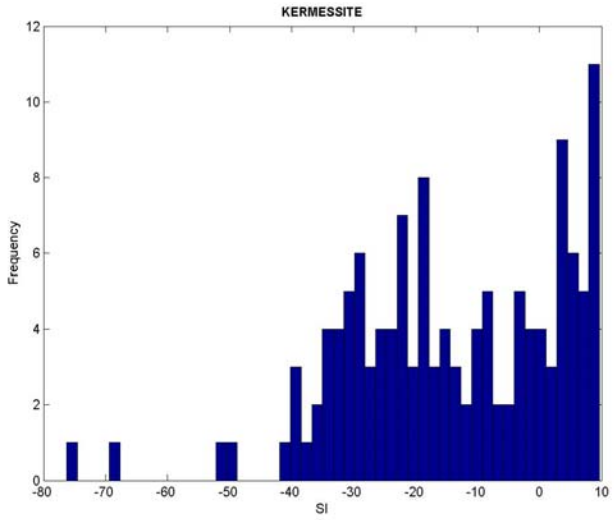

(e)

Fig. 3.30. Frequency Distribution of Saturation Indices of (a) Gudmundite, (b) Berthierite, (c) Stibnite, (d) Antimonselite and (e) Kermesite. The Saturation Indices are calculated using a selected set of groundwaters from the NWIS, and assuming Eh to be defined by Fe(III)/Fe(II) in solution.

Figures 3.30a, b, c, and d, showing the SI histograms for gudmundite, berthierite, stibnite, and antimonselite respectively, all suggest that Sb activity in groundwaters is unlikely to be controlled by their presence as discrete phases, since the majority of SI's suggest moderate to extreme undersaturation. However, for all four minerals, local maxima are observed at SI ~ 0. Under rare situations where strongly reducing conditions prevail, one of these minerals could be present, coexisting with pyrite or another iron sulfide phase at a given pH (Williams-Jones and Normand, 1997). Further analysis to substantiate this conjecture is presently beyond the scope of this study. In contrast to the antimony minerals referred to above, a significant population of SI's for kermesite is in positive territory. It is therefore probable that this mineral controls Sb activity in potable groundwaters.

Selenium. Selenium ranks as particularly important, not only as a hazardous constituent in its own right, but because of its potential as Se(-II) to complex strongly with other hazardous constituents in solution and to form extremely insoluble selenides. In Figure 3.31, we assemble SI histograms of all potential activity controlling selenides under consideration, i.e., ferroselite ($FeSe_2$), cadmoselite, tiemannite, clausthalite, and antimonselite.

The SI histogram for ferroselite displays a bimodal distribution with SI(max) at SI ~ -17 and –3. A similar distribution is also displayed in Run 1 (Figure 3.40), where SI(max) ~ -16 and –7.5. The less negative peak probably represents Se substitution for S in pyrite and indicates that insufficient Se is present in most potable water aquifer host rocks for saturation with respect to ferroselite. Spectroscopic studies have revealed the presence of dzharkenite, a ferroselite polymorph coexisting with selenian pyrite in shales associated with Western phosphate deposits (Ryser et al., 2005). However the average concentration of Se in these shales approaches 300 mg/kg, which is over three orders of magnitude greater than is believed to occur in most domestic potable water aquifer host rocks (see Section 3.6). An explanation for the peak centered about SI ~ -17 is not presently forthcoming.

Cadmoselite, tiemannite and clausthalite all appear to be at or close to saturation, suggesting that these selenides could co-exist with or supplant the corresponding sulfide, provided that the Gibbs Phase Rule is obeyed at equilibrium. The very limited SI data available for antimonselite suggests that this mineral, like its sulfide analogue, stibnite, is unlikely to be present and control Sb activity in NWIS potable groundwaters. However, it is interesting to speculate whether Se analogues of kermesite with formulas such as Sb_2SSeO or Sb_2Se_2O, although never observed or described, might be present in small quantities. Further study to define their stability fields as functions of Sb and Se abundance and pH and Eh is merited.

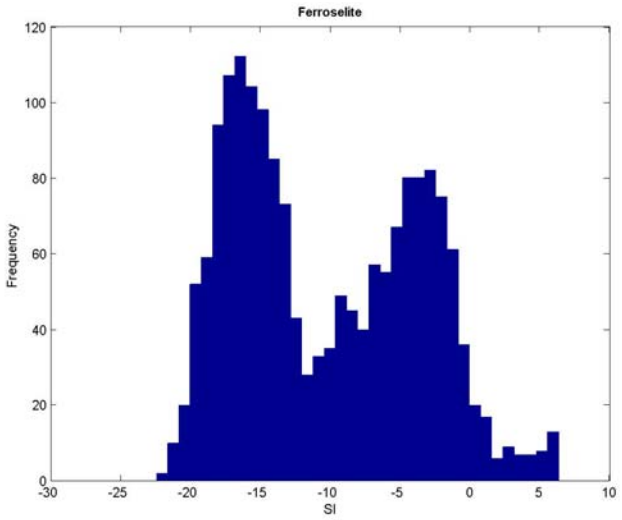

(a)

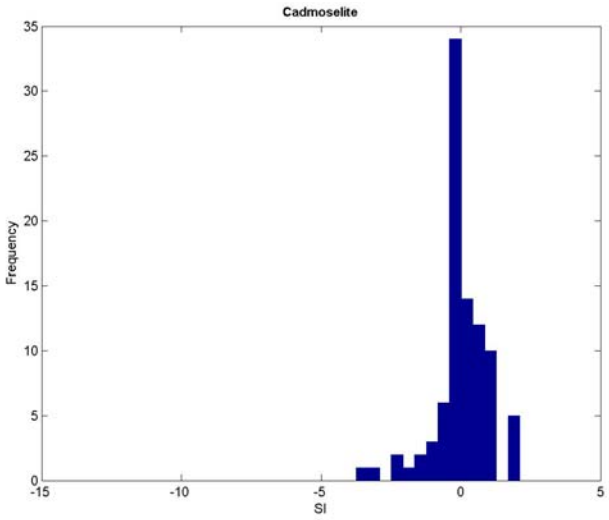

(b)

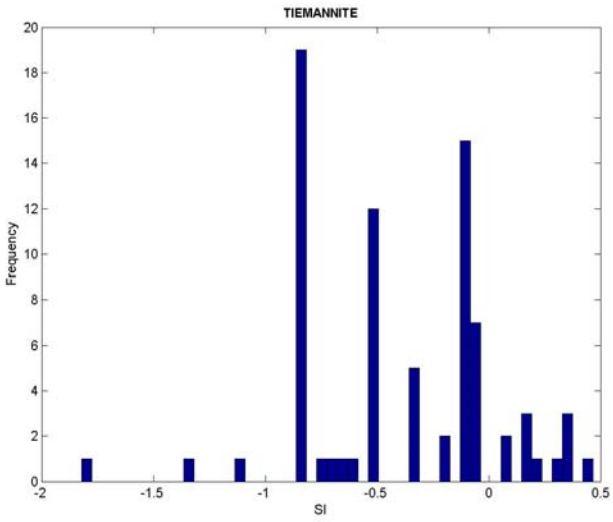

(c)

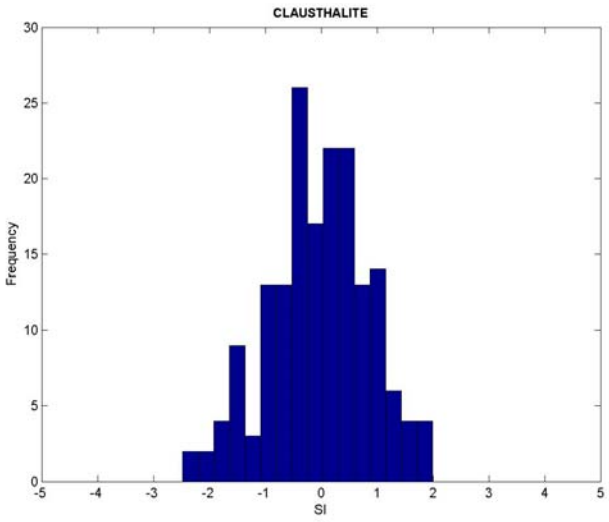

(d)

Fig. 3.31. (Part 1)

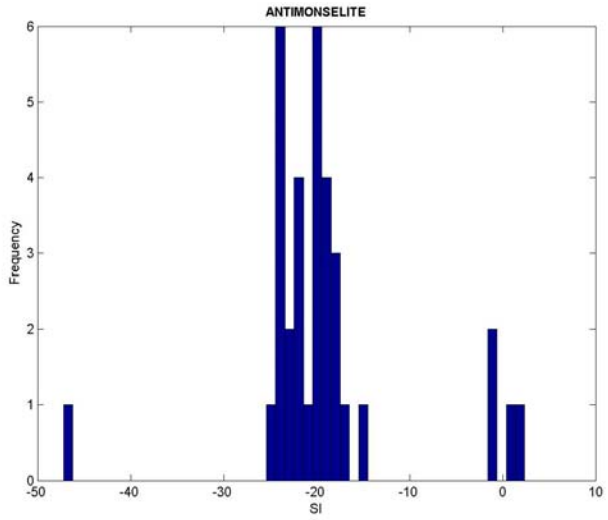

(e)

Fig. 3.31. Frequency Distribution of Saturation Indices of (a) Ferroselite, (b) Cadmoselite, (c) Tiemannite, (d) Clausthalite, and (e) Antimonselite. The Saturation Indices are calculated using a selected set of groundwaters from the NWIS, and assuming Eh to be defined by Fe(III)/Fe(II) in solution.

Uranium. Figure 3.32 gives SI histograms for uraninite (UO_2), coffinite ($USiO_4$) and a typical and fairly common oxidation product of uraninite, uranophane ($Ca(UO_2)_2SiO_3(OH)_2.5H_2O$). A relatively sharp peak in the frequency histogram for uraninite (UO_2) is observed at SI ~ +1. A similar result is obtained for coffinite at SI ~ +1.5. Bearing in mind that SiO_2(aq) had been set to be in equilibrium with respect to opal C-T, and that the SiO_2(aq) activity for this silica polymorph is about 5 times higher than for the most stable polymorph, quartz, these results suggest that U activity in solution is probably controlled by either uraninite, coffinite, or both. The reason for the observed modest degree of supersaturation is not known, and further review to investigate the cause is warranted. This finding is consistent with field observations of sediment hosted uranium deposits, where the co-existence of the two minerals is not uncommon (Abdel-Gaward and Kerr 1961; Drew Ilger et al., 1987). Furthermore, the finding is strongly indicative that most groundwaters are sufficiently reducing to stabilize one or both minerals. The histograms of uraninite and coffinite can be compared with that for uranophane, where U is present in the (VI) instead of the (IV) state. It is obvious that all groundwaters examined are

unsaturated with respect to this mineral, further substantiating the conclusion that the groundwaters are sufficiently reducing to stabilize U^{+4} instead of UO_2^{+2}.

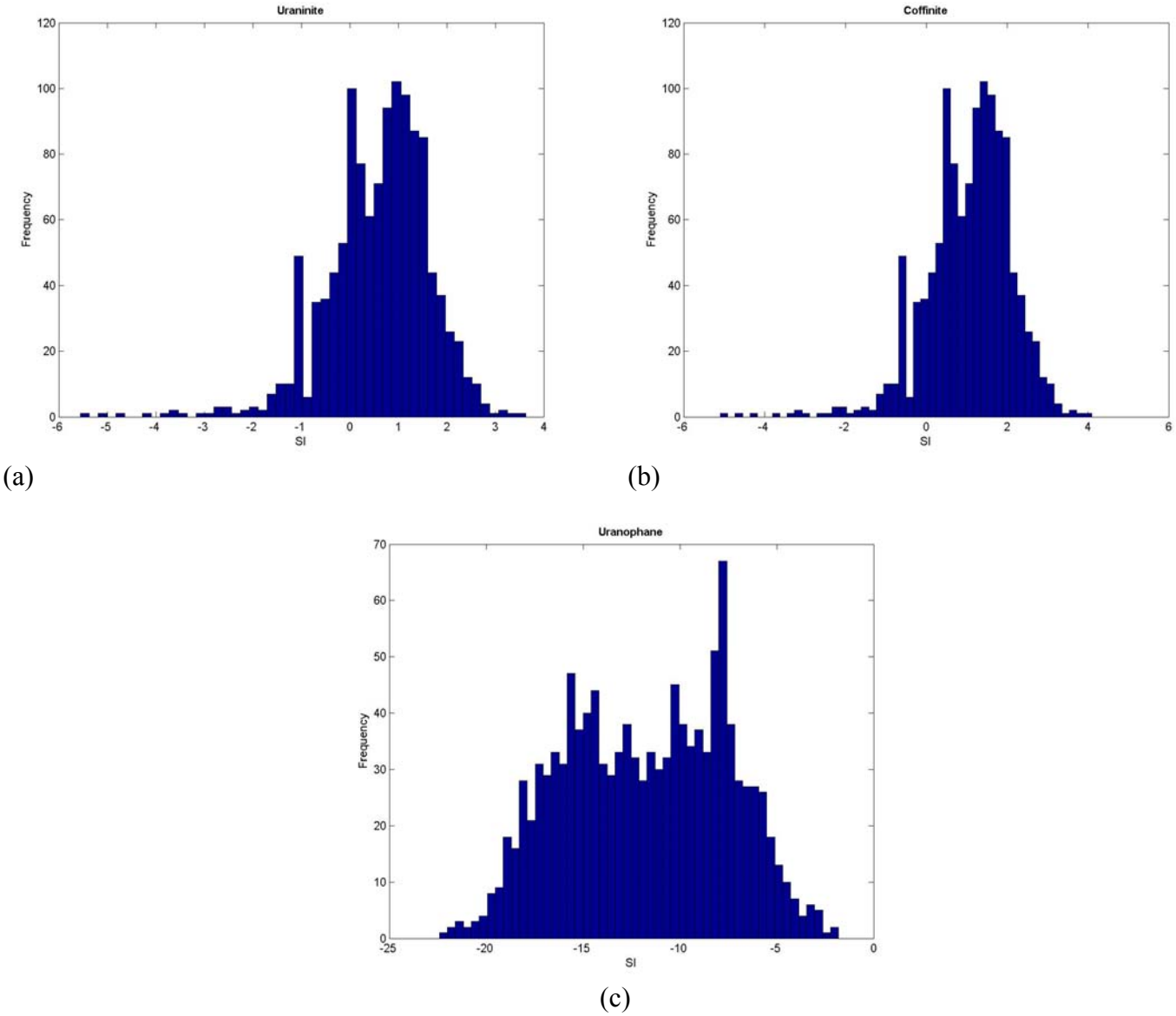

Fig. 3.32. Frequency Distribution of the Saturation Index of (a) Uraninite, (b) Coffinite and (c) Uranophane. The Saturation Indices are calculated using a selected set of groundwaters from the NWIS, and assuming Eh to be defined by Fe(III)/Fe(II) in solution.

Zinc. Figures 3.33a, b, c, and d provide the SI histograms for sphalerite (ZnS), smithsonite ($ZnCO_3$), hydrozincite ($Zn_5(CO_3)_2(OH)_6$) and hemimorphite ($Zn_4Si_2O_7(OH)_2.H_2O$).

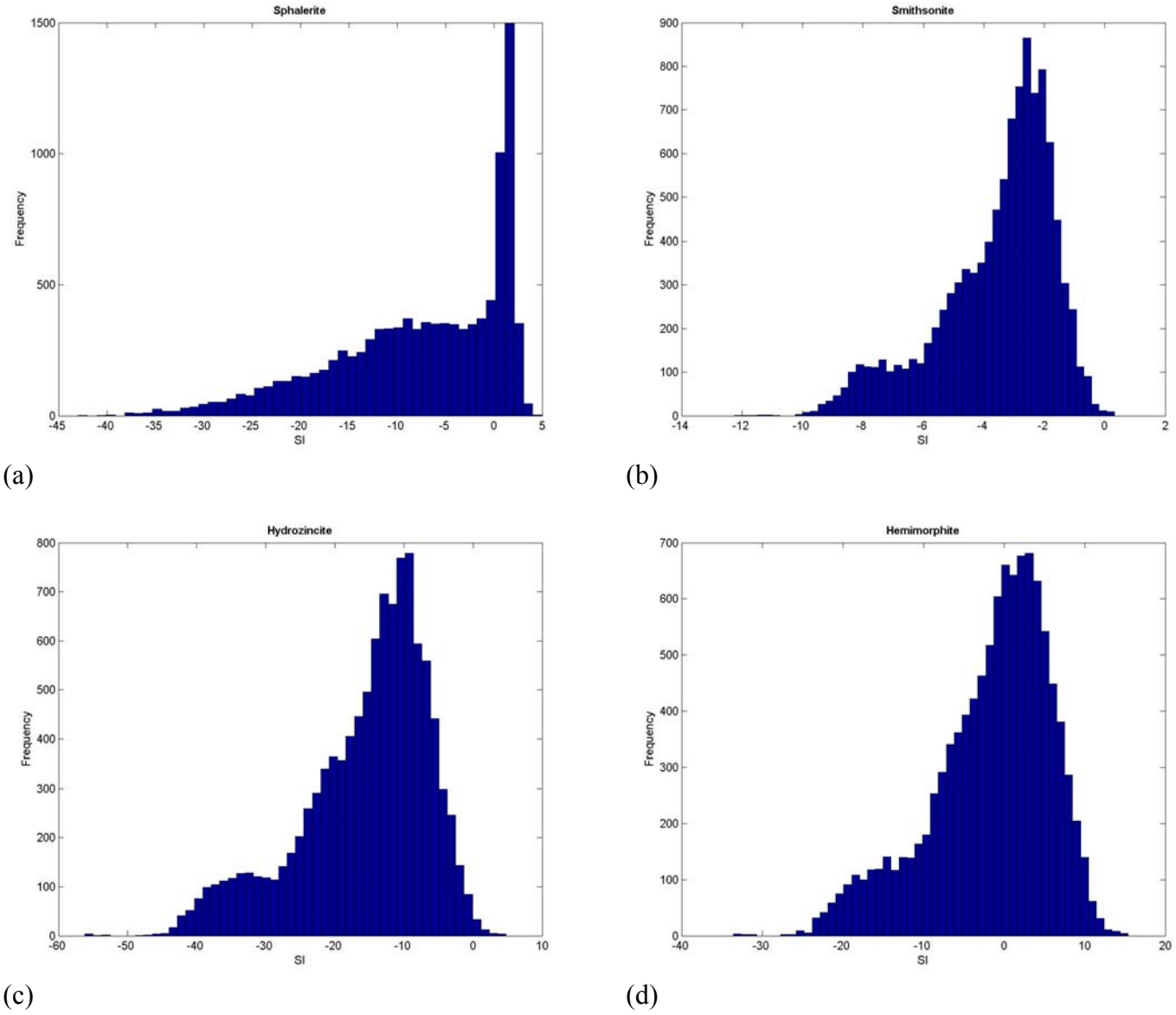

Fig. 3.33. Frequency Distribution of the Saturation Indices of (a) Sphalerite, (b) Smithsonite, (c) Hydrozincite and (d) Hemimorphite. The Saturation Indices are calculated , using a selected set of groundwaters from the NWIS, and assuming Eh to be defined by Fe(III)/Fe(II) in solution.

The histogram for sphalerite shows a maximum at SI ~ +2. This observation suggests that the Zn concentration in reducing groundwaters could be controlled by sphalerite. The reason for the positive SI deviation from zero is not clear. Interpretation is further complicated by the observation that the SI frequency for hemimorphite, SI ~ +2. The SiO_2(aq) activity in the analysis is defined by opal-CT, which is approximately 0.7 log units higher than that for quartz saturation. For groundwaters saturated with respect to quartz, the saturation index would be approximately zero. This suggests that control of Zn activity in groundwaters may be determined by either sphalerite and/or hemimorphite. Control of Zn activity by smithsonite or hydrozincite appears to be unlikely in all but significantly alkaline groundwaters.

3.4.5.2 Discussion of Results from Run 1

A spread of Eh values is observed in Run 0 above, depending on pH and the availability of Fe(II), Fe(II) plus Fe(III), or Fe(total) analyses, together with the assumption of goethite saturation in all analyses. Run 1, in contrast, defines the Eh at a given pH through the coexistence of goethite and pyrite, which constitutes an Eh buffer. It is thus assumed that all groundwaters are reducing, even though it is probable that a minor fraction might actually be oxidizing. This concession to expediency in the absence of feasible methods for characterizing the oxidation state of groundwaters other than through the method adopted for Run 0 should be borne in mind when considering the following analysis of thermodynamic controls.

Arsenic. SI histograms for arsenopyrite, scorodite, and symplesite are given in Figures 3.34a, b and c. They differ substantially from those generated under Run 0, because Eh is now tightly constrained, and the variability induced by transitions in oxidation state from As(III) to As(V) is no longer a factor. The SI profile for arsenopyrite peaks at SI ~ -3.5, suggesting that As activity is controlled primarily by arsenopyrite in solid solution in pyrite (arsenian pyrite). Neither scorodite nor symplesite could be present in the aquifers from which the sampled population of potable groundwaters are taken, since both are strongly undersaturated.

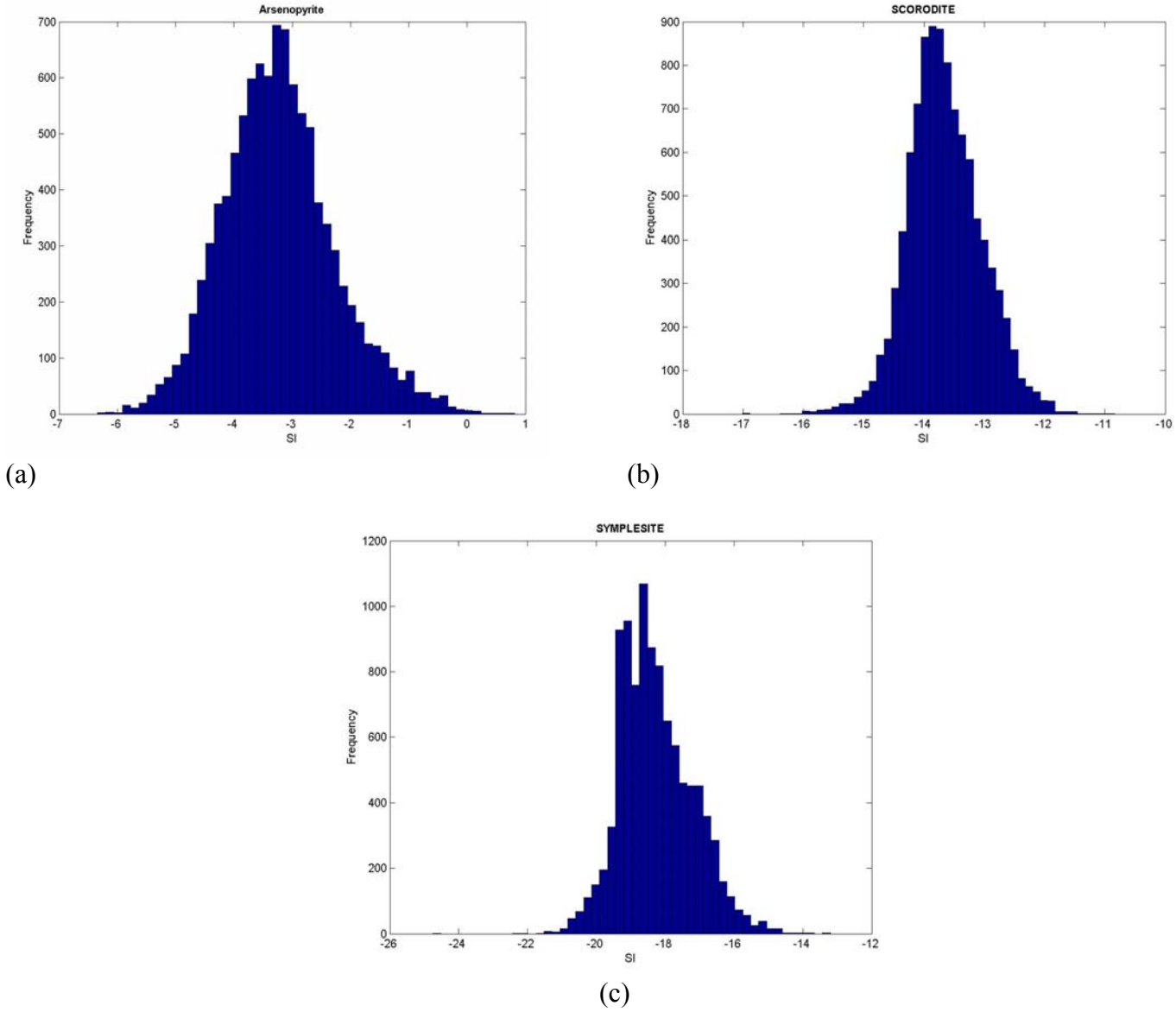

Fig. 3.34. Frequency Distribution of Saturation Indices of (a) Arsenopyrite, (b) Scorodite, and (c) Symplesite. The Saturation Indices are calculated using a selected set of groundwaters from the NWIS, and assuming Eh to be defined by the coexistence of pyrite and goethite.

Barium. The histogram for barite, Figure 3.35, is similar to that of Figure 3.26a. The profile clearly shows a negative skew rather than being symmetrical. The latter would be expected if all groundwaters were saturated with respect to barite, thus suggesting a bias towards undersaturation in the population of sampled groundwaters. Presentation of the corresponding

histogram for witherite is omitted, since it would be essentially identical to that displayed under barium in Run 0.

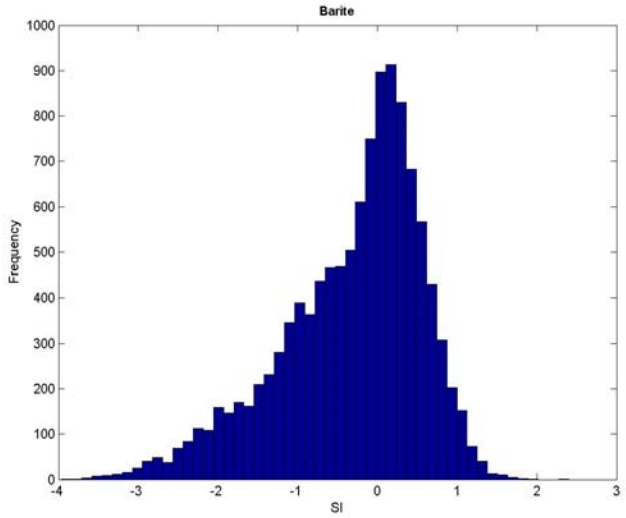

Fig. 3.35. Frequency Distribution of the Saturation Index of Barite. The Saturation Indices are calculated for a selected set of groundwaters from the NWIS. Eh is defined by the coexistence of pyrite and goethite, but does not significantly affect barite saturation.

Cadmium. The CdS SI histogram, Figure 3.36a, displays a trimodal distribution with SI maxima at ~ -3, -0.5, and +1. This complex distribution is probably in part an artifact caused by the bi-modal distribution of analyzed Cd concentrations (Figure 3.6d). The analysis conducted in Appendix B2 suggests that SI(max) ~ -0.5 is more credible, and is supported by further selection and evaluation of only those groundwater analyses conducted using the most sensitive analytical methods under Runs 4 and 5 (see Section 3.4.6, below). The cause of the peak where SI(max) ~ -3 might be explained by the presence of competitive selenide complexing depressing the activity of Cd^{+2} in those groundwater samples also reporting Se. If this supposition is true, then saturation with respect to CdS is not achieved, and the Cd^{+2} activity reflects a solid solution in sphalerite and/or galena. However, the possibility remains that greenockite could be saturated at potable water aquifer temperatures, because solid solution substitution in sphalerite and/or galena would decrease with falling temperature. Further examination of the water quality analyses, and evaluation of the temperature-dependent behavior of Cd substitution in sphalerite and/or galena,

are needed to resolve this matter. The SI histogram for cadmoselite in Figure 3.36b is relatively well defined, with SI(max) at ~ 0, although a small scattering of SI values occur between SI = -4 and –1. Saturation suggests that Cd^{+2} activity may actually be controlled by the presence of cadmoselite. The findings are consistent with those of Run 0 in Figure 3.27b.

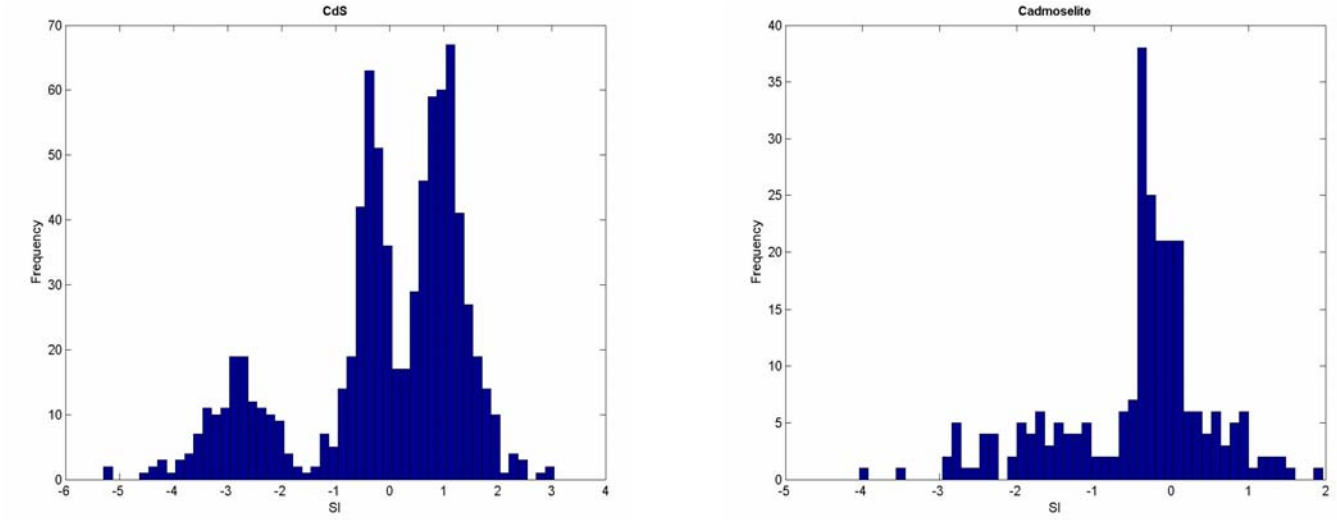

(a) (b)

Fig. 3.36. Frequency Distribution of Saturation Indices of (a) CdS (Greenockite) and (b) Cadmoselite. The Saturation Indices are calculated assuming Eh to be defined by the coexistence of pyrite and goethite, using a selected set of groundwaters from the NWIS.

Mercury. Figures 3.37a-c show the SI histograms for cinnabar, tiemannite and quicksilver. Peak frequencies in SI for all three minerals are generally consistent with the findings of Run 0 (Figure 3.28). The supersaturation revealed in the histogram for cinnabar, where SI ~ 1.0, indicates its likely presence in aquifers, whereas tiemannite could also be present occasionally, as SI(max) ~ -0.5, and therefore close to saturation. The observed saturation with respect to quicksilver (SI(max) ~ 0) is inconsistent with the reducing conditions imposed by the goethite/pyrite buffer. Taken together, the supersaturation with respect to cinnabar and saturation with respect to quicksilver suggest an error in calculated Hg^{+2} activity by approximately one log unit. Several alternative explanations are possible, and further refinement of the analysis in this report is needed. However, uncertainties associated with the thermodynamic parameters used in the analysis (see discussion under mercury in the preceding Section 3.4.5.1) preclude drawing a

definitive conclusion at this time. If a systematic error in Hg^{+2} activity were confirmed, then SI (tiemannite) would fall to ~ -1.5, and would be unlikely to be present in other than Se-rich environments.

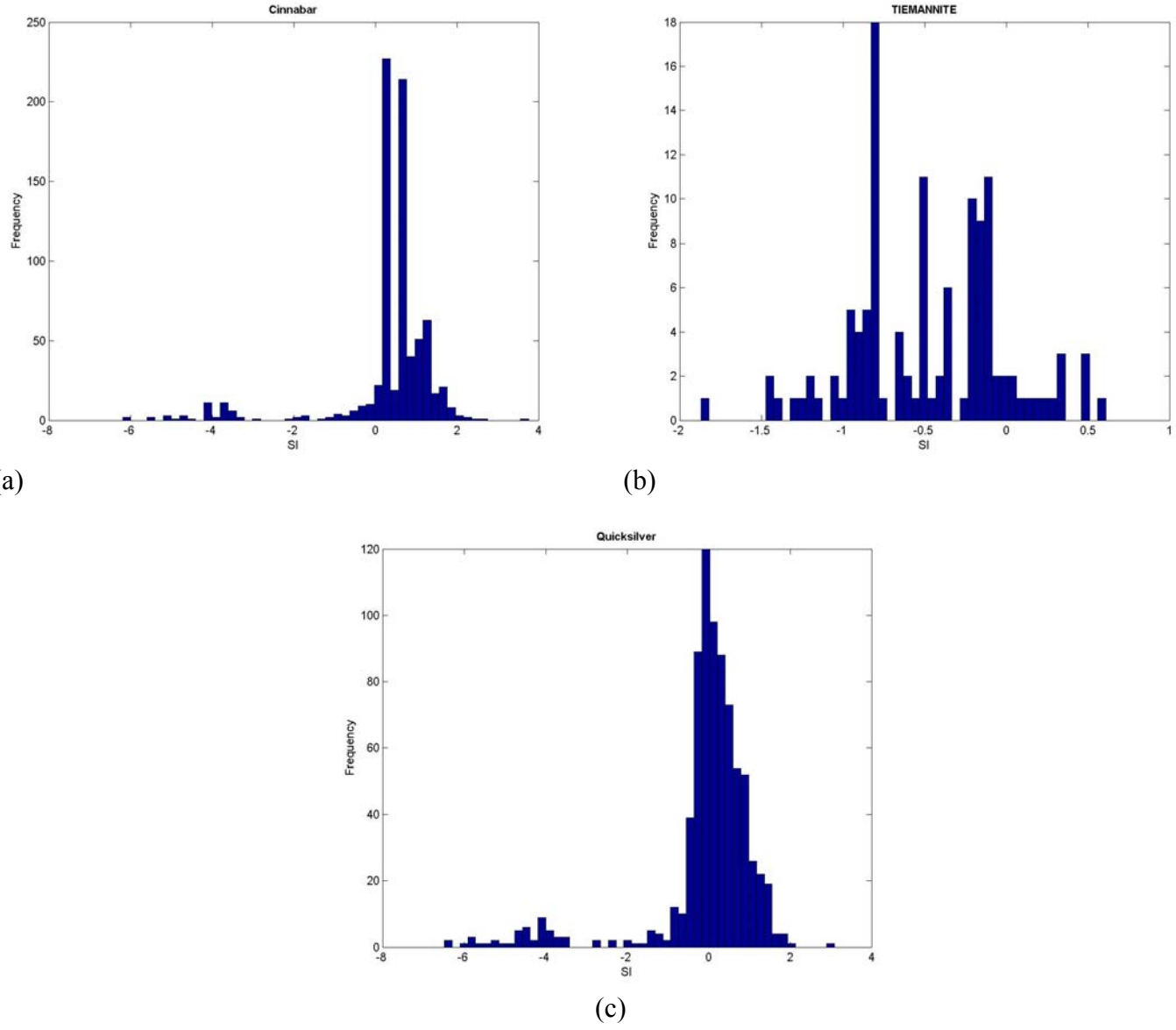

Fig. 3.37. Frequency Distribution of the Saturation Index of (a) Cinnabar, (b) Tiemannite and (c) Quicksilver. The Saturation Indices are calculated assuming Eh to be defined by the coexistence of pyrite and goethite, using a selected set of groundwaters from the NWIS.

Lead. SI histograms for galena, clausthalite and cerussite are presented in Figures 3.38a, b, and c. The histogram for galena is represented by a ragged single peak with a maximum at about SI ~ +1.0. In contrast to the corresponding histogram for Run 0 (Figure 3.29a), the dispersion is far smaller owing to the uniform treatment whereby all analyses are saturated with respect to goethite and pyrite. The maximum frequency for clausthalite is at SI ~ -0.5, which compares well with Figure 3.29b from Run 0. Both analyses support the belief that either galena, clausthalite, or both could control the Pb^{+2} activity in potable groundwaters.

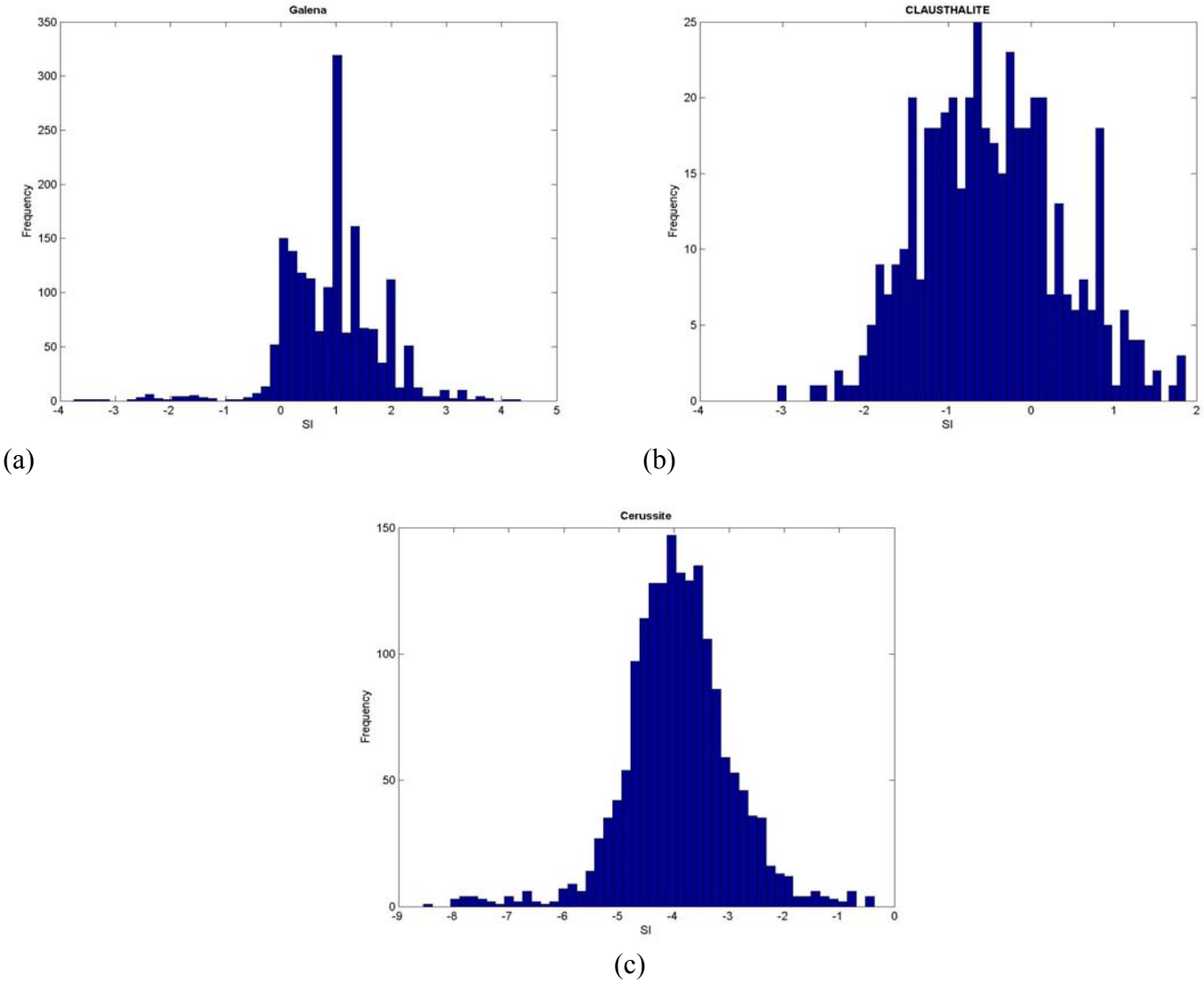

Fig. 3.38. Frequency Distribution of Saturation Indices of (a) Galena, (b) Clausthalite and (c) Cerussite. Eh is defined by the coexistence of pyrite and goethite, but does not significantly affect cerussite saturation.

The SI histogram for cerussite indicates that this mineral does not control Pb activity in most groundwaters under reducing conditions. However, the small secondary peak at SI ~ 0 suggests that a small percentage, ~ 5%, of potable groundwaters could be saturated with respect to this mineral. It should be noted that, were this to be the case, the groundwater would be oxidizing, and the assumption of goethite/pyrite equilibrium would no longer be applicable.

Antimony. SI histograms for gudmundite, stibnite, antimonselite and kermesite are presented in Figures 3.39a, b, c, and d. The very sparse dataset represented in the corresponding Figures 3.30a, b, c, and e is augmented in Run 1, because a significant number of Sb analyses were eliminated in Run 0, due to the absence of analyses for Fe in the same groundwater sample. Nevertheless, the results are largely comparable and the conclusions reached under the discussion for antimony in Section 3.4.5.1 are generally applicable. The bimodal distributions, especially evident with respect to stibnite and kermesite, result from the bimodal distribution in Sb concentration observable in Figure 3.6f. As discussed elsewhere in this report (Section 3.3.5, Appendix B2), the more positive peaks in SI are artifacts caused by the application of insufficiently sensitive analytical methods, and therefore reference should be made to the more negative peak. The histogram for gudmundite, Figure 3.39a, is more clearly defined than its counterpart, Figure 3.30a, due to the constraints imposed on Eh by the pyrite/goethite couple. All SI values are negative and peak at SI(max) ~ -5. The result is consistent with the likely solid solution of the gudmundite component in pyrite, in analogy with the corresponding arsenopyrite solid solution. The stibnite and antimonselite histogram shows SI(max) ~ -13 and -20, respectively, indicative that neither mineral is likely to be present in potable water aquifers. The peak value in SI frequency for kermesite occurs at SI ~ -0.5, which again suggests its potential occurrence as a mineral controlling the activity of Sb(III) in solution, especially in aquifers deficient in pyrite.

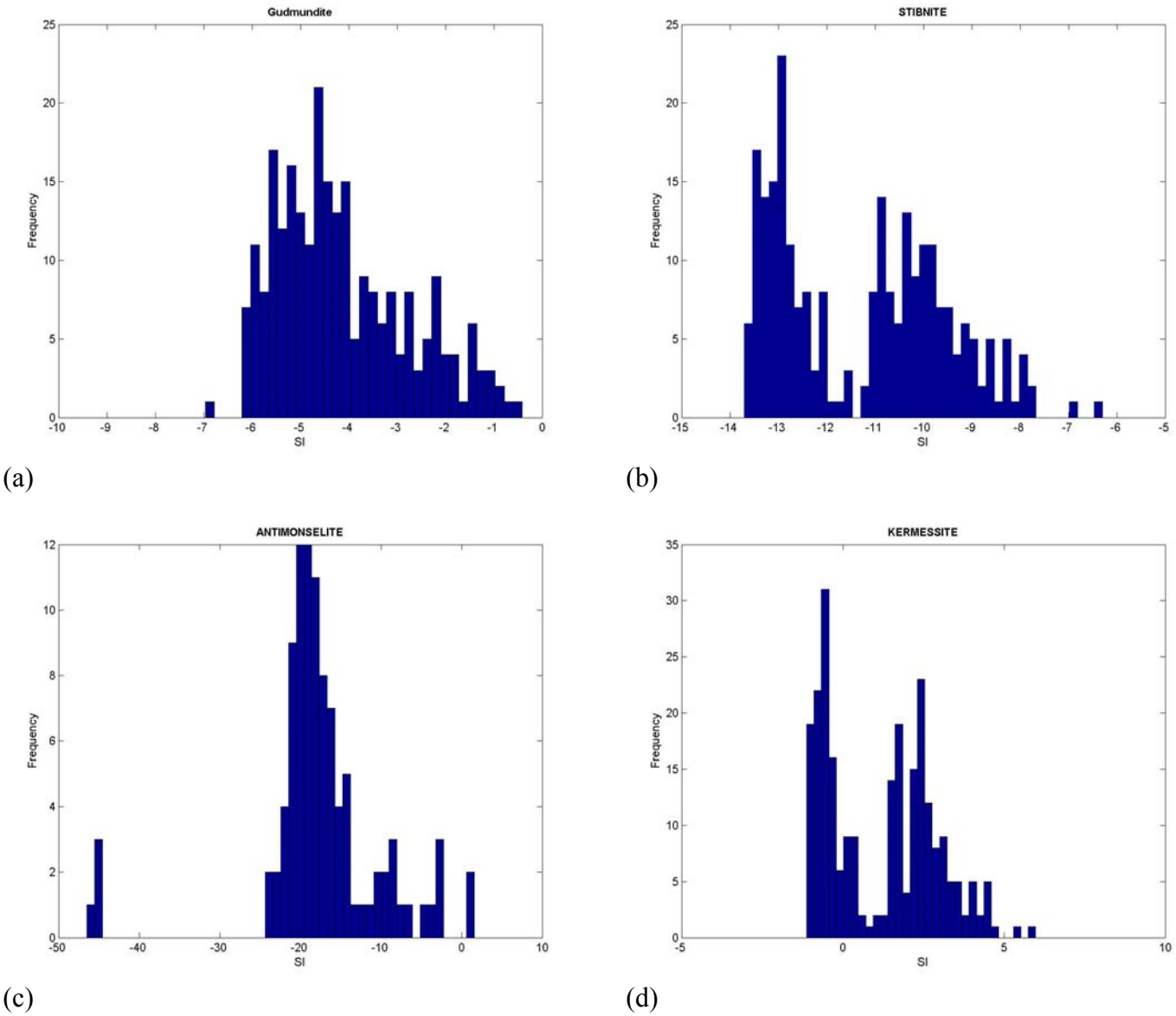

Fig. 3.39. Frequency Distribution of Saturation Indices of (a) Gudmundite, (b) Stibnite, (c) Antimonselite and (d) Kermesite. The Saturation Indices are calculated assuming Eh to be defined by the coexistence of pyrite and goethite, using a selected set of groundwaters from the NWIS.

Selenium. SI histograms for all selenium minerals are again assembled in Figures 3.40. The ferroselite SI histogram gives a bimodal distribution, potentially attributed to the omission of analyses of species in solution that complex selenium, i.e., Cd, Hg, Pb, Zn, thus giving rise to

elevated HSe^- activities in the groundwaters. However, this artifact requires further confirmation. The profile at SI(max) ~ -15 probably represents the true state of saturation with respect to ferroselite in the evaluated set of NWIS groundwaters. With the exception of antimonselite, the remaining minerals all appear to be close to or at saturation, and therefore could be effective in controlling SE(II) activity in potable groundwaters.

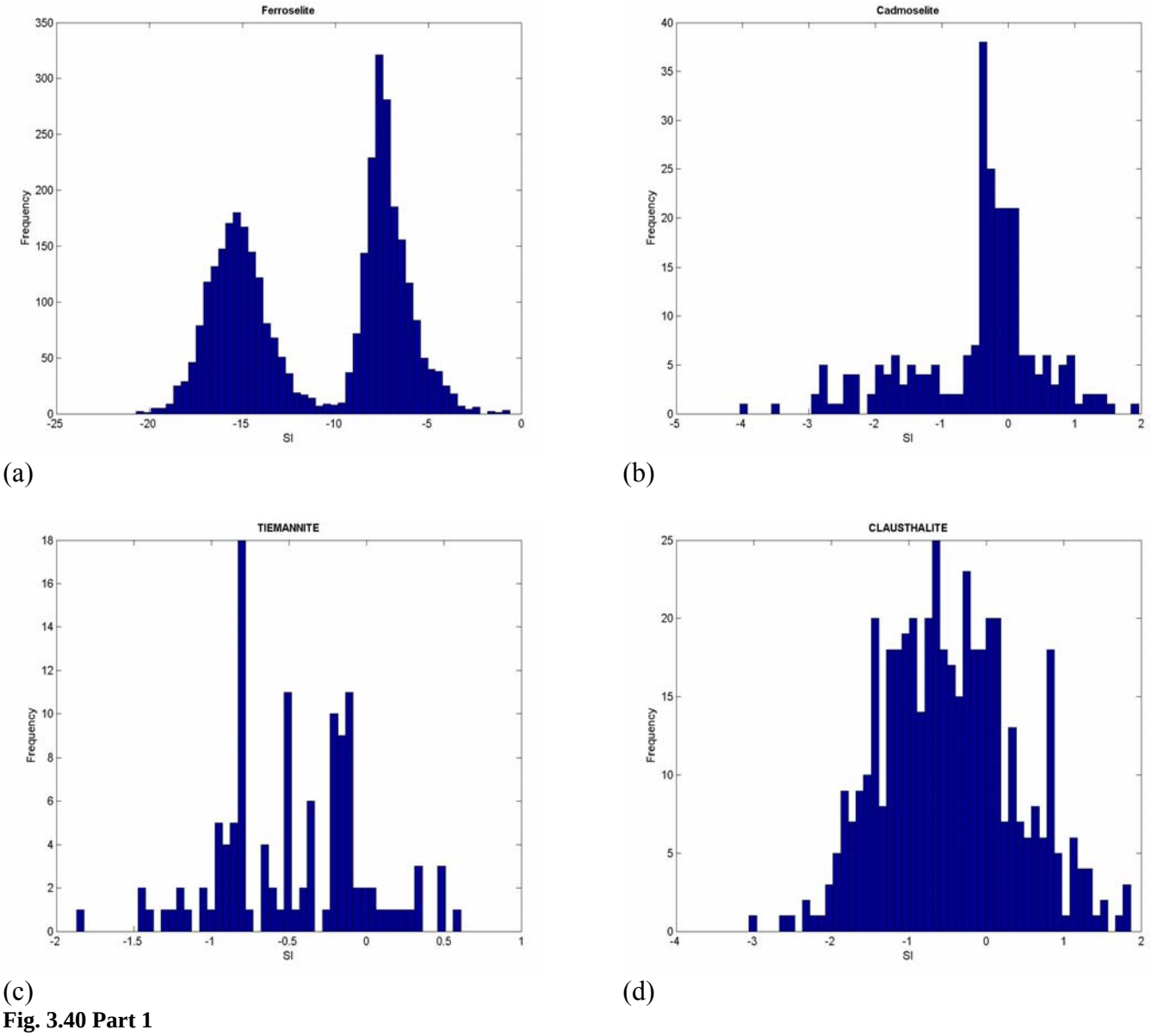

Fig. 3.40 Part 1

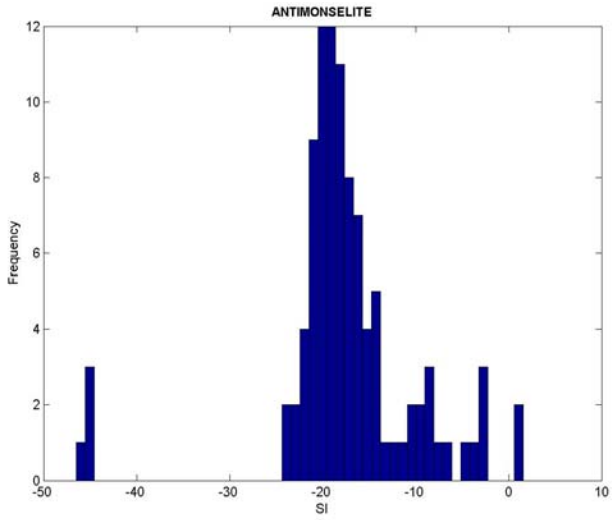

(e)

Fig. 3.40. Frequency Distribution of Saturation Indices of (a) Ferroselite, (b) Cadmoselite, (c) Tiemannite, (d) Clausthalite and (e) Antimonselite. The Saturation Indices are calculated assuming Eh to be defined by the coexistence of pyrite and goethite, using a selected set of groundwaters from the NWIS.

Uranium. Results for uranium in Figure 3.41 are similar to those of Run 0. Uraninite shows SI ~ +1, whereas coffinite shows SI ~ +1.5. In correcting for SiO_2(aq) from saturation with respect to opal-CT and quartz, coffinite SI would be approximately +0.7, which suggests that the occurrence frequency of coffinite would be comparable to that of uraninite, consistent with field observations of sediment-hosted uranium deposits (Abdel-Gaward and Kerr, 1961; Drew Ilger et al., 1987).

Zinc. The single peak in SI in the histogram for sphalerite, Figure 3.42, is consistent with the conservative assumptions of Run 1, leading to SI ~ +1, which is comparable with that given by Run 0. The negative skew suggests that not all groundwaters are saturated with respect to sphalerite. The histogram for hemimorphite is also given, even though this mineral is more likely to be present under more oxidizing conditions where pyrite is no longer stable. The peak SI frequency occurs at SI ~ -2, suggesting that hemimorphite is less likely to be found coexisting with sphalerite and pyrite, even though the relative stabilities for all three minerals are comparable.

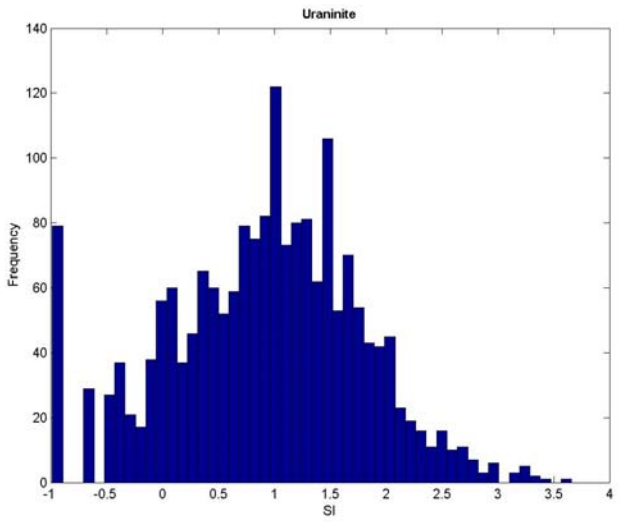

(a)

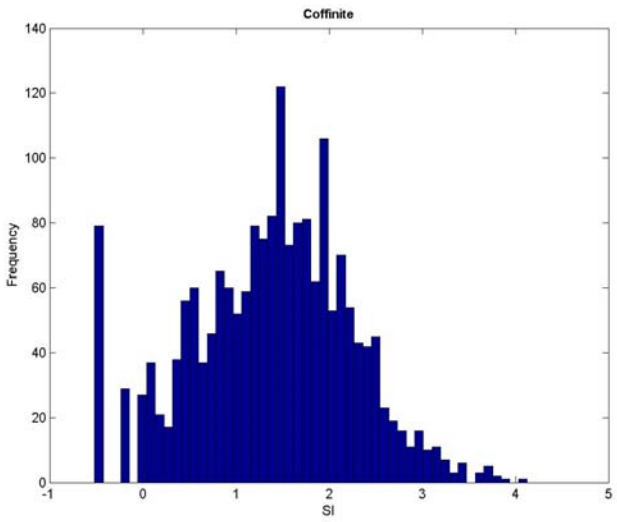

(b)

Fig. 3.41. Frequency Distribution of the Saturation Index of Uraninite. The Saturation Indices are calculated assuming Eh to be defined by the coexistence of pyrite and goethite, using a selected set of groundwaters from the NWIS.

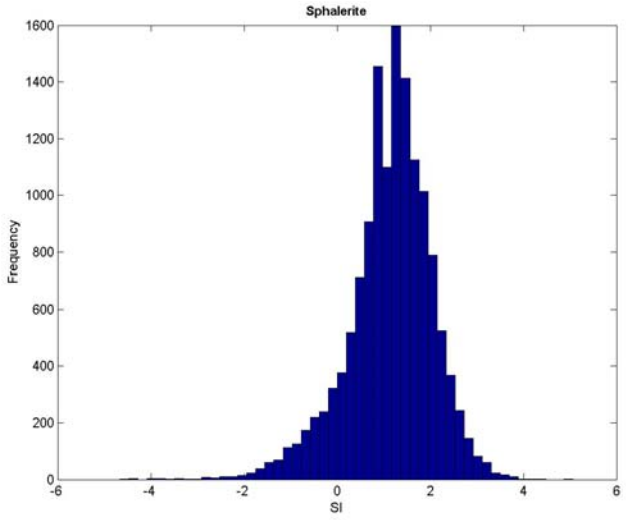

(a)

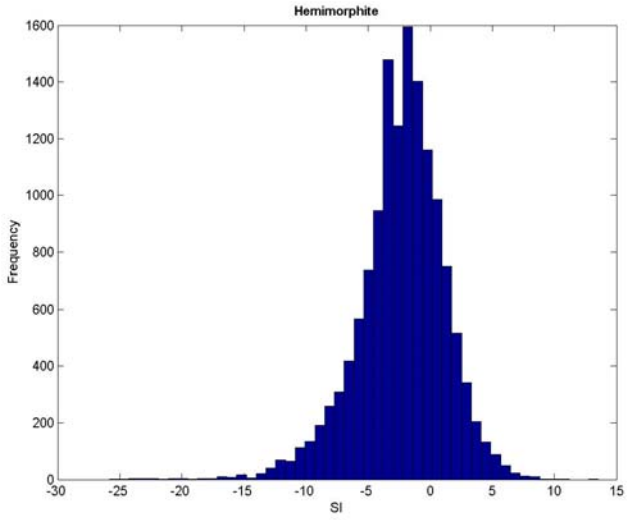

(b)

Fig. 3.42. Frequency Distribution of the Saturation Index of (a) Sphalerite, and (b) Hemimorphite. The Saturation Indices are calculated assuming Eh to be defined by the coexistence of pyrite and goethite, using a selected set of groundwaters from the NWIS.

3.4.6 Variation of Lead, Cadmium, and Zinc Concentration with Redox Potential

A wealth of information has been presented in the previous ections (3.4.5.1 and 3.4.5.2), and apparent conflicts between the alternative distributions of SI's for the same mineral have been observed, as different specified equilibrium conditions are compared, especially in relation to defining the redox potential, or Eh, of the system. As is noted at the outset of this section, the purpose of conducting alternative runs is to gain insight into the chemical controls affecting the collective set of all groundwaters selected for geochemical analysis in the face of uncertainties in the quality of the analyses, uncertainties in the identities of aqueous species and minerals that may control the activities of hazardous inorganic constituents in solution, uncertainties in the quality of thermodynamic data used to calculate the mineral solubility products and aqueous species dissociation constants in the EQ3/6 Data0.dat database, and uncertainties defining the redox potential of the groundwaters when *in situ*. Despite the uncertainties, the results generally show a consistent pattern, allowing the investigator to use expert judgment in reaching a number of reasonable conclusions.

The principal finding drawn from a comparison of the results obtained in Runs 0 and 1 is that the majority of groundwaters are reducing, and that the assumption that they are buffered by the pyrite/goethite couple is probably a good approximation, even though more refined evaluations considering other natural redox buffers are justified in future studies. The large variations in redox state generated through the assumption of goethite equilibrium with respect to total Fe in solution causes substantial and unrealistic scatter in data relating to certain sulfide minerals, especially pyrite, galena, kermesite, and CdS. Furthermore, a comparison between cinnabar and quicksilver saturation profiles suggests that the unrealistically high levels of quicksilver saturation are the result of treating a solution in equilibrium with cinnabar, and containing abundant Hg sulfide complexes in solution, that are not taken into account because an erroneously elevated redox potential has been specified. Likewise, the extreme degrees of undersaturation of arsenates, as well as the low concentrations of Cd, Pb, and U, and their undersaturation with respect to alteration products under mildly reducing conditions—all suggest

that the groundwaters were reducing and that the Fe analyses in these groundwaters were erroneously low. This is hardly surprising, given that neutral reduced-state groundwaters, if exposed to air, will immediately lead to oxidation and precipitation of any Fe(II) present. Thus, we believe that the results presented for Run 1 are more credible and can be relied upon with greater confidence than those of Run 0. However, this assertion is made with the caveat that a small proportion of the groundwaters with an imposed pyrite/goethite redox buffer may in fact have been drawn from an aquifer where oxidizing conditions actually prevailed.

Some of the issues involved in variations between reducing and oxidizing conditions are discussed with respect to Pb, cadmium, and zinc in the following paragraphs.

Lead. Figure 3.43 illustrates some of the controls that determine Pb concentration in groundwaters. The solubilities of galena and cerussite in a representative groundwater with a pH = 7.6 (a pH typical of the groundwaters studied), and slightly supersaturated with respect to calcite, are calculated as a function of Eh, which is treated as an independent parameter. Coexisting values of As, Cd, Hg, Sb, Se, and Zn were set to plausible average values in NWIS groundwaters, as shown in Figure 3.6, recognizing artifacts due to application of insufficiently sensitive analytical methods. The figure is a vertical section through an Eh–pH, or Pourbaix diagram, at a specified pH. Where Eh < -0.23 V, the Pb concentration is defined by the coexistence of pyrite and galena. The Pb concentration remains essentially invariant, because most of the available S(VI) in solution is reduced to S(-II). At Eh ~ -0.23 V, pyrite becomes unstable and decomposes to goethite, at the invariant point where galena, goethite, and pyrite coexist. Between Eh ~ -0.23 and ~ -0.18 V, galena and goethite coexist, and the Pb concentration increases steeply until saturation is achieved with respect to cerussite, and galena becomes unstable. At Eh ~ -0.18 V, cerussite, galena and goethite coexist, whereas at higher Eh, the Pb concentration is defined by cerussite alone in the presence of goethite. Because no further redox reactions are involved in the system under consideration, the Pb concentration thereafter remains essentially invariant with increasing Eh.

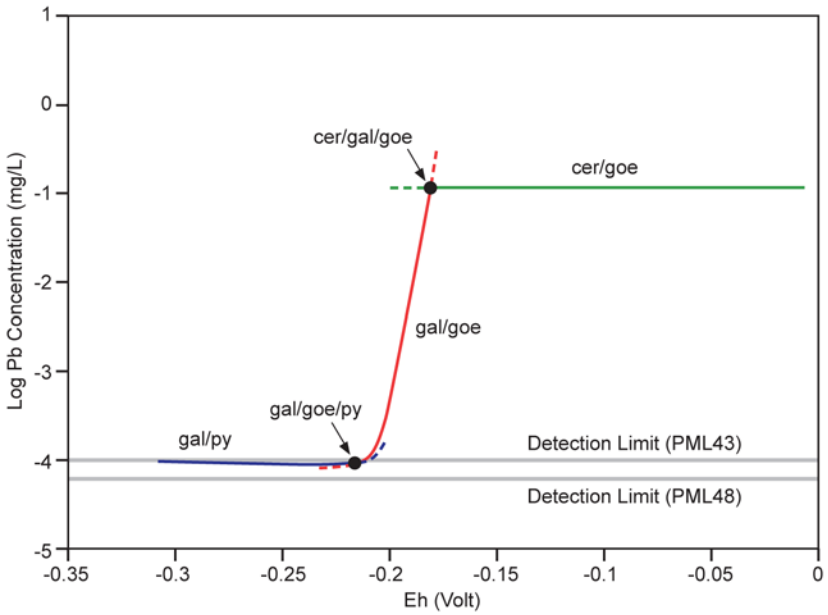

Fig. 3.43. Calculated Pb Concentration in Groundwater as a Function of Eh and saturated with respect to Galena and Cerussite in the Presence of Goethite and Pyrite. Cerussite = cer; galena = gal; goe = goethite; py = pyrite.

Also included in Figure 3.43 are the minimum detection limits for the analytical methods PLM43 and PLM48 at 0.0001and 0.00006 mg/L, respectively. These two methods are currently the most sensitive used routinely in the measurement of Pb in groundwaters. Pb was detected in nearly 50% of the analyses using method PLM43 and in over 80% using the more sensitive method PLM48.

The solubility product of galena, K(gal), is defined by the dissolution reaction:

$$PbS + H^{+} = Pb^{+2} + HS^{-}$$

Values reported in the literature for logK(gal) vary over two orders of magnitude, from -12.78 to –14.85, the highest value being based on an experimental determination of galena solubility, and the lowest value, currently specified in Data0.dat of EQ3/6 (Appendices A and D), being based on thermochemical properties of galena. This large variation in reported values would have had a pronounced impact in determining whether the presence of Pb in solution could have been detected were galena to coexist with pyrite. However, detailed investigations summarized in

Appendices D and E revealed the underlying cause for the discrepancies in LogK(gal), and allowed reconciliation of experimental determinations of galena solubility with those predicted using thermochemical determinations of $\Delta G^0_{f,P_r,T_r}$(galena). A major factor in achieving reconciliation came with the recognition that the saturated concentration of Pb in solution is determined not only by the presence of known monomeric complexes, but also by the presence of previously unrecognized oligomeric sulfide and selenide complexes. These additional complexes contributed significantly to elevating the concentration of Pb to such an extent that it should be just detectable using the most sensitive analytical methods. Furthermore, it became clear that Pb concentrations in equilibrium with galena depend not only on the ambient activity of HS^-, but also on that of HSe^-, the latter being dependent on saturation with respect to some other coexisting solid selenide mineral such as cadmoselite, clausthalite, or tiemannite, for example.

Figure 3.44 shows the calculated frequency of SI's for galena in groundwaters analyzed for Pb by analytical methods PLM43 and PLM48, while assuming that logK(gal) = –14.85 (Appendix D, Table D2) and that Eh is specified either by (a) the Fe(III)/Fe(II) couple and goethite saturation, or (b) by the goethite/pyrite couple. The two representations illustrate, respectively, the minimum and maximum likely calculated frequencies of galena saturation. Both histograms indicate that SI(max) ~ +0.5, suggesting galena saturation in the subset of NWIS groundwaters examined. It should be noted that all thermodynamic calculations are made assuming that the temperature of the groundwater is 25ºC. In fact, most shallow groundwaters have temperatures closer to 10ºC, and correction for temperature would result in a correction to logK(gal) of approximately –1.0. Given that the uncertainties associated with the evaluation could be as high as ±1.0 in SI, overall agreement is excellent.

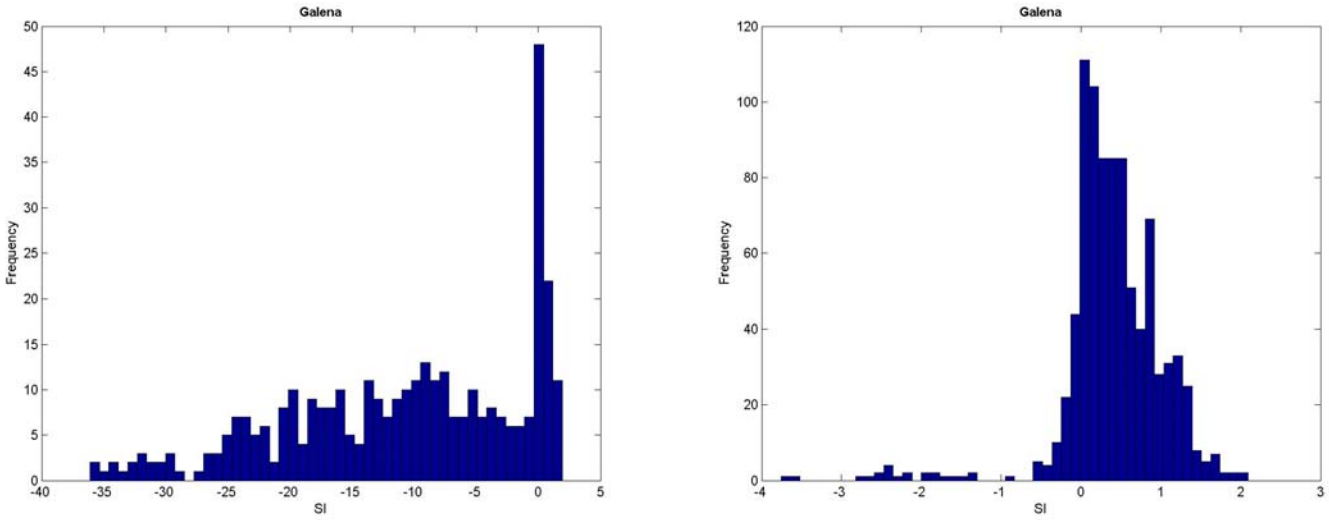

(a) (b)

Fig. 3.44. Frequency Distribution of Saturation Indices of Galena in Groundwater Samples analyzed for Pb using PLM43 and PLM48. (a) Eh is defined by Fe(III)/Fe(II) in solution in the presence of goethite. (b) Eh is defined by the coexistence of pyrite and goethite.

Because of the role that Se plays in complexing Pb in solution, and the fact that the corresponding selenide analogue of galena might control the Pb concentration, SI histograms for clausthalite (Pb selenide) were also calculated using the same analytical data for Pb as used in the calculation of the corresponding galena histograms. These are illustrated in Figure 3.45. Both histograms indicate that SI(max) ~ -1. When compared with galena (Figure 3.44), these findings suggest that clausthalite is undersaturated in the suite of groundwaters examined. However, the overall uncertainties in both thermochemical data for clausthalite, estimates of sulfide and selenide Pb complexation constants, and other factors relating to the groundwater quality analyses preclude making such an assertion with confidence.

The frequency distribution of SI's for pyrite in the selected groundwater samples used in the construction of Figures 3.44 and 3.45 is presented in Figure 3.46a (where Eh is again defined by Fe(III)/Fe(II) in solution in the presence of goethite). Only a small fraction of samples are saturated with respect to pyrite, and as noted above, it is not clear whether these results are meaningful. Figure 3.46b also shows that most of the groundwaters analyzed for Pb by PLM43

and PLM48 are saturated with respect to calcite, consistent with the groundwater composition used to calculate the Pb concentration in Figure 3.43.

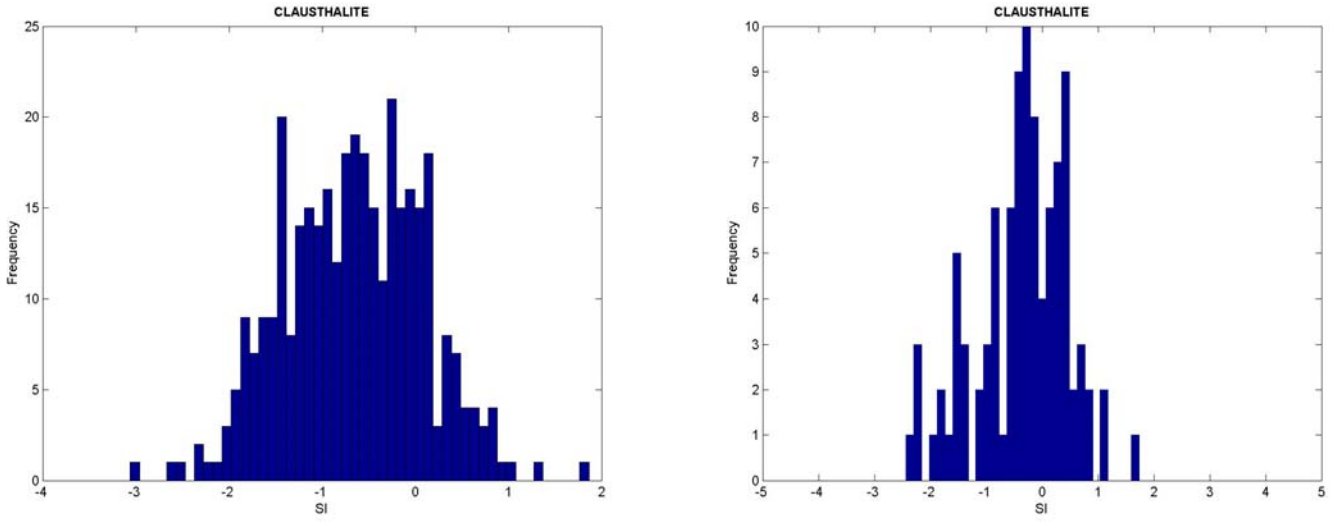

(a) (b)

Fig. 3.45. Frequency Distribution of Saturation Indices of Clausthalite in Groundwater Samples analyzed for Pb using PLM43 and PLM48. (a) Eh is defined by Fe(III)/Fe(II) in solution in the presence of goethite. (b) Eh is defined by the coexistence of pyrite and goethite.

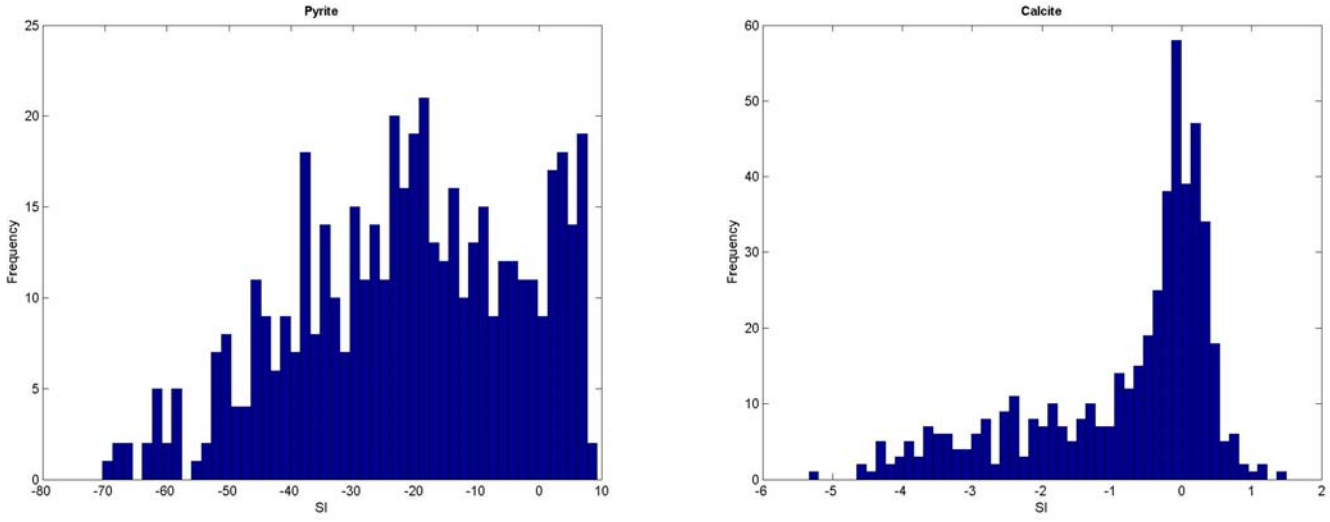

(a) (b)

Fig. 3.46. Frequency Distribution of Saturation Indices of (a) Pyrite and (b) Calcite in Groundwater Samples analyzed for Pb using PLM43 and PLM48. The Saturation Indices are calculated assuming Eh to be defined by Fe(III)/Fe(II) in solution in the presence of goethite.

Cadmium. Figure 3.47 illustrates the variation in cadmium concentration in solution as a function of Eh for the same groundwater, with pH = 7.6, as used in the analysis of Pb solubility in the preceding section. Below Eh ~ -0.22 V, CdS (greenockite) coexists with pyrite. Between Eh ~ -0.22 and ~ -0.17 V, CdS coexists with goethite. Above Eh ~ -0.17 V, CdS decomposes, and Cd concentration is controlled by otavite ($CdCO_3$), and is independent of Eh. It should be noted that the leveling off of Cd concentration at Eh < -0.22 V is due to the conversion of all available S(VI) in solution into S(-II) species, i.e., HS^- and H_2S(aq). The saturation control of Cd in solution by otavite has been shown to occur under field conditions, as demonstrated by Carroll et al. (1998) and McGrath et al. (2007). White et al. (2004) have also shown that Cd is readily leached from soils by dilute acid treatment, suggesting the presence of Cd as a carbonate. This is in contrast to the leaching behavior of Zn, which suggests stabilization as a silicate (see below).

As noted in Appendix B2, most of the reported analyses for Cd in groundwaters appear to be artifacts, due to insufficient sensitivity of past analytical methods. The detection limit by the most sensitive analytical methods used routinely in the analysis of Cd in groundwaters, PLM43 and PLM47, is 0.00004 mg/L, as included in Figure 3.47. Only 24% of the analyses using PLM43 and 17% of the analyses using PLM47 detected Cd in solution.

Independent determinations of greenockite solubility logK(CdS), represented by the reaction

$$CdS + H^+ = Cd^{+2} + HS^-$$

have been reported in the literature, as noted in Appendix D, and differ by nearly two orders of magnitude, i.e., logK(CDS) = -14.36 and –15.91, respectively. The smaller value is currently specified in Data0.dat of EQ3/6. As noted above, the discrepancies were reconciled as described in Appendices D and E, and a LogK(CdS) was chosen based on a thermochemical determination of $\Delta G^0_{f,P_r,T_r}$ (CdS). If CdS were to coexist with pyrite, Cd in solution would be about one order of magnitude above the detection limit of PLM43 and PLM47 at 0.00004 mg/L. In the absence of pyrite, Cd concentrations in equilibrium with CdS should be even more easily detectable as saturation with respect to otavite is approached. A few of the Cd analyses fall within the range of

otavite solubility, i.e., circa Log Cd ~ -1.5 (mg/L), as shown in Figure 3.6d, and probably represent conditions in oxidized aquifers, in analogy with cerussite saturation with respect to Pb (Figure 3.43). The calculated solubility is therefore about one order of magnitude greater than the apparent marginal detectability of Cd in solution, but correction for lower ambient temperatures than the 25ºC reference and other factors could easily allow for reconciliation of this discrepancy.

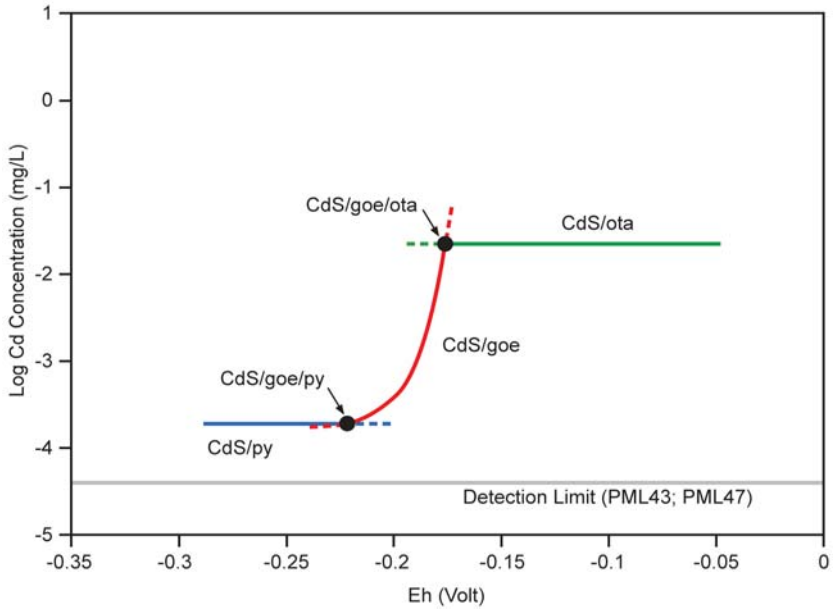

Fig. 3.47. Calculated Cd Concentration in Groundwater as a Function of Eh and saturated with respect to CdS and Otavite in the Presence of either Pyrite or Goethite. CdS = CdS; goe = goethite; ota = otavite; py = pyrite.

Figure 3.48 illustrates the SI histograms for CdS where Eh is defined either by Fe(III)/Fe(II) in the presence of goethite (Figure 3.48a), or by the coexistence of goethite and pyrite (Figure 3.48b). Both figures show SI(max) ~ 0, indicating saturation. However, Figure 3.48b also displays a bimodal distribution with a secondary peak at SI(max) ~ -3. An explanation for this secondary peak is not readily available. It cannot be caused by an insufficiently sensitive analytical method, because the histogram is based on only those analyses for Cd using PLM43 and PLM47, both of which have the same detection limits. A more likely explanation is that the two peaks arise from the omission of Se analyses from those samples comprising the peak where

SI(max) ~ 0. In this case, the lower peak, where selenide complexing is taken into account, would indicate that CdS must be a component of either sphalerite or galena in solid solution. However, this would imply that CdS saturation would be about two log units higher than calculated in Figure 3.48, in which selenide complexation is accounted for.

SI frequency histograms for cadmoselite are given in Figure 3.49. Both indicate SI(max) ~ 0, and the results are relatively unambiguous. Furthermore, the population of analyses permitting calculation of SI(cadmoselite) in Figure 3.49b is approximately equivalent to that populating the secondary peak in Figure 3.48b. From this comparison, one is drawn to the tentative postulate that, with respect to the NWIS groundwaters studied and analyzed for Cd using PLM43 and PLM47, CdS is unsaturated in solution, and that the phase controlling Cd solubility is cadmoselite. Clearly, further review of the composition of the affected groundwater analyses, thermodynamic data refinement, and additional corroboration is required before this finding can be accepted.

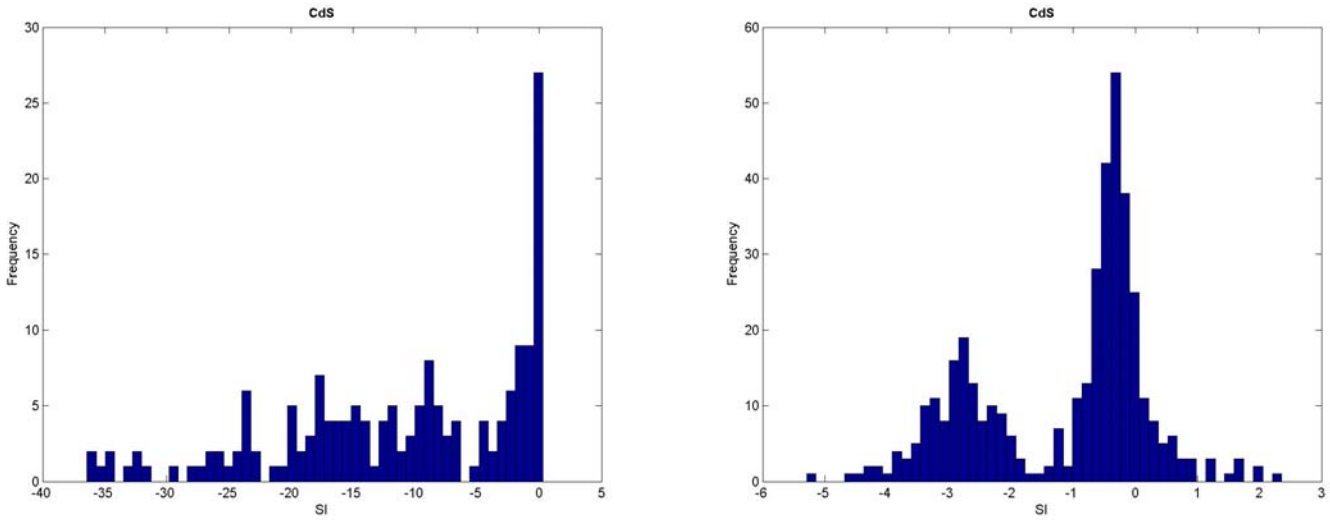

(a) (b)

Fig. 3.48. Frequency Distribution of Saturation Indices of CdS in Groundwater Samples analyzed for Cd using PLM43 and PLM47. (a) Eh is defined by Fe(III)/Fe(II) in solution in the presence of goethite. (b) Eh is defined by the coexistence of pyrite and goethite.

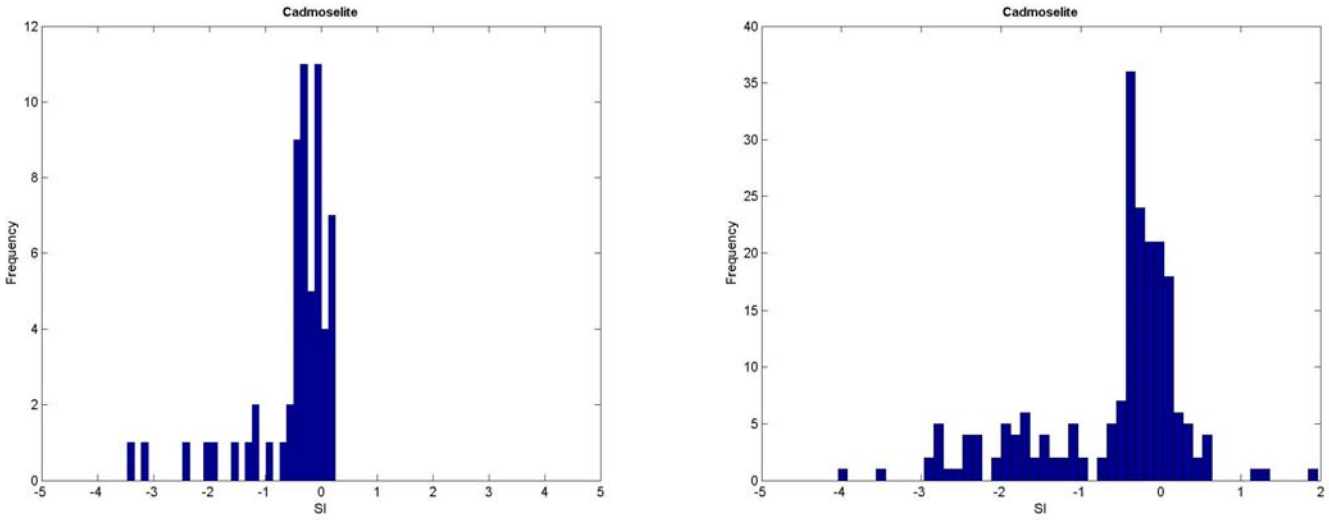

(a) (b)

Fig. 3.49. Frequency Distribution of Saturation Indices of Cadmoselite in Groundwater Samples analyzed for Cd using PLM43 and PLM47. (a) Eh is defined by Fe(III)/Fe(II) in solution in the presence of goethite. (b) Eh is defined by the coexistence of pyrite and goethite.

Zinc. It is instructive to compare the behavior of Zn in solution with that of Cd under similar conditions, since their sulfides are crystallographically similar, i.e., sphalerite is the structural analogue of hawleyite, and wurtzite is the analogue of greenockite (CdS). However, in contrast to Cd, the detection and quantification of Zn in groundwaters is readily achieved with current analytical methods (Figure 3.6i). For example, although the minimum detection limit using the most sensitive analytical method routinely available for Zn, PLM43, is higher at 0.0006 mg/L compared to 0.00004 mg/L for Cd, Zn was detected in 94% of the samples analyzed, in contrast with only 24% for Cd. Furthermore, Figure 3.6i does not show any obvious indications of analytical artifacts, so clearly suggested by the corresponding Figure 3.6d for Cd.

Figure 3.50 shows the calculated Zn concentration as a function of Eh in the same groundwater as that for Cd in Figure 3.47. The coexistence of sphalerite with pyrite and goethite occurs at a Zn concentration of approximately 0.002 mg/L, which is in contrast with the corresponding three-phase coexistence where Cd concentration is 0.0002 mg/L. Under oxidizing conditions, sphalerite is transformed to hemimorphite ($Zn_4Si_2O_7(OH)_2.(H_2O)$) (McPhail et al., 2006). That a

silicate such as hemimorphite is likely to immobilize Zn is substantiated by leaching studies on soils distal to sulfide mineralization in Australia, where no more than 50% Zn is mobilized by acid leaching of the <65µm fraction, but Hf/aqua regia is required to solubilize the remainder (White et al., 2004). This is in contrast to Cd, where almost all in the <65 µm fraction was mobilized by acid leaching alone. The solubility product for hemimorphite at 25ºC was retrieved from preliminary data presented by McPhail et al. (2003), and utilized in the construction of Figure 3.50. The limitation of the minimum Zn concentration to approximately log Zn = -10 is due also to the conversion of all S(VI) to S(-II) species. The concentration of Zn in solution where goethite, sphalerite, and hemimorphite coexist is calculated to be 0.004 mg/L.

As noted in Appendix D, two independent determinations of sphalerite solubility logK(sph), represented by the reaction ($ZnS + H^+ = Zn^{+2} + HS^-$) are in substantial agreement, i.e., logK(sph) = -11.44 and 11.46, respectively, the higher value being currently specified in Data0.dat of EQ3/6. The value derived from thermochemical measurements was used to calculate LogK(sph), and the potential participation of neutral oligomeric neutral sulfide and selenide complexes was taken into account as described in Appendices D and E.

The SI frequency histogram for sphalerite in Figure 3.33a gives SI(max) = +1, where Eh is calculated on the basis of Fe(III)/Fe(II) ratio in a solution saturated with respect to goethite. Figure 3.42a shows a corresponding histogram giving SI(max) = +1, where Eh is calculated assuming a goethite/pyrite buffer. The maximum frequency of Zn concentration is circa Log Zn = -1.5 (mg/L), which is about one log unit higher than the calculated concentrations illustrated in Figure 3.50 for both sphalerite and hemimorphite, and is consistent with the SI frequency diagrams cited above. This discrepancy suggests that either the predicted $\Delta G^0_{f,P_r,T_r}$ (sph) and Log K(hemi) have imposed excessive stability on these minerals in solution, or, in the case of sphalerite, that the stabilities of the sulfide and selenide complexes are greater than predicted on the basis of the evaluations given in Appendices D and E. Because of the complexity of the system and uncertainties associated with the thermodynamic parameters used, together with significant variations in water quality, a more rigorous evaluation will be needed than that presented in this scoping study. Given the cumulative uncertainties inherent in this analysis, the

close correspondence between predicted and observed degrees of saturation with respect to sphalerite and hemimorphite is very good.

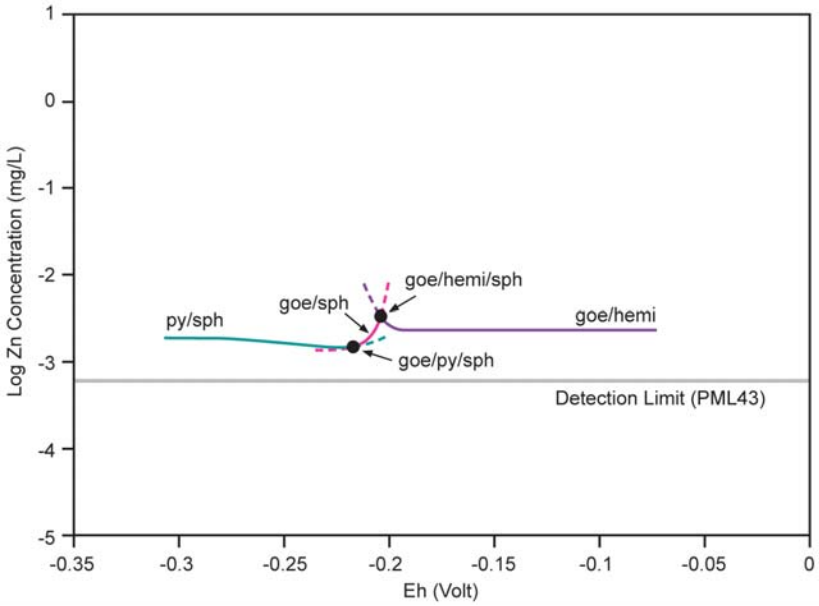

Fig. 3.50. Calculated Zn Concentration in Groundwater as a function of Eh and Saturated with respect to either Sphalerite or Hemimorphite in the Presence of Goethite and Pyrite. goe = goethite; py = pyrite; sph = sphalerite; hemi = hemimorphite.

In conclusion, the theoretical calculations provide a basis for explaining field observations and substantiate the proposition that sphalerite controls Zn concentrations in groundwaters under moderate to strongly reducing conditions, and hemimorphite under mildly reducing to oxidizing conditions.

3.4.7 Summary of Thermodynamic Controls

Conclusions as to which minerals thermodynamically control the activities of the selected hazardous constituents in NWIS potable groundwaters in the United States are summarized in Table 3.13. Most groundwaters, at least 75% of all samples from the NWIS data base, are moderately to strongly reducing, with the lower bound to the redox state most likely buffered by pyrite, or other ferrous sulfide, and another mineral containing iron in either the Fe(II) or Fe(III)

state. A small fraction of groundwaters, estimated to be perhaps as low as 5 percent, may be mildly reducing or even oxidizing, as suggested by the behavior of certain hazardous constituents such as As, Cd and Pb that they might. Table 3.13 recognizes the distinction between these two categories of groundwater, as defined broadly by their redox states.

The claims presented in Table 3.13 are generalizations that apply to potable groundwaters of average composition and pH. They are used to construct a geochemical model of general applicability for addressing problems related to groundwater contamination, as demonstrated in Section 4 of this report. Overall model uncertainty is difficult to estimate; rigorous site-specific characterization would be necessary to further evaluate model uncertainty. Model uncertainties are evaluated in greater detail in the following Section 3.5. The selection of water quality data meeting more stringent criteria, a more critical review of thermodynamic data already used in geochemical model analysis, and incorporation of additional aqueous species relevant to the modeling effort could limit model uncertainty in future studies.

Table 3.13. Summary of minerals identified as controlling the thermodynamic activity of selected hazardous constituents in potable groundwaters

Con-stituent	Thermodynamic Control on Groundwater Activity		
	Moderately - Strongly Reducing, i.e., Pyrite/Goethite Buffer	**Mildly Reducing - Oxidizing**	**Comments**
As	(1) Arsenopyrite in solid solution in pyrite (arsenian pyrite) (2) Arsenopyrite	Adsorption on host rock mineral surfaces, especially iron oxides, or through substitution for SO_4^{-2} in anionic clays such as green rust	No mineral in which As is an essential component, other than arsenopyrite, has been identified controlling As activity in solution in the groundwaters examined.
Ba	Barite	Barite	Barium activity is controlled by barite alone, regardless of oxidation state. No other Ba minerals controlling Ba activity have been identified.

Con-stituent	Thermodynamic Control on Groundwater Activity		
	Moderately - Strongly Reducing, i.e., Pyrite/Goethite Buffer	**Mildly Reducing - Oxidizing**	**Comments**
Cd	(1) CdS (greenockite) substitution in either galena or sphalerite (2) Cadmoselite	Otavite	Further evaluation is required to resolve ambiguities. Greenockite could saturate at potable water aquifer temperatures, as solid solution substitution in sphalerite and/or galena decreases with falling temperature. The observed saturation with respect to cadmoselite suggests that this phase may control Cd^{+2} activity in the evaluated NWIS groundwaters for which Cd and Se analyses are available. Equilibrium concentrations in solution are so low, however, that current analytical methods are marginally effective in providing quantitative measurements. Under oxidizing conditions, cadmium activity is controlled by otavite. Otavite cannot be present in the majority of potable groundwaters analyzed for Cd in the NWIS database, because Cd concentrations would be easily detected by current state-of-the art analytical methods. This observation indirectly supports the conclusion that most groundwaters are reducing.
Hg	(1) HgS solid solution in pyrite (2) Cinnabar (3) Tiemannite	Native Mercury	
Pb	(1) Galena (2) Clausthalite	Cerussite	A small fraction, ≈ 5%, of groundwaters is sufficiently oxidizing that Pb activity is defined with respect to cerussite saturation. This observation indirectly supports the conclusion that most groundwaters are reducing. Pb mineralogy under mildly reducing – oxidizing conditions is complex, and it is possible that secondary Pb silicates might also control Pb activity in groundwaters under these conditions.
Sb	(1) Gudmundite solid solution in pyrite. (2) Kermesite (red antimony)	Kermesite (red antimony).	
Se	(1) Cadmoselite (2) Tiemannite (3) Clausthalite (4) Dzharkenite solid solution in pyrite	None recognized	Solid solution substitution of the dzharkenite ($FeSe_2$) component in pyrite, when present, could also be responsible for defining Se(-II) activity. No potential selenite of selenate minerals are recognized as activity controlling under mildly reducing - oxidizing conditions.
U	(1) Uraninite and/or (2) Coffinite	None recognized	Uranophane is strongly undersaturated in all cases when the redox state of the groundwater was specified by the goethite-Fe(III)/Fe(II) Eh buffer at a given pH.
Zn	Sphalerite	Hemimorphite	

3.5 The Variation of Hazardous Constituent Concentrations with Partial Pressure of Carbon Dioxide in Groundwaters

3.5.1 Introduction

Given certain assumptions and approximations, changes in the groundwater equilibrium concentrations of hazardous inorganic constituents caused by changes in the partial pressure of CO_2 can be calculated using a distribution-of-species code. In this section, we present such calculations, performed with the distribution-of-species simulator EQ3/6, and discuss their significance and limitations. The equilibrium calculations reflect the direct calibration of the model to the pertinent field data for the hazardous constituents and give preliminary estimates of the potential magnitude of the impact of CO_2 intrusion on groundwater quality. Further, the results indicate which hazardous constituents are sensitive to CO_2 intrusion and which are not.

In the following subsections, we first discuss the inputs to the thermodynamic model (Section 3.5.2) and then present the base case results from the equilibrium calculations (Section 3.5.3). In Section 3.5.4, we evaluate the overall uncertainties associated with the model and the chemical analyses, and show the impact that such uncertainties may have on the results. Finally, we examine how aqueous complexation impacts the total concentrations of each constituent in groundwaters with changing $P(CO_2)$ (Section 3.5.5).

3.5.2 Input Specifications

Before providing further details regarding this thermodynamic analysis, it is important to understand the relationship between (1) the thermodynamic model of the geochemistry of groundwaters used to predict equilibrium concentrations of given hazardous constituents under specified equilibrated CO_2 partial pressures, and (2) the observed concentrations of these same constituents in NWIS groundwaters. The thermodynamic model was developed entirely independently of any of the chemical analyses of NWIS groundwaters. It was based on the existing thermochemical database in EQ3/6, which was revised and augmented using recent literature on calorimetrically or experimentally derived solubility products (Section 3.4.2;

Appendices C, D, and E). This independent thermodynamic model was then used in Section 3.4.5 to evaluate the chemical analyses and to determine to what extent the groundwaters were saturated with respect to minerals that might control the activities of the selected hazardous constituents. The candidate minerals are present at such low abundances, however, that their direct detection is practically impossible without using advanced spectroscopic techniques. Therefore, with rare exceptions, we can only surmise their presence through thermodynamic evaluation.

In the evaluation of solubility controls for hazardous constituents presented in Section 3.4.5, the modes of the histograms of the logarithm of the SI of each candidate mineral are determined. The calculated mode differs from the ideal value of zero by ± some incremental value, reflecting a "closing error" between model prediction and actual field observation. This deviation is a measure of the overall uncertainty of all parameters that go towards construction of the model, including the uncertainties and variabilities associated with the 38,000 chemical analyses of the NWIS groundwaters as well as uncertainty as to whether the candidate mineral is a plausible thermodynamic control. It is desirable to ensure that the calculated model variations in hazardous constituent concentrations as a function of $P(CO_2)$ are consistent with the field observations. This was done here by adjusting in the model the Log K values of the dissolution constants of the minerals plausible mineral candidates so that the calculated log SI's of the mode for each are now zero, rather than showing a closing error. In other words, the model is now calibrated to the selected modes of the histograms of the SI's calculated from NWIS groundwater analyses.

Table 3.14 summarizes the imposed input constraints for the base case runs, including the modifications made in the calibration. The list of minerals identified as controlling hazardous constituent concentrations is based on the thermodynamic evaluations summarized in Section 3.4.7. Thermochemical data, including the measured solubilities of most of these minerals, are available (Appendix C, D, and E), and calorimetrically or experimentally derived solubility products at 25°C were entered in the EQ3/6 Data0.dat database where needed. Calculations were performed using a typical groundwater composition. The redox state was defined by the assumed equilibrium between pyrite and goethite at a given pH to simulate reducing conditions typical of

shallow confined aquifers. The groundwater was also assumed to be saturated with respect to calcite, opal-CT, and low Fe, Mg smectite. (The effect of these minerals on the solubilities of the hazardous inorganic constituents is negligible.) Electrical neutrality was achieved by adjustment of pH. Also, as mentioned before, previously unrecognized metal sulfide and selenide complexation in solution is taken into account in the Data0.dat database.

Calibration adjustments to the log K values of the solubility products of minerals that control the concentrations of Pb, Hg, Se, U and Zn in NWIS groundwaters were made to cinnabar, galena, and tiemannite, uraninite and sphalerite, respectively, as indicated in Column 4 of the Table 3.14, the purpose being to ensure consistency between the modal concentrations of these constituents and the thermodynamic model. Corrections were also made to the solubility products of arsenopyrite and gudmundite, to reflect the assumption that both As and Sb are substituting in solid solution in pyrite as FeAsS and FeSbS components. The magnitude of each correction is based on the calculated mode of the SI distribution determined through the analysis of NWIS groundwaters given in Section 3.4.5.2. No adjustments were made to the log K values of barite or CdS (greenockite). In the former, there appears to be substantial agreement between model predictions and observed concentrations of Ba. Regarding the latter, considerable ambiguity remains regarding the saturation state in NWIS groundwaters, and calibration was not attempted.

3.5.3 Results from Equilibrium Calculations

Results from the calculations of the saturation concentrations for each hazardous constituent as a function of $P(CO_2)$ are presented graphically in Figure 3.51. The figure shows the most likely expected concentrations (black lines) as well as a prediction of the uncertainty band (shaded areas) based on the uncertainty analsyis described in Section 3.5.4. Also included in the figure are the relevant MCLs (or SWDL for Zn), the detection limits for the most sensitive analytical methods, and the estimated $\pm 2\sigma$ variation about the mean of the log concentration of each hazardous constituent at log $P(CO_2) = -2$, i.e., the average natural partial pressure of CO_2 in NWIS groundwaters (see Figure 3.17). The estimated $\pm 2\sigma$ variation about the mean is assumed to be $\approx \pm 1.5$ log(mg/L), and is based on the observed log-normal distributions of Ba, U and Zn in

NWIS potable groundwaters, all of which gave quantitative measurements for ≥90% of all samples (see Table 3.17 below). For Pb and Se, the lower "tail" of the distribution falls below the limits of detection for the most sensitive analytical methods used, whereas for Cd. Hg and Sb, the estimated mean value falls below the corresponding most sensitive detection limits. For Cd, Hg, and Sb, therefore, the variation in natural groundwaters was estimated assuming that the percentage of detectable values represents an observed upper "tail" of the log-normal distribution.

We shall start discussing the general trends observed for most likely results shown as black lines in Figure 3.51. The concentrations of some of the hazardous constituents are quite sensitive to changes in $P(CO_2)$, whereas others remain relatively unaffected. For example, Hg, Se, and U are insensitive to changes. Ba is slightly affected, but the maximum concentration at elevated $P(CO_2)$ (~ 1.1 mg/L at 10 bar) remains below the MCL (maximum contaminant level) of 2 mg/L. Cd, Pb, and Zn show marked increases after log $P(CO_2)$ rises above -1. However, only in the case of lead is the maximum concentration at elevated $P(CO_2)$ (~ 0.02 mg/L at 10 bar) higher than the MCL of 0.015 mg/L. Arsenic concentration changes sympathetically with increasing $P(CO_2)$, with a maximum concentration (~ 0.46 at 10 bar) significantly higher than the MCL of 0.01 mg/L. Sb initially increases in parallel with As, then saturates with respect to kermesite at Log $P(CO_2) > -2$, and thereafter remains at a concentration level significantly below the MCL of 0.006 mg/L. The reasons for these differing behaviors can be understood by reference to variations in pH and Eh, and to variations in the nature and distributions of complexes of each element in aqueous solution. These variations are discussed further in Section 3.5.5.

Table 3.14. Input specifications for base case EQ3 runs to calculate the equilibrium concentrations of hazardous inorganic constituents in groundwater at 25°C as a function of $P(CO_2)$. SS = Solid Solution.

Aqueous Basis Species	Concentration (mg/L)	Mineral Saturation[1]	Adjustments[2]	
			Specified Change	Explanation
H^+	-	-	Charge balance	Electrical neutrality
Na^+	45.8	-		
K^+	5.04	-		
Mg^{+2}	2.01	-		
Ca^{+2}	Set by mineral saturation	calcite		
Fe^{+2}	Set by mineral saturation	pyrite		
Al^{+3}	Set by mineral saturation	low Fe,Mg smectite		
$SiO_2(aq)$	Set by mineral saturation	opal-CT		
$O_2(g)$	Set by mineral saturation	goethite		
HCO_3^-	Set by $P(CO_2)$ saturation	log $P(CO_2)$	-4, –3, -2, -1, 0, +1	Variation from background due to CO_2 intrusion
Cl^-	7.14	-		
SO_4^{-2}	18.4	-		
$H_2AsO_4^-$	Set by mineral saturation	arsenopyrite SS	Change Log K from +58.66 by -3.00 to +55.66	Calibration. Change also accounts for solid solution
Ba^{+2}	Set by mineral saturation	barite	Log K = -9.97 (no change)	No calibration needed
Cd^{+2}	Set by mineral saturation	CdS (greenockite)	Log K = -14.09 (no change)	No calibration needed
Hg^{+2}	Set by mineral saturation	cinnabar	Change Log K from -38.08 to -37.50	Calibration
Pb^{+2}	Set by mineral saturation	galena	Change Log K from -14.87 to -14.40	Calibration
$Sb(OH)_3(aq)$	Set by mineral saturation	gudmundite SS, kermesite	Change Log K from +38.76 by -5.00 to +33.76	Calibration. Change also accounts for solid solution
SeO_3^{-2}	Set by mineral saturation	tiemannite	Change Log K from -43.27 to -44.10	Calibration
UO_2^{+2}	Set by mineral saturation	uraninite	Change Log K from -4.83 to –3.83	Calibration
Zn^{+2}	Set by mineral saturation	sphalerite	Change Log K from -11.27 to -10.00	Calibration

1. Mineral saturation is specified, which determines the aqueous concentration of the basis species identified in column 1 through the law of mass action.
2. Adjustments specified in the input file of EQ3. All adjustments with the exception of H^+ and HCO_3^- involve corrections to Log K values of mineral solubility products in order to calibrate the thermodynamic geochemical model with the mode of the corresponding mineral saturation indices in the sampled NWIS groundwaters. Charge balancing is assumed through adjustment of H^+ by the EQ3 code algorithm. HCO_3^- is specified through successive incremental adjustment of log $P(CO_2)$ to explore the effect on hazardous constituent concentrations of the full range of $P(CO_2)$ anticipated in the subsurface environment.

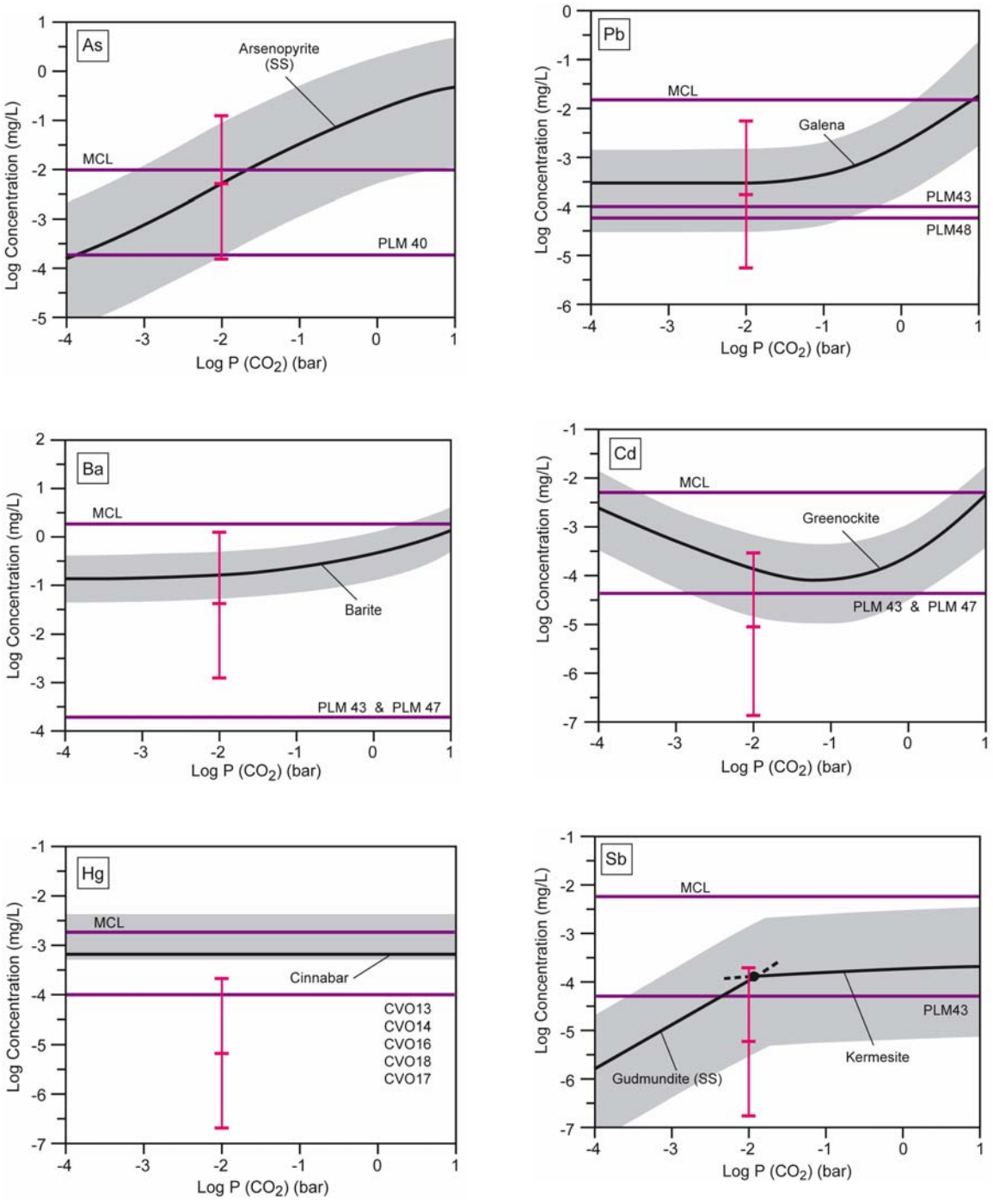

Figure 3.51 Part 1.

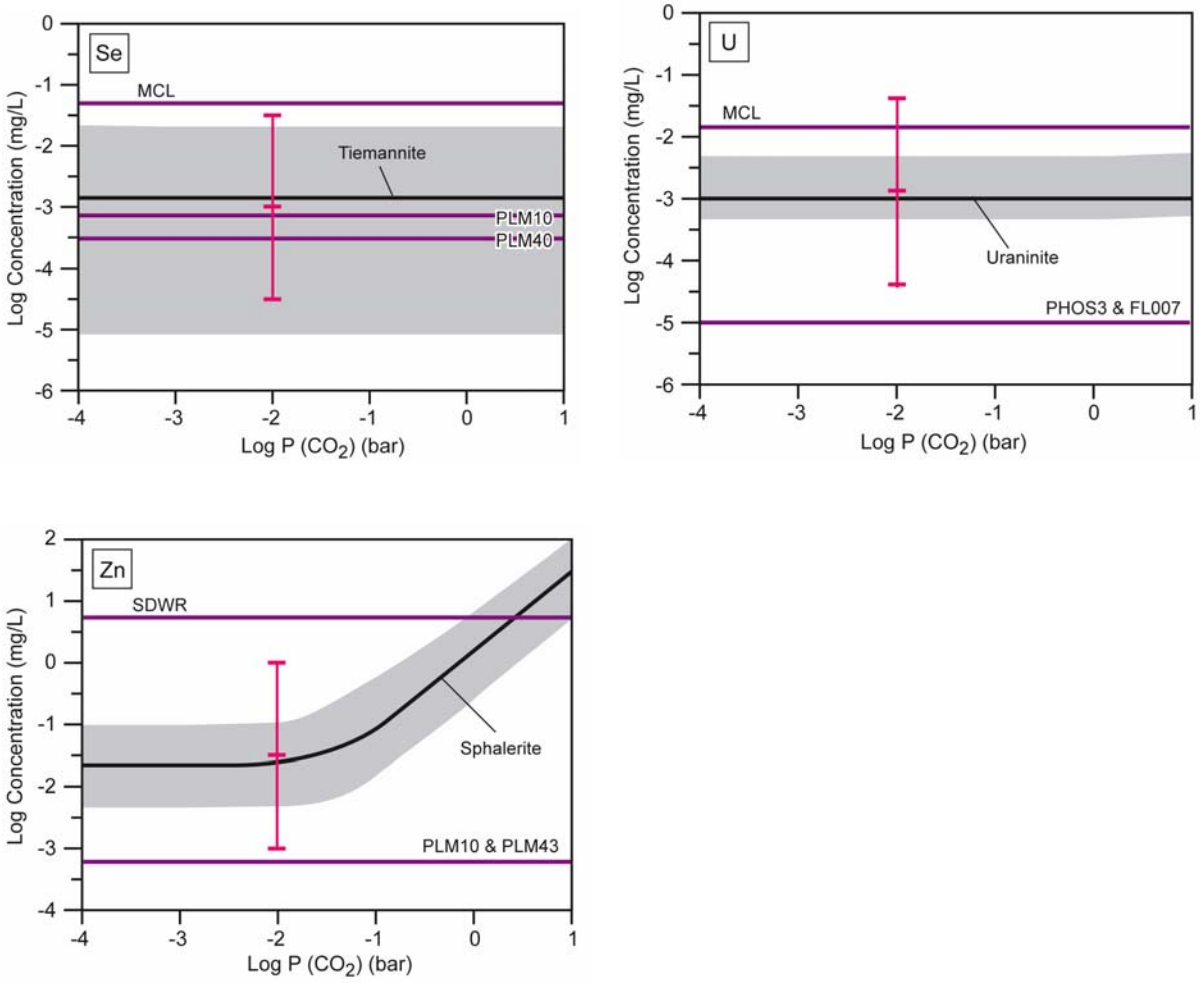

Fig. 3.51. Variation of trace metal concentrations in equilibrium with host minerals as a function of CO_2 partial pressure taking into account both sulfide and selenide complexation, and with solubility products calculated using thermochemical data and adjusted to ensure consistency with hazardous constituent concentrations in NWIS waters (see Table 3.14). (SS) refers to solid solution. CV013, CV014, CV016, XV017, CV018, FL007, PH0S3, PLM10, PLM40, PLM43, PLM47 and PLM48 are analytical methods cited in the NWIS database. See Table A2 in Appendix A.

3.5.4 Uncertainties Associated with Equilibrium Calculations

3.5.4.1 Estimation of Aggregate Uncertainties

The overall uncertainty related to predictions of hazardous constituent concentrations in potable groundwaters as a function of $P(CO_2)$ is difficult to estimate, as so many factors affect the analysis and interpretation. Briefly, four components are involved: (1) the validity of assumptions relating to the geochemical model, (2) uncertainties in geochemical model parameters, (3) uncertainties relating to the chemical analyses of NWIS groundwaters, and (4) uncertainties relating to the natural variability in sampled NWIS groundwater compositions. Tables 3.15-3.18 list the various uncertainties under these four categories, and their potential impact on hazardous constituent behavior is discussed.

The treatment of uncertainty in this section is at best semi-quantitative. Most of the listed estimates of uncertainty are based on professional judgment, and not on quantitative evaluation, the reason being that it would otherwise take an inordinate amount of time and effort to accomplish such a task, even if technically feasible. The term "uncertainty" is assumed to be the standard deviation of the mean, i.e., $\pm\sigma$, except where otherwise noted. The listed uncertainties in Table 3.15-3.17 are then selectively used to calculate the aggregate uncertainties associated with the calibrated log K values of the solubility products of the hazardous constituent host minerals. This information is summarized in Table 3.19.

Uncertainties listed in Table 3.18 are not utilized in the calculation of aggregate uncertainties, because these natural-variability uncertainties are accounted for in the estimated $\pm 2\sigma$ variation observed in hazardous element concentrations at the modal $\log P(CO_2) \approx -2$. Furthermore, it is the purpose of the analysis to compare the aggregate geochemical model uncertainty in calculated hazardous concentrations with the observed apparent natural variability in order to obtain some measure as to whether or not the natural variability exceeds modeled uncertainty.

Table 3.15. Uncertainties associated with geochemical model assumptions

No.	Item	Principal Concern	Impact on Findings	Justification for Current Assumptions
1	Specified mineral hosts control hazardous constituent concentrations.	Identification of mineral hosts was made through indirect thermodynamic comparison of predicted mineral solubilities with those in 38,000 potable groundwaters. The presence of mineral hosts in the subject aquifers has not been verified.	If selected minerals have been incorrectly identified, then the predicted response to changing $P(CO_2)$ could differ markedly, and the present interpretation would be invalid	The correlation between predicted solubilities and the modes of the compositions for all selected constituents in 38,000 groundwaters is consistent with thermodynamic control by the selected minerals.
2	Mineral hosts are pure substances, except where otherwise noted.	In the case of Cd, Sb and Se, it is not entirely clear whether pure substances or solid solutions control these constituent concentrations.	If the hazardous constituent were a minor component in solid solution in a mineral other than that identified, the thermodynamic response to $P(CO_2)$ changes would differ from that in the present model.	Identified pure substances containing Cd, Sb and Se, where relevant, are consistent with observed concentrations in groundwaters. Both field observations and thermodynamic analyses are consistent with the assumption that As is present in solid solution in pyrite.
3	Oligomeric sulfide and selenide complexes of Cd, Hg, Pb, and Zn are present in solution and impact equilibrium concentrations of these constituents.	The exact compositions of the S and Se oligomers have not been determined. Selenide speciation is assumed to be analogous to that of sulfide speciation, based on correlation between Hg-S(-II) and Se(-II) species.	If incorrect, both the concentrations and the thermodynamic response to changes in $P(CO_2)$ would differ from that in the present model for the listed species and Se.	The assumption that oligomeric sulfide and selenide complexes of Cd, Hg, Pb, and Zn are present in solution, and that the thermodynamic properties of selenide complexes correlate with those of sulfide complexes is necessary to achieve consistency between model predictions of hazardous constituent concentrations and field observations.
4	The pyrite/goethite pair buffers Eh at a given pH.	Goethite is metastable with respect to hematite, i.e., pyrite/hematite might be operative in some aquifers. Other buffers might be operative, e.g., pyrite/magnetite, pyrite/siderite, pyrite/chlorite, etc. A systematic study as to the ranges of conditions under which these alternative buffers might operate, and how they would impact results has not been conducted. It is further assumed, but not proven, that the Eh buffer is in thermodynamic equilibrium with the aqueous phase.	Variations in Eh at a given pH due to control by alternative buffers could impact mineral host solubilities, possibly by ±1 to 2 log units.	Most of the alternative Eh – pH buffers control Eh at a given pH in a range that lies within the overall uncertainty of the calculations. Groundwater analyses are generally consistent with the assumption that the pyrite/goethite buffer closely represents conditions in most potable water aquifers. An alternative assumption that Eh was defined by goethite saturation in the presence of measured Fe^{+2} concentration at a given pH did not yield results consistent with hazardous constituent concentrations saturated with respect to the specified host mineral hosts.

No.	Item	Principal Concern	Impact on Findings	Justification for Current Assumptions
5	Reversible chemical equilibrium is assumed with respect to selected mineral hosts.	Some geochemical systems, especially those involving redox reactions, are notoriously slow at achieving chemical equilibrium (see No. 4, above). This is especially pertinent where reactions involve transformations between S(-II) and S(VI).	If partial oxidation in the field leads to dissolution of sulfides of Cd, Hg, Pb, and Zn with formation of native sulfur or other intermediate species instead of SO_4^{-2}, the stability fields of these sulfides would be extended to higher oxidation states. This would in turn lead to a broader distribution of observed concentrations.	The statistical dispersion of the SIs of the identified mineral hosts is suggestive that not all groundwaters are in thermodynamic equilibrium. The agreement between predicted and modal values with respect to redox-sensitive mineral hosts indicate, however, that substantial equilibrium has been achieved in many groundwaters under buffered redox (i.e., pyrite/goethite) conditions.
6	Temperature and pressure is assumed to be 25ºC and one bar, respectively.	The temperatures of most groundwaters within the 48 contiguous states fall between 5ºC and 30ºC with a mode at aroud 12ºC (see Figure 3.52). Hydrostatic pressures in potable water aquifers are unlikely to exceed 10 bars.	Correction of log K for the dissolution reaction of a host mineral from 25ºC to 10ºC ranges from ≈ –2.0 to ≈ +0.75 for the host minerals under consideration. Pressure changes of only one bar would have negligible impact on thermodynamic equilibria and can be ignored. With respect to most hazardous constituent complexes, the values of their dissociation constants at other than 25º are unavailable, and therefore corrections for temperature cannot be made at present.	With the exception of uraninite, none of the corrections of host mineral solubility products for temperature would improve the correlation between model predictions and field observations. Such corrections are generally within the overall uncertainty of the model and the field data used for comparison.
7	Activity coefficients of some sulfide and selenide complexes of hazardous constituents in supporting electrolytes in experiments were assumed to be unity.	Supporting electrolytes were sometimes seawater, or 1 N perchlorate solutions (e.g., Hg selenide complexes).	Failure to correct for ionic strength in such solutions could lead to errors in associated dissociation constants of as high as ±1 log unit.	Activity coefficient corrections, especially for ill-defined oligomeric species, are difficult to implement. In general, corrections to calculated dissociation constants would be less than ±0.5 log units, and even less for oligomeric neutral species, and are therefore within the uncertainty of the model predictions.
8	TDS is assumed to be zero.	Corrections for ionic strength are not made.	Errors thereby introduced are very small, as most potable waters have very low (≤1000 mg/L) TDS.	Impact on hazardous constituent concentrations is negligible.

No.	Item	Principal Concern	Impact on Findings	Justification for Current Assumptions
9	All hazardous constituent mineral hosts are coarsely crystalline.	Some minerals, especially those formed as secondary precipitates, could be amorphous or very finely crystalline. Amorphous or finely crystalline phases are more soluble than their coarsely crystalline counterparts.	Failure to account for increased solubility of hazardous constituent host minerals could lead to predictions of hazardous constituent concentrations 1 – 2 orders of magnitude lower than actually occurs.	Hazardous constituent mineral hosts are assumed to have coarsened through the mechanism of Ostwald ripening over perhaps millions of years, and therefore mineral crystallinity or surface free energy effects are expected to be negligible.
10	Silica activity in solution is controlled by saturation with repect to opal-CT.	Not all waters are saturated with respect to opal-CT; many are expected to be saturated with respect to quartz.	Choice of silica mineral affects predictions of coffinite saturation.	The assumption that silica is saturated with respect to opal-CT in shallow aquifers is reasonable, and consistent with field observations of such systems undergoing diagenesis.
11	Aluminum in solution is controlled by saturation with repect to low Fe,Mg smectite.	Aluminium concentration is under-predicted when compared with field observations.	In general, the impact of incorrectly simulating Al concentrations on predictions of the concentrations of hazardous constituents is small.	Because the underlying problem concerning Al concentration discrepancies has not yet been resolved, selection of low Fe,Mg smectite is appropriate in the context of the present geochemical model.
12	Calcium in solution is controlled by saturation with respect to calcite.	Not all groundwaters are saturated with respect to calcite.	Calcite will buffer pH changes due to changing $P(CO_2)$ more strongly than would be the case if it were absent.	The evaluation of NWIS groundwaters indicated that most are saturated with respect to calcite.
13	Concentrations of major species in groundwater.	Concentrations were fixed and chosen to be representative of the modes of major species analyses in NWIS groundwaters. Variations could impact predictions of hazardous constituent concentrations	The sulfate concentration will affect predictions of Ba concentration in groundwaters by $\approx \pm 0.3$ log unit, as it is assumed that barite is the host mineral. The sulfate concentration will also affect the redox potential through equilibrium with the pyrite/goethite couple by a similar uncertainty. Other species will have negligible effect, as none participate directly in mass action reactions defining hazardous constituent concentrations.	Selection of representative values for the major species is appropriate to ensure model verisimilitude with field observations.

Table 3.16. Uncertainties in geochemical model parameters

No.	Parameter	Estimated Uncertainty	Impact on Findings
1	Mineral solubility products of hazardous constituent mineral hosts.	The primary uncertainty is associated with thermochemical (calorimetric) determinations of ΔH_f^o, which display standard deviations of ≈ ±0.5 - 1.0 kcal/mol in typical cases. Errors associated with the ΔG_f^o of aqueous basis species are generally small, i.e., ≈ ±0.2 kcal/mol, although the uncertainty associated with some basis species could be larger, e.g., for Fe^{+2}, Fe^{+3}, HSe^-	In general, uncertainties associated with mineral solubility products could lead to over- or under-predicting the concentration of a hazardous constituent by ≈ ±1 order of magnitude.
2	Dissociation constants of sulfide and selenide complexes of hazardous constituents.	Experimentally determined uncertainties of dissociation constants of sulfide complexes are usually less than ±0.5 log unit. However, with the exception of Hg selenide complexes, all other selenide complex dissociation complexes have been estimated with potential uncertainties that could be as high as ±2 log units.	Uncertainties associated with the correct identification and stoichiometry of sulfide and selenide complexes can lead to significant errors in estimated concentrations of some hazardous constituents, especially with respect to Cd, Hg, Pb, Se and Zn. Uncertainties are most acute where selenide complexes dominate over corresponding sulfide complexes, as is the case with the solubility of cinnabar (Hg,) and tiemannite (Se). The solubilities of CdS (greenockite), galena (Pb) and sphalerite (Zn) are affected only incrementally by selenide complexation. Therefore the uncertainties in predicted concentrations of Hg and Se are likely to be much larger, i.e., ±2 log units, than for Cd, Pb and Zn, i.e., ±0.5 log units.
3	Arsenopyrite and gudmundite solid solution proxies.	Field evidence suggests that the abundances of As and Sb in potable water aquifers are normally insufficient to cause saturation with respect to either arsenopyrite or gudmundite, although, with respect to Sb, it is probable that kermesite saturates under more acid conditions induced by higher $P(CO_2)$. Therefore, it was assumed that both As and Sb exist in solid solution in pyrite as arsenopyrite and gudmundite components, respectively, and their solid solution saturations were calibrated against the estimated modes of the concentrations of these elements in potable NWIS groundwaters. Uncertainties are approximately ±1 log unit for arsenopyrite SS, and ±2 log unit for gudmundite SS.	The uncertainties in arsenopyrite SS and gudmundite SS likewise affect calculated concentrations of As and Sb in solution, except where the latter saturates with respect to kermesite.
4	Activity coefficient estimates.	The *a* parameter in the extended form of the Debye Huckel expression is estimated for almost all sulfide and all selenide complexes of hazardous constituents.	Because potable waters have low total dissolved solids concentrations, uncertainties associated with the *a* parameter have minor and inconsequential effect on calculated concentrations of hazardous constituents in solution.

No.	Parameter	Estimated Uncertainty	Impact on Findings
5	Rock-forming mineral solubility products.	Uncertainties range from very low in the case of silica polymorphs (±0.1 log unit) to significant, as is the case with several clay minerals (≥ ±1.5 log unit) depending on mineral stoichiometry.	The rock forming minerals equilibrate with the groundwater and buffer pH and Eh. They therefore define the environmental conditions, which in turn affect the solubilities of the hazardous constituent mineral hosts. The pH and Eh of most groundwaters are buffered within a fairly narrow range. The impact of uncertainties in the solubility products of rock-forming minerals is not explicitly evaluated in this study, but general consistency with field observations suggests that these uncertainties have a small effect on predicted hazardous constituent concentrations in most cases.

Table 3.17. Uncertainties in chemical analyses of potable groundwaters

No.	Parameter	Estimated Uncertainty	Comments	Impact on Findings
Basic Chemistry				
1	pH	±0.1 pH unit	Errors introduced through improper custodial handling could increase the uncertainty to ±0.5 pH units or greater	Associated uncertainty could result in errors in the calculated SI of hazardous constituent host minerals and hazardous constituent concentrations of as large as ±1.0 unit, although for most analyses, the error is likely to be much smaller, and the solubilities of several constituents are insensitive to pH.
2	Major cations (Na, K, Mg, Ca)	±5 %	These analyses are usually quite reliable, especially those made during the last 15 years.	Impact on the calculated SI of hazardous constituent host minerals and hazardous constituent concentrations is expected to be small, i.e., < ±0.1 unit.
3	Major anions (Cl, SO_4)	±5 %	These analyses are usually quite reliable, especially those made during the last 15 years.	Impact on the calculated SI of hazardous constituent host minerals and hazardous constituent concentrations is expected to be small, i.e., < ±0.1 unit.
4	Total HCO_3^-	±10 %	Errors introduced through improper custodial handling could increase the uncertainty to ±30% or greater.	The calculated extent of carbonate complexing by Ba, Cd, Pb, U and Zn in groundwaters would be affected, but because carbonate complexes are not predominant, except for Pb at >0.1 bar $P(CO_2)$, the impact on calculated SI of host minerals is expected to be minor, i.e., << ±0.1 unit.
5	Minor cations (e.g., Al, Fe^{+2}, Fe^{+3})	±10 %	When at the limits of detection, uncertainties could exceed ±50%. Errors introduced through improper custodial handling could increase the uncertainty to the point where the analytical result is essentially meaningless.	Uncertainties associated with measurements of Fe^{+2} in potable waters could lead to very large errors (>> 5 units) in the calculated SI of hazardous constituent host minerals when used to calculate Eh.Uncertainties associated with measurement of Al in the calculated SI of hazardous constituent host minerals are likely to be small, i.e., < ±0.1 unit.
6	Minor Anions (e.g., F, PO_4)	±10 %	When at the limits of detection, uncertainties could exceed ±50%. Errors introduced through improper custodial handling could increase the uncertainty to the point where the analysis is essentially meaningless.	Impact on calculated hazardous constituent concentrations is expected to be minor, as no analyses of minor anions were used in the calculation of either SIs of hazardous constituent host minerals or hazardous constituent concentrations.
7	SiO_2(aq)	±5 %	Analyses are usually fairly reliable.	Uncertainties in the calculated SI of hazardous constituent host minerals and hazardous constituent concentrations, associated with measurement of SiO2(aq), are likely to be small, i.e., < ±0.1 unit.
8	Charge imbalance	±30 %	The calculated charge imbalance of many potable NWIS groundwaters is larger than generally considered acceptable. The root causes of such large imbalances are difficult to determine.	Charge imbalance was ignored in the calculation of SIs of hazardous constituent host minerals. However, the large statistical dispersion in values of charge imbalance suggests cumulative uncertainties in the chemical analyses of individual constituents, especially pH and HCO_3^-, or to the omission of analyses of one or more major species.

No.	Parameter	Estimated Uncertainty	Comments	Impact on Findings
Hazardous Constituents				
9	As	±10 %	For the most part, only the most sensitive analytical method, i.e. PLM40 with a detection limit of ≈ 0.0002 mg/L, yields 87% quantitative measurements.	The potential error in SI, due to analytical uncertainty, is ≈ 0.1 unit for the most sensitive analytical method.
9	Ba	±5 %	Modern analytical methods, e.g., PLM43 and PLM47 with a detection limit of 0.0002 mg/L, yield >95% quantitative measurements.	The potential error in SI, due to analytical uncertainty, is <0.1 units for the most sensitive analytical methods.
10	Cd	±50 %	Only the most sensitive analytical methods, i.e. PLM43 and PLM47 with a detection limit of ≈ 0.00004 mg/L, yield meaningful measurements, of which only 24 and 17% respectively are quantitative.	The potential error in SI, due to analytical uncertainty, is ≈ 0.2 unit for the most sensitive analytical method.
11	Hg	±70 %	Most analytical methods have detection limits of ≈ 0.0001 mg/L, but only 0 - 14% yield quantitative measurements.	The potential error in SI, due to analytical uncertainty, is ≈ 0.1 unit for the most sensitive analytical method.
12	Pb	±20 %	Only the most sensitive analytical methods, i.e. PLM43 and PLM48 with a detection limit of ≈ 0.0001 mg/L and ≈0.00006 mg/L, yield meaningful measurements, with 49% and 82% giving quantitative data.	The potential error in SI, due to analytical uncertainty, is ≈ 0.1 unit for the most sensitive analytical methods.
13	Sb	±50 %	Only the most sensitive analytical method, i.e. PLM43 with a detection limit of ≈0.00005 mg/L, yields meaningful measurements, of which only 18% are quantitative.	The potential error in SI, due to analytical uncertainty, is ≈ 0.2 unit for the most sensitive analytical method.
14	Se	±30 %	Only the most sensitive analytical methods, i.e. PLM10 and PLM40 with detection limits of 0.0008 and 0.0003 mg/L respectively, yield meaningful measurements, of which 75 and 54% are quantitative.	The potential error in SI, due to analytical uncertainty, is > 0.1 unit for the most sensitive analytical method.
14	U	±20 %	The most sensitive analytical methods, i.e., PHOS3 with a detection limit of ≈0.0004 mg/L and FL007 with a detection limit of ≈ 0.00001 mg/L respectively, yield 67% and 97% quantitative measurements.	The potential error in SI, due to analytical uncertainty, is ≈ 0.1 unit for the most sensitive analytical methods.
16	Zn	±5 %	Modern analytical methods, e.g., PLM10 and PLM43, both with a detection limit of ≈ 0.0006 mg/L respectively, yield 82% and 94% quantitative measurements.	The potential error in SI, due to analytical uncertainty, is <0.1 units for the most sensitive analytical methods.

Table 3.18. Uncertainties relating to environmental variability in sampled NWIS groundwater compositions

No.	Parameter	Estimated Variability	Impact on Findings
1	Temperature and pressure	The temperatures of most groundwaters within the 48 contiguous states probably fall between 5 ºC and 30ºC (see Figure 3.52). Hydrostatic pressures in potable water aquifers likely range from 1 to 10 bar.	Variations in log K for the dissolution reaction of a host mineral between 5 and 25º range from ≈ –1.0 to ≈ +2.5 for the host minerals under consideration. Pressure changes of up to 10 bars would have negligible impact on thermodynamic equilibria.
2	Oxidation state	Oxidation state could range from highly reducing, i.e., close to the decomposition of water with respect to the evolution of H_2, to oxidizing, i.e., in equilibrium with air.	Such large variations in oxidation state would lead to changes in the identities of mineral hosts controlling hazardous constituent saturations. Variations in SI of specified mineral hosts are likely to range over ± 2 – 3 log units. A general consistency of SI distributions in NWIS potable groundwaters suggests that most fall into a narrower range of oxidation states.
3	Natural variations in hazardous constituent concentrations	Examination of hazardous constituent distributions of concentration in soils and sediments in the National Geochemistry Database shows that the standard deviation of an approximated log normal distribution averages about 0.3. Therefore at 3 standard distributions (accounting for 99.7% of all), the range is approximately ±1 log unit. If the same constituent distributions apply to potable water aquifer host rocks, then whether or not a mineral host controls the aqueous concentration of a hazardous constituent would depend on whether the concentration distribution in the aquifer host rock permits saturation.	Estimating the natural variability of hazardous constituent concentrations in potable waters from the corresponding distributions in aquifer host rocks is difficult to establish without detailed analysis, as many geochemical factors are involved. The measured distributions, based on chemical analyses are confounded with analytical uncertainties, and are therefore broader than would be found in nature. If the concentration distributions of Ba, U and Zn in NWIS potable waters are examined, it appears that natural variability does not exceed ± 1.2, ±2.0 and ± 1.5 log units, respectively. It is expected that the other hazardous constituent concentrations would fall into similar ranges, but they cannot be accurately estimated because the mean of the distribution is at or below the detection limit.
4	Host rock mineralogy	Aquifer host rocks range in mineralogy from essentially pure arenites through impure arkoses to dolomitic limestones. Some shallow unconfined aquifers may be hosted in unconsolidated sediments. Under reducing conditions, the stability of these identified mineral hosts is relatively unaffected by these differing mineralogical environments. The pH of groundwaters in partial equilibrium with the mineral assemblages may vary by as much as ±2 pH units, which, under oxidizing conditions could destabilize the mineral hosts found under these conditions, e.g., cerussite or otavite, and perhaps hemimorphite for Pb, Cd and Zn, respectively.	Most of the hazardous constituent concentrations in NWIS potable groundwaters strongly suggest equilibrium with mineral hosts under reducing conditions in the presence of a pyrite/goethite or similar buffer. Observed concentration distributions of several hazardous constituents also suggest a positive skew, which may be due to equilibration under oxidizing conditions with respect to higher-solubility oxidized mineral hosts at varying pH values, or the skew may be due to analytical artifacts. We conclude that under reducing conditions, mineralogical variations could cause small changes, i.e., ≤ 1 log unit in concentration. A very minor population of NWIS groundwaters has been determined to reside under mildly reducing to oxidizing conditions. This lead to an increase in equilibrium concentration over reducing conditions by +2 to 3 log units, or greater.

No.	Parameter	Estimated Variability	Impact on Findings
5	Extent to which system is at equilibrium	Few studies have been conducted to rigorously analyze the extent to which sedimentary systems have attained equilibrium with pore waters. Generally, when equilibrium between detrital silicates and the groundwater is not attained, diagenetic processes reflect a progressive approach to equilibrium, which may involve the production of metastable secondary minerals such as opal-CT and smectites. As noted above (Table 3.3, Item 5) the lack of thermodynamic equilibrium between rock-forming minerals and groundwaters generally does not materially affect the aqueous concentrations of hazardous constituents. With respect to hazardous constituent mineral hosts, it is expected that most will closely approach equilibrium in reducing groundwater provided that the system is not perturbed through the ingress of oxygen. One issue of concern, however, relates to attainment of equilibrium between SO_4^{-2} and $H_2S(aq)$. Redox equilibrium in this reaction may not be achieved, and this should be borne in mind when conducting model analyses. Non attainment of equilibrium between these species also impacts perturbations in equilibrium between sulfide mineral hosts and the groundwater due to changing pH, where increased solubility can lead to only partial oxidation of S(-II) to native sulfur rather than S(VI).	Non-attainment of equilibrium between aqueous sulfur species could lead to significant dispersion in the calculated SIs of sulfide mineral hosts. However, the statistical dispersion of the calculated SIs for sphalerite (ZnS) is not significantly different from that of barite ($BaSO_4$) or uraninite (UO_2). Because the SI was calculated using the measured SO_4^{-2} concentration, and calculation of $H_2S(aq)$ was based on assumed equilibrium between SO_4^{-2} and $H_2S(aq)$, this observation lends credence to the belief that non-attainment of equilibrium between aqueous sulfur species is not a significant issue in the sampled NWIS potable groundwaters.
6	Anthropogenic contaminants	Anthropogenic contamination by certain hazardous constituents, e.g., As, Hg, Pb, Se, in surficial soils and sediments could be the source of subsequent groundwater contamination, due to solubilization and infiltration. Clear indications of such processes are usually localized, and inadvertent exploitation of potable waters that have been contaminated in that manner are rare.	It is not expected that anthropogenic contamination of groundwaters materially affects the compositions of the NWIS groundwaters selected for this study.

Table 3.19. Estimated Uncertainties contributing to the Aggregate Uncertainty in Log K of the Solubility Product of the Hazardous Constituent Mineral Host[1]

Item	As	Ba	Cd	Hg	Pb	Sb	Se	U	Zn
Host mineral	**Arseno-pyrite SS**	**Barite**	**CdS**	**Cinna-bar**	**Galena**	**Gudmun-dite SS**	**Tieman-nite**	**Uraninite**	**Sphale-rite**
Relevant Uncertainty Contributions from Table 3.15									
Item 6	0.85	0.26	0.7	1.7	0.7	0.85	1.8	0.6	0.3
Item 7	0	0	0	0.5	0	0	0.5	0	0
Item 11	0.3	0.3	0.3	0.3	0.3	0.3	0	0.	0.3
Relevant Uncertainty Contributions from Table 3.16									
Item 1	0.5	0.3	0.23	0.48	0.35	0.5	0.5	0.3	0.26
Item 2	0	0	0.5	1.0	0.5	0	1.0	0	0
Item 3	1.0	0	0	0	0	1.0	0	0	0
Relevant Uncertainty Contributions from Table 3.17									
Item 1	0.1	0	0	0	0.1	0.1	0.1	0	0
Item Haz. Const.	0.1	0.1	0.2	0.1	0.1	0.2	0.1	0.1	0.1
Aggregate Uncertainty									
$\sigma(+)$	1.17	0.44	0.66	1.26	0.69	1.18	1.23	0.68	0.65
$\sigma(-)^2$	1.49	0.51	0.96	2.11	0.99	1.50	2.18	0.32	0.71
Log K + $\sigma(+)$	56.83	-9.53	-13.43	-36.24	-13.71	34.97	-46.28	3.15	-9.35
Log K[3]	55.66	-9.97	-14.09	-37.50	-14.40	33.76	-44.10	3.83	-10.00
Logk - $\sigma(-)$	54.17	-10.48	-14.09	-39.61	-15.39	32.26	-42.87	4.15	-10.71

[1] Values refer to one σ, i.e., one standard deviation from the mean.

[2] The larger negative uncertainty takes into account the bias introduced by assuming a model temperature that is about 10-15ºC higher than average ambient aquifer temperatures.

[3] Best-estimate value used in equilibrium calculation. See Table 3.14.

Because the geochemical model is calibrated against field measurements, as discussed in Section 3.5.2, the major uncertainty associated with identification of the specific redox buffers defining oxidation state is implicitly taken into account. Uncertainties in log K of the solubility products of the mineral hosts due to differences between the modeled and observed temperatures are also partially compensated by the calibration step. A biased uncertainty arising from model calculations made at 25ºC is, however, included to account for the modal ambient temperature of ~12ºC observed in potable water aquifers, as shown in Figure 3.52. This figure gives the frequency histogram for the temperatures of the NWIS groundwaters evaluated in this study. For convenience, uncertainties associated with sulfide and selenide complexation are folded into the uncertainty associated with the log K values of the solubility products. Although this approach is not strictly correct, it is adopted in order to facilitate calculation of the overall model uncertainty. The aggregate uncertainty in Table 3.19 is estimated by taking the square root of the sum of the

squares of the uncertainties associated with each parameter, an approach that is commonly adopted as a convenient technique for estimating this value. Note that the upper and lower uncertainties differ to reflect the bias introduced by assuming a 25ºC temperature.

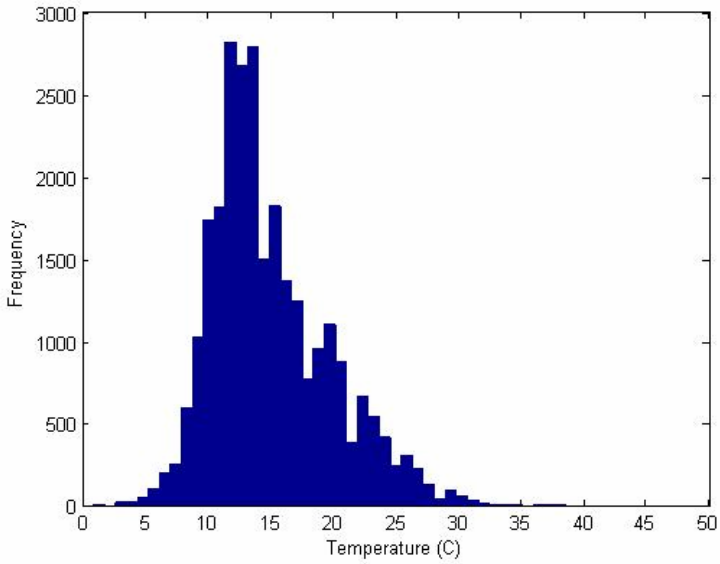

Fig. 3.52. Histogram showing the temperature (ºC) distribution of more than 35,000 groundwater analyses selected from the NWIS Database.

In order to generate an uncertainty envelope for the equilibrium calculations, the computed upper and lower values of Log K for the solubility products of the respective mineral hosts for each element were used to calculate the concentrations of the respective hazardous constituents at discrete intervals of log $P(CO_2)$. The calculations were performed by varying the log K value separately for each hazardous constituent, while fixing all other log K values for the other hazardous constituents at the calibrated value. The results are plotted in Figure 3.51 in the form of a grey envelope, which delineates the $\pm\sigma$ limits of uncertainty about the calibrated value. Note that the total concentrations of Cd, Hg, Pb and Zn are affected in varying degrees by complexation with selenide, as would result from the $\pm\sigma$ variation in log K for tiemannite (HgSe). These variations are not taken into account in the present analysis, but further study of this phenomenon is merited in future more rigorous studies. The assumption that the Se concentration in solution is determined by tiemannite saturation has the unintended consequence

of swamping out variations in Hg aqueous concentration imposed by the -σ variation in log K for cinnabar, because Hg selenide complexation accounts for a substantial fraction of the total Hg concentration in solution. Hence an artifact is created in the form of a highly asymmetric grey uncertainty envelope about the calibrated value displayed by Hg in Figure 3.51.

3.5.4.2 Discussion Relating to Uncertainties

Inspection of the graphs presented in Figure 3.51 in most cases shows excellent agreement between the calculated equilibrium concentration of a given constituent at log $P(CO_2)$ = -2 and the measured or estimated mean concentration in NWIS groundwaters at the same $P(CO_2)$. In other words, the predicted concentration from the geochemical model agrees reasonably well with the observed data from groundwater analyses. This agreement is expected as a consequence of the calibration process, which is applied to all constituents, except Ba and Cd, as described in Section 3.5.2. Furthermore, the calculated aggregate uncertainties at ±1σ, illustrated with the grey shading, are on average about half the ±2σ range estimated independently for the variability in hazardous constituent concentrations in NWIS potable groundwaters. Thus, despite the obvious crudity in estimating aggregate uncertainty, it is comparable with the statistical dispersion actually observed in potable groundwater.

Significant discrepancies arise, however, with respect to the calculated concentrations of Cd, Hg, and Sb when compared with the corresponding field estimates of the mean concentrations in NWIS potable groundwaters. This requires further comment. In all three, the initial calibration was based on the selection of the mode of the SI for the minerals CdS (Figure 3.36a), cinnabar (Figure 3.37a) and gudmundite solid solution (Figure 3.39a), bearing in mind the fact that the analyses most trustworthy are those made with the most sensitive analytical methods currently available. The evaluation did not take into account the most likely statistical distribution based on the percentage of quantitative measurements versus non-detects in NWIS waters using the most sensitive analytical method for a given constituent, as is evaluated in this section. The fact that only 24(17)% have detects for Cd, only 12% for Hg, and only 18% for Sb (see Table 3.9, for all samples analyzed with the most sensitive analytical methods) suggests that many low-

concentration samples for these constituents are not accounted for. In other words, the real mean values of the log concentrations for Cd, Hg and Sb falls below the detection limits of the most sensitive analytical methods currently in routine use. An attempt was made in Figure 3.51 to show an adjusted real concentration range in NWIS potable groundwaters, assuming the the percentage of detectable values represents an observed upper "tail" of lognormally distributed values. However, the calibration of log K values for the geochemical model was conducted without taking this bias into account; thus the presently predicted concentrations of these constituents as a function of $P(CO_2)$ are overstated, and are therefore inherently conservative. A reappraisal of the thermodynamic controls affecting the concentrations of Cd, Hg and Sb in potable groundwaters is clearly necessary. Such corrections would lead to the conclusion that these three constituents would be even less likely to adversely impact water quality upon CO_2 intrusion than the present equilibrium concentrations indicate.

If the revised estimated mean concentration of Cd in NWIS goundwaters was taken into account, then the modal value of SI for CdS would be ≈ -1.5, rather than -0.5, indicating that CdS is even less likely to be present as a discrete phase, and is most probably present in solid solution in sphalerite or possibly galena, although saturation with respect to cadmoselite still remains a plausible option in some groundwaters. It should be noted that the SI for CdS is unlikely to be depressed significantly be selenide complexing of Cd^{+2}, as such species appear to be relatively minor contributors (see Table 3.21 under CdS (greenockite)). Figure 3.51 shows that the predicted versus estimated mean concentration of Hg in solution at log $P(CO_2)$ = -2 differs by about 2 log units. Such a large correction would depress the modal SI for cinnabar and quicksilver to ≈ -2 in both cases. Saturation with respect to tiemannite is likely to be similarly affected. The extent of undersaturation could be offset by assuming that the log K value of the solubility product is -38.08 (Appendix D, Table D1), based on calorimetric data, rather than the calibrated value of -37.5. A correction of this magnitude would still leave cinnabar undersaturated, and is consistent with several field observations suggesting that Hg normally partitions preferentially in pyrite (see Section 3.2). With respect to Sb, Figure 3.51 suggests a correction of approximately -1.5 log units to the calibrated value of gudmundite in solid solution. Such a correction would defer saturation with respect to kermesite until log $P(CO_2)$ exceeds -0.5.

3.5.5 System Variations with $P(CO_2)$ and the Impact of Complexation

The underlying reasons for the response of hazardous constituent concentrations in potable groundwaters to increasing $P(CO_2)$ can be better understood through an examination of the induced variations in pH, Eh and $P(H_2S)$, and the progressive redistribution of participating aqueous complexes in solution in response to these changes. This examination is conducted in the following sections.

3.5.5.1 Variation of pH, Eh and $P(H_2S)$ with $P(CO_2)$

Species distributions were made at 25°C over a range of CO_2 partial pressures from log $P(CO_2)$ = -4 to +1, reflecting the full range of partial pressures either in natural shallow groundwaters, or in those intruded by CO_2 escaping from an underlying deeply buried aquifer. The variation in the equilibrium partial pressure of CO_2 leads to variations in the concentration of CO_2(aq), which, being a weak acid, hydrolyses and lowers pH, as shown in Table 3.20. The pyrite/goethite phase boundary also defines the Eh at any specified pH, where Eh is inversely related to pH.

Table 3.20. Variation of key dependent compositional parameters in groundwaters with variation in CO_2 partial pressure

Log $P(CO_2)$ (bar)	pH	Eh (V)	Log$P(H_2S)$ (bar)
-4	8.906	-0.314	-8.713
-3	8.136	-0.257	-8.815
-2	7.378	-0.200	-8.912
-1	6.684	-0.149	-8.999
0	6.051	-0.103	-9.075
+1	5.574	-0.069	-9.127

The calculated values of log $P(H_2S)$ are also listed in Table 3.15 as a function of Log $P(CO_2)$. As noted under Section 3.4.5.1, $P(H_2S)$ is a measure of the hydrogen sulfide activity in solution, and has an important bearing on the extent of sulfide complexing of heavy metals in solution, including Cd, Hg, Pb and Zn. The calculated log $P(H_2S)$ at log $P(CO_2)$ = -2 , the modal value

calculated for NWIS groundwaters illustrated in Figure 3.17, is –8.91, which corresponds closely to the calculated NWIS groundwater modal value for this species, -8.95, in Figure 3.18. It is interesting to note that the variation in $P(CO_2)$ over five orders of magnitude, from log $P(CO_2)$ = -4 to +1, results in only a minor variation in log $P(H_2S)$, i.e., from –8.7 to –9.1 for the specified base case conditions given in Table 3.20.

3.5.5.2 Nature of Aqueous Complexation and its Impact on Mineral Solubility

The shift in pH and Eh contributes to the changing solubilities of the trace-element host minerals and their stability in relation to other potential mineral hosts. It is, therefore, instructive to investigate the underlying reasons why the concentrations of some elements are sensitive to changes in the partial pressure of CO_2, whereas others are not, and why. Table 3.21 lists how the principal aqueous species in equilibrium with the host minerals vary with $P(CO_2)$ for each of the elements studied. All species are listed that constitute greater than 0.001% of the total speciation at any value of log $P(CO_2)$ between -4 and +1.

For most minerals, the changing solubility as a function of $P(CO_2)$ can be ascribed primarily to a change in pH, and not to increased complexation by carbonate species. For Hg, As, Sb, and Se, neutral and anionic species are predominant, and carbonate species play no part. Enhanced solubility due to carbonate complexation occurs with Ba, Cd, and Pb. However, only with Pb does carbonate complexation, as $PbCO_3(aq)$, dominate the aqueous speciation. The molal percentage of $PbCO_3(aq)$ increases only incrementally over a 5-order of magnitude change in both total Pb in solution and $P(CO_2)$. With Ba and Cd, the predominant carbonate species is the bicarbonate, $MHCO_3^-$ (M = Ba or Cd), but it never becomes the major species contributing to aqueous solubility with either element. Uranium solubility is dominated by the neutral U(IV) species $UO_2(aq)$. Although the U(VI) species UO_2^{+2} complexes strongly with carbonate, this species is present in inconsequential concentrations under reducing conditions, and therefore the carbonate complexes, $UO_2(CO_3)_3^{-4}$, $UO_2(CO_3)_2^{-2}$ and $UO_2CO_3(aq)$, are present only in minor amounts, even at the highest $P(CO_2)$ studied.

.

Table 3.21. Concentration of aqueous species of hazardous constituents in aqueous solution in equilibrium with specified host minerals as a Function of CO_2 partial pressure.

Arsenopyrite Solid Solution Component

Species	Log $P(CO_2)$ (bar)											
	-4		-3		-2		-1		0		+1	
	Concentration											
	mol/kgH^2O	mol %	mol/kgH^2O	mol %	mol/kgH^2O	mol %	mol/kgH^2O	mol %	mol/kgH^2O	mol %	mol/kgH^2O	mol %
H_3AsO_3(aq)	1.2617E-09	63.60	1.0346E-08	91.12	7.8402E-08	98.30	4.7269E-07	99.64	2.2437E-06	99.91	6.1197E-06	99.97
$H_2AsO_3^-$	7.1869E-10	36.23	1.0059E-09	8.86	1.3530E-09	1.70	1.6980E-09	3.579E-01	1.9655E-09	8.752E-02	1.9302E-09	3.153E-02
AsS(OH)(SH)-	3.0122E-12	1.518E-01	2.6413E-12	2.326E-02	2.2651E-12	2.840E-03		<0.001		<0.001		<0.001
$HAsO_4^{-2}$	3.6050E-13	1.817E-02	2.2218E-13	1.957E-03		<0.001		<0.001		<0.001		<0.001
$MgAsO_4^-$	5.2383E-14	2.640E-03		<0.001		<0.001		<0.001		<0.001		<0.001
$CaAsO_4^-$	4.5689E-14	2.303E-03		<0.001		<0.001		<0.001		<0.001		<0.001
$MgHAsO_4$(aq)	1.2901E-14	6.503E-04		<0.001		<0.001		<0.001		<0.001		<0.001
$CaHAsO_4$(aq)	1.0005E-14	5.043E-04		<0.001		<0.001		<0.001		<0.001		<0.001
$FeAsO_4$(aq)		<0.001		<0.001		<0.001	4.1048E-12	8.653E-04	3.9021E-11	1.738E-03	1.6940E-10	2.767E-03

Barite

Species	Log $P(CO_2)$ (bar)											
	-4		-3		-2		-1		0		+1	
	Concentration											
	mol/kgH^2O	mol %	mol/kgH^2O	mol %	mol/kgH^2O	mol %	mol/kgH^2O	mol %	mol/kgH^2O	mol %	mol/kgH^2O	mol %
Ba^{+2}	9.0983E-07	97.35	9.7134E-07	97.78	1.1677E-06	96.97	1.6138E-06	94.71	2.6912E-06	89.92	6.4937E-06	77.82
$BaCO_3$(aq)	1.4885E-08	1.59	4.4642E-09	4.494E-01	1.5267E-09	1.268E-01	7.6410E-10	4.484E-02	5.6868E-10	1.900E-02	1.0489E-09	1.257E-02
$BaHCO_3^+$	9.8517E-09	1.05	1.7525E-08	1.76	3.4959E-08	2.90	8.9372E-08	5.24	3.0107E-07	10.06	1.8491E-06	22.16
$BaCl^+$	4.6233E-11	4.947E-03	4.8169E-11	4.849E-03	5.4081E-11	4.491E-03	6.6273E-11	3.889E-03	9.1111E-11	3.044E-03	1.5387E-10	1.844E-03
BaOH+	1.9472E-11	2.083E-03		<0.001		<0.001		<0.001		<0.001		<0.001

Table 3.21. Continued.

CdS (Greenockite)

Species	Log $P(CO_2)$ (bar)											
	-4		-3		-2		-1		0		+1	
	Concentration											
	mol/kgH^2O	mol %	mol/kgH^2O	mol %	mol/kgH^2O	mol %	mol/kgH^2O	mol %	mol/kgH^2O	mol %	mol/kgH^2O	mol %
$Cd(OH)_2(HS)^-$	2.3468E-08	97.03	4.0056E-09	87.40	7.1093E-10	56.15	1.4793E-10	19.51	3.6015E-11	1.48	1.2793E-11	3.338E-02
CdS(aq)	5.1286E-10	2.12	5.1286E-10	11.19	5.1286E-10	40.51	5.1286E-10	67.63	5.1286E-10	21.01	5.1286E-10	1.34
$Cd(OH)_2(HSe)^-$	1.6923E-10	6.997E-01	2.8885E-11	6.303E-01	5.1265E-12	4.049E-01	1.0667E-12	1.407E-01	2.5971E-13	1.064E-02		<0.001
CdSe(aq)	3.5481E-11	1.467E-01	3.5481E-11	7.742E-01	3.5481E-11	2.80	3.5481E-11	4.68	3.5481E-11	1.45	3.5481E-11	9.259E-02
Cd^{+2}		<0.001	3.4753E-14	7.583E-04	1.5300E-12	1.208E-01	5.1586E-11	6.80	1.3747E-09	56.32	2.0165E-08	52.62
$CdHCO_3^+$		<0.001		<0.001	1.3916E-13	1.099E-02	8.6793E-12	1.14	4.6725E-10	19.14	1.7446E-08	45.53
$CdCl^+$		<0.001		<0.001	2.0816E-14	1.644E-03	6.2233E-13	8.207E-02	1.3672E-11	5.601E-01	1.4037E-10	3.663E-01
$CdCO_3$(aq)		<0.001		<0.001		<0.001	5.5262E-14	7.288E-03	6.5727E-13	2.693E-02	7.3700E-12	1.923E-02
$CdOH^+$		<0.001		<0.001		<0.001	1.4958E-14	1.973E-03	8.0528E-14	3.299E-03	3.0067E-13	7.846E-04
$CdSO_4$(aq)		<0.001		<0.001		<0.001		<0.001	5.4951E-14	2.251E-03	3.3405E-13	8.717E-04

Cinnabar

Species	Log $P(CO_2)$ (bar)											
	-4		-3		-2		-1		0		+1	
	Concentration											
	mol/kgH^2O	mol %	mol/kgH^2O	mol %	mol/kgH^2O	mol %	mol/kgH^2O	mol %	mol/kgH^2O	mol %	mol/kgH^2O	mol %
HgSe(aq)	2.1380E-09	68.12	2.1380E-09	68.13	2.1380E-09	68.13	2.1380E-09	68.13	2.1380E-09	68.13	2.1380E-09	68.13
HgS(aq)	1.0000E-09	31.86	1.0000E-09	31.87	1.0000E-09	31.87	1.0000E-09	31.87	1.0000E-09	31.87	1.0000E-09	31.87
HgS_2^{-2}	4.2968E-13	1.369E-02		<0.001		<0.001		<0.001		<0.001		<0.001
$HgS(HS)^-$	2.5805E-13	8.222E-03	3.4863E-14	1.111E-03		<0.001		<0.001		<0.001		<0.001

Table 3.21. Continued.

Galena

Species	Log $P(CO_2)$ (bar)											
	-4		-3		-2		-1		0		+1	
	Concentration											
	mol/kgH^2O	mol %	mol/kgH^2O	mol %	mol/kgH^2O	mol %	mol/kgH^2O	mol %	mol/kgH^2O	mol %	mol/kgH^2O	mol %
$PbCO_3$(aq)	2.6250E-13	1.918E-02	3.3164E-12	2.417E-01	4.1534E-11	2.94	5.0714E-10	26.59	6.0318E-09	74.20	6.7635E-08	84.71
Pb^{+2}			1.7060E-14	1.243E-03	7.5210E-13	5.327E-02	2.5440E-11	1.33	6.8289E-10	8.40	1.0222E-08	12.80
PbS(aq)	1.2589E-09	91.97	1.2589E-09	91.75	1.2589E-09	89.16	1.2589E-09	65.99	1.2589E-09	15.49	1.2589E-09	1.58
$Pb(CO_3)_2^{-2}$	4.5836E-14	3.348E-03	1.7084E-13	1.245E-02	6.9837E-13	4.946E-02	3.9345E-12	2.063E-01	3.0843E-11	3.794E-01	5.4452E-10	6.820E-01
PbSe(aq)	1.0965E-10	8.01	1.0965E-10	7.99	1.0965E-10	7.77	1.0965E-10	5.75	1.0965E-10	1.35	1.0965E-10	1.373E-01
$Pb(OH)^+$	7.1397E-15	5.216E-04	5.3504E-14	3.899E-03	3.9085E-13	2.768E-02	2.4377E-12	1.278E-01	1.3123E-11	1.614E-01	4.8999E-11	6.137E-02
$PbCl^+$		<0.001		<0.001		<0.001	8.8924E-14	4.662E-03	1.9536E-12	2.403E-02	2.0057E-11	2.512E-02

Gudmundite Solid Solution Component

Species	Log $P(CO_2)$ (bar)											
	-4		-3		-2		-1		0		+1	
	Concentration											
	mol/kgH^2O	mol %	mol/kgH^2O	mol %	mol/kgH^2O	mol %	mol/kgH^2O	mol %	mol/kgH^2O	mol %	mol/kgH^2O	mol %
$Sb(OH)_3$(aq)	1.2617E-11	99.72	1.0346E-10	99.95	1.1415E-09	99.99	1.3935E-09	100.00	1.6553E-09	100.00	1.8374E-09	100.00
$Sb(OH)_4^-$	3.5686E-14	2.820E-01	4.9945E-14	4.825E-02	9.7811E-14	8.568E-03	2.4850E-14	1.783E-03	7.1924E-15	4.345E-04	2.8552E-15	1.554E-04

Table 3.21. Continued.

Tiemannite

Species	Log $P(CO_2)$ (bar)											
	-4		-3		-2		-1		0		+1	
	Concentration											
	mol/kgH^2O	mol %	mol/kgH^2O	mol %	mol/kgH^2O	mol %	mol/kgH^2O	mol %	mol/kgH^2O	mol %	mol/kgH^2O	mol %
ZnSe(aq)	1.4454E-08	85.46	1.4454E-08	86.20	1.4454E-08	86.33	1.4454E-08	86.35	1.4454E-08	86.36	1.4454E-08	86.36
HgSe(aq)	2.1380E-09	12.64	2.1380E-09	12.75	2.1380E-09	12.77	2.1380E-09	12.77	2.1380E-09	12.77	2.1380E-09	12.77
PbSe(aq)	1.0965E-10	6.483E-01	1.0965E-10	6.539E-01	1.0965E-10	6.548E-01	1.0965E-10	6.550E-01	1.0965E-10	6.551E-01	1.0965E-10	6.551E-01
CdSe(aq)	3.5481E-11	2.098E-01	3.5481E-11	2.116E-01	3.5481E-11	2.119E-01	3.5481E-11	2.120E-01	3.5481E-11	2.120E-01	3.5481E-11	2.120E-01
FeSe(aq)	6.0651E-12	3.586E-02	3.0077E-12	1.794E-02	1.5312E-12	9.145E-03	8.4127E-13	5.026E-03	5.0044E-13	2.990E-03	3.5737E-13	2.135E-03
$Cd(OH)_2(HSe)^-$	1.6923E-10	1.00	2.8885E-11	1.722E-01	5.1265E-12	3.062E-02	1.0667E-12	6.373E-03	2.5971E-13	1.552E-03	9.2254E-14	5.512E-04

Uraninite

Species	Log $P(CO_2)$ (bar)											
	-4		-3		-2		-1		0		+1	
	Concentration											
	mol/kgH^2O	mol %	mol/kgH^2O	mol %	mol/kgH^2O	mol %	mol/kgH^2O	mol %	mol/kgH^2O	mol %	mol/kgH^2O	mol %
UO_2(aq)	4.0476E-09	99.92	4.0476E-09	99.99	4.0476E-09	100.00	4.0476E-09	100.00	4.0476E-09	99.99	4.0476E-09	99.82
$UO_2(CO_3)_3^{-3}$	2.8238E-15	6.971E-05	6.5828E-15	1.626E-04	4.1055E-14	1.014E-03	4.1055E-14	1.014E-03	4.2100E-13	1.040E-02	5.5480E-12	1.368E-01
$UO_2(CO_3)_2^{-2}$	6.8029E-16	1.679E-05	5.1132E-15	1.263E-04	1.9863E-14	4.907E-04	1.9863E-14	4.907E-04	1.2075E-13	2.983E-03	1.5798E-12	3.896E-02
UO_2CO_3(aq)	6.4301E-19	1.587E-08	1.6382E-17	4.047E-07	4.0298E-16	9.956E-06	4.0298E-16	9.956E-06	8.9561E-15	2.212E-04	1.7907E-13	4.416E-03
UO_2^+	2.0264E-17	5.002E-07	1.9186E-16	4.739E-06	1.7552E-15	4.336E-05	1.7552E-15	4.336E-05	1.3367E-14	3.302E-04	8.5589E-14	2.111E-03
HUO_3^-	3.3530E-12	8.277E-02	5.7230E-13	1.414E-02	1.0158E-13	2.509E-03	1.0158E-13	2.509E-03	2.1140E-14	5.222E-04	5.1510E-15	1.270E-04

Table 3.21. Continued.

Sphalerite

Species	Log $P(CO_2)$ (bar)											
	-4		-3		-2		-1		0		+1	
	Concentration											
	mol/kgH^2O	mol %	mol/kgH^2O	mol %	mol/kgH^2O	mol %	mol/kgH^2O	mol %	mol/kgH^2O	mol %	mol/kgH^2O	mol %
ZnS(aq)	3.1623E-07	95.59	3.1623E-07	95.28	3.1623E-07	88.66	3.1623E-07	28.97	3.1623E-07	1.44	3.1623E-07	7.635E-02
ZnSe(aq)	1.4454E-08	4.37	1.4454E-08	4.36	1.4454E-08	4.05	1.4454E-08	1.32	1.4454E-08	6.583E-02	1.4454E-08	3.490E-03
$ZnOH^+$	9.2743E-11	2.804E-02	6.9500E-10	2.094E-01	5.0770E-09	1.42	3.1665E-08	2.90	1.7047E-07	7.764E-01	6.3648E-07	1.537E-01
$ZnS(HS)^-$	1.2125E-11	3.665E-03	1.6382E-12	4.936E-04		<0.001		<0.001		<0.001		<0.001
Zn^{+2}	9.4721E-12	2.863E-03	4.2567E-10	1.283E-01	1.8690E-08	5.24	6.2637E-07	57.38	1.6471E-05	75.02	2.3312E-04	56.28
ZnO(aq)	5.6732E-12	1.715E-03	7.1675E-12	2.160E-03	8.9764E-12	2.517E-03	1.0960E-11	1.004E-03		<0.001		<0.001
$ZnCO_3$(aq)	2.7953E-12	8.450E-04	3.5315E-11	1.064E-02	4.4229E-10	1.240E-01	5.4004E-09	4.947E-01	6.4231E-08	2.925E-01	7.2023E-07	1.739E-01
$ZnHCO_3^+$	2.6012E-13	7.863E-05	1.9493E-11	5.874E-03	1.4240E-09	3.992E-01	8.8814E-08	8.14	4.7813E-06	21.78	1.7852E-04	43.10
$ZnSO_4$(aq)		<0.001	9.5241E-12	2.870E-03	3.4878E-10	9.779E-02	8.5090E-09	7.795E-01	1.3598E-07	6.193E-01	8.2664E-07	1.996E-01
$ZnCl^+$		<0.001		<0.001	4.3321E-12	1.215E-03	1.2951E-10	1.186E-02	2.8454E-09	1.296E-02	2.9213E-08	7.053E-03
Zn(OH)Cl(aq)		<0.001	2.4503E-13	7.383E-05	1.7271E-12	4.842E-04	1.0107E-11	9.259E-04		<0.001		<0.001

Arsenic and Sb behave similarly to each other, where aqueous species are dominated by neutral oxy-complex molecules of each element in the (III) state. Traces of As(V) oxy-anionic and neutral species are present, including $H_2AsO_4^-$ and complexes of Mg^{+2}, Ca^{+2} and Fe^{+3}. The omission of corresponding species in the Sb system does not mean that they are absent, only that thermodynamic data are unavailable and no evidence has so far indicated they might be important. Both As and Sb complex with sulfide, but under the conditions of the current simulation, such complexation is negligible. Selenium complexation is also found to be negligible. Neither sulfide nor selenide complexes of either Ba or U are known.

At low $P(CO_2)$, Cd speciation is dominated by $Cd(OH)_2(HS)^-$ (relative concentration = 97 mol%) at $P(CO_2)$ = 0.0001 bar, but declines progressively with increasing $P(CO_2)$ until it becomes inconsequential at $P(CO_2)$ = 10 bar. CdS(aq), a minor species at low $P(CO_2)$, increases to a maximum relative concentration of 68 mol% at $P(CO_2)$ =0.1 bar, but falls with further increase in $P(CO_2)$. CdSe(aq) and $Cd(OH)_2(HSe)^-$ are present as minor species, CdSe(aq) following CdS(aq) and reaching a maximum relative concentration of about 5 mol% at $P(CO_2)$ = 0.1 bar. With increasing $P(CO_2)$, Cd^{+2} increases progressively to a maximum relative concentration at $P(CO_2)$ = 1 bar, then begins to decline as $CdHCO3^+$, whose relative importance increases progressively with increasing $P(CO_2)$, and becomes predominant at $P(CO_2)$ = 10 bar, with a relative concentration of 53 mol%. The complex interaction between sulfide, selenide, bicarbonate and the uncomplexed Cd cation leads to complex CdS (greenockite) solubility behavior with respect to $P(CO_2)$, as is illustrated in Figure 3.51.

Hg speciation is almost completely dominated by neutral oligomeric species represented by HgS(aq) and HgSe(aq), and the solubility of cinnabar is consequently essentially independent of $P(CO_2)$. The presence of selenide in solution effectively increases cinnabar solubility by approximately 50 mol%.

The behavior of galena solubility as a function of $P(CO_2)$ is dominated primarily by the oligomeric species PbS(aq) at low $P(CO_2)$, but with increasing $P(CO_2)$, the carbonate complex, PbCO3(aq), becomes increasingly important until it predominates at $P(CO_2)$ > 1 bar. PbSe(aq) follows PbS(aq) in behavior, but increases galena solubility by only about 10 mol%. Pb+2

increases progressively to a maximum relative concentration of 13 mol% at $P(CO_2)$ = 10 bar. By analogy with Cd^{+2}, it is possible that the relative concentration of this species would decline at even greater $P(CO_2)$, as carbonate species become predominant. The increase in galena solubility with $P(CO_2)$ is due to the formation of the Pb(CO3)(aq) complex, and occurs when Log $P(CO_2)$ exceeds -1.

In specifying the input parameters, we recognize that cadmoselite, tiemannite and clausthalite are all potential candidates for controlling Se(II) activity in solution, but it is not clear which is most plausible. Tiemannite was selected, because of the availability of thermochemical data for Hg selenide complexes (Mehra and Gubeli, 1971). A further constraint is imposed by Gibbs Phase Rule for equilibrium assemblages, which requires that only one selenide can be selected, unless saturation with respect to one or more sulfides of Cd, Hg, Pb, and Zn is suppressed. With the selection of tiemannite, and incorporation of selenide complexes, the saturation index for ferroselite is depressed to ~ -15 (Section 3.4.5.2). This suggests that Se substitution for S in pyrite is probably small. Although Ryser et al. (2005) have identified the association of selenian pyrite and dzharkenite, a ferroselite polymorph in shales associated with Western phosphate deposits in the United States, we believe that such an occurrence is unusual and is not representative of potable aquifer host rocks in general. Western phosphate shales are exceedingly rich in Se, averaging about 275 mg/kg rock. This contrasts with the average abundance of Se measured in surficial sediments and soils in the United States of no more than 1 mg/kg of material (Section 3.6). Western shales therefore represent a case of extreme selenium enrichment by a factor of perhaps as much as 1,000, where it must be presumed that all Cd, Hg, Pb, and perhaps some or all of the Zn are stabilized as selenides rather than sulfides, and there is sufficient Se in excess to precipitate $FeSe_2$.

Selenium speciation in solution saturated with respect to tiemannite is completely dominated by complexation with Zn and Hg as the oligomeric species ZnSe(aq) and HgSe(aq). Because sphalerite is relatively soluble in groundwaters, Zn complexing predominates, constituting 86 mol% of Se species in solution, the balance being made up primarily by HgSe(aq). Under alkaline conditions where $P(CO_2)$ = 0.0001 bar, the Cd species $Cd(OH)_2(HSe)^-$ begins to make

an appearance, but only to the extent of about 1 mol% in relative concentration. Other selenide species, including CdSe(aq), PbSe(aq), and FeSe(aq), never reach significant concentrations in the current simulation.

The solubility of sphalerite at low $P(CO_2)$ is determined primarily by the oligomeric species represented by ZnS(aq), which predominates in solution (~ 90+ mol%) until $P(CO_2)$ exceeds 0.01 bar, thereafter falling to insignificant concentrations as $P(CO_2)$ reaches 10 bar. The Se analogue, ZnSe(aq), behaves similarly, but constitutes no more than 5 mol% of the total relative concentration. With increasing $P(CO_2)$, uncomplexed Zn^{+2} and $ZnHCO_3^-$ become predominant, representing 56 and 43 mol% respectively of the relative concentration at 10 bar. The behavior of Zn species with respect to sphalerite saturation is somewhat analogous to that of Cd species with respect to CdS (greenockite) saturation, but with the important distinction that a Zn analogue to the species $Cd(OH)_2(HS)^-$ has not been identified. The variation of sphalerite solubility with $P(CO_2)$ actually shows greater affinity with that of galena, where both are insensitive to $P(CO_2)$ until it exceeds ~ 0.01 bar as carbonate complexes progressively overwhelm the sulfide complexes.

Finally, it should be noted that other species, including complexes of Cl^- and SO_4^{-2} with Ba, Pb, Zn, or Cd are evident, even at the low concentrations of these species in the representative groundwater composition used in the analysis. Higher concentrations of either species could have a marked impact on the distributions reported in Table 3.20, which highlights the fact that complex geochemical systems must be fully described to account for all possible interactions.

3.5.6 Conclusions from Equilibrium Calculations

Figure 3.51 shows that the most serious water quality issue resulting from CO_2 intrusion may be the enhanced dissolution of pyrite with consequent solubilization of arsenic, with a high probability that the MCL would be exceeded. At plausible $P(CO_2)$ levels representative of maximum possible values in shallow groundwaters, Ba, Pb and Zn may approach or exceed regulatory concentration limits. For those elements, however, model uncertainties, kinetic factors, and post-withdrawal water treatment methods all suggest diligence rather than alarm. Of

the remaining elements, the calculated concentrations of Cd, Hg and Sb are somewhat higher than are believed to occur naturally, but analytical methods are insufficiently sensitive for accurate quantification. None are expected to exceed MCLs with increasing $P(CO_2)$. Hg, Se and U concentrations are unaffected by CO_2 intrusion.

From the foregoing discussion and the results depicted in Figure 3.51, it is apparent that of the hazardous constituents investigated, only As and to a lesser extent Pb and Zn have the potential to exceed MCLs (or SDWRs) through imposition of elevated partial pressures of CO_2. The focus of subsequent reactive transport simulations in Section 4 is on the mobilization and transport of As and Pb in potable water aquifers following intrusion of CO_2 from deep storage.

3.6 Representative Aquifer Host Rock Mineralogies

3.6.1 Background

This section provides a basis for defining the mineralogy of representative aquifers exploited for potable water, with the objective of illustrating a range of geochemical responses to CO_2 intrusion (e.g., a well buffered aquifer vs. a poorly buffered aquifer). The resulting suite of realistic "representative" mineralogies are used in the simulation study in Section 4 to evaluate the effect of CO_2 intrusion on the chemical composition of the groundwater, and particularly on the potential changes in the concentrations of hazardous constituents. Our attempt to correlate aquifer mineral composition with host rock and groundwater chemical analyses is part of an overall strategy to develop a geochemical model capable of representing any potable water aquifer.

Previous modeling of heavy metal mobilization and transport in potable water aquifers assumed grossly simplified mineral compositions (Wang and Jaffe, 2004), consisting of 50 wt.% galena and 50 wt.% of either calcite or of quartz. In subsequent work, we formulated more realistic aquifer mineralogies (Birkholzer et al., 2008; Xu et al., 2007), based on extensive studies of Gulf Coast oil field arenaceous aquifers and associated confining shales (Xu et al., 2005), as well as on deep carbonaceous sandstone from the Ohio Basin (Zerai et al., 2006; Xu et al., 2006). To simulate to potential mobilization of these contaminants under elevated CO_2 partial pressures, we assumed that a 1% volume fraction of either galena or arsenopyrite was present, in addition to the known major minerals. However, as discussed before, these volume fractions of trace minerals such as galena or arsenopyrite in potable water aquifer host rocks are still unrealistically high. Furthermore, the Gulf Coast aquifer mineralogy, which can be classified as a lithic arkose (see Figure 3.53 below), was based on that of deep arenaceous horizons in the Frio Formation of Texas, which is not necessarily representative of shallow potable water aquifers over most of the contiguous 48 U.S. states.

Below, we develop "representative" mineralogies for domestic shallow potable aquifers. These mineralogies are (1) an impure sandstone typical of those that are found underlying the Atlantic

Coastal Plain, the Gulf Coast, and deposited in the Central Valley of California; (2) a relatively pure arenite, characteristic of the St. Peter sandstone underlying the Illinois basin; and (3) a typical dolomitic limestone, found underlying extensive tracts of the Appalachians. These mineralogies are a compromise in representing broad ranges of aquifer host rock compositions found throughout the United States, with focus on aquifers that may overlie future CO_2 storage sites and are expected to be vulnerable to CO_2 intrusion. This compromise is a necessity in a global assessment of groundwater vulnerability, because it would be impossible to explore fully the impact on hazardous metals transport under the diverse range of aquifer mineralogies that probably exist throughout the United States, even if such mineralogies had been fully characterized.

In practice, such a restriction is not generally a critical issue. The main reason for this is the nature of the thermodynamic controls affecting the partitioning of heavy metals between the solids of which they form an essential component and the aqueous phase (i.e., groundwater). As discussed in Section 3.4.1, equilibrium between the solid and the aqueous phase is governed by the relationship specified in Equation (3.1). This relationship can be redefined in terms of activity ratios of ionic species or in terms of chemical potentials, both of which are intensive parameters, i.e., they are independent of mass. This means that as long as a particular mineral is present, it does not matter how much is present. Likewise, if the mineralogy of a host rock is in thermodynamic equilibrium, the groundwater composition would not be affected by the relative concentrations of the minerals are present.

Composition-dependent differences may arise, however, upon perturbation of the geochemical system, where the reaction path leading to re-establishment of thermodynamic equilibrium is defined by chemical kinetic and transport processes. Such a perturbation would arise from CO_2 intrusion where, for example, a certain mineral might dissolve entirely, or a secondary mineral might precipitate in one aquifer, but would not occur in another containing the same mineralogy, but with differing mass fractions. Also, the rate of dissolution or precipitation would be mass- or rather surface-dependent. Mass-dependent differences could become important to water quality, where pH or Eh buffering minerals are present in low concentrations, or where the activities of

hazardous inorganic constituents are determined by trace concentrations of minerals containing the constituents as essential components. Although such kinetic issues must be recognized in simulating aquifer responses to CO_2 intrusion, we believe as a general rule that only substantial variations in aquifer host rock mineralogy would lead to major differences in the evolution of the system due to CO_2 intrusion. Thus, selection of the three mentioned mineralogies should cover a broad range of likely geochemical environments. Furthermore the methodology developed here has flexibility, by allowing simulations to be conducted for site-specific conditions with actually measured aquifer mineralogies, physical properties, temperatures, and other relevant properties.

3.6.2 Approach at Mineralogy Characterization

3.6.2.1 Distribution of Major and Accessory Minerals

The Groundwater Atlas of the United States, published by the United States Geological Survey (U.S. Geological Survey, 1992-1997), was consulted to identify the extent and importance of major aquifer host rock types in the Unites States. The atlas is subdivided into 12 segments, of which four were selected for further evaluation: Segment 1 (California, Nevada), Segment 9 (Iowa, Michigan, Minnesota, Wisconsin), Segment 10 (Illinois, Indiana, Kentucky, Ohio, Tennessee), and Segment 11 (Delaware, Maryland, New Jersey, North Carolina, Pennsylvania, Virginia, West Virginia).

Although confined aquifers most likely to be affected by leakage from future underlying CO_2 storage reservoirs were of particular interest, the review showed that by far the largest source of drinking water in the four identified regions was from unconfined aquifers, which would be less likely to retain and trap intruding CO_2. In Segments 9 and 10, the sources of many potable waters are locally shaley limestone and dolomites, typically less critical with regards to the impacts of CO_2 intrusion. A host rock mineral composition that is predominantly composed of carbonates would mitigate groundwater compositional changes in response to CO_2 intrusion because of the buffering effect of the carbonates. The main remaining potable water sources in Segment 9 are relatively pure sandstones of Cambrian-Ordovician age, principally the St. Peter-Prairie du Chien-Jordan, Ironton-Gatesville, and Mount Simon aquifers. In Segment 11, arenaceous

aquifers of the North-Atlantic Coastal Plain are the principal sources of drinking water, notably the Chesapeake, Castle Hayne-Aquia, Severn-Magothy, Peedee-Upper Cape Fear, and Potomac aquifers. The predominant source of underground drinking water in the Segment 1 states of California and Nevada is the Central Valley Aquifer System.

Major aquifers vary substantially in mineralogy, both vertically and laterally, reflecting temporal and areal facies and depositional changes during palaeogeographical evolution. Furthermore, subsequent diagenetic and metasomatic processes also vary in areal extent and intensity, depending on postburial history and subsequent exhumation. Thus, the identification of a specific aquifer does not result in a unique characterization of its mineralogy. Furthermore, variations characteristically overlap with other formations of similar provenance.To characterize the mineralogy, we used the principal formations identified from the review of the four segments in a series of literature searches, with the objective of identifying mineralogical analyses. Results from these searches were disappointing; few papers yielded critical quantitative information of the type desired, and those that did were not considered representative.

After failing to locate suitable representative mineralogical analyses of major aquifers in the regions studied, a different approach was taken to characterize the principal mineral composition of arenaceous rocks, as discussed in the following paragraphs. Less attention was paid to the characterization of carbonate aquifer mineralogy, because the aqueous buffering capacity is insensitive to large mass and compositional variations in the essential minerals composing such rocks, i.e., calcite and dolomite, and therefore significant mass and compositional variations in these minerals are not critical.

Recently published textbooks on sedimentary petrology (i.e., Greensmith, 1989; Tucker, 1991; Blatt, 1992; Boggs, 2003) were reviewed to find a classification that would define the mineralogical characteristics of arenaceous rocks in a manner consistent with geochemical model development and the objectives of the project. A further requirement was that the classification would provide a framework for incorporating and exploring variations in the mineralogy of any chosen domestic potable-aquifer host rock. Although the authors of the cited textbooks pointed out a long-term problem regarding inconsistent, conflicting, and confusing classification

schemes, a general consensus has emerged that a scheme broadly based on the classic text of Pettijohn et al. (1987) may be most reasonable.

This scheme by Pettijohn et al. (1987), illustrated in Figure 3.53, as based on Tucker (1991, Fig. 2.57, p.49), considers only the detrital material comprising the rock, ignoring subsequent post-depositional mineralogical changes arising from diagenesis and metamorphism. The mineralogy of the rock "framework," or large particles, is represented on a triangular diagram in terms of three major components: quartz, feldspar, and lithic fragments, while in the plane perpendicular to the triangular diagram, the increasing fraction of included "matrix" or interstitial fine-grained (<30 μm) material is considered. In further refining a selection of a specific mineralogy for the purposes of model development, use was also made of Figure 3.54, also from Tucker (1991, Fig. 2.62, p. 53), where the petrologic characteristics of arenaceous sediments derived under differing tectonic conditions are plotted onto the triangular diagram of the principal framework constituents.

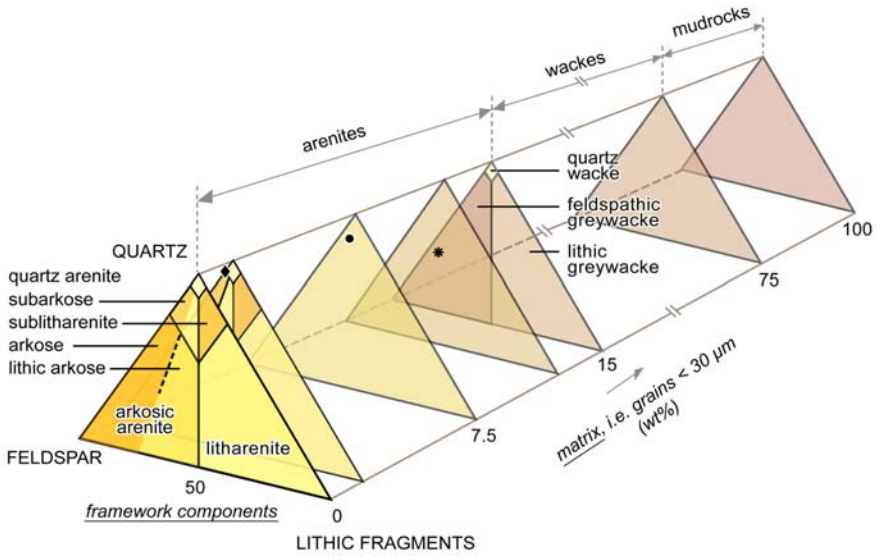

Fig. 3.53. Classification of arenaceous sediments in terms of detrital framework grains (quartz, feldspars and lithic fragments) and a detrital (clay) interstitial matrix (after Tucker, 1991). The spot on the 7.5-wt% matrix triangle represents the base-case aquifer host rock introduced in Section 3.6.3.1. The diamond represents the St Peter Sandstone described in Section 3.6.3.3. For comparison, the star illustrates the Gulf Coast Lithic Arkose described in Xu et al. (2006).

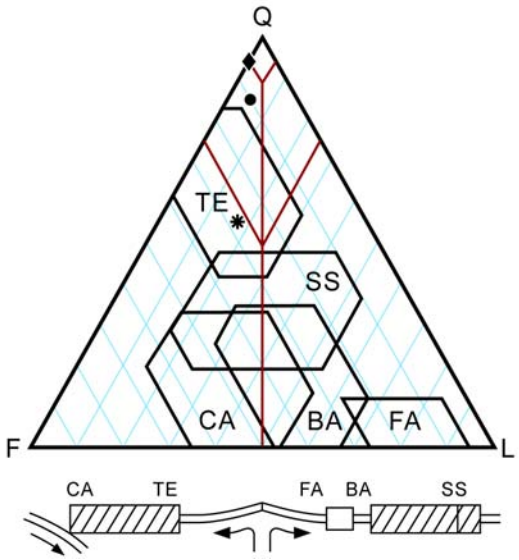

Fig. 3.54. Representation of the tectonic provenances of framework grains of arenaceous rocks (after Tucker, 1991). TE = trailing edge or passive continental margin; SS = strike slip continental margin; CA = converging arc margin; BA = back arc basin and FA = fore arc basin. The black spot indicates the base-case aquifer host rock introduced in Section 3.6.3.1. The diamond represents the St Peter Sandstone described in Section 3.6.3.3. For comparison, the star illustrates the Gulf Coast Lithic Arkose described in Xu et al. (2005).

After defining the composition of the arenite in terms of the Pettijohn et al. (1987) sandstone classification scheme, a further characterization of the basic mineralogy is required. This characterization includes (1) identifying the nature and composition of detrital feldspars, (2) the composition of the lithic fragments, and (3) the composition of the clay minerals in the matrix. Because the provenances of most detrital feldspars were exposed granitic to granodioritic batholiths, their composition is presumed to be primarily feldspar and relatively sodic plagioclases, i.e., oligoclase. For simplicity, it is assumed that lithic fragments likewise are represented by granitic or granodioritic mineralogy. Clay minerals occupy the matrices of arenaceous rocks. The clay mineralogy is based on the average clay-mineral composition of some shales and mudstones reported in the literature (Boggs, 2003, Table 7.6, p. 289). Table 3.22 summarizes this mineralogy, and how it is redistributed to conform to limitations in model input.

Table 3.22. Matrix clay mineralogy.

Clay Mineral	Concentration, Wt.%	Model Distribution, Wt.%
Kaolinite	14.4	22.9
Smectite	10.7	19.5
Illite	34.2	40.9
Chlorite	8.2	16.7
Mixed-layer illite/smectite	13.0	-
Kaolinite/chlorite	17.0	-
Montmorillonite/mixed-layer clays	2.3	-
Total	99.8	100.0

The actual characterization of the mineralogy under the three categories listed above is somewhat arbitrary, and reflects the lack of critical evaluations necessary to permit generalization. Because each clay mineral differs in its site complexation characteristics for each hazardous constituent in solution, variations in clay content and composition can markedly affect their partitioning between the host rock and migrating pore water in aquifers, and likewise strongly affect the mobilization of metals caused by CO_2 intrusion, both of which is demonstrated by reactive transport modeling in Section 4. It is therefore an important consideration that the clay mineralogy be evaluated for any site that becomes a candidate for a more detailed evaluation. Through the use of spreadsheets, the mineralogies developed in this study can be recalculated for any specific set of site-specific conditions when required. See Section 3.6.3 for the four selected mineralogies defined based on the above approach.

The final step in defining the mineralogy involves the inclusion of minor, albeit critical secondary minerals that commonly form during authigenesis and diagenesis, and occasionally through epigenesis. These include (1) organic matter (primarily kerogen), (2) carbonates and sulfates, both of which act as cement, and (3) iron oxides and sulfides, the former acting as adsorbents and the latter acting as hosts for the hazardous inorganic chemical elements that form the subject of this study. The concentrations of these constituents in arenaceous sedimentary rocks are usually small, and quantitative surveys defining their observed concentration ranges

have not been made. We therefore estimated suitable values, all of which are probably somewhat higher than average, but not unrealistically so.

We must emphasize that the mineralogical descriptions of the aquifer host rocks, which are defined further in the following sections, are based on field observations and are almost never assemblages at thermodynamic equilibrium. It is inevitable that incompatible assemblages are defined, which can never achieve thermodynamic equilibrium without mineralogical changes. Preliminary simulations of aquifer chemistry prior to CO_2 intrusion occasionally necessitated *ad hoc* adjustments, and therefore minor differences between the initial and simulation mineralogies occur, of necessity to ensure initial steady state, if not thermodynamic equilibrium.

3.6.2.2 Distribution of Trace-Element Minerals

The specification of both the identity and the concentrations of trace minerals containing hazardous metals as essential components is based on two sources of information: (1) identification of the minerals likely to act as hosts through a review of published scientific literature bearing on the subject (Section 3.2), and evaluation of potential host minerals controlling the saturation concentration of hazardous constituents in NWIS groundwaters (Sections 3.3 and 3.4), and (2) specification of their concentrations in soils and sediments estimated from information supplied by the National Geochemical Survey (NGS) Database, maintained by the United States Geological Survey. This second step is described in the following paragraphs.

The NGS database was searched to find the average concentrations of As, Ba, Cd, Hg, Pb, Sb, Se, U, and Zn in all analyzed soils and sediments from the contiguous forty-eight states. Several analytical methods are reported in the database. Unfortunately, not all methods actually measure the total concentration, but rather a partial amount depending on the effectiveness of treatment used in liberating a particular element for the analytical method. In this respect, neutron activation is the preferred method, because it does actually measure total concentration. (However, not all elements under consideration were analyzed by this method.) The concentration, in ppm, was rounded up to the nearest significant figure, and it was then assumed

that the source rock from which the sediment or soil was derived contains the same concentration of that element in a specified mineral where the element is an essential component. The resulting concentrations are given in Table 3.23.

The concentrations of the selected elements were further checked against two other referenced sources of elemental abundances; (a) calculated crustal abundances based on the averages of values presented by Turekian (1970), Wanke et al. (1984), Weaver and Tamey (1984), Shaw et al. (1985), Taylor and McLennan (1985), Ernshaw and Greenwood (1997), Lide (2005), and (b) abundances in domestic coals (Kuhn et al., 1981; Golightly and Simon, 2006; Bragg et al., 1998; USGS, 2001), both of which are also included in Table 3.23. The latter source is subject to deviation from expected norms in potable aquifers, because of the overwhelming content of organic matter, which over geologic time could lead to enhanced sequestration of chalcophilic elements. However, because most of the elements under consideration are chalcophilic, their relative abundances are likely to be minimally fractionated. Furthermore, as noted in Section 3.2, an incentive exists for investigating the nature and distribution of hazardous trace elements in coals that are discharged into the atmosphere during combustion. As a consequence, many minerals containing trace elements have been identified in coal, which are easier to observe and characterize than in typical aquifer host rocks.

With the exception of cadmium and selenium, the elemental abundances characterizing the selected elements are generally consistent with corresponding average crustal abundances and are therefore believed to be reasonably representative for most aquifer host rocks. The assumption that each hazardous element is concentrated in one mineral alone is conservative, since each element is expected to be distributed over exchange and adsorption sites in the mineral assemblage, co-precipitated with secondary minerals, and in solid solution in primary detrital minerals. Indeed, several of the selected constituents may be present entirely in substitution as minor components in other minerals, rather being present in minerals listed in Table 3.23, where the constituent is an essential component. Under such circumstances, calculated equilibrium concentrations in the aqueous phase would represent the expected upper limit under reducing conditions.

Table 3.23. Representation of the mineralogy of hazardous inorganic substances in an arenaceous aquifer host rock

Element	Concentration, ppm								Host Mineral	Formula
	National Geochemical Survey Database (Mainly Sediments and Soils)					Average Crustal Abundance (1)	Coal (2)	Values selected for this Study		
	ICP	Part. ICP	AA	NAA	NURE					
As	10	1.3	5.3	10	4.7	1.69	6.8	10	Arsenopyrite (SS)	FeAsS
Ba	549	-	-	500	522	539	237	500	Barite	$BaSO_4$
Cd	2	0.09	-	5	5	0.131	0.98	5	Greenockite	CdS
Hg	-	0.04	0.03	0.04	500	0.0617	0.17	0.04	Cinnabar	HgS
Pb	18	10	-	20	12	13.9	29	20	Galena	PbS
Sb	-	1	0.6	0.5	2	0.2	11.1	0.5	Gudmundite (SS) Kermesite	FeSbS Sb_2S_2O
Se		0.241	0.2	0.25	1	0.067	2.6	0.25	Tiemannite	$FeSe_2$
U	100	-	-	3	-	1.91	2.3	3	Uraninite	UO_2
Zn	64	29		100	58	72	832	100	Sphalerite	ZnS
Fe	25400	-	-	See notes	24,500	50,000	19,600	See notes	Pyrite, goethite, chlorite, etc.	FeS_2, etc.
S	-	-	-	See Notes	-	468	39,000	See Notes	Pyrite, barite greenockite, galena, etc.	FeS_2, etc.

Notes: ICP: Inductively coupled plasma emission spectroscopy
AA: Atomic absorption spectroscopy
NAA: Neutron activation analysis
NURE: National Uranium Resource Evaluation, a program utilizing various analytical methods
(1): Average of five reported values
(2): Data from Kuhn et al. (1980), except for Cd (Golightly & Simon, 2006) and Hg (USGS, 2001)
Concentrations of Fe and S were not selected, as they are defined by the mineralogies specified for the aquifer host rocks.
Both arsenopyrite and gudmundite are expected to be present in solid solution (SS) in pyrite. Greenockite might be in solid solution in sphalerite, but it is assumed for the purpose of subsequent reactive transport modeling that it is present as a pure substance.

Note that all representative mineralogies developed in Section 3.6.3 (with the exception of an aquifer in oxidizing conditions), utilized for the reactive transport simulation studies in Section 4, use the same set of trace minerals given in Table 3.23. In other words, we make the assumption that trace minerals are present where the hazardous inorganic constituent is either a major component or incorporated in solid solution. Based on the discussion in Sections 3.2 and 3.3.3, the presence of such trace minerals is a reasonable possibility in many aquifers. The

concentration of these trace minerals, however, are very small, much smaller than was assumed in previous studies (Wang and Jaffe, 2004; Birkholzer et al., 2008; Xu et al., 2007).

3.6.3 Representative Mineralogies

3.6.3.1 Coastal Plain Aquifer Host Rock

Most arenaceous sediments of the northeast and southeast Atlantic seaboard, as well as the Gulf Coast, fall into the subarkose classification, and are characteristic of trailing edge (TE) or passive continental margins (Figure 3.53). Sediments of the Central Valley of California were laid down in a fore arc (FA) basin, but their mineralogy is characterized by weathering products of the Sierra batholith. A decision was therefore made to choose a framework mineralogy that is a compositional compromise between a subarkose and a quartz arenite, consisting of 85 wt.% quartz, 10 wt.% feldspar, and 5 wt.% lithic fragments, as identified by the solid circle on Figure 3.53. Additionally, the clay content in the matrix was arbitrarily chosen to be 7.5 wt.% of the total, i.e., the framework comprises the remaining 92.5 wt.% of the rock, intermediate in composition between an arenite and a greywacke.

We then defined the nature and composition of detrital feldspars, the composition of the lithic fragments, and the composition of the clay minerals in the matrix. The feldspars were divided equally between K-feldspar and oligoclase, reflecting a granite-granodiorite provenance. The lithic fragments consist of equal parts quartz, K-feldspar, and oligoclase. The clay mineralogy was based on the average clay mineral composition, appropriately modified to account for thermodynamic limitations of the model, as described under Section 3.6.2.

In the final step, the trace minerals defined in Section 3.6.2.2 were added to the basic mineralogy. The resulting mineralogy is summarized in Table 3.24. Notice that the expected realistic volume fractions of Pb-bearing galena or As-bearing arsenopyrite are far smaller than the previously used volume fractions of 50% or 1%, respectively. The specified concentrations can be modified, if warranted, to reflect definitive determinations from any specific site.

3.6.3.2 Coastal Plain Aquifer Host Rock - Oxidizing Conditions

Many potable water aquifers are unconfined, in which case continuous recharge with oxygenated water may eventually lead to oxidation of residual organic matter and secondary sulfides, such as pyrite and sulfides containing hazardous inorganic constituents. Furthermore, any ferrous iron present in detrital and secondary clays would also be oxidized to the ferric state, although not necessarily with any modification to their stability or crystal structure (Fialips et al., 2002). The recharge of aquifers by oxygenated groundwaters is a common phenomenon, leading on occasion to the formation of a migrating redox front (McMahon and Chapelle, 2008). Pervasive *in situ* oxidation can occur when penetration is rapid, particularly in response to anthropogenic extraction of potable water (Thornberg and Sahai 2004) or injection for the purpose of aquifer storage and recovery (ASR) (Arthur et al., 2005). Such oxygenation can lead to the mobilization of heavy metals, particularly As, Cd, Pb and U, with adverse consequences to water quality. In fact, oxidative dissolution may result in a higher degree of heavy-metal dissolution than a decrease in pH due to CO_2 intrusion. In fact, the oxidative dissolution can lead, under arid conditions, to the almost quantitative solubilization of all As present, as the natural abundance of As in many rocks, if partitioned completely into the groundwater, would be insufficient to achieve saturation with respect to any arsenate minerals after all Pb present has been co-precipitated as mimetite.

As discussed in Section 3.4, the mineral host limiting Pb concentration in solution under oxidizing conditions would be cerussite, which would lead to equilibrium Pb concentrations approximately four orders of magnitude greater that under reducing conditions, where galena is likely to coexist with pyrite. Because of the likelihood of greatly enhanced solubility of cerussite in the presence of elevated CO_2 partial pressures, it is considered important to conduct one simulation case evaluating the potential behavior of an oxidized aquifer affected by CO_2 intrusion.

Table 3.24 contains a listing of a modified mineralogy of a representative Coast Plain Aquifer host rock, where all minerals likely to buffer the redox state under reducing conditions have been eliminated, and only cerussite is present as hazardous inorganic host mineral.

3.6.3.3 St Peter Sandstone

The principal arenaceous aquifer rocks of Segments 9 and 10, e.g., the St Peter Sandstone, are reworked sands associated with a relatively stable cratonic environment, virtually devoid of residual feldspathic or lithic fragments and containing only a very small percentage of clay matrix. They therefore fall near or within the classification of quartz arenite (Figure 3.53). Because of their limited buffer capacity, extensive distribution, and the fact that they overlie much of the Illinois Basin, which is a likely candidate for the storage of CO_2 in deep underlying saline aquifers, it was decided that a representative mineralogy for the St Peter's Sandstone should be formulated for the reactive transport modeling purposes. Mineralogical data, cited in the literature for St Peter Sandstone in Illinois (Thiel, 1935; Odom et al., 1977; Hoholick, 1980; Hoholick et al., 1984; Barnes et al., 1992; Girard and Barnes, 1995; Pitman et al., 1997) were used to develop the representative mineralogical composition as listed in Table 3.24. Noteworthy is the addition of dolomite to the carbonate mineralogy. Otherwise, the minerals present are similar, but in significantly differing proportions to those of the Coastal Plain Aquifer. The framework mineralogy selected for St Peter Sandstone falls within the pure arenite field, as indicated by the diamond symbol in Figure 3.53. The matrix mineralogy consisting of carbonates, clays, goethite, pyrite and kerogen, in total, comprise only 2 wt.% of the rock, of which clays constitute about 1 wt.%. The specific mineral hosts for the hazardous inorganic constituents were retained with the concentrations as those specified in Section 3.6.1.2.

3.6.3.4 Dolomitic Limestone

Wang and Jaffe (2004) pointed to the fact that the presence of carbonates tends to buffer the pH of the groundwater, even in the presence of elevated CO_2 partial pressures up to 10 bars. However, even though most arenaceous aquifers contain traces to minor concentrations of carbonates (principally calcite), the continuous ingress of CO_2, leaking from an underlying storage reservoir, could eventually dissolve all the calcite in the vicinity of the point of ingress. With the buffering capacity gone, the pH would fall and further enhance the solubility of minerals containing hazardous inorganic constituents as essential components.

Many potable groundwaters are drawn from aquifers consisting predominantly of limestones, some quite shaley or dolomitic, especially in regions aligned with the west flanks of the Appalachians and the Cumberland Plateau of Tennessee, such as the upper Knox Limestone. Representative dolomitic limestones contain up to 20 wt.% dolomite. In our study, the mineralogy of an impure dolomitic limestone was formulated to represent the extreme case where complete dissolution due to (even long-term) ingress of CO_2 would be implausible. The clay composition of the dolomitic limestone differs significantly from those of the other rocks specified for study, not only in quantity, but also in kind. Of the total clay concentration of 16 wt.%, 7 wt.% is illite and 5wt.% is kaolinite, chlorite and smectite making up the balance in equal proportions. The clay mineralogy is dictated partly by the diagenetic history of dolomitic limestone, where it is assumed that both dolomitization and illitization of smectitic clays were the result of thermogenic processes caused by deep burial. The contrasting clay mineralogy impacts the adsorption of hazardous constituents, as adsorption sites on illite differ from those of smectite in magnitude and character, which is demonstrated in Section 4.7.2. This mineralogy is given in Table 3.24. The specific mineral hosts for the hazardous inorganic constituents were retained with the concentrations of those specified in Section 3.6.2.2.

Table 3.24. Representative mineralogies of aquifer host rocks used in reactive chemical transport simulations

				Coastal Plain Aquifer (Arenite) Reducing Env.		St Peter Sandstone		Dolomitic Limestone		Coastal Plain Aquifer (Arenite) Oxidizing Env.	
Mineral	Element	gfw	V, cm^3/mol	Wt. %	Vol Fraction	Wt. %	Vol Fraction	Wt. %	Vol Fraction	Wt. %	Vol Fraction
Quartz		60.084	22.688	80.165	0.77666	92.756209	0.926778	5.009065	0.05144173	79.28271411	0.79592773
K-feldspar		278.33	108.87	6.165	0.06187	4.881906	0.0505281	0.000000	0.00000000	6.097148787	0.06340635
Oligoclase		1327.094	502.477	6.175	0.09998	0.244095	0.00244551	0.000000	0.00000000	6.107038728	0.06147562
Kaolinite		258.159	99.52	1.72	0.01701	0.097638	0.00099595	5.009065	0.05251716	1.701069897	0.01743424
Smectite-Ca		365.394	132.51	1.46	0.01358	0.244095	0.0023423	2.003626	0.01976175	1.443931424	0.01392168
Illite		383.899	138.94	3.07	0.0285	0.390552	0.00374012	7.012692	0.0690266	3.036211967	0.02921461
Chlorite		634.653	210.26	1.25	0.0106	0.195276	0.00171185	2.003626	0.01805338	0.000000000	0.000000000
Kerogen-OS		1881.97	1738.37	0.1125	0.002666	0.097638	0.00238641	1.001813	0.02516736	0.000000000	0.000000000
Pyrite		119.977	23.94	1	0.00512	0.097638	0.00051551	0.500907	0.00271834	0.000000000	0.000000000
Dolomite		184.40	64.365	0.000000	0.000	0.488191	0.00450893	15.027196	0.14265542	0.000000000	0.000000000
Calcite		100.087	36.934	1.6	0.01514	0.097638	0.00095337	60.108785	0.60326492	0.988994126	0.00970287
Goethite		88.852	20.82	1	0.0601	0.097638	0.00060538	2.003626	0.01276885	0.988994126	0.0061612
Apatite	P	502.31	158.957	0.270287	0.0021945	0.263904	0.00220978	0.270778	0.00233047	0.267313153	0.00224898
Barite	Ba	233.39	52.1	0.08496	0.00048944	0.027654	0.00016334	0.028374	0.00017227	0.084032816	0.00049873
Arsenopyrite	As	162.83	26.272	0.002100	9.0484E-06	0.002122	9.0594E-06	0.002177	9.5542E-06	0.000000000	0.000000000
Greenockite	Cd	144.48	26.42	0.000621	3.0327E-06	0.000628	3.0363E-06	0.000644	3.2022E-06	0.000000000	0.000000000
Cinnabar	Hg	232.66	28.416	0.000004	1.4622E-08	0.000005	1.4640E-08	0.000005	1.5439E-08	0.000000000	0.000000000
Galena	Pb	239.27	31.49	0.002232	7.8433E-06	0.002255	7.8529E-06	0.002314	8.2817E-06	0.000000000	0.000000000
Cerussite	Pb	267.21	31.49	0.000000	0.00000000	0.000000	0.00000000	0.000000	0.00000000	0.00255086	7.9922E-06
Gudmundite	Sb	121.75	73.352	0.000024	3.8866E-07	0.000068	3.8913E-07	0.000070	4.1038E-07	0.000000000	0.000000000
Tiemannite	Se	213.77	30.003	0.000033	1.2256E-07	0.000033	1.2271E-07	0.000034	1.2941E-07	0.000000000	0.000000000
Uraninite	U	270.03	24.616	0.000329	8.0056E-07	0.000332	8.0154E-07	0.000341	8.4531E-07	0.000000000	0.000000000
Sphalerite	Zn	96.98	23.83	0.014335	9.4066E-05	0.014485	9.418E-05	0.014862	9.9324E-05	0.000000000	0.000000000
Total	-	-	-	100.	1	100	1	100	1	100	1

3.7 Summary Results and Implications for Reactive Transport Model of CO_2 Intrusion

Section 3 of this report covers the development of necessary input for the reactive chemical transport simulations of high-pressure CO_2 intrusion into shallow potable water aquifers, which are described in Section 4. A comprehensive geochemical model was developed representing typical conditions in many freshwater aquifers in the United States. An important step in developing this geochemical model was to use a distribution-of-species code, EQ3/6, for the evaluation of the thermodynamic controls influencing the initial aqueous concentration and CO_2-related mobilization of selected hazardous inorganic constituents. By evaluating the chemical analyses of more than 38,000 groundwaters from the USGS NWIS database, minerals hosts were identified containing one or more of the hazardous constituents, either as essential components or in solid solution. These hosts, upon equilibration with groundwater, are able to assume partial or complete control of the aqueous trace-metal concentrations and their changes upon ingress of CO_2, depending on the nature of the mineralogy of the aquifer host rock. A representative trace-element mineralogy was developed for the solubility-controlling minerals identified above, including their expected (typically very small) concentrations in the aquifer solid phase, and was subsequently used for the reactive transport model in Section 4.

Identification of thermodynamic controls necessitated the development and testing of a large supporting thermodynamic database comprising the solubility products of minerals of interest, and of complexes that could affect the concentrations of the hazardous constituents in aqueous solution. In addition, the bulk mineralogy of the aquifer host rocks also had to be specified, which was accomplished through review of the scientific literature. The bulk mineralogy was combined with the trace element mineralogy involving the hazardous inorganic constituents, whose abundance were defined in terms of the natural abundances of the hazardous constituents in soils and sediments in the United States. The integrated mineralogy was normalized in terms of molar volume fractions and passed through for TOUGHREACT simulations described in Section 4. In addition, thermodynamic data, in the form of mineral solubility products and

aqueous complex dissociation constants used in the database of EQ3/6, were also passed through and formatted for the corresponding TOUGHREACT database.

Prior to the complex reactive-transport modeling in Section 4, a preliminary assessment of CO_2-related water quality changes was conducted by calculating the expected equilibrium concentrations of hazardous inorganic constituents as a function of the partial pressure of CO_2 in water with a typical potable groundwater composition, defined based on the above geochemical evaluation. Results indicate that the concentrations of some of the constituents are quite sensitive to changes in $P(CO_2)$, whereas others remain relatively unaffected. This assessment was used in Section 4 to focus the reactive transport simulations on those constituents that have the clear potential to exceed maximum contaminant levels through imposition of elevated partial pressures of CO_2.

The foregoing paragraphs cannot do justice in summarizing the many tasks that formed part of the overall geochemical evaluation in Section 3. Nor can they touch on the assumptions, approximations, and compromises that were necessary to bring such a complex study to fruition in the time available. In the following paragraphs, we summarize in greater detail the several tasks accomplished in Section 3 of this report, and indicate further steps that would be desirable in refining the geochemical modeling with the objective of quantifying and decreasing current uncertainties. These tasks are described in the following order: (1) literature review providing preliminary identification of thermodynamic controls for hazardous inorganic constituents, (2) review and modification of an extensive thermodynamic database for relevant minerals and aqueous species and site complexation constants, (3) evaluation of more than 38,000 groundwater quality analyses from potable water aquifers throughout the United States, with final specification of solubility-controlling minerals for hazardous inorganic constituents, (4) evaluation of the natural abundances of these hazardous constituents in sedimentary formations hosting potable water, (5) determination of typical aquifer host-rock mineralogies, and (6) calculation of equilibrium concentrations as a function of partial pressure of CO_2.

(1) Preliminary Assessment of Solubility-Controlling Minerals via Literature Review

Thermodynamic equilibrium of a given hazardous inorganic constituent can be established between the aqueous phase and (a) adsorption sites on mineral surfaces (e.g., iron oxides, silicates, sulfides, carbonates, etc.), (b) on functional groups on organic matter, (c) by ion exchange sites in clays, zeolites, etc., (d) in solid solution in primary and secondary minerals, and (e) in discrete minerals where the element in question is an essential component. Because of the extremely low solubilities of many of the minerals falling under Category (d) and (e), such minerals are most likely to act as the primary thermodynamic controls determining the concentrations of the constituents in groundwaters. Not many studies are reported in the literature that would help identify such solubility-controlling minerals for the relevant hazardous constituents and the range of geochemical conditions observed in United States aquifers. We therefore based our initial assessment of possible minerals controlling aqueous concentrations in groundwater on the extensive literature describing the mineralogy of coals and marine sediments (Section 3.2). (For the final assessment, we conducted a rigorous thermodynamic evaluation of more than 38,000 groundwater analyses from potable aquifers throughout the United States, using the distribution-of-species code, EQ3/6.)

Because coal is burned, and hazardous inorganic constituents can be released in volatile or particulate form to the atmosphere, there is considerable interest in the mode of occurrence of such constituents, and several quite elaborate studies have been undertaken over the past 40 years to establish where and how they are distributed in coal. (Although coal can hardly be considered representative of aquifer host rocks, its component parts, which crudely classify the potential host materials listed above, are found in both, although their respective mass fractions differ greatly.) The chemistry of each component has been determined through application of a sequential procedure using progressively more aggressive lixiviants, supplemented by suitable analytical and diagnostic procedures to characterize the elemental and mineralogical composition together with microscopic techniques. A limited number of similar studies have also been undertaken to examine the sedimentology of surficial marine sediments during authigenesis, the goal being to determine the immobilization of heavy metals through reduction and co-

precipitation with pyrite. Finally, the descriptive literature on the metallography of polymetallic ore deposits is a helpful adjunct in identifying anticipated phase and solid solution relationships among ore minerals, especially those most likely to form in minute and usually undetectable concentrations in potable water aquifers.

Based on the literature review, a list of potential mineral hosts was generated for the selected hazardous inorganic constituents and average geochemical conditions. This list was used as a suitable starting point for the rigorous thermodynamic evaluation conducted in a second step (see Task (3) below).

(2) Modification and Augmentation of Thermodynamic Data

The geochemical models used in the current study require solubility products of solid phases and dissociation constants for complexes. Both parameters are defined by equations relating the solid phases or complex to basis species in solution. The respective solubility products and complex dissociation constants can be calculated as a function of temperature and pressure, provided that sufficient thermodynamic parameters are available. To ensure a realistic thermodynamic description of the complete geochemical system, we reviewed the available literature and, if necessary, revised and augmented the thermodynamic databases associated with EQ3/6, the distributions-of-species code, and TOUGHREACT, the reactive transport simulator. This process was conducted for the hazardous inorganic constituents, as well as for a variety of additional rock forming and accessory minerals (Section 3.4.2).

In many cases, changes to the existing thermodynamic databases for EQ3/6 and TOUGHREACT were necessary not only to ensure that the geochemical model realistically represented aquifer conditions, but also to eliminate obsolete and/or erroneous data. Most importantly, several significant errors and omissions were discovered that entailed a complete revision of mineral solubility and aqueous sulfide and selenide complexation data for Cd, Hg, Pb and Zn. The revision was undertaken in an expedient, though not completely rigorous manner. The raw data from a substantial number of refereed papers related to sulfide and selenide mineral solubilities will eventually require a complete re-analysis to meet archival standards. Such a re-analysis,

however, is not expected to significantly impact the findings in this report. All changes and revisions in the thermodynamic databases are described in great detail in Appendix C.

For many of the minerals and some of the aqueous species, the SUPCRT92 code was used to calculate solubility products and complex dissociation constants as a function of pressure and temperature from given thermodynamic parameters. However, some constants were also taken directly from the literature, most of which were specified at 25ºC and 1 atmosphere pressure. Because of the magnitude of the task in compiling data for all the constituents under study, certain approximations and assumptions were made as documented in Appendices C, D, and E, which could introduce minor inconsistencies. These inconsistencies are believed to be small, and well within the overall uncertainty of the model.

The modified and augmented thermodynamic database was used in Section 3.4.5 to evaluate the groundwater quality data from the NWIS database and to identify minerals that control the activities of the selected hazardous constituents (see summary below). It was observed that some solubility-controlling minerals exhibited moderate discrepancies between the ideal saturation index value of zero and the calculated modes of the 38,000 chemical analyses. This closing error between the actual field observation and the thermodynamic model prediction was reconciled by further adjusting the log K values of the dissolution constants so that the calculated mode for each hazardous constituent was shifted to zero (Section 3.5.2). This was done in both the EQ3/6 and the TOUGHREACT databases prior to modeling the geochemical impact of CO_2 intrusion. In other words, a geochemical model calibrated to the NWIS groundwater analyses was used for the equilibrium calculations conducted in Section 3.5 as well as for the reactive transport simulations conducted in Section 4.

(3) Evaluation of Groundwater Quality Data from the NWIS Database and Identification of Thermodynamic Controls

Over 38,000 groundwater analyses were retrieved from the NWIS database, with the main objective of identifying thermodynamic controls that govern the concentrations of hazardous inorganic constituents in groundwaters. Prior to conducting the geochemical calculations using

the distribution-of-species code, EQ3/6, the concentration distributions of these constituents were examined for artifacts caused by the use of insufficiently sensitive analytical methods. In some cases, these resulted in spurious distributions in concentrations of elements whose ambient concentrations were near or at the limits of detectability. This applied in particular to Cd, Pb, Sb, and possibly Hg. The analytical methods and their ability to measure constituent concentrations in groundwaters are listed in Appendix A. A discussion of the analytical artifacts introduced by the use of insufficiently sensitive analytical methods is given in Appendix B2.

A preliminary examination of all water quality analyses was also conducted to assess analytical integrity. This examination showed that the majority of analyses possessed charge imbalances that were comparably large according to recognized standards. Although the principal cause could be attributed to inadequate custodial handling, leading to sample CO_2 degassing and probable precipitation of carbonate, no single correction method could be identified that would eliminate these errors without introducing others. Therefore all analyses were used in subsequent geochemical evaluations, but with due consideration being paid to the limitations of the data.

A major challenge with the evaluation of the water quality analyses was finding a way to define the redox state of the groundwaters, given the absence of reliable field measurements for this parameter. Two approaches were taken: (1) Eh was calculated based on the Fe(III)/Fe(II) couple at a given pH, using analytical data for dissolved iron together with the assumption that the groundwater was saturated with respect to goethite, and (2) Eh was defined at a given pH by the pyrite/goethite buffer. Two sets of runs were conducted with EQ3/6, in which the more than 38,000 analyses were speciated assuming the calculated Eh. The calculated saturation indices were the examined with respect to all those minerals containing a hazardous constituent as an essential component. Runs were conducted at 25ºC and 1 atmosphere pressure rather than at ambient temperatures (which were probably lower), because the NWIS data did not report the ambient temperature and because some of the thermodynamic data used in the databases of the code was specified only at 25ºC. This assumption introduces an uncertainty in the results, which is smaller than the overall uncertainty associated with the water quality analyses and smaller than the natural variability in the large population of groundwaters studied.

Several iterative refinements and augmentations to the thermodynamic data were made in successive runs, during which obvious errors were identified and tracked down. In total, approximately one million species distributions were made. The results of the analysis turned out to be in good agreement with the data, giving a strong indication that the model assumptions are robust. Solubility-controlling minerals were identified with reasonable confidence where the predicted saturation indices of many of the candidate host minerals were close to or at zero, and the identified minerals correlated well with the limited quantity of information regarding their occurrence in the field, especially with respect to the coal data. Results were also consistent with the detectability of the hazardous constituents in groundwaters as determined by the analytical method used and its sensitivity.

Perhaps the most important observation stemming from the analysis using two methods of independently computing the groundwater Eh was that average mineral solubilities were consistent with conditions close to or defined by the pyrite/goethite buffer, thereby indirectly substantiating the argument that the majority of groundwaters comprising the data set examined are moderately to strongly reducing. Only a small number of analyses, such as those consistent with cerussite saturation, are indicative of more oxidizing conditions. The information derived from the database analysis also showed that the average pH of all groundwaters was about 7.6, and that the calculated average ambient Log $P(CO_2)$ was about –2.5, one unit higher than that of the atmosphere, and that most aquifers tested were saturated with respect to calcite.

For a representative groundwater at reducing conditions, the most likely mineral hosts controlling the concentration of the hazardous inorganic constituents studied are as follows. Arsenic is present as the arsenopyrite component in solid solution in pyrite. Ba is saturated with respect to barite. Cd is either in solid solution in sphalerite and/or is present as greenockite or cadmoselite. Hg is present as cinnabar and possibly as tiemannite, but its presence in solid solution in pyrite, perhaps in minor amounts, cannot be ruled out. Pb is present as galena, and/or possibly as clausthalite. Sb is present as the gudmundite component in solid solution in pyrite, and probably as kermesite, especially in neutral to acid conditions. Se could be present as either clausthalite, tiemannite, or cadmoselite. U is present as uraninite and/or coffinite. and zinc is

present as sphalerite and/or hemimorphite. Some of the uncertainty associated with the specific identification of one particular mineral can be attributed to variations in the redox potential and pH between aquifers (owing to the presence of differing redox buffers from the standard), variations in the absolute abundances of the hazardous constituents in the aquifer host rocks, and the fact that the Gibbs Phase Rule with zero degrees of freedom at the specified pressure and temperature would not be violated in some cases were both cited minerals to be present.

The mean saturation indices of some of the mineral hosts, identified as controlling the concentrations of certain hazardous inorganic constituents, deviate positively from zero. Examples include uraninite and coffinite for uranium, and sphalerite and/or hemimorphite or zinc. Such deviations could be caused by any of a number of reasons relating to the thermodynamic properties of the participating solid phases and aqueous species in solution, to systematic deviations in the calculated redox potential, or to differences between the reference temperature and mean formation temperature. Further targeted investigations are warranted to identify the underlying causes of the saturation differences between calculated and field measurements (as defined by the saturation index), and to decrease ambiguity in a few cases. Where the mean saturation indices of some of the mineral hosts deviate negatively from zero, it is likely that a solid solution may exist in another mineral host. For example, arsenopyrite, gudmundite, or dzarkenite (ferroselite) components can represent As, Sb, and Se substitution in pyrite. The geochemical model does not currently account for such solid solutions, and therefore the magnitude of such occupancies cannot be directly calculated. Therefore, approximations were made in the current study to offset the omission of a solid solution model for arsenopyrite and gudmundite. Future model refinements would enhance the overall accuracy of geochemical simulations.

The dispersion revealed in the saturation index histograms for the minerals displayed in Section 3.4.4, 3.4.5, and 3.4.6 are a measure of the total uncertainty and variability of the analyzed systems. Uncertainties in geochemical model parameters, as well as the natural variations expected in groundwaters of differing provenances, contribute to this dispersion. A systematic examination of the uncertainties of each parameter, and their impact on the overall dispersion of

specific mineral saturation indices, is feasible but time consuming. Such an analysis would provide much insight as to what extent each parameter contributes to geochemical model uncertainty. The evaluation presented in this report can therefore be a point of departure for the study of general issues relating to the validity of geochemical models in both a scientific and regulatory environment.

We emphasize that the approach of determining thermodynamic controls chosen in this study is an indirect one; it does not provide a direct confirmation of the existence of the minerals hosting the inorganic constituents. Direct confirmation is achievable only through verification of their presence through mineralogical, spectroscopic, or separation procedures. Such procedures are extremely challenging, because the quantities present are minute, and particle sizes may be extremely small. We recommend conducting such procedures in future site-specific studies to demonstrate the validity of the general geochemical model developed here.

(4) Natural Abundances of the Trace Elements of Interest

The reactive transport model utilized in Section 4 requires specification of the volumetric fractions of the solubility-controlling mineral hosts for hazardous inorganic constituents identified above. It is important that the specified concentrations of these hazardous constituents in the aquifer host rocks are representative of those found in the United States. A search of the literature showed that such information was not generally available, and therefore use was made of the National Geochemistry Database giving average elemental abundances in surficial soils and sediments in the United States, to act as a proxy for abundances in aquifer host rocks. Several alternative analytical methods were used in the compilation of the National Geochemistry Database, each having differing detection levels and characteristics. Average values were selected from among those different analytical methods deemed most representative. A comparison was also made between the selected average concentrations and the average crustal abundances of those same elements reported in the literature, and it was found that they were for the most part comparable. Average abundances of hazardous inorganic constituents ranged from $< 10^{-7}$ for Hg to $>10^{-4}$ for Ba (Section 3.6.2.2). While the above abundances are very small compared to the major minerals, all hazardous constituents targeted for study in this report

occur ubiquitously in soils, sediments, and aquifer rocks throughout the world, indicating that the problem of mobilization of these constituents in response to CO_2 intrusion can be a widespread one in United States aquifers (Section 3.3.2).

(5) Typical Aquifer Host Rock Mineralogies

The mineralogy of the host rock of a potable water aquifer can have a significant influence on the water quality, and similarly impact the nature of compositional changes due to the ingress of high pressure CO_2. In this report, one goal was to characterize the mineralogies of a selected group of host rocks that would be considered representative of the majority of confined and unconfined potable water aquifers in the United States. Another consideration was that the selected aquifers should also be those most likely to be affected by intruding CO_2 from deep saline storage reservoirs. At the outset of the study, it was presumed that the mineralogies of candidate aquifers would be sufficiently well characterized that the appropriate information need only be lifted from suitable literature sources. It turned out that such information is not widely available, nor is it of sufficient quality or detail to be used for the simulations contemplated in this study. Representative mineralogies therefore were created using standard sedimentological classifications, and these were augmented with the trace quantities of the minerals identified as being at equilibrium with the selected hazardous inorganic constituents in the NWIS groundwaters (Section 3.6). The specification of different mineralogical compositions was facilitated by the utilization of Excel™ spreadsheets. If necessary, site-specific mineralogies can be entered and suitable inputs for the TOUGHREACT or other simulators generated to suit specific needs.

The created mineralogical assemblages, when contacted by the aqueous phase, are not necessarily able to come to equilibrium without progressive destruction of one or more minerals, because the mineralogy is commonly overspecified, and the Gibbs phases rule is violated. However, this condition is also typical of real sedimentary assemblages and is characteristically responsible for observed authigenic and diagenetic processes. Therefore, the modeled groundwater composition generated after attempting a simulated equilibration in reactive transport modeling invariably represents a quasi- rather than true equilibrium state. Despite this

limitation, the simulated groundwater composition with specified initial concentrations of conservative components, such as chloride ion and Cl^-, should fall within the range of groundwater compositions downloaded from the NWIS database (see Section 4.4).

(6) Concentrations of Hazardous Inorganic Constituents as a Function of $P(CO_2)$

A preliminary assessment was made of how the partial pressure of CO_2 affected the equilibrium concentrations of hazardous inorganic constituents in water with a typical potable groundwater composition, assuming reducing conditions defined by the pyrite/goethite buffer (Section 3.5). The assessment incorporated both sulfide and selenide complexing of chalcophilic elements. Log $P(CO_2)$ was varied between –4 and +1, leading to a corresponding pH variation between 8.9 and 5.6. Of the nine hazardous constituents studied, only As, and to a lesser extent Pb and Zn, are of have the potential for exceeding maximum contaminant levels at elevated $P(CO_2)$. In Section 4 of this report, primary emphasis is placed on the evaluation of the response and transport of As and Pb under intruding CO_2.

4. Systematic Geochemical Modeling

This section describes a systematic modeling study conducted with a reactive transport simulator to quantify the effect of CO_2 intrusion into a shallow aquifer. The goal was to determine the potential amount of hazardous constituents that can be mobilized by the ingress of CO_2, to predict the fate and migration of these constituents in the groundwater, and to evaluate the likelihood that drinking water standards might be exceeded. A variety of scenarios and aquifer conditions was considered in a sensitivity evaluation. These scenarios and conditions, in particular those describing the geochemistry and mineralogy of potable aquifers, have been selected based on the geochemical model definition described in the previous section.

4.1 TOUGHREACT Simulator

We conduct our geochemical modeling with TOUGHREACT, a simulation program for nonisothermal multiphase reactive transport in variably saturated media (Xu et al., 2006). TOUGHREACT has been widely applied to many geologic systems and environmental problems, including geothermal systems, diagenetic/weathering processes, subsurface waste disposal, acid mine drainage remediation, contaminant transport, and CO_2 geologic storage (e.g., Xu et al., 2005). The simulator was developed by introducing reactive chemistry into the existing framework of a nonisothermal, multiphase, multicomponent fluid and heat flow code (Pruess et al., 1999).

TOUGHREACT considers a wide range of thermo-physical-chemical conditions of pressure, temperature, water saturation, ionic strength, pH, and Eh. The major processes for fluid and heat flow are: (1) fluid flow in liquid and gas phases under pressure, viscous, and gravity forces, (2) interactions between flowing phases represented by characteristic curves (relative permeability and capillary pressure), (3) heat transfer by conduction and convection, and (4) diffusion of water vapor and noncondensable gases. Transport of aqueous and gaseous species by advection and diffusion is considered in both liquid and gas phases (Xu et al., 2005; 2006).

A specific fluid property module within TOUGHREACT for CO_2 sequestration includes a comprehensive description of the thermodynamics and thermophysical properties of a H_2O–NaCl -CO_2 system. Flow processes can be modeled isothermally (as done in this study) or nonisothermally, and phase conditions may include a single (aqueous or CO_2-rich) phase, as well as two-phase mixtures. Depending on the temperature-pressure conditions, CO_2 may be in supercritical or gaseous form. Aqueous chemical complexation and gas (CO_2) dissolution/exsolution are assumed to be at local equilibrium. For the conditions assumed in this study, the intrusion of gaseous CO_2 into a freshwater aquifer is modeled as a two-phase flow system, with dissolution of CO_2 into water occurring instantaneously until equilibrium concentration is reached. Excess CO_2 migrates within the aquifer, driven mainly by buoyancy forces.

The geochemical model implemented in TOUGHREACT considers a variety of equilibrium and kinetic chemical reactions (Xu et al., 2005; 2006). Aqueous complexation, acid-base, redox, and cation exchange are considered under equilibrium assumptions. The activity of aqueous species is equal to the product of the activity coefficient and the molal concentration. Aqueous species activity coefficients with the exception of CO_2(aq) are calculated from the extended Debye-Hückel equation (Helgeson et al., 1981). The CO_2(aq) activity and CO_2(gas) fugacity coefficients are determined as functions of pressure, temperature, and salinity, with details given in Xu et al. (2004). The thermodynamic data incorporated in TOUGHREACT have been derived from a comprehensive review of the published literature. Originally based on the equilibrium constants for aqueous species and minerals given in the EQ3/6 V7.2b database (Wolery, 1992), many substitutions and changes to this data base have been incorporated into TOUGHREACT over the years in response to revised or improved information on the given thermodynamic properties (Xu et al., 2005, 2006). In addition to these changes, Xu et al. (2005) have incorporatedthe thermodynamic properties of several phases relevant to geologic sequestration of CO_2, among these various carbonate phases. Mineral dissolution and precipitation can be modeled in TOUGHREACT, subject to either local equilibrium or kinetic conditions. For kinetically controlled mineral dissolution and precipitation, a general form of rate law is used, based on that used by Steefel and Lasaga (1994). The TOUGHREACT version with the geochemical model

described in Xu et al. (2005; 2006) was the starting point for the modeling studies performed in this study. However, further modifications were made, as briefly summarized below.

4.1.1 Thermodynamic Data and Kinetic Data

Because of the unusual requirements of the current study, the thermodynamic data incorporated within the TOUGHREACT version described in Xu et al. (2005; 2006) are insufficient for adequately modeling the complex chemistry associated with the behavior of hazardous inorganic constituents in groundwaters. Therefore, the available literature was reviewed and the database used for the reactive transport simulation has been significantly modified and, if necessary, the thermodynamic database in TOUGHREACT was revised and augmented within this study, as described in Section 3.4.2 and Appendix C. Specific consideration was given to the thermodynamic data of the metal sulfide minerals and aqueous complexes (see Appendix D for details), as well as metal selenide minerals and aqueous complexes (see Appendix E). Further modification of thermodynamic parameters was necessary to reconcile differences between the measured and predicted solubility controls in the more than 38,000 groundwater analyses from the NWIS database. The modifications made to "calibrate" the geochemical model are described in Section 3.5.1.

Mineral dissolution and precipitation rates are a product of the kinetic-rate constant and the reactive surface area (Xu et al., 2006). Mineral reactive surface areas (except those for illite, kaolinite, smectite and goethite) used in this study are taken from Xu et al. (2006, 2007), which are based on the work of Sonnenthal et al. (2005). The values developed in Xu et al. (2006, 2007) are typically two orders of magnitude smaller than measured surface areas based on surface roughness evaluation, because only part of the total mineral surface is involved in the chemical reaction, due to coatings, reduced exposure to the aqueous phase, and channeling of reactive flow. The reactive surface areas of illite, kaolinite, smectite and goethite are taken from published BET surface areas (Bradbury and Baeyens, 2005; Gu and Evans, 2007; Lackovic et al., 2003; Muller and Sigg, 1991) in conformity with the surface area used for surface complexation reaction involved in adsorption/desorption. Kinetic rate parameters for most minerals are taken from Xu et al. (2006, 2007), which are based on work by Palandri and Kharaka (2004), with the

exception of galena and arsenopyrite. Kinetic rate parameters for galena are taken from Zhang et al. (2003). Those for arsenopyrite are assumed to be the same as those for galena, based on their structural similarity. All parameters are given in Table 4.3 and other tables throughout Section 4 that detail the basic mineralogies used in the simulations. The impact of uncertainy in the kinetic rate parameters has been evaluated in a sensitivity analysis (Section 4.6.2).

4.1.2 Improved Adsorption Models

Adsorption via surface complexation has been widely studied (Dzombak and Morel, 1990; Lutzenkirchen, 2006) and is a key process with respect to the fate and transport of heavy metals (e.g., Bradl, 2004) or other hazardous constituents such as As (Goldberg, 2002; Goldberg et al., 2005; Manning and Goldberg, 1997). We have therefore incorporated into TOUGHREACT a model considering adsorption via surface complexation, using nonelectrostatic, constant capacity, and double layer models (Dzombak and Morel, 1990). The surface complexation model implemented in TOUGHREACT was verified by comparison with other codes such as PHREEQC (Parkhurst and Appelo, 1999) and CRUNCH (Steefel, 2001).

Adsorption of heavy metal (and As) ions on minerals is influenced by a variety of factors, the most important of which are pH, type, and speciation of metal ion involved, as well as competition among different ions (Bradl, 2004). In this study, we consider goethite, illite, kaolinite, and smectite as principal adsorbents, mainly because these minerals have strong adsorption capacities with respect to Pb and As**.** A literature analysis was conducted to determine relevant surface-complexation reactions and their thermodynamic constants for these cations and minerals, as summarized in Appendix F.

Usually, the surface complexation reaction is composed of the formation of outer-sphere and inner-sphere complexes. The formation of outer-sphere complexes is relatively rapid and usually treated as an equilibrium process, which is known as steady-state approximation (Selim and Amacher, 1996). The formation of inner-sphere complexes is relatively slow, and is often calculated by a kinetic law. If the formation of outer-sphere and inner-sphere complexes occurs sequentially, the overall rate is determined by the formation of the inner-sphere complexes; if the

formation of outer-sphere and inner-sphere complexes occurs in parallel reactions, the overall rate is determined by the formation of the outer-sphere complexes. Because in our model, the formation of outer-sphere complex and inner-sphere complex are treated as parallel reactions, all surface complexation reactions are treated as an equilibrium process. It is worth noting that the time range to attain equilibrium of sorption reactions is from seconds to days while that for mineral dissolution is from days to years or even thousands of years (Selim and Amacher, 1996). Therefore, considering the simulation period of interest in current study (100 year), it is safe to assume that sorption via surface complexation can be modeled as an equilibrium process, while mineral dissolution is kinetically controlled.

4.2 Model Setup

The basic model setup for most of the simulations presented here is depicted in Figure 4.1. The hydrogeological configuration considered is relatively simple. We consider a confined aquifer with a uniform vertical thickness of 10 m at a reference depth of 50 m. The simulation domain comprises an area of this aquifer 500 m in length and 200 m in width. Water flows from left to right with a flow velocity of 10 m per year (transport velocity). Hydrostatic pressure is assumed; i.e., the initial fluid pressure is 5 bar. Hydrogeologic properties, as given in Table 4.1, are homogeneous, isotropic, and constant over time. Carbon dioxide is assumed to migrate from a deeper geological storage site into the aquifer, representing, for example, local leakage through a fault zone. Specifics of these leakage conditions at depth are not important in the context of this study; only the rate of CO_2 leakage and the area over which it arrives at the freshwater resource are relevant. We assume in the base model a continuous CO_2 leakage rate of 7.5×10^{-5} kg/s, which corresponds to 2.36 tonnes per year, entering from below over an area of 100 m^2 (10 m × 10 m) at x = 105 m and y = 0 m.

With the intrusion of 2.36 tonnes per year of CO_2, a small, two-phase zone evolves where water and gaseous CO_2 coexist (see simulation results in Section 4.5). However, most of the gaseous CO_2 quickly dissolves into the groundwater. With time, the CO_2-charged groundwater flows downstream from the intrusion location, with the result that the acidity of the affected

groundwater increases, along with the potential for mobilizing hazardous inorganic constituents. The simplified model setup is represented, in most simulation cases, as a two-dimensional (2D) horizontal depth-averaged model. A sensitivity case simulating a fully three-dimensional (3D) setup is described in Section 4.9.

The potential rate of CO_2 leakage into an aquifer may vary widely in field situations. We have selected the above rate leakage rate of 7.5×10^{-5} kg/s, roughly based on the amount of CO_2 that can dissolve into the groundwater without forming a large two-phase zone of gaseous CO_2 and water. (The chosen leakage rate was based on a simple back-of-the-envelope analysis, using as input the volume of water affected in the aquifer at given flow velocity and the CO_2 solubility at given pressure and temperature conditions.) Excess CO_2 (i.e., gaseous CO_2 not dissolving into water) would likely migrate upwards and, in an unconfined aquifer, would escape into the vadose zone without further impacting groundwater quality. In a confined aquifer, which is the situation assumed in this study, excess CO_2 would accumulate under the confining layer, largely bypassed by the migrating groundwater. We have conducted sensitivity studies varying the CO_2 leakage rate, as described in Sections 4.6.9 and 4.9.3.

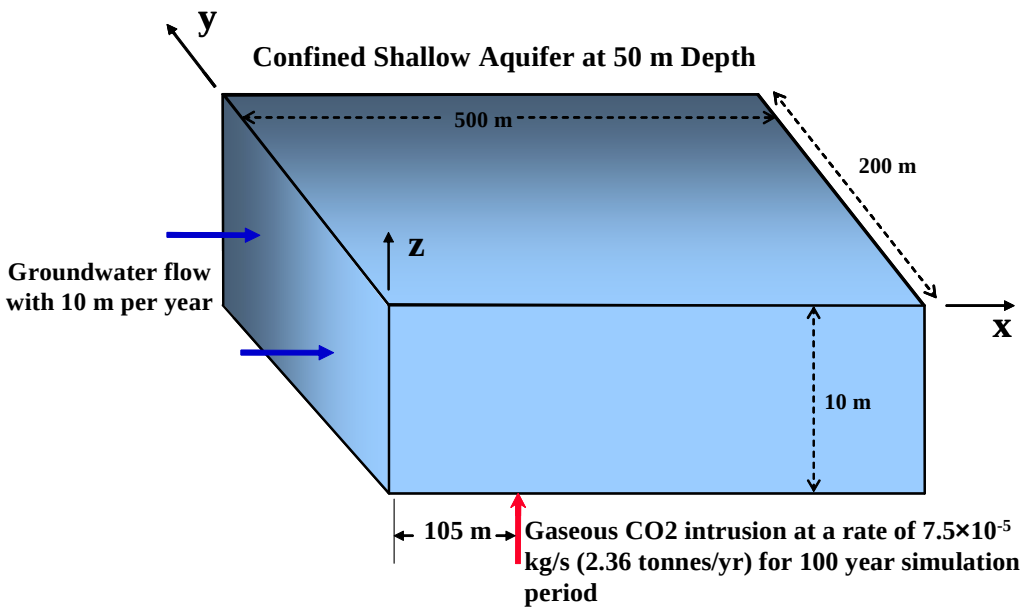

Fig. 4.1. Simplified model setup for initial geochemical model

Table 4.1. Hydrodynamic parameters

Porosity	0.3
Intrinsic permeability	1×10^{-12} m^2 (hydraulic conductivity of ≈ 0.86 m/day)
Relative permeability (van Genuchten-Mualem model)	$k_{rl}=\sqrt{S^*}\left\{1-\left(1-\left[S^*\right]^{1/0.457}\right)^{0.457}\right\}^2$ with $S^*=(S_l-0.3)/(1.0-0.3)$ where S_l is the liquid saturation degree
Gas relative permeability	$k_{rg}=\left(1-\hat{S}\right)^2\left(1-\hat{S}^2\right)$ with $\hat{S}=\left(S_l-0.3\right)/\left(1-0.3-0.05\right)$
Capillary pressure function	$P_{cap}=-\frac{1}{5.1\times10^{-5}}\left(\left[S^*\right]^{-1/0.457}-1\right)^{1-0.457}$ with $S^*=S_l/0.999$ and subject to restriction $-10^7\le P_{cap}\le 0$
Molecular diffusion coefficient	10^{-9} m^2/s

Due to its simplicity, the hydrogeological situation assumed in this study does not account for effects that may affect the system behavior in field situations. These effects include, for example, the impact of internal heterogeneity, which could lead to fast preferential transport in the aquifer, or the impact of vertical anisotropy in the aquifer's permeability (e.g., due to bedding), which could affect the vertical spreading of the CO_2 plume. We chose an idealized hydrogeological situation in this simulation study to bring out more clearly the geochemical changes in response to intrusion of CO_2 and to more easily interpret related sensitivities; in other words, we focused on a very complex geochemical system rather than a very complex hydrogeological system. It is understood that our simulations are idealized representations that can only serve as a guide to actual field behavior, which can vary strongly from place to place. As discussed in Section 6, we recommend conducting site-specific model predictions in future studies—ideally combined with adequately designed field experiments—where the local hydrogeological conditions would be represented in great detail.

In the base model, the background CO_2 partial pressure was set to 0.002 bar (which corresponds to a Log P(CO_2) value of -2.7). This is about one order of magnitude higher than CO_2 levels in the atmosphere, consistent with the fact that most groundwaters have elevated P(CO_2) levels due to the decay of organic matter. The selected background concentration of 0.002 bar falls into the range of values calculated from the database analysis described in Section 3.4.3 (Figure 3.17). Appelo and Postma (1994) report partial pressures of CO_2 dissolved in natural groundwaters ranging from 0.0002 bar to 0.01 bar, depending on the host-rock mineralogy. Background partial pressure of CO_2 in the groundwater may be important in the context of this study, because the higher initial P(CO_2) values would correlate to lower initial pH in the water, and thus the pH change would be less than expected with intrusion of CO_2. The initial CO_2 partial pressure furthermore impacts the initial distribution of Pb, Cd, and As in the aqueous phase or as adsorbed species. See Section 4.6.6 for a sensitivity study with respect to initial CO_2 concentration.

Note that the base model assumes reducing conditions with a redox potential of about -0.23 at pH around 7.6, defined by the coexistence of pyrite and goethite. The thermodynamic analysis of potable groundwater reported in Section 3.4 has demonstrated that the majority of groundwater samples represent waters from reducing environments. To evaluate the implications of oxidizing conditions, we conducted one simulation study with a redox potential of approximately +0.37 V (Section 4.8).

In this simulation study, we focus on the behavior of Pb and As as the hazardous constituents that may be mobilized by the intrusion of CO_2. Of the hazardous constituents studied in this report, the concentration of Ba, Cd, Sb, and Zn are also affected by the acidic conditions after CO_2 leakage (Section 3.5). Pb and As have been selected here because these two are most likely to exceed MCLs in potable waters as a result of CO_2 intrusion (see Section 3.5.)

The chemical reactions considered in this modeling study include aqueous complexation, mineral dissolution/precipitation, and adsorption/desorption via surface complexation, the latter considering goethite, illite, kaolinite, and smectite as principal adsorbents. Ion exchange is not explicitly considered, since earlier analysis suggested a less significant effect on the chemical evolution of As and Pb. Solid solutions are not explicitly considered, because the

TOUGHREACT simulator offers currently only a very simplified solid-solution model. Approximations are made in the current modeling work to offset the omission of an explicit solid solution model. As pointed out in Section 3.5, corrections were made to the solubility products of arsenopyrite and gudmundite to reflect the assumption that both As and Sb are likely to occur in solid solution in pyrite as FeAsS and FeSbS components. The magnitude of each correction was based on the calculated maximum SI frequency determined through the analysis of the more than 38,000 NWIS groundwaters given in Section 3.4.5.2.

4.3 Model Sequence and Sensitivity Cases

All simulations were performed using a two-step procedure. First, equilibrium runs were conducted with a specified mineralogical composition to establish the initial (steady state) chemical composition of the groundwater at equilibrium condition with minerals and adsorbed matter before the intrusion of CO_2 (see, for example, results described in Section 4.4). Second, reactive transport simulations were conducted for the hydrogeological environment shown in Figure 4.1, with the initial aqueous chemical composition obtained from the equilibrium run. CO_2 intrusion starts at time zero and continues for the entire simulation period of 100 years. In other words, it is assumed that the CO_2 leakage remains undetected and that no remedial measures are undertaken.

Various geochemical sensitivity cases are evaluated to (1) account for the wide range of conditions found in domestic potable aquifers and their host rocks, and (2) to encompass the uncertainty associated with geochemical processes and model parameters. In addition, we have varied certain hydrogeological aquifer conditions, such as the depth of the freshwater resource, the groundwater flow rate and CO_2 intrusion rates. We have also evaluated the fidelity of the 2D model by comparing the results to those of the 3D model.

Most of the sensitivity cases described in this report assume the basic mineralogy of a Coastal Plain Sandstone aquifer, as described in Section 3.6.3.1. This mineralogy is representative of an impure sandstone—with a composition consisting of mostly quartz plus some feldspar, lithic

fragments, and clays—expected to represent one of the more vulnerable aquifers, because the pH buffering capacity to CO_2 intrusion is limited. We describe in Section 4.4 the initial geochemical conditions derived for this type of aquifer and discuss how these conditions compare with the measured concentrations of major constituents in potable groundwater described in Section 3.3.2. We then provide the simulation results for CO_2 intrusion into a Coastal Plain Sandstone, starting with the base model (Section 4.5) and followed by various sensitivity cases (Section 4.6).

Table 4.2. Summary of sensitivity cases

Base Model	**Coastal Plain Sandstone Mineralogy**	**Section 4.5**
Geochemical Processes and Parameters	**Sensitivity to Adsorption**	**Section 4.6.1**
	Sensitivity to Kinetic Rate Parameters	**Section 4.6.2**
	Sensitivity to PbS(aq) Association Constant	**Section 4.6.3**
	Sensitivity to Mineral Solubility	**Section 4.6.4**
	Sensitivity to Initial Mineral Volume Fraction	**Section 4.6.5**
Model Setup, Initial and Boundary Conditions	**Sensitivity to Background CO_2 Concentration**	**Section 4.6.6**
	Sensitivity to Depth of Aquifer	**Section 4.6.7**
	Sensitivity to Groundwater Flow Rate	**Section 4.6.8**
	Sensitivity to CO_2 Leakage Rate	**Section 4.6.9**
Other Mineralogies	**St. Peter Sandstone Mineralogy**	**Section 4.7.1**
	Dolomitic Limestone Mineralogy	**Section 4.7.2**
Oxidizing Conditions	**Coastal Plain Sandstone Mineralogy**	**Section 4.8**
Dimensionality of Model	**3D Model**	**Section 4.9**

Returning to the base model setup, we report (in Section 4.7) simulations using other mineralogical compositions. These include two end-member cases: (a) one having the mineralogical characteristics of St Peter Sandstone, which is an almost pure arenite and expected to be most vulnerable to CO_2 intrusion, and (b) another having the mineralogy of a Dolomitic Limestone aquifer, where the pH is well buffered and expected to be less vulnerable to CO_2 intrusion. A modified mineralogy representing a Coastal Plain Sandstone in an oxidizing environment is used in Section 4.8. All specified mineral compositions contain trace amounts of

minerals containing hazardous metals or As as essential components, as detailed in Section 3.6.2.2. A complete list of all sensitivity cases is given below. Some other relevant factors and their potential importance are qualitatively discussed in Section 4.10.

4.4 Initial Geochemical Conditions for Base Model with Coastal Plain Sandstone

The base model simulates the groundwater disturbance by CO_2 intrusion into a Coastal Plain Sandstone aquifer, as described in Section 3.6.3.1. The base model setup, introduced in Section 4.2, assumes a two-dimensional depth-averaged model domain with homogeneous properties. Gaseous CO_2 intrudes from the bottom into the shallow, confined aquifer groundwater with groundwater flowing at 10 m per year. Reducing conditions are assumed.

The basic mineralogy of Coastal Plain Sandstone aquifer, including the hazardous-constituent-bearing minerals, is listed in Table 4.3. With respect to minerals containing hazardous substances, we consider galena (Pb), arsenopyrite solid solution (As), barite (Ba), greenockite (Cd), cinnabar (Hg), gudmundite solid solution (Sb), tiemannite (Se), uraninite (UO_2^{+2}), and sphalerite (Zn). However, in our current simulation study, we focus only on the evolution of Pb and As. The other listed hazardous constituents are included in the reactive transport simulations, but are not further reported here, because either their MCLs are not exceeded in reducing groundwaters, or they are believed to be insensitive to CO_2 intrusion (Section 3.5). The selection of these minerals, as well as their solubilities, is based on the thermodynamic evaluation conducted in Section 3.4.5 and is consistent with the equilibrium calculations conducted in Section 3.5. Notice the relatively small volume fraction of the hazardous-constituent-bearing minerals in Table 4.3, which is a realistic representation based on the review of trace element concentrations in soils and sediments given in Section 3.6.2.2.

Table 4.3 also gives the selected parameters for the rate law used for kinetically controlled mineral dissolution and precipiation. TOUGHREACT (Xu et al., 2006) uses a general form of

rate expression, which is based on transition state theory (TST) (Lasaga et al., 1994; Steefel and Lasaga, 1994):

$$r = kA\left[1-\left(Q/K\right)^{\theta}\right]^{\eta} \tag{4.1}$$

where r is the kinetic rate (positive values indicate dissolution, negative values indicate precipitation), k is the rate constant (moles per unit mineral surface area and unit time) which is temperature dependent, A is the specific reactive surface area per kg H_2O, K is the equilibrium constant for the mineral–water reaction written for the destruction of one mole of mineral, and Q is the reaction quotient. The parameters θ and η must be determined by experiments, but are commonly set equal to unity when experimental quantification is unavailable. The kinetics rate constant can be summed from three mechanisms (Lasaga et al., 1994):

$$\begin{aligned} k = {} & k_{25}^{nu}\exp\left[\frac{-E_a^{nu}}{R}\left(\frac{1}{T}-\frac{1}{198.15}\right)\right] + k_{25}^{H}\exp\left[\frac{-E_a^{H}}{R}\left(\frac{1}{T}-\frac{1}{198.15}\right)\right]\alpha_H^{n_H} \\ & + k_{25}^{OH}\exp\left[\frac{-E_a^{OH}}{R}\left(\frac{1}{T}-\frac{1}{198.15}\right)\right]\alpha_H^{n_{OH}} \end{aligned} \tag{4.2}$$

where subscripts nu, H, and OH indicate neutral, acid, and base mechanisms, respectively, E is the activation energy, k_{25} is the rate constant at 25 °C, R is gas constant, T is absolute temperature, a is the activity of the species, and n is a power term (constant). Notice that parameters θ and η (see Eq. (4.2)) are assumed to be the same for each mechanism. TOUGHREACT also provides a general form of species-dependent rate constant, which is detailed in Xu et al. (2006).

Prior to modeling the reactive transport processes related to the intrusion of CO_2 (with results reported in Section 4.5), an equilibrium run is performed to establish the initial conditions for the reactive transport model. We discuss results from this equilibrium run below, to evaluate consistency between the simulated initial state of the aqueous phase composition and the concentration ranges revealed by the evaluation of groundwater from the NWIS database, as described in Section 3.3. A reasonable agreement would demonstrate that our reactive transport

model, along with its input geochemical properties and thermodynamic data, has been adequately defined. Results are given in Tables 4.4 and 4.5, listing the initial chemical compositions with respect to major and trace constituents. Additional information is provided in Tables 4.6 and 4.7, giving the aqueous speciation of Pb and As for comparison with Table 3.15.

Table 4.3. Mineral volume fractions, possible secondary minerals, and kinetic properties for a Coastal Plain Sandstone. Kinetic parameters from Xu et al. (2006).

Mineral	**Volume Fraction of solid**	**A (cm^2/g)**	**Parameters for Kinetic Rate Law**							
			Neutral Mechanism		**Acid Mechanism**			**Base Mechanism**		
			k_{25} ($mol/m^2/s$)	**E_a (KJ /mol)**	**k_{25}**	**E_a**	**$n(H^+)$**	**k_{25}**	**E_a**	**$n(H^+)$**
***Primary*:**										
Quartz	0.77	9.8	1.02×10^{-14}	87.7						
K-feldspar	0.0618	9.8	3.89×10^{-13}	38	8.71×10^{-11}	51.7	0.5	6.31×10^{-12}	94.1	-0.823
Oligoclase	0.06	9.8	1.45×10^{-12}	69.8	2.14×10^{-10}	65	0.457			
Kaolinite	0.017	1.95×10^{5}	6.92×10^{-14}	22.2	4.89×10^{-12}	65.9	0.777	8.91×10^{-18}	17.9	-0.472
Smectite-Ca	0.0136	5.64×10^{5}	1.66×10^{-13}	35	1.05×10^{-11}	23.6	0.34	3.02×10^{-17}	58.9	-0.4
Illite	0.0285	6.68×10^{5}	1.66×10^{-13}	35	1.05×10^{-11}	23.6	0.34	3.02×10^{-17}	58.9	-0.4
Chlorite	0.0106	9.8	3.02×10^{-13}	88	7.76×10^{-12}	88	0.5			
Kerogen-os	2.67×10^{-3}	9.8	3.02×10^{-13}	88	7.76×10^{-12}	88	0.5			
Pyrite	0.00512	12.9	2.52×10^{-12}	62.76	2.34×10^{-7}	43.54	1			
Calcite	0.0151	Assumed at equilibrium								
Goethite	0.00601	1.47×10^{5}	2.52×10^{-12}	62.76	2.34×10^{-7}	43.54	1			
Apatite	2.2×10^{-3}	12.9			2.34×10^{-7}	43.54	1			
Barite	4.89×10^{-4}	12.9			2.34×10^{-7}	43.54	1			
Arsenopyrite	9.05×10^{-6}	12.9			2.34×10^{-7}	43.54	1			
Greenockite	3.03×10^{-6}	12.9			2.34×10^{-7}	43.54	1			
Cinnabar	1.46×10^{-8}	12.9			2.34×10^{-7}	43.54	1			
Galena	7.84×10^{-6}	12.9			2.34×10^{-7}	43.54	1			
Gudmundite	3.88×10^{-7}	12.9			2.34×10^{-7}	43.54	1			
Tiemannite	1.22×10^{-7}	12.9			2.34×10^{-7}	43.54	1			
Uraninite	8.005×10^{-7}	12.9			2.34×10^{-7}	43.54	1			
Sphalerite	9.4×10^{-5}	12.9			2.34×10^{-7}	43.54	1			
Secondary:										
Dolomite		12.9	2.52×10^{-12}	62.76	2.34×10^{-7}	43.54	1			
Magnesite		9.8	4.57×10^{-10}	23.5	4.17×10^{-7}	14.4	1			
Ankerite		9.8	1.26×10^{-9}	62.76	6.46×10^{-4}	36.1	0.5			
Dawsonite		9.8	1.26×10^{-9}	62.76	6.46×10^{-4}	36.1	0.5			
Smectite-Na		151.6	1.66×10^{-13}	35	1.04×10^{-11}	23.6	0.34	3.02×10^{-17}	58.9	-0.4
Pyromorphite		12.9			2.34×10^{-7}	43.54	1			
Ferroselite		12.9			2.34×10^{-7}	43.54	1			
Clausthalite		12.9			2.34×10^{-7}	43.54	1			

Table 4.4 shows the initial total aqueous concentration of major constituents, plus some other geochemical properties, obtained from the initial equilibrium run. These are compared with the respective values obtained at maximum frequency in histograms of the major constituents in more than 38,500 potable groundwaters evaluated in the NWIS database analysis, as given in Table 3.7. The water composition calculated in the initial equilibrium run with Coastal Plain Sandstone is characterized by slightly higher Na and K, slightly lower Ca and Fe, and fairly similar concentrations of SiO_2, SO_4^{-2}, and Cl^-. The observed differences are quite moderate, considering the fact that the reported peak histogram values in Table 3.7 typify very broad concentration distributions, characterized by the range and variety of geochemical conditions encountered. The water compositions show slightly different values for the partial pressure of CO_2, pH, and Eh. The difference with respect to Ca is in part caused by the fact that the water composition calculated for the Coastal Plain Sandstone had lower alkalinity and higher pH, assuming the water is in equilibrium with calcite—whereas the measured concentrations at peak value are slightly oversaturated with respect to calcite (based on a EQ3 run using the analytical peak concentrations). There are, however, considerable differences with respect to Mg and Al (respectively 40 times and 2,000 times smaller in the simulated concentration). These discrepancies are caused by some limitations in the current geochemical model, which we discuss briefly in the following paragraphs.

Normalized saturation indices of a suite of minerals commonly encountered in sedimentary environments are listed in Table 4.4a for initial secular equilibrium conditions generated for the Coastal Plain Sandstone and for modal chemical analyses of NWIS potable water composition. The saturation indices are normalized to unit silica stoichiometry for silicates and unit carbonate stoichiometry for carbonates. This normalization procedure affords a better basis for intercomparison of mineral saturations, because the saturation index is an extensive parameter that can vary depending on how the chemical formula of a mineral is written. Both the Coastal Plain Sandstone aquifer initial condition and the potable water compositions are concordant in displaying significant supersaturation with respect to quartz, the former due to kinetic constraints and the latter due to specification of saturation with respect to opal-CT. Both also display significant undersaturation with respect to dolomite, consistent with field observations indicating

that de-dolomitization can occur in shallow freshwater aquifers. Otherwise, the saturation indices of most silicates and carbonates indicate a relatively close approach to saturation, and fall within the range of uncertainty expected from the level of accuracy in log K values of mineral solubility products.

Table 4.4. Initial total aqueous concentration of major constituents obtained by initial equilibrium run for Coastal Plain Sandstone and analytical concentration at the maximum frequency in the histogram of 38,500 potable groundwaters and saturation indices of some major minerals

Species	**Total Aqueous Concentration (mol/L)**	**Total Aqueous Concentration (mg/L)**	**Modal values of Analytical Concentrations at (mg/L)**
Eh	-0.215 (volt)		-0.18 (volt)
pH	7.61		7.3
Ca	9.00E-04	36.0	63.1
Mg	2.17E-05	0.52	20
Na	1.97E-03	45.36	12.6
K	2.68E-04	10.47	1.6
Fe	5.63E-06	0.31	1.3
Si	9.31E-04	55.9	75
TIC as HCO_3^-	3.33E-03	203.1	316
SO_4^{-2}	1.95E-04	18.7	20
Al	4.19E-11	1.1E-06	0.002
Cl	2.07E-04	7.3	15.8
$P(CO_2)$ (log bar)	-2.3	-2.3	-1.86
ionic strength (mol/L)	0.0051		0.0078

Noteworthy in both cases is the relatively close approach to saturation with respect to K-feldspar, in contrast to significant undersaturation with respect to low albite. However, the degree of supersaturation of Ca- and Na-smectites in the potable waters suggests deficiencies in the thermodynamic data for these minerals. Furthermore, the very large level of supersaturation predicted for chlorite ($Mg_{2.5}Fe_{2.5}Al_2Si_3O_{10}(OH)_8$) in the potable water suggests that either the computed solubility product for this mineral was inadequate, or that some other Mg-bearing mineral is controlling the Mg activity at metastably elevated levels in potable groundwaters. In this regard, note that talc ($Mg_3Si_4O_{10}(OH)_2$) is close to saturation. It is geochemically

unreasonable to expect talc to occur in most shallow arenaceous aquifers, but the presence of an otherwise unrecognized poorly crystallized magnesian-rich phyllosilicate metastably saturating such aquifers, especially in aquifers undergoing dedolomitization, cannot be discounted.

The observed apparent chlorite supersaturation may also be attributed to the higher Al concentration reported in potable groundwaters than predicted from thermodynamic calculations. A partial explanation for this phenomenon is given in Section 3.3.2, where it is noted that the precipitation of metastable amorphous hydrated aluminum silicates caused by the dissolution of unstable detrital feldspars is not accounted for, a process recognized by Paces (1978) several decades ago. Both the kinetics of feldspar alteration and the associated precipitation of amorphous hydrated aluminum silicates are poorly understood, and further insight into the dissolution/precipitation mechanisms involved is needed before this process can be incorporated satisfactorily in geochemical models. However, recognition of this process may also explain the apparent chlorite supersaturation noted above.

The very large discrepancy between the modeled Al concentration in the Coastal Plain Sandstone aquifer initial condition and the modal value of analytical concentrations in NWIS groundwaters, as shown in Table 4.4 is primarily caused by the model deficiency described above. However, a further contribution, also discussed in Section 3.3.2, is the omission from the TOUGHREACT database of alumino-silicate complexes described by Tagirov and Schott (2001). These complexes can increase the total Al concentration in solution by a factor of ten. In conclusion, we may infer that the primary cause for the discrepancies between modeled and observed aqueous concentrations in both Mg and Al is the failure to account for secondary precipitation of amorphous or cryptocrystalline Mg- and Al-hydroxy-silicates. It is beyond the scope of this study to investigate this matter further, particularly when it is recognized that failure to take this issue into account has an insubstantial impact on the thermodynamic and kinetic controls affecting the concentrations of hazardous inorganic constituents in groundwaters, the primary subject of investigation. There are several contributing reasons why the observed Mg and Al discrepancies are not relevant in the context of this study, as explained below.

First, the activities of all of the hazardous constituents under study are determined by the solubilities of their mineral hosts, which have been identified as sulfides or selenides, carbonates and a silicate. None involve the participation of minerals containing alumina. Second, the pH of the aqueous phase is normally buffered primarily by carbonate minerals, especially by calcite. In the absence of carbonates, aluminosilicates, especially clays, may play an important role in buffering pH, but it is the well-defined amphoteric equilibrium between aqueous hydroxy-alumina species that determines buffering capacity, rather than the solubility product of aluminosilicates. It should be noted that the solubility products of most aluminosilicate minerals incorporated in both EQ3/6 and TOUGHREACT thermodynamic databases are derived from calorimetric measurements, rather than from direct measurement of their solubilities. In geochemical modeling of aqueous systems in which aluminosilcates play a part, the system is specified by Gibbs phase rule, and the concentration of Al in solution, defined in relation to the basis species, Al^{+3} in EQ3/6, or AlO_2^- in TOUGHREACT, is a dependent variable that is generally ignored, unless, as in the present study, an attempt is made to validate model predictions against field observation. Finally, Eh is specified primarily through equilibria between pyrite and goethite at a given pH. Dissolved Al does not play a role in defining the redox state of the system, yet it is the redox state that is generally critical in specifying the activities of the studied hazardous constituents when in equilibrium with their mineral hosts. In summary, aluminum speciation in solution does not play a direct role in modifying the thermodynamics or kinetics of the activities of hazardous constituents in solution, and its amphoteric behavior in buffering pH is also not at issue.

Table 4.5 lists the initial aqueous concentration of all hazardous inorganic constituents in groundwater. The predicted total aqueous Pb concentration is 1.3×10^{-9} mol/L (2.68×10^{-4} mg/L), which corresponds to a local maximum in the histogram of measured Pb concentrations from the NWIS database for potable groundwaters (see Figure 3.6a in Section 3.3.3). The predicted total aqueous As concentration is 4.42×10^{-8} mol/L (3.31×10^{-3} mg/L), which falls close to the maximum frequency of As concentration observed in NWIS analyses (see Figure 3.6b in Section 3.3.3). Similarly good agreement between the simulated initial concentrations and the range of values reported from the database is also observed for the other hazardous inorganic constituents.

Notice, furthermore, that the initial aqueous concentrations are fully consistent with the trace metal concentrations displayed in Figure 3.51 (at the selected log $P(CO_2)$ level of -2.3), where equilibrium concentrations as a function of CO_2 partial pressure have been determined from EQ3/6 calculations. The above comparisons, for both major and trace elements, demonstrate that the geochemical conditions in the base model at initial equilibrium state are reasonably consistent with the average conditions observed in a large number of United States aquifers.

Table 4.4a. Comparison of normalized saturation indices of some major minerals from the initial equilibrium run for Coastal Plain Sandstone with those calculated for potable groundwater with analytical concentrations at the maximum frequency in 38,500 potable groundwaters

Mineral	Normalized Saturation Index[1]		Comments
	Initial condition, Coastal Plain Sandstone	At maximum frequency in potable NWIS groundwaters	
***Primary*:**			
Quartz	+0.71	+0.84	
Opal-CT	-	0.00	Saturation specified
K-feldspar	-0.11	+0.16	
Albite_low	-0.90	-0.48	
Kaolinite	-1.23	+0.25	
Talc	-	+0.24	
Smectite-Ca	-0.02	+0.75	
Smectite-low-Fe-Mg	-	0.00	Saturation specified in NWIS groundwater
Illite	+0.02	+0.03	
Chlorite	+0.00	+2.21	
Pyrite	0.00	0.00	Saturation specified
Calcite	0.00	+0.09	Saturation specified in simulation
Goethite	0.00	0.00	Saturation specified
Secondary:			
Dolomite	-1.77	-1.07	
Magnesite	-1.91	-4.19	
Ankerite	-0.35	+0.08	
Siderite	-0.58	-0.05	
Na-smectite	-0.11	+0.61	

[1]Normalized to unit SiO_2 for silicates, and unit CO_3 for carbonates

Table 4.5. Initial chemical composition of trace elements of groundwater from the TOUGHREACT equilibrium simulation in comparison

Species	Total Aqueous Concentration (mol/L)	Total Aqueous Concentration (mg/L)
Pb	1.30E-09	2.69E-04
As	4.42E-08	3.31E-03
Ba	1.12E-06	1.53E-01
Cd	1.76E-09	1.98E-04
Hg	2.53E-09	5.08E-04
Sb	3.57E-10	4.34E-05
Se	1.69E-08	1.33E-03
U	4.48E-09	1.07E-03
Zn	3.40E-07	2.22E-02

With respect to aqueous speciation, the concentrations of Pb aqueous species listed in Table 4.6 are consistent with the findings discussed in Section 3.5.4 and the values presented in Table 3.15. At the selected CO_2 partial pressure of –2.3 (in log10), the most important Pb aqueous complex is PbS(aq), which accounts for about 85% of the total aqueous Pb. PbSe(aq) accounts for about 14% and $PbCO_3$(aq) for about 1%. Table 4.7, which shows aqueous As speciation, indicates that arsenite (As III) is the dominant species at the selected initial conditions and mainly exists as a complex of H_3AsO_3(aq), while arsenate (As V) can be neglected. These results are consistent with those derived from EQ3/6 calculations (Table 3.16).

Table 4.6. Concentrations of aqueous species of Pb

Species	Concentration (mol/L)	Percentage
$PbCO_3(aq)$	1.50E-11	1.15%
$Pb(HS)_2(aq)$	7.93E-18	0.00%
$Pb\ (HS)_3^-$	9.63E-26	0.00%
$PbCl^+$	8.67E-16	0.00%
$PbCl_2(aq)$	5.50E-19	0.00%
$PbCl_3^-$	5.50E-23	0.00%
$PbCl_4^{-2}$	8.57E-27	0.00%
$PbOH^+$	1.75E-13	0.01%
$Pb(OH)_2(aq)$	2.07E-15	0.00%
$Pb\ (OH)_3^-$	9.25E-19	0.00%
$Pb\ (CO_3)_2^{-2}$	1.15E-14	0.00%
PbO(aq)	2.58E-15	0.00%
$PbHCO_3^+$	3.59E-13	0.03%
Pb^{+2}	2.06E-13	0.02%
$Pb(HSe)_2(aq)$	6.56E-24	0.00%
$Pb(HSe)_3$-	4.76E-38	0.00%
PbS(aq)	1.11E-09	84.80%
PbSe(aq)	1.83E-10	13.99%
Total Pb	**1.30E-09**	**100%**

Table 4.7. Speciation of aqueous species of As

Species	Concentration (mol/L)	Percentage
$H_3AsO_3(aq)$	4.28E-08	96.79%
$H_2AsO_3^-$	1.41E-09	3.19%
$H_2AsO_4^-$	1.77E-13	0.00%
$H_3AsO_4(aq)$	6.89E-19	0.00%
$HAsO_4^{-2}$	1.63E-12	0.00%
$H_3As_3S_6(aq)$	7.84E-46	0.00%
$H_2As_3S_6^-$	8.36E-42	0.00%
$HAs_3S_6^{-2}$	4.20E-42	0.00%
$H_3As_3Se_6(aq)$	3.93E-77	0.00%
$H_2As_3Se_6^-$	1.39E-73	0.00%
$HAs_3Se_6^{-2}$	5.75E-75	0.00%
$HAsS_2(aq)$	6.51E-20	0.00%
$AsSe(OH)(HSe)^-$	1.63E-19	0.00%
$AsS(OH)(HS)^-$	8.83E-12	0.02%
Total As	**4.42E-08**	**100%**

4.5 Results for CO_2 Intrusion into Coastal Plain Sandstone

4.5.1 Prediction of CO_2 Plume Evolution and Changes in Acidity

In our simulation scenario, CO_2 gas enters the aquifer from the bottom at x = 105 m and y = 0 m, over a horizontal area of 10 m × 10 m. The dissolution of CO_2 into water leads to the formation of various aqueous carbonate complexes and therefore the total amount of dissolved CO_2 is given by the concentration of total inorganic carbon (TIC). The intrusion of CO_2 leads to an increase of TIC (Figure 4.2 left) and a corresponding decrease of pH (Figure 4.2 right). Note that the variation in concentration of TIC is the combined effect of CO_2 intrusion, dissolution of CO_2 in water, and chemical reactions (mainly as calcite dissolution in the current simulation). While initially all CO_2 dissolves almost instantaneously into the groundwater, a gas phase evolves after around 3 years close to the intrusion area (Figure 4.3). Both water and gaseous CO_2 are present in this area, forming a small two-phase zone that remains present until the end of the simulation period at 100 years (Figure 4.4). The CO_2 gas dissolves into the groundwater and is transported downstream (Figure 4.5). The plume of dissolved CO_2 (total carbonate) migrates primarily along the groundwater flow direction, while lateral spreading of dissolved CO_2 is minor, penetrating only up to 20 m in the y-axis direction (direction perpendicular to groundwater flow). The spatial distribution of pH shown in Figure 4.6 closely follows the distribution of TIC. The two-phase zone has the highest partial pressure of CO_2 and thus largest TIC concentration, and therefore, the pH in the two-phase zone is the lowest.

Notice in this context that the TOUGHREACT transport model has been set up without consideration of hydrodynamic (longitudinal or transverse) dispersion, which would induce more spreading. The process of hydrodynamic dispersion is often represented by a Fickian diffusion analogue (convection–dispersion equation) that has some flaws and limitations (Xu and Pruess, 2001). A Fickian model for dispersion is not used in TOUGHREACT. Instead, hydrodynamic dispersion is introduced through spatial resolution. The discretization used for the transport simulations employs a grid size of 10 m in the horizontal directions, implying that both the longitudinal and transverse dispersivities are on the order of about 10 m. In our study, modeling

without explicit consideration of hydrodynamic dispersion means that less spreading and dilution of the dissolved CO_2 plume occurs, thus maximizing (at least locally) the impacts of CO_2 intrusion on the geochemistry of the system. If hydrodynamic dispersion was significantly larger than assumed here, the area affected by dissolved CO_2 would increase, but the maximum concentrations would be reduced due to enhanced dilution of the plume.

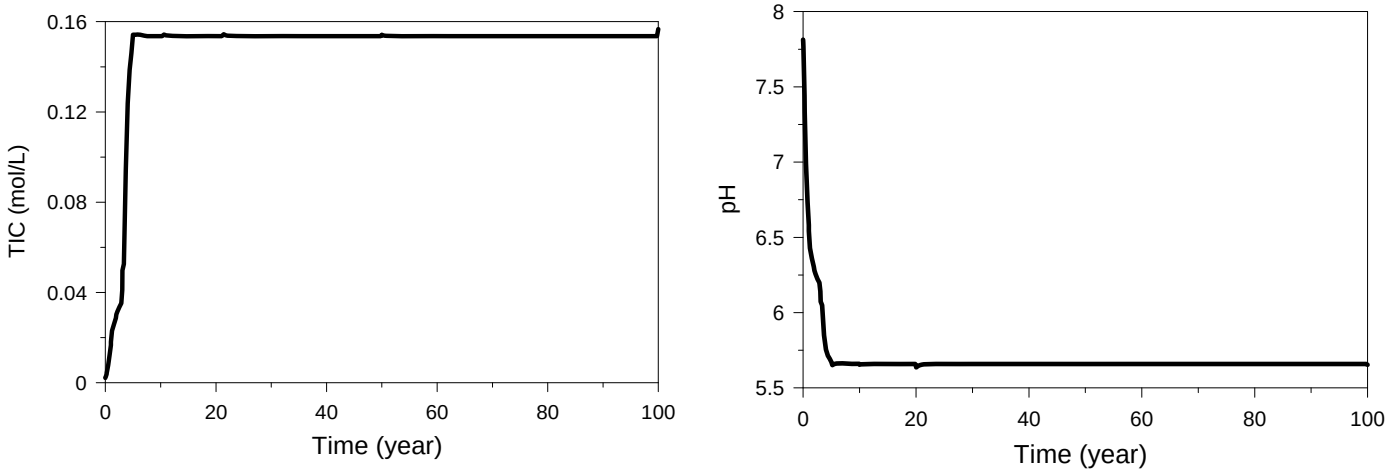

Fig. 4.2. Time evolution of total inorganic carbon (TIC) (left) and pH (right) at CO_2 intrusion location

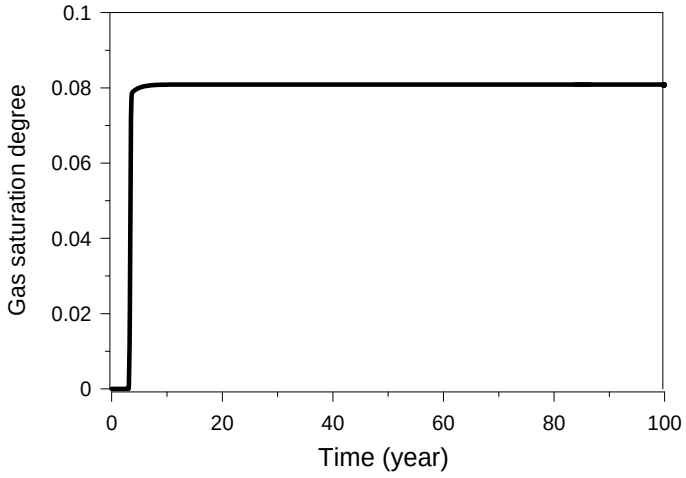

Fig. 4.3. Time evolution of gas saturation degree at CO_2 intrusion location

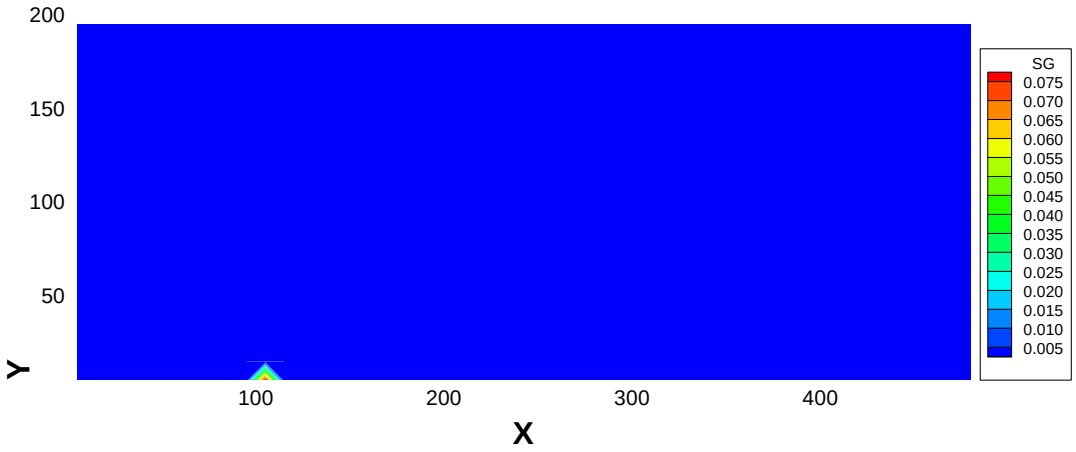

Fig. 4.4. Spatial distribution of saturation degree of CO_2 gas after 100 years of intrusion

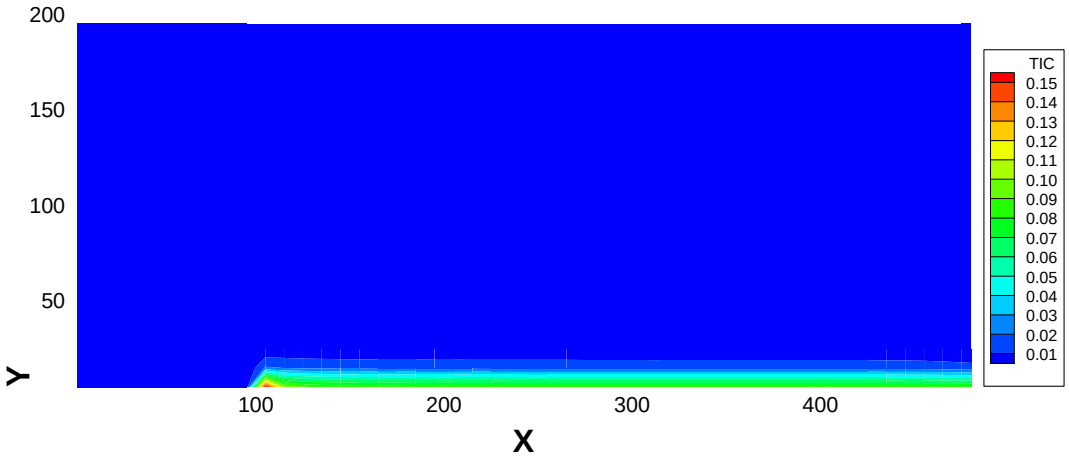

Fig. 4.5. Spatial distribution of total inorganic carbon (TIC) (mol/L) after 100 years of intrusion

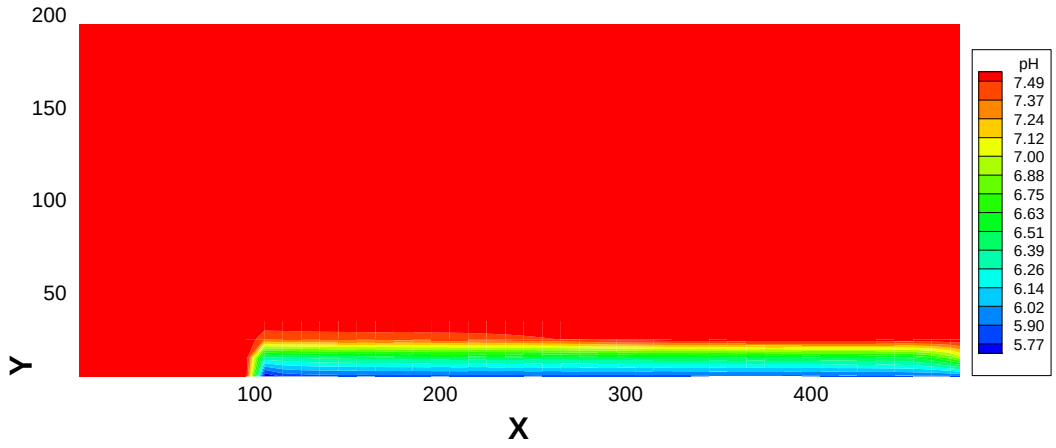

Fig. 4.6. Spatial distribution of pH after 100 years of intrusion

Figure 4.7 shows profiles of TIC (left) and pH (right) at four times after the start of intrusion of CO_2, i.e., at 5, 20, 50, and 100 years. The profiles are taken along the direction of flow (x-axis) at y = 0 m. The plume of dissolved CO_2 migrates with the groundwater flow over time, extending further and further downstream until a steady state is reached within the model domain. The evolution of pH closely follows the evolution of TIC, with pH decreasing as the concentration of TIC rises. After about 50 years, the region of decreased pH extends from the CO_2 intrusion point downstream to the boundary of the model domain. Notice that the lowest pH is around 5.87 outside of the two-phase zone, which is higher than the expected pH in a system without any buffering capacity. (For a nonbuffered system, a pH around 4.5 would be expected). The moderation in pH decrease is caused primarily by the dissolution of calcite. Figure 4.8 shows the volumetric change in calcite caused by dissolution. Almost all of the calcite initially present near the two-phase zone has dissolved after 100 years. This significant dissolution of calcite buffers the pH response to the increasing CO_2 levels in the water; however, this buffering effect would cease locally if CO_2 intrusion were to continue after 100 years, since calcite would eventually be depleted.

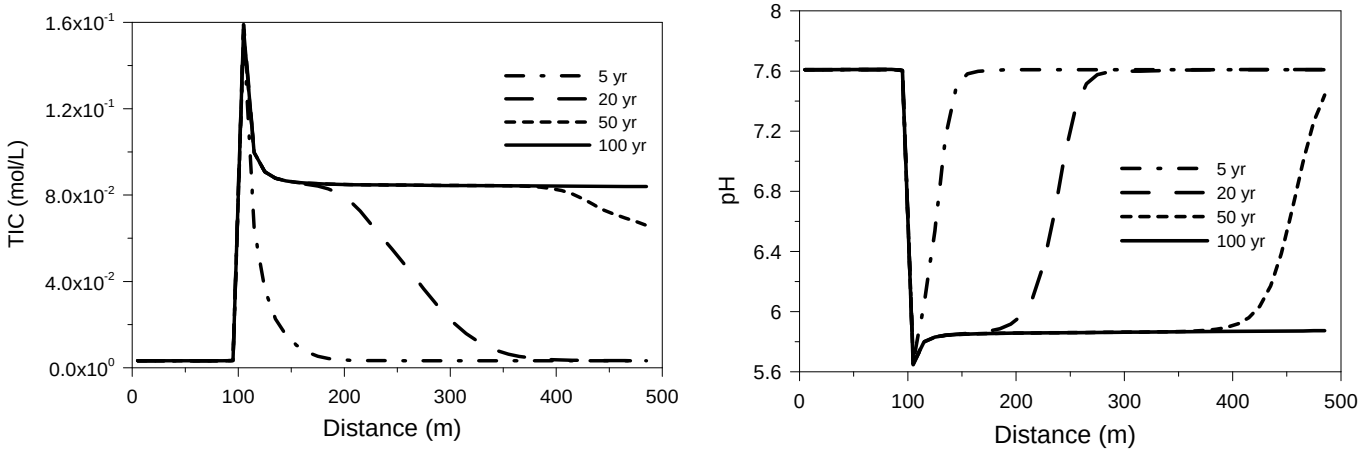

Fig. 4.7. Total inorganic carbon (left) and pH (right) along the x-axis at y = 0 m, for Coastal Plain Sandstone.

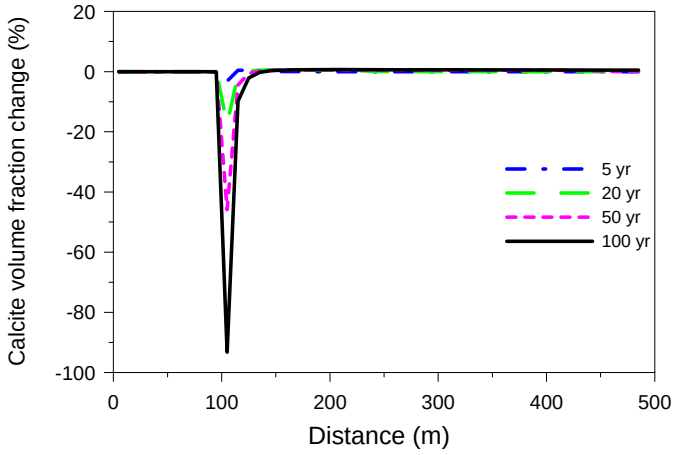

Fig. 4.8. Calcite volume fraction change profiles along x-axis at y = 0 m, for Coastal Plain Sandstone.

4.5.2 Prediction of Pb and As Concentrations

The processes that control the changes in aqueous Pb and As concentration in response to CO_2 intrusion include desorption/adsorption from the surface of minerals, dissolution/precipitation of relevant minerals (galena for Pb and arsenopyrite in solid solution for As), and the dissociation/association of aqueous complexes. The resulting concentrations are moreover affected by complex interaction between these processes.

Figure 4.9 shows the contour map of total aqueous Pb concentration after 100 years, which resembles closely the spatial distribution of the pH decrease. The highest concentration occurs along the y=0 profile. Transport in the longitudinal direction is dominant. Figure 4.10 shows the total aqueous Pb concentration profile along the x-axis at y = 0 m for different times. The peak value of aqueous Pb is 3.4×10^{-8} mol/L in the small two-phase zone at the intrusion location after 5 years, which then decreases to 1.8×10^{-8} mol/L after 50 years. As time progresses, the peak moves incrementally downstream, and after 100 years falls to 1.6×10^{-8} mol/L. The aqueous Pb concentration downstream approaches a stable value around 1.1×10^{-8} mol/L. This value is significantly higher (about one order of magnitude) than the initial concentration, but remains below the MCL (maximum contamination level), which is 7.24×10^{-8} mol/L (15 ppb). The observed Pb concentration profiles reflect a combination of dissolution/precipitation and adsorption/desorption effects, as discussed below.

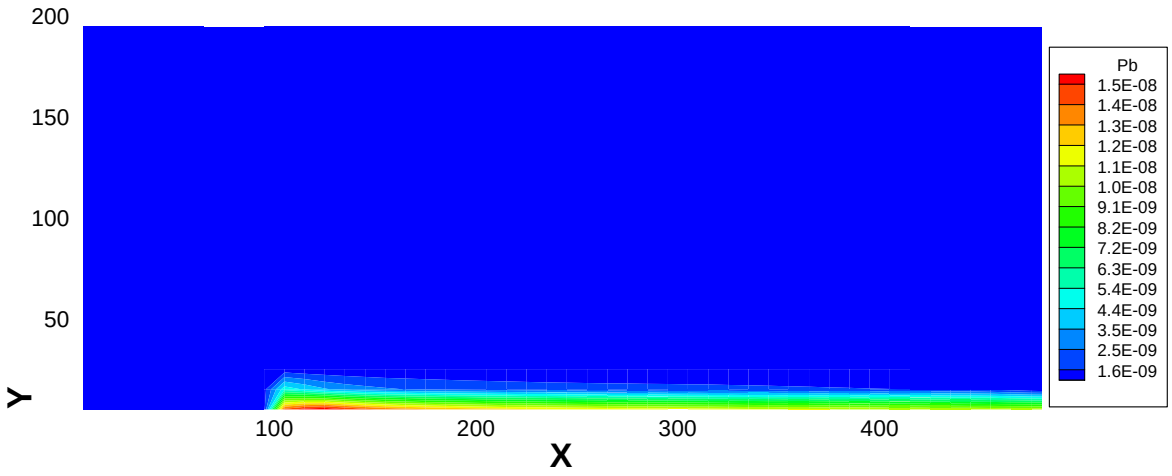

Fig. 4.9. Spatial distribution of total aqueous Pb after 100 years of intrusion

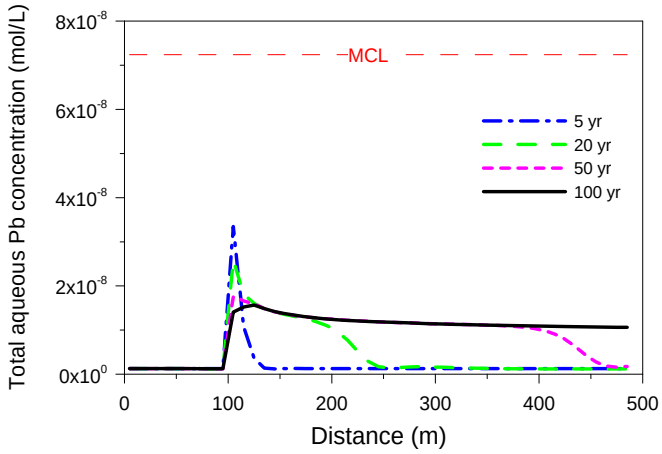

Fig. 4.10. Total aqueous Pb concentration profile along x-axis at y = 0 m.

Our results for the base-case model suggest that adsorption and desorption of Pb^{+2} ion from mineral surfaces are more important to the evolution of aqueous Pb concentrations than the precipitation and dissolution of galena. Figure 4.11 exemplifies the complexity of these processes by illustrating the change in the surface complex concentrations for illite. The surface complex concentration is expressed in mol/L solution. Desorption and adsorption constitute, respectively, the net effects of decreasing and increasing the concentration for all relevant surface complexes. Illite is the most important adsorbent of Pb. $Ill^{s}\_OPb^{+}$ is a surface complex of Pb on illite (Appendix F), which represents the mass of Pb on the strong site at the surface of illite, while $Ill^{w}\_OPb^{+}$ represents the mass of Pb on the weak site at the surface of illite. The increase of $Ill^{s}\_OPb^{+}$ (Figure 4.11 left) compared to the initial levels indicates that aqueous Pb is adsorbed on the strong site, whereas the decrease of $Ill^{w}\_OPb^{+}$ (Figure 4.11 right) indicates that aqueous Pb is released from the weak site on illite. Another important surface complex that adsorbs Pb is $sme^{s}\_OPb^{+}$, which represents the mass of Pb on the strong site at the surface of smectite.

Figure 4.12 shows the relative change of total Pb concentration on adsorption sites (which is a summation of the concentration of all Pb surface complexes), calculated as:

$$\frac{S^{t} - S^{ini}}{S^{ini}} \tag{4.3}$$

where S^t is the total Pb concentration on adsorption sites at a given time *t*, and S^{ini} is the initial total Pb concentration on adsorption sites (both given in mol/L solution). The figure indicates that significant desorption of Pb occurs in the two-phase zone (depleting the initially sorbed Pb by about 60% after 100 years), thereby increasing the aqueous Pb concentration. Less effective desorption occurs further downstream, although the Ph there is similarly small. The overall effect of desorption is smaller because the aqueous Pb mobilized in the two-phase zone migrates downstream, inhibiting further desorption.

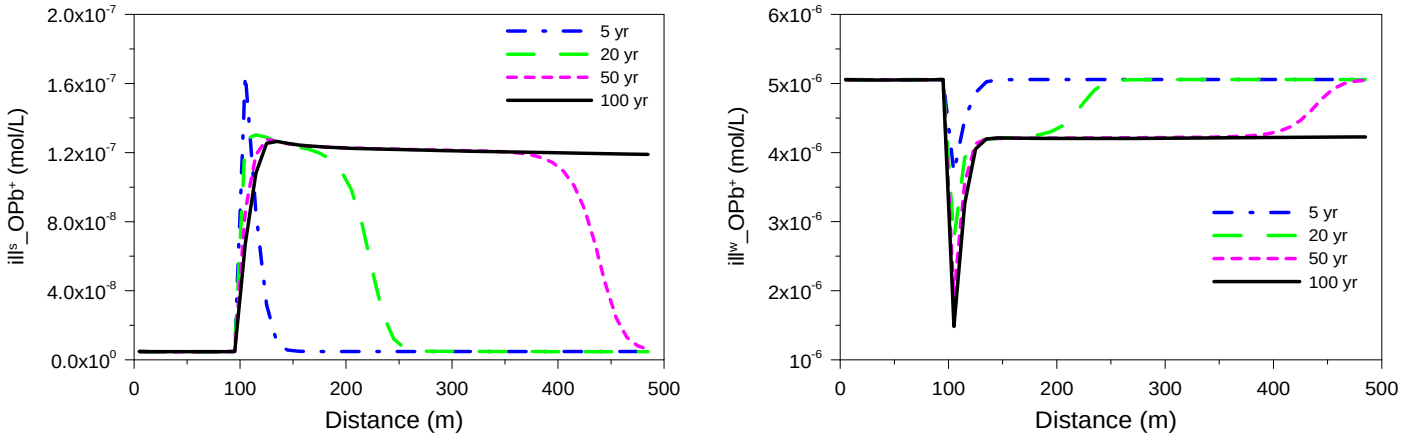

Fig. 4.11. Surface complex of Pb on the strong (left) and weak site (right) of illite along x-axis at y = 0 m for Coastal Plain Sandstone.

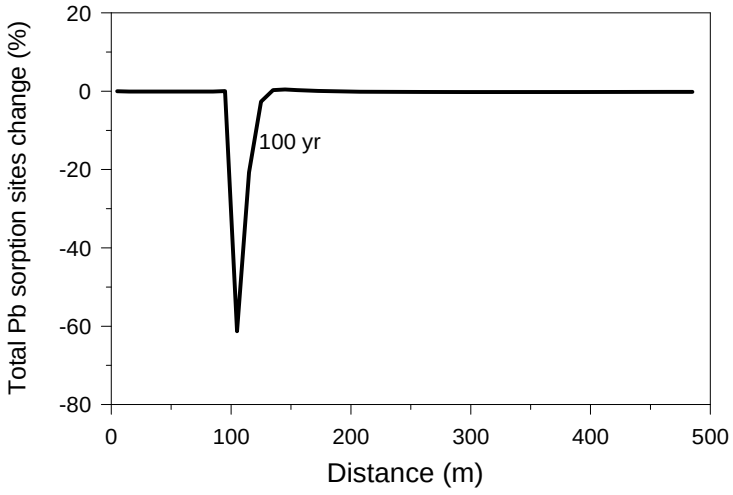

Fig. 4.12. Relative change of total Pb surface complexes concentration along the x-axis at y = 0 m for Coastal Plain Sandstone.

Section 3.5 illustrated how the solubility of galena increases with the partial pressure of CO_2 and presented the expected equilibrium concentrations of Pb and other inorganic hazardous constituents at various $P(CO_2)$ levels. It is important to point out, however, that these calculations (in Section 3.5.3) represent an equilibrium state, which does not take into account transient changes in adsorption/desorption and precipitation/dissolution. The ingress of CO_2 immediately disturbs both adsorption and solubility equilibria, but whereas adsorption reactions are always assumed to re-equilibrate instantaneously, the dissolution precipitation of a hazardous mineral host is kinetically controlled and typically much slower. As we can observe from the transient runs conducted here, the relatively sudden release of Pb from adsorption sites increases the aqueous Pb concentration so significantly that the solution becomes in fact supersaturated with respect to galena (even though the groundwater becomes more acidic, suggesting a higher galena solubility), and galena precipitation occurs in the two-phase zone.

Figure 4.13 exemplifies this process, giving the relative change in the galena volume fraction as a function of time. The volume fraction change is calculated as:

$$\frac{V^t - V^{ini}}{V^{ini}} \tag{4.4}$$

where V^t is the volume fraction of mineral at given time *t*, and V^{ini} is the initial volume fraction of mineral. Negative values indicate dissolution, positive values indicate precipitation. Notice that galena continues to precipitate in the two-phase zone over the entire simulation period of 100 years. At later stages, however, galena may start dissolving, because the Pb on adsorption sites will have eventually depleted.

As pointed out in Section 3.5, sulfide and selenide aqueous complexation play a very important role in the behavior and evolution of several of the hazardous constituents, most notably Pb, but also cadmium, mercury, and zinc. Because very stable neutral complexes form in solution, the impact that elevated CO_2 levels have on increasing the solubility of galena (PBS), for example, is reduced compared to a case where no complexation is considered, due to the competition between chalcogenide complexes and carbonate complexes. While not reported here, we have

conducted reactive transport simulations without accounting for sulfide and selenide complexes in solution. These resulted in higher overall aqueous Pb concentrations after CO_2 intrusion compared to the base model, because both desorption and galena dissolution caused Pb mobilization in the two-phase zone.

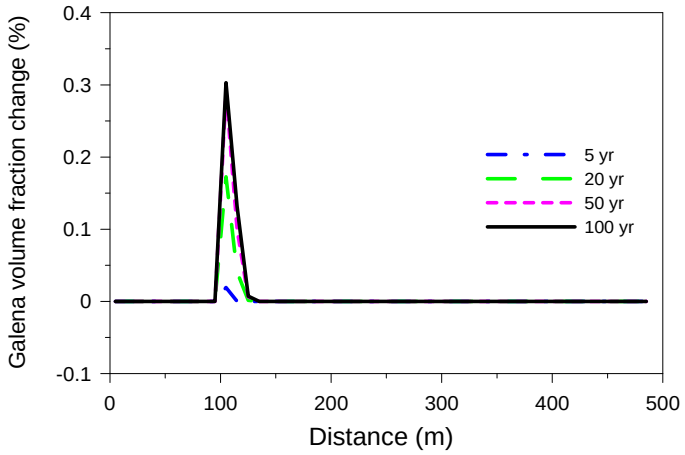

Fig. 4.13. Galena volume fraction change profiles along x-axis at y = 0 m, for Coastal Plain Sandstone.

Figures 4.14 and 4.15 (left) show, respectively, the spatial distribution of As concentration at 100 years and the evolution of As concentration in a profile along the x-axis. The peak concentration of As is 1.29×10^{-7} mol/L, with the As concentration stabilizing at 1.19×10^{-7} mol/L downstream, slightly less than the MCL (1.33×10^{-7} mol/L or 10 ppb). The increases in As concentration are constrained to a narrow area downstream of the CO_2 intrusion point.

As was the case with Pb, the observed As concentrations are significantly affected by adsorption/desorption processes. In the base model, illite is the most important adsorbent for both Pb and As, but as conditions change, other minerals may become more relevant, depending on the thermodynamic solubility, specific adsorption site density, and volume fraction of minerals present in the aquifer host rock. The adsorption/desorption of As exhibits even more complexity than that of Pb. For example, H_2AsO_3 (aq) is adsorbed on illite as three types of surface complexes: ill $\_H_2AsO_3$, ill $\_HAsO_3^-$, and ill $\_AsO_3^{2-}$. Desorption or adsorption is the net effect of increase or decrease of As concentration on all three surface complexes, as well as

surface complexes on other minerals. For example, a decrease in ill_$HAsO_3^-$ (Figure 4.16, left) indicates the release of initially adsorbed As into water, whereas an increase in ill _H_2AsO_3 (Figure 4.16, right) indicates that aqueous As is adsorbed. The relative change of total As surface-complex concentration shown in Figure 4.17 (left) indicates that desorption occurs in the two-phase zone, thus increasing the aqueous As concentration, whereas adsorption occurs further downstream, thus limiting further increases in aqueous As.

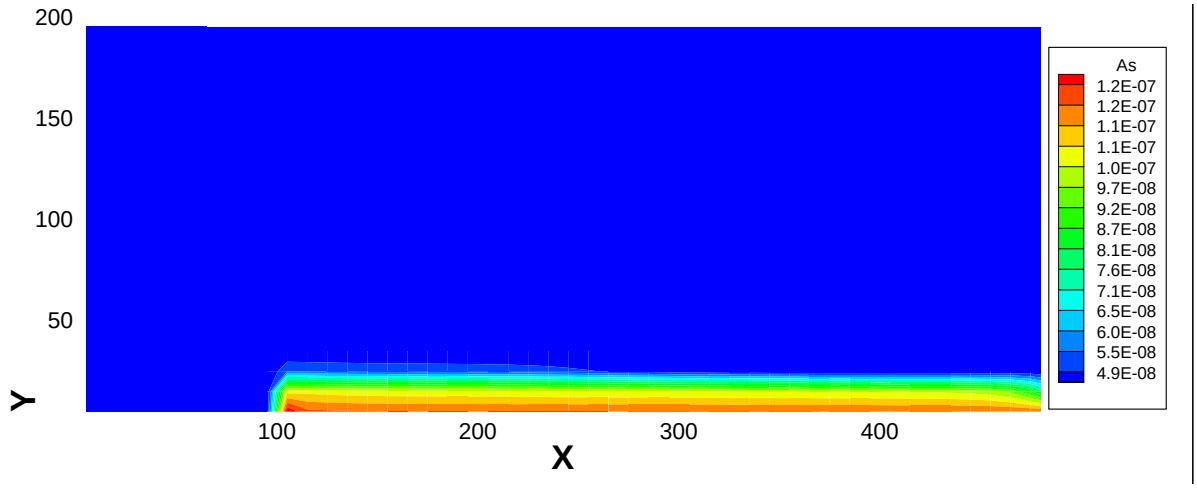

Fig. 4.14. Spatial distribution of total aqueous As concentration after 100 years of intrusion

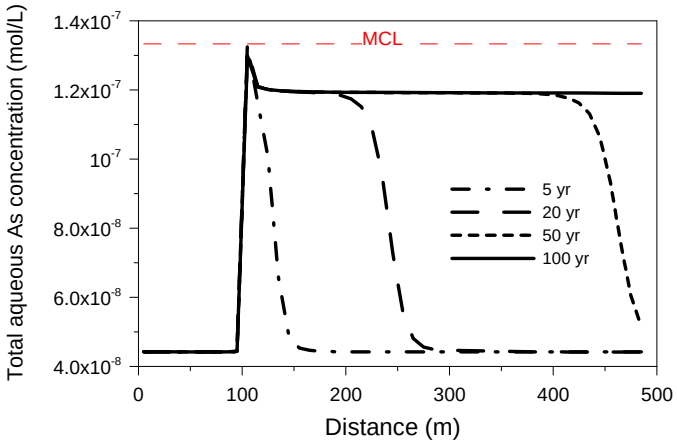

Fig. 4.15. Total aqueous As concentration profiles along the x-axis at y = 0 m, for Coastal Plain Sandstone.

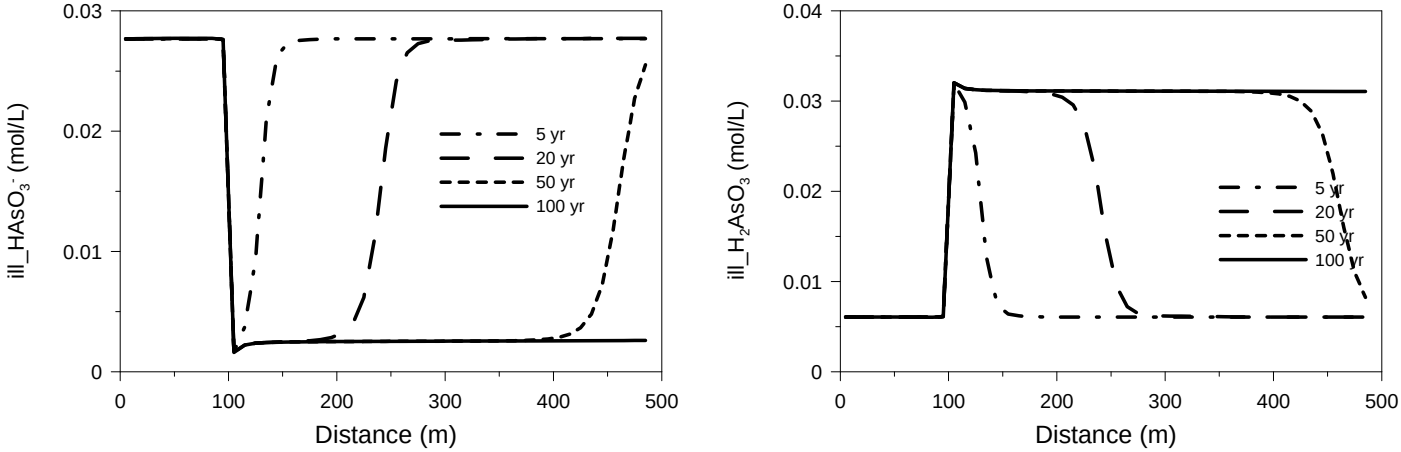

Fig. 4.16. Surface complex Ill _$HAsO_3^-$ (left) and Ill _H_2AsO_3 (right) profiles along the x-axis at y = 0 m, for Coastal Plain Sandstone.

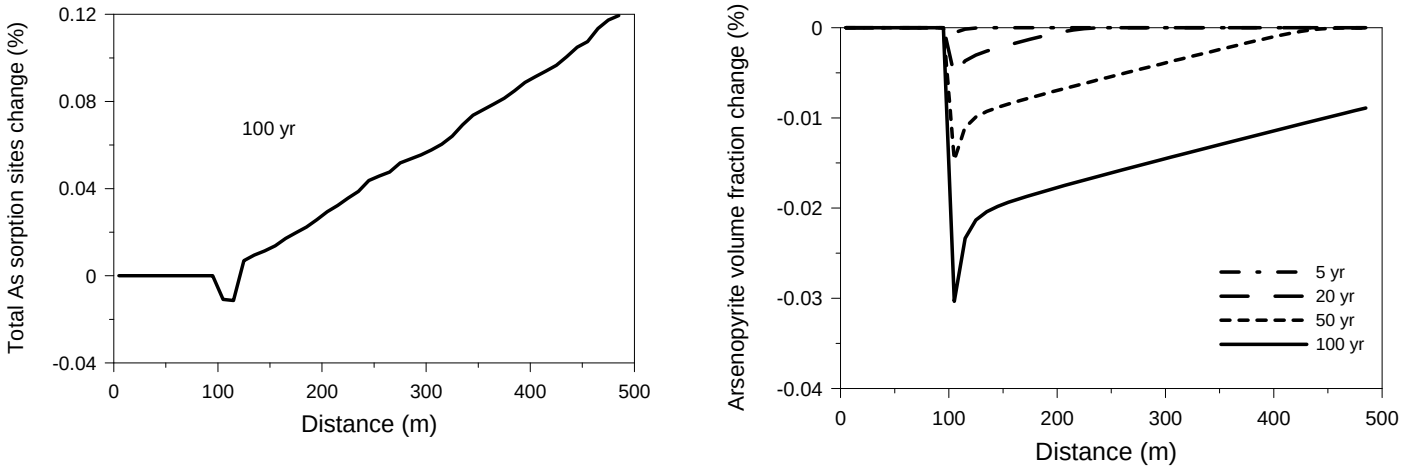

Fig. 4.17. Relative change of total As surface complexes concentration (left) and arsenopyrite volume fraction change (right) along the x-axis at y = 0 m for Coastal Plain Sandstone.

Figure 4.17 (right) shows the volume fraction change of arsenopyrite in solid solution. In contrast to the Pb observations, where the metal-hosting mineral (galena) actually precipitates after intrusion of CO_2, As is mobilized by arsenopyrite dissolution in the two-phase zone and, to a lesser degree, in the downstream region. Thus, in the case of As, the decrease of pH in the two-phase zone causes both desorption of As from the mineral surface (Figure 4.17 left) and dissolution of arsenopyrite (Figure 4.17 right), generating a concentration increase almost to the

MCL. Further increases of As concentrations downstream of the two-phase zone are limited, because the water arriving from upstream already has elevated As concentrations. As a result, the dissolution of arsenopyrite becomes less effective, and aqueous As sorbs back to the mineral surfaces (Figure 4.17 left). That the dissolution of arsenopyrite is a rather slow process becomes evident in Figure 4.17 (right), where the maximum volumetric change of arsenopyrite after 100 years is only about 0.03% of its initial volume fraction. This suggests that the rather small initial volume of arsenopyrite in solid solution can be a long-lasting source of aquifer contamination.

The differences in the two-phase-zone behavior of Pb and As in response to CO_2 intrusion—desorption combined with galena precipitation in the case of Pb compared to desorption and arsenopyrite dissolution in the case of As—point to the complexities involved in reactive transport modeling and the interplay between the various processes involved. For example, as shown in Figure 3.51 (see Section 3.5.3), the solubility of arsenopyrite increases more significantly with the partial pressure of CO_2 than the solubility of galena, because sulfide and selenide complexation effectively inhibit PbCO3(aq) complexation. This is one of the main reasons why the desorption of As does not cause supersaturation with respect to arsenopyrite, while the desorption of Pb causes supersaturation with respect to galena. However, variations in the kinetic rates or changes in other geochemical parameters could affect the observed trends.

The following tables show how Pb and As are initially distributed in the aquifer between solid and aqueous phases, and how this initial distribution changes during the 100 years of CO_2 intrusion. Table 4.8 expresses the mass (mol/L solution) of Pb and As in solid (as an essential component in a mineral and adsorbed on mineral surfaces) and aqueous phases in the two-phase zone near the CO_2 intrusion point, at t = 0 and t = 100 years. Table 4.9 gives the same information, but relative to the initial (t = 0) total mass of Pb and As, respectively.

Initially, most Pb resides in the solid phase: about 99% as an essential component in galena and about 1% on adsorption sites, while the relative amount of Pb in the aqueous phase is very low (around 2×10^{-4} %). After 100 years, the total mass of Pb on adsorption sites has decreased by about two-thirds as a result of desorption, while Pb as an essential component in galena increases marginally as a result of the galena precipitation. In contrast, the mass of Pb dissolved in the

aqueous phase has increased by almost one order of magnitude compared to the initial value. In absolute numbers, however, the relative amount of Pb in the aqueous phase is still marginal compared to the solid phases. This points out that there is enough Pb in the aquifer rock to provide a long-lasting source for aqueous contamination. Total mass of Pb in all phases decreases by about 0.3%, indicating that part of the dissolved Pb is transported downstream.

Arsenic in the solid phase, both on adsorption sites and in arsenopyrite, decreases only marginally during the 100 years of CO_2 intrusion, while the mass of As dissolved in the aqueous phase increases by a factor of about three. Note that adsorbed mass accounts for the majority of As in the solid phase (about 98% adsorbed compared to about 2% as an essential component in arsenopyrite).

Table 4.8. Mass distribution (mol/L solution) of Pb and As on solid (as an essential component in minerals or adsorbed on mineral surfaces) and liquid phase in two-phase zone at initial (t=0) and final time (t=100 years)

Species	Aqueous Phase (mol/L solution)	Solid Phase		Total Mass (mol/L solution)	Time
		Mineral (mol/L solution)	Surface (mol/L solution)		
Pb	1.30E-09	0.000578	5.62E-06	0.000583	t=0
Pb	1.41E-08	0.000580	1.97E-06	0.000582	t=100 year
As	4.42E-08	0.000795	0.0383625	0.039157	t=0
As	1.29E-07	0.000794	0.0383584	0.039153	t=100 year

Table 4.9. Mass distribution (%) of Pb and As on solid (as essential an component in minerals or adsorbed on mineral surfaces) and liquid phase in two-phase zone at initial (t=0) and final time (t=100 years)

Species	Aqueous Phase	Solid Phase		Total	Time
		Mineral	Surface		
Pb	2.23E-04	99.036	0.964	100	t=0
Pb	2.41E-03	99.336	0.338	99.68	t=100 year
As	1.13E-04	2.029	97.971	100	t=0
As	3.30E-04	2.029	97.960	99.989	t=100 year

4.6 Sensitivity Analyses

In this section, we discuss the results of a series of sensitivity analyses with respect to geochemical processes, model setup, and initial and boundary conditions. The base model is described in Section 4.2, and the modeling results concerning this case are given in Section 4.5. These results suggest that adsorption/desorption and mineral dissolution/precipitation act together as the most important processes that control the evolution of aqueous Pb and As. Previous work on the subject by Wang and Jaffe (2004) did not consider adsorption/desorption. Therefore, to explore the role of adsorption/desorption, we conducted a sensitivity analysis as described below, evaluating the geochemical effects of CO_2 intrusion with or without consideration of adsorption/desorption. Further sensitivity analyses were performed on other key chemical parameters, including solubility parameters, the volume fraction of minerals containing hazardous constituents, and surface complexation constants. Finally, sensitivity analyses were performed on the hydrodynamic assumptions of the base model: background CO_2 concentration, aquifer depth, groundwater flow rate, and CO_2 intrusion rate.

4.6.1 Sensitivity to Adsorption

4.6.1.1 Sensitivity Run without Adsorption

In the base model, adsorption and desorption processes are included in the simulation through a surface complexation model. In this section, we present results for a simulation without adsorption/desorption, and compare these with the base model. A simulation run without adsorption allows quantitative evaluation of the role of adsorption/desorption on the evolution of the aqueous concentration of hazardous constituents. Because of this change, the initial distribution of hazardous constituents in the aquifer is different. Specifically, no initial mass is sorbed onto mineral surfaces, which is otherwise released with the ingress of CO_2 (see previous section). Thus, in the sensitivity run without adsorption, dissolution of galena is the only process mobilizing Pb and increasing the aqueous Pb concentrations, while dissolution of arsenopyrite (in solid solution) is the only process producing changes in aqueous As concentrations.

In the base run, desorption in the two-phase zone releases Pb into the aqueous phase; the solution there becomes supersaturated with respect to galena, and consequently galena precipitates (Figure 4.18 right). In the sensitivity run, the increased acidity caused by the ingress of CO_2 in turn causes dissolution of galena (Figure 4.18 left). Spatial distributions of the resulting aqueous Pb concentration at different times are shown in Figure 4.19. The Pb dissolved close to the intrusion zone migrates downstream, where galena continues to dissolve because of the lowered pH. As a result, the initially relatively small aqueous Pb concentrations in the two phases continue to build up with travel distance (Figure 4.19, left); however, the trend observed in the profiles is very moderate, and it is not clear whether Pb concentrations above the MCL could be reached much further downstream, should the simulation interval be sufficiently long. During the 100-year period shown here, the resulting Pb concentration is smaller in the sensitivity run compared to the base case (Figure 4.19 right), indicating that desorption has the potential to release more Pb than dissolution of galena.

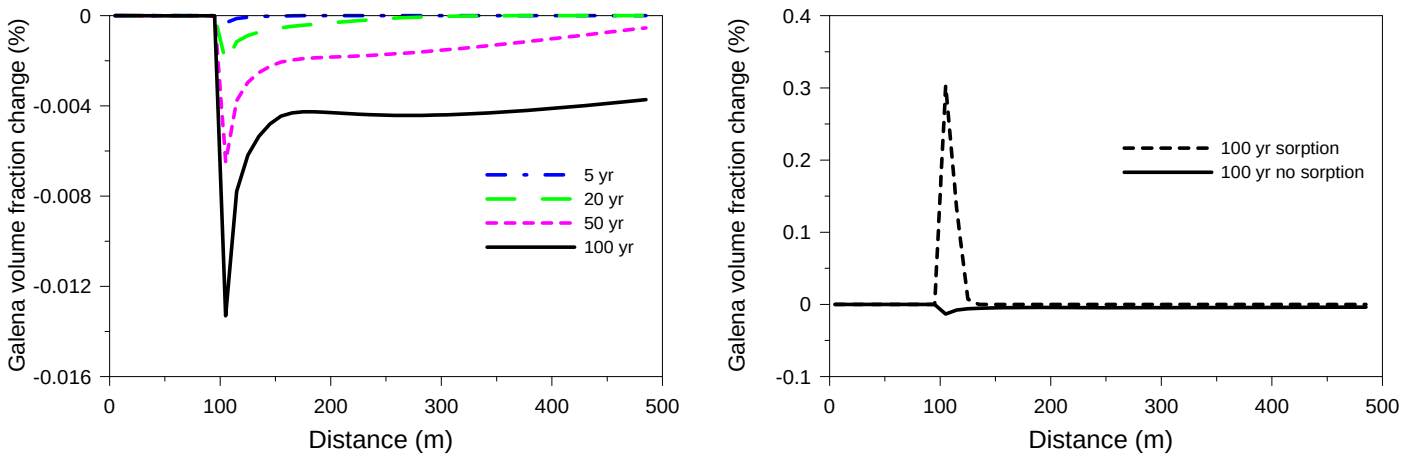

Fig. 4.18. Galena volume fraction change profiles along x-axis at y = 0 m 0 at different times in a sensitivity run without adsorption/desorption (left), and comparison of galena volume fraction change profile along x at y=0 after 100 years of CO_2 intrusion with base model (right).

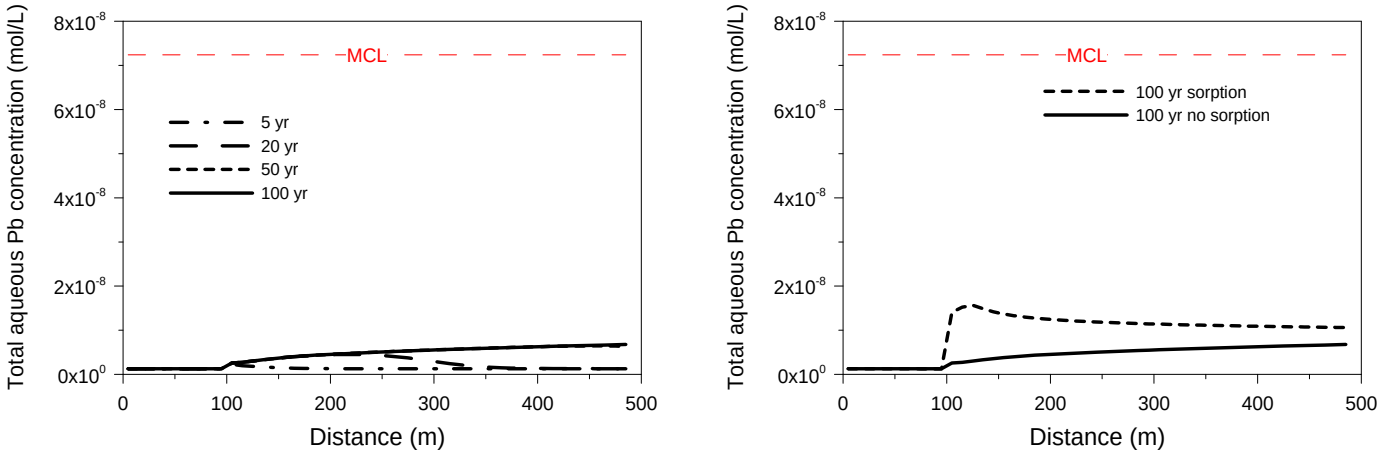

Fig. 4.19. Aqueous Pb concentration profile along x at y=0 at different times in a sensitivity run without adsorption/desorption (left), and comparison of model results for total aqueous Pb concentration profile along x at y=0 after 100 years of CO_2 intrusion with base model (right).

The omission of adsorption/desorption processes is similarly important for As. Without adsorption, the As concentrations increase significantly with travel distance (Figure 4.20, left). The trend seen in the profiles suggests that the MCL for As would be exceeded further downstream, and that the maximum concentration of As would be limited by the solubility of arsenopyrite (see Section 3.5.3). This is in contrast to the base model, where adsorption stabilizes the aqueous As to a relatively uniform level that is smaller than the MCL (Figure 4.20 right). That the base-model results show much higher concentration values in the two-phase zone near the CO_2 intrusion location is caused by the significant mobilization of initially sorbed As.

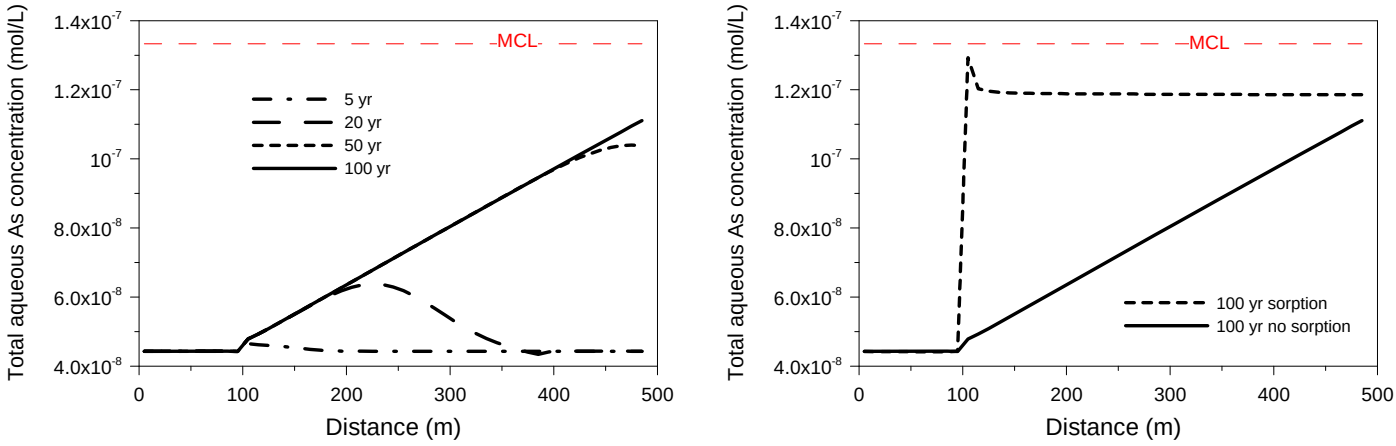

Fig. 4.20. Aqueous As concentration profile along x at y=0 at different time in a sensitivity run without adsorption/desorption (left) and comparison of model results of As concentration profile along x at y=0 after 100 years of CO_2 intrusion with base model (right).

In the TOUGHREACT model, adsorption/desorption processes are calculated assuming a local equilibrium, which means that the surface complex responds instantaneously to pH changes. This is a reasonable assumption, because adsorption reactions are fast compared to the kinetically controlled dissolution/precipitation of hazardous mineral hosts. As a result, desorption is the dominant process affecting aqueous Pb and As in the short term (see Figure 4.21 for the situation after 1 year of CO_2 intrusion).

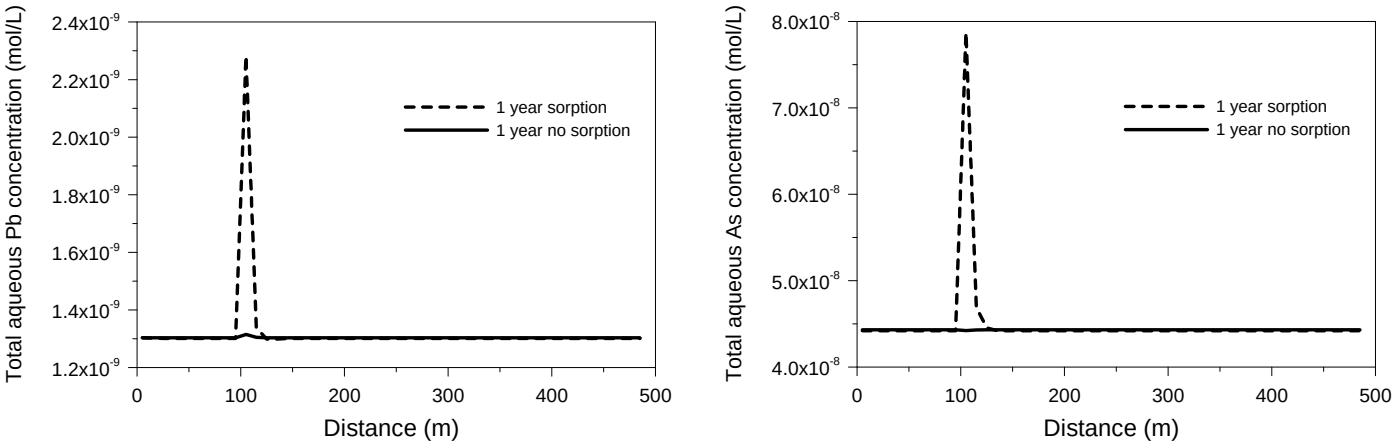

Fig. 4.21. Comparison of model results for sensitivity case without adsorption/desorption and base model, showing aqueous Pb (left) and As (right) concentration profiles along x at y=0 after 1 year of CO_2 intrusion.

We may conclude that adsorption/desorption processes are extremely important when predicting changes in aqueous concentrations of Pb and As (for the given mineralogical composition). Incorporation of these processes has two main effects: (1) initially sorbed matter will be released as pH changes, leading to increased concentration of Pb and As near the intrusion zone, and (2) adsorption of dissolved or desorbed mass tends to stabilize its downstream concentration. Compared to the relatively slow dissolution rate of galena or arsenopyrite, desorption acts much more rapidly, leading to increased local Pb or As concentrations.

4.6.1.2 Sensitivity Run with Lower Site Density

The role adsorption/desorption plays in the mobilization of hazardous constituents depends strongly on the total number of adsorption sites, which is the product of adsorption-site density and specific surface area of mineral. In the base run, illite is the most important mineral that adsorbs or desorbs both Pb and As. In the base model, the specific surface area (66.8 m^2/g) and site density (1.3×10^{-6} mol/m^2 for strong sites and 2.27×10^{-6} mol/m^2 for weak sites) for this mineral are taken from Gu and Evans (2007). However, Lackovic et al. (2003) pointed out that surface properties vary widely for illites from different sources. To study the effect of uncertainties of surface properties of illite on the evolution of Pb and As after CO_2 intrusion, we use the published site density (2×10^{-7} mol/m^2 for strong sites and 6×10^{-7} mol/m^2 for weak sites) from Lackovic et al. (2003) in the sensitivity run.

In the current simulation, the chemical evolution of Pb depends on the dynamic balance of galena dissolution/precipitation and adsorption/desorption from mineral surfaces. If these two processes are considered separately, the increase in acidity triggers desorption as well as galena dissolution. In a coupled system, however, depending on the respective geochemical parameters, desorption may release sufficient Pb to the aqueous phase to precipitate galena, or in contrast, when galena dissolution may release sufficient Pb to the aqueous phase, such that adsorption takes place. In the base model, galena precipitates (Figure 4.22 right) because desorption of Pb from illite surface releases sufficient Pb such that the solution becomes supersaturated with respect to galena. In the sensitivity run, because the site density on illite is much smaller, the mass of Pb released from adsorption sites decreases correspondingly, the solution becomes undersaturated with respect to galena, and thus dissolution of this mineral occurs (Figure 4.22 left).

Figure 4.23 shows the spatial distribution of aqueous Pb at different times, exhibiting a very complex transient behavior. The aqueous Pb concentration actually decreases during the first two years, although galena dissolves and desorption occurs. This is because dissociation of important aqueous complexes affects the early-time aqueous concentration of Pb. Remember that at initial conditions, Pb^{+2} and $PbCO_3(aq)$ account for only 0.02% and 1% of the total aqueous Pb,

respectively, while PbS(aq) accounts for about 85% (see Table 4.4). When the solution becomes more acidic, the complexation of $PbCO_3$(aq) tends to generate an increase of aqueous Pb, whereas the dissociation of PbS(aq) tends to work against an increase of aqueous Pb, both of which are assumed to be equilibrium reactions in TOUGHREACT. The dissociation of PbS(aq) does not increase the total aqueous Pb, but releases Pb^{+2}, which is adsorbed on mineral surfaces, leading to a decrease in total aqueous Pb. Since this decrease is initially not fully compensated by the dissolution of galena, we observe a decrease of total aqueous Pb concentration in the two-zone (Figure 4.23 left), which migrates downstream with time (Figure 4.23 right, 5 and 20 years). As time progresses, the long-term effect of dissolution of galena eventually surpasses the short-term effect of dissociation of PbS(aq). We observe an increase in aqueous Pb concentration with peaks in the two-phase zone and an elevated Pb concentration downstream, which is about two times the initial concentration.

Figure 4.24 (left) shows the time evolution of total aqueous Pb concentration measured at the CO_2 intrusion location. The early concentration decrease during the first two years is followed by a gradual increase up to the peak concentration observed in the profile plots. This early-time transient behavior is controlled by the complex interaction of the dissociation of PbS(aq), adsorption of Pb^{+2} onto mineral surfaces, dissolution of galena, transport of all Pb species downstream, all of which are affected by a gradually increasing partial pressure of CO_2. (The partial pressure of CO_2 increases slowly until a two-phase zone forms after about 3 years—see Figures 4.2 and 4.3.) Figures 4.24 (right) shows the total aqueous Pb concentration after 100 years for the sensitivity case (in comparison with the base model). The base run leads to much higher Pb concentrations, because desorption is more effective and more Pb is released into solution.

The results for As indicate a simpler behavior than for Pb. Without complex aqueous-dissociation processes occurring, arsenopyrite dissolves in response to pH changes, while adsorption occurs in the two-phase region and desorption takes place further downstream. Because of the lower site density on illite in the sensitivity run, less As is released from adsorption sites, and therefore a lower As concentration is observed in the two-phase zone.

Subsequently, less aqueous As is transported downstream, and the aqueous As concentration is smaller compared to the base model (Figure 4.25).

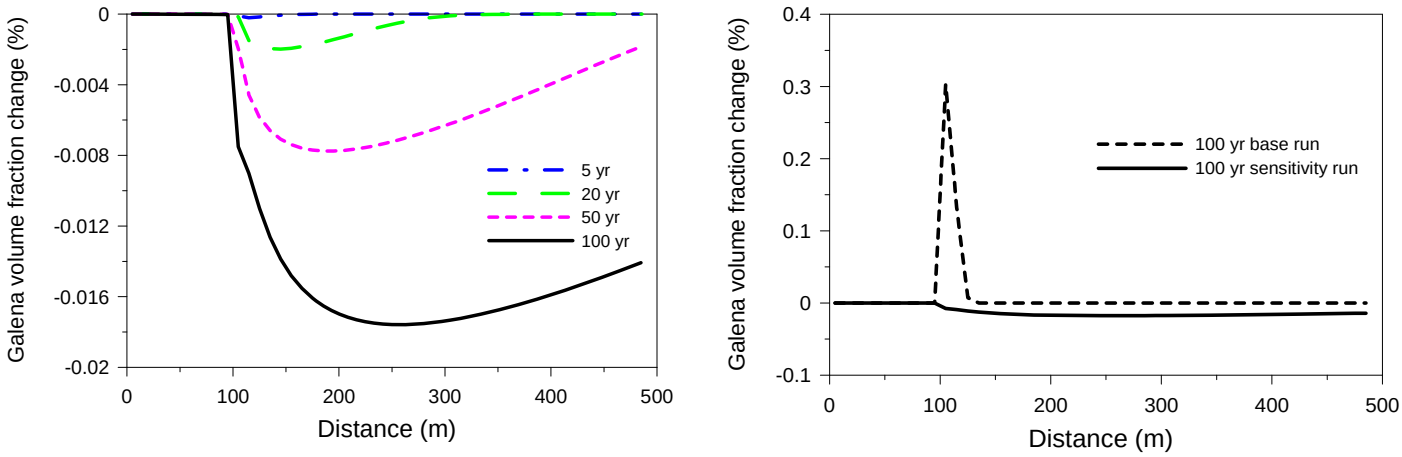

Fig. 4.22. Galena volume fraction change profiles along x-axis at y = 0 m 0 at different times in a sensitivity run with lower site density for illite and comparison of galena volume fraction change profile along x at y=0 after 100 years of CO_2 intrusion with base model (right).

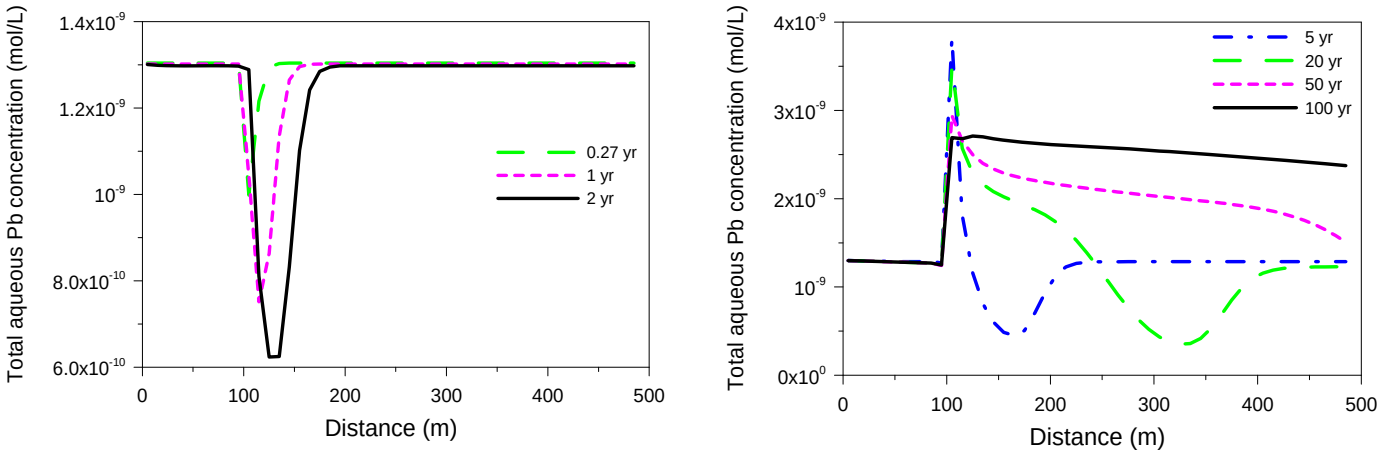

Fig. 4.23. Aqueous Pb concentration profile along x at y=0 at different times in a sensitivity run with lower site density on illite.

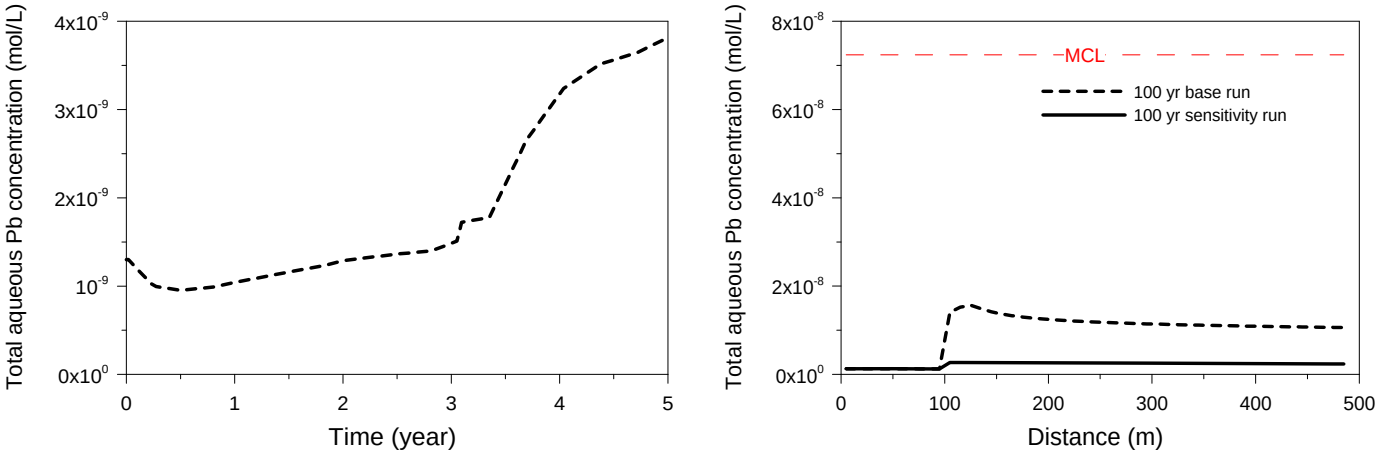

Fig. 4.24. Time evolution of total aqueous Pb concentration at the intrusion location (left) and comparison of model results for total aqueous Pb concentration profile along x at y=0 after 100 years of CO_2 intrusion in sensitivity and base model (right).

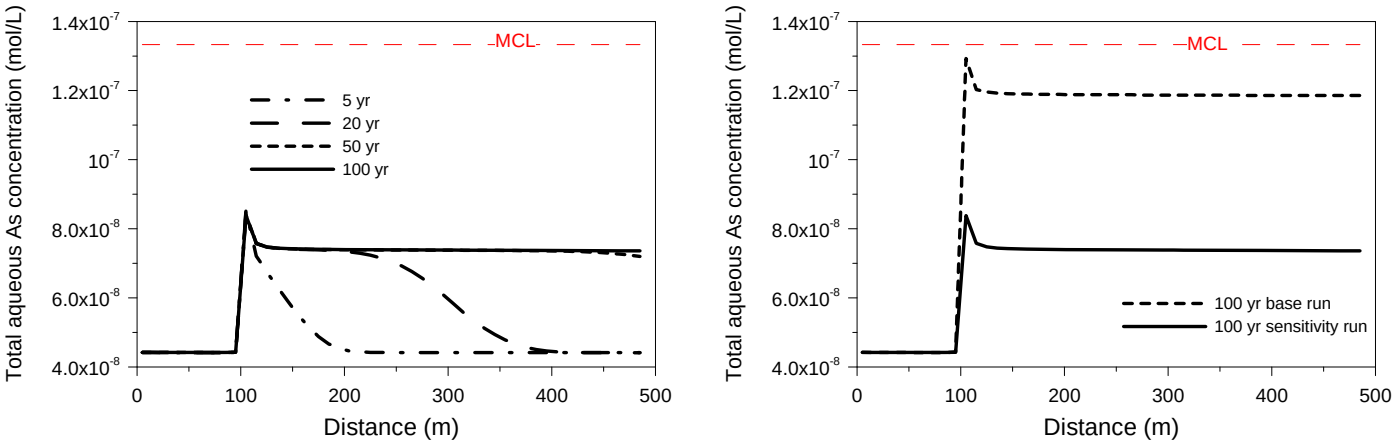

Fig. 4.25. Aqueous As concentration profile along x at y=0 at different time in a sensitivity run with lower site density and comparison of model results of As concentration profile along x at y=0 after 100 years of CO_2 intrusion with base model (right).

The sensitivity run with lower site density reveals to what extent adsorption affects the chemical evolution of Pb and As in relation to the total number of sites on a mineral surface. Overall, decreasing site density lowers aqueous Pb and As concentrations. However, the transient chemical evolution of Pb is affected by a dynamic balance between mineral dissolution, adsorption, and dissociation of aqueous complexes.

4.6.1.3 Sensitivity to Surface Complexation Constant

Illite is considered the most important adsorbent of As in this study, and the following surface complexation reaction

$$Ill\_OHAsO_3^- + H_2O + H^+ \rightleftharpoons Ill\_OH + H_3AsO_3 \qquad (4.5)$$

is most relevant. In the base model, the surface complexation constant (logK) in reaction (4.3) is taken to be -2.12 (Manning and Goldberg, 1997). However, according to Goldberg (2002), the value of the surface complexation constant (logK) may be as low as -3. With this in mind, we conducted a sensitivity run using logK = -3.

Figure 4.26 indicates that the evolution of aqueous As is quite sensitive to the change in the complexation constant. A decreased complexation constant corresponds to less effective adsorption of As and thus a higher aqueous As concentration. It should be noticed that adsorption/desorption is determined as the net effect of surface complexation on different mineral surfaces for different surface complexes. Thus, variation of the constant for one surface complexation reaction changes not only the concentration of its own surface complex, but also the concentration of other surface complexes. For example, when the constant of $Ill\_OHAsO_3^-$ changes from -2.12 to -3, the concentration of $Ill\_OHAsO_3^-$ decreases (Figure 4.27 left), while the concentration of $Ill\_OH_2AsO_3$ increases (Figure 4.27 right). The fact that more As is adsorbed when the constant for reaction 4.3 changes is the result of variation in As related surface complexes on the illite, as well as on other minerals.

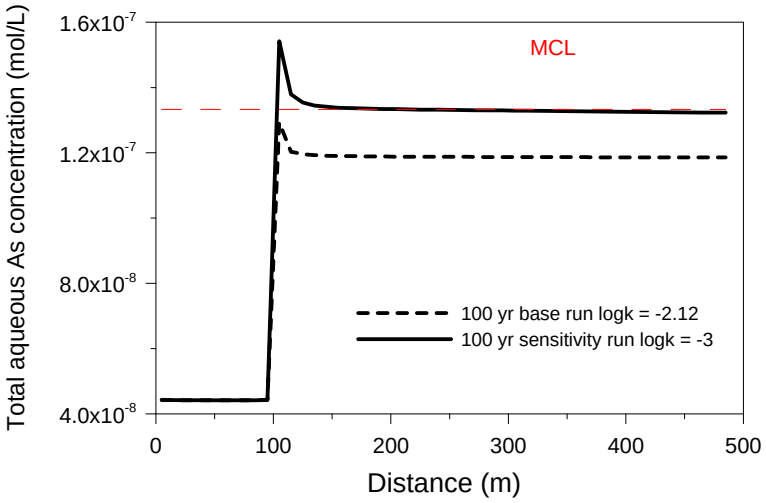

Fig. 4.26. Computed As concentration after 100 years of CO_2 intrusion in a sensitivity run (logK = -3) and base model (logK = -2.12)

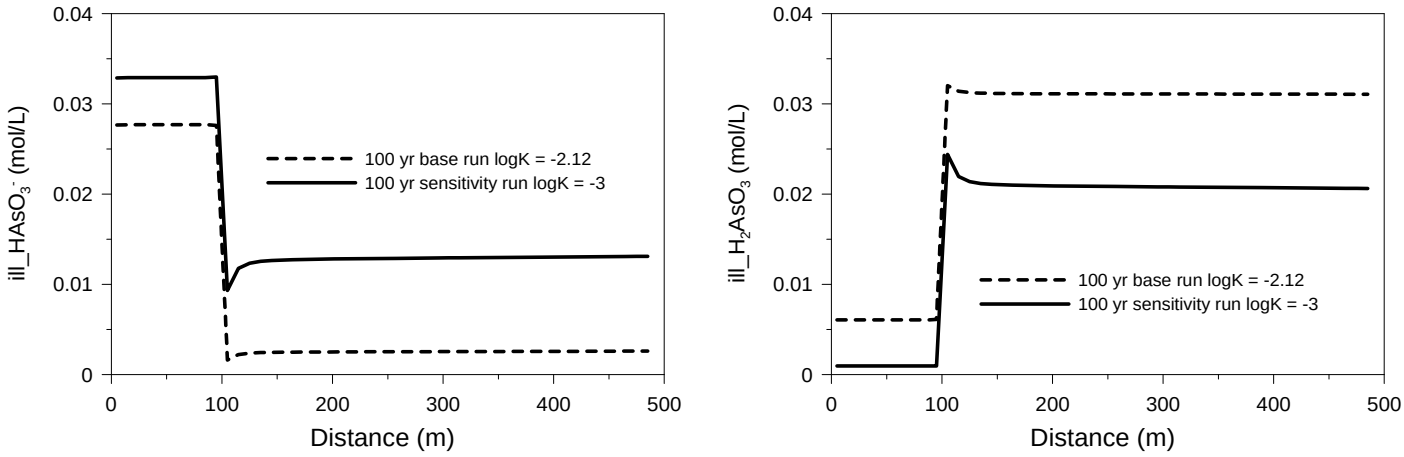

Fig. 4.27. Surface complex Ill _$HAsO_3^-$ (left) and Ill _H_2AsO_3 (right) profiles along the x-axis at y = 0 m, in a sensitivity run (logK = -3) and base model (logK = -2.12).

4.6.2 Sensitivity to Kinetic Rate Parameter

4.6.2.1 Sensitivity to Kinetic Rate Parameter for Galena

In the current model, the dissolution of galena is mainly caused by the increase of acidity as CO_2 intrudes into the aquifer. A literature search for nonoxidative rates of galena dissolution was conducted. Published values, determined by laboratory experiments, vary over several orders of magnitude, with most values obtained at pH less than 4. Zhang et al. (2003) conducted an experiment on dissolution kinetics of galena in 1 mol/L NaCl solutions at pH 0.43–2.45 and 25–75 ^{o}C. The kinetic-rate constant for galena dissolution is given by the equation: $k = 2.34 \times 10^{-7} \alpha_{H^+}$ at 25 ^{o}C. Acero et al. (2007) reported a galena dissolution kinetic-rate constant as: $k = 10^{-5.7 \pm 0.4} e^{\frac{-23 \pm 3}{RT}} a_{H^+}^{0.43 \pm 0.05}$ for pH below 2. Apart from the large variation in measured rates from laboratory experiments, discrepancies between field estimates and laboratory measurements of reaction rates have also been observed, with differences of up to four orders of magnitude (Brantley and Velbel, 1993). These discrepancies may result from a lack of understanding of the reaction mechanism, experimental errors, differences in solution chemistry, inaccuracies in reactive surface area and estimates of water-mineral contact area, temperature variability, or biological activity (Brantley and Velbel, 1993). Note that the kinetic rate (r) is a product of kinetic-rate constant (k) and reactive surface area (A) (see Eq. 4.1). The magnitude of the reactive surface area is also highly uncertain, which further aggravates the uncertainty associated with the kinetic rate.

Sensitivity simulations have been performed to partially address the impact of large uncertainties of the kinetic rate. Below, we have varied the kinetic-rate constant by two orders of magnitude. Because the kinetic rate is a product of the kinetic-rate constant and the reactive surface area, a two-order of magnitude variation of the reactive surface area would lead to the same variation of the kinetic rate; therefore, we have not conducted a separate sensitivity simulation varying the reactive surface area. In the current simulation, the precipitation rate is assumed to be the same as the dissolution rate.

As discussed in Section 4.2 for the base run, galena precipitates rather than dissolves upon intrusion of CO_2. It follows that in the sensitivity run, a lower kinetic rate leads to less precipitation of galena (Figure 4.28 left). Consequently, more aqueous Pb remains in the aqueous phase and the concentration of Pb in the two-phase zone is slightly higher (Figure 4.28 right). Overall, the simulated concentrations of aqueous Pb after 100 years of CO_2 intrusion are rather insensitive to the variation of the kinetic rate, because desorption is the dominant process that controls the evolution of aqueous Pb concentration, effectively dampening the effect of mineral precipitation. In order to illustrate how the kinetic rate would affect the aqueous Pb concentration with less dominant sorption, we also performed two sensitivity simulations varying the kinetic rate constant in the absence of sorption. Without sorption, galena dissolves, causing corresponding increases in aqueous Pb concentrations. An increase in the kinetic-rate constant by two orders of magnitude leads to more effective dissolution, which results in a slight increase of aqueous Pb concentration after 100 years of CO_2 intrusion (see Figure 4.29)

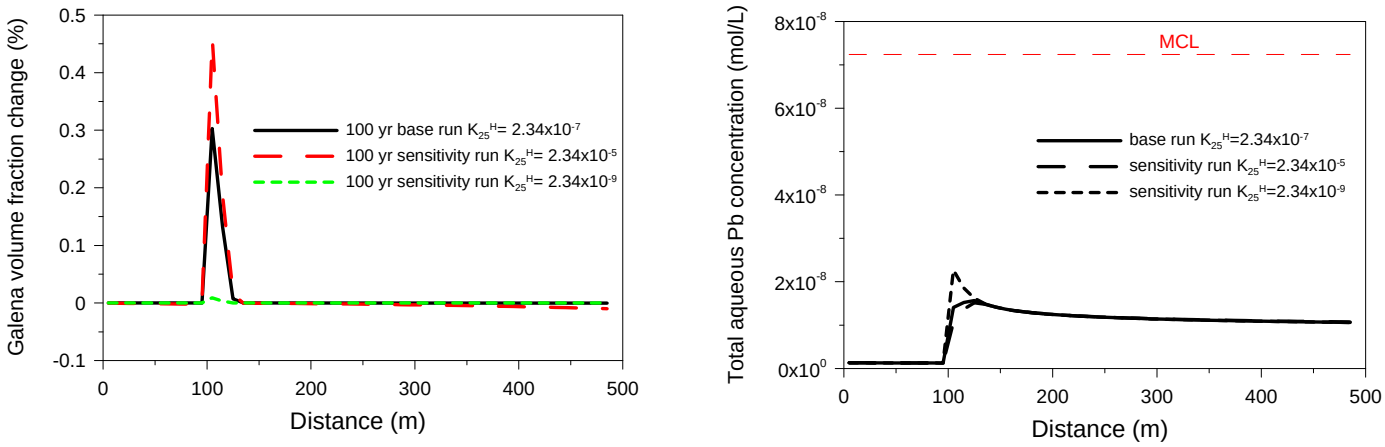

Fig. 4.28. Computed galena volume fraction change (left) and (right) total adsorbed Pb change after 100 years of CO_2 intrusion with different kinetic-rate constant.

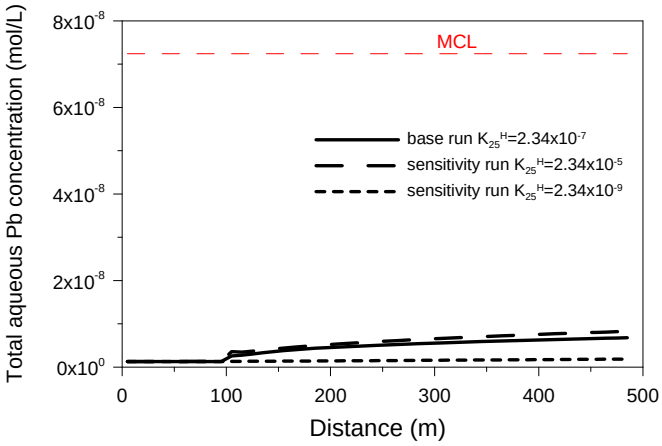

Fig. 4.29. Sensitivity of computed Pb concentration after 100 years of CO_2 intrusion to kinetic-rate constant (k) for simulations without considering sorption.

4.6.2.2 Sensitivity to Kinetic Rate Parameter for Arsenopyrite

Although the kinetic rates of arsenopyrite oxidation have been widely studied (McKibben et al., 2008; Walker et al., 2006; Yu et al., 2007), nonoxidative rates for arsenopyrite dissolution have been rarely reported, and do not permit parameters estimation for the purpose of this study. In the current model, the kinetic-rate constant for arsenopyrite is assumed to be the same as for galena (Zhang et al., 2003). We conducted a sensitivity analysis varying the kinetic-rate constant for arsenopyrite by two orders of magnitude.

Figure 4.30 shows the sensitivity of the resulting aqueous As concentration to the kinetic-rate constant. As discussed in the Section 4.2, while desorption of As from sorption sites and dissolution of arsenopyrite both release As into the aqueous phase, the contribution of dissolution is comparably small in the base run. A decrease of the kinetic-rate constant makes the contribution of dissolution even smaller, only marginally affecting the total release of As. An increase of the rate constant results in increased mobilization of As, which shows in a slightly higher aqueous As concentration. Overall, the model results are rather insensitive to the kinetic rate constant. As with Pb, the dominant process affecting aqueous concentration is adsorption/ desorption rather than precipitation/dissolution. For the purpose of comparison, sensitivity

simulations were conducted for a case without sorption (Figure 4.31). For this case, a two-order-of-magnitude higher kinetic rate leads to a dramatic increase in aqueous As concentration.

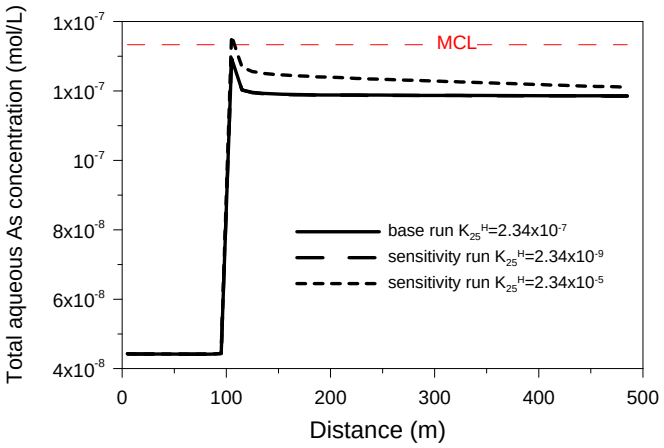

Fig. 4.30. Computed As concentration after 100 years of CO_2 intrusion in sensitivity runs with different kinetic-rate constant (k).

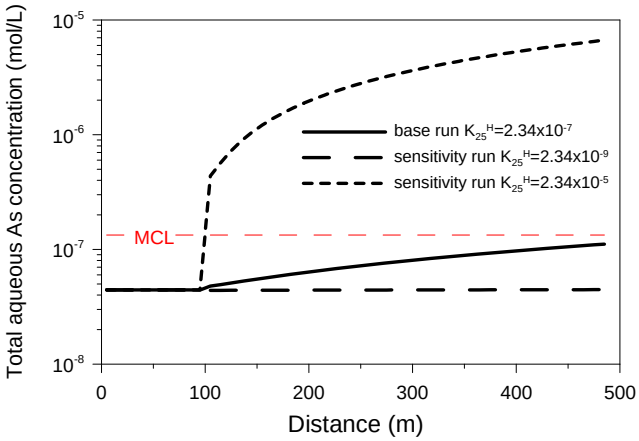

Fig. 4.31. Sensitivity of computed As concentration after 100 years of CO_2 intrusion to rate constant (k) for simulations without considering sorption.

4.6.3 Sensitivity to PbS(aq) Dissociation Constant

As discussed in Sections 4.4 and 3.5.3, PbS(aq) is the most important aqueous complex at ambient (low) partial pressure of CO_2 partial pressure; it accounts for about 85% of the total aqueous Pb at a log$P(CO_2)$ of -2.3. For reasons reported in preceding sections, the existence of Pb sulfide complexes can strongly retard solubility changes of galena when $P(CO_2)$ increases. This result is based on a dissociation constant (logK) of -5.5 for the following reaction:

$$PbS(aq) + H^+ \rightleftharpoons HS^- + Pb^{+2} \qquad \log K = -5.5 \tag{4.6}$$

There is some uncertainty associated with the magnitude of the dissociation constant, as is discussed in Appendix D. Therefore, a sensitivity study to evaluate changes in the magnitude of this constant is called for, which was conducted by changing $\log K_{PbS(aq)}$ by one order of magnitude up and down.

Table 4.10 shows the concentration of some Pb aqueous species obtained from the initial equilibrium run. Variation of $\log K_{PbS(aq)}$ affects the initial concentration of PbS(aq) and also the total Pb concentration, while other important species like Pb^{+2} and $PbCO_3$ (aq) remain the same. When the initially equilibrated system is disturbed as a result of CO_2 intrusion, important processes involved in the evolution of aqueous Pb concentration are association/dissociation of PbS(aq), desorption/adsorption of Pb^{+2}, precipitation of galena, and dissolution of pyrite. Note that precipitation of galena and dissolution of pyrite are both kinetically controlled. In the short term (within the first 2 years), dissolution of pyrite does not produce enough HS^-. Therefore, PbS(aq) dissociates (see Section 4.6.1.1), and the desorption of Pb^{+2} is consequently retarded. In the long term (after 5 years), dissolution of pyrite produces sufficient HS^- so that PbS(aq) associates, and the desorption of Pb^{+2} is accelerated. As a result, the sensitivity case with $\log K_{PbS(aq)}$=-6.5 leads to greater desorption after 100 years of CO_2 intrusion (see Figure 4.32 left), while less galena precipitates, because the association of PbS(aq) retards the precipitation of galena (Figure 4.32 right). In summary, the case with $\log K_{PbS(aq)}$=-6.5 results in more desorption, less galena precipitation, and higher Pb concentration, both initially and after CO_2 intrusion (see Figure 4.33). The opposite behavior can be seen for the case with $\log K_{PbS(aq)}$=-4.5.

Table 4.10. Concentration (in mol/L) of some Pb aqueous species calculated by different dissociation constants of PbS(aq) at initial condition with $\log P(CO_2) = -2.3$

Species	$\log K_{PbS(aq)}$=-5.5	$\log K_{PbS(aq)}$=-6.5	$\log K_{PbS(aq)}$=-4.5
$PbCO_3(aq)$	1.50E-11	1.50E-11	1.50E-11
Pb^{+2}	2.06E-13	2.06E-13	2.06E-13
PbS(aq)	1.11E-09	1.11E-08	1.11E-10
PbSe(aq)	1.83E-10	1.83E-10	1.83E-10
Total Pb	1.30E-09	1.13E-08	3.03E-10

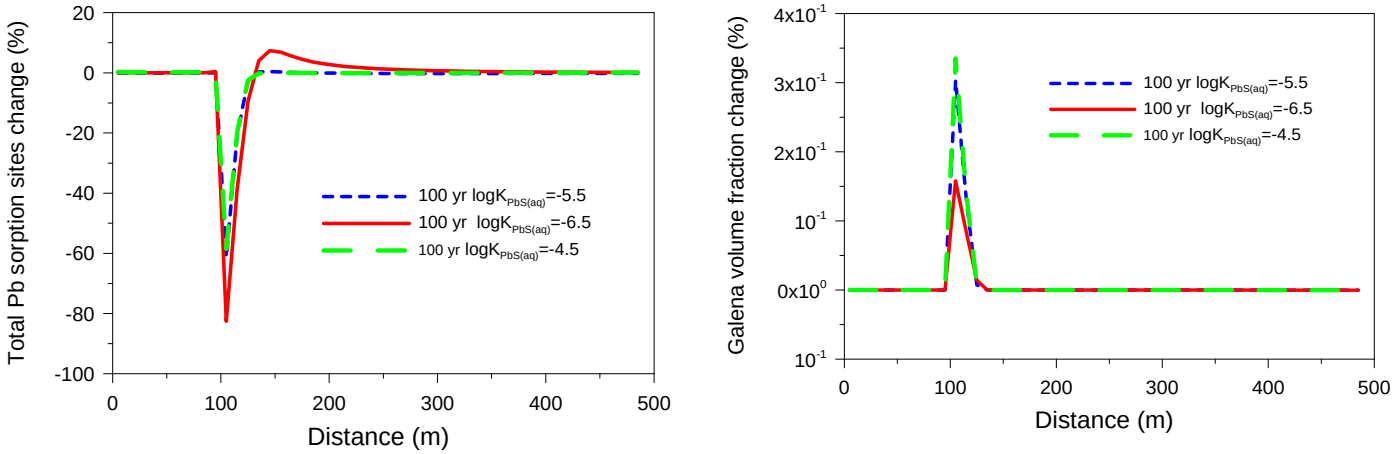

Fig. 4.32. Computed total adsorbed Pb change (left) and galena volume fraction change (right) after 100 years of CO_2 intrusion with different $\log K_{PbS(aq)}$.

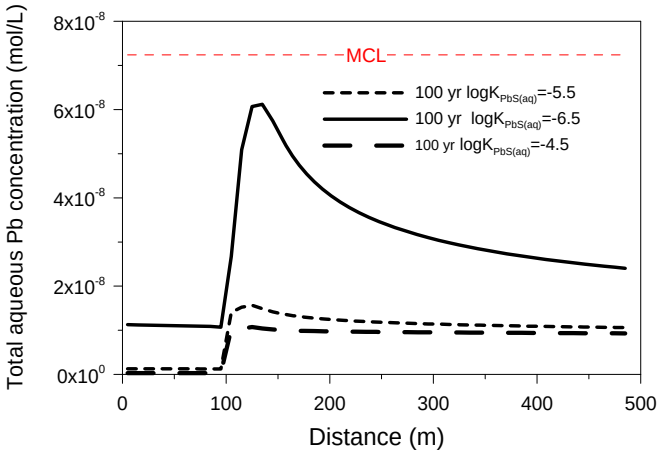

Fig. 4.33. Computed total aqueous Pb concentration after 100 years of CO_2 intrusion with different $\log K_{PbS(aq)}$.

4.6.4 Sensitivity to Mineral Solubility

4.6.4.1 Sensitivity to Solubility of Galena

The solubility of hazardous-constituent-bearing minerals, with galena and arsenopyrite (in solid solution) being the focus in the current model, is the most critical parameter for dissolution-related increases in aqueous concentrations of Pb or As. With this in mind, we conducted a sensitivity run in which the solubility of galena is changed. In TOUGHREACT, the dissolution reaction of galena is written as:

$$PbS + H^+ \rightleftharpoons HS^- + Pb^{+2} \qquad \log K = -14.4 \tag{4.7}$$

The value of logK (-14.4) for reaction (4.5) has been selected based on the thermodynamic analysis conducted in Section 3 (Table 3.13). However, as discussed in detail in Appendix D, published values for logK, derived either from solubility measurements or from thermochemical measurements, show significant discrepancies, which were resolved through consideration of the neutral complex PbS(aq). However, thermochemical data used in the calibration of logK (galena) have uncertainties of ± 1 kcal/mol, which translate into an uncertainty in logK of about 0.5. The MINTEQ (Allison et al., 1991) database cites a logK value for reaction (4.5) of -13.97. In the sensitivity run, we arbitrarily change logK of reaction 4.5 to this value.

As mentioned in Section 4.2, our simulations include two steps: (1) an equilibrium run, establishing the initial equilibrium conditions before CO_2 intrusion and (2) a reactive transport run, simulating the chemical evolution after CO_2 intrusion. Increasing the solubility of galena changes the initial distribution of Pb in the aqueous phase and changes the amount of Pb adsorbed on mineral surfaces. Table 4.11 shows that the initial total aqueous Pb concentration in the sensitivity run is higher (by a factor of 2.5) than that in the base model. What should be mentioned here is that the initial Pb concentration on adsorption sites for a given mineral surface (for example, illite) is affected by the initial aqueous concentration of the corresponding ion (Pb^{+2}) as well as other ions (for example, H_3AsO_3(aq)) that participate in surface complexation reactions on this mineral surface (for example, $ill^s\_OPb^+$). In this sensitivity run, the initial total

number of Pb adsorption sites is higher, because the initial aqueous concentration of Pb^{+2} is higher. Consequently, more desorption occurs in the sensitivity run (see Figure 4.34 left), and the simulated total aqueous Pb concentration is significantly higher than that in the base run (see Figure 4.34 right), but still does not exceed the MCL.

Table 4.11. Concentration (in mol/L) of some Pb aqueous species after initial equilibrium in base model and in the sensitivity run

Species	Base model	Sensitivity run
PbS(aq)	1.11E-09	2.98E-09
PbSe(aq)	1.83E-10	1.78E-10
$PbCO_3$(aq)	1.77E-11	4.77E-11
Pb^{+2}	2E-13	5.5E-13
Total aqueous Pb	1.30E-09	3.21E-09
Total adsorbed Pb	5.09E-6	1.36E-5

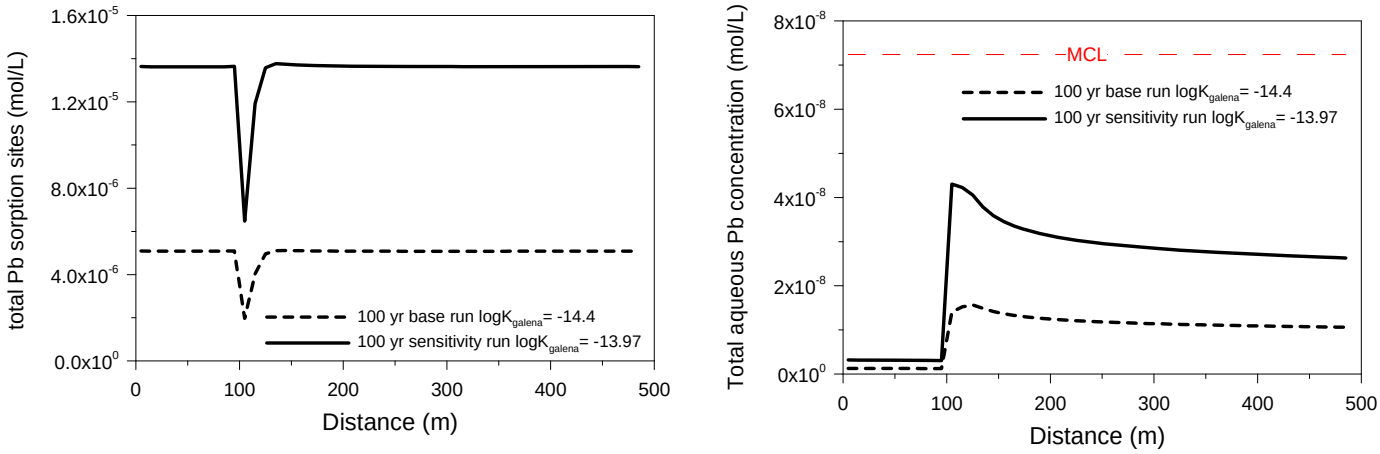

Fig. 4.34. Computed total adsorbed Pb (left) and aqueous Pb concentration (right) after 100 years of CO_2 intrusion in sensitivity run (logK galena = -13.97) and base model (logK galena = -14.4)

4.6.4.2 Sensitivity to Solubility of Arsenopyrite

As pointed out before, the initial As concentration is likely controlled by arsenopyrite in solid solution in pyrite in most groundwaters, based on the evaluation of thermodynamic controls in Section 3.4. Since TOUGHREACT cannot explicitly treat the dissolution of solid solutions, arsenopyrite is instead incorporated in the model as a stand-alone pseudophase, possessing the same properties and stoichiometry as the pure end-member of arsenopyrite, but with a solubility product lowered to reflect the reality that the As is present in solid solution. Considering the uncertainties in the calibration of this solubility product—using measured groundwater analysis from the NWIS database (Section 3.4)—we conducted a sensitivity run in which the base model solubility is reduced by a one-half order of magnitude (from logK = 55.66 to logK = 55.16). Decreasing the solubility of arsenopyrite has two effects. First, the initial total aqueous As concentration is lower, which also causes the total As concentration on adsorption sites to be smaller. In the base model, the initial total aqueous As concentration is 4.4×10^{-8} mol/L and the initial total As concentration on adsorption sites is 3.83×10^{-2} mol/L, whereas the respective values in the sensitivity run are 1.4×10^{-8} mol/L and 3.78×10^{-2} mol/L. Second, the total aqueous As concentration after intrusion of CO_2 is smaller than in the base model, because both desorption from mineral surfaces and dissolution of arsenopyrite are less significant.

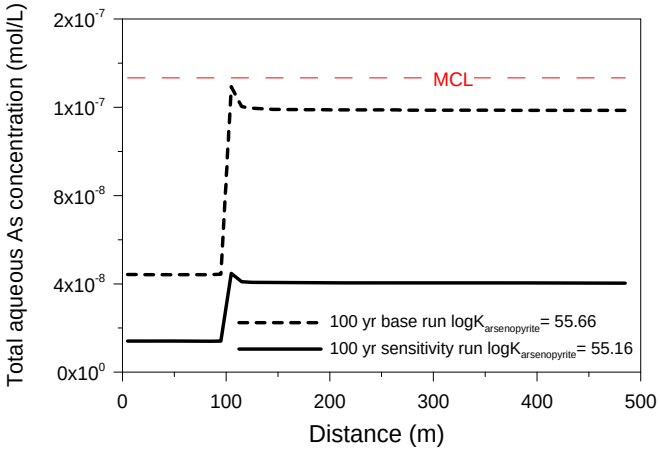

Fig. 4.35. Computed aqueous As concentration after 100 years of CO_2 intrusion in a sensitivity run (logK arsenopyrite = 55.16) and base run (logK arsenopyrite = 55.66)

4.6.5 Sensitivity to Initial Mineral Volume Fraction

4.6.5.1 Sensitivity to Initial Volume Fraction of Galena

In the base model, the initial volume fraction of galena is set to 7.84×10^{-6}, based on the extensive discussion of minor secondary minerals described in Section 3.6.2.2. To account for the possible variability and to understand the impact of an increase in volume fraction, we conducted a sensitivity run with an initial volume fraction for galena of 7.84×10^{-3}. While this is three orders of magnitude larger than in the base model, the volume fraction is still much smaller than the unrealistic 50% volume fraction for galena assumed in earlier studies by Wang and Jaffe (2004). The increase in initial volume fraction of galena means not only that a larger amount of galena is available for dissolution, but also that the dissolution kinetics change, through an assumed increase in reactive surface area. However, as shown in Figure 4.36, the total aqueous Pb concentrations at 100 years are not sensitive to the volume fraction of galena. As discussed in Section 4.5.2, the dominant process for increasing aqueous Pb concentrations is desorption rather than galena dissolution, which explain why galena volume changes, within reasonable ranges reflecting natural variability, have no significant impact.

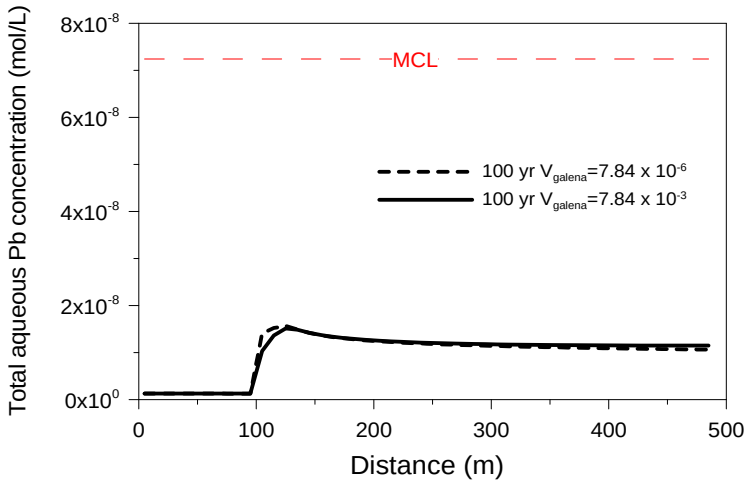

Fig. 4.36. Sensitivity of total aqueous Pb concentration after 100 years along the x-axis at y = 0 m to the initial volume fraction of galena.

4.6.5.2 Sensitivity to Initial Volume Fraction of Arsenopyrite

The volume fraction of arsenopyrite used in the model is based on the mean abundance of As in soils and sediments, as reported by the National Geochemistry Survey database of the USGS, and used as a proxy for As abundance in aquifer host rocks (Section 3.6.2.2). It is furthermore assumed, as pointed out before, that arsenopyrite occurs in solid solution in pyrite. The volume fraction of arsenopyrite is therefore that of the FeAsS component in pyrite with an assumed ideal partial molar volume of unity. To account for variability and uncertainty in the magnitude of the volume fraction of arsenopyrite, we have increased the value chosen in the base model by two orders of magnitude, from about 9×10^{-6} to about 9×10^{-3}. The increase in initial volume fraction of arsenopyrite means not only that a larger amount of arsenopyrite is available for dissolution, but also that the dissolution kinetics change, through an assumed increase in reactive surface area. Figure 4.37 shows that the total aqueous As concentrations are moderately sensitive to the volume fraction of arsenopyrite. Increasing the volume fraction of arsenopyrite leads to faster dissolution of arsenopyrite and, thus, the sensitivity results arrive at higher aqueous As concentrations after 100 years. The reason that As concentrations are affected by a change in the volume fraction of its solubility-controlling mineral host, while Pb concentrations are not (see earlier section), has been given before. Pb concentration increases are caused by desorption (while galena actually precipitates instead of dissolving), whereas As concentration increases are generated from both desorption and dissolution of arsenopyrite.

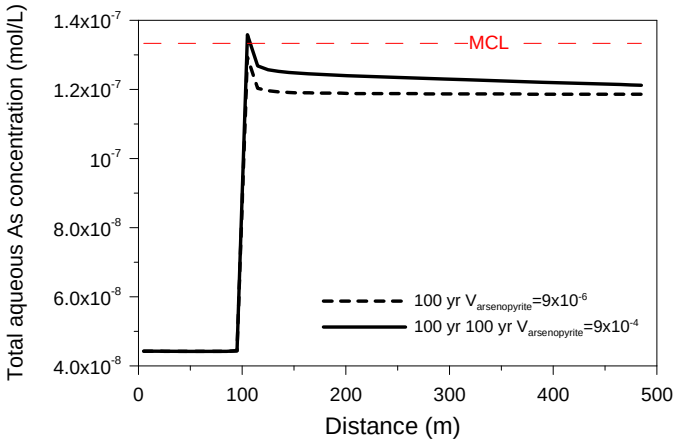

Fig. 4.37. Sensitivity of total aqueous As concentration after 100 years along the x-axis at y = 0 m to the initial volume fraction of arsenopyrite.

4.6.6 Sensitivity to Initial Partial Pressure of CO_2

In the base model, the initial chemical composition is in equilibrium with a specified CO_2 partial pressure around 0.005 bar (which corresponds to a Log P(CO_2) value of -2.3). The specified value falls into the medium range of measured CO_2 partial pressures calculated from the groundwater database analysis (Section 3.4.3, Figure 3.17). The high end of these measured CO_2 partial pressures is on the order of –1.5 in Log P(CO_2). To evaluate the impact of the higher initial partial pressure of CO_2 in the groundwater, we conducted a sensitivity study using this high-end value of -1.5. First, a equilibrium run was carried out to establish the initial chemical composition, and then a reactive transport simulation was conducted, modeling the ingress of CO_2 into the equilibrated system.

Table 4.12 shows the initial chemical composition in equilibrium with a Log P(CO_2) value to be –1.5. The increase of initial partial pressure of CO_2 results in a higher bicarbonate concentration and a lower pH. Consistent with the equilibrium analysis in Section 3.5 and the trends shown in Figure 3.51, the total aqueous Pb concentration increases slightly compared to the base model, due to the increase in $PbCO_3$(aq), while the initial As concentration in equilibrium with a Log P(CO_2) value of –1.5 is significantly higher. In fact, the equilibrium concentration for As is approximately 1.4×10^{-7} mol/L, which exceeds the MCL of 1.33×10^{-7} mol/L (or 10 ppb). It is possible that samples with elevated ambient CO_2 concentrations could be responsible for some occurrences of high As concentrations in groundwaters, as shown in Figure 3.6(b).

We shall now compare the Pb concentration profiles for base model and sensitivity run at 100 years of CO_2 intrusion, shown in Figures 4.34. In the base model (initial Log P(CO_2) = -2.3), the Pb concentration increases with the ingress of CO_2 from 1.3×10^{-10} mol/L to about 1.57×10^{-8} mol/L in the two-phase zone near the intrusion location, and to about 1.1×10^{-8} mol/L downstream. In the sensitivity run (initial Log P(CO_2) = -1.5), the aqueous Pb concentration increases from initially 1.4×10^{-9} mol/L to about 1.55×10^{-8} mol/L near the intrusion location and to 1.15×10^{-8} mol/L downstream. Thus, in absolute values, the situation after CO_2 intrusion is

almost identical in both cases; only the starting point is slightly different, owing to differences in the initial Pb concentration (Figure 4.38).

Table 4.12. Initial chemical composition (mol/L) of groundwater in equilibrium with partial pressures of -2.3 (base model) and -1.5 (sensitivity run) in Log $P(CO_2)$

Species	**Partial pressure of CO_2 Log $P(CO_2)$ = -2.3**	**Partial pressure of CO_2 Log $P(CO_2)$ = - 1.5**
Eh	-0.215 (volt)	-0.195 (volt)
pH	7.61	7.36
Ca	9.00E-04	4.98E-04
Mg	2.17E-05	9.62E-05
Na	1.97E-03	1.97E-03
K	2.68E-04	3.85E-04
Fe	5.63E-06	2.31E-05
Si	9.31E-04	9.18E-04
TIC	3.33E-03	1.26E-02
SO_4^{-2}	1.95E-04	1.92E-04
HS^-	1.44E-08	1.36E-08
Al	4.19E-11	2.92E-11
Cl	2.07E-04	2.07E-04
P	1.78E-06	6.72E-06
Pb	1.30E-09	1.40E-09
As	4.42E-08	1.43E-07
Ba	1.04E-07	1.04E-07
Hg	8.37E-10	9.77E-10
Sb	2.10E-09	2.05E-09
U	7.18E-11	4.18E-11
Zn	1.15E-08	1.22E-08
Se	1.72E-09	1.86E-09
Cd	1.80E-09	1.29E-09

As mentioned before, the increase in Pb concentration caused by CO_2 intrusion is mainly controlled by two processes: adsorption/desorption of Pb on adsorption sites and galena precipitation/dissolution. Although the aqueous Pb concentrations after 100 years are almost

identical in the two simulation cases, the underlying processes affecting them differ somewhat. The total Pb concentration on adsorption sites is lower in the sensitivity run (see Figure 4.39 left), because of the smaller concentration of $ill^{w}\_OPb^{+}$ (Figure 4.39 right). Less desorption in the sensitivity run induces less precipitation of galena (see Figure 4.40 left), while the computed pH is similar in both cases (Figure 4.40 right).

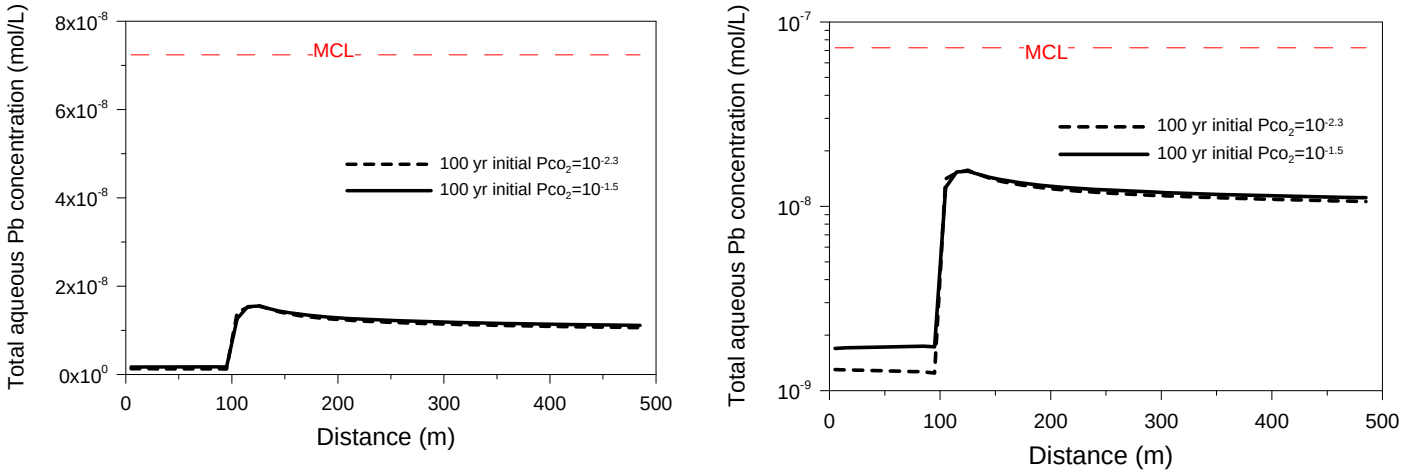

Fig. 4.38. Sensitivity of Pb concentration to initial partial pressure of CO_2. The figure on the right is the same as the one on the left but in semi-log scale.

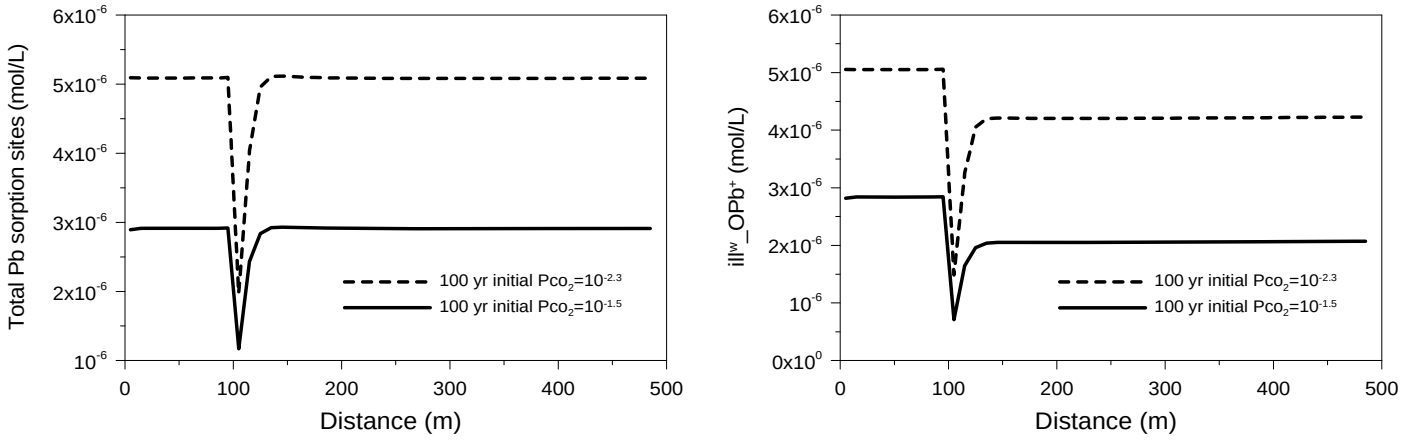

Fig. 4.39. Total Pb concentration on adsorption sites (left) and concentration of $ill^{w}\_OPb^{+}$ (right) along x-axis at y = 0 m in the base and sensitivity run.

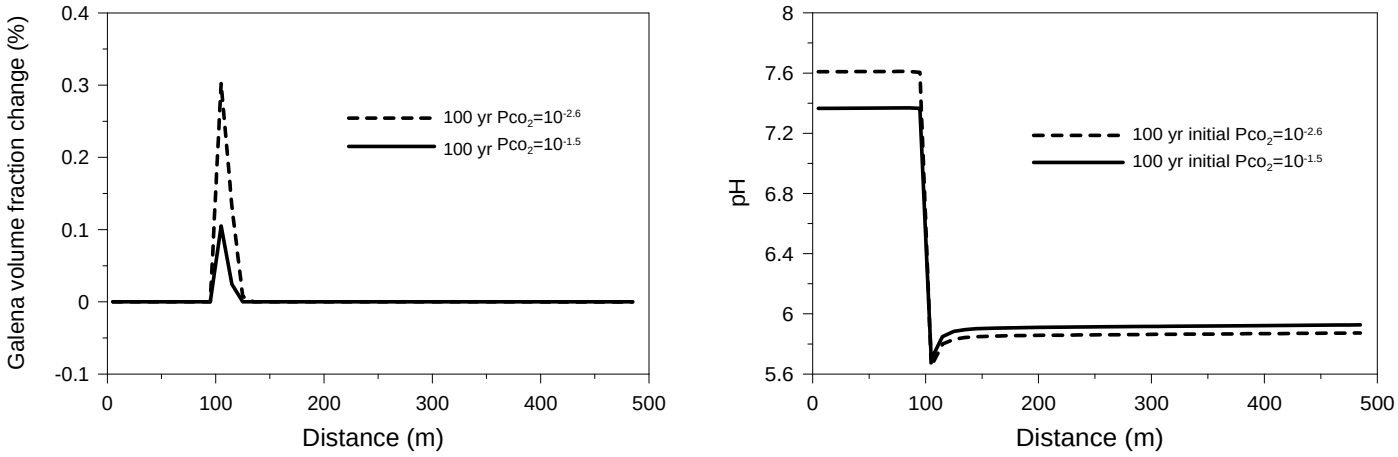

Fig. 4.40. Galena volume fraction change (left) and pH (right) along x-axis at y = 0 m in the base and sensitivity run.

Figure 4.41 shows concentration profiles of total aqueous As after 100 years in the sensitivity run (initial Log $P(CO_2)$ = -1.5) and the base run (initial Log $P(CO_2)$ = -1.5). The increase in initial Log $P(CO_2)$ results in increases of comparable magnitude in both the initial As concentration and the final As concentration after intrusion of CO_2. Thus, the main difference between the two simulation cases is the initial As concentration, which is much higher in the sensitivity run using a Log $P(CO_2)$ of -1.5. As mentioned above, the initial As concentration is already higher than the MCL; the ingress of CO_2 leads to a further increase (Figure 4.41).

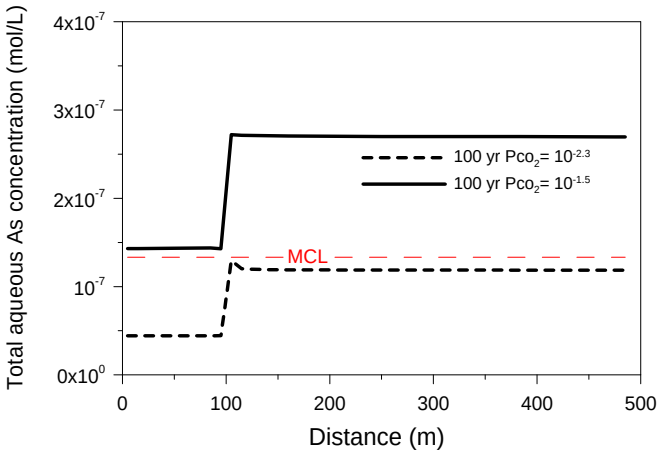

Fig. 4.41. Sensitivity of As concentration to initial partial pressure of CO_2.

4.6.7 Sensitivity to Initial Fluid Pressure (Depth of Aquifer)

In the base model, the initial pressure in the aquifer is set to 5 bar, corresponding to an aquifer at a depth of about 50 m. Because the solubility of CO_2 in water is a function of CO_2 partial pressure, a change in the initial aquifer pressure controls, upon intrusion of CO_2, how much of the gaseous CO_2 dissolves in the groundwater (and may affect pH) versus how much remains in gas phase and migrates under buoyant forces. In a shallower aquifer, the maximum amount of dissolved CO_2 would be smaller than in a deeper aquifer, and vice versa. To understand the implications of this dependence, we conducted a sensitivity run assuming CO_2 intrusion at 3 bar initial pressure (i.e., equivalent to an aquifer depth of about 30 m). All other model assumptions and parameters are identical to the base model.

Figure 4.42 shows a slightly larger two-phase zone forms in the sensitivity run with a slightly higher gas saturation (Figure 4.42 left), while less CO_2 is dissolved in the water (Figure 4.42 right). As a result, the pH obtained in the sensitivity run (fluid pressure of 3 bar) is higher than in the base run (Figure 4.43). Consequently, the Pb and As concentrations (Figure 4.40) observed after 100 years of CO_2 intrusion are slightly lower in the sensitivity run due, in the case of Pb, not only to the higher pH, but also to less complexing of dissolved CO_2 with Pb^{+2}. In summary, the geochemical impact of CO_2 intrusion into a drinking water aquifer is moderately affected by initial fluid pressure (or aquifer depth), with smaller effects expected in a shallower aquifer. A drinking water aquifer would have to be significantly deeper (resulting in a higher maximum amount of dissolved CO_2), and a CO_2 would have to leak into the aquifer at a higher rate (resulting in an increase in dissolved CO_2 up to or exceeding the maximum amount) to be exhibit stronger effects from CO_2 intrusion and related pH changes.

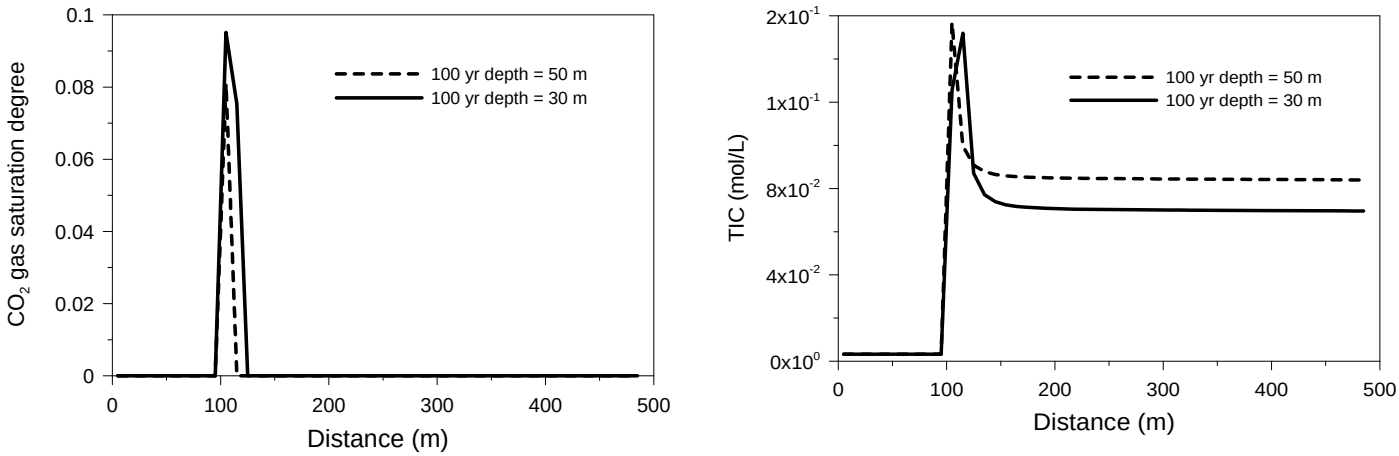

Fig. 4.42. Sensitivity of CO_2 gas saturation degree (left) and total inorganic carbon (TIC) to the depth of aquifer.

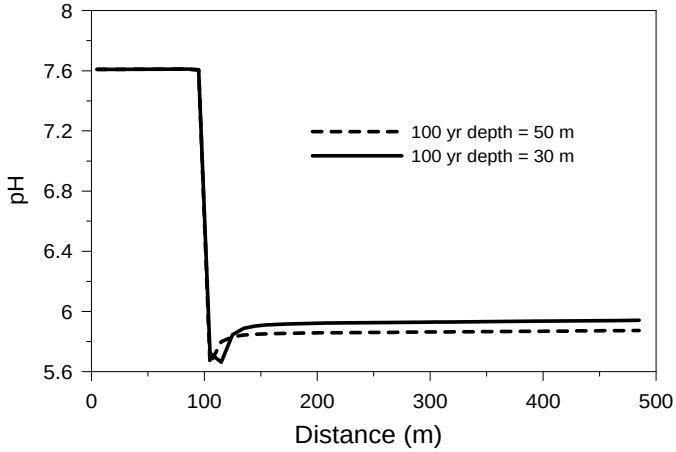

Fig. 4.43. Sensitivity of pH to the depth of aquifer.

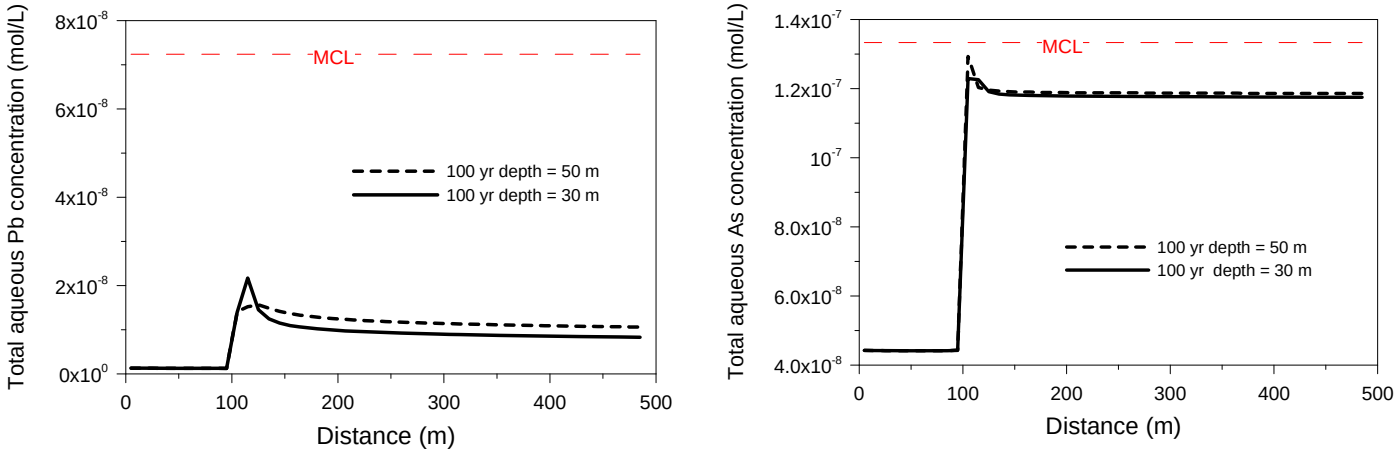

Fig. 4.44. Sensitivity of Pb (left) and As concentration (right) to the depth of aquifer.

4.6.8 Sensitivity to Groundwater Flow Velocity

In all simulation cases conducted so far, we have assumed a groundwater flow velocity of 10 m/year (transport velocity). A sensitivity run with lower flow rate of 1 m/year was performed to study the effect of the groundwater flow conditions on the evolution of hazardous constituents. When the flow velocity decreases (while the CO_2 intrusion rate remains the same), an enlarged two-phase zone is observed compared to the base model (see Figure 4.45). The two-phase zone is larger because less fresh water flows past the intrusion zone and thus less CO_2 can dissolve in the water. The highest CO_2 gas saturation degree is 0.14 in the sensitivity run, whereas in the base run it is 0.08 (Figure 4.47 left). The corresponding area with elevated TIC is larger in the sensitivity run compared to the base run (Figure 4.46 and Figure 4.47 right). Because groundwater flow is much slower, the enhanced TIC front has not advanced sufficiently to intersect the right boundary of the simulated zone after 100 years. (Note that the larger two-phase zone observed in this simulation case raises the question as to whether the assumption of depth-averaged processes remains valid, as the gaseous CO_2 region is more pronounced. We refer to Section 4.9 for a three-dimensional test case to address this issue.)

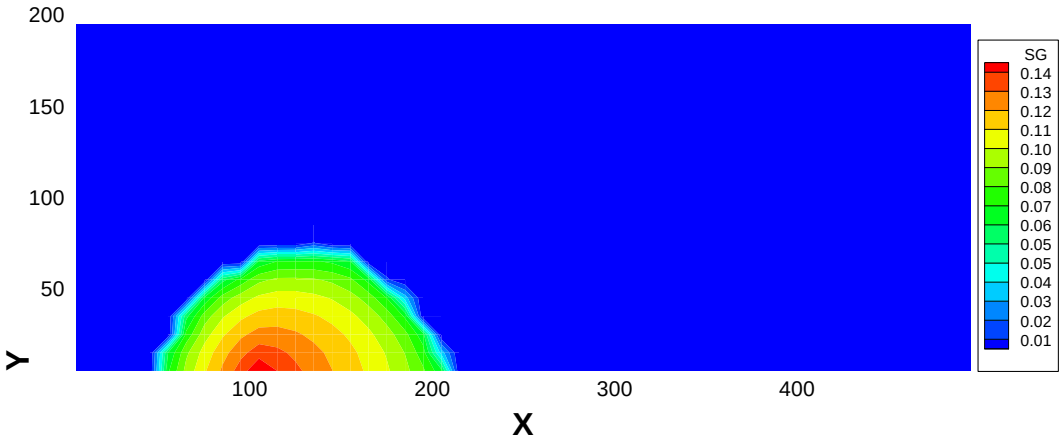

Fig. 4.45. Spatial distribution of saturation of CO_2 in a sensitivity run with flow rate of 1m/year after 100 years of intrusion

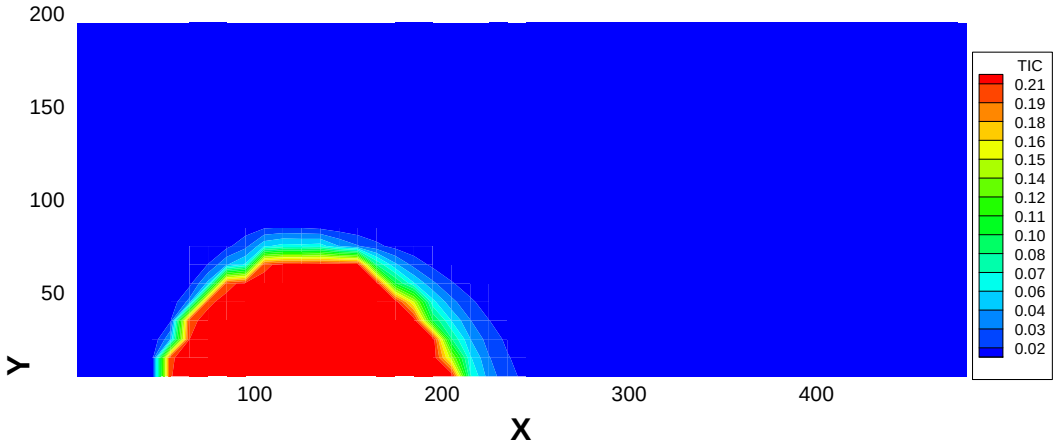

Fig. 4.46. Spatial distribution of TIC in a sensitivity run with flow rate of 1m/year after 100 years of intrusion

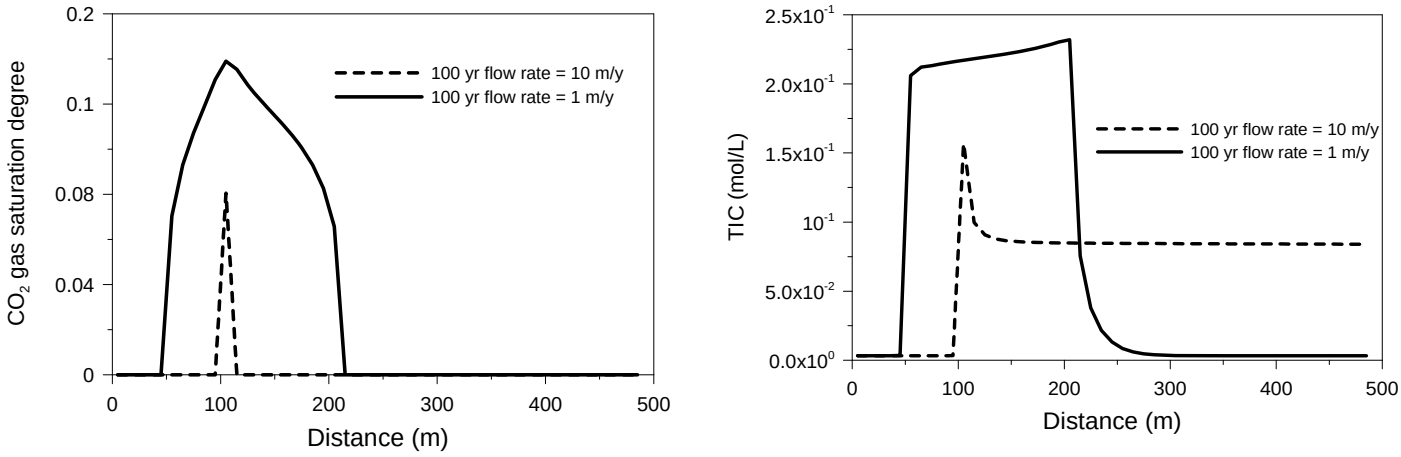

Fig. 4.47. Comparison of CO_2 gas saturation degree (left) and TIC (right) along x-axis at y = 0 m in the sensitivity case and the base run

When the groundwater flow velocity decreases to 1 m/year, diffusion rather than just advection becomes important in controlling the transport of aqueous species. Figure 4.48 (left) shows the evolution of pH at different times. As a result of diffusion, the low pH profile moves not only downstream with the groundwater flow, but also in the upstream direction (right-hand side of the figure). Elevated aqueous Pb and As concentrations correspond to the areas where pH is low (Figure 4.49 and 4.50). We may conclude that for a case with low groundwater velocity, the impact of CO_2 intrusion can be more significant, but is also more localized.

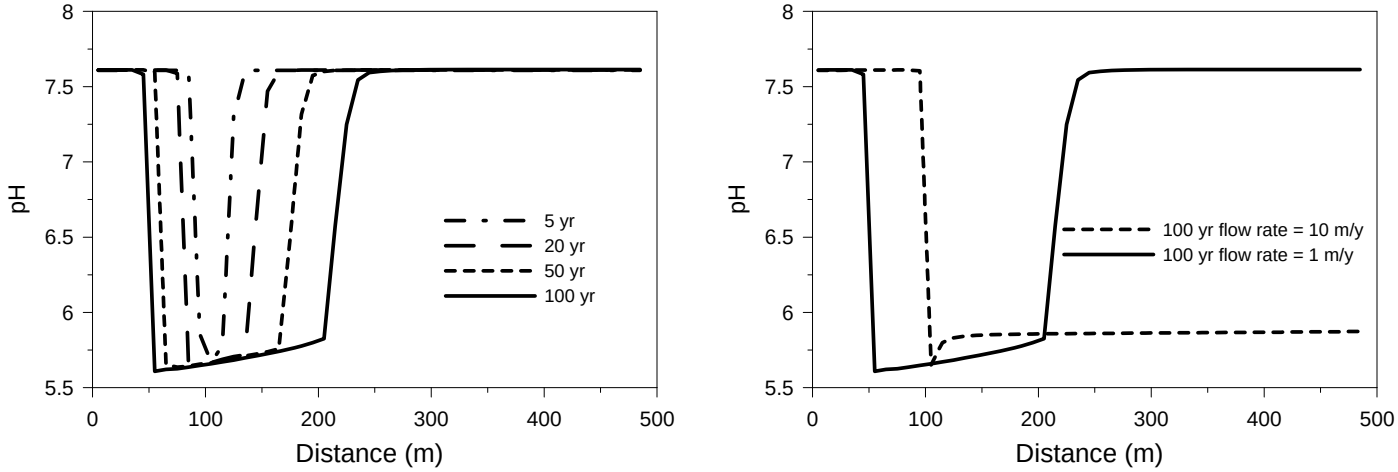

Fig. 4.48. Evolution of pH at different times (left) along the x-axis at y = 0 m where groundwater flow velocity is 1m/year, and sensitivity of pH to groundwater flow velocity after 100 years (right)

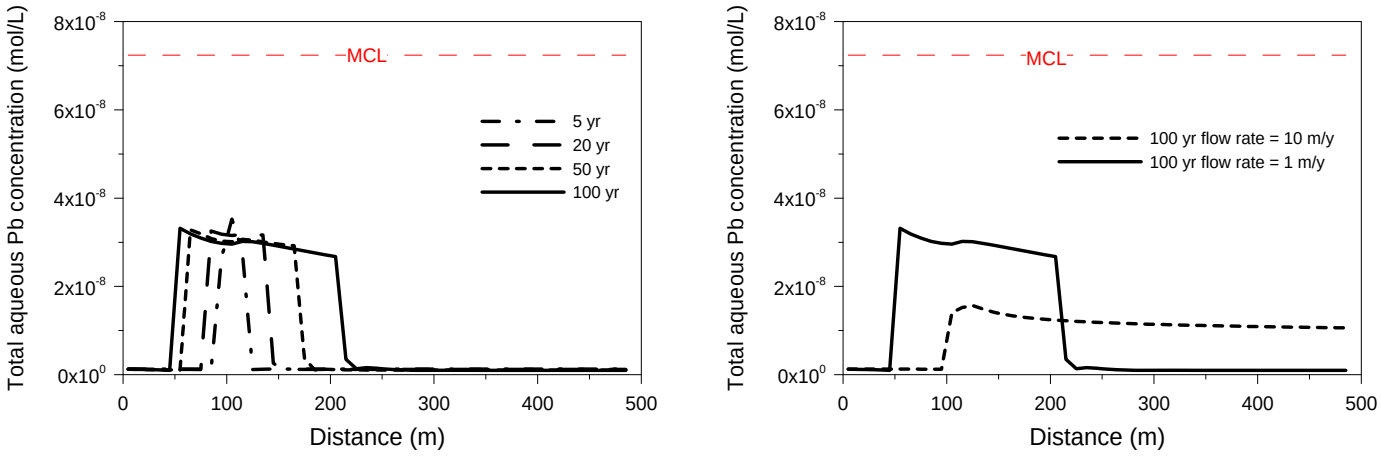

Fig. 4.49. Total aqueous Pb concentration at different times (left) along the x-axis at y = 0 m where groundwater flow velocity is 1m/year, and sensitivity to groundwater flow velocity after 100 years (right)

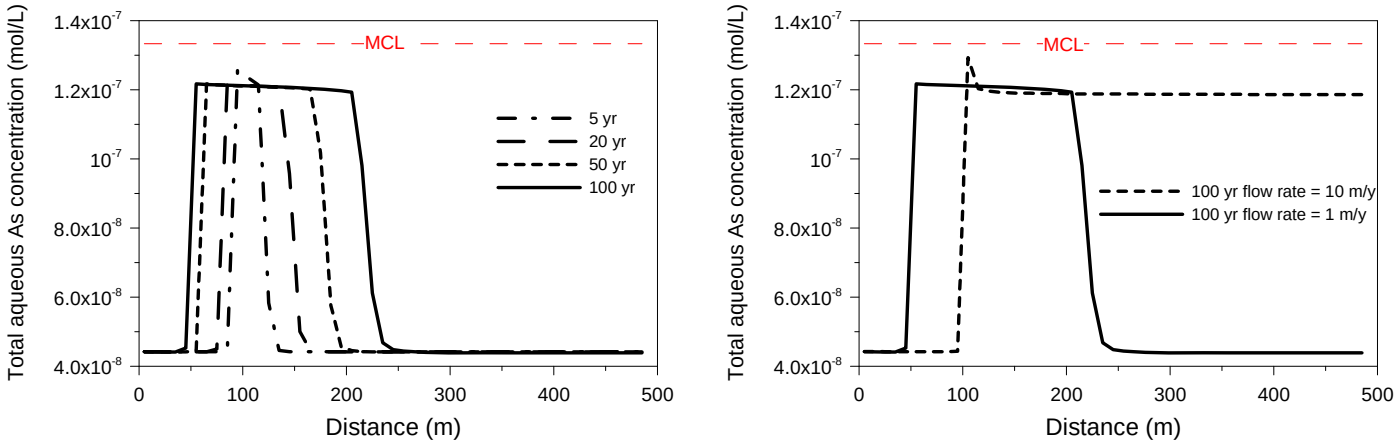

Fig. 4.50. Total aqueous As concentration at different times (left) along x-axis at y = 0 m where groundwater flow velocity is 1m/year and sensitivity to groundwater flow velocity after 100 years (right).

4.6.9 Sensitivity to CO_2 Leakage Rate

The base model assumes a gaseous CO_2 intrusion rate of 7.5×10^{-5} kg/s, which corresponds to 2.36 tonnes of CO_2 per year. This rate was selected based on the amount of CO_2 that can dissolve in the aquifer without forming a large two-phase zone. To understand the implications of more CO_2 leaking into the aquifer, we performed a sensitivity run with a CO_2 intrusion rate of 6×10^{-4} kg/s. When the CO_2 intrusion rate increases, we observe a much larger two-phase region (see Figure 4.51 and Figure 4.53 left) and a correspondingly larger region with elevated TIC (see Figure 4.52 and Figure 4.53, right). As a result, in this two-phase zone, the CO_2 partial pressure is larger than in the base run and the pH is lower (Figure 4.54, right). This pH decrease has implications for the mobilization of hazardous constituents, giving rise to significant increases in aqueous Pb concentrations, (Figure 4.55, right), and moderate increases in As concentrations downstream (Figure 4.56, right). Another reason for the significant increase of total aqueous Pb concentration is that the Pb carbonate aqueous complex, $PbCO_3(aq)$, becomes the most important aqueous species containing Pb. An increase of the carbonate concentration gives rise to an increase of Pb carbonate aqueous complex and thus elevates the total aqueous Pb concentration.

Even more so than in the previous section, the large two-phase zone forming in this sensitivity case implies that the assumption of depth-averaged processes may not be valid for the model being studied. Because of buoyancy, CO_2 would tend to accumulate under the confining layer at the top of the aquifer, possibly bypassing much of the groundwater flow in the aquifer. See Section 4.9 for a three-dimensional simulation of this sensitivity case.

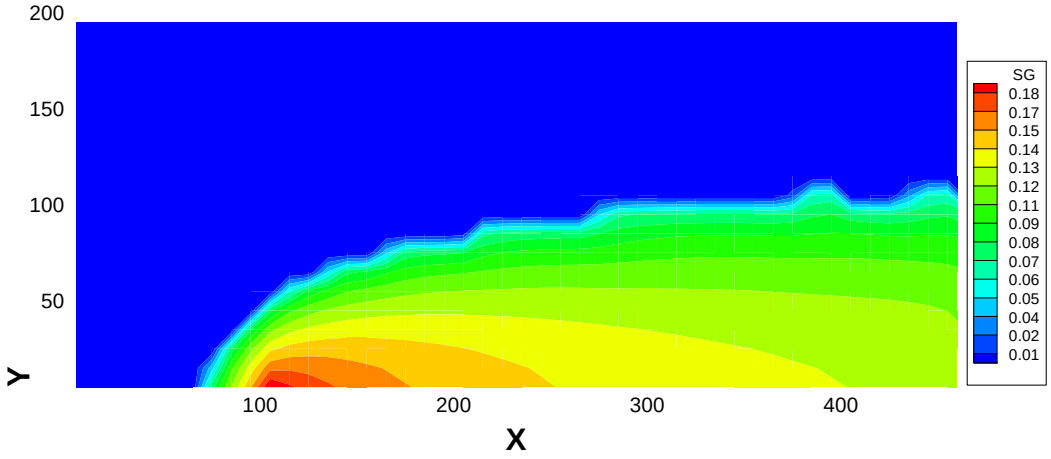

Fig. 4.51. Spatial distribution of saturation for CO_2 in a sensitivity run with CO_2 intrusion rate of 6×10^{-4} kg/s after 100 years of intrusion

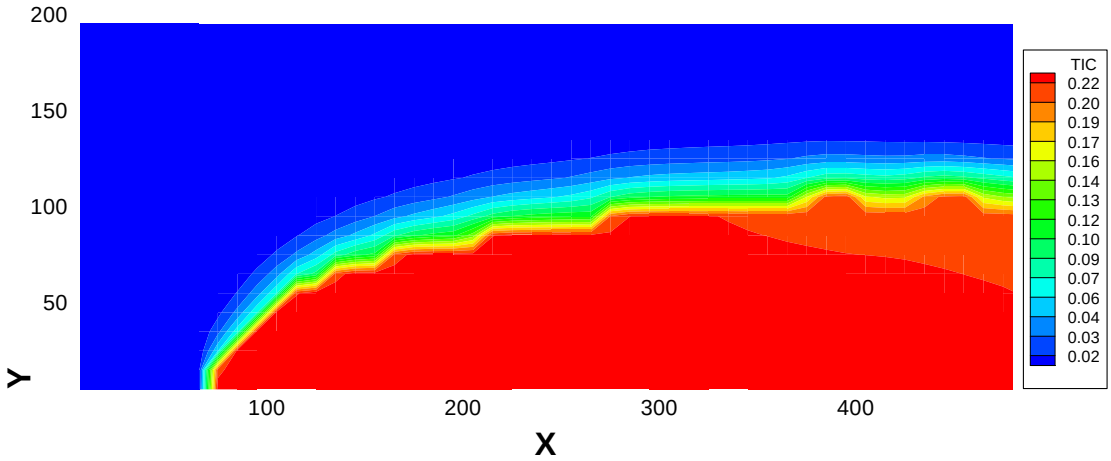

Fig. 4.52. Spatial distribution of TIC in a sensitivity run with CO_2 intrusion rate of 6×10^{-4} kg/s after 100 years of intrusion

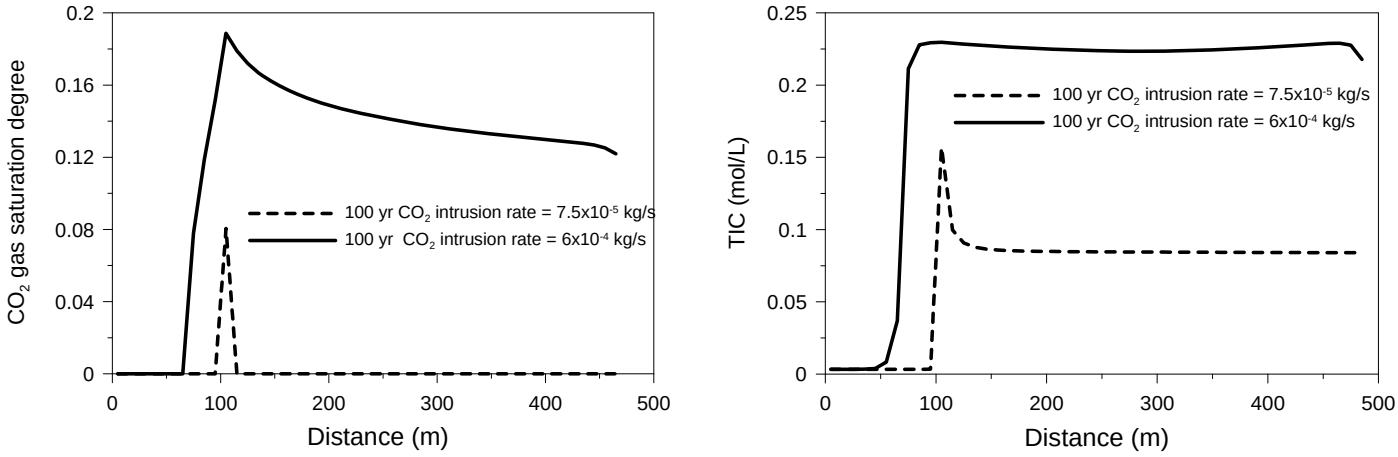

Fig. 4.53. Comparison of CO_2 gas saturation degree (left) and dissolved CO_2 mass fraction (right) along x-axis at y = 0 m in the sensitivity and base run.

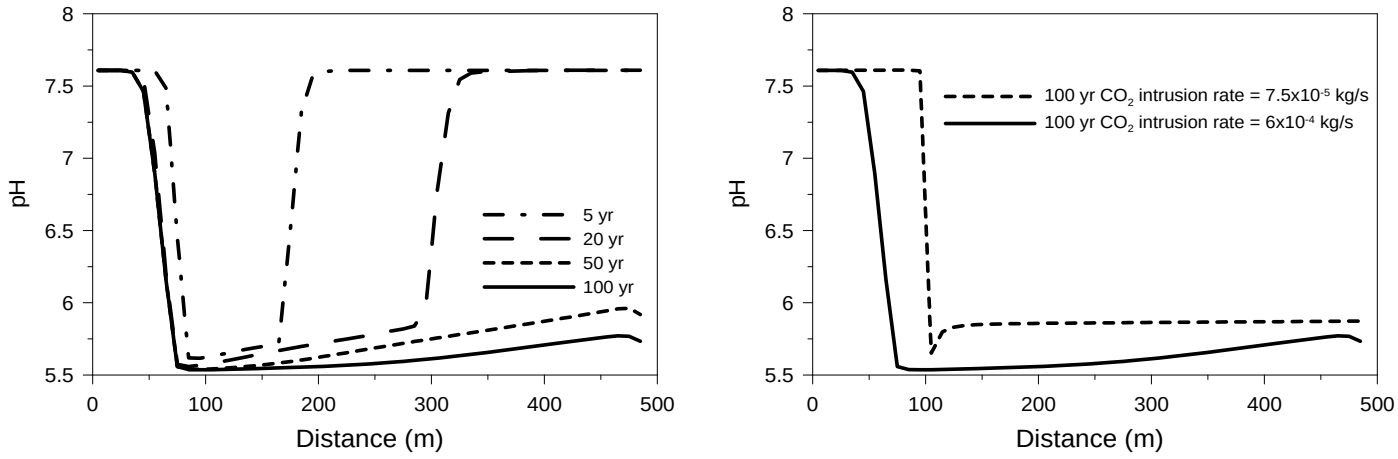

Fig. 4.54. pH evolution at different times (left) along the x-axis at y = 0 m for CO_2 intrusion rate of 6×10^{-4} kg/s, and sensitivity of pH to CO_2 intrusion rate.

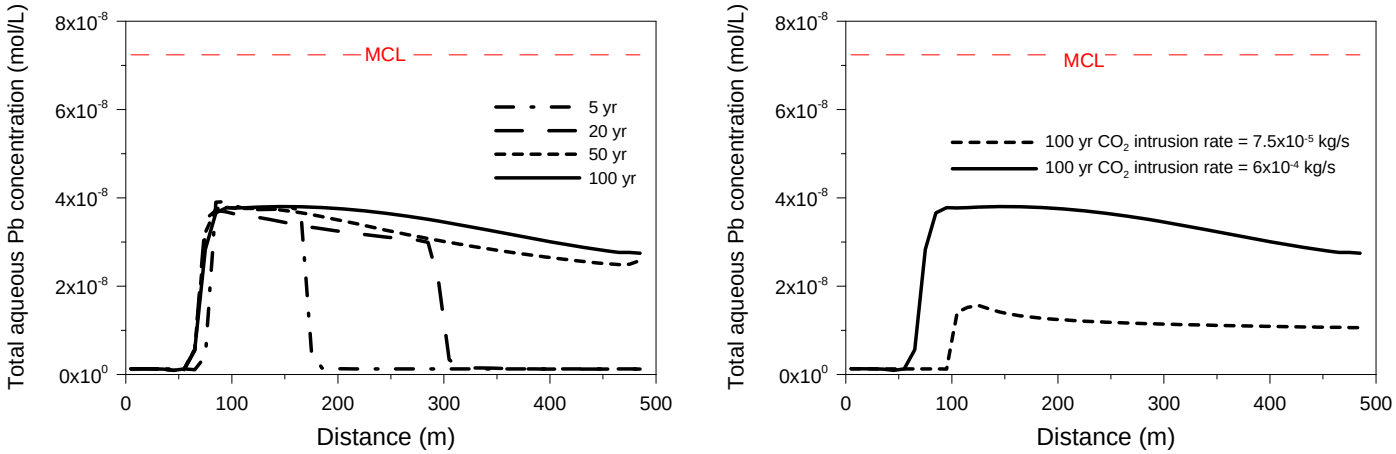

Fig. 4.55. Total aqueous Pb concentration at different times (left) along the x-axis at y = 0 m for CO_2 intrusion rate of 6×10^{-4} kg/s, and sensitivity of Pb concentration to CO_2 intrusion rate.

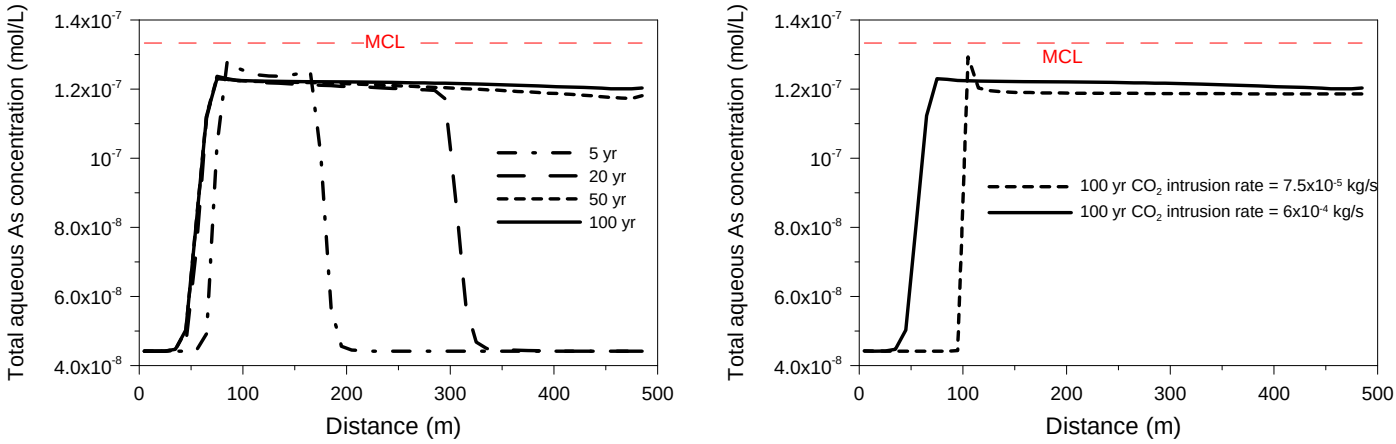

Fig. 4.56. Total aqueous As concentration at different times (left) along the x-axis at y = 0 m for CO_2 intrusion rate of 6×10^{-4} kg/s, and sensitivity of As concentration to CO_2 intrusion rate.

4.7 Results for Other Mineralogies

The base run and all sensitivity cases conducted thus far have all assumed the basic mineralogy of a Coastal Plain Sandstone aquifer, as introduced in Section 3.6.3.1. This mineralogy is representative of an impure arenite, with a composition mostly consisting of quartz plus some feldspars, lithic fragments, and clays. Below, we evaluate other basic mineralogies, otherwise simulating the base model setup described in Section 4.2. The first is representative of an almost pure arenite typical of the mineralogy of a St Peter Sandstone aquifer, and the second is the mineralogy of a dolomitic limestone aquifer. The St Peter Sandstone, which consists primarily of quartz sand, has a poor pH buffering capacity and is presumed to be the type of aquifer most vulnerable to mobilization of hazardous inorganic constituents through CO_2 intrusion. The dolomitic limestone, which is dominated by calcite and dolomite, should have good pH buffering capacity and is assumed to be least vulnerable to the mobilization of hazardous constituents during CO_2 intrusion. All basic mineral compositions contain the same volumetric fractions of trace minerals containing metals or As as essential components (Section 3.6.2.2).

4.7.1 St Peter Sandstone

The mineralogy of the St Peter Sandstone, Illinois, as presented in Section 3.6.3.3, is an example of an aquifer with limited pH buffering capability. The most obvious feature of this mineralogy is that it consists mainly of quartz sand with small amounts of calcite and dolomite, both of which are important pH buffering minerals. The clay matrix content is very small. Table 4.13 lists the mineralogical composition and gives the kinetic properties for minerals in this aquifer. An equilibrium run reveals the initial chemical composition in equilibrium with St Peter Sandstone before intrusion of CO_2 (Table 4.14), which has a lower pH and Eh compared with the Coastal Plain Sandstone aquifer assumed in the base model. Slightly larger initial As aqueous concentrations are obtained, while the initial Pb concentration is virtually identical. Overall, the differences in the initial conditions are not significant.

Table 4.13. Mineral volume fractions, possible secondary minerals, and kinetic properties for a St Peter Sandstone

Mineral	Volume Fraction of solid	A (cm^2/g)	Parameters for Kinetic Rate Law							
			Neutral Mechanism		Acid Mechanism			Base Mechanism		
			k_{25} ($mol/m^2/s$)	E_a (KJ /mol)	k_{25}	E_a	$n(H^+)$	k_{25}	E_a	$n(H^+)$
Primary:										
Quartz	0.926778	9.8	1.023×10^{-14}	87.7						
K-feldspar	0.0505281	9.8	3.890×10^{-13}	38	8.710×10^{-11}	51.7	0.5	6.310×10^{-12}	94.1	-0.823
Oligoclase	0.00244551	9.8	1.445×10^{-12}	69.8	2.138×10^{-10}	65	0.457			
Kaolinite	0.00099595	1.95×10^{5}	6.918×10^{-14}	22.2	4.898×10^{-12}	65.9	0.777	8.913×10^{-18}	17.9	-0.472
Smectite-ca	0.0023423	5.64×10^{5}	1.660×10^{-13}	35	1.047×10^{-11}	23.6	0.34	3.020×10^{-17}	58.9	-0.4
Illite	0.00374012	6.68×10^{5}	1.660×10^{-13}	35	1.047×10^{-11}	23.6	0.34	3.020×10^{-17}	58.9	-0.4
Chlorite	0.00171185	9.8	3.02×10^{-13}	88	7.762×10^{-12}	88	0.5			
Kerogen-os	0.00238641	9.8	3.02×10^{-13}	88	7.762×10^{-12}	88	0.5			
Pyrite	0.000515	12.9	2.52×10^{-12}	62.76	2.34×10^{-7}	43.54	1			
dolomite	0.0045	12.9	2.52×10^{-12}	62.76	2.34×10^{-7}	43.54	1			
Calcite	0.00095337	Assumed at equilibrium								
Goethite	0.00060538	1.47×10^{5}	2.52×10^{-12}	62.76	2.34×10^{-7}	43.54	1			
Apatite	0.00220978	12.9			2.34×10^{-7}	43.54	1			
Barite	0.00016334	12.9			2.34×10^{-7}	43.54	1			
Arsenopyrite	9.0594E-06	12.9			2.34×10^{-7}	43.54	1			
Greenockite	3.0363E-06	12.9			2.34×10^{-7}	43.54	1			
Cinnabar	1.4640E-08	12.9			2.34×10^{-7}	43.54	1			
Galena	7.8529E-06	12.9			2.34×10^{-7}	43.54	1			
Gudmundite	3.89×10^{-7}	12.9			2.34×10^{-7}	43.54	1			
Tiemannite	1.22×10^{-7}	12.9			2.34×10^{-7}	43.54	1			
Uraninite	8.015×10^{-7}	12.9			2.34×10^{-7}	43.54	1			
Sphalerite	9.42×10^{-5}	12.9			2.34×10^{-7}	43.54	1			
Secondary:										
Dolomite		12.9	2.52×10^{-12}	62.76	2.34×10^{-7}	43.54	1			
Magnesite		9.8	4.571×10^{-10}	23.5	4.169×10^{-7}	14.4	1			
Ankerite		9.8	1.260×10^{-9}	62.76	6.457×10^{-4}	36.1	0.5			
Dawsonite		9.8	1.260×10^{-9}	62.76	6.457×10^{-4}	36.1	0.5			
Na-smectite		151.6	1.660×10^{-13}	35	1.047×10^{-11}	23.6	0.34	3.020×10^{-17}	58.9	-0.4
Pyromorphite		12.9			2.34×10^{-7}	43.54	1			
Ferroselite		12.9			2.34×10^{-7}	43.54	1			
Clausthalite		12.9			2.34×10^{-7}	43.54	1			

Table 4.14. Initial chemical composition (mol/L) of groundwater in equilibrium with Coastal Plain Sandstone and St Peter Sandstone

Species	Base Model with Coastal Plain Sandstone	St Peter Sandstone
Eh	-0.215 (volt)	-0.2 (volt)
pH	7.61	7.45
Ca	9.00E-04	1.94E-03
Mg	2.17E-05	4.23E-05
Na	1.97E-03	1.97E-03
K	2.68E-04	4.17E-04
Fe	5.63E-06	8.45E-06
Si	9.31E-04	6.35E-04
TIC	3.33E-03	2.38E-03
SO_4^{-2}	1.95E-04	1.97E-04
HS^-	1.44E-08	1.37E-08
Al	4.19E-11	6.58E-11
Cl	2.07E-04	2.07E-04
P	1.78E-06	1.04E-06
Pb	1.30E-09	1.30E-09
As	4.42E-08	5.44E-08
Ba	1.12E-06	1.27E-06
Cd	1.76E-09	1.41E-09
Hg	2.53E-09	2.52E-09
Sb	3.57E-10	4.19E-10
Se	1.69E-08	1.67E-08
U	4.48E-09	3.15E-09
Zn	3.40E-07	3.51E-07

Intrusion of CO_2 into the St Peter Sandstone aquifer gives rise to geochemical changes similar to those observed in the base model. With gaseous CO_2 dissolving into the aqueous phase, the pH drops and mobilization of hazardous constituents occurs. Figure 4.57 (left) shows the simulated pH in profiles along the x-axis at y=0 m for different times. Note that the pH in the two-phase zone close to the intrusion location is significantly smaller at 100 years than at 50 years. Slight

decreases in pH can also be seen along the first 100 m downstream of the two-phase zone. This further pH drop is caused by the partial loss of pH buffer capability as the initially small volumes of calcite and dolomite minerals dissolve and eventually become depleted in the two-phase area and the immediate downstream region.

Figure 4.58 (left) shows the calcite volume fraction changes at different times. After 20 years, a small region of complete calcite depletion develops in the two-phase zone, which means that calcite ceases acting as a pH buffer. With time, this region extends further downstream. The dissolution of dolomite (Figure 4.59 right) is less rapid; dolomite is fully depleted only in a small region, after about 100 years. In the two-phase region, where both calcite and dolomite are fully depleted at the end of the simulation period, the pH decreases to about 4.5 at 100 years (Figure 4.57). In the region immediately downstream, where calcite is depleted, but dolomite is still present, the pH value is slightly lower than further downstream. As shown in Figure 4.57 (right), the regions with complete dissolution of calcite/dolomite correspond to the regions where the St Peter Sandstone and the Coastal Plain Sandstone differ most with respect to pH.

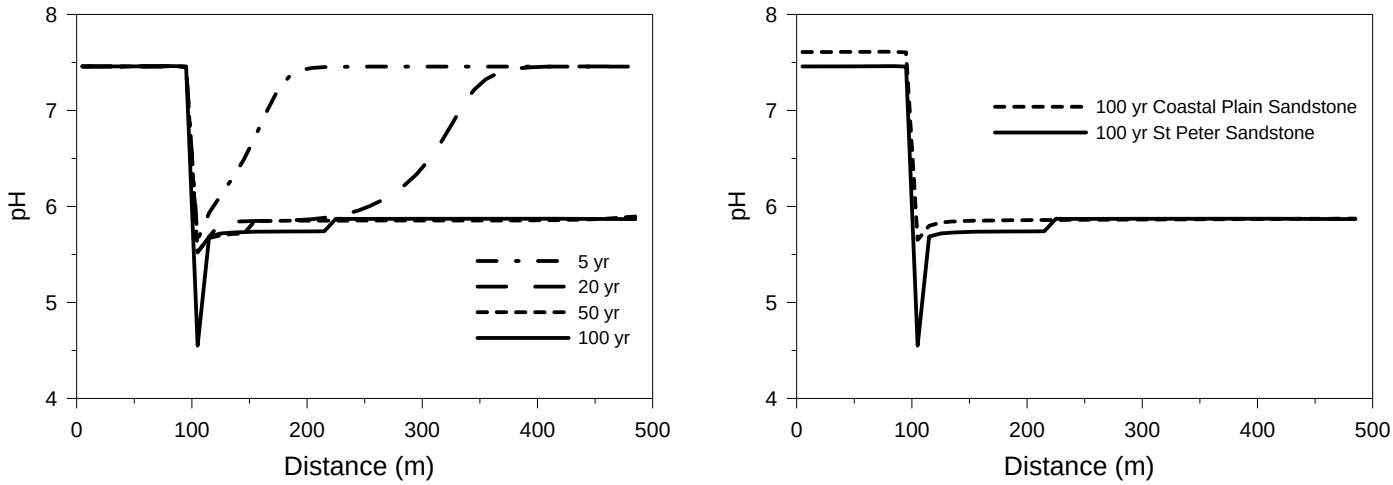

Fig. 4.57. pH profiles (left) along the x-axis at y = 0 m at different times for St Peter sandstone, and comparison of pH computed for Coastal Plain Sandstone and St Peter Sandstone (right)

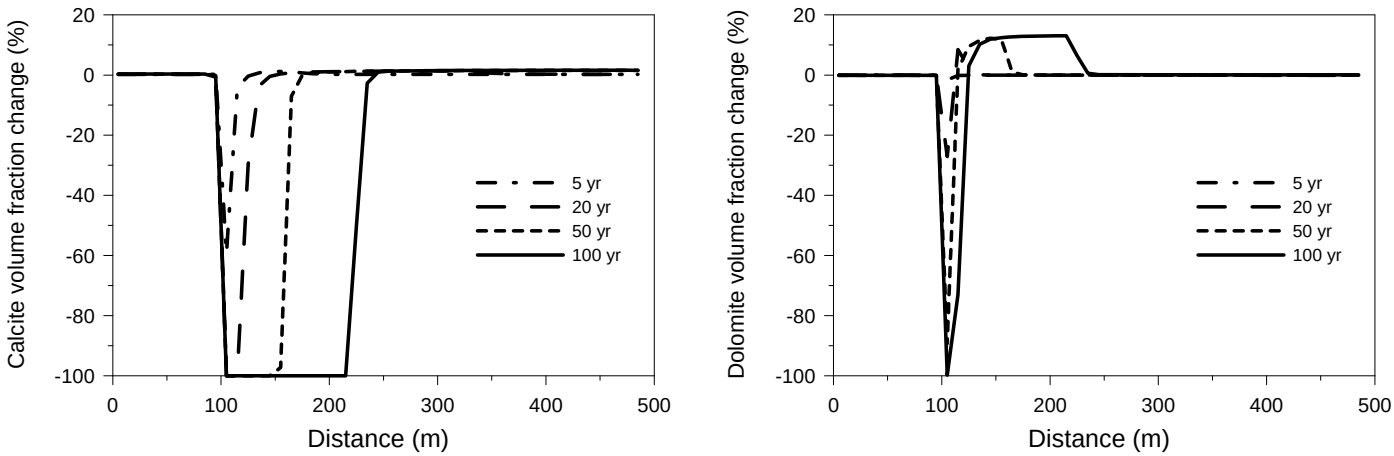

Fig. 4.58. Volume fraction of calcite (left) and dolomite (right) along x-axis at y = 0 m

Figures 4.55 (left) shows the resulting Pb concentrations for the St Peter Sandstone at different times after CO_2 intrusion, exhibiting a complex transient behavior. Early on, the Pb concentrations increase strongly in the two-phase zone, as observed in the base model, but decrease at later stages. From the observed evolution of pH, which decreases at later stages because buffering minerals become depleted, one would have expected the opposite behavior. Analysis of the adsorption characteristics for Pb reveals that the trend of decreasing Pb concentrations in the two-phase zone is caused by a corresponding depletion of Pb on adsorption sites (Figures 4.56). Similar to the base model, the early increase in aqueous Pb is mainly caused by desorption of initially sorbed Pb. Since the St Peter sandstone contains less clay mineral than the Coastal Plain Sandstone, the initial amount of sorbed Pb is smaller and thus becomes fully depleted in the two-phase zone after about 50 years, taking away a significant source of Pb in solid phase.

Figures 4.55 (right) shows a comparison of Pb concentrations after 100 years of CO_2 intrusion for the St Peter Sandstone and Coastal Plain Sandstone, respectively. The sensitivity run has smaller Pb concentrations in and near the two-phase zone, because of the above-discussed depletion of sorbed Pb. In contrast, the area further downstream shows slightly higher aqueous Pb concentrations for the St Peter Sandstone, apparently caused by the less effective re-adsorption of Pb migrating in downstream direction. We may conclude that the differences in Pb

concentrations observed in the sensitivity run compared to the base model are mostly related to differences in the adsorption/desorption characteristics (the clay content is different), while the differences in the pH buffer characteristics play a lesser role.

A different behavior is seen in the As results. The As concentration in the groundwater increases strongly in the two-phase zone between 50 years to 100 years (Figure 4.61 left), consistent with the further decrease of pH during this period. The obvious difference to the results observed for Pb is that there is enough As initially sorbed on mineral sites such that depletion of sorbed matter is not an issue. In fact, the plot showing the total As concentration on adsorption sites at 100 years in Figure 4.62 (left) is a straight line (for both the St Peter Sandstone and Coastal Plain Sandstone) because the spatial variation is too small to be detected. That significant desorption of As occurs in the two-phase zone between 50 and 100 years is evident in Figure 4.62 (right), which shows the change in sorbed As compared to the initial conditions. The resulting differences between the sensitivity case and the base model (Figure 4.61 right) are consistent with the observed differences in pH within and near the two-phase zone. The St Peter Sandstone aquifer arrives at higher As concentration than the Coastal Plain Sandstone because (1) As desorbs more strongly and (2) dissolution of arsenopyrite is enhanced.

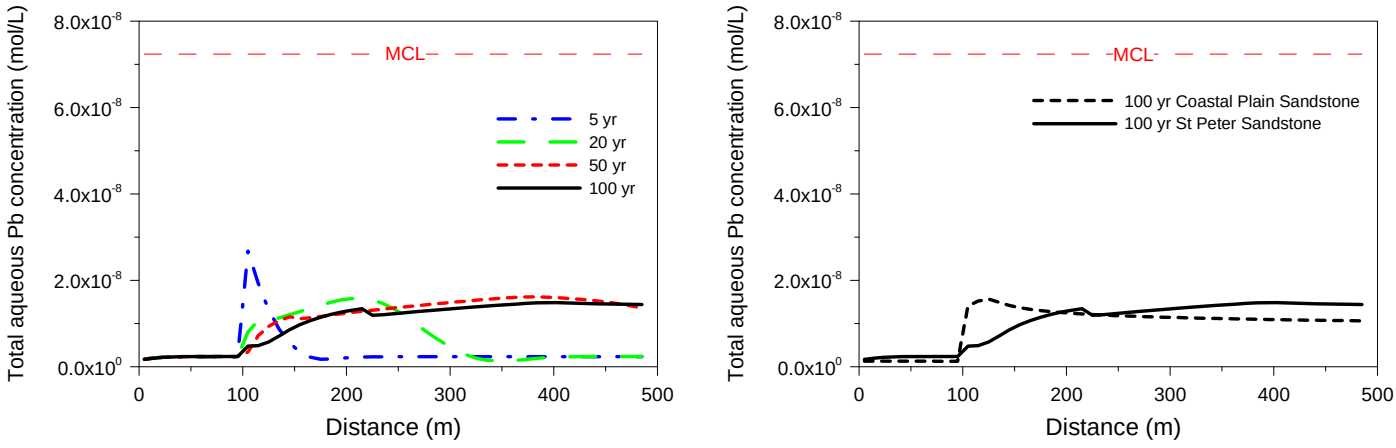

Fig. 4.59. Total aqueous Pb concentration profiles (left) along x-axis at y = 0 m at different times for St Peter Sandstone, and comparison of computed Pb concentration for Coastal Plain Sandstone and St Peter Sandstone with adsorption/desorption (right)

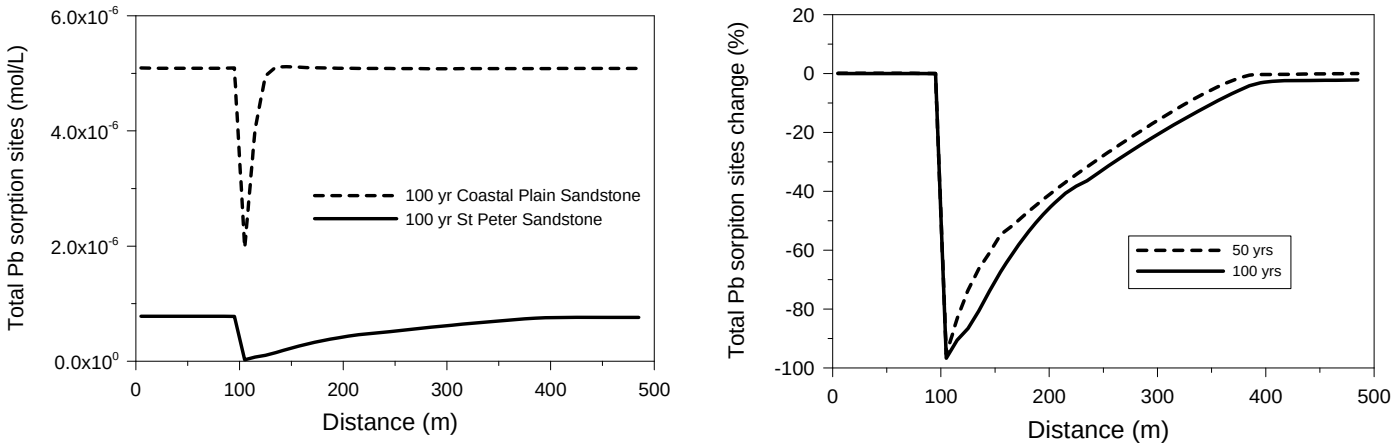

Fig. 4.60. Comparison of total Pb concentration on adsorption sites in mol/L for Coastal Plain Sandstone and St Peter Sandstone (left), and relative change in concentration on adsorption sites for St Peter Sandstone at 50 and 100 years (right)

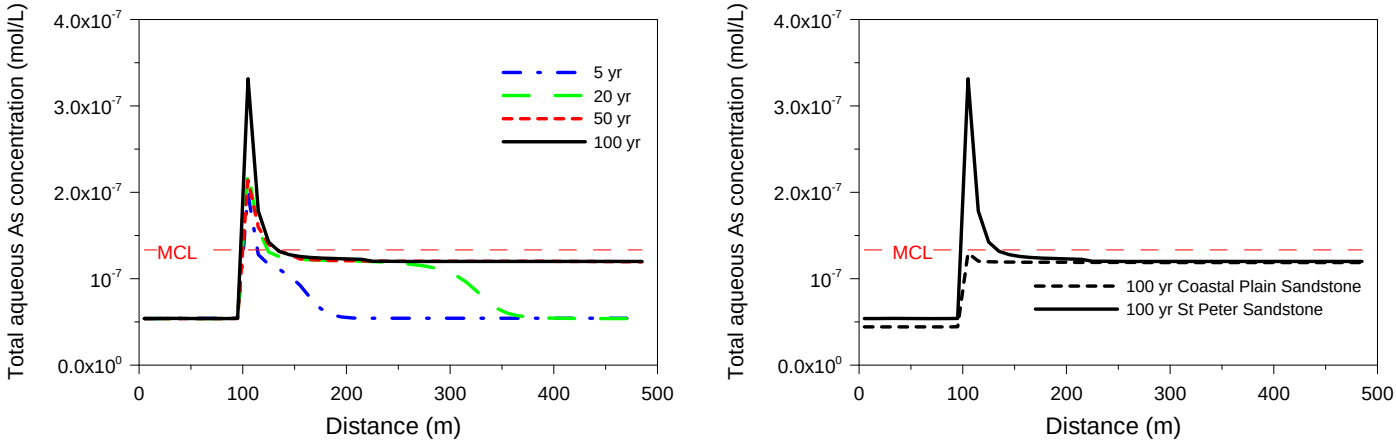

Fig. 4.61. Total aqueous As concentration profiles (left) along x-axis at y = 0 m at different times for St Peter Sandstone, and comparison of computed As concentration for Coastal Plain Sandstone and St Peter Sandstone (right)

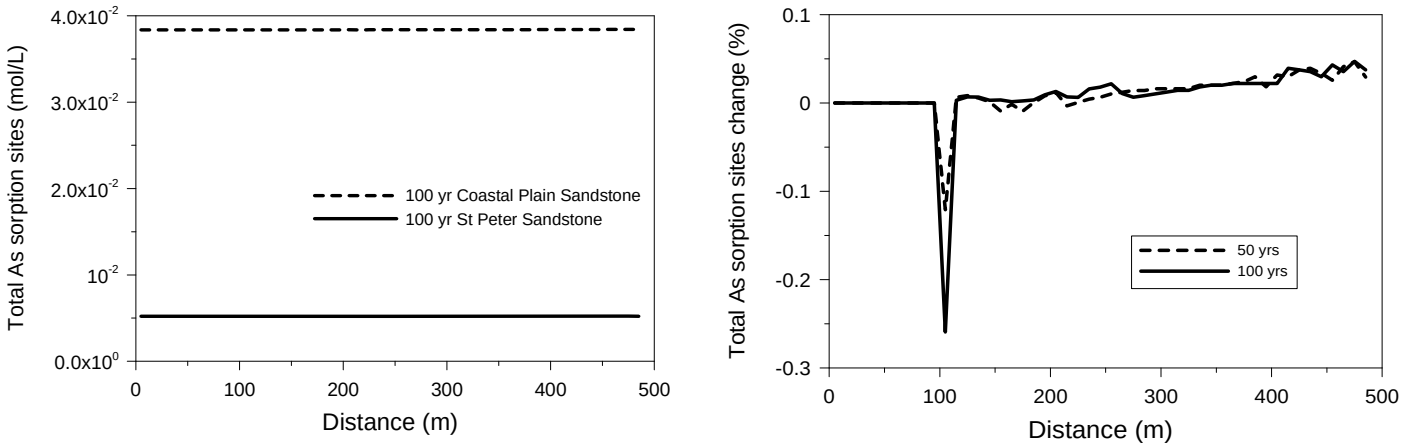

Fig. 4.62. Comparison of total As concentration on adsorption sites in mol/L for Coastal Plain Sandstone and St Peter Sandstone (left), and relative change in concentration on adsorption sites for St Peter Sandstone at 50 and 100 years (right)

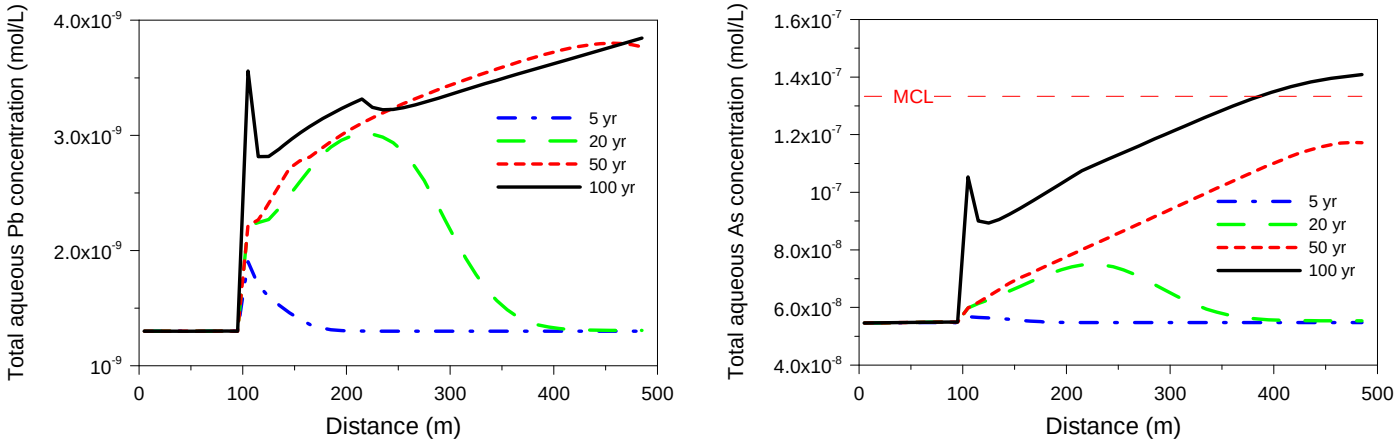

Fig. 4.63. Total aqueous Pb (left) and As (right) concentration profiles (left) along x-axis at y = 0 m at different times for St Peter Sandstone obtained by a simulation *without* adsorption/desorption

4.7.2 Dolomitic Limestone

A dolomitic limestone aquifer is considered in this section as an example of a mineralogy in which complete dissolution of buffering carbonates due to even long-term ingress of CO_2 would be implausible. A brief introduction to the slightly impure Dolomitic Limestone assumed below is given in Section 3.6.3.4, while Table 4.15 lists its mineralogical composition and provides kinetic parameters. The most obvious feature of the Dolomitic Limestone mineralogy is that it contains large amounts of calcite (>60% volume fraction) and dolomite (>14% volume fraction), both of which strongly buffer pH.

An equilibrium run provides the initial chemical composition in equilibrium with Dolomitic Limestone, prior to intrusion of CO_2 (Table 4.16). Compared to the initial chemical composition for the Coastal Plain Sandstone, the Dolomitic Limestone aquifer has a slightly higher initial pH and a lower Eh. Identical initial Pb and slightly lower As concentrations are obtained compared with those of the Coastal Plain Sandstone aquifer.

Figure 4.64 shows profiles of simulated pH for the Dolomitic Limestone at different times during ingress of CO_2 (left figure) and compares the 100-year profile to the Coastal Plain Sandstone aquifer from the base model (right figure). Both mineralogies have an almost identical pH profile, which indicates that: (1) the slight difference in initial pH of the groundwater does not affect the pH after CO_2 intrusion; and (2) the actual volume fraction of buffering minerals is not relevant so long as the minerals are present. However, because the Dolomitic Limestone aquifer contains much more calcite and dolomite than the Coastal Plain Sandstone, the relative volume changes caused by dissolution of these minerals are different. For example, only 1% of the calcite fraction dissolves in the sensitivity case during 100 years of CO_2 intrusion, compared to almost 100% in the Coastal Plain aquifer (Figure 4.65). It can be anticipated that the Coastal Plain Sandstone would be depleted of calcite shortly after 100 years, whereas the Dolomitic Limestone would buffer pH for thousands of years.

Table 4.15. Mineral volume fractions, possible secondary minerals, and kinetic properties for a Dolomitic Limestone

Mineral	Volume Fraction of solid	A (cm^2/g)	Parameters for Kinetic Rate Law							
			Neutral Mechanism		Acid Mechanism			Base Mechanism		
			k_{25} ($mol/m^2/s$)	E_a (KJ /mol)	k_{25}	E_a	$n(H^+)$	k_{25}	E_a	$n(H^+)$
Primary:										
Quartz	0.05144173	9.8	1.023×10^{-14}	87.7						
K-feldspar	0.00000000	9.8	3.890×10^{-13}	38	8.710×10^{-11}	51.7	0.5	6.310×10^{-12}	94.1	-0.823
Oligoclase	0.00000000	9.8	1.445×10^{-12}	69.8	2.138×10^{-10}	65	0.457			
Kaolinite	0.05251716	1.95×10^{5}	6.918×10^{-14}	22.2	4.898×10^{-12}	65.9	0.777	8.913×10^{-18}	17.9	-0.472
Smectite-ca	0.01976175	5.64×10^{5}	1.660×10^{-13}	35	1.047×10^{-11}	23.6	0.34	3.020×10^{-17}	58.9	-0.4
Illite	0.0690266	6.68×10^{5}	1.660×10^{-13}	35	1.047×10^{-11}	23.6	0.34	3.020×10^{-17}	58.9	-0.4
Chlorite	0.01805338	9.8	3.02×10^{-13}	88	7.762×10^{-12}	88	0.5			
Kerogen-os	0.02516736	9.8	3.02×10^{-13}	88	7.762×10^{-12}	88	0.5			
Pyrite	0.00271834	12.9	2.52×10^{-12}	62.76	2.34×10^{-7}	43.54	1			
dolomite	0.14265542	12.9	2.52×10^{-12}	62.76	2.34×10^{-7}	43.54	1			
Calcite	0.60326492	Assumed at equilibrium								
Goethite	0.01276885	1.47×10^{5}	2.52×10^{-12}	62.76	2.34×10^{-7}	43.54	1			
Apatite	0.00233047	12.9			2.34×10^{-7}	43.54	1			
Barite	0.00017227	12.9			2.34×10^{-7}	43.54	1			
Arsenopyrite	9.5542E-06	12.9			2.34×10^{-7}	43.54	1			
Greenockite	3.2022E-06	12.9			2.34×10^{-7}	43.54	1			
Cinnabar	1.5439E-08	12.9			2.34×10^{-7}	43.54	1			
Galena	8.2817E-06	12.9			2.34×10^{-7}	43.54	1			
Gudmundite	4.1038E-07	12.9			2.34×10^{-7}	43.54	1			
Tiemannite	1.2941E-07	12.9			2.34×10^{-7}	43.54	1			
Uraninite	8.4531E-07	12.9			2.34×10^{-7}	43.54	1			
Sphalerite	9.9324E-05	12.9			2.34×10^{-7}	43.54	1			
Secondary:										
Dolomite		12.9	2.52×10^{-12}	62.76	2.34×10^{-7}	43.54	1			
Magnesite		9.8	4.571×10^{-10}	23.5	4.169×10^{-7}	14.4	1			
Ankerite		9.8	1.260×10^{-9}	62.76	6.457×10^{-4}	36.1	0.5			
Dawsonite		9.8	1.260×10^{-9}	62.76	6.457×10^{-4}	36.1	0.5			
Na-smectite		151.6	1.660×10^{-13}	35	1.047×10^{-11}	23.6	0.34	3.020×10^{-17}	58.9	-0.4
Pyromorphite		12.9			2.34×10^{-7}	43.54	1			
Ferroselite		12.9			2.34×10^{-7}	43.54	1			
Clausthalite		12.9			2.34×10^{-7}	43.54	1			

Table 4.16. Initial chemical composition (mol/L) of groundwater in equilibrium with Coastal Plain Sandstone and Dolomitic Limestone.

Species	Coastal Plain Sandstone	Dolomitic Limestone
Eh	-0.215 (volt)	-0.22 (volt)
pH	7.61	7.68
Ca	9.00E-04	6.61E-04
Mg	2.17E-05	1.69E-05
Na	1.97E-03	1.97E-03
K	2.68E-04	2.39E-04
Fe	5.63E-06	4.86E-06
Si	9.31E-04	9.72E-04
TIC	3.33E-03	3.85E-03
SO_4^{-2}	1.95E-04	1.95E-04
HS^-	1.44E-08	1.45E-08
Al	4.19E-11	4.23E-11
Cl	2.07E-04	2.07E-04
P	1.78E-06	1.88E-06
Pb	1.30E-09	1.30E-09
As	4.42E-08	4.32E-08
Ba	1.12E-06	5.11E-07
Cd	1.76E-09	1.95E-09
Hg	2.53E-09	2.57E-09
Sb	3.57E-10	3.27E-10
Se	1.69E-08	1.41E-08
U	4.48E-09	5.28E-09
Zn	3.40E-07	3.31E-07

With the pH differences almost negligible, the effects of galena precipitation or arsenopyrite dissolution should be fairly similar between the two sensitivity cases. However, the resulting concentrations of Pb and As do show small but noticeable differences. The reason is that the

adsorption/desorption characteristics differ because the content of illite and smectite differs between the Dolomitic Limestone and the Coastal Plain Sandstone mineralogies.

4.66 shows the spatial distribution of total aqueous Pb concentrations at different times for Dolomitic Limestone (left) and compares them with those for the Coastal Plain Sandstone (right). The sensitivity case has a slightly higher Pb concentration in the two-phase region and marginally lower Pb concentration downstream. The weak site on illite is the principal surface complex that releases Pb, while the strong site on smectite is the principal surface complex that adsorbs Pb. Desorption is stronger in the two-phase zone for the Dolomitic Limestone than for the Coastal Plain Sandstone (Figure 4.67 and Figure 4.68 left), because the former contains more illite than the latter. The Dolomitic Limestone also contains more smectite, which explains why more Pb sorbs back onto the strong site on smectite in the downstream region (Figure 4.68 right). Overall, the sensitivity run shows a very small amount of Pb in the downstream region, whereas the base model exhibits a minor amount of desorption. While hard to observe in Figure 4.68 (right), the relative changed of total Pb sorbed is +0.15% for the sensitivity case compared to -0.2% for the base model.

Figure 4.69 shows the spatial distribution of total aqueous As concentrations at different times for the Dolomitic Limestone (left) and a comparison of the 100-year results with those for the Coastal Plain Sandstone (right). The sensitivity case shows higher aqueous As concentration than the base model. This result is somewhat counterintuitive when considering the large amounts of pH buffering minerals present in the Dolomitic Limestone. However, as pointed out before, the pH evolution after ingress of CO_2 is largely identical for both mineralogies, because the actual volume fraction of buffering minerals is not relevant as long as these minerals remain present. The difference in the As concentrations is rather caused by the larger illite content in the Dolomitic Limestone, which leads to stronger desorption in the two-phase zone and subsequent transport of elevated aqueous As in downstream direction.

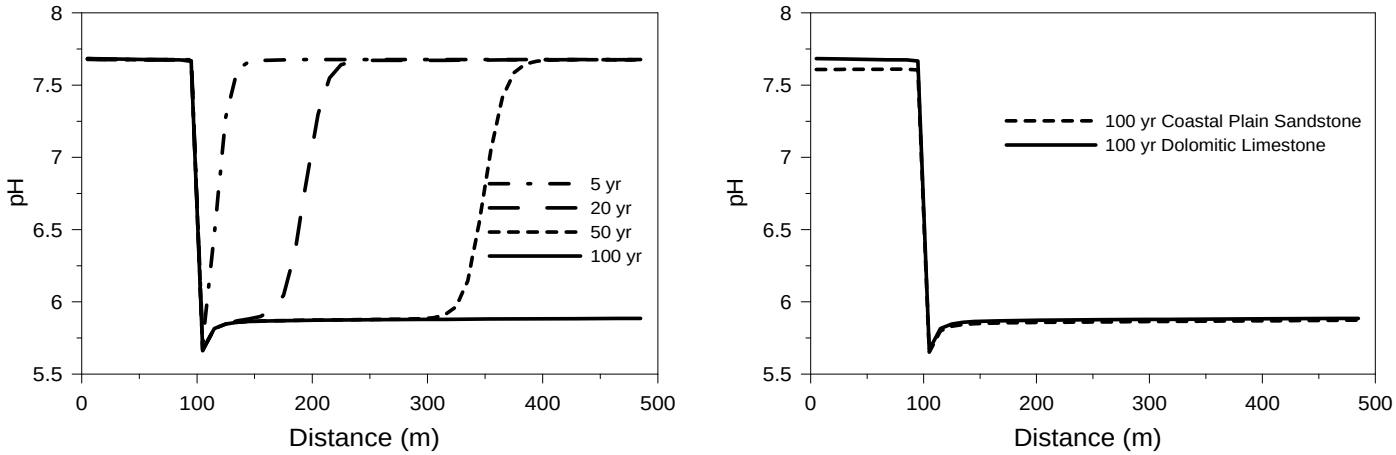

Fig. 4.64. pH profiles (left) along x-axis at y = 0 m at different times for Dolomitic Limestone, and comparison of computed pH with Coastal Plain Sandstone (right).

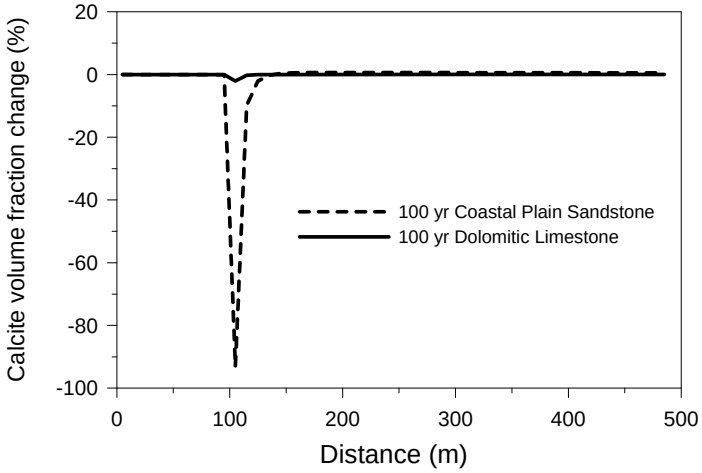

Fig. 4.65. Comparison of calcite volume fraction change for Coastal Plain Sandstone and Dolomitic Limestone.

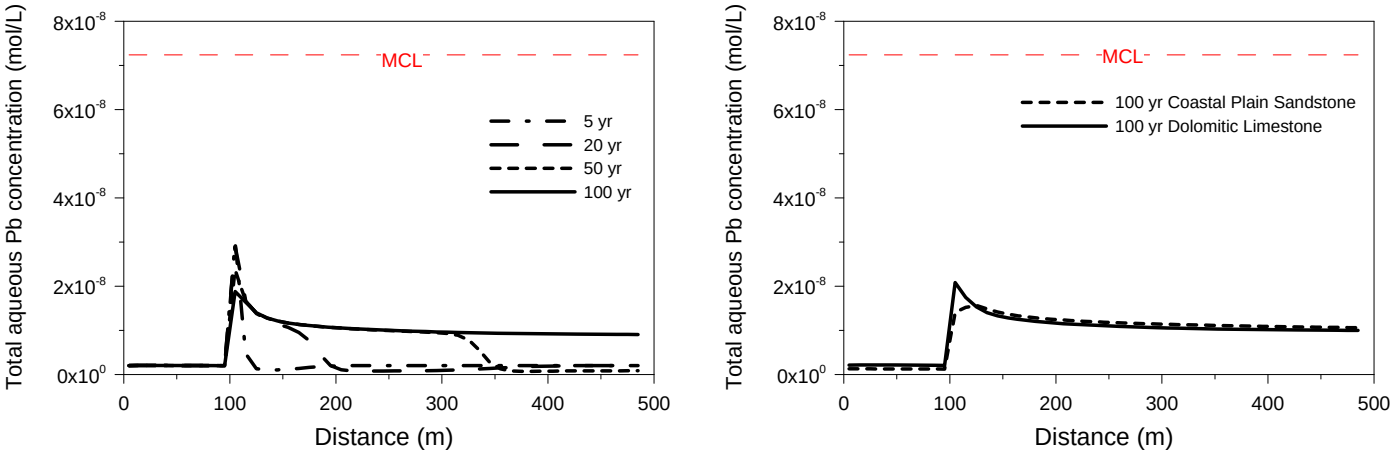

Fig. 4.66. Total aqueous Pb concentration profiles (left) along x-axis at y = 0 m at different times for Dolomite Limestone, and comparison of computed Pb concentration with Coastal Plain Sandstone (right)

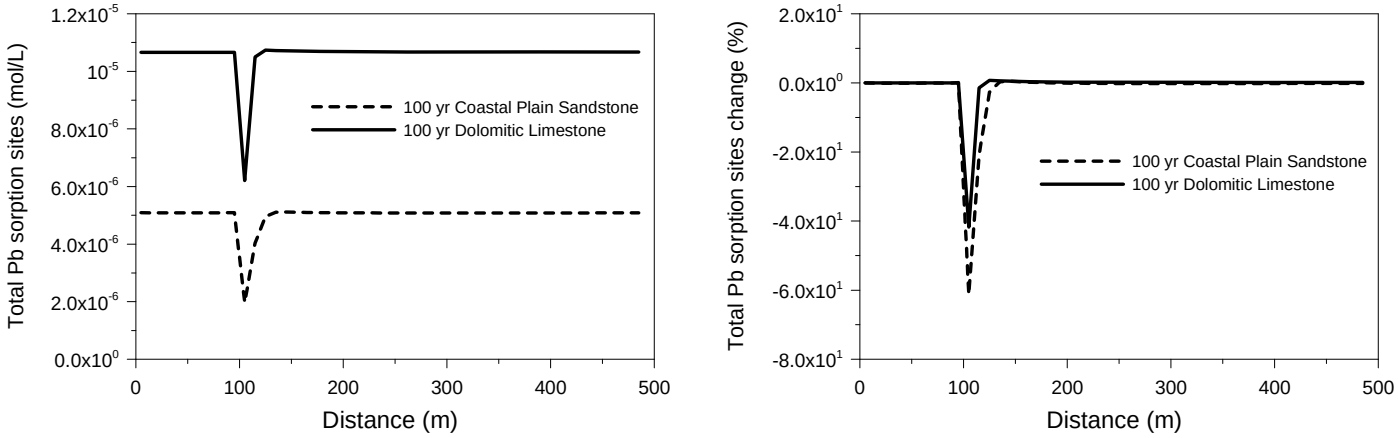

Fig. 4.67. Comparison of total Pb concentration on adsorption sites (left) and change (right) for Coastal Plain Sandstone and Dolomitic Limestone.

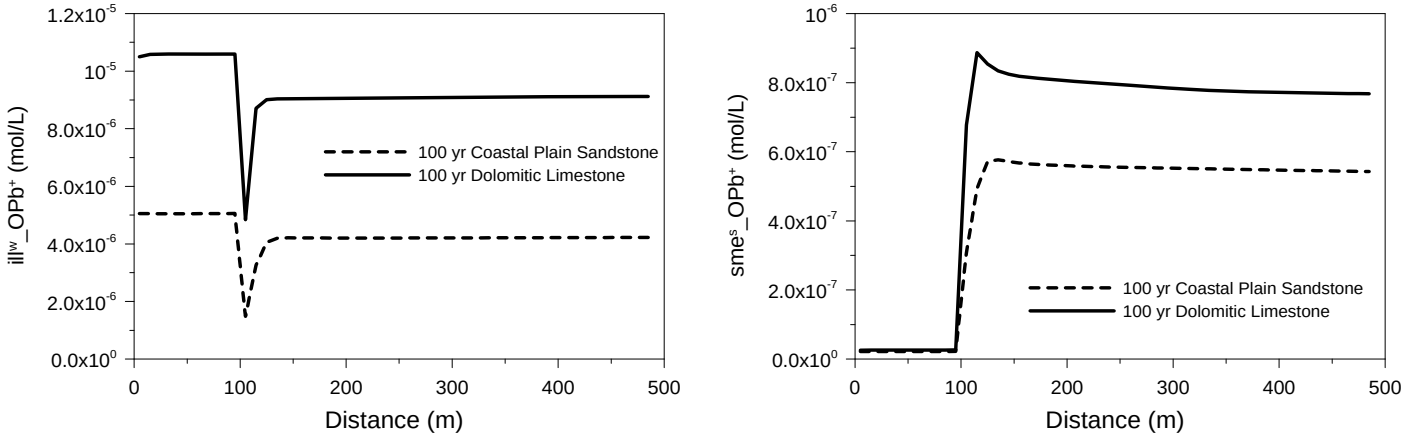

Fig. 4.68. Comparison of surface complex ill^{w}_OPb^{+} (left) and sme^{s}_oPb^{+}for Coastal Plain Sandstone and Dolomitic Limestone.

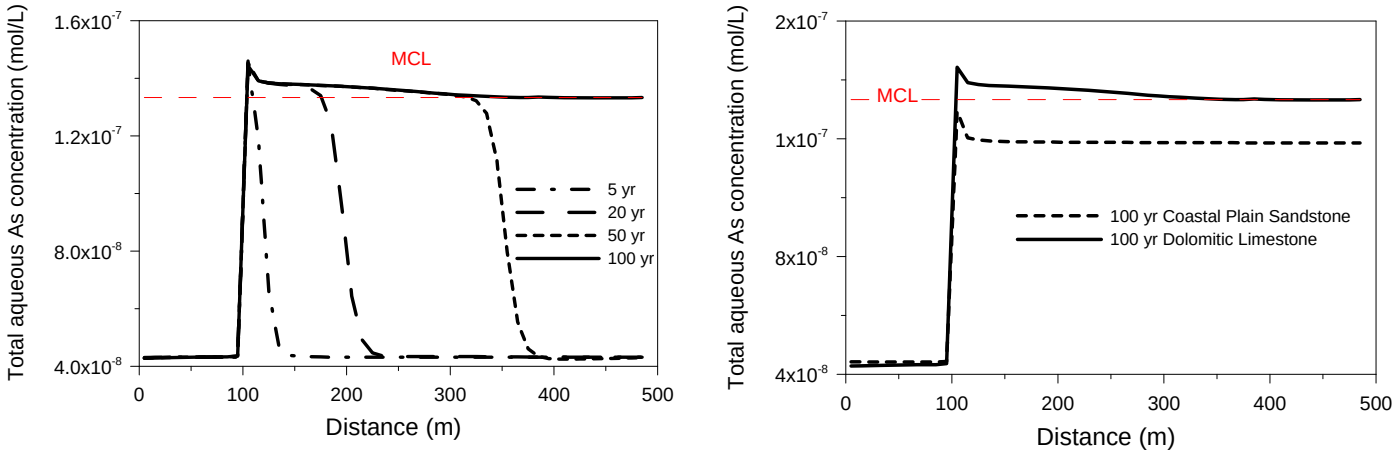

Fig. 4.69. Total aqueous As concentration profiles (left) along x-axis at y = 0 m at different times for Dolomitic Limestone, and comparison of computed As concentration with Coastal Plain Sandstone (right)

4.8 Oxidizing Conditions

Section 3.6.3.2 introduces the mineralogy of a Coastal Plain Sandstone under oxidizing conditions. Oxidizing conditions may result from continuous recharge with oxygenated water in unconfined aquifers, or in response to anthropogenic extraction of potable water. In this section, we investigate the behavior of an oxidized aquifer affected by CO_2 intrusion. Notice, however, that oxygenation itself can lead to the mobilization of heavy metals as a result of oxidative dissolution, an effect that is often more relevant than the pH decrease caused by CO_2 intrusion.

As discussed in Section 3.6.3.2, the mineralogical composition of an oxidized aquifer differs from an aquifer under reducing conditions. The most significant differences with respect to the Coastal Plain Sandstone are that (1) pyrite is oxidized and that (2) cerussite instead of galena would be the mineral controlling Pb concentration. Table 4.17 lists the modified mineralogical composition of a representative Coastal Plain Sandstone under oxidizing conditions. All minerals likely to buffer the redox state under reducing conditions have been eliminated, and only cerussite is present as a host mineral for Pb. We focus in this sensitivity case only on the potential for Pb contamination; the behavior of As under analogous conditions may be studied in a future analysis.

An equilibrium run reveals the initial chemical composition in equilibrium with the oxidized Coastal Plain Sandstone, before the intrusion of CO_2. Well-oxidized soils have redox potentials of +0.4 to +0.8 V, while extremely reduced soils may have potentials of -0.1 to -0.5 V (Dragun, 1988). In the equilibrium run, Eh is specified by the redox couple of O_2/H_2O, giving an Eh value of +0.37 V. An Eh value of +0.37 V represents an end case of groundwater redox condition, which probably only exists near the recharge area of an aquifer where the water table is direct contact with air. The objective of conducting a simulation with Eh of +0.37 V is to establish the maximum effect of redox potential on the mobilization of Pb. Table 4.18 compares the chemical composition of groundwater for the Coastal Plain Sandstone aquifer under both reducing and oxidizing conditions. The latter composition is characterized by vanishingly small concentrations for Fe(II) and HS^-; pH is similar. The most relevant difference, of course, is the initial aqueous

Pb concentration in the oxidized aquifer, which is more than three orders of magnitude larger than under reducing conditions. In fact, the initial Pb concentration of 1.36×10^{-6} mol/L in the oxidized aquifer is significantly above the MCL of 7.24×10^{-8} mol/L (or 15 ppb). This difference is due to cerussite, rather than galena, controlling the aqueous Pb concentration under oxidizing conditions (see Section 3.4.6). Note that the following reaction defines cerussite solubility in the presence of CO_2. According to the PHREEQC (Parkhurst and Appelo, 1999) database, one has:

$$PbCO_3(S) \rightleftharpoons Pb^{+2} + CO_3^{-2} \qquad \log K = -13.13 \tag{4.8}$$

Table 4.17. Mineral volume fractions, possible secondary minerals, and kinetic properties for an oxidized Coastal Plain Sandstone aquifer.

Mineral	Volume fraction of solid	A (cm^2/g)	Parameters for kinetic rate law							
			Neutral mechanism		Acid mechanism			Base mechanism		
			k_{25} ($mol/m^2/s$)	E_a (KJ /mol)	k_{25}	E_a	$n(H^+)$	k_{25}	E_a	$n(H^+)$
***Primary*:**										
Quartz	0.796	9.8	1.023×10^{-14}	87.7						
K-feldspar	0.0634	9.8	3.890×10^{-13}	38	8.710×10^{-11}	51.7	0.5	6.310×10^{-12}	94.1	-0.823
Oligoclase	0.0614	9.8	1.445×10^{-12}	69.8	2.138×10^{-10}	65	0.457			
Kaolinite	0.0174	151.6	6.918×10^{-14}	22.2	4.898×10^{-12}	65.9	0.777	8.913×10^{-18}	17.9	-0.472
Ca-smectite	0.0139	151.6	1.660×10^{-13}	35	1.047×10^{-11}	23.6	0.34	3.020×10^{-17}	58.9	-0.4
Illite	0.029	151.6	1.660×10^{-13}	35	1.047×10^{-11}	23.6	0.34	3.020×10^{-17}	58.9	-0.4
Calcite	0.0097	Assumed at equilibrium								
Goethite	0.00616	12.9	2.52×10^{-12}	62.76	2.34×10^{-7}	43.54	1			
Apatite	2.2×10^{-4}	12.9	2.52×10^{-12}	62.76	2.34×10^{-7}	43.54	1			
Barite	4.9×10^{-4}									
Cerussite	7.99×10^{-6}	12.9	2.52×10^{-12}	62.76	2.34×10^{-7}	43.54	1			
Secondary:										
Magnesite		9.8	4.571×10^{-10}	23.5	4.169×10^{-7}	14.4	1			
Ankerite		9.8	1.260×10^{-9}	62.76	6.457×10^{-4}	36.1	0.5			
Dawsonite		9.8	1.260×10^{-9}	62.76	6.457×10^{-4}	36.1	0.5			
Pyromorphite		12.9	2.52×10^{-12}	62.76	2.34×10^{-7}	43.54	1			
Na-smectite		151.6	1.660×10^{-13}	35	1.047×10^{-11}	23.6	0.34	3.020×10^{-17}	58.9	-0.4

Table 4.18. Chemical composition (mol/L) of groundwater in equilibrium with Coastal Plain Sandstone aquifer under reducing and oxidizing and conditions.

Species	Reducing Conditions (Base Model)	Oxidizing Conditions
Eh	-0.215 (volt)	0.37 (volt)
pH	7.61	7.78
Ca	9.00E-04	1.33E-03
Mg	2.17E-05	1.52E-14
Na	1.97E-03	1.35E-02
K	2.68E-04	1.27E-05
Fe	5.63E-06	6.50E-17
Si	9.31E-04	1.02E-03
TIC	3.33E-03	2.27E-03
SO_4^{-2}	1.95E-04	6.65E-03
HS^-	1.44E-08	2.18E-16
Al	4.19E-11	1.08E-09
Cl	2.07E-04	2.08E-05
P	1.78E-06	1.52E-06
Pb	1.30E-09	1.36E-06

Except for the difference in mineralogy and initial chemical conditions, the simulation of CO_2 intrusion into the oxidized Coastal Plain Sandstone was conducted for a model setup similar to the base model (Section 4.2). Although oxidizing conditions would typically exist in very shallow aquifers, we did not change the aquifer depth.

Figure 4.70 shows the evolution of pH along the x-axis at y=0, which is almost identical with the base model under reducing conditions. The pH decrease in the two-phase zone near the intrusion location induces the release of Pb from adsorption sites. Figure 4.71, for example, shows a decrease in the concentration of surface complexes on illite in the two-phase zone for both the strong (left) and weak sites (right). Within 100 years of CO_2 intrusion, the total mass of Pb on adsorption sites drops by about 6% in the two-phase zone (Figure 4.72 left). The elevated aqueous Pb concentrations, mostly induced by desorption in the two-phase zone, migrate

downstream with the groundwater flow, where a small amount of Pb adsorbs onto surface complexes (note the minor increase in adsorbed mass downstream of the intrusion zone in Figure 4.72 left). Note that the solution becomes oversaturated with respect to cerussite in both the two-phase zone and downstream of it, which causes Pb to precipitate out as cerussite (note the few percent increase in the cerussite volume fraction in Figure 4.72, right). Thus, while cerussite controls the initial equilibrium concentrations of Pb within the groundwater and on adsorption sites, the increase in aqueous Pb in response to CO_2 intrusion is not actually caused by cerussite dissolution, but rather by desorption of initially sorbed matter. This could be different if adsorption processes were less relevant in the aquifer, e.g., if less clay minerals were present or the site density was lower.

Figure 4.73 shows the resulting evolution of aqueous Pb concentrations along the x-axis. The peak in the two-phase zone observed at 5 years is caused by the strong desorption occurring with the change in pH. Because surface complexation is a relatively fast process, considered as an equilibrium reaction in the current simulations, desorption ceases when the pH in two-phase zone stops decreasing. After 100 years, the downstream Pb concentrations have attained a fairly uniform concentration, which is about 30 times larger than the initial Pb concentration. Both initial and final conditions have Pb concentrations significantly larger than the MCL of 7.24×10^{-8} mol/L (15 ppb).

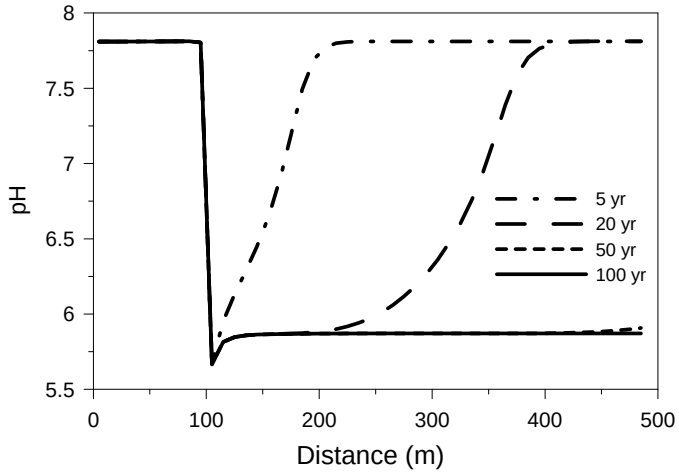

Fig. 4.70. pH profiles along x-axis at y = 0 m, for oxidized Coastal Plain Sandstone.

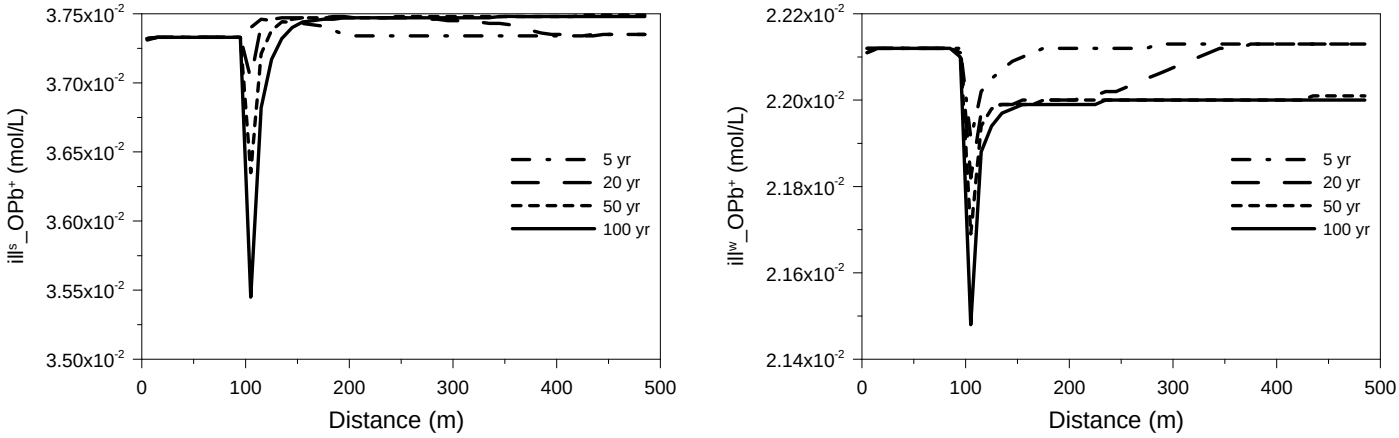

Fig. 4.71. Surface complex of Pb on the strong (left) and weak site (right) of illite along x-axis at y = 0 m for oxidized Coastal Plain Sandstone.

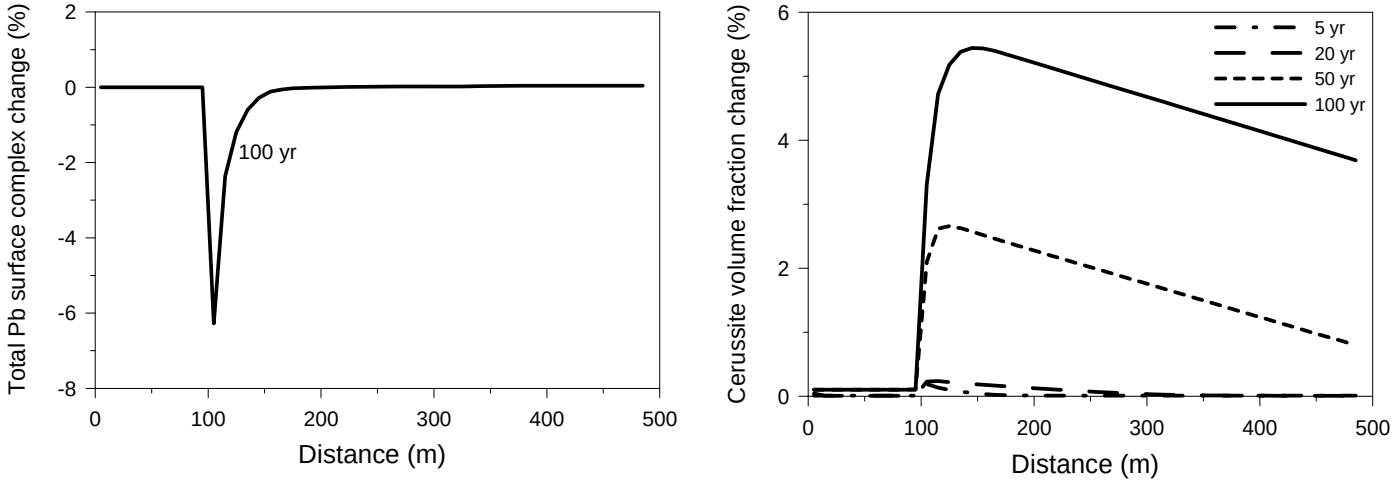

Fig. 4.72. Relative change of total Pb concentration on adsorption sites (left) and cerussite volume fraction change (right) profiles, along x-axis at y = 0 m (left) for oxidized Coastal Plain Sandstone.

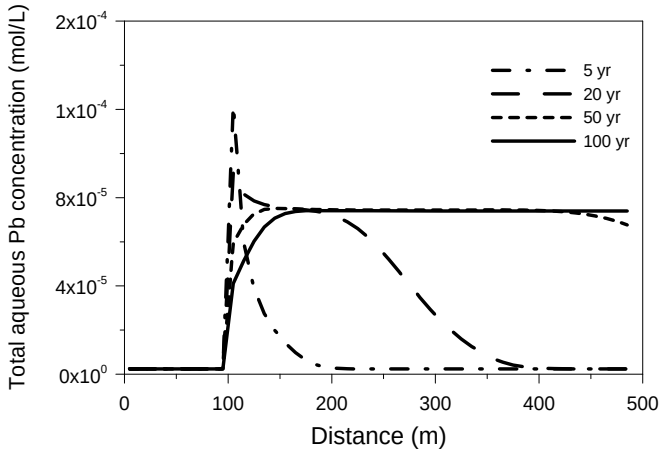

Fig. 4.73. Total aqueous Pb concentration profiles (left) along x-axis at y = 0 m at different times for oxidized C

4.9 Three-Dimensional (3D) Simulation of CO_2 Intrusion

A two-dimensional depth-averaged model is used in all simulations described in the previous sections. Thus, the vertical variation in gaseous and aqueous CO_2, as well as the vertical variation in the resulting geochemical changes, has been neglected so far. This raises questions regarding the limitations of the 2D assumption. For example, if a 3D model with vertical variation were used, how different would be the spatial distribution and magnitude of CO_2 in the gas phase and dissolved in the aqueous phase? How would these differences affect the pH as well as the aqueous concentrations of Pb and As? Would the observed discrepancies between 2D and 3D modeling be less relevant for the base model described in Section 4.5, where most of the gaseous CO_2 readily dissolves in water, compared to the sensitivity cases described in Sections 4.6.8 and 4.6.9, where much larger CO_2 gas plumes are observed suggesting that buoyancy is more relevant?

To answer these questions, a three-dimensional model was developed using the same model setup and similar model dimensions as in the 2D simulations. Like the 2D model, the 3D domain is 500 m long and has a uniform thickness of 10 m. However, the vertical extent of the model is now discretized using five model layers of 2 m thickness each. To increase computational efficiency, the lateral extent of the 3D model is reduced to 100 m, which was shown to be sufficient in the 2D simulations. CO_2 enters the model domain from below. Three simulation cases are considered: The first one uses a model setup identical to the 2D base model described in Section 4.5, except that vertical variability is now considered (Section 4.9.1). The second case is identical to the 2D sensitivity case described in Section 4.6.8, featuring a reduced groundwater flow velocity (Section 4.9.2). The third case is identical to the 2D case described in Section 4.6.9, where a higher CO_2 leakage rate is assumed (Section 4.9.3). Note that in all cases, a confined aquifer has been assumed, so that gaseous CO_2 cannot escape into the overlying vadose zone. This is a conservative assumption because excess CO_2 (i.e., gaseous and buoyant CO_2 not dissolving into the groundwater), which would otherwise escape into the vadose zone, is forced to remain in the aquifer.

4.9.1 Results from 3D Simulation of Base Model

The CO_2 leakage rate assumed in the base-case simulation is 7.5×10^{-5} kg/s, which is about 2.4 tonnes per year. As pointed out in Section 4.2, this leakage rate was chosen roughly based on the amount of CO_2 that can dissolve into the groundwater at a flow velocity of 10 m per year. Thus, buoyancy effects should be less relevant in this case, and the 2D model simplification should be a reasonable surrogate for the more complex 3D simulations. We will demonstrate this in the following discussion of 3D simulation results, starting with a set of figures with a close-in viewing of the intrusion zone and immediate vicinity.

Figures 4.74 and 4.75 show CO_2 gas saturation after 100 years of leakage, both in a 3D contour plot and in several y-z cross-sections. Consistent with the 2D results described in Section 4.5.1, the two-phase zone predicted by the 3D model is relatively small, extending about 30 m in the direction of groundwater flow (x-direction) and about 10 m perpendicular to it (y-direction). Vertically, the two-phase zone extends almost to the top of the aquifer, but does not accumulate there, as most of the gaseous CO_2 effectively dissolves into the groundwater. Plots of dissolved CO_2 (which is given by the concentration of total inorganic carbonate (TIC)) are shown in Figures 4.76 and 4.77. Qualitatively, the 3D results are again similar to those obtained from the 2D model. An elevated concentration of TIC is observed in the two-phase region near the intrusion location and further downstream, resulting from slow advective transport with the groundwater, while lateral spreading of dissolved CO_2 is minor. TIC contours indicate a fairly uniform distribution of dissolved CO_2 with depth.

While qualitatively similar, there are some differences between 2D and 3D results. For example, the peak CO_2 gas saturation and the peak concentrations of dissolved CO_2 as predicted from the 3D model, observed near the intrusion point at the base of the aquifer, are higher than those in the 2D model. As a result, the lowest pH value calculated in the 3D model is around 5.5 (see Figure 4.78 and 4.79), which is more acidic than in the 2D model (pH is equal to 5.65). However, outside of the immediate intrusion location, the predicted pH changes from CO_2 intrusion are in fair agreement between the 3D and 2D models. Reasonable agreement between

3D and 2D can also be seen in the predicted Pb and As concentrations, which correlate well with the groundwater volume experiencing pH changes (Figure 4.80 to 4.83). Elevated Pb and As have peak values near the intrusion location and slightly smaller values in the downstream direction. Except for the uppermost portion of the aquifer, aqueous Pb and As are well equilibrated over the depth of the aquifer.

Figures 4.84 through 4.87 provide, respectively, contours of TIC, pH, Pb, and As from the 3D model, showing the entire length (in the x-direction) of the model domain rather than focusing on the intrusion location. These figures reiterate qualitatively what was observed before in the 2D results. Transport in the longitudinal direction is dominant, with little lateral spreading. They also show that, while there is some vertical variability further downstream, the observed geochemical behavior is relatively uniform with depth.

A direct and quantitative comparison of predicted 3D and 2D results is provided in Figures 4.88 and 4.89. Figure 4.88 shows total aqueous Pb concentration along the x-axis at y = 0 m for different aquifer depths (top at z = 0 m, middle at z = -5 m, and bottom at z = -10 m) in the 3D model, together with the depth-averaged results from the 2D model. The highest Pb concentrations are observed at the bottom and in the middle of the aquifer, much higher than those observed at the top. As discussed above, this is because gaseous CO_2 dissolves before reaching the aquifer top. The 2D concentration profiles resemble those of the 3D simulations, but deviate from them by about 20-30% when comparing the aquifer bottom and top. Figure 4.89 shows the comparison of As concentrations for 3D and 2D models. Results from the depth-averaged 2D model are very similar to those predicted at the bottom and in the middle of the 3D domain.

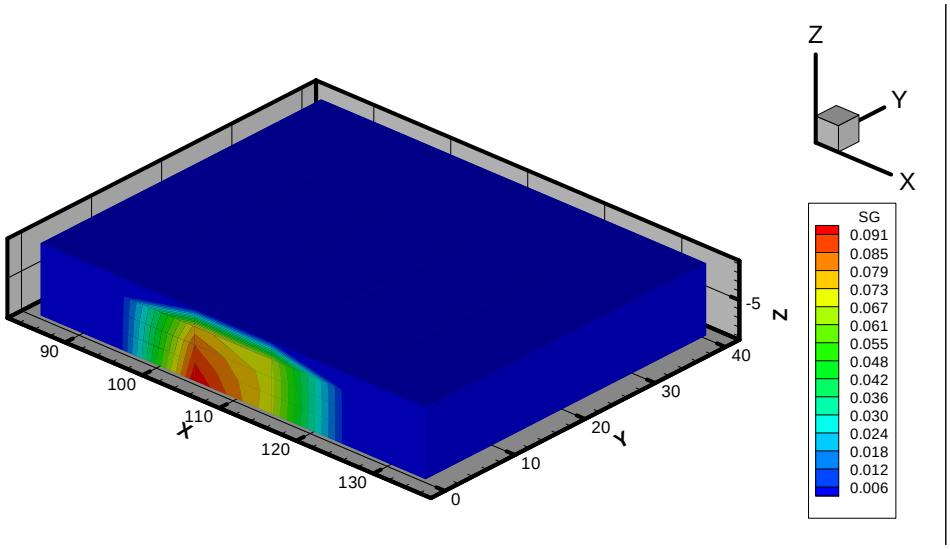

Fig. 4.74. Close-up view of spatial distribution of CO_2 gas saturation after 100 years of CO_2 intrusion in 3D model with CO_2 leakage rate of 7.5×10^{-5} kg/s.

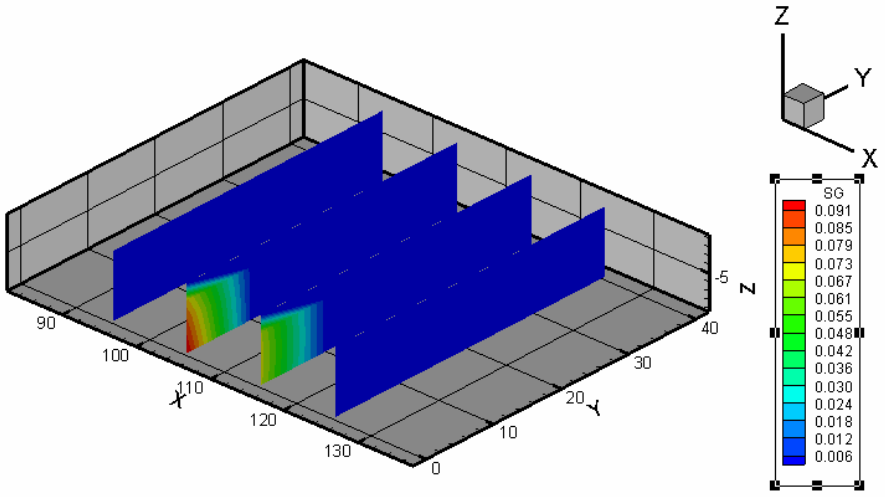

Fig. 4.75. Profiles CO_2 gas saturation at x= 95 m, x =105 m, x = 115 m, and x = 125 m after 100 years of CO_2 intrusion in the 3D model with CO_2 leakage rate of 7.5×10^{-5} kg/s.

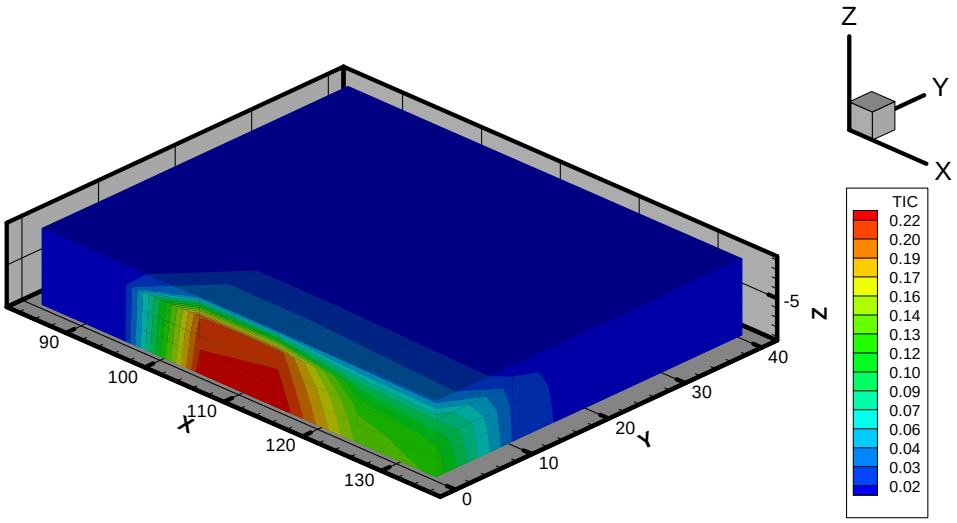

Fig. 4.76. Close-up view of spatial distribution of Total Inorganic Carbon (TIC) after 100 years of CO_2 intrusion in 3D model with CO_2 leakage rate of 7.5×10^{-5} kg/s.

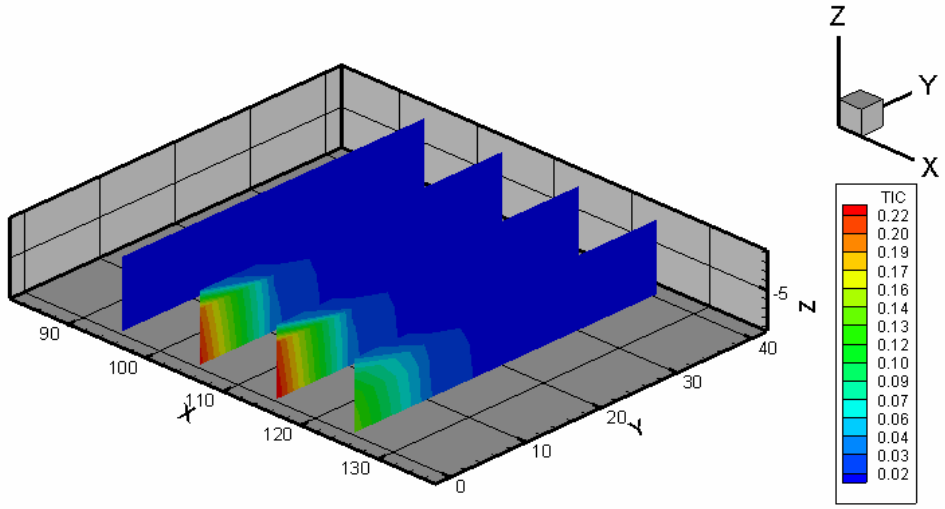

Fig. 4.77. Profiles of concentration of Total Inorganic Carbon (TIC) at x= 95 m, x =105 m, x = 115 m, and x = 125 m after 100 years of CO_2 intrusion in the 3D model with CO_2 leakage rate of 7.5×10^{-5} kg/s.

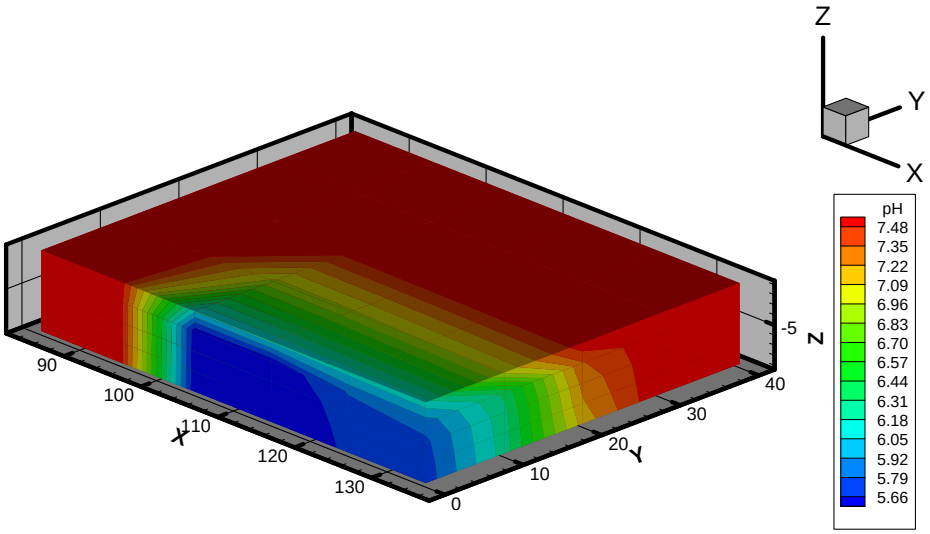

Fig. 4.78. Close-up view of spatial distribution of pH in 3D model after 100 years of CO_2 intrusion in the 3D model with CO_2 leakage rate of 7.5×10^{-5} kg/s.

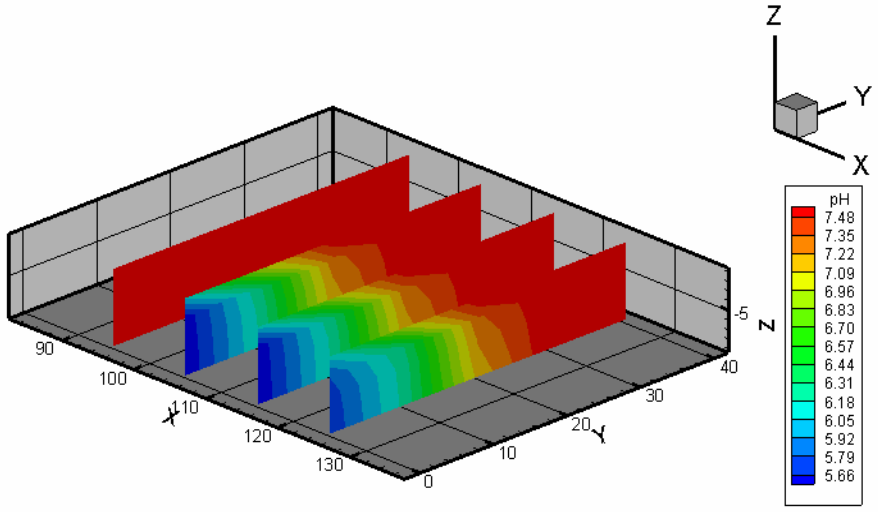

Fig. 4.79. Profiles of pH at x= 95 m, x =105 m, x = 115 m, and x = 125 m after 100 years of CO_2 intrusion in the 3D model with CO_2 leakage rate of 7.5×10^{-5} kg/s.

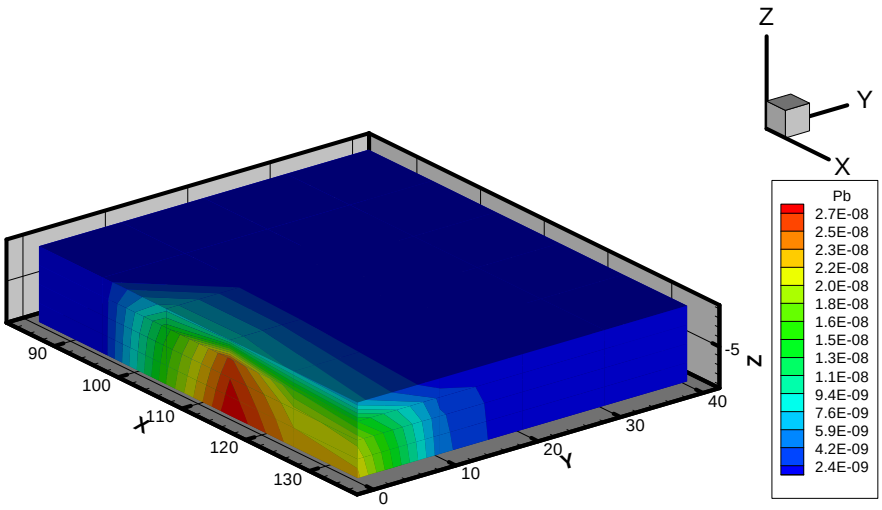

Fig. 4.80. Close-up view of spatial distribution of total aqueous Pb concentration after 100 years of CO_2 intrusion in the 3D model with CO_2 leakage rate of 7.5×10^{-5} kg/s.

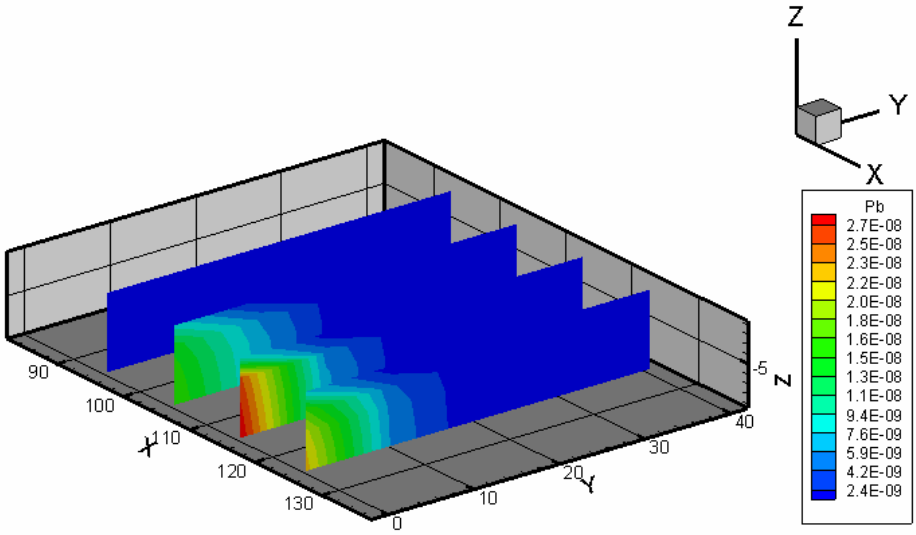

Fig. 4.81. Profiles of total aqueous Pb concentration at x= 95 m, x =105 m, x = 115 m, and x = 125 m after 100 years of CO_2 intrusion in the 3D model with CO_2 leakage rate of 7.5×10^{-5} kg/s.

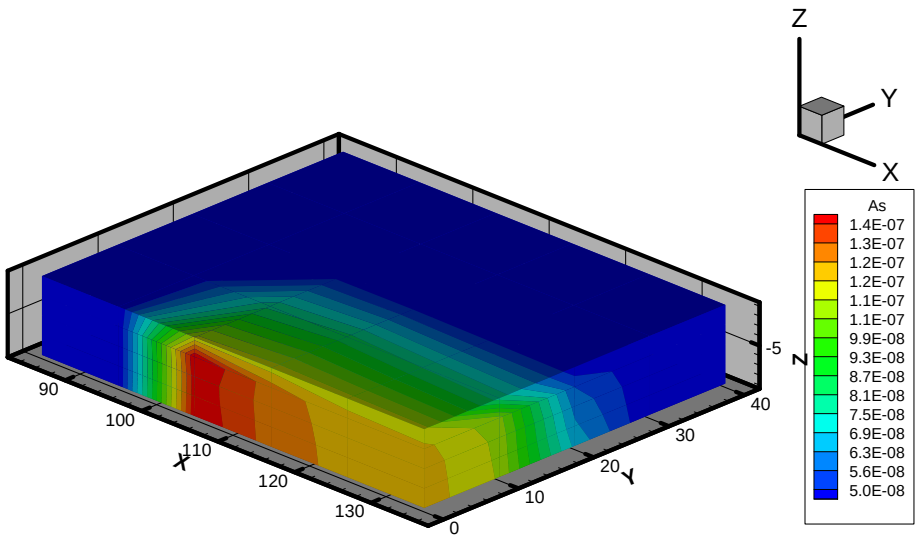

Fig. 4.82. Close-up view of spatial distribution of total aqueous As concentration after 100 years of CO_2 intrusion in the 3D model with CO_2 leakage rate of 7.5×10^{-5} kg/s.

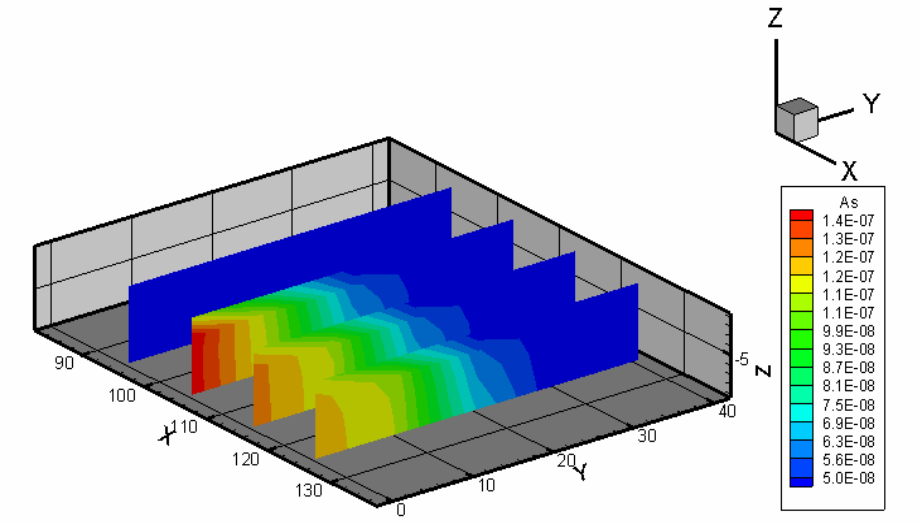

Fig. 4.83. Profiles of total aqueous As concentration at x= 95 m, x =105 m, x = 115 m, and x = 125 m after 100 years of CO_2 intrusion in the 3D model with CO_2 leakage rate of 7.5×10^{-5} kg/s.

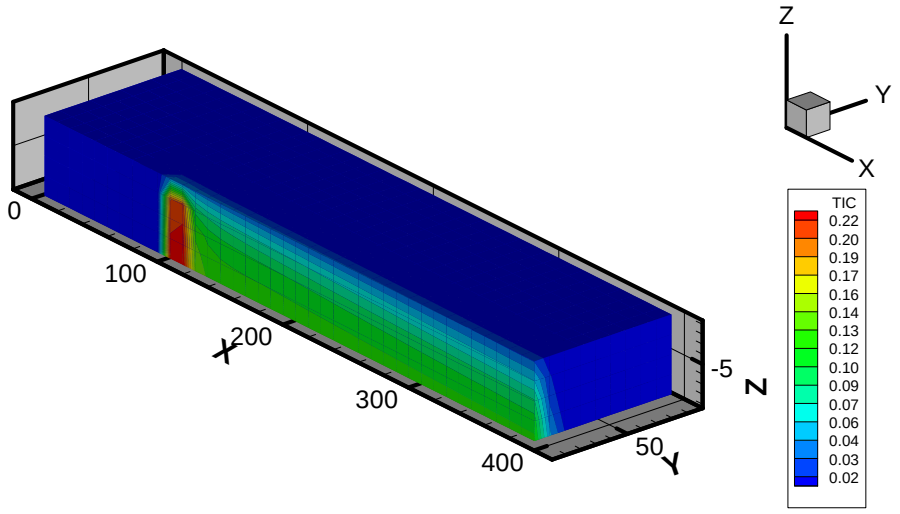

Fig. 4.84. Spatial distribution of Total Inorganic Carbon (TIC) after 100 years of CO_2 intrusion in 3D model with CO_2 leakage rate of 7.5×10^{-5} kg/s.

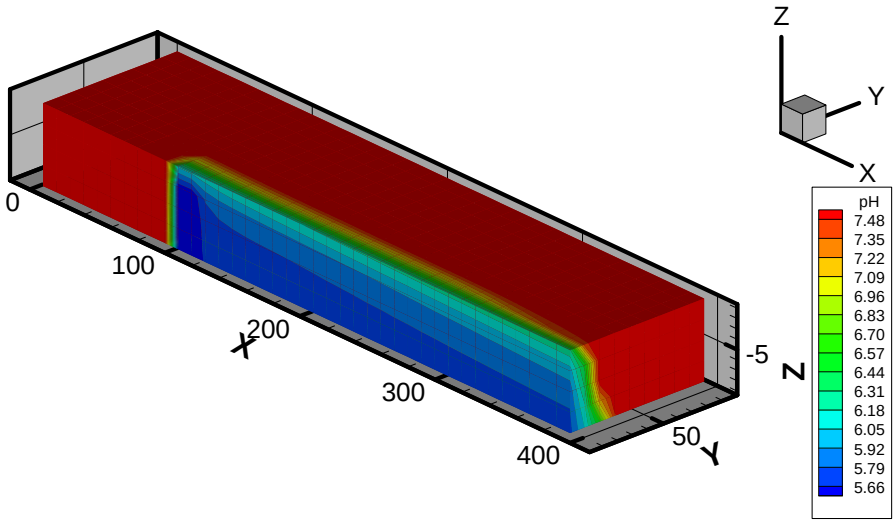

Fig. 4.85. Spatial distribution of pH after 100 years of CO_2 intrusion in 3D model with CO_2 leakage rate of 7.5×10^{-5} kg/s.

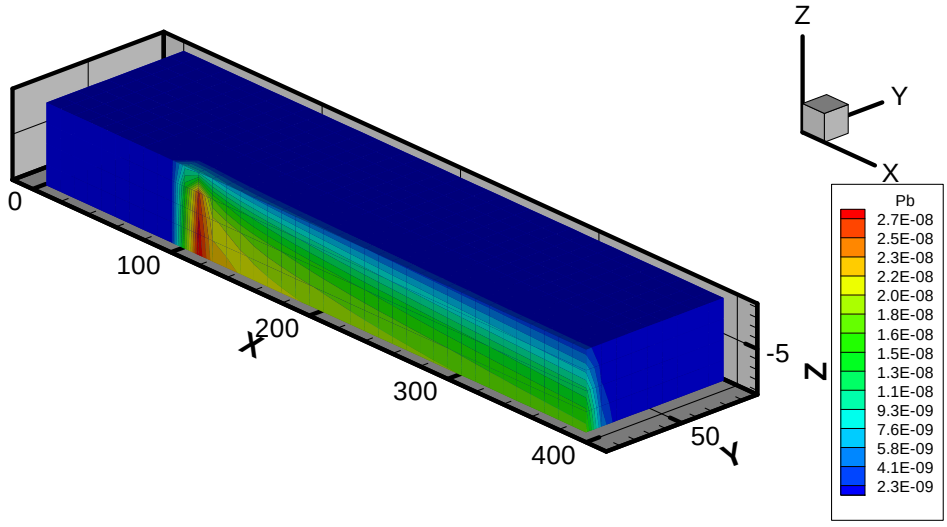

Fig. 4.86. Spatial distribution of total aqueous Pb concentration after 100 years of CO_2 intrusion in 3D model with CO_2 leakage rate of 7.5×10^{-5} kg/s.

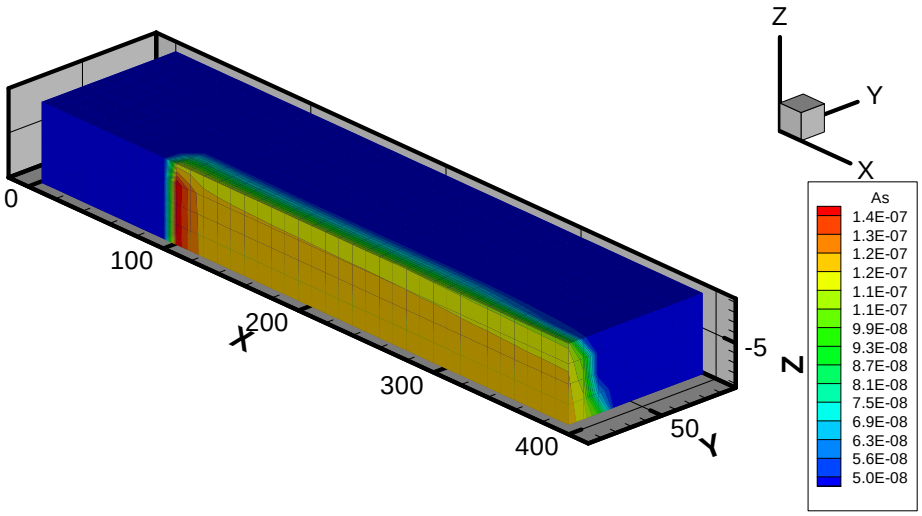

Fig. 4.87. Spatial distribution of total aqueous As concentration after 100 years of CO_2 intrusion in 3D model with CO_2 leakage rate of 7.5×10^{-5} kg/s.

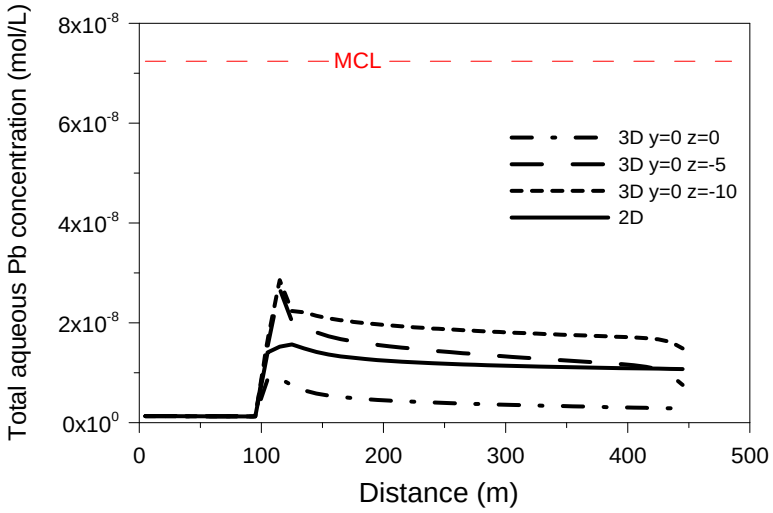

Fig. 4.88. Total aqueous Pb concentration along x-axis at y = 0 m and different aquifer depths (z = 0, -5 and -10 m) for 3D model and total aqueous Pb concentration along x-axis at y = 0 m for 2D model.

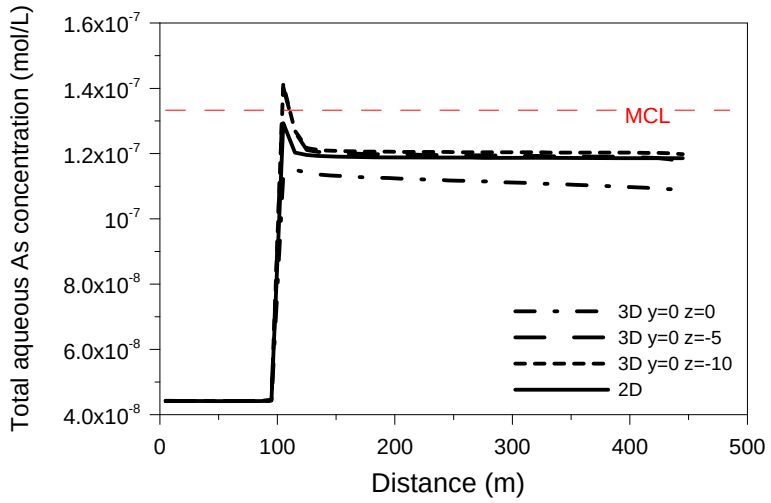

Fig. 4.89. Total aqueous As concentration along x-axis at y = 0 m and different aquifer depth (z = 0, -5 and -10 m) for 3D model and total aqueous As concentration along x-axis at y = 0 m for 2D model.

We may conclude that the 2D results provide a reasonable approximation of the three-dimensional system behavior. The differences observed between 3D and 2D are well within the range stemming from uncertainties in many of the geochemical parameters. Of course, this is a conclusion specific to the considered case, which has a small zone of gaseous CO_2 and is therefore not dominated by buoyancy effects. Furthermore, we point out that the

TOUGHREACT transport model has been set up such that lateral and vertical mixing is limited (i.e., by setting hydrodynamic dispersion to zero, or by choosing homogenous rather than spatially distributed parameters). More vertical mixing in the 3D model would lead to stronger equilibration over the thickness of the aquifer, thus further improving the agreement between 2D and 3D models.

4.9.2 Sensitivity to Groundwater Flow Velocity—3D Model

Our 2D simulation of the sensitivity to groundwater flow velocity case indicates that a much larger two-phase zone with gaseous CO_2 and water evolves when the groundwater flow rate decreases to 1 m/y (Section 4.6.8). In such a case, buoyancy forces should be more relevant than in the base model, suggesting that a 3D model representation may be necessary. Figures 4.90 and 4.91 show the 3D model results of CO_2 gas saturation after 100 years of CO_2 intrusion in an aquifer with a groundwater flow rate of 1 m/yr. With less water flowing towards the intrusion zone, dissolution of CO_2 is less effective. As a result, most of the leaking CO_2 remains in the gas phase, migrates upward until it reaches the upper closed boundary of the confined aquifer, and then spreads out laterally. A strongly three-dimensional behavior can be seen, with significant vertical variability, which is not captured by the 2D model results shown in Section 4.6.8.

Figures 4.92 and 4.93 provide contours of dissolved CO_2 (given as total inorganic carbon, TIC) as predicted by the 3D model. CO_2 has dissolved into the aqueous phase wherever gaseous CO_2 is in contact with water. Thus the region of elevated TIC corresponds roughly with the CO_2 plume volume, with high levels of TIC near the intrusion location and at the aquifer top. However, some advective and diffusive transport of dissolved CO_2 also widens the region somewhat, with elevated TIC observed mainly in the downstream direction from the intrusion location.

The spatial distributions of pH, total aqueous Pb, and total aqueous As concentration shown in Figures 4.94 through 4.99 correlate well with the TIC contours. Due to the buoyancy of the CO_2 gas, contamination occurs mainly near the top of aquifer. In this region, increased acidity and

elevated contaminant concentrations extends far from the intrusion location, both downstream and upstream as well as laterally. In the lower portions of the aquifer, contamination occurs primarily near the location of intrusion.

A direct and quantitative comparison of predicted 3D and 2D results for this sensitivity case is provided in Figures 4.100 and 4.101. Figure 4.100 shows the total aqueous Pb concentration along the x axis for different aquifer depths (top at z = 0 m, middle at z = -5 m, and bottom at z = -10 m) in the 3D model, together with the depth-averaged results from the 2D model. The top figures are for x-axis profiles at y = 0 m; i.e., they intersect the CO_2 intrusion location. The bottom figures are at y = 50 m, away from the intrusion location. While the predicted maximum concentrations are similar, the 2D results clearly underestimate the extent of contamination at the top of the aquifer and do not capture the spatial characteristics of contamination in the lower aquifer body. Figure 4.101 for As shows similar discrepancies. We conclude that this sensitivity case clearly demonstrates the necessity of using a 3D model, especially in aquifers where advective velocity is low. The 2D results can, at best, provide a first-order approximation of the system behavior.

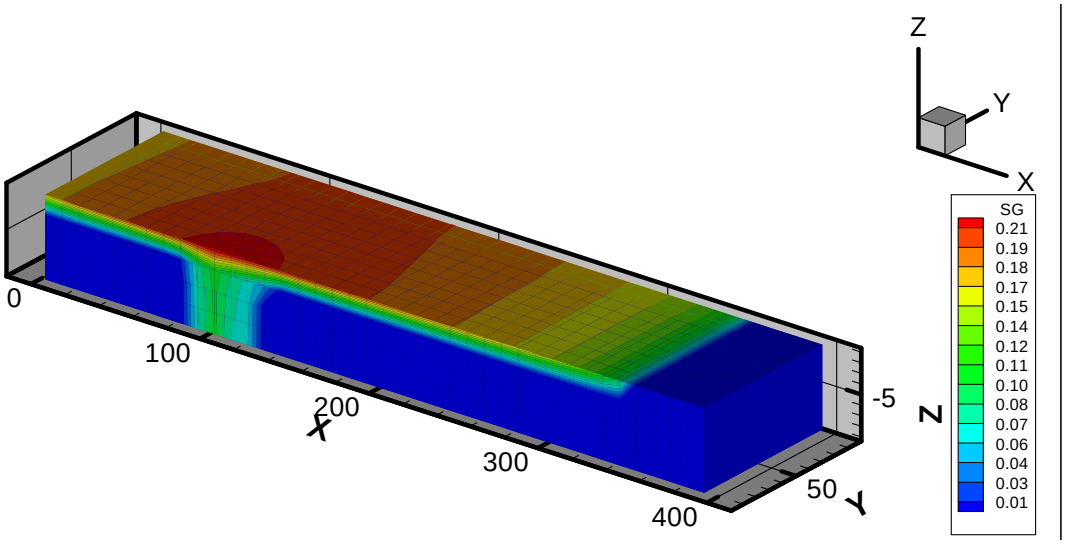

Fig. 4.90. Spatial distribution of CO_2 gas saturation after 100 years of CO_2 intrusion in 3D model with flow rate of 1 m/y.

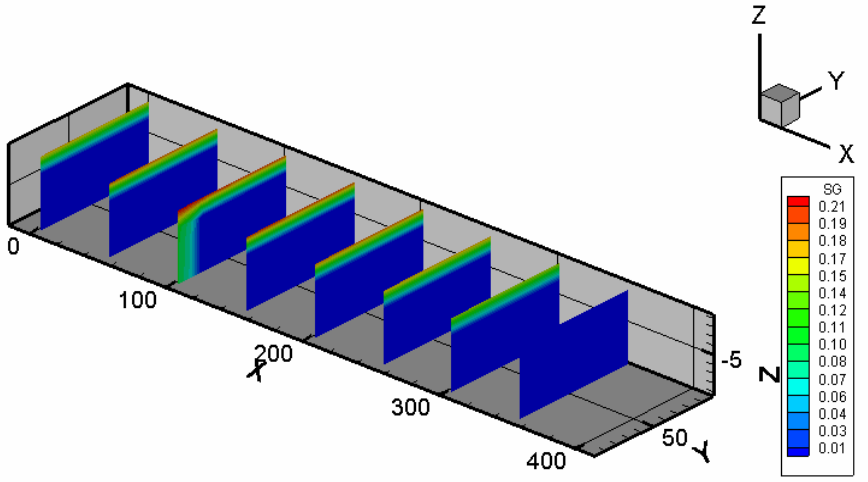

Fig. 4.91. Profiles of CO_2 gas saturation at different locations after 100 years of CO_2 intrusion in 3D model with flow rate of 1 m/y.

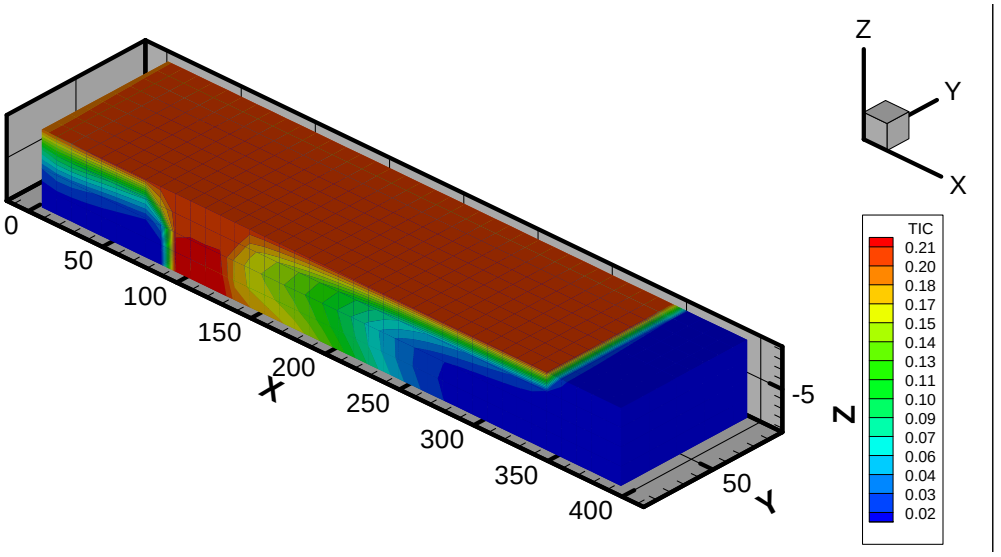

Fig. 4.92. Spatial distribution of total inorganic carbon (TIC) after 100 years of CO_2 intrusion in 3D model with flow rate of 1 m/y.

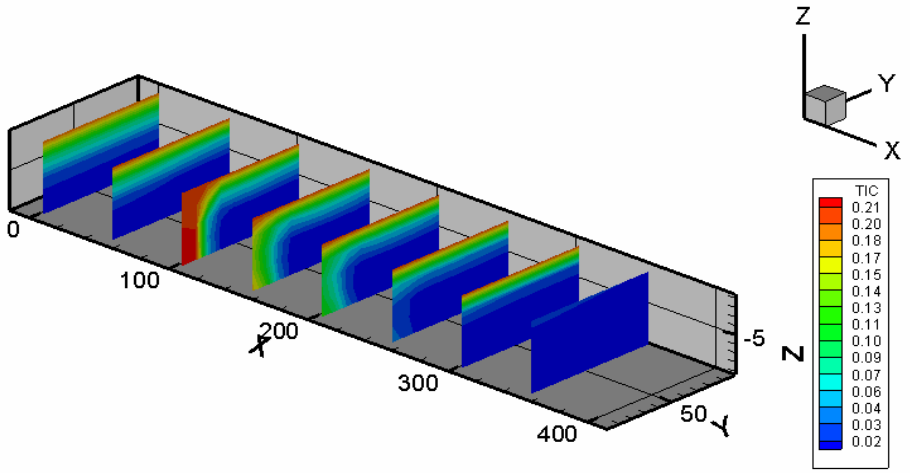

Fig. 4.93. Total inorganic carbon (TIC) y-z profile at different locations after 100 years of CO_2 intrusion in 3D model with flow rate of 1 m/y.

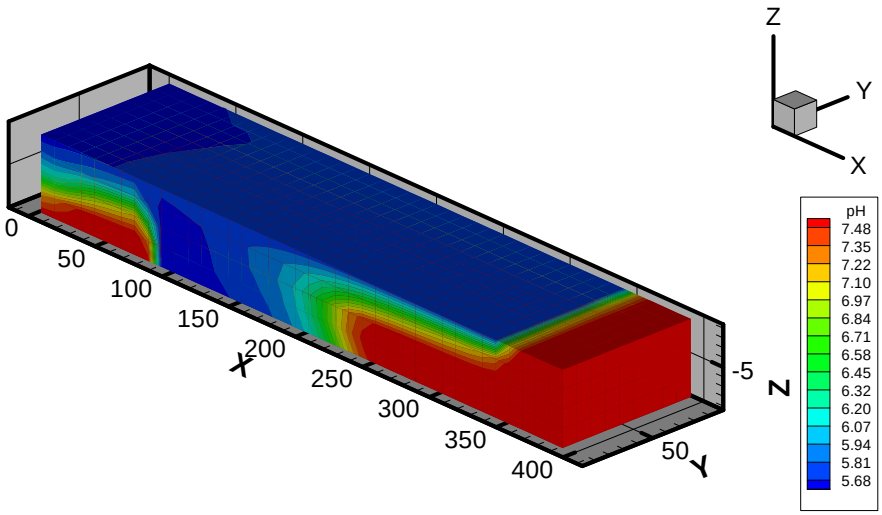

Fig. 4.94. Spatial distribution of pH after 100 years of CO_2 intrusion in 3D model with flow rate of 1 m/y.

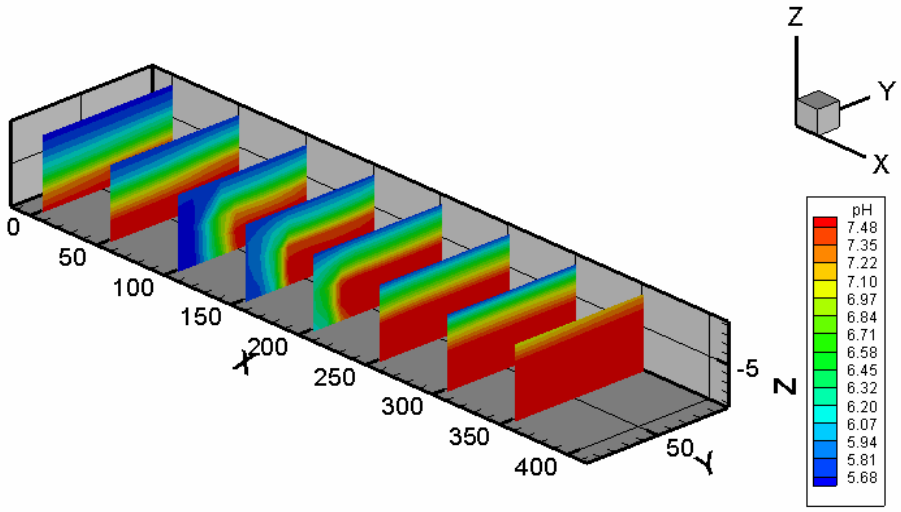

Fig. 4.95. Profiles of pH at different locations after 100 years of CO_2 intrusion in 3D model with flow rate of 1 m/y.

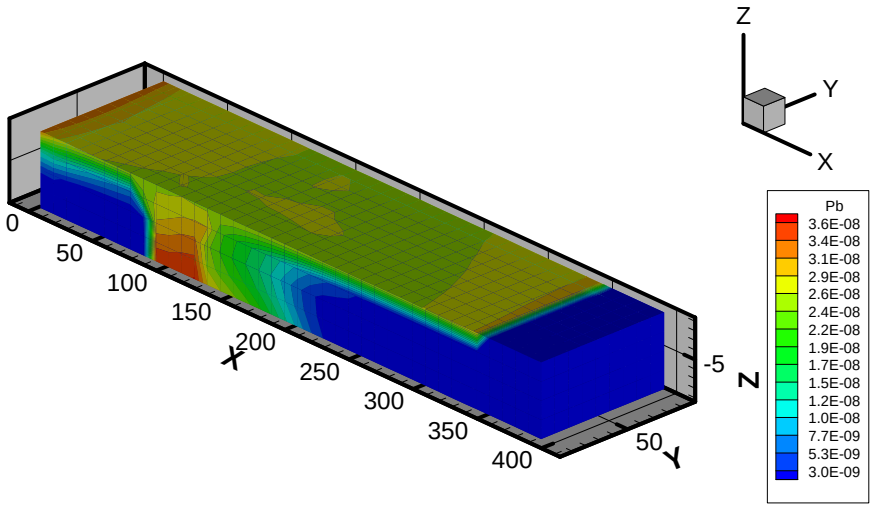

Fig. 4.96. Spatial distribution of total aqueous Pb concentration after 100 years of CO_2 intrusion in 3D model with flow rate of 1 m/y.

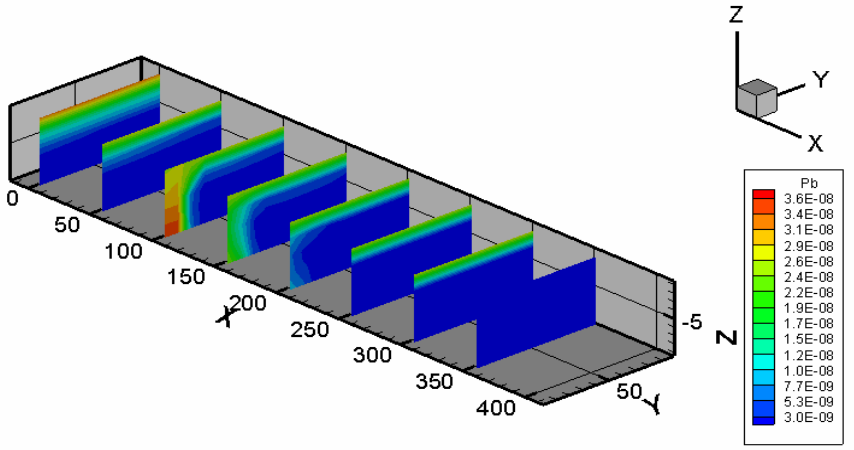

Fig. 4.97. Profiles of total aqueous Pb concentration at different locations after 100 years of CO_2 intrusion in 3D model with flow rate of 1 m/y.

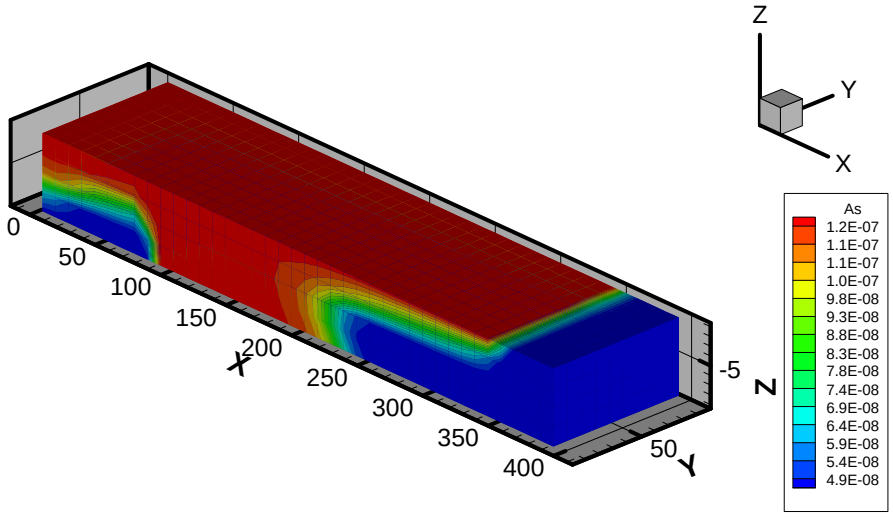

Fig. 4.98. Spatial distribution of total aqueous As concentration after 100 years of CO_2 intrusion in 3D model with flow rate of 1 m/y.

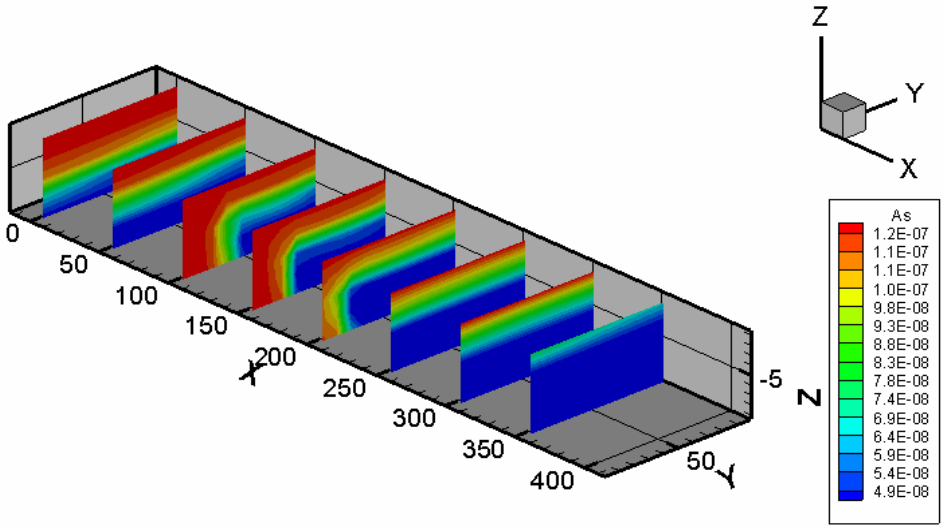

Fig. 4.99. Profiles of total aqueous As concentration at different locations after 100 years of CO_2 intrusion in 3D model with flow rate of 1 m/y.

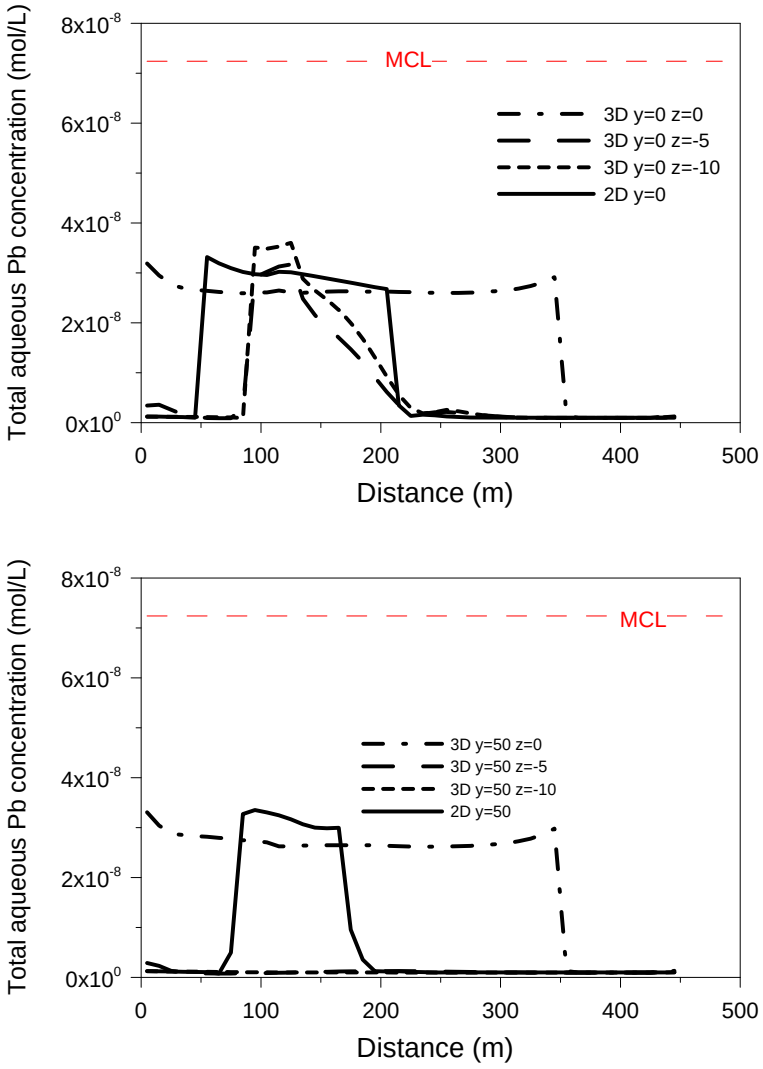

Fig. 4.100. Total aqueous Pb concentration along x-axis at different aquifer depths (z = 0, -5 and -10 m) for 3D model and total aqueous Pb concentration along x-axis for 2D model (both models have a flow rate of 1 m/y). Top figure shows x-axis profiles at y = 0 m, bottom figure shows profiles y = 50 m.

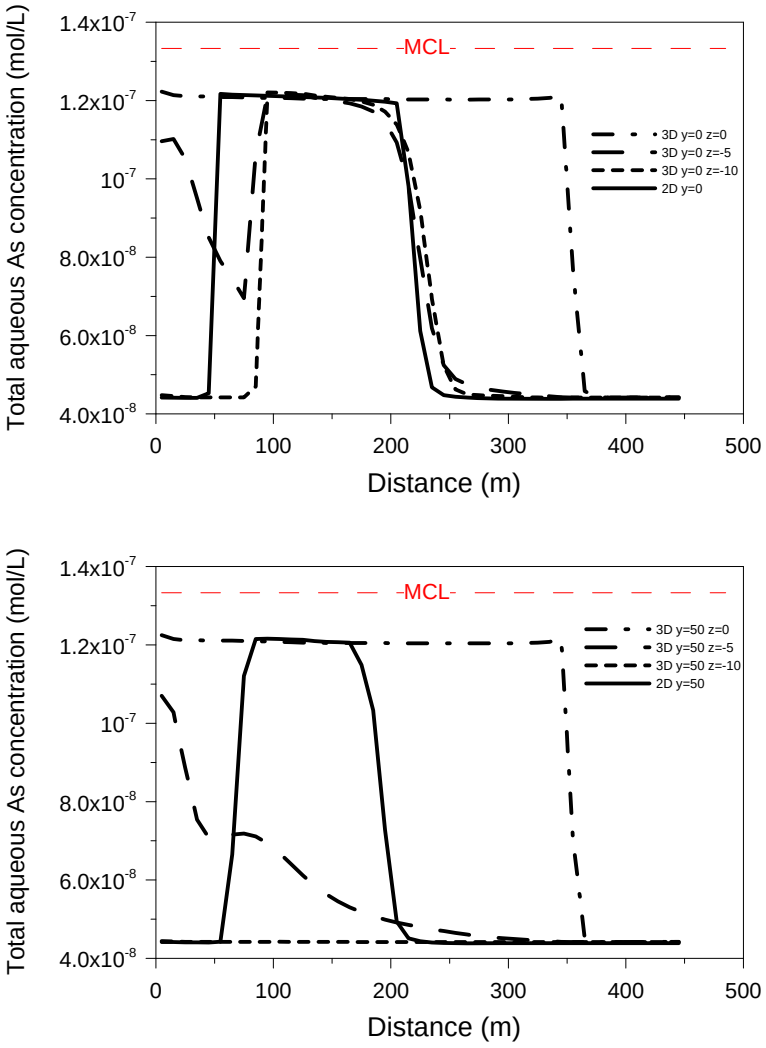

Fig. 4.101. Total aqueous As concentration along x-axis at different aquifer depths (z = 0, -5 and -10 m) for 3D model and total aqueous As concentration along x-axis for 2D model (both models have a flow rate of 1 m/y). Top figure shows x-axis profiles at y = 0 m, bottom figure shows profiles at y = 50 m.

4.9.3 Sensitivity to CO_2 Leakage Rate — 3D Model

An increased CO_2 leakage rate (by a factor of 8) has shown that a large CO_2 gas plume is generated, as evident in the 2D results (Section 4.6.9), suggesting that buoyancy forces are relevant and that a 3D model should provide a better simulation. Figures 4.102 and 4.103 show model results of CO_2 gas saturation, as predicted by the 3D model, for the situation after 100 years of CO_2 leakage into the aquifer. As expected, the buoyancy of CO_2 leads to accumulation of a gaseous plume at the top of the aquifer and induces significant vertical variation in gas saturation. Note that the groundwater flow direction affects the distribution of the CO_2 plume at the aquifer top, which extends much further downstream than upstream.

Figures 4.104 and 4.105 show contours of dissolved CO_2 (total inorganic carbon). Two principal factors affect the spatial distribution of TIC: (1) the distribution of the CO_2 plume, and (2) the advective-diffusive transport of dissolved CO_2 with the groundwater flow. The dissolved CO_2 concentrations thus follow the general pattern of the CO_2 plume (e.g., the spreading of the plume at the top), but also show a significant migration of CO_2-charged water from the intrusion location further downstream (evident at the bottom of the aquifer along the x-axis). The spatial distributions of pH, total aqueous Pb, and total aqueous As concentration (Figure 4.106 to 4.111) follow similar trends as TIC. Areas with increased acidity as well as high Pb and As correspond to areas with elevated TIC. Overall, a strongly three-dimensional behavior can be seen in these plots, with significant vertical variability, which is not well represented by the 2D model results shown in Section 4.6.9.

A direct and quantitative comparison of predicted 3D and 2D results for this sensitivity case is provided in Figures 4.112 and 4.113. The figures show, respectively, total aqueous Pb and As concentration along the x-axis for different aquifer depths (top at z = 0 m, middle at z = -5 m, and bottom at z = -10 m) in the 3D model, together with the depth-averaged results from the 2D model. The top figures are for profiles at y = 0 m, intersecting the CO_2 intrusion location. The bottom figures are for profiles at y = 50 m. Interestingly, the 3D and 2D results are not too different for the top figures; there is no significant vertical variation in the 3D results measured

along the x-axis. One reason is that the groundwater above the intrusion location appears to be completely saturated with CO_2, meaning that the TIC does not increase further even though gaseous CO_2 continues to transit upward from the bottom to the top of the aquifer. Carbon dioxide is thus relatively well equilibrated in the vertical direction near the intrusion location, and vertically uniform geochemical conditions are observed. This uniformity does not deviate significantly further downstream, because the CO_2-charged and possibly contaminated water travels sufficiently far within the 100-year simulation time to reach the downstream model boundary. In other words, contamination via transport of dissolved CO_2 in the lower portion of the aquifer is comparable with contamination where extensive spreading of the gas plume occurs at the top of aquifer. However, as Figures 4.106 through 4.111 suggest, vertical variability of TIC, pH, Pb, and As is much stronger for all locations offset from that immediately downstream of the intrusion location (i.e., away from y = 0 m), indicating that indeed a 3D model is preferred for this sensitivity case. This is clearly evident from the x-axis profiles at y = 50 m in Figures 4.112 and 4.113, where the 2D results are in good agreement with the 3D concentrations at the top of the aquifer (where gaseous CO_2 accumulates), but strongly overpredict those in the lower aquifer portions.

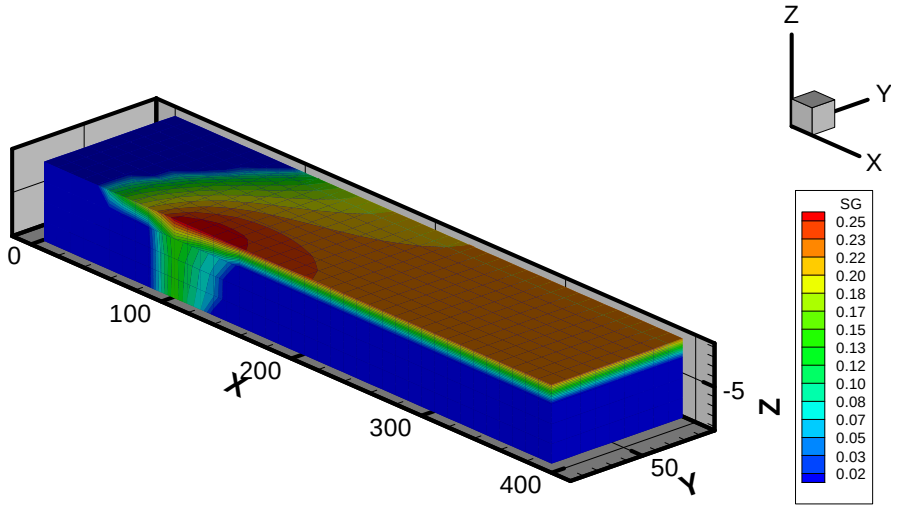

Fig. 4.102. Spatial distribution of CO_2 gas saturation after 100 years of CO_2 intrusion in 3D model with CO_2 leakage rate of 6×10^{-4} kg/s.

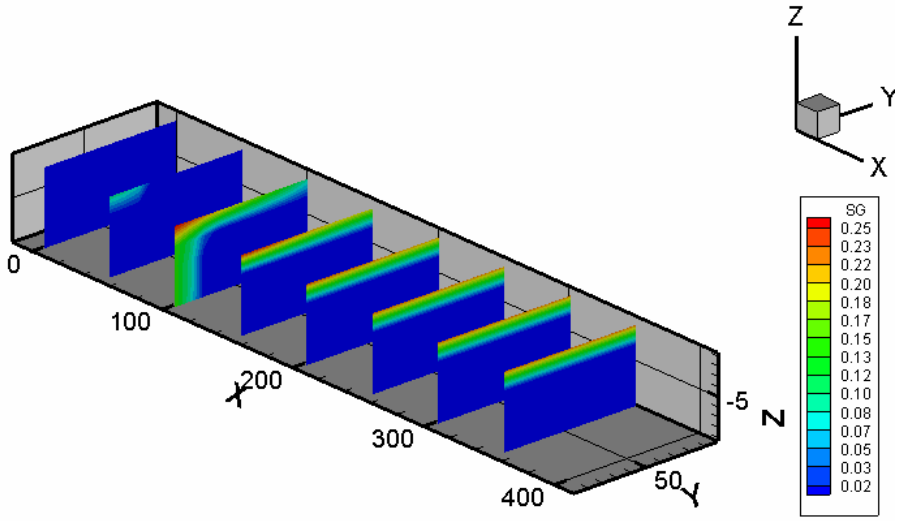

Fig. 4.103. Profiles of CO_2 gas saturation at different locations after 100 years of CO_2 leakage in the 3D model with CO_2 intrusion rate of 6×10^{-4} kg/s.

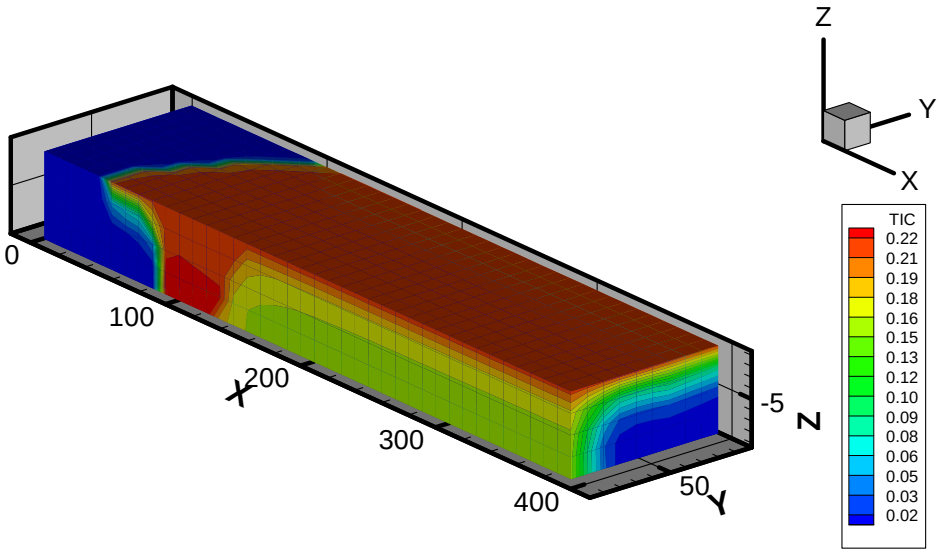

Fig. 4.104. Spatial distribution of TIC after 100 years of CO_2 intrusion in 3D model with CO_2 leakage rate of 6×10^{-4} kg/s.

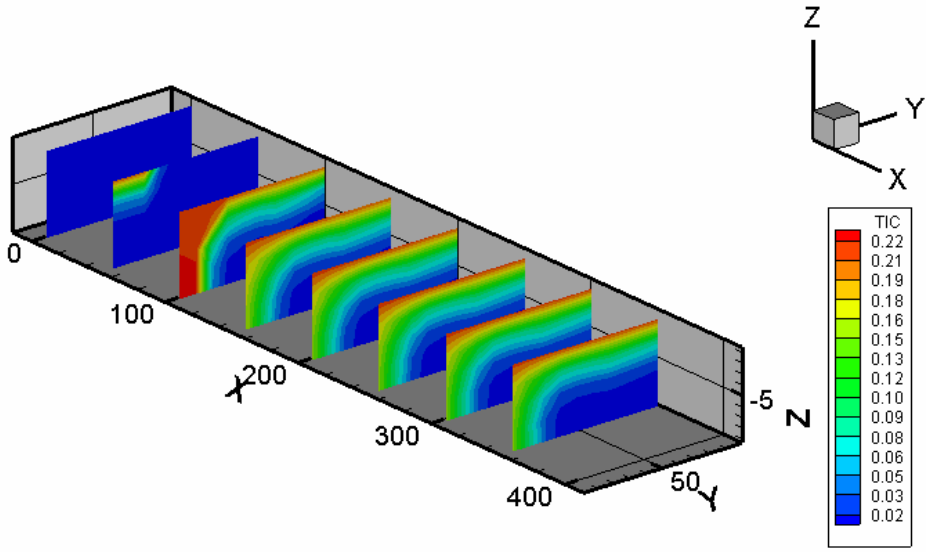

Fig. 4.105. Profiles of Total Inorganic Carbon (TIC) at different locations after 100 years of CO_2 intrusion in the 3D model with CO_2 leakage rate of 6×10^{-4} kg/s.

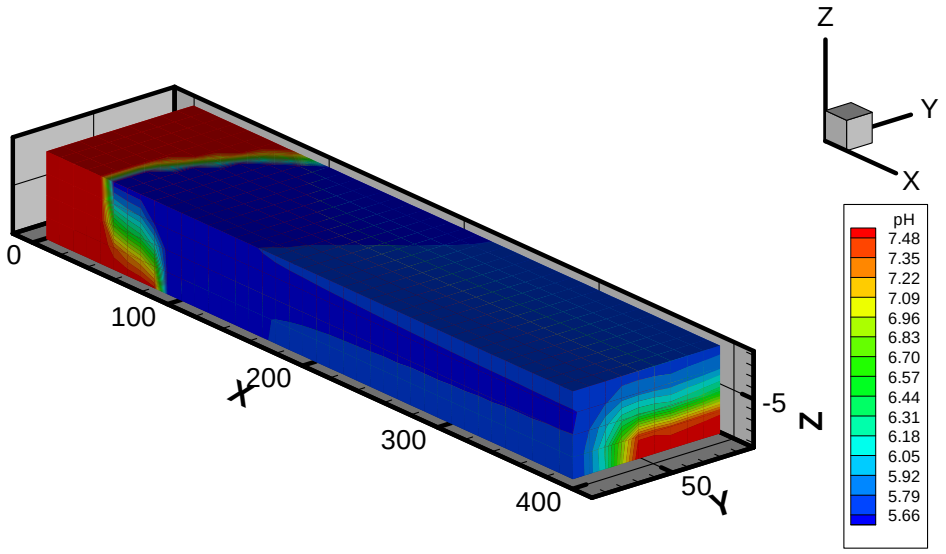

Fig. 4.106. Spatial distribution of pH after 100 years of CO_2 intrusion in 3D model with CO_2 leakage rate of 6×10^{-4} kg/s.

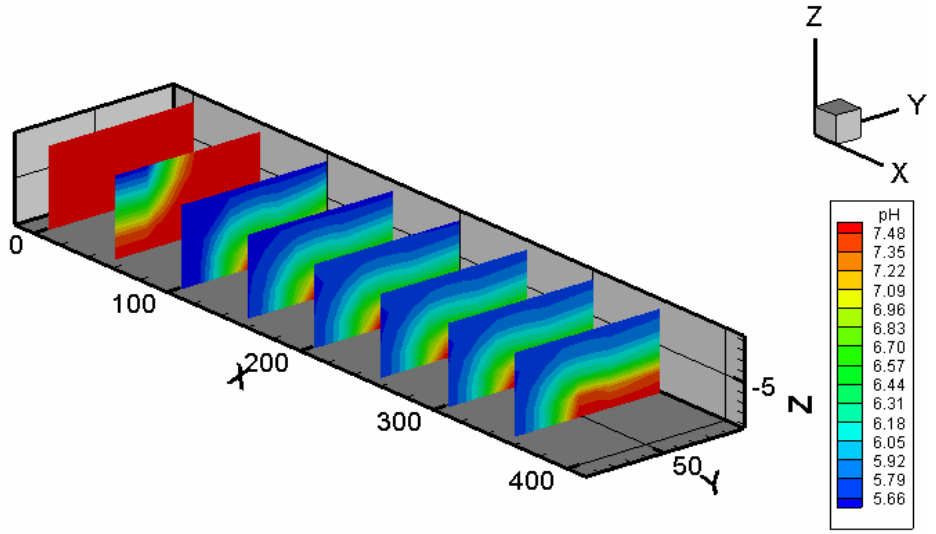

Fig. 4.107. Profiles of pH at different locations after 100 years of CO_2 intrusion in the 3D model with CO_2 leakage rate of 6×10^{-4} kg/s.

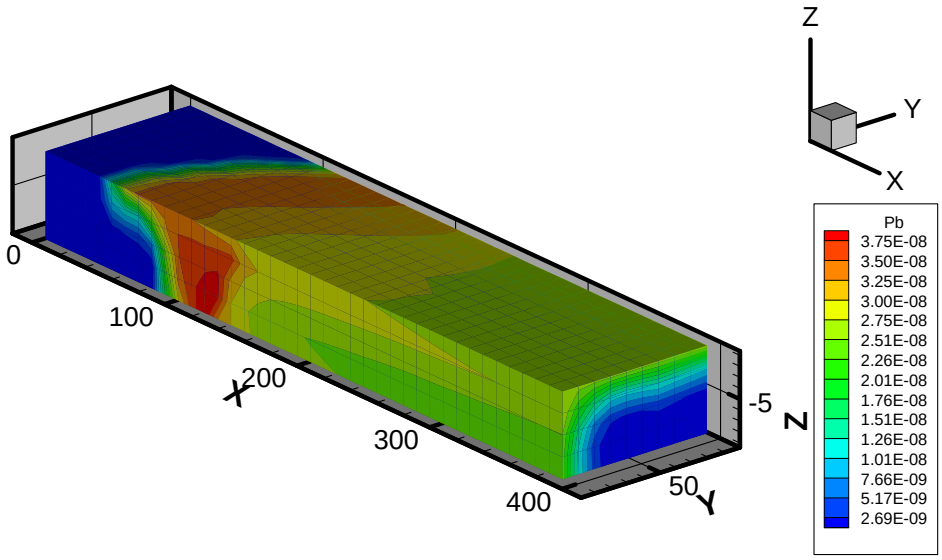

Fig. 4.108. Spatial distribution of total aqueous Pb concentration after 100 years of CO_2 intrusion in 3D model with CO_2 leakage rate of 6×10^{-4} kg/s.

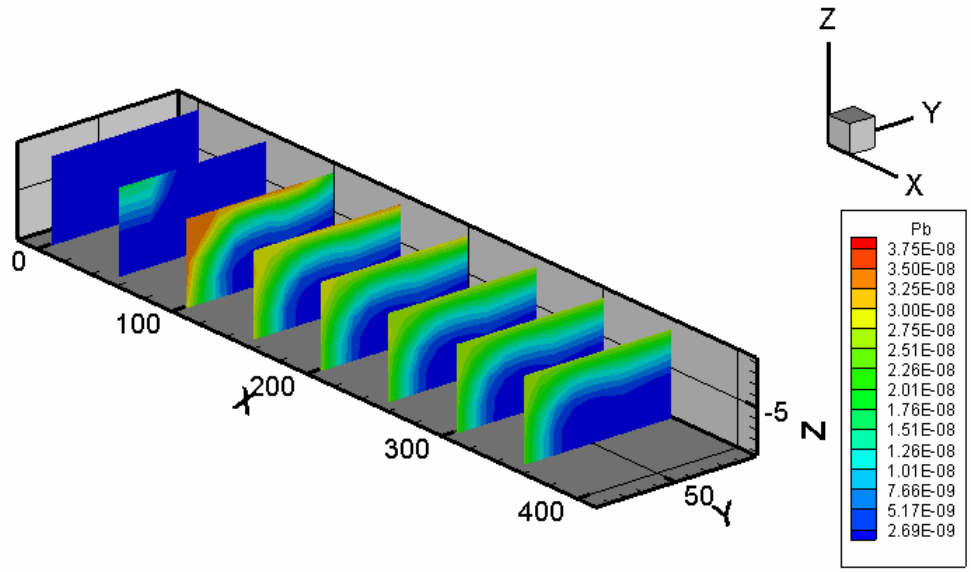

Fig. 4.109. Profiles of total aqueous Pb concentration at different locations after 100 years of CO_2 intrusion in the 3D model with CO_2 leakage rate of 6×10^{-4} kg/s.

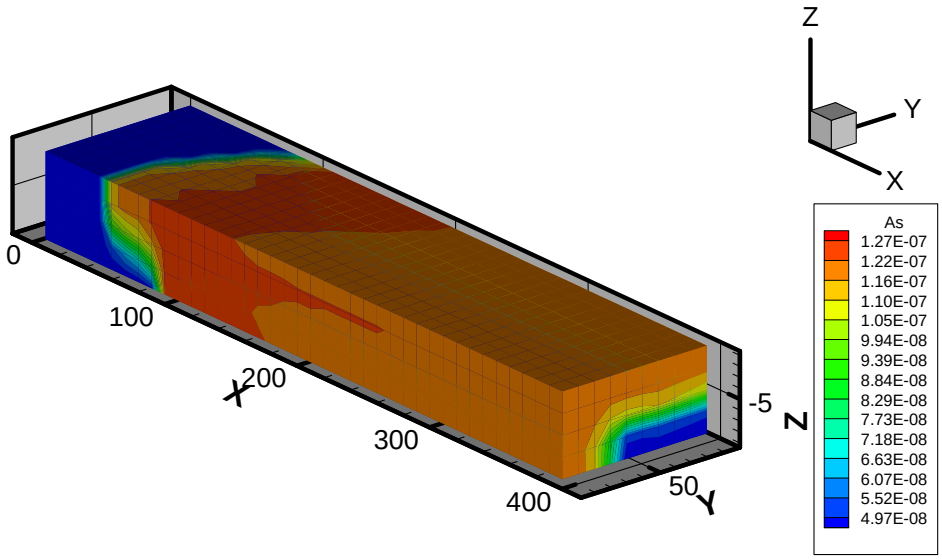

Fig. 4.110. Spatial distribution of total aqueous As concentration after 100 years of CO_2 intrusion in 3D model with CO_2 leakage rate of 6×10^{-4} kg/s.

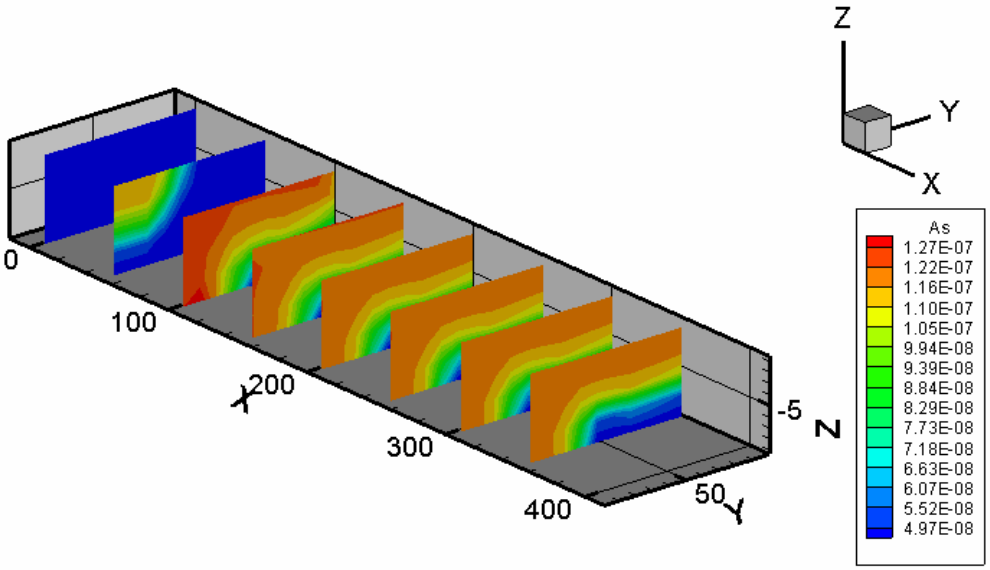

Fig. 4.111. Profiles of total aqueous As concentration at different locations after 100 years of CO_2 intrusion in the 3D model with CO_2 leakage rate of 6×10^{-4} kg/s.

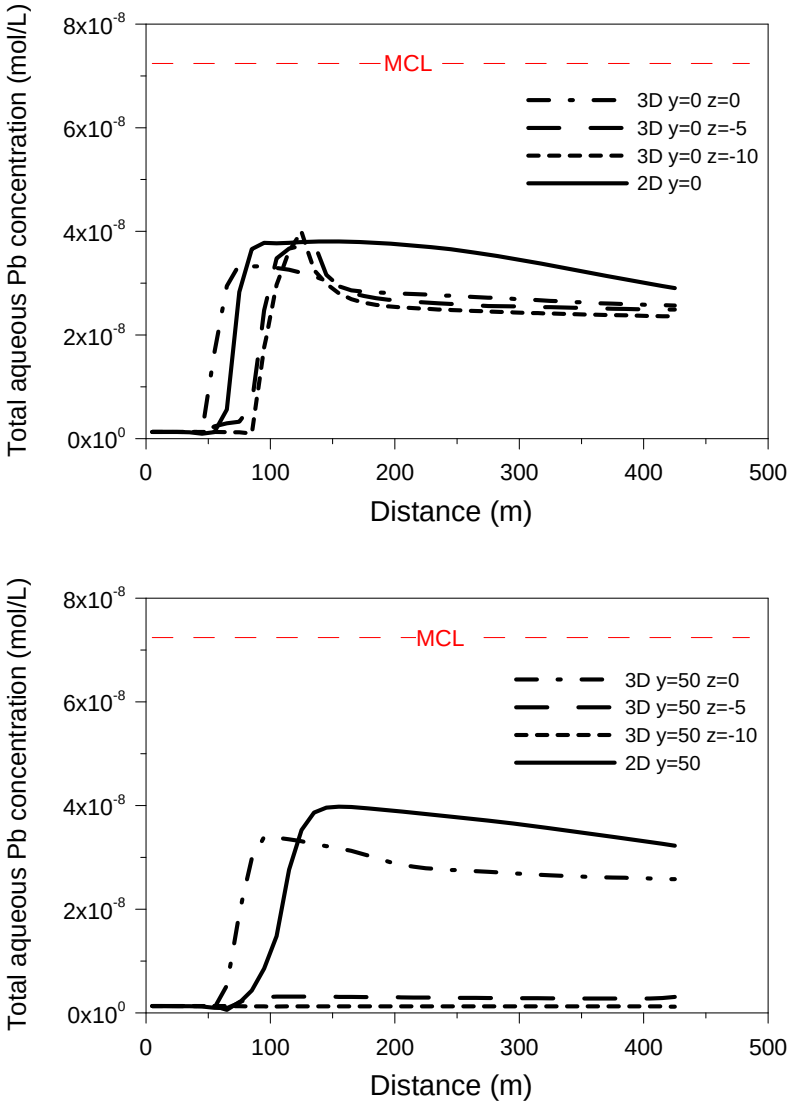

Fig. 4.112. Total aqueous Pb concentration along x-axis at different aquifer depths (z = 0, -5 and -10 m) for 3D model and total aqueous Pb concentration along x-axis for 2D model (both models have a CO_2 intrusion rate of 6×10^{-4} kg/s). Top figure shows x-axis profiles at y = 0 m, bottom figure shows profiles y = 50 m.

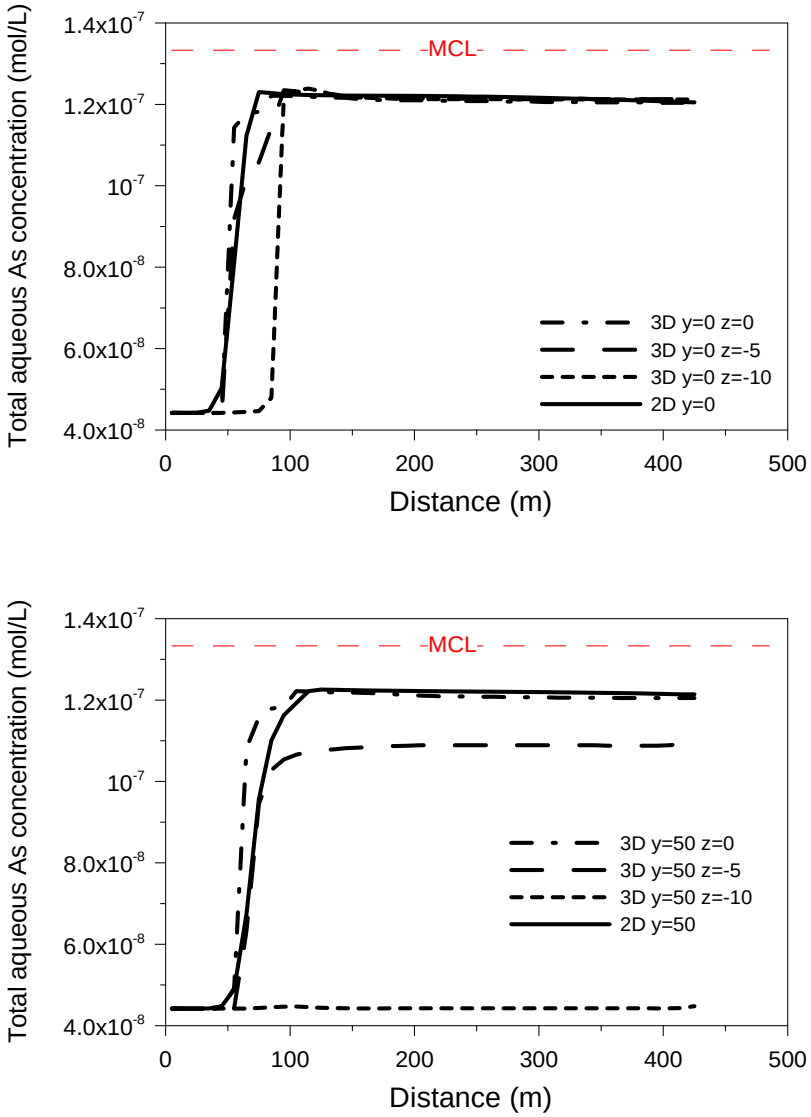

Fig. 4.113. Total aqueous As concentration along x-axis at different aquifer depths (z = 0, -5 and -10 m) for 3D model and total aqueous As concentration along x-axis for 2D model (both models have a CO_2 intrusion rate of 6×10^{-4} kg/s). Top figure shows x-axis profiles at y = 0 m, bottom figure shows profiles y = 50 m.

4.10 Summary of Modeling Results

Systematic reactive transport simulations have been conducted to evaluate the effect of CO_2 intrusion into domestic shallow potable aquifers. A synthetic simplified hydrogeological situation was considered as described in Section 4.2. The model starts with the basic assumption that CO_2 stored in deep geologic units can escape via preferential pathways, such as a fault zone, and enter the shallow aquifer locally from below at a constant rate. The reactive transport model is used to predict the transport of gaseous and dissolved CO_2 within the shallow aquifer as well as the geochemical changes introduced by the presence of CO_2, in particular the mobilization of potentially hazardous constituents and their migration in the groundwater. Various sensitivity studies have been conducted for different hydrological, geochemical, and mineralogical conditions, to (1) account (partially) for the range of conditions found in domestic potable aquifers and their host rocks, and (2) to evaluate the uncertainty associated with geochemical processes and model parameters. The base model setup and the sensitivity scenarios have been selected based on the geochemical model definition described in Section 3.

With respect to hazardous constituents, the focus in this modeling study is on Pb and As mobilization. It is assumed in all simulation cases that small volume fractions of minerals containing hazardous constituents are present in the aquifers, including those containing Pb and As as essential components. Based on the discussion in Sections 3.3.3 and 3.6.2.2, the presence of such trace minerals can be considered a reasonable possibility in all aquifers. The minerals that are considered to control the aqueous concentrations of Pb and As are, respectively, galena and arsenopyrite (the latter in solid solution in pyrite). These were identified in Section 3.4 as likely solubility-controlling mineral hosts under reducing conditions, a conclusion obtained from thermodynamic evaluation of more than 35,000 groundwater analyses in the NWIS database.

Equilibrium runs were conducted prior to modeling CO_2 intrusion to establish the initial chemical composition of the groundwater at equilibrium with the selected mineralogy. This initiation step also establishes equilibrium between mineral solubilities and adsorption sites, essentially “loading” these up. Thus, the selection of solubility-controlling minerals for

hazardous inorganic constituents not only defines the initial aqueous concentration in the groundwater, but also affects the amount of contaminants initially sorbed onto clays or goethite.

Starting with the equilibrated initial conditions, the impact of CO_2 intrusion was then modeled with the reactive transport simulator TOUGHREACT, for a simulation time period of 100 years with continuous ingress of CO_2. Our simulation results suggest that CO_2 ingress into a shallow aquifer can lead to significant and long-lasting mobilization of Pb and As, contaminating the groundwater near the intrusion location and further downstream of it. However, while strong increases in aqueous concentrations are predicted to occur compared to the initial water composition, the MCL for As in groundwater has been exceeded in only a few simulation cases, whereas the MCL for Pb has not been exceeded at all. According to our sensitivity study, many conditions and factors impact the severity and spatial distribution of groundwater contamination in response to CO_2 intrusion. Below, we summarize the important implications from the sensitivity study and discuss the relative importance of various conditions and factors.

Base Model

The base model described in Sections 4.2 and 4.5 assumes CO_2 entering a shallow aquifer of 10 m thickness at an annual rate of about 2.4 tonnes. The aquifer is in a reducing environment. The host rock mineralogy, referred to as Coastal Plain Sandstone, is representative of an impure sandstone aquifer. According to the model predictions, the local ingress of CO_2 results in a small two-phase zone and an elongated elevated dissolved CO_2 zone along the flow direction. This leads to moderate increases in acidity within the two-phase zone as well as in the downstream area, followed by mobilization of Pb and As. The mobilization of Pb and As depends on the complex transient interaction between adsorption/desorption onto/from mineral surfaces and dissolution/ precipitation of relevant minerals.

In the case of Pb, desorption of initially sorbed mass is the main contributor to the observed increase in aqueous concentrations. In fact, desorption releases enough Pb from adsorption sites that the solution becomes supersaturated with respect to galena, and precipitation of this mineral occurs. The resulting aqueous concentrations of Pb are about one order of magnitude higher than

the initial concentrations, but lower than the MCL (less than 3 ppb compared to the MCL of 15 ppb) within the small two-phase zone and the elongated downstream plume. As pointed out in Section 3.5, sulfide and selenide aqueous complexation play a very important role in the behavior and evolution of Pb in response to CO_2 intrusion. Because very stable neutral complexes form in solution, the impact that elevated CO_2 levels have on increasing the solubility of galena (PbS), for example, is reduced compared to the case where no complexation is considered. While not reported here, we have conducted reactive transport simulations without accounting for sulfide and selenide complexes in solution. These resulted in higher overall aqueous Pb concentrations after CO_2 intrusion compared to the base model, because both desorption and galena dissolution caused Pb mobilization in the two-phase zone.

Contrary to what is observed for Pb, desorption processes do not release sufficient As into solution to inhibit the dissolution of arsenopyrite. Therefore, desorption of As from mineral surface and dissolution of arsenopyrite occur simultaneously and lead to a substantial increase of aqueous As concentrations. The maximum concentration almost reaches the MCL (10 ppb) within the small two-phase zone and is slightly lower (about 9 ppb) than the MCL within the elongated area of increased acidity downstream of the intrusion location.

The mobilization of Pb and As, from minerals and from adsorption sites, causes only very small changes to the initial contaminant mass in the solid phase, even after a time period of 100 years of CO_2 intrusion. For example, although the initial volume fraction of arsenopyrite in the aquifer is very small, on the order of 10^{-5} of the total mineral volume, this mineral is far from being depleted after 100 years of increased acidity. Very small amounts of Pb and As contained in the aquifer solid phase can provide a long-lasting source of contamination.

Importance of Adsorption/Desorption Processes

Our simulations indicate that adsorption/desorption via surface complexation is arguably the most important process controlling the fate of hazardous constituents mobilized by CO_2 leakage when sorbing minerals are present. Adsorbed species are modeled in the TOUGHREACT simulations via a surface complexation model that takes into account the competitive

complexation of As and Pb on several clays and goethite. Our simulation results suggest that desorption of initially sorbed As and dissolution of arsenopyrite act together in mobilizing As near the region of CO_2 intrusion, whereas the desorption of Pb from mineral surfaces is so significant that galena precipitates instead of dissolving. The opposite behavior is seen further downstream. There, adsorption removes significant amounts of Pb and As from the solution, dampening further increases of contaminant concentrations.

The importance of adsorption is clearly demonstrated in Section 4.6.1.1, where a simulation without adsorption is compared to the base model considering adsorption. Without adsorption, the resulting long-term contamination of an aquifer would be less significant near the region where CO_2 enters, whereas aqueous concentrations would keep increasing with travel distance (eventually exceeding MCLs), as acidic water migrates further and more dissolution occurs. Thus, without adsorption, an important process mitigating the long-term impact of CO_2 intrusion would be neglected. Furthermore, whereas adsorption/desorption reactions are always assumed to equilibrate instantaneously, the dissolution or precipitation of galena or arsenopyrite is a kinetically controlled, slow process, and, therefore, restoration of a complete equilibrium state following perturbation of the system can take years or decades or even longer, depending on the parameters of the system. Thus, desorption of initially sorbed matter is the dominant process in mobilizing contaminants in the short term.

The relative importance of dissolution/precipitation versus adsorption/desorption is controlled by many factors including adsorption parameters and aquifer mineralogy, but also reaction kinetics, aqueous complexation processes, and solubility constants. For example, the role that adsorption/desorption plays in the mobilization of hazardous constituents depends highly on the total number of adsorption sites, which is the product of adsorption site density and specific surface area of the sorbing minerals. A sensitivity run (Section 4.6.1.2) with lower site density reveals that the increases in aqueous Pb and As are much less significant, because desorption is less relevant in mobilizing contaminants.

Different Host Rock Mineralogies

A suite of "representative" host rock mineralogies was simulated in a sensitivity study representing broad ranges of aquifer host rock compositions found throughout the United States (Section 4.7). In addition to the Coastal Plain Sandstone aquifer considered in the base case, we evaluated two other representative cases: (1) a mineral composition representative of a St Peter Sandstone and (2) a mineral composition representative of a Dolomitic Limestone. The St Peter Sandstone is composed primarily of quartz sand and has a poor pH buffering capacity, whereas the dolomitic limestone is dominated by calcite and dolomite, and has a good pH buffering capacity. Note that the host rock mineralogies differ with respect to major and accessory minerals, including clays and other adsorbents, but all have the same (small) volumetric fractions of trace minerals, including those containing Pb and As as essential components. The following conclusions can be drawn from the comparison of different host rocks:

- Even small amounts of calcite or dolomite help moderate the pH changes caused by CO_2 intrusion. The typical range of pH observed in our simulations is between 5.5 and 6, whereas values as low as 4.5 could be expected in the absence of buffering from aquifer minerals. Buffer capacity is effective as long as these minerals have not completely dissolved. In other words, the actual volumetric fraction of carbonate minerals is less relevant for buffer capacity, as long as the minerals remain present in the host rock. The St Peter Sandstone represents the most vulnerable aquifer, because the small initial amount of carbonate minerals is depleted after some time and the pH buffer capacity is lost. The dolomitic limestone is less vulnerable from the perspective of long-term effects, because it contains large amounts of carbonate minerals, which can can buffer pH for a long time.
- While buffer capacity is relevant, differences in adsorption/desorption behavior have equal or more important effects on the resulting contaminant concentrations. The host rocks considered in this study differ with respect to clay minerals and clay volumetric fractions. The dolomitic limestone, for example, results in higher As concentrations after 100 years of CO_2 intrusion, because it contains more clay minerals and thus releases more initially sorbed As into the groundwater, despite the fact that carbonate minerals provide long-term buffering capacity.

Oxidizing Versus Reducing Conditions

Although most groundwaters analyzed in Section 3 suggest reducing conditions, one sensitivity run was conducted to evaluate the potential for Pb contamination in an oxidized aquifer. The mineralogical composition of an oxidized aquifer was developed in Section 3.6.3.2, with the most relevant differences compared to the base case that pyrite is oxidized and cerussite instead of galena controls the aqueous concentration of Pb. The simulated behavior of the oxidized aquifer is very different from an aquifer in a reducing environment. Because of the much higher solubility of cerussite, the initial aqueous Pb concentration is already considerably higher than the MCL, even without considering CO_2 leakage into the aquifer. This confirms the well-known fact that oxidative dissolution can lead to significant mobilization of hazardous constituents, an effect that is often more relevant than the decrease in pH caused by CO_2 intrusion. A further increase in Pb concentration is predicted as CO_2 enters the oxidized aquifer. As discussed in Section 4.8, Pb is mobilized near the CO_2 intrusion region primarily from desorption. Further downstream, Pb precipitates out as cerussite, stabilizing the downstream Pb concentrations.

Sensitivity to Other Geochemical Parameters and Conditions

- It is known that the kinetic rate of mineral dissolution/precipitation is highly uncertain. Sensitivity simulations have been conducted varying the kinetic rate by two orders of magnitude. However, the simulated concentrations of aqueous Pb and As after 100 years of CO_2 intrusion are rather insensitive to a variation of the kinetic rate, due to the dominance of adsorption/desorption processes. Strong sensitvities were observed for simulation case in which sorption processes were neglected, with aqueous concentrations of As increasing significantly with an increase in the kinetic rate.
- The solubilities of hazardous-constituent-bearing minerals and the association constant used in the aqueous complexation of Pb are critical geochemical parameters that are not well defined in all cases. In exploratory sensitivity runs we conducted, these parameters were varied based on the variability of values found in the literature. Changes in the solubilities of galena and arsenopyrite (by about a half-order of magnitude) give rise to strong differences in the resulting aqueous concentrations of Pb and As. As discussed in Sections 4.6.4, these

differences result in part from the different dissolution behavior, but more importantly are caused by changes in the adsorption/desorption characteristics (the initial distribution of Pb and As in the aqueous phase and adsorbed on mineral surfaces changes with a variation of solubility). A variation in the PbS(aq) association constant also leads to significant changes in aqueous Pb concentrations after CO_2 intrusion.

- The initial volume fraction of galena was increased by three orders of magnitude in a sensitivity run, to understand the consequences of natural variability in trace-element minerals (Section 4.6.5.1). However, the changes in aqueous Pb concentrations were negligibly small in this sensitivity case, mainly because Pb mobilization is dominated by desorption processes, not by galena dissolution. In contrast to what was observed for Pb, an increase in the arsenopyrite volume fraction (by two orders of magnitude) gives rise to a moderate increase in the aqueous As concentrations, mainly because the dissolution kinetics are assumed to change with variation in the reactive surface area.
- One sensitivity run was conducted to evaluate the impact of a comparatively high initial partial pressure of CO_2 in the groundwater (Section 4.6.6). This has minor impact on the resulting aqueous Pb concentrations, but causes significant increases in As concentrations, both at initial conditions and after intrusion of CO_2.

Sensitivity to Hydrogeologic Conditions and CO_2 Leakage Rate

- The maximum amount of CO_2 dissolved in water is a function of fluid pressure. Thus, in a shallower aquifer, fewer CO_2-related pH changes and, consequently, smaller increases in aqueous Pb and As concentrations would be expected. A sensitivity run using an initial fluid pressure of 3 bar (30 m head), instead of 5 bar (50 m head) as in the base model, showed moderate impact, slightly decreasing the change in pH as well as the resulting contaminant concentrations compared to the base case (Section 4.6.7).
- A sensitivity run with a flow rate of 1 m per year (instead of 10 m per year in the base model) was conducted to study the effect of groundwater flow conditions on the evolution of hazardous constituents. One major effect of a reduced flow rate is that dissolution of CO_2 is

less effective, because a smaller volume of groundwater undersaturated with respect to CO_2 flows past the location where CO_2 enters the aquifer. As a result, most of the leaking CO_2 remains in the gas phase, migrates upward towards the top of the confined aquifer, and spreads out laterally. Initially modeled as a 2D depth-averaged process (Section 4.6.8), it became clear that this strongly buoyancy-driven behavior should be modeled in 3D (Section 4.9.2). Except for the uppermost portion of the aquifer, where contamination spreads widely following the dissolution of the gaseous CO_2 plume, the area affected by contamination is smaller than in the base case, because the transport of aqueous species is driven by diffusion rather than by advection (i.e., downstream transport of TIC, Pb, and As is minimal). The maximum concentrations are moderately higher than in the base case, because of less effective dilution.

- Similar 3D effects occur in a sensitivity case with increased CO_2 leakage rate (Section 4.9.3). Since the rate of CO_2 entering from below exceeds the dissolution capacity of the groundwater, the gaseous plume rises to the top of the aquifer, thereby bypassing most of the groundwater body. The resulting impact on aqueous contamination is influenced by the general pattern of the CO_2 plume (e.g., the spreading of the plume at the top of the aquifer) and the subsequent migration of CO_2-charged and contaminated water further downstream. Maximum concentrations are moderately higher than in the base case, mostly at the top of the aquifer.

- The above cases showing the evolution of larger CO_2 plumes demonstrate that the rate of CO_2 entering an aquifer has only a minor effect on the maximum contaminant concentrations. Once the groundwater reaches its solubility limit, which occurs at relatively small intrusion rates, there is no further increase in total inorganic carbon and acidity. Consequently, no further mobilization of hazardous constituents occurs once local equilibrium has been achieved. Excess CO_2 remains in the gas phase and migrates elsewhere, thereby changing the spatial distribution of possible groundwater contamination, but the contamination level remains essentially the same.

Discussion of Conservatisms and Mitigating Effects

Some assumptions made in the model setup and in the geochemical model represent conservative choices. Below, we list these choices and discuss the expected implications on the geochemical system.

- A confined aquifer was considered, meaning that excess CO_2 not dissolving into groundwater accumulates at the aquifer top, potentially causing widespread pH changes and mobilization of contaminants. Excess CO_2 in an unconfined aquifer would escape into the vadose zone, causing no further harm.
- Contaminant transport was modeled without consideration of hydrodynamic dispersion, meaning that less spreading and dilution of the dissolved CO_2 plume occurs. This tends to maximize the contaminant concentrations predicted by the model.
- CO_2 continuously enters the aquifer for an extended period of time (100 years), implying that the CO_2 leakage remains undetected and no remedial measures are undertaken.
- While the reactive transport simulations demonstrate the potential for increased concentration of Pb and As, it is not clear that the problem would remain after pumping and standard treatment of the water for potable purposes. Water recovery from the aquifer would lead to degassing of CO_2, probably causing supersaturation with respect to calcite, which would likely induce co-precipitation of these contaminants.

5. Analogues

Both natural and man-made analogues of CO_2 intrusion into groundwater may help us to better understand corresponding changes in water quality. The natural leakage of CO_2 (plus additional acid gases in some cases) from geologic reservoirs into groundwaters is discussed in Section 5.1, with emphasis on the resulting groundwater chemical compositions (based on Lewicki et al., 2006, 2007). While changes in groundwater chemistry were observed to be related to CO_2 (and sulfur gas) leakage as caused by acidification and interaction with host rocks along flow paths, waters remained potable in most cases. Section 5.2 describes the geochemical impacts of CO_2 releases from a landfill into a shallow aquifer, causing cadmium levels in the groundwater to increase to levels above the maximum contaminant level of 5 ppb (McGrath et al., 2007)

5.1 Natural Analogues

5.1.1 San Vittorino, Italy

The San Vittorino plain, located 100 km northeast of Rome in central Italy, is a sparsely populated intramontane basin that is used primarily for agriculture. Carbonate rocks are prevalent in the region (e.g., bedrock limestones and surface travertines). Numerous CO_2-rich mineral springs, gas vents, and sinkholes, many of which pose hazards to local infrastructure, are located throughout the plain and are believed to be associated with migration of CO_2 from depth along major faults in the area. In an effort to understand the influence of this CO_2 leakage on groundwater chemistry and sinkhole formation, NASCENT (Natural Analogs for the Storage of CO_2 in the geological ENvironmenT) (2005) conducted soil gas, bubble gas, dissolved gas, and groundwater geochemistry surveys throughout the plain. They found that anomalously high soil gas concentrations (up to 70% CO_2, 80 ppm He, and 2% CH_4) were closely correlated with the locations of sinkholes. Gas bubbles in springs, sinkholes, and wells had concentrations of CO_2 from 36 to 85%, CH_4 from 150 to 2100 mg L^{-1}, He from 6 to 400 mg L^{-1}, and N_2 from 7 to 60%. H_2S was also present, but unquantified. Dissolved gases had CO_2 concentrations from <0.2 to 0.8 L gas per L water at ambient pressure and temperature. The highest CO_2 concentrations were

close to the solubility limit of CO_2 in water at 1 atm pressure. Chemical analysis of waters collected from springs, wells, and sinkholes indicated that most are classified as Ca-HCO_3 waters, while a few are classified as Ca-Mg-HCO_3 waters. The total dissolved constituents varied widely between samples, with Total Dissolved Solids (TDS) ranging from 330 to 1843 mg L^{-1} and hardness ranging from 307 to 1843 mg L^{-1} as $CaCO_3$. The concentrations of major elements were well correlated in samples. Concentrations ranged from 89 to 550 mg L^{-1} for Ca, 17 to 97 mg L^{-1} for Mg, 10 to 795 mg L^{-1} for SO_4, 43 to 1945 mg L^{-1} for B, and 230 to 2900 mg L^{-1} for Sr. Some waters were also enriched in Mn, Al, Zn, Pd, and Rb. Samples with the highest concentrations of dissolved constituents were located in the north-central part of the plain and also had the highest CO_2 concentrations in both dissolved and excluded gases. The leakage of CO_2 (and H_2S) typically resulted in a 5 to 10 fold increase in most major and trace elements in springs. Despite elevated concentrations of dissolved chemical constituents in groundwaters, these waters are potable, according to current international groundwater standards for major ions.

Correlations between dissolved chemical constituents in waters were interpreted to reflect the dissolution of carbonate rocks along flow paths of groundwaters that have become acidified by CO_2 and H_2S rising along high permeability pathways in fault zones. The formation of sinkholes was found to be closely associated with groundwaters having anomalously high dissolved chemical constituents. These features were likely formed by the dissolution of fine-grained rocks by acidified groundwaters and collapse triggered by earthquakes. NASCENT (2005) developed and deployed a continuous groundwater chemistry monitoring station in the San Vittorino plain, designed to detect anomalous changes that might serve as precursors to sinkhole formation.

5.1.2 Florina Basin, Greece

Two aquifers are present in the Florina basin. The first is a confined aquifer in clastic sedimentary rocks capped by silts and clays that extends throughout most of the basin and hosts the CO_2 reservoir. The second is an unconfined aquifer hosted in karstic carbonates on the eastern and southern margins of the basin. To evaluate the effects of CO_2 leakage from depth on groundwater quality in the Florina basin, Beaubien et al. (2004) conducted an investigation of the

chemistry of waters from wells and springs throughout the basin. They analyzed major element concentrations in 132 samples and trace element concentrations in 17 of these samples, and found that total dissolved solids ranged from 150 to 4230 mg L^{-1} and hardness ranged from 70 to 1950 mg L^{-1} as $CaCO_3$. Waters collected from shallow wells and springs were Ca-HCO_3 type, while those collected from deep boreholes were Mg-HCO_3 type. Most water samples were potable. However, samples collected close to the CO_2 field had higher total dissolved chemical constituents and hardness, and consequently were of poorer drinking water quality. Beaubien et al. (2004) interpreted the spatial trends in the chemical compositions of groundwaters as reflecting the interaction of CO_2-rich groundwaters with host rocks along flow paths.

5.1.3 Albani Hills, Italy

Three main hydrogeologic units have been identified in the Albani Hill region (Boni et al., 1995). From depth to the surface, these include: (1) a calcareous-siliceous-marly basal complex constituting a multilayered aquifer hosted in fractured carbonates interbedded with confining clay layers, (2) a clayey-marly intermediate complex that acts as a groundwater flow boundary due to its low permeability, and (3) the Albani Hills volcanic complex, which displays wide variation in permeability and acts as a multilayered aquifer with radial groundwater flow. Chiodini and Frondini (2001) conducted a geochemical study of groundwaters collected from 293 wells and 63 springs in the region (Figure 5.1), and found high CO_2 partial pressures (average = 0.2 bar), indicating a high CO_2 leakage rate into the regional aquifers. HCO_3 is the major anion in most waters, with only a few samples characterized by high Cl and SO_4 concentrations. The SO_4-rich waters in the northern part of the study area are associated with an influx of deep sulfur-rich gases into shallow groundwaters, while the Cl-rich waters are located on the coastal plain and are associated with fossil seawater. The relative concentrations of cations (e.g., Na/K ratios, Figure 3.1) in waters reflect the interaction of CO_2-rich groundwaters with host rocks. In particular, many samples have high HCO_3, Ca, and Mg contents, which can be explained by the influx of CO_2-rich fluids from depth and subsequent interaction with sedimentary rocks.

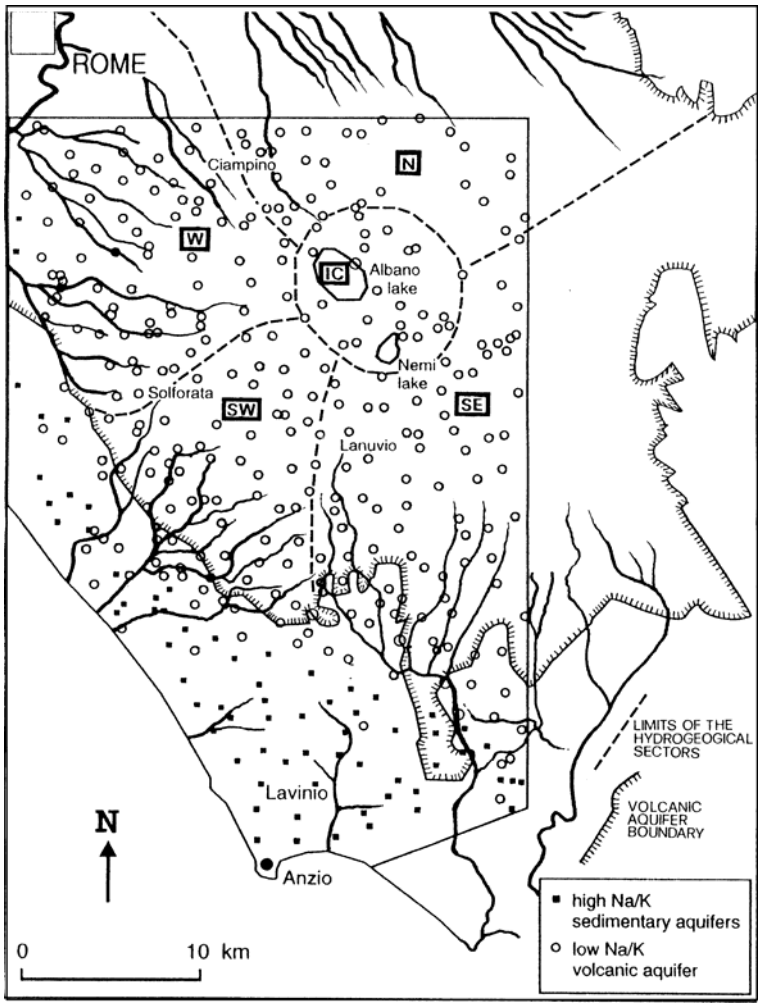

Fig. 5.1. Map of the Albani Hills region showing major drainage basins and locations of water samples from Chiodini and Frondini (2001).

5.1.4 Central Italy

Throughout Tyrrhenian Central Italy, widespread nonvolcanic CO_2 degassing (likely originating from a crustally-contaminated mantle or a mixture of magmatic and crustal components) occurs from vent and diffuse soil gas emissions and from CO_2-enriched groundwaters (Chiodini et al., 1999). From the Tyrrhenian Sea to the Apennine Mountains, buried structural highs act as gas traps. Widespread CO_2 leakage occurs at the surface throughout the region in the form of diffuse and vent gas emissions or by dissolution in groundwaters and subsequent release at surface

springs. Chiodini et al. (1999, 2000, 2001) conducted geochemical investigations of regional aquifers and found that CO_2 partial pressure values for springs are up to four orders of magnitude greater than that of the atmosphere. They also found that in geographic regions characterized by thick regional carbonate-evaporite aquifers, most or part of the deeply derived gas is dissolved by the aquifers, whereas in regions characterized by small aquifers, these aquifers cannot dissolve a large quantity of the CO_2, and extensive vent and soil CO_2 emissions occur at the surface. Chiodini et al. (2000) used mass-balance equations coupled with carbon isotopic analyses and hydrologic data to estimate fluxes of deeply derived CO_2 of up to 0.29 g $m^{-2}d^{-1}$ into the aquifers. For waters with high CO_2 partial pressures, the CO_2 flux lost to the atmosphere is of the same order of magnitude as the influx of deep CO_2.

Based on the analysis of major dissolved chemical constituents in 52 springs, 65% were classified as Ca(Mg)-HCO_3 in composition, 10% as Ca-Mg-SO_4 in composition, 10% as Na-Cl in composition, and the remaining as intermediate in composition (Chiodini et al., 2000). A major process controlling the chemical composition of most groundwaters was the dissolution of calcite, while the dissolution of gypsum or halite was important in the springs of a few aquifers. Total dissolved inorganic carbon concentrations in springs ranged from 0.00244 to 0.05080 mol/kg.

5.1.5 Mammoth Mountain, California, USA

Mammoth Mountain in eastern California has numerous CO_2-rich cold springs located on its lower flanks, primarily associated with leakage from the high-pressure gas reservoir beneath the volcano (Evans et al., 2002). Evans et al. (2002) conducted a geochemical study of these springs to quantify the magmatic carbon discharge in cold groundwaters. Based on measured spring flow rates and concentrations and isotopic compositions of dissolved inorganic carbon in spring discharges, they found that Mammoth discharges 2×10^4 t yr^{-1} of magmatic carbon (as CO_2); this discharge varies seasonally from 30 to 90 t d^{-1}. While most springs contain high concentrations of dissolved CO_2, they are otherwise dilute, with specific conductance ranging from 100 to 300 $\mu S\ cm^{-1}$.

5.1.6 Paradox Basin, Utah, USA

A number of natural springs and well bores discharge CO_2-rich groundwater along the Little Grand Wash and Salt Wash faults in the Paradox basin of Utah. Samples collected from springs along the Little Grand Wash and Salt Wash faults and from Crystal Geyser were analyzed to determine the contents of major dissolved chemical constituents in groundwaters (Shipton et al., 2004). Concentrations (in mmol L^{-1}) were as follows: 2.37-20.83 for Ca, 7.86 to 9.30 for Mg, 167.82-236.38 for Na, 7.62 to 10.44 for K, 0.00 to 0.14 for Fe, 0.00 to 0.02 for Mn, 0.01 to 0.16 for Sr, 46.40-75.70 for HCO_3, 91.15-204.52 for Cl, and 24.33-30.81 for SO_4. Waters were high in total dissolved solids, which ranged from 13,555 to 21,188 mg L^{-1}. Shipton et al. (2004) determined that the chemical compositions of groundwaters were primarily controlled by the dissolution of calcite and evaporites along groundwater flow paths.

5.2 Landfill Gas Impacts

McGrath et al. (2007) report on a study evaluating the potential impact of carbon dioxide contained in municipal solid waste (MSW) landfill gas on the release of cadmium from uncontaminated native soils. Elevated aqueous cadmium was detected in groundwater monitoring wells downgradient of the landfill but not in the landfill leachate or monitoring wells located upgradient. Based on soil leaching experiments and geochemical modeling, the authors concluded that the observed increases in aqueous cadmium in the field were likely caused by the CO_2 dissolution into the groundwater and the related increase of acidity, causing mobilization of cadmium from the natural soils. Both the soil leaching experiments and the modeling results showed strong increases in cadmium concentrations with increasing partial pressure of CO_2. Naturally occurring otavite (or cadmium carbonate) was reported to be the primary mineral controlling cadmium solubility, which suggests oxidizing conditions. In response to these findings, the landfill operator initiated a soil vapor extraction system in the vadose zone overlying the aquifer. Since then, aqueous cadmium concentrations in the formerly impacted wells have fallen to below detection limits (McGrath et al., 2007).

6. Overall Conclusions and Recommendations

This report describes a systematic evaluation of the possible water quality changes in response to localized CO_2 intrusion into aquifers currently used as sources of potable water in the United States. Our goal was to develop a general understanding of the potential vulnerability of United States potable groundwater resources in the event of CO_2 leakage from deep geologic sequestration reservoirs. This goal was achieved in two main tasks, the first to develop a comprehensive geochemical model representing typical conditions in many freshwater aquifers (Section 3), the second to conduct a systematic reactive-transport modeling study to quantify the effect of CO_2 intrusion into shallow aquifers for a variety of scenarios and aquifer conditions (Section 4). To ensure adequate model setup, the scenarios and conditions modeled in the reactive transport simulations—in particular those describing the geochemistry and mineralogy of potable aquifers—were selected based on the comprehensive geochemical model developed in Section 3. Detailed summaries of results from the two tasks are given, respectively, in Sections 3.7 and 4.10.

An important step in developing the comprehensive geochemical model in Section 3 was the identification of those mineral hosts containing hazardous constituents, which control their equilibrium concentration in potable groundwaters. Thermodynamic controls were evaluated using geochemical data for 38,000 potable groundwaters extracted from the USGS NWIS database, using a distribution-of-species code to test for their thermodynamic saturation in solution. This necessitated the iterative improvement and augmentation of a large supporting thermodynamic database comprising the solubility products of minerals of interest, and of complexes that affect the concentrations of the hazardous constituents in aqueous solution. Considering a representative groundwater under reducing conditions (a condition met in the large majority of all evaluated groundwaters), the most likely solubility-controlling mineral host for Pb is galena, while As would typically be controlled by the arsenopyrite component as a solid solution in pyrite. These mineral hosts are assumed to partially or completely control the initial aqueous concentrations of hazardous constituents as well as subsequent changes due to the ingress of CO_2. The thermodynamic controls obtained for other hazardous constituents are

summarized in Section 3.7, together with other necessary input for the reactive transport simulations such as the evaluation of relevant aquifer conditions (e.g., oxidation state, initial CO_2 concentrations in the aquifer) and the definition of the bulk/trace-element mineralogy in typical aquifer host rocks.

Starting with the comprehensive geochemical model, a preliminary assessment of CO_2-related water quality changes was conducted by calculating the expected equilibrium concentrations of hazardous inorganic constituents as a function of the partial pressure of CO_2. $P(CO_2)$ was varied from 10^{-4} bar to 10 bar, leading to a corresponding pH variation between 8.9 and 5.6. Equilibrium concentrations were determined using a distribution-of-species code, assuming a representative groundwater in reducing conditions and incorporating the thermodynamic controls identified in above-mentioned database evaluation. Results indicate that the concentrations of some of the studied constituents, for example Ba, Cd, Sb, and Zn, are sensitive to changes in $P(CO_2)$, but that As, and to a lesser extent Pb and Zn, have shown the potential for exceeding their respective MCLs at elevated CO_2 concentrations. In the systematic reactive-transport modeling study discussed below, primary emphasis was placed on the evaluation of the response and transport of As and Pb under intruding CO_2.

The reactive-transport simulator TOUGHREACT was used to predict the transport of gaseous and dissolved CO_2 within a shallow aquifer, as well as induced geochemical changes caused by the presence of CO_2, in particular those changes leading to the mobilization of Pb and As and their migration in the groundwater (Section 4). Our simulation results suggest that CO_2 ingress into a shallow aquifer can lead to significant and long-lasting mobilization of Pb and As, contaminating the groundwater near the intrusion location and further downstream. However, while substantial increases in aqueous concentrations are predicted to occur compared to the initial water composition, the MCL for As in groundwater has been exceeded in only a few simulation cases, whereas the MCL for Pb has not been exceeded at all.

Various sensitivity cases were simulated for different hydrological, geochemical, and mineralogical conditions, (1) to account for a range of conditions found in domestic potable aquifers and their host rocks, and (2) to evaluate the uncertainty associated with geochemical

processes and model parameters, results of which are summarized in Section 4.10. Adsorption/desorption via surface complexation is arguably the most important process controlling the fate of hazardous constituents mobilized by CO_2 leakage when sorbing minerals are present. In a simulation case without adsorption/desorption taken into account, the resulting long-term contamination of the aquifer is less significant near the region where CO_2 enters, whereas aqueous concentrations keep increasing with travel distance (eventually exceeding MCLs), as acidic water migrates further and more dissolution occurs. The relative importance of dissolution/precipitation versus adsorption/desorption is controlled by many factors, including adsorption parameters and aquifer mineralogy, reaction kinetics, aqueous complexation processes, and mineral solubility constants. For example, the role that adsorption/desorption plays in the mobilization of hazardous constituents depends highly on the total number of adsorption sites. A sensitivity run with lower site density reveals that early increases in aqueous Pb and As are much less significant, because desorption is less relevant in mobilizing contaminants.

Moderate to strong sensitivities in the resulting Pb and As concentrations have been obtained for several other geochemical parameters (such as the solubilities of hazardous-constituent-bearing minerals, the kinetic rates for precipitation and dissolution, and the aqueous complexation constants) and conditions (such as the redox environment, with the simulated behavior in a oxidized aquifer being very different from an aquifer in a reducing environment). With respect to the typical aquifer mineralogies assumed in our study (ranging from almost pure arenites to dolomitic limestone), the most important effects resulted from differences in clay content, which affect the adsorption/desorption behavior, as well as from differences in the presence of carbonate minerals, which can moderate the pH changes caused by CO_2 intrusion. An increase in the leakage rate does not necessarily lead to increases in the maximum contaminant concentrations in the aquifer. Once the groundwater reaches its solubility limit with respect to CO_2, which occurs at relatively small intrusion rates, there is no further change in total inorganic carbon and acidity. Consequently, no further mobilization of hazardous constituents occurs once local equilibrium has been achieved. Excess CO_2 remains in the gas phase and rises to the top of the aquifer, thereby bypassing most of the groundwater body. The resulting impact on aqueous

contamination is then influenced by the general pattern of the CO_2 plume (e.g., the spreading of the plume at the top of the aquifer in the case of a confined aquifer) and the subsequent migration of CO_2-charged and contaminated water further downstream.

As stated before, the goal of this study was to better understand, in a global sense, the vulnerability of representative and relevant aquifer types in the case of CO_2 intrusion, thereby providing sound scientific information to regulators and the public. It is understood, however, that even the most comprehensive sensitivity study cannot encompass all possible aquifer conditions and CO_2 intrusion scenarios. Neither can it account for all relevant uncertainties. While the geochemical evaluation conducted in Section 3 was extremely comprehensive, it was also pointed out that several assumptions, approximations, and compromises were necessary in this effort, mostly because of incomplete characterization of important parameters such as dissolution and dissociation constants. We recommend that our study should now be followed up with site-specific model predictions, and that laboratory or field experiments should be performed to test uncertain model assumptions and parameters. Such experiments would involve exposing initially undisturbed groundwater in laboratory samples or *in situ* in the field to elevated levels of CO_2. One could also attempt to test the developed geochemical models using measured data from natural analogue sites, such as those described in Section 5.

Our studies suggest that the fate of inorganic hazardous constituents in the presence of elevated CO_2 levels ultimately depends on their initial abundance and distribution in the aquifer minerals. For example, contaminants released from adsorption sites are expected to cause short-term perturbation in aqueous heavy-metal concentrations, while contaminants in host minerals would be mobilized in slower, longer duration processes. As pointed out before, the required information on hazardous constituents and their distribution in the mineral hosts is not easy to come by, because relevant mineral hosts in the aquifer rocks are difficult to identify where the concentrations are too small to be detected with standard mineralogical characterization methods. Therefore, an indirect approach was developed to determine their initial abundance and distribution, based on evaluation of geochemical data that are more easily measurable (i.e., by using a large number of groundwater analyses to test for saturation with respect to postulated

mineral hosts in conjunction with a supporting literature review, and analyses of trace elements in soils and sediments). While the approach demonstrated a high level of consistency, we recommend corroborating our findings through direct measurements of the form, distribution, and association of trace hazardous constituents within associated rock samples, which would involve, for example, synchroton-based microspectroscopic analysis at extremely high spatial resolution.

7. Acknowledgments

We are grateful to Guoxiang Zhang and Dan Hawkes of LBNL for constructive review of this manuscript. We thank the US Environmental Protection Agency, Office of Water and Office of Air and Radiation, for funding this study under an Interagency Agreement with the U.S. Department of Energy at the Lawrence Berkeley National Laboratory, Contract No. DE-AC02-05CH11231. Special thanks go to Jonathan Scott of the U.S. Geological Survey, Oklahoma City, Oklahoma, who provided indispensable contributions to this report by extracting and supplying over 38,000 groundwaters from the NWIS database.

8. References

Abdel-Gaward, A.M. and P.F. Kerr (1961), Urano-organic mineral association. *American Mineralogist, 46*, 402–419.

Abdul-Samad, F.A., J.H. Thomas, P.A. Williams, and R.F. Symes (1982), Chemistry of formation of lanarkite. *Mineralogical Magazine, 46*, 499–501.

Abercrombie, H.J., I.E. Hutcheon, J.D. Bloch, and P. de Caritat (1994), Silica activity and the smectite-illite reaction. *Geology, 22*, 539–542.

Acero, P., J. Cama and C. Ayora, 2007. Rate law for galena dissolution in acidic environment. Chemical Geology, 245: 219-229.

Adami, L.H. and E.G. King (1964), Heats and free energies of formation of sulfides of manganeses, iron, zinc, and cadmium. *U.S. Bur. Mines Rept. Inv. 6495*, 10 p.

Akinfiev N.N., A.V. Zotov, and N.D. Shikina (1994), Experimental investigation and thermodynamic correlation in the Sb(III)-S(II)-O-H system. *Geochem. Intern. 31*, 27–40.

Al-Farawati, R. and C.M.G. van den Berg (1999), Metal – sulfide complexation in seawater. Marine Chemistry 63, 331-352

Anderko, A. and P.J. Shuler (1998), Modeling the formation of iron sulfide scales: Using thermodynamic simulation software. Unpublished Report, OLI Systems Inc., 108 American Road, Morris Plains, NJ 07950, USA. 20 p.

Anfalt, T., D. Dyrssen, E. Ivanova, and D. Jagner (1968), State of divalent mercury in natural waters. *Svensk Kemisk Tidskrift, 80*(10), 340–342 [in Swedish].

Appelo, C.J.A., and D. Postma (1994), *Geochemistry, Groundwater and Pollution*. A.A.Balkema, Rotterdam, Netherlands.

Apps, J.A. (2004), Re-evaluation of the thermodynamic properties of SiO_2(aq) and those of H_2O low-pressure silica polymorphs. Appendix A in: *Data Qualification for Thermodynamic Data Used To Support THC Calculations*. N. Spycher and J.A. Apps, *Bechtel SAIC Company Report No. ANL-NBS-HS-000043 Rev 00B*., 99 p. plus appendices. Prepared for U.S. Department of Energy, Office of Civilian Radioactive Waste Management by Bechtel SAIC Company, LLC, 1180 Town Center Drive, Las Vegas, Nevada 89144.

Aravena, R., L. I. Wassenaar, and L. N. Plummer (1995), Estimating 14C groundwater ages in a methanogenic aquifer. *Water Resources Research, 31*(9), 2307–2317.

Arthur, J.D., A. A. Dabous, and J. B. Cowart (2005), Water-rock geochemical considerations for aquifer storage and recovery: Florida case studies. In: *Underground Science and Technology*, C.-F. Tsang and J. A. Apps, eds., *Development in Water Sciences, 52*, Chapter 24., pp. 327–339, Elsevier, Amsterdam.

Babcan, J. (1976), Entstehung und Stabilitaet von Antimonmineralen im System Sb3+-S2--H+-OH-. (Formation and stability of antimony minerals in the Sb3+-S2--H+-OH- system), *Chemie der Erde*, v. 35, p. 281-284.

Back, W., B. B. Hanshaw, L.N. Plummer, P.H. Rahn, C.T. Rightmire, and M. Rubin (1983), Process and rate of dedolomitization; mass transfer and 14 C dating in a regional carbonate aquifer. *GSA Bulletin, 94*(12), 1415–1429.

Baas Becking, L.G.M., L.R. Kaplan, and D. Moore (1960), Limits of the natural environment in terms of pH and oxidation- reduction potentials. *J. Geol. 68*, 243–284.

Ball, M.C., and M.J. Casson (1977), Thermal studies on lead(II) salts-V. Enthalpies of formation of lead(II) oxide carbonates by scanning calorimetry. *J. Inorg. Nucl. Chem., 39*, 1456–1457.

Ballirano, P. and A. Maras (2002), Refinement of the crystal structure of arsenolite, As_2O_3. *Zeitschrift fur Kristallographie*, *217*, 177-178.

Barbanson, L., D. Saulas, D., and J.C. Touray, (1985), Les blendes mercuriferes de la region de Cabezon de la Sal (Santander, Espagne). *Bulletin Mineralogique, 108*, 483-486.

Barnes, D.A., C.E. Lundgren, and M.W. Longman (1992), Sedimentology and diagenesis of the St. Peter Sandstone, Central Michigan Basin, United States. *American Association of Petroleum Geologists Bulletin, 76*, 1507–1532.

Barrett, T.J., and G.M. Anderson (1982), The solubility of sphalerite and galena in NaCl brines. *Economic Geology, 77*, 1923–1933.

Barrett, T.J., and G.M. Anderson (1988), The solubility of sphalerite and galena in 1–5 m NaCl brines to 300ºC. *Geochimica Cosmochimica Acta, 52*, 813–820.

Barton P.B. Jr, and P. Toulmin(1966), Phase relations involving sphalerite in the Fe-Zn-S system. *Econ. Geol.*, 61:815-849.

Bayliss, P. (1977), Crystal structure refinement of a weakly anisotropic pyrite cubic model. *American Mineralogist, 62*, 1168–1172.

Bayliss, P., and W. Nowacki (1972), Refinement of the crystal structure of stibnite, Sb_2S_3. *Zeitschrift fur Kristallographie*,*135*, 308–315.

Beaubien, S.E., S. Lombardi, G. Ciotoli, A. Annunziatellis, G. Hatziyannis, A. Metaxas, and J.M. Pearce (2004), Potential hazards of CO_2 leakage in storage systems—Learning from natural systems, *GHGT7*, Vancouver, Sept. 5–8.

Behra, P., P. Bonnissel-Gissinger, M. Alnot, R. Revel, and J. J. Ehrhardt (2001), XPS and XAS study of the sorption of Hg(II) onto pyrite. *Langmuir, 17*, 3970–3979.

Belcher, R.W., A. Rozendaal, and W. J. Przybylowicz (2004), Trace element zoning in pyrite determined by PIXE elemental mapping: evidence for varying ore-fluid composition and electrochemical precipitation of gold at the Spitskop deposit, Saldania Belt, South Africa. *X-Ray Spectrom., 33*, 174–180.

Benoit, J.M., C. C. Gilmour, R. P. Mason, and A. Wheyes (1999), Sulfide controls on mercury speciation and bioavailability to methylating bacteria in sediment pore waters. *Environ. Sci. Technol., 33*, 951–957.

Berner, R.A. (1967), Thermodynamic stability of sedimentary iron sulfides. *Am J Sci., 265* (9), 773–785.

Bessinger, B. (2000), The geochemistry of gold, arsenic, and antimony in the Carlin-type gold deposits and the mechanics of geologic fractures. Ph.D. Thesis, University of California, Berkeley, California. Ernest Orlando Lawrence Berkeley National Laboratory, *Report LBNL-46525*, 2000.

Bethke, P.M. and P.B. Barton, Jr. (1971), Sub-solidus relations in the system PbS-CdS. *American Mineralogist, 56*, 2034–2039.

Bexfield, L.M. and Plummer, L.N., (2003), Occurrence of arsenic in ground water of the Middle Rio Grannde Basisn, central New Mexico. Chapter11 in *Arsenic in Ground Water*, A.H. Welch and K.G. Stollenwerk, eds., Kluwer Academic Publishers, Boston, pp. 295-327.

Bigham, J.M., L. Carlson, and E. Murad (1994), Schwertmannite, a new iron oxyhydroxy-sulphate from Pyhasalmi, Finland, and other localities. *Mineralogical Magazine; 58*(4), 641–648.

Birkholzer, J.T., J.A. Apps, Y. Zhang, L. Zheng, and T. Xu (2008): Prediction of Groundwater Quality Changes in Response to CO2 Leakage from Deep Geological Storage, Abstract in: *Proceedings 7th Annual Conference on Carbon Capture and Sequestration*, Pittsburgh, PA, May 2008

Blake, R L, R.E. Hessevick, T. Zoltai, and L.W. Finger (1966), Refinement of the hematite structure. *American Mineralogist, 51*, 123–129.

Blanchard, M., M. Alfredsson, J. Brodholt, K. Wright, and C.R.A. Catlow (2007), Arsenic incorporation into FeS_2 pyrite and its influence on dissolution: A DFT study. *Geochimica et Cosmochimica Acta, 71*, 624–630.

Blatt, H. (1992), *Sedimentary Petrology*. W.H. Freeman and Company, New York. 2nd Edition, 514 p.

Boggs, S., Jr. (2003), *Petrology of Sedimentary Rocks*. The Blackburn Press, Caldwell, New Jersey. Reprint of the 1st Edition of 1992. 707 p.

Boivin, J.-C., D. Thomas, and G. Tridot (1968), Etude chimique et cristallographique du sulfate de plomb dibasique. *C. R. Acad. Sci. Paris*, *267*, Series C, 532–535.

Bonazzi, P, S. Menchetti, and G. Pratesi (1995), The crystal structure of pararealgar. *American Mineralogist, 80*, 400–403.

Bonazzi, P, S. Menchetti, and C. Sabelli (1987), Structure refinement ofkermesite: symmetry, twinning, and comparison with stibnite. *Neues Jahrbuch fur Mineralogie, Monatshefte 1987*, 557–567

Boni, C., P. Bono, S. Lombardi, L. Mastrorillo, and C. Percopo (1995), Hydrogeology, fluid geochemistry, and thermalism. In: *The Volcano of the Alban Hills, Rome*, R. Triglia, ed., pp. 221–242.

Bostick, B.C., S. Fendorf, and M. Fendorf (2000), Disulfide disproportionation and CdS formation upon cadmium sorption on FeS_2. *Geochimica et Cosmochimica Acta, 64*(2) 247-255.

Bothe, J.V. and P.W. Brown (1999), The stabilities of calcium arsenates. *J. Hazard. Mat., B69*, 197–207.

Bowers, T., J. Jackson, and H. Helgeson (1985), *Equilibrium Activity Diagrams*. Elsevier Press, New York.

Bradbury, M.H. and B. Baeyens (2005), Modelling the sorption of Mn(II), Co(II), Ni(II), Zn(II), Cd(II), Eu(III), Am(III), Sn(IV), Th(IV), Np(V) and U(VI) on montmorillonite: Linear free energy relationships and estimates of surface binding constants for some selected heavy metals and actinides. *Geochimica et Cosmochimica Acta, 69*(4), 875–892.

Bradl, H.B. (2004), Adsorption of heavy metal ions on soils and soils constituents. *Journal of Colloid and Interface Science, 277*, 1–18.

Bragg, L.J., J.K. Oman, S.J. Tewalt, C.L. Oman, N.H. Rega, P.M. Washington, and R.B. Finkelman (1998), The U.S. Geological Survey Coal Quality (COALQUAL) Data-Base,Version 2.0. *U.S. Geological Survey Open-File Report 97-134*, one CD-ROM.

Brantley, S.L. and M.A. Velbel (1993), Geochemical kinetics of mineral-water reactions in the field and the laboratory. Chem. Geol., 105(1-3): 7-9.

Brasseur (1940), Etude roentgenographique de la laurionite PbOHCI. *Bull. Soc. Roy. Sc. Liege*, 9, 166-169.

Brownfield, M.E., R.H. Affolter, J.D. Cathcart, S.Y. Johnson, I.K. Brownfield, and C.A. Rice (2005), Geologic setting and characterization of coals and the modes of occurrence of selected elements from the Franklin coal zone, Puget Group, John Henry No. 1 Mine, King County, Washington, USA. *International Journal of Coal Geology, 63*, 247–275.

Buffle, J., R.R. deVitre, D. Perret, and G.G. Leppard (1988), Combining field measurements for speciation in non perturbable waters. In: *Metal Speciation: Theory, Analysis and Application.* J.R. Kramer and E.E.Allen, eds., Lewis Publishers, Inc., 99–124.

Buerger, M.J., W.A. Dollase, and I. Garaycochea-Wittke (1967), The structure and composition of the mineral pharmacosiderite. *Zeitschrift fur Kristallographie, 125*, 92–108.

Buerger, M.J. (1939), The crystal structure of gudmundite. American Mineralogist 24, 183–184.

Bur'yanova, E.Z., G.A. Kovalev, and A.A. Komkov (1957), The new mineral cadmoselite. Zapiski Vses. *Mineralog. Obshch., 86*, 626–628 (in Russian).

Caracas, R. and X. Gonze (2005), First-principles study of the electronic properties of A2B3 minerals, with A=Bi,Sb and B=S,Se. *Physics and Chemistry of Minerals, 32*, 295–300.

Carroll, S.A., P.A. O'Day, and M. Piechowski (1998), Rock-water interactions controlling zinc, cadmium, and lead concentrations in surface waters and sediments, U.S. Tri-State Mining District. 2. Geochemical Interpretation. *Environ. Sci. Technol., 32*, 956–965.

Catti, M, G. Chiari, and G. Ferraris (1980), The structure of ferrarisite, $Ca_5(HAsO_4)_2(AsO_4)_2*9H_2O$: Disorder, hydrogen bonding, and polymorphism with guerinite. *Bulletin de Mineralogie 103*, 541–546.

Catti, M. and G. Ferraris (1974), Crystal structure of $Ca_5(HAsO_4)_2(AsO_4)_2*9H_2O$ (guerinite). *Acta Crystallographica, B30*, 1789–1794.

Catti, M, G. Ferraris, and G. Ivaldi (1981), The crystal structure of picropharmacolite, $Ca_4Mg(HAsO_4)_2(AsO_4)_2*11H_2O$. *American Mineralogist, 66*, 385–391.

Catti, M, G. Ferraris, and G. Ivaldi G. (1977), Hydrogen bonding in the crystalline state. Structure of talmessite,. $Ca_2(Mg,Co)(AsO_4)_2*2H_2O$, and crystal chemistry of related minerals. *Bulletin de Mineralogie, 100*, 230–236.

Cesbron, F. and H.J. Schubnel (1968), Nouvelles donnees sur la penfieldite. *Bull. Soc. Fr. Mineral. Cristallogr., 91*, 407–408.

Chai, L. and A. Navrotsky (1996), Synthesis, characterization, and energetics of solid solution along the dolomite-ankerite join, and implications for the stability of ordered $CaFe(CO_3)_2$. *Am. Mineral., 81*, 1141–1147.

Chase, M.W., C.A. Davies, J.R. Downey, D.J. Frurip, R.A. McDonald, and A.N. Syverud (1985), *JANAF Thermochemical Tables, 3rd Edition. J. Phys.Chem. Data*, 14 (Suppplement No. 1).

Chen L., Zhang Q., Li D., and Wang G. (1993): Antimonselite - A new mineral. Acta Mineralogica Sinica 13(1), 7-11 (in Chinese with English abstract).

Cherry, J.A., A.V. Shaikh, D.E. Tallman, and R.V. Nicholson (1979), Arsenic species as an indicator of redox conditions in groundwater. *J. Hydrol., 43*, 373–392.

Chiodini, G., F. Frondini, D.M. Kerrick, J. Rogie, F. Parello, L. Peruzzi, and A.R. Zanzari (1999), Quantification of deep CO_2 fluxes from Central Italy: Examples of carbon balance for regional aquifers and of soil diffuse degassing. *Chem. Geol., 159*, 205–222.

Chiodini, G., F. Frondini, C, Cardellini, F. Parello, and L. Peruzzi (2000), Rate of diffuse carbon dioxide Earth degassing estimated from carbon balance of regional aquifers: The case of the central Apennine, Italy. *J. Geophys. Res., 105*, 8423–8424.

Chiodini, G., F. Frondini, C. Cardellini, D. Granieri, L. Marini, and G. Ventura (2001), CO_2 degassing and energy release at Solfatara volcano, Campi Flegrei, Italy, *J. Geophys. Res., 106,* 16, 213–16,221.

Chiodini G. and F. Frondini (2001), Carbon dioxide degassing from the Albani Hills volcanic region, Central Italy. *Chem. Geol.*, 177, 67–83.

Cowan, C. E. (1988), Review of selenium thermodynamic data: Final report. Electric Power Research Institute Report *EPRI-EA-5655*, 73 pp, Palo Alto, CA.

Dai, Y. S. and J.M. Hughes (1989), Crystal-structure refinements of vanadinite and pyromorphite. *The Canadian Mineralogist, 27*, 189–192.

Daskalakis, K.D. and G.R. Helz (1992), Solubility of CdS (greenockite) in sulfidic waters at 25ºC. *Environ. Scl. Technol., 26*, 2462–2468.

Daskalakis, K.D. and G.R. Helz (1993), The solubility of sphalerite (ZnS) in sulfidic solutions at 25°C and 1 atm pressure. *Geoch. Cosmochim. Acta*, *57*, 4923–4931.

Davies-Colley, R.J., P.O. Nelson, and K.J. Williamson (1985), Sulfide control of cadmium and copper concentrations in anaerobic estuarine sediments. *Marine Chemistry, 16*, 173–186.

DeKock, C.W. (1986), Thermodynamic properties of selected metal sulfates and their hydrates. *U.S. Bureau of Mines Information Circular 9081*. 59.p.

Deore, S. and A. Navrotsky (2006), Oxide melt solution calorimetry of sulfides: Enthalpy of formation of sphalerite, galena, greenockite, and hawleyite. *American Mineralogist, 91*, 400–403.

Derriche, Z. and P. Perrot (1976), Etude thermodynamique des phses solides et liquide dans le systeme PbO-$PbSO_4$. *Revue de Chimie Minerale, 13*(4), 310–323.

Diehl, S.F., M.B. Goldhaber, and J.R. Hatch (2004), Modes of occurrence of mercury and other trace elements in coals from the warrior Weld, Black Warrior Basin, Northwestern Alabama. *Internat. J. Coal Geol., 59*, 193Ð208.

Dixit, S. and J.G. Hering (2003), Comparison of arsenic(V) and arsenic(III) sorption onto iron oxide minerals: Implications for arsenic mobility. *Environ. Sci. Technol., 37*, 4182–4189

Dragun, J. (1988), *The Soil Chemistry of Hazardous Materials*. Hazardous Materials Control Research Institute, Silver Spring, MD.

Drew Ilger, J., W.A. Ilger, R.A. Zingaro, and M.S. Mohan (1987), Modes of occurrence of uranium in carbonaceous uranium deposits: Characterization of uranium in a South Texas (U.S.A.) lignite. *Chemical Geology, 63*, 197–216.

Dubessy, J., M. Pagel, J.M. Beny, H. Christensen, B. Hickel, C. Kosztolanyi, and B. Poty (1988), Radiolysis evidenced by H_2-O_2-bearing fluid inclusions in three uranium deposits. *Geochimica et Cosmochimica Acta, 52*, 1155–1167.

Dunn, P.J., D.R. Peacor, and N. Newberry (1980), Johnbaumite, a new member of the apatite group from Franklin, New Jersey. *American Mineralogist, 65*, 1143–1145.

Dutkiewicz, A., J. Ridley, and R. Buick (2003), Oil-bearing CO_2-CH_4-H_2O fluid inclusions: Oil survival since the Palaeoproterozoic after high temperature entrapment. *Chemical Geology, 194*(1–3), 51–79.

Dyrssen, D. and M. Wedborg (1991), The sulphur-mercury system in natural waters. *Water Air Soil Pollut., 56*, 507–519.

Dyrssen, D. and K. Kremling (1990), Increasing hydrogen sulfide concentration and trace metal behavior in the anoxic Baltic waters. *Marine Chemistry, 30*, 193–204.

Dyrssen, D. (1989), Biogenic sulfur in two different marine environments. *Marine Chem., 28*, 241–249.

Dyrssen, D. and M.Wedborg, (1989), The state of dissolved trace sulphide in seawater. *Marine Chem., 26*, 289–293.

Dyrssen, D. (1988), Sulphide complexation in surface seawater. *Marine Chem., 24*, 143–153.

Dyrssen, D. (1985), Metal complex formation in sulphidic seawater. *Marine Chem., 15*, 285–293.

Dzombak, D.A. and F.M.M. Morel (1990), *Surface Complexation Modeling—Hydrous Ferric Oxide*. John Wiley & Sons, New York, 393 pp.

Earley, J.W. (1950), Description and syntheses of the selenide minerals. *American Mineralogist, 35*, 337–364.

Earnshaw, A. and N. Greenwood (1997), *Chemistry of the Elements*, *2nd edition*. Butterworth-Heinemann, (1997). ISBN 0-7506-3365-4, Appendix 4, Abundance of Elements in Crustal Rocks.

Edmunds, W.M., A.H. Bath, and D.L. Miles (1982), Hydrochemical evolution of the East Midlands Triassic sandstone aquifer, England. *Geochimica et Cosmochimica Acta 46,* 2069–2081.

Ehrhardt, J-J., P. Behra, P. Bonnissel-Gissinger, and M. Alnot (2000), XPS study of the sorption of Hg(II) onto pyrite FeS_2. *Surf. Interface Anal., 30*, 269–272.

Esdaile, J.D. (1966), The lead oxide-lead sulfate system. *J. Electrochem. Soc., 113*(1), 71–75.

Evans, W.C., M.L. Sorey, A.C. Cook, B.M. Kennedy, D.L. Shuster, E.M. Colvard, L.D. White, and M.A. Huebner (2002), Tracing and quantifying magmatic carbon discharge in cold groundwaters: Lessons learned from Mammoth Mountain, USA, *J. Volcanol. Geotherm. Res., 114*, 291–312.

Felmy, A.R., D. Girvin, and E.A. Jenne (1984), MINTEQ: A computer program for calculating aqueous geochemical equilibria. U.S. Environmental Protection Agency *Report EPA-600/3-84-032*.

Ferraris, G. and G. Chiari (1970), The crystal structure of $CaHAsO_4$ (weilite). *Acta Crystallographica, B26*, 403–409.

Ferraris, G., D.W. Jones, and J. Yerkess (1972), A neutron and X-ray refinement of the crystal structure of $CaHAsO_4$*H_2O (haidingerite). *Acta Crystallographica, B28*, 209–214.

Ferraris, G., D.W. Jones, and J. Yerkess (1971), Determination of hydrogen atom positions in the crystal structure of. pharmacolite, $CaHAsO_4(H_2O)_2$, by neutron diffraction. *Acta Crystallographica, B27*, 349–354.

Fialips, C.-I., D. Huo, L. Yan, J. Wu, and J.W. Stucki (2002b), Effect of iron oxidation state on the IR spectra of Garfield nontronite. *American Mineralogist, 87*, 630-641.

Finkelman, R.B. (1981), Modes of occurrence of trace elements in coal. *U.S. Geological Survey Open-File Report 81–99*. 301 p.

Finkelman, R.B. and H. Klemic (1976), Brannerite from the Penn Haven Junction uranium occurrence, Carbon County, Pennsylvania. *U.S. Geol. Surv. J. Res., 4*(6), 715–716.

Fish, W. (1993), Sub-surface redox chemistry: A comparison of equilibrium and recction-based approaches. Chapter 3 in *Metals in Groundwater* (Herbert E. Allen, E. Michael Perdue, David S. Brown, Eds). CRC, 464 p.

Fleet, M.E., P.J. MacLean, and J. Barbier (1989), Oscillatory-zoned As-bearing pyrite from strata-bound and stratiform gold deposits: An indicator of ore fluid evolution. *Econ. Geol. Monogr. 6,* 356Ð362.

Flis, J., M. Manecki, and T. Bajda (2007), Solubility of pyromorphite-mimetite solid solutions at 5–65ºC: Variability of thermodynamic stability of minerals from pyromorphite-mimetite series at 5–65ºC. *Goldschmidt Conference Abstracts*.

Focazio, M.J., Tipton, D., Dunkle Shapiro, S., and L.H. Geiger (2006), The chemical quality of self-supplied domestic well water in the United States. *Ground Water Monitoring & Remediation*, 26(3), pages 92–104.

Framson, P.E. and J.O. Leckie (1978), Limits of coprecipitation of cadmium and ferrous sulfides. *Environmental Science & Technology, 12*(4), 465–469.

Frueh, A J. (1951), The crystal structure of claudetite (monoclinic As_2O_3). *American Mineralogist, 36*, 833–850.

Giannetti, B.F., W.A. Moreira, S.H. Bonilla, C.M.V.B. Almeida, and T. Raboczkay (2006), Towards the abatement of environmental mercury pollution: An electrochemical characterization. *Colloids and Surfaces A: Physicochem. Eng. Aspects, 276*, 213–220.

Giordano, T.H. and H.L. Barnes, (1979), Ore solution chemistry IV: PbS solubility in bisulfide solutions to 300°C. *Econ. Geol., 74*, 1637–1646.

Girard, J.-P. and D.A. Barnes (1995), Illitization and paleothermal regimes in the Middle Ordovician St. Peter Sandstone, central Michigan Basin: K-Ar, oxygen isotope, and fluid inclusion data. *AAPG Bulletin, 79*(1), 49–69.

Gluskoter, H.J. and P.C. Lindahl (1973), Cadmium: Mode of occurrence in Illinois coals. *Science, 181*, 264–266.

Goldberg, S. (2002), Competitive adsorption of arsenate and arsenite on oxides and clay minerals. *Soil Sci. Soc. Am. J., 66*, 413–421.

Goldberg, S., S.M. Lesch, D.L. Suarez and N.T. Basta (2005), Predicting arsenate adsorption by soils using soil chemical parameters in the Constant Capacitance Model. *Soil Sci. Soc. Am. J.,* 69(5), 1389–1398.

Goldhaber, M.B., R.C. Lee, J.R. Hatch, J.C. Pashin, and J. Treworgy (2003), Role of large scale fluid flow in subsurface arsenic enrichment. Chapter 5 in *Arsenic in Ground Water*, A.H. Welch and K.G. Stollenwerk, eds., Kluwer Academic Publishers, Boston, pp. 127–164.

Golightly D.W. and F.O. Simon (Eds) (2006), Methods for Sampling and Inorganic Analysis of Coal. U.S. Geological Survey Bulletin 1823

Greensmith, J.T. (1989), *Petrology of the Sedimentary Rocks*. Unwin Hyman, London. 7th Edition, 262 p.

Grundl, T.J. and D.L. Macalady (1989), Electrode measurements of redox potential in anaerobic ferric/ferrous chloride systems. *J. Contam. Hydrol. 5*, 97–117.

Gu, X. and L.J. Evans (2007), Modelling the adsorption of Cd(II), Cu(II), Ni(II), Pb(II), and Zn(II) onto Fithian illite. *Journal of Colloid and Interface Science, 307*, 317–325

Gubeli, A.O. and J. Ste-Marie (1967), Constantes de stabilité de thiocomplexes et produits de solubilité de sulfures de métaux. II Sulfure de zinc. *Can. J. Chem., 45*(18), 2101–2108.

Hansen, H.C.B., O.K. Borggaard, and J. Sorensoen (1994), Evaluation of the free energy of formation of Fe(II)-Fe(III) hydroxide-sulphate (green rust) and its reduction of nitrite. *Geochim. et Cosmochim. Acta, 58*, 2599–2608.

Helean, K.B., A. Navrotsky, G.R. Lumpkin, M. Colella, J. Lian, R.C. Ewing, B. Ebbinghaus, and J.G. Catalano (2003), Enthalpies of formation of U-, Th-, Ce-brannerite: implications for plutonium immobilization. *Journal of Nuclear Materials, 320*, 231–244.

Helgeson, H.C., J.M. Delany, H.W. Nesbit, and D.K. Bird (1978), Summary and critique of the thermodynamic properties of minerals. *American Journal of Science*, *278A*, 229 p.

Helgeson, H.C. (1990), Note 18 to the SUPCRT SPRONS92.DAT database, Johnson et al., (1992).

Hemley, J. J. (1953), A study of PbS solubility and its relation to ore deposition. *Econ. Geol.*, 48, 13-138.

Heyding, R D, and R.M. (1976), Crystal structures of Cu1.8Se, Cu_3Se_2, alpha- and gamma=CuSe, $CuSe_2$, and $CuSe_2$II. *Canadian Journal of Chemistry, 54*, 841–848.

Hill R. J. (1985), Refinement of the structure of orthorhombic PbO (massicot) by Rietveld analysis of neutron powder diffraction data. *Acta Crystallographica*, Section C, 41 p.1281-1284.

Hizal, J. and R. Apak, 2006. Modeling of copper(II) and lead(II) adsorption on kaolinite-based clay minerals individually and in the presence of humic acid. *Journal of Colloid and Interface Science, 295*, 1–13.

Hoholick, D.J. (1980), Porosity, grain fabric, water chemistry, cement, and depth of the St. Peter Sandstone in the Illinois Basin. University of Cincinnati, Master's Thesis, 72 p.

Hoholick, J.D., T. Metarko, and P.E. Potter (1984), Regional variations of porosity and cement: St. Peter and Mount Simon Sandstones in Illinois Basin. *American Association of Petroleum Geologists Bulletin, 68*, 753–764.

Holland, T.J.B. and R. Powell (1998), An internally consistent thermodynamic data set for phases of petrological interest. *Journal of Metamorphic Geology*, *16*(3), 309–343.

Hopkins, J. and P. Putnam (2000), Fabric alteration and isotopic signature of carbonates in a recharge area of the Madison Aquifer, Montana, USA. *Journal of Geochemical Exploration*, 69–70 (June 2000), 235–238.

Hower, J.C. and J. D. Robertson (2003), Clausthalite in coal. *International Journal of Coal Geology*, 53, 219–225.

Howie, R.A. and W. Moser (1968), Structure of Tin(II) "Hydroxide" and Lead(II) "Hydroxide". *Nature*, 219, 372 – 373.

Huerta-Diaz, M.A. and J.W. Morse (1992), Pyritization of trace metals in anoxic marine sediments. *Geochemica et Cosmochimica Acta, 56*, 268l–2702.

Humphreys, D.A., J.H. Thomas, and P.A. Williams (1980), The chemical stability of mendipite, diaboleite, chloroxiphite, and cumengeite, and their relationships to the secondary lead minerals. *Mineralogical Magazine, 43*, 901–904.

HydroGeoLogic, Inc. and Allison Geoscience Consultants, Inc. (1999), MINTEQA2/ PRODEFA2, A Geochemical Assessment Model for Environmental Systems: User Manual Supplement for Version 4.0. Prepared for U.S. Environmental Protection Agency, National Exposure Research Laboratory, Ecosystems Research Division, Athens, Georgia, June 1998 (revised September 1999). 76 p. Available at http://www.epa.gov/ceampubl/mmedia/minteq/index.htm

Irving, H.M.N.H. (1977), Dithizone. Analytical Science Monographs No. 5. The Chemical Society, London, 106 p.

James, Noel P., Yvonne Bone, and T. Kurtis Kyser (1993), Shallow burial dolomitization and dedolomitization of mid-Cenozoic, cool-water, calcitic, deep-self limestones, Southern Australia. *Journal of Sedimentary Petrology, 63*(3) (May), 528–538.

Jansen, M. (1977), Crystal structure of As_2O_5. *Angew. Chem. Int. Ed. Engl., 16*(5), 314–315.

Janssens, A. (1973), Stratigraphy of the Cambrian and lower Ordovician rocks of Ohio. *Bull. 64*, Ohio Department of Natural Resources, Division of the Geological Survey.

Kovacevic, D., A. Pohlmeier, G. Ozbas, H.D. Narres, and M.J.N. Kallay (2000), The adsorption of lead sepecies on goethite. *Colloids and Surfaces A: Physicochem. Eng. Aspects, 166*, 225–233

Kuhn, J., F. Fiene, R. Cahill, H. Gluskoter, and N. Shimp (1981), Abundance of Trace and Minor Elements in Organic and Mineral Fractions of Coal. U.S. Environmental Protection Agency, Washington, D.C., EPA/600/7-80/003, 67 p.

Riley, R.A., J.A. Harper, M.T. Baranoski, C.D. Laughrey, and R.W. Carlton (1993), Measuring and predicting reservoir heterogeneity in complex deposystems: the late Cambrian Rose Run Sandstone of Eastern Ohio and Western Pennsylvania. US Department of Energy.

Johnson, J.W., E.H. Oelkers, and H.C. Helgeson (1992), SUPCRT92: A software package for calculating the standard molal thermodynamic properties of minerals, gases, aqueous species, and reactions from 1 to 5000 bars and 0 to 1000 degrees C. *Computers and Geosciences, 18*, 899–947.

Johnston, R.B. and P.C. Singer (2007), Solubility of symplesite (ferrous arsenate): Implications for reduced groundwaters and other chemical environments. *Soil Sci Soc. Am. J., 71*, 101–107.

Kelley, K.K. (1960), High-Temperature Heat-Content, Heat-Capacity, and Entropy Data for the Elements and Inorganic Compounds. *Contributions to the Data on Theoretical Metallurgy XIII. Bulletin*, 584. Washington, D.C.: U.S Government Printing Office. 232 p.

Kellog H. H. and S.K. Basu (1960), Thermodymamic properties of the system Pb-S-O to 1100K. *Trans TMS-AIME*, 218(2): 70-81.

Kellog, H.H. (1989), Critical evaluation of the thermochemical properties of lead sulfates. *Metallurgical Trans. B, 20B*, 77–85.

Kitahama, K, R. Kiriyama, and B. Yoshihisa (1975), Refinement of the crystal structure of scorodite. *Acta Crystallographica B31*, 322–324.

Kiukkola, K. and C. Wagner (1957), Measurements on galvanic cells involving solid electrolytes. Journal of the Electrochemical Society, 104 (6), 379–387.

Kolker, A., S.J. Mroczkowski, C.A. Palmer, K.O. Dennen, R.B. Finkelman, and J.H. Bullock, Jr. (2002), Toxic xubstances from coal combustion- A comprehensive assessment, Phase II: Element modes of occurrence for the Ohio 5/6/7, Wyodak, and North Dakota coal samples. *Open-File Report 02-224*, U.S. Geological Survey, U.S. Department of the Interior. 79 p.

Kolker, A., C.L. Senior, and J.C. Quick (2006), Mercury in coal and the impact of coal quality on mercury emissions from combustion systems. *Applied Geochemistry, 21*, 1821–1836.

Kuzel, H.-J. (1973), Hydrothermalesynthese basicher Bleisulfate (hydrothermal synthesis of basic lead-sulfates). *Neues Jahrbuch fur Mineralogie Monatshefte*, 110–116.

Kyono, A., M. Kimata, and T. Hatta (2005), Light-induced degradation dynamics in realgar: in situ structural investigation. using single crystal X-ray diffraction and X-ray photoelectron spectroscopy. *American Mineralogist, 90*, 1563–1570.

Lackovic, K., M.J. Angove, J.D. Wells, and B.B. Johnson (2003), Modeling the adsorption of Cd(II) onto Muloorina illite and related clay minerals. Journal of Colloid and Interface Science, 257: 31-40.

Langmuir, D., J. Mahoney, and J. Rowson (2006), Solubility products of amorphous ferric arsenate and crystalline scorodite ($FeAsO_4.2H_2O$) and their application to arsenic behavior in buried mine tailings. *Geochim. et Cosmochim. Acta, 70*, 2942–2956.

Lasaga, A.C., J.M. Soler, J. Ganor, T.E. Burch and K.L. Nagy (1994), Chemical weathering rate laws and global geochemical cycles. Geochimica et Cosmochimica Acta, 58: 2361-2368.

Lee, J.S. and J.O. Nriagu (2007), Stability constants for metal arsenates. *Environ. Chem., 4*, 123–133.

Lemoine, P., D. Carre, and F. Robert (1991), Structure du sulfure de fer et d'antimoine, FeSb2S4 (Berthierite). *Acta Crystallographica, C47*, 938–940.

Lennie, A R, S.A.T. Redfern, P.F. Schofield, and D.J. Vaughan (1995), Synthesis and Rietveld crystal structure refinement of mackinawite, tetragonal FeS. *Mineralogical Magazine, 59*, 677–683.

Levinson, A.A. (1977), Hydrogen—A reducing agent in some uranium deposits. *Canadian Journal of Earth Sciences, 14*, 2679–2681.

Lewicki, J.L., J.T. Birkholzer, and C.-F. Tsang (2006), Natural and industrial analogues for release of CO_2 from storage reservoirs: identification of features, events, and processes, and lessons learned, Lawrence Berkeley National Laboratory report, LBNL-59784.

Lewicki, J.L., J.T. Birkholzer, and C.-F. Tsang (2007), Natural and industrial analogues for leakage of CO_2 from storage reservoirs – identification of features, events, and processes and lessons learned, *Journal of Environmental Geology*, 52(3), pp. 457-467.

Lide, D.R. (ed.) (2005), *CRC Handbook of Chemistry and Physics, 85th Edition*. CRC Press. Boca Raton, Florida (2005). Section 14, "Geophysics, Astronomy, and Acoustics; Abundance of Elements in the Earth's Crust and in the Sea."

Lindberg, R.D. and D.D. Runnels (1984), Ground water redox reactions: An analysis of equilibrium state applied to Eh measurements and geochemical modeling. Science, 225, 925-927.

Liu, J., Z. Li, J. Liu, J. Wang, C. Feng, and W. Lu (2005), Mineralogy of the stibnite-antimonselite series in nature. *Journal of Jilin University (Earth Science Edition), 35*(5), 545–553.

Lozar, J., L. Schuffenecker, G. Cudey, and J. B. Bourdet (1984), Determination a 25°C des proprietes thermodynamiques des complexes chlores du plomb divalent a partir de mesures de solubilite dans des solutions aqueuses de force ionique inferieure a 1 mol kg-1. *Thermochimica Acta*, v. 79, Pages 171-186.

Lutzenkirchen, J. (2006), *Surface Complexation Modelling*. Academic Press, Amsterdam, London, 638 p.

Manning, B.A. and S. Goldberg (1997), Adsorption and stability of arsenic(III) at the clay mineral-water interface. *Environ. Sci. Technol., 31*, 2005–2011.

Martinez Garcia, E., C. Luque, R. Burkhardt, R., and M. Guiterrez-Claverol (1991), Hozarco: Un ejemplo de mineralizacion de Pb-Zn-Hg de edad permica (Cordillera Cantabrica, NW de Espana). *Boletin Sociedad Espanola de Mineralogica, 14*, 107–118.

Majzlan, J., B.E. Lang, R. Stevens, A. Navrotsky, B.F. Woodfield, and J. Boerio-Goates (2003), Thermodynamics of Fe oxides: Part I. Entropy at standard temperature and pressure and heat capacity of goethite (α-FeOOH), lepidocrocite (γ-FeOOH), and maghemite (γ-Fe_2O_3). *American Mineralogist, 88*(5–6), 846–854.

Majzlan, J., K.D. Grevel, and A. Navrotsky (2003). Thermodynamics of Fe oxides: Part II. Enthalpies of formation and relative stability of goethite (α-FeOOH), lepidocrocite (γ-FeOOH), and maghemite (γ-Fe_2O_3). *American Mineralogist, 88*(5–6), 855–859.

Majzlan, J., A. Navrotsky, and U. Schwertmann (2004), Thermodynamics of Fe oxides: Part III. Enthalpies of formation and stability of ferrihydrite (~$Fe(OH)_3$), schwertmannite (~$FeO(OH)_{3/4}(SO4)_{1/8}$), and e-Fe_2O_3. *Geochimica et Cosmochimica Acta, 68*(5), 1049–1059.

McGrath, A.E., G.L. Upson, and M.D. Caldwell (2007), Evaluation and mitigation of landfill gas impacts on cadmium leaching from native soils. *Ground Water Monitoring & Remediation, 27*, 99–109.

McKibben, M.A., B.A. Tallant and J.K.d. Angel (2008), Kinetics of inorganic arsenopyrite oxidation in acidic aqueous solutions. Applied Geochemistry, 23: 121-135.

McMahon, P.B., and F.H. Chapelle (2008), Redox processes and water quality of selected principal aquifer systems, *Ground Water*, v. 46, no. 2, p. 259-271.

McPhail, D.C., E. Summerhayes, S. Welch, and J. Brugger (2003), The geochemistry and mobility of zinc in the regolith. In: *Advances in Regolith*, I.C. Roach, ed., pp. 287–291, CRC for Landscape Environments and Mineral Exploration, PO Box 1130, Bentley, Western Australia 6102 Australia. ISBN 0-7315-4815-9 (CD-ROM).

McPhail, D.C., E. Summerhayes, V. Jayaratne, and A. Christy (2006), Hemimorphite solubility and stability of low-T zinc minerals. *Geochimica et Cosmochimica Acta, 70*. 16th Annual Goldschmidt Conference, 27 August to 1 September, Melbourne, Australia.

Mehra, M.C. and A.O. Gubeli (1970a), Complexing characteristics of insoluble selenides. II. Manganese selenide. *Journal of the Less-Common Metals*, 22(3), 281-285.

Mehra, M.C. and A.O. Gubeli (1970b), Complexing characteristics of insoluble selenides. I. Silver selenide. *Canadian Journal of Chemistry, 48*, 3491–3497.

Mehra, M.C. and A.O. Gubeli (1971), Complexing characteristics of insoluble selenides. III. Mercuric selenide. *Journal of the Less-Common Metals, 25*(3), 221–224.

Michel, F.M., L. Ehm, S.M. Antao, P.L. Lee, P.J. Chupas, G. Liu, D.R. Strongin, M.A.A. Schoonen, B.L. Phillips, and J.B. Parise (2007), The structure of ferrihydrite, a nanocrystalline material. *Science*, published online 24 May 2007 (10.1126/science.1142525).

Michel, F. M., L. Ehm, G. Liu, W.Q. Han, X.S.M. Antao, P.J. Chupas, P.L. Lee, K. Knorr, H. Eulert, J. Kim, C.P. Grey, A.J. Celestian, O.J. Gillow, M.A.A. Schoonen, D.R. Strongin, and J.B. Parise (2007), Similarities in 2- and 6-line ferrihydrite based on pair distribution function analysis of x-ray total scattering. *Chem. Mater*, *19,* 1489–1496.

Mills, K.C. (1974), *Thermodynamic Data for Inorganic Sulfides, Selenides and Tellurides*. Butterworths, London, 845 p.

Min, M.-Z., Z.-W. Meng , G.-Y. Sheng , Y.-S. Min , and X. Liu (2000), Organic geochemistry of paleokarst-hosted uranium deposits, South China. *Journal of Geochemical Exploration, 68*, 211–229.

Mohan, M.S., R.A. Zingaro, R.D. Macfarlane, and K.J. Irgolic, K.J. (1982), Characterization of a uranium-rich organic material obtained from South Texas lignite. *Fuel, 61*, 853–858.

Morimoto, N. and L.A. Clark (1961), Arsenopyrite crystal-chemical relations from Freiberg, Germany. *American Mineralogist, 46*, 1448–1469.

Morin, G., G. Rousse, and E. Elkaim (2007), Crystal structure of tooeleite, $Fe_6(AsO_3)_4SO_4(OH)_4{\cdot}4H_2O$, a new iron arsenite oxyhydroxy-sulfate mineral relevant to acid mine drainage. *American Mineralogist; 92*(1), 193–197.

Mullen, D.J.E. and W. Nowacki (1972), Refinement of the crystal structures of realgar, AsS and orpiment, As_2S_3. *Zeitschrift fur Kristallographie, 136*, 48–65.

Muller, B. and L. Sigg (1991), Adsorption of lead(ll) on the goethite surface: Voltammetric evaluation of surface complexation parameters. *Journal of Colloid and Interface Science, 148*(2), 517–532.

NASCENT (2005), Natural analogs for the geological storage of CO_2, *NASCENT Report 2005/6,* March 2005.

Nefedov, V.I., Yu.A. Teterin, A.M. Lebedev, A.Yu. Teterin, A.P. Dementjev, M. Bubner, T. Reich , S. Pompe, K.H. Heise, and H. Nitsche (1998), Electron spectroscopy for chemical analysis investigation of the interaction of uranyl and calcium ions with humic acids. *Inorganica Chimica Acta, 273*, 234–237.

Nordstrom, D.K. (1984), Partial compilation and revision of basic data in the Wateq programs. *U.S. Geol. Surv. WRI Rept. #84-4186*, 40 p.

Nordstrom, D.K. and D.G. Archer (2003), Arsenic thermodynamic data and environmental geochemistry. An evaluation of thermodynamic data for modeling the aqueous environmental geochemistry of arsenic. Chapter 1 in *Arsenic in Ground Water*, A.H. Welch and K.G. Stollenwerk, eds., Kluwer Academic Publishers, Boston, pp. 1–33.

Odom, I. E., T.M. Willand, and R.J. Lassin (1977), Paragenesis of authigenic minerals in St. Peter Sandstone. *American Association of Petroleum Geologists Bulletin, 61*, 1384–1385.

Paar, W.H., D. Topa, A.C Roberts, A.J Criddle, G. Amann, and R.J. Sureda (2002), The new mineral species brodtkorbite, Cu_2HgSe_2, and the associated selenide assemblage from Tuminico, Sierra de Cacho, La Rioja, Argentina. *The Canadian Mineralogist, 40*(1), 225–237.

Paces, T. (1978), Reversible control of aqueous aluminum and silica during the irreversible evolution of natural waters. *Geochim. Cosmochim. Acta 42*, 1487-1493.

Pacheco, Fernando A.L., and T. Szocs (2006), Dedolomitization reactions driven by anthropogenic activity on loessy sediments, SW Hungary. *Applied Geochemistry 21*, 614–631.

Pagnanelli, F., L. Bornoroni, E. Moscardini, and L. Toro (2006), Non-electrostatic surface complexation models for protons and lead(II) sorption onto single minerals and their mixture. *Chemosphere, 63*, 1063–1073.

Palache, C., H. Berman, and C. Frondel (1951), The System of Mineralogy, *7th edition,* vol II. *Halides, Nitrates, Borates, Sulfates, Phosphates, Arsenates, Tungstates, Molybdates*, etc. John Wiley and Sons, Inc. New York.

Palandri, J. and Y.K. Kharaka (2004), A compilation of rate parameters of water-mineral interaction kinetics for application to geochemical modeling. Open File Report 2004-1068, US Goelogical Survey.

Palenik, C.S., S. Utsunomiya, M. Reich, S.E. Kesler, and R.C. Ewing (2004), Invisible gold revealed: direct imaging of gold nanoparticles in a Carlin-type deposit. *Am. Mineral., 89*, 1359–1366.

Pankratz, L.B. and E.G. King (1987), Thermodynamic properties of sulfides. U.S. Bur. Mines Bull., 689, 427 p.

Paquette, K.E and G. Helz (1997), Inorganic speciation of mercury in sulfidic waters: the importance of zero-valent sulfur. *Environmental Science and Technology, 31*, 2148–2153.

Paquette, K.E and G. Helz (1995), Solubility of cinnabar (red HgS) and implications for mercury speciation in sulfidic waters. *Water, Air, and Soil Pollution, 80*, 1053–1056.

Parker, V.B. and I.L. Khodakovskii, (1995), Thermodynamic properties of the aqueous ions (2+ and 3+) of iron and key compounds of iron. *J. Phys. Chem. Ref. Data, 24*(5), 1699–1745.

Parkhurst, D.L. and C.A.J. Appelo (1999), User's guide to PHREEQC (version 2)—A computer program for speciation, batch-reaction, one-dimensional transport, and inverse geochemical calculations. *U.S. Geological Survey Water-Resources Investigations Report 99-4259*, Denver, CO, Http://Wwwbrr.Cr.Usgs.Gov/Projects/GWC_Coupled/Phreeqc/Html/Final.Html

Pecharroman, C, T. Gonzalez-Carreno, and J.E. Iglesias (1995), The infrared dielectric properties of maghemite, gamma-Fe_2O_3, from reflectance measurement on pressed powders. *Physics and Chemistry of Minerals, 22*, 21–29

Penn, R.L. (2007), Resolving an elusive structure. *Science*, published online 24 May 2007 (10.1126/science.1144002).

Perfetti E., G.S. Pokrovski, K. Ballerat-Busserolles, V. Majer, and F. Gibert (2008), Densities and heat capacities of aqueous arsenious and arsenic acid solutions to 350 °C and 300 bar, and revised thermodynamic properties of As(OH)3(aq), AsO(OH)3(aq) and iron sulfarsenide minerals. Geochimica et Cosmochimica Acta 72 (2008) 713–731

Pertlik, F. (1975), Die kristallstruktur der monoklinen form von As_2O_3 (Claudetit II). *Monatshefte fur Chemie, 106*, 755–762.

Pettijohn, F.J., P.E. Potter, and R. Siever (1987), *Sand and Sandstone*, Springer Verlag.

Piatak, N.M., R.R. Seal, II, and J.M. Hammarstrom (2004), Environmental significance of cadmium and other trace-element concentrations in sphalerite from mineral deposits. *Geological Society of America, Abstracts with Program, 36*(5), 27–28. Online at http://gsa.confex.com/gsa/2004AM/finalprogram/abstract_79382.htm.

Pickardt, J., B. Reuter, E. Riedel, and J. Sochtig (1975), On the formation of $FeSe_2$ single crystals by chemical transport reactions. Journal of Solid State Chemistry, 15, 366–368.

Pitman. A.L., M. Pourbaix, and N. de Zoubov (1957), Potential-pH diagram of the antimony-water system: Its applications to properties of the metal, its compounds, its corrosion, and antimony electrodes. *Journal of the Electrochemical Society, 104*(10), 594–600.

Pitman, J.K., M.B. Goldhaber, and C. Spoetl (1997), Regional diagenetic patterns in the St. Peter Sandstone: Implications for brine migration in the Illinois Basin. *Evolution of Sedimentary Basins—Illinois Basin*, *U.S. Geological Survey Bulletin 2094-A*, pp. A1–A17.

Plummer, L., J. Busby, R. Lee, and B. Hanshaw (1990), Geochemical modeling of the Madison Aquifer in parts of Montana, Wyoming, and South Dakota. *Water Resour. Res., 26*(9), 1981–2014.

Plummer, L.N., and E. Busenberg (1982), The solubilities of calcite, aragonite, and vaterite in CO_2-H_2O solutions between 0 and 90ºC and an evaluation of the aqueous model of the system $CaCO_3$-CO_2-H_2O. *Geochim. Cosmochim. Acta, 46*, 1011–1040.

Pokrovski, G., R. Gout, J. Schott, A. Zotov, and J. Harrichoury (1996), Thermodynamic and stoichiometry of As (III) hydroxide complexes at hydrothermal conditions. *Geochim. Cosmochim. Acta, 60*, 737–749.

Pokrovski, G.S., S. Kara, and J. Roux (2002), Stability and solubility of arsenopyrite, FeAsS, in crustal fluids. *Geochim. et Cosmochim. Acta, 66*(13), 2361–2378.

Preis, W. and H. Gamsjager (2002), Critical evaluation of solubility data: Enthalpy of formation of siderite. *Phys. Chem. Chem. Phys., 4*, 4014–4019.

Pruess, K., C. Oldenburg, and G. Moridis (1999), TOUGH2 User's Guide, Version 2.0, LBL-43134, Lawrence Berkeley National Laboratory, Berkeley, CA.

Reardon, E.J. and R.D. Beckie (1987), Modelling chemical equilibria of acid mine drainage: The $FeSO_4$-H_2SO_4-H_2O system. *Geochim. et Cosmochim. Acta, 51*, 2355–2368.

Reich, M. and U. Becker (2006), First-principles calculations of the thermodynamic mixing properties of arsenic incorporation into pyrite and marcasite. *Chem. Geol., 225*, 278–290.

Reich, M., S.E. Kesler, S. Utsunomiya, C.S. Palenik, S.L. Chryssoulis, and R.C. Ewing (2005), Solubility of gold in arsenian pyrite. *Geochimica et Cosmochimica Acta*, *69*(11), 2781–2796.

Rickard, D. (2006), The solubility of FeS. *Geochimica et Cosmochimica Acta, 70*, 5779–5789.

Rickard, D. and G.W. Luther III. (2006), Metal sulfide complexes and clusters. Chapter 8 in Reviews in Mineralogy and Geochemistry (David J. Vaughan, Ed.), p. 421-504. The Mineralogical Society of America, Chantilly, Va, USA.

Rieder, M., J.C. Crelling, O. Sustai, M. Drabek, Z. Weiss, and M. Klementova (2007), Arsenic in iron disulfides in a brown coal from the North Bohemian Basin, Czech Republic. *International Journal of Coal Geology, 71*, 115–121.

Robie, R.A. (1967), Selected x-ray crystallographic data, molar volumes, and densities of minerals and related substances. *U.S.G.S. TIC: 248724* (1248, p. 87), Denver, CO.

Robie, R.A. and B.S. Hemingway (1995), Thermodynamic properties of minerals and related substances at 298.15 K and 1 bar (10^5 pascals) pressure and at higher temperatures. *U.S. Geol. Surv. Bull. 2131*, 461 p.

Rock, P.A., G.K. Mandell, W.H. Casey, and E.M. Walling (2001), Gibbs energy of formation of dolomite from electrochemical cell measurements and theoretical calculations. *Am. J. Sci., 301*, 103–111.

Rojo, J.M., J.L. Mesa, J.L. Pizarro, L. Lezama, M.I. Arriortua, and T. Rojo (1996), Spectroscopic and magnetic study of the $(Mg,M)_3(AsO_4)_2*8H_2O$ ($M = Ni^{2+}$, Co^{2+}) arsenates. *Materials Research Bulletin, 31*, 925–934.

Rozan, T.F., Luther, G.W. III, Ridge, D. and Robinson, S. (2003). Determination of Pb complexation in oxic and sulfidic waters using pseudovoltammetry. Environ. Sci. Technol. 2003, 37, 3845-3852.

Ruaya, J.R. and T.M. Seward (1986), The stability of chlorozinc (11) complexes in hydrothermal solutions up to 350ºC. *Geochimica Cosmochimica Acta, 50*, 651–662.

Ryser, A.L., D.G. Strawn, M.A. Marcus, J.L. Johnson-Maynard, M.E. Gunter, and G. Möller (2005), Micro-spectroscopic investigation of selenium-bearing minerals from the Western US Phosphate Resource Area. *Geochemical Transactions, 6*, 1–11.

Sacks, L.A. and A.B. Tihansky (1996), Geochemical and isotopic composition of ground water, with emphasis on sources of sulfate, in the Upper Floridan Aquifer and Intermediate Aquifer System in Southwest Florida. *U.S. Geological Survey Water-Resources Investigations Report 96-4146*, 67 p.

Stanton, M.R., P.A. Gemery-Hill, W.C.S. III and C.D. Taylor (2008), Rates of zinc and trace metal release from dissolving sphalerite at pH 2.0–4.0. *Applied Geochemistry*, 23(136-147).

Sato, M. (1992), Persistency-field Eh-pH diagrams for sulfides and their application to supergene oxidation and enrichment of sulfide ore bodies. *Geochimica et Cosmochimica Acta, 56*(8), 3133–3156.

Savage, K.S., T.N. Tingle, P.A. ODay, G.A. Waychunas, and D.K. Bird (2000), Arsenic speciation in pyrite and secondary weathering phases, Mother Lode gold district, Tuolumne County, California. *Appl. Geochem., 15*, 1219–1244.

Schaefer, S.C. and N.A. Gokcen (1982), Electrochemical determination of the thermodynamic properties of sphalerite, ZnS(beta). *High Temperature Science, 15*, 225–237.

Schiferl, D. and C.S. Barrett (1969), The crystal structure of arsenic at 4.2, 78 and 299 K. *Journal of Applied Crystallography, 2*, 30–36.

Schoonen, M.A.A. and Barnes, H.L. (1988). An approximation of the second dissociation constant for H_2S. Geochim. Cosmochim. Acta, vol. 52, p. 649-654.

Schwarzenbach, G. and M. Widmer (1963), Die Löslichkeit von Metallsulfiden: I. Schwarzes Quecksilbersulfid. *Helv. Chim. Acta*, 46, 2613–2628.

Seal, R.R., R.A. Robie, P.B. Barton, and B.S. Hemingway (1992), Superambient heat capacities of synthetic stibnite, berthierite, and chalcostibnite: Revised thermodynamic properties and implications for phase equilibria. *Econ. Geol., 87*, 1911–1918.

Seby, F., M. Potin-Gautier, E. Giffaut, G. Borge, and O.F.X. Donard (2001), A critical review of thermodynamic data for selenium species at 25ºC. *Chemical Geology, 171*, 173–194.

Selim, H. M. and Amacher, M. C. (1996). Reactivity and transport of heavy metal in soil. Lewis Publishers, 201 pp.

Seward, T.M. (1984), The formation of lead (II) chloride complexes to 300°C: A spectrophotometric study. *Geochimica Cosmochimica Acta, 48*, 121–134.

Shaw, D.M., J. Dostal, and R.R. Keays (1985), Additional estimates of continental surface Precambrian shield composition in Canada. *Geochim. Cosmochim. Acta, 40*, 73–83.

Shea, D. and G.R. Helz (1989), Solubility product constants of covellite and a poorly crystalline copper sulfide precipitate at 298 K. *Geochimica et Cosmochimica Acta, 53*, 229–236.

Shelton, R.A.J. (1970), $PbCl_2$, $SnCl_2$ and CuCl from emf measurements on galvanic cells with a solid electrolyte. *Trans. Inst. Min. and Met., C, 79*, C215–C220.

Shipton, Z.K., J.P. Evans, B. Dockrill, J. Heath, A. Williams, D. Kirchner, and P.T. Kolesar (2004), Natural leaking CO_2-charged systems as analogues for failed geologic sequestration reservoirs. In: *Geological Storage of Carbon Dioxide*, S.J. Baines and R.H. Worden, eds., Geological Society, London, Special Publications, *233*, pp. 43–58.

Shock, E.L. and H.C. Helgeson (1988), Calculation of the thermodynamic and transport properties of aqueous species at high pressures and temperatures: Correlation algorithms for ionic species and equation of state predictions to 5 kb and 1000°C. *Geoch. Cosmochim. Acta*, *52*, 2009–2036.

Shock, E.L., H.C. Helgeson, and D.A. Sverjensky (1989), Calculation of the thermodynamic and transport properties of aqueous species at high pressures and temperatures: Standard partial molal properties of inorganic neutral species. *Geoch. Cosmochim. Acta*, *53*, 2157–2183.

Shock, E.L., E.H. Oelkers, J.W. Johnson, D.A. Sverjensky, and H.C. Helgeson (1992), Calculation of the thermodynamic and transport properties of aqueous species at high pressures and temperatures: Effective electrostatic radii to 1000C and 5 kb. *J. Chem. Soc. London Faraday Trans.*, *88*, 803–826.

Shock E.L., D.C. Sassani, M. Willis, and D.A. Sverjensky (1997), Inorganic species in geologic fluids: Correlations among standard partial molal thermodynamic properties of aqueous ions and hydroxide complexes. *Geoch. Cosmochim. Acta*, 61, 907–950.

Shpanov E. P., G. A. Sidorenko, and T. I. Stolyarova (1970), Akdalaite, a new hydrous modification of alumina: Zap. Vses. Mineral. Obshch., 99, 333-339 [in Russian].

Simon, G., H. Huang, J.E. Penner-Hahn, S.E. Kesler, and L.-S. Kao (1999a), Oxidation state of gold and arsenic in gold-bearing arsenian pyrite. *Am. Mineral.*, 84, 1071– 1079.

Simon, G., S.E. Kesler, and S. Chryssoulis (1999b), Geochemistry and textures of gold-bearing arsenian pyrite, Twin Creeks, Nevada; implications for deposition of gold in Carlin-type deposits. *Econ. Geol., 94*, 405–421.

Simon, L., M. François, P. Refait, G. Renaudin, M. Lelaurain, and J.-M.R. Génin (2003), Structure of the Fe(II-III) layered double hydroxysulphate green rust two from Rietveld analysis. *Solid State Sciences, 5*, 327–334.

Singer, P.C. and W. Stumm (1968), Oxygenation of ferrous iron: The rate determining step in the formation of acidic mine drainage. *Federal Water Pollution Control Administration Research Series Report*. *NTIS Report No. PB-189-233*.

Singer, P.C. and W. Stumm (1970), Acid mine drainage: The rate-determining step. *Science, 167*, 1121–1123.

Skinner, B.J., R.C. Erd, and F.S. Grimaldi (1964), Greigite, the thio-spinel of iron; a new mineral. *American Mineralogist, 49*, 543–555.

Smedley, P. L. and W. M. Edmunds (2002), Redox patterns and trace-element behavior in the East Midlands Triassic Sandstone Aquifer, U.K. *Ground Water, 40*(1), 44–58.

Smedley, P.L. (2003), Arsenic in groundwater – south and east Asia. Chapter 7 in *Arsenic in Ground Water*, A.H. Welch and K.G. Stollenwerk, eds., Kluwer Academic Publishers, Boston, pp. .

Smith, E.H., W. Lu, T. Vengris, and R. Binkiene (1996), Sorption of heavy metals by lithuannian glauconite. *Water Research, 30*(12), 2883–2892.

Smith, F.G. (1963), *Physical Geochemistry*. Addison-Wesley Publishing Company, Inc., Reading, Massachusetts, 624 p

Solans-Huguet, J. and M. Font-Altaba (1967) Estudio de un modelo teoretico de la formacion del mineral cotunnita. *Bol. R. Soc. Espanola Hist. Nat. (Geol)*, 65, 51–56.

Sonnenthal, E., A. Ito, N. Spycher, M. Yui, J. Apps, Y. Sugita, M. Conrad and S. Kawakami (2005), Approaches to modeling coupled thermal, hydrological, and chemical processes in the Drift Scale Heater Test at Yucca Mountain. Int. J. Rock Mech. Min. Sci., 42: 6987–719.

Steefel, C.I. and A.C. Lasaga (1994), A coupled model for transport of multiple chemical species and kinetic precipitation/dissolution reactions with applications to reactive flow in a single-phase hydrothermal system. *Am. J. Sci,* 294, 529–592.

Steefel, C.I. (2001), *GIMRT, Version 1.2: Software for Modeling Multicomponent, Multidimensional Reactive Transport: Users Guide*. Lawrence Livermore National Laboratory, Livermore, California.

Stefansson, A., S. Arnorsson, and A.E. Sveinbjornsdottir (2005), Redox reactions and potentials in natural waters at disequilibrium. *Chemical Geology, 221*, 289–311.

Ste-Marie, J., A.E. Torma, and A.O. Gübeli (1964), The stability of thiocomplexes and solubility products of metal sulphides: I. Cadmium sulphide. *Can. J. Chem., 42*(3), 662–668.

Stevenson, R.K. and R.F. Martin (1986). Implications of the presence of amazonite in the Broken Hill and Geco metamorphosed sulfide deposits. *Canadian Mineralogist, 24*, 729–745.

Stubbles, J.R. and C.E. Birchenall (1959), Redetermination of the lead sulfide equilibrium between 585 and 920ºC. *Trans. Met. Soc. AIME, 215*, 535–539.

Suzuki, Y., S.D. Kelly, K.M. Kemner, and J.F. Banfield (2005), Direct microbial reduction and subsequent preservation of uranium in natural near-surface sediment. *Applied and Environmental Microbiology*, Apr. 2005, 1790–1797.

Svensson, C. (1974), The crystal structure of orthorhombic antimony trioxide, Sb_2O_3. *Acta Crystallographica, B30*, 458–461.

Svensson, C. (1975), Refinement of the crystal structure of cubic antiomony trioxide, Sb_2O_3. *Acta Crystallographica, B31*, 2016–2018.

Sverjensky, D.A., E. Shock, and H.C. Helgeson (1997), Prediction of the thermodynamic properties of aqueous metal complexes to 1000 degrees C and 5 kb. *Geoch. Cosmochim. Acta*, *61*, 1359–1412.

Szalay, A. (1964), Cation exchange properties of humic acids and their importance in the geochemical enrichment of UO_2^{++} and other cations. *Geochimica et Cosmochimira Acta, 28*, 1605-1614.

Tagirov, B. and J. Schott (2001), Aluminum species in crustal fluids revisited. *Geochim. Cosmochim. Acta, 65*(21), 3965–3992.

Tanger J.C. and H.C. Helgeson (1988), Calculation of the thermodynamic and transport properties of aqueous species at high pressures and temperatures: Revised equations of state for the standard partial molal properties of ions and electrolytes. *Amer. J. Sci.*, *288*.

Taylor, P. and V.J. Lopata (1984), Stability and solubility relationships between some solids in the system PbO-CO_2-H_2O. *Can. J. Chem., 62*, 395–402.

Taylor, S.R. and S.M. McLennan (1985), *The Continental Crust: Its Composition and Evolution*. Blackwell Sci. Publ., Oxford, 330 pp.

Tewalt, S.J., L.J. Bragg, and R.B. Finkelman (2001), Mercury in U.S. coal—Abundance, distribution, and modes of occurrence. *USGS Fact Sheet FS-095-01*, U.S. Geological Survey, U.S. Department of the Interior, 3 p.

Theberge, S. and G.W. Luther (1997), Determination of the electrochemical properties of a soluble aqueous FeS species present in sulfide solutions. *Aquatic Geochem. 3*, 191–211.

Thiel, G.A. (1935), Sedimentary and petrographic analysis of the St. Peter Sandstone. *Geological Society of America Bulletin, 46*, 559–614.

Thornberg, K. and N. Sahai, (2004), Arsenic occurrence, mobility, and retardation in sandstone and dolomite formations of the Fox River valley, Eastern Wisconsin. *Environ. Sci. Technol., 38*, 5087–5094.

Tissot, B.P. and D.H. Welte (1978), *Petroleum Formation and Occurrence: A New Approach to Oil and Gas Exploration*. Springer Verlag, New York, 538 p.

Tilley, D.B. and Eggleton, R.A. (1994), Tohdite ($5A1_2O_3.H_2O$) in bauxites from Northern Australia. Clays and Clay Minerals, Vol. 42, No. 4, 485-488.

Tolkachev, S. S., E.V. Stroganov., I. Kozina (1958), The structure of lead oxide monohydrate. *Vestn. Leningr. Univ. Ser. Fizik. Khim*.,16, 134-139. [In Russian]

Toptygina, G.M., A.A. Soldatov, and V.I. Evdokimov (1984), The reaction of lead chloride with calcium hydroxide in aqueous solution. Russian Journal of Inorganic Chemistry, 29(11) 1580–1582. [Translated from Zhurnal Neorganicheskoi Khimii, 29, 2757-2759 (1984)].

Tossell, J.A. (1999), Theoretical studies on the formation of mercury complexes in solution and the dissolution and reactions of cinnabar. *American Mineralogist, 84*, 877–883.

Tridot, G., J.-C. Boivan, and D. Thomas, (1969), Contribution a l'etude du systeme $PbO\text{-}PbSO_4$. *J. Thermal Analysis, 1(1)*, 35–46 Doi:10.1007/BF01911244.

Tronc, E., C. Chaneac, and J. P. Jolivet (1998), Structural and magnetic characterization of e-Fe_2O_3. *Journal of Solid State Chemistry, 139*, 93–104.

Tucker, M.E. (1991), *Sedimentary Petrology: An Introduction to the Origin of Sedimentary Rocks*. Blackwell Scientific Publications, Oxford. 2nd Edition, 260 p.

Turekian, K.K. (1970), in *McGraw-Hill Encyclopedia of Science and Technology*, *4*, 627.

Uhler, A.D. and G.R. Helz (1984), Solubility product of galena at 298 K: A possible explanation for apparent supersaturation in nature. *Geochimica et Cosmochimica Acta, 48*, 1155–60.

USGS (2008), National Geochemical Survey database. http://tin.er.usgs.gov/geochem/

USGS, (2001), Mercury in U.S. Coal -- Abundance, Distribution, and Modes of Occurrence. U.S. Geological Survey Fact Sheet FS-095-01, 6 p.

Utsunomiya, S., S.C. Peters, J.D. Blum, and R.C. Ewing (2003), Nanoscale mineralogy of arsenic in a region of New Hampshire with elevated As-concentrations in the groundwater. *Am. Miner. 88*, 1844–1852.

Vaughan, D.J. and J.R. Craig (1978), Mineral Chemistry of Metal Sulfides. Cambridge Earth Science Series. Harland, W.B., ed. New York: Cambridge University Press. 493 p.

Vikre, Peter G. (2005), Se-rich precious metal deposits and the significance of Se in sinter, Northern Great Basin (Abstract). *Paper No. 235-8*, The Geological Society of America 2005 Salt Lake City Annual Meeting (October 16–19, 2005).

Wagman, D.D., W.H. Evans, V.B. Parker, I. Halow, S.M. Bailey, and R.H. Schumm (1968), Selected values of chemical thermodynamic properties. *Nat. Bur. Stand. (U.S.). Tech. Note*, 270–3, 264 p.

Wagman, D.D., W.H. Evans, V.B. Parker, R.H. Schumm, I. Halow, S.M. Bailey, K.L. Churney, and R.L. Nuttall (1982), The NBS Tables of Chemical and Thermodynamic Properties. *Jour. Phys. Chem. Ref. Data*, v. 11, Supplement no. 2, 392 p.

Walker, F.P., M.E. Schreiber and J.D. Rimstidt, 2006. Kinetics of arsenopyrite oxidative dissolution by oxygen. Geochimica et Cosmochimica Acta, 70: 1668-1676.

Wang, S. and P.R. Jaffe (2004), Dissolution of a mineral phase in potable aquifers due to CO_2 releases from deep formations; effect of dissolution kinetics. *Energy Conversion and Management, 45*, 2833–2848.

Wänke, H., G. Dreibus, and E. Jagoutz (1984), Mantle chemistry and accretion history of the Earth. In: *Archean Geochemistry*, A. Kröner, G.N. Hanson, A.M. Goodwin, eds., pp. l–24, Springer-Verlag, Berlin.

Weast, R.C., Astle, M.J. and W.H. Beyer (Eds). (1984), CRC Handbook of Chemistry and Physics CRC Press, Inc., Boca Raton, Florida.

Weaver, B.L. and J. Tamey (1984), Major and trace element composition of the continental lithosphere. In *Physics and Chemistry of the Earth, 15*, H.N. Pollack, V.R. Murthy, eds., pp. 39–68, Pergamon, Oxford.

White, D., D.C. McPhail, and D. Lawie (2004), Fractionation of Zn and Cd in soils proximal and distal to sulphide mineralistion. In: *Regolith 2004*, I.C. Roach, ed., , pp. 394–397, CRC for Landscape Environments and Mineral Exploration, Bentley, Western Australia, Australia, ISBN 0-9756895-1-7 (CD-ROM).

Whitfield, M. and D.R. Turner (1980), The theoretical studies of the chemical speciation of lead in seawater. In: *Lead in the Marine Environment*, M. Branica and Z. Konrad eds., pp. 109–148, Pergamon, New York.

Wiegers, G A. (1971), The crystal structure of the low-temperature form of silver selenide. *American Mineralogist, 56*(1971), 1882–1888.

Wieser, M. E. (2006), Atomic weights of the elements 2005, (IUPAC Technical Report). *Pure Appl. Chem., 78*(11), 2051–2066.

Wise, W.S. and S.E. Loh (1976), Equilibria and origin of minerals in the system Al_2O_3-$AlPO_4$-H_2O. *American Mineralogist, 6I*, 409–413.

Williams Jones, A.E. and C. Normand (1997), Controls of mineral parageneses in the system Fe-Sb-S-O. *Economic Geology, 92*(3), 308–324.

Wolfe, C.W. (1940), Classification of minerals of the type $A_3(XO_4)_2 \cdot nH_2O$ (concluded) American Mineralogist, 25(12), 787–809.

Wolery, T.J.(1992), EQ3NR, A computer program for geochemical aqueous speciation-solubility calculations: Theoretical manual, user's guide, and related documentation (Version 7.0). Lawrence Livermore National Lab. UCRL-MA-110662 PT III.

Wolery, T.J. (1993), EQ3/6, A software package for geochemical modelling of aqueous systems (Version 7.2). Lawrence Livermore Nat. Lab. UCRL-MA 110662.

Wood, R.H. (1958), The second ionization constant of hydrogen selenide. *J. Am. Chem. Soc., 80*, 1559–1562.

Wright, H.D., W.M. Barnard, and J.R. Halbig (1965), Solid solution in the systems ZnS-ZnSe and PbS-PbSe at 300°C. and above. *American Mineralogist, 50*, 1802–1815.

Wyckoff, R.W.G. (1963), [Antimony] In: *Crystal Structures 1*, pp. 7–83. Second edition. Interscience Publishers, New York, New York

Wyckoff, R.W.G. (1963), [Clausthalite]. In: *Crystal Structures, 1*, pp. 85–237, Second edition. Interscience Publishers, New York, New York.

Wyckoff, R.W.G. (1963), [Greenockite cell parameters.]. In: *Crystal Structures, 1*, pp. 85–237, Second edition. Interscience Publishers, New York, New York

Wyckoff, R.W.G. (1963), [Lepidocrocite structure]. In: *Crystal Structures, 1*, 290–295 Second edition. Interscience Publishers, New York, New York.

Wyckoff, R.W.G. (1963), [Uraninite cell parameters.]. In *Crystal Structures, 1*, 239-444, Second edition. Interscience Publishers, New York, New York.

Xiong, Y. (2003), Predicted equilibrium constants for solid and aqueous selenium species to 300°C: Applications to selenium-rich mineral deposits. *Ore Geology Reviews, 23*, 259–276.

Xu, T., J.A. Apps, and K. Pruess (2003), Reactive geochemical transport simulation to study mineral trapping for CO2 disposal in deep arenaceous formations. *J. Geophys. Res*., 108(B2), 2071-2084.

Xu, T., E. Sonnenthal, N. Spycher, and K. Pruess (2006), TOUGHREACT: A simulation program for non-isothermal multiphase reactive geochemical transport in variably saturated geologic media. *Computers and Geosciences, 32*, 145–165.

Xu, T., J. Apps, and J. Birkholzer (2007), Contamination of groundwater by hazardous inorganic chemical constituents through induced acidification due to CO_2 leakage from a storage formation. Abstract in: *Proceedings of the 6th Annual Conference on Carbon Capture and Sequestration*, Pittsburgh, PA, May 2007.

Xu, T., J.A. Apps, K. Pruess and H. Yamamoto, (2007). Numerical modeling of injection and mineral trapping of CO_2 with H_2S and SO_2 in a sandstone formation. Chemical Geology, 242: 319-346.

Xu, Y., G.P. Zhou, and X.F. Zheng (2007), Redetermination of iron(III) arsenate dihydrate. *Acta Crystallographica, E63*, i67–i69.

Yakovleva, V.A., E.V. Belogub, and K.A. Novoselov (2003), Supergene iron sulpho-selenides from the Zapadno-Ozernoe copper-zinc massive sulphide deposit, South Urals, Russia: A new solid- solution series between pyrite FeS_2 and dzharkenite $FeSe_2$. *Mineralogical Magazine, 67*(2).

Yang, H., R. Lu, R.T. Downs, and G. Costin (2006), Goethite, alpha-FeO(OH), from single-crystal data. *Acta Crystallographica, E62*, i250–i252.

Yongshan, D., J.M. Hughes, and P.B. Moore (1991), The crystal structures of mimetite and clinomimetite, $Pb_5(AsO_4)_3Cl$. *The Canadian Mineralogist, 29*, 369–376.

Yu, Y., Y. Zhu, Z. Gao, C.H. Gammons and D. Li (2007), Rates of arsenopyrite oxidation by oxygen and Fe(III) at pH 1.8-12.6 and 15-45 °C. Environ. Sci. Technol., 41: 6460-6464.

Zacharias, J., J. Fryda, B. Paterova, and M. Mihaljevic (2004), Arsenopyrite and As-bearing pyrite from the Roudny deposit, Bohemian Massif. *Mineralogical Magazine, 68*(1), 31-46.

Zerai B., B.Z. Saylor, and G. Matisoff (2006), Computer simulation of CO_2 trapped through mineral precipitation in the Rose Run Sandstone, Ohio. *Appl. Geochem.*, *21*, 223–240.

Zhang, J.-Z. and Millero, F.J. (1994), Investigation of metal sulfide complexes in sea water using cathodic stripping square wave voltammetry. Analytica Chimica Acta, 284, 497-504.

Zhang, S., J. Li, Y. Wang and G. Hu (2003), Dissolution kinetics of galena in acid NaCl solutions at 25—75 ^{o}C. Applied Geochemistry, 19: 835-841.

Zhu, Y.N., X.H. Zhang, Q.L. Xie, D.Q. Wang, and Q.W. Cheng (2006), Solubility and stability of calcium arsenates at 25ºC. *Water, Air and Soil Pollution, 169*, 221–238.

Zotov, A.V., N.D. Shikina, and N.N. Akinfiev (2003), Thermodynamic properties of Sb(III) hydroxide complex $Sb(OH)_3(aq)$ at hydrothermal conditions. *Geoch. Cosmochim. Acta, 67*, 1821–1836.

Research Project on CO_2 Geological Storage and Groundwater Resources

Water Quality Effects Caused by CO_2 Intrusion into Shallow Groundwater

Appendices A-F

Appendix A:
Lists of Analytical Methods for Groundwater Analysis

Table A1. Summary of Groundwater Analyses Data Available for Trace Elements (see list of analytical methods in Table A2)

(a) Summary of Arsenic (As) Analyses

Analytical Method Code	PCode	Total No. of Analyses	Detection Limit (mg/L)	No. below Detn Limit	No. at or above Detn Limit	Percentage at or above Detn. Limit (%)	Notes
GF042	01000	135	0.001	124	11	8.15	
GF044	01002	2	0.001	1	1	50.00	
GF073	01002	9	0.005	1	8	88.89	
PL120	01002	2	0.001	1	1	50.00	
PLA06	01000	5	0.002	4	1	20.00	
GF085	01000	652	0.001 0.002 0.004	175 91 1	385	59.05	
GF096	01002	157	0.002 0.003 0.004 0.008	60 2 2 1	92	58.60	
GF031	01002	69	0.001	44	25	36.23	
HY010	01000	5522	0.001 0.005 0.01	2309 1 9	3203	58.00	
HY013	01002	137	0.001	81	56	40.88	
PLA07	01002	117	0.002 0.004	33 66	99	84.62	
PLM10	01000	76	0.00012	6	70	92.11	
PLM27	01000	174	0.002 0.001 0.01	104 24 2	144	82.76	
PLM40	01000	2782	0.0002 0.0003 0.0004 0.0009	201 72 1 87	2421	87.02	
Unknown		11610	>0.1 0.01-0.1 0.01 0.005-0.01 0.005 0.004 0.003-0.004 0.003 0.002 0.001 0.000001- 0.001 0	82 131 3366 11 593 36 1 10 94 2586 149 14	3688	31.77	40 presence verified but not quantified. 788 analyzed but not detected 1 greater than 1.e6 mg/L

(b) Summary of Barium (Ba) Analyses

Analytical Method Code	PCode	Total No. of Analyses	Detection Limit (mg/L)	No. below Detn Limit	No. at or above Detn Limit	Percentage at or above Detn. Limit (%)	Notes
AA003	01005	117	0.10	70	47	40.17	
GF046	01005	16	-	0	16	100.00	
PLA06	01005	24	0.0005	1	23	95.83	
PLM27	01005	177	0.1	18	159	89.83	
PLA11	01005	5178	0.0009 0.001 0.002 0.003 0.006 0.1	6 9 100 3 1 6	5053	97.59	
PLM43	01005	1252	0.0002 0.001	2 29	1206	96.33	15 Presence verified but not quantified
PLM47	01007	87	0.0002	1	86	98.85	
GF033	01007	18	-	0	18	100.00	
PLA15	01007	13	-	0	13	100.00	
PLA07	01007	120	-	0	120	100.00	
PLA06	01007	24	-	0	24	100.00	
unknown		7337	0.0001 0.0002 0.001 0.002 0.005 0.01 0.025 0.03 0.04 0.05 0.06 0.07 0.1 0.2 0.3 0.4 0.5 10	2875	4462	60.82	

(c) Summary of Cadmium (Cd) Analyses

Analytical Method Code	PCode	Total No. of Analyses	Detection Limit (mg/L)	No. below Detn Limit	No. at or above Detn Limit	Percentage at or above Detn. Limit (%)	Notes
AA005	01025	39	0.01	38	1	2.56	
CX002	01025	39	0.001 0.004 0.01	31 1 1	6	15.38	
GF086	01025	2421	0.00001 0.001	1 2405	15	0.62	
CX013	01027	27	0.001	19	8	29.63	
GF097	01027	67	0.001	67	0	0.00	
PLA06	01025	23	0.0005	22	1	4.35	
PLA07	01027	118	0.0005	114	4	3.39	
PLA11	01025	2403	0.001 0.002 0.003 0.005 0.008 0.009 0.01	1964 12 18 7 49 1 4	348	14.48	
PLM27	01025	177	0.001 0.002	31 145	1	0.56	
PLM43	01025	3290	0.00004 0.001 others	1385 1093 15	797	24.22	
PLM47	01027	64	0.00004	53	11	17.19	
Unknown	01025 or 01027	12201	0 0-0.0002 0.0002 0.0005 0.0006 0.001 0.001-0.005 0.005 0.005-0.01 0.01 0.02	225 89 229 1339 117 2653 2628 484 11 940 1095	319	2.6	1118 Analyzed for but not detected 953 Presence verified but not quantified

(d) Summary of Mercury (Hg) Analyses

Analytical Method Code	PCode	Total No. of Analyses	Detection Limit (mg/L)	No. below Detn Limit	No. at or above Detn Limit	Percentage at or above Detn. Limit (%)	Notes
CV013	71890	2534	0.0001 0.0002 0.0003 0.001	2210 14 1 6	303	11.96	
CV014	71890	112	0.0001 0.0002	78 24	10	8.93	
CV016	71900	111	0.0001 0.0002	94 1	16	14.41	
CV017	71900	58	0.0001	58	0	0.00	
CV018	71900	69	0.0001 0.0002	36 25	8	11.59	

(e) Summary of Lead (Pb) Analyses

Analytical Method Code	PCode	Total No. of Analyses	Detection Limit (mg/L)	No. below Detn Limit	No. at or above Detn Limit	Percentage at or above Detn. Limit (%)	Notes
AA019	01049	74	0.1	71	3	4.05	
CX007	01049	501	0.001 0.004 0.005 0.01	300 1 54 11	135	26.95	
CX017	01049	40	0.005	22	18	45.00	
GF031	01051	47	0.001	29	18	38.30	
GF056	01051	1	0.005	1	0	0.00	
GF078	01049	1	0.005	1	0	0.00	
GF089	01049	2876	0.001 0.002 0.1	2531 1 1	341	11.86	2 empty values
GF100	01051	94	0.001 0.005	36 1	57	60.64	
PLA06	01049	23	1.001 0.002	16 5	2	8.70	
PLA07	01051	123	0.001 0.002	39 76	8	6.50	
PLA11	01049	1657	0.001 0.01 0.02 0.03 0.05 0.1	1 1368 9 15 7 40	215	12.98	2 empty values
PLM43	01049	1970	0.0001 0.0001- 0.001 0.001 0.002 0.004	285 6 701 7 1	970	49.24	
PLM48	01051	100	0.00006 0.001	6 12	82	82.00	
Unknown		12374	0 0.000001 0.00001 0.00001- 0.0001 0.0001- 0.001 0.001 0.001-0.01 0.01 0.01-0.1 0.1 0.1-1 >1	187 55 4 24 81 417 3932 (3337 of them are 0.005) 3466 499 271 18 11	438	3.54	971 Analyzed for but not detected 2000 Presence verified but not quantified

(f) Summary of Antimony (Sb) Analyses

Analytical Method Code	PCode	Total No. of Analyses	Detection Limit (mg/L)	No. below Detn Limit	No. at or above Detn Limit	Percentage at or above Detn. Limit (%)	Notes
GF032	01095	1	0.001	1	0	0.00	
GF040	01097	115	0.001	115	0	0.00	
PLM48	01097	54	0.0002 0.0006 0.0009	49	5	9.26	
HY009	01095 01097	516	0.001	432	84	16.28	
PLM43	-	1274	0.00005 0.0001 0.0002 0.0003 0.0004 0.0006 0.0008 0.001 0.002 >=0.003	105 1 219 148 1 1 2 555 7 2	233	18.29	Trivial No. of other misc. detn limits
Unknown	01095	790	Misc: 0.00005-0.3	761	29	3.67	

(g) Summary of Selenium (Se) Analyses

Analytical Method Code	PCode		Detection Limit (mg/L)	No. below Detn Limit	No. at or above Detn Limit	Percentage at or above Detn. Limit (%)	Notes
GF060	01145		0.001	16	6	27.27	
PLM10	01145		0.0008	17	52	75.36	
GF091	01145		0.001 0.002 0.006 0.014	297 41 6 4	80	18.69	
PLM27	01145		0.01	153	21	12.07	
HY011	01145		0.001 0.002 0.003 0.005 0.01	3240 61 1 3 10	752	18.49	
PLM40	01145		0.0003 0.0004 0.0005 0.0007 0.002	365 250 230 160 1	1411	58.38	
Unknown	01145		0 <0.001 0.001 0.001-0.01 0.01 0.01-0.1 >=0.1	192 112 932 248 2170 53 53	1108	22.76	

(h) Summary of Uranium (U) Analyses

Analytical Method Code	PCode	Total No. of Analyses	Detection Limit (mg/L)	No. below Detn Limit	No. at or above Detn Limit	Percentage at or above Detn. Limit (%)	Notes
PHOS1	22703	218	0.0004	72	146	66.97	
PHOS2	22703	4	0.09	1	3	75.00	
PHOS3	22703	141	0.00001	10	131	7.09	
PHOS4	22703	1	0.00024	1	0	0.00	
PHOS5	22703	162	0.00	8	149	4.94	5 of them are “Presence verified but not detected”
PHOS6	22703	61	0.001	44	2	3.28	15 of them are “Presence verified but not detected”
PLM43	22703	1310	0.004 0.003 0.002 0.001 0.00016 0.00007 0.00004 0.00002	1 1 4 315 1 1 31 43	913	69.70	
PLM48	28011	62	-	0	62	100.	
FL001	22703	163	0.001	120	43	26.38	
FL002	75990	122	-	0	122	100.00	
FL003	28011 28011 75993	56	0.001	21	35	60.00	
FL004	22703	4	-	0	4	100.00	
FL006	22703	59	0.0004	18	41	69.49	
FL007	80020	33	0.00001	1	32	96.97	
Unknown		848	0.00001 0.0001 0.0002 0.0003 0.0004 0.0005 0.0006 0.0007 0.0011 0.007 0.013 0.02	11 56 38 1 12 16 20 3 2 1 63 6	618	72.88	

(i) Summary of Zinc (Zn) Analyses

Analytical Method Code	PCode	Total No. of Analyses	Detection Limit (mg/L)	No. below Detn Limit	No. at or above Detn Limit	Percentage at or above Detn. Limit (%)	Notes
AA039	01090	187	0.01	75	112	59.89	
AA071	01092	125	0.01	26	99	79.20	
PLM48	01092	89	0.002	9	80	89.89	
GF084	01090	1		0	1	100.00	
PLA06	01090	83	0.001 0.002 0.01	2 16 1	64	77.11	
PLA07	01092	141	0.001 0.002	4 14	123	87.23	
PLA15	01092	17	0.006 0.031 0.04	6	11	64.71	
PLM10	01090	11	0.0006	2	9	81.82	
PLM27	01090	175	0.01	120	55	31.43	
PLA11	01090	5407	0.003 0.004 0.005 0.006 0.007 0.009 0.01 0.014 0.02 0.024 0.06 0.08	587 8 7 5 1 5 11 1 342 7 6 1	4426	81.86	
PLM43	01090	1554	0.0006 0.001 0.001-0.01 0.0101	4 87 7 1	1455	93.63	
Unknown	01090 01092	14304	0 0-0.0001 0.001 0.001-0.01 0.01 0.02 0.03 0.04 0.05 0.05-0.1 0.1 >0.1	64 21 9 392 1378 1924 8 13 2010 65 103 16	8301(1225 are zeros)	58.03	

Table A2. List and Explanation of Analytical Methods from USGS NWIS Database Used in Table A

Analytical Method Code	Short Info	Long Info	Database Citation	Method Number	Method Owner
AA003	Barium, wf, direct AAS	Barium in filtered water by direct AAS	TWRI 5-A1/1989, p. 89	I-1084-85:USGS	USGSNWQL
AA005	Cadmium, wf, direct AAS	Cadmium in filtered water by direct AAS	TWRI 5-A1/1989, p. 127	I-1135-85:USGS	USGSNWQL
AA019	Lead, wf, direct AAS	Lead in filtered water by direct AAS	TWRI 5-A1/1989, p. 247	I-1399-85:USGS	USGSNWQL
AA039	Zinc, wf, direct AAS	Zinc in filtered water by direct AAS	TWRI 5-A1/1989, p. 507	I-1900-85:USGS	USGSNWQL
AA071	Zinc, wu, USGS digest, AAS	Zinc recoverable from unfiltered water by dilute HCl (USGS) digestion and direct AAS	TWRI 5-A1/1989, p. 507	I-3900-85:USGS	USGSNWQL
CV013	Mercury, wf, auto CVAAS	Mercury in filtered water by automated-sequential CVAAS	TWRI 5-A1/1989, p. 289	I-2462-85:USGS	USGSNWQL
CV014	Mercury, wf, CV-AFS	Mercury in Filtered Water by Cold Vapor-Atomic Fluorescence Spectrometry	WRI 01-4132	I-2464-01:USGS	USGSNWQL
CV016	Mercury, wu, CVAAS (NWQL)	Mercury recoverable from unfiltered water by CVAAS	TWRI 5-A1/1989, p. 285	I-3462-85:USGS	USGSNWQL
CV017	Mercury, wu, CVAAS (NWQL)	Mercury recoverable from unfiltered water by CVAAS	TWRI 5-A1/1989, p. 285	I-3462-85:USGS	USGSOCFL
CV018	Mercury, wu, CV-AFS	Mercury in Unfiltered Water by Cold Vapor-Atomic Fluorescence Spectrometry	WRI 01-4132	I-4464-01:USGS	USGSNWQL
CX002	Cadmium, wf, APDC & MIBK, AAS	Cadmium in filtered water by chelation-extraction with APDC and MIBK, and AAS	TWRI 5-A1/1989, p. 125	I-1136-85:USGS	USGSOCFL
CX007	Lead, wf, APDC & MIBK, AAS	Lead in filtered water by chelation-extraction with APDC and MIBK, and AAS	TWRI 5-A1/1989, p. 245	I-1400-85:USGS	USGSOCFL
CX013	Cadmium, USGS digest,extract AAS	Cadmium recoverable from unfiltered water by dilute HCl (USGS) digestion, chelation-extraction with APDC and MIBK, and AAS	TWRI 5-A1/1989, p. 125	I-3136-85:USGS	USGSOCFL
CX017	Lead, USGS digest, extract AAS	Lead recoverable from unfiltered water by dilute HCl (USGS) digestion, chelation-extraction with APDC and MIBK, and AAS	TWRI 5-A1/1989, p. 245	I-3400-85:USGS	USGSOCFL
FL001	U (natural), wf, fluorometric	Dissolved fluorometric			USGSNWQL
FL002	U (natural) 2SPE, wf,fluorimetry	Fluorimetry, Uranium, FIL			USGSNWQL
FL003	U (natural), water, fluorometric	U, Fluorometric, TOT			USGSNWQL
FL004	U (natural), wf, FL-DIR GR-W	U-FIL, fluorometric method--direct (FL-DIR.), ground water (GR-W)			USGSNWQL
FL006	U (natural), wf, direct fluorom	U-FIL, fluorometric method--direct (FLUOR-direct)			USGSNWQL
FL007	Uranium, wf,extract fluorometric	U-FIL, fluorometric method--extracted sample (FLUOR-ext)			USGSNWQL
GF031	Elements, drinking water, GFAA	EPA 200.9 determination of total recoverable trace elements in drinking water by GFAA		200.9:USEPA	USGSNWQL
GF032	Antimony, drinking wtaer, GFAA	GFAA, Antimony, dissolved, EPA 200.9, Drinking Water		200.9:USEPA	USGSNWQL
GF040	Antimony, wu, GFAA	ANTIMONY TOTAL (GFAA)		204.2:USEPA	USGSOCFL
GF042	Arsenic, wf, GFAA	ARSENIC DISSOLVED (GFAA)		206.2:USEPA	USGSOCFL
GF044	Arsenic, wu, GFAA	ARSENIC TOTAL GFAA		206.2:USEPA	USGSOCFL
GF046	Barium, wf, GF	BARIUM DISSOLVED (GF)		208.2:USEPA	USGSOCFL
GF056	Lead, LL, wu, GFAA	LEAD TOTAL LL (GFAA)		239.2:USEPA	USGSOCFL

GF060	Selenium, wf, GFAA (Ocala)	SELENIUM DISSOLVED (GFAA)		270.2:USEPA	USGSOCFL
GF073	Arsenic and selenium, wu, GFAA	Graphite furnace atomic absorption		I-0000-91:USGS	USGSNWQL
GF078	Lead, LIS, GFAAS	Lead in low ionic strength water by GFAAS	TWRI 5-A1/1989, p. 249	I-1401-85:USGS	USGSNWQL
GF084	Zinc, LIS, GFAAS	Zinc in low ionic strength water by GFAAS	TWRI 5-A1/1989, p. 509	I-1901-85:USGS	USGSNWQL
GF085	Arsenic, wf, GFAAS	Arsenic in Filtered Water by GFAAS	OF 98-639	I-2063-98:USGS	USGSNWQL
GF086	Cadmium, wf, GF-AAS	Cadmium in filtered water, by GF-AAS	OF 93-125, p. 53	I-2138-89:USGS	USGSNWQL
GF089	Lead, wf, GF-AAS	Lead in filtered water, by GF-AAS	OF 93-125, p. 87	I-2403-89:USGS	USGSNWQL
GF091	Selenium, wf, GFAAS (NWQL)	Selenium in Filtered Water by GFAAS	OF 98-639	I-2668-98:USGS	USGSNWQL
GF096	Arsenic, wu, GFAAS	Arsenic Recoverable from Unfiltered Water by GFAAS	OF 98-639	I-4063-98:USGS	USGSNWQL
GF097	Cadmium, wu, GF-AAS	Cadmium in unfiltered water, by GF-AAS	OF 93-125, p. 53	I-4138-89:USGS	USGSNWQL
GF100	Lead, wu, GF-AAS	Lead recoverable from unfiltered water, by GF-AAS	OF 93-125, p. 87	I-4403-89:USGS	USGSNWQL
HY010	Arsenic, wf, auto hydride AAS	Arsenic in filtered water by automated sulfuric acid potassium persulfate digestion or ultraviolet radiation, hydride generation, and tube furnace AAS	TWRI 5-A1/1989, p. 77	I-2062-85:USGS	USGSNWQL
HY011	Selenium, wf, auto hydride AAS	Selenium in filtered water by automated hydride generation and AAS	TWRI 5-A1/1989, p. 403	I-2667-85:USGS	USGSNWQL
HY013	Arsenic, wu, digest & hydrideAAS	Total arsenic in unfiltered water by automated sulfuric acid potassium persulfate digestion or ultraviolet radiation, hydride generation, and tube furnace AAS	TWRI 5-A1/1989, p. 77	I-4062-85:USGS	USGSNWQL
PHOS1	Laser phosphorim, dir (Eberline)	Laser-induced phosphorimetry, direct (analysis by Eberline Services)			USGSNWQL
PHOS2	Laser phosphorimetry, dir (NWQL)	Laser-induced phosphorimetry, direct (analysis by NWQL)			USGSNWQL
PHOS3	Laser phosphorim, ext (Eberline)	Laser-induced phosphorimetry, extracted (analysis by Eberline Services)			USGSNWQL
PHOS4					
PHOS5	Uranium, wf, dir phosphorescence	Uranium, Water, Filtered, by Direct Laser Induced Phosphorescence			USGSNWQL
PHOS6	Uranium, wf, ext phosphorescence	Uranium, Water, Filtered, by Extraction and Laser Induced Phosphorescence			USGSNWQL
PL120	Metals, wu, ICP-OES or ICP-MS	Metals Recoverable from Unfiltered Water ICP-OES or ICP-MS	OF 98-165	I-4471-97:USGS	USGSNWQL
PLA06	Trace elements, wf, ICP/T (Ocala	Ocala Lab analysis of dissolved trace elements by Inductively Coupled Plasma--Atomic Emission Spectrometry (ICP/T)		200.7:USEPA	USGSOCFL
PLA07	Trace elements, wu,ICP/T (Ocala)	Ocala Lab analysis of total trace elements by Inductively Coupled Plasma--Atomic Emission Spectrometry (ICP/T)		200.7:USEPA	USGSOCFL
PLA11	Metals, wf, ICP-AES	Metals, filtered water, Inductively coupled plasma-atomic emmission spectrometry	OF 93-125, p. 101	I-1472-87:USGS	USGSNWQL
PLA15	Metals, wu, ICP-AES	Metals, unfiltered water, Inductively coupled plasma-atomic emission spectrometry	OF 98-165	I-4471-97:USGS	USGSNWQL
PLM10	Collision/reaction cell ICPMS	Elements in Natural-Water, Biota, Sediment, and Soil Samples Using Collision/Reaction Cell Inductively Coupled Plasma-Mass Spectrometry	USGS TMR 5-B1	:USGS	USGSNWQL
PLM27	Elements, wf, ICP-MS w/o digest	Trace elements in water and wastes by inductively coupled plasma - mass spectrometry without digestion	EPA-600/R-94/111	200.8:USEPA	USGSOKWC
PLM40	Metals, water, ICP-MS	Metals in Water by ICP-MS	OF 92-634	I-2477-92:USGS	USGSNWQL

PLM43	Metals, wf, ICP-MS	Metals, filtered water, Inductively coupled plasma-mass spectrometry	OF 92-634	I-2477-92:USGS	USGSNWQL
PLM47	Metals, wu, ICP-MS	Metals, unfiltered water, Inductively coupled plasma-mass spectrometry	OF 98-165	I-4471-97:USGS	USGSNWQL
PLM48	Metals, wu, ICP-MS	Metals, unfiltered water, Inductively coupled plasma-mass spectrometry	OF 98-165	I-4471-97:USGS	USGSNWQL

Appendix B:
Discussion of Spatial Distributions and Analytical Artifacts in Groundwater Analyses from NWIS Database

B1. Spatial Distribution of Groundwater Analyses from NWIS Database

With reference to discussion in Section 3.3.3, we further analyze here the spatial distributions of measured aqueous concentrations of lead in groundwater analyses from the NWIS database (Figure 3.8(a) and Figure B.1(a)). The question is why the measurable lead concentrations are so sparsely distributed over many parts of the country. A possible reason is that less water quality analyses for hazardous inorganic constituents have been conducted in certain parts of the country or that analyses have been conducted using analytical methods with insufficient detection limits. For evaluation, we have plotted in Figure B1(b) the spatial distribution of all samples that have been declared "non-detects" for lead, with the color scheme indicating the detection limit of the analytical method used (in Log mg/L). In Figure B1(c), we furthermore plot the location of samples that have been declared in the NWIS database as "presence verified, but not quantified".

Figures B1(a) through B1(c) together indicate that both possible reasons stated above are valid. Clearly, there are many states and regions where almost no water analyses for lead have been conducted, or at least these analyses have not been reported in the NWIS database. There are furthermore several states and regions with many lead analyses in the NWIS database, but the majority of those with insufficient detection limits. A good example are the states of Iowa and Illinois, where numerous samples have detection limits of about 0.01 mg/L, two orders of magnitude above the expected equilibrium lead concentration of 0.0001 mg/L for a typical reducing groundwater where galena coexists with pyrite and goethite (Section 3.3.5). The "hot spots" of measurable lead concentrations in Figure B1(a) are clearly correlated to states or regions where large numbers of high-quality analyses (i.e., with low enough detection limits) have been conducted. In contrast, states or regions with no or only few detectable lead concentrations in Figure 3B1(a) correspond to locations with either no measurements or analyses

with insufficient detection limits. We may conclude that almost all groundwaters in the United States would exhibit small (mostly below MCLs), but non-zero lead concentrations if measured with appropriate analytical techniques, which is consistent with the above finding that lead occurs ubiquitously in soils, sediments and aquifer rocks throughout the United States. While not reported here, the same conclusions can be drawn for the other hazardous inorganic constituents of interest in this study.

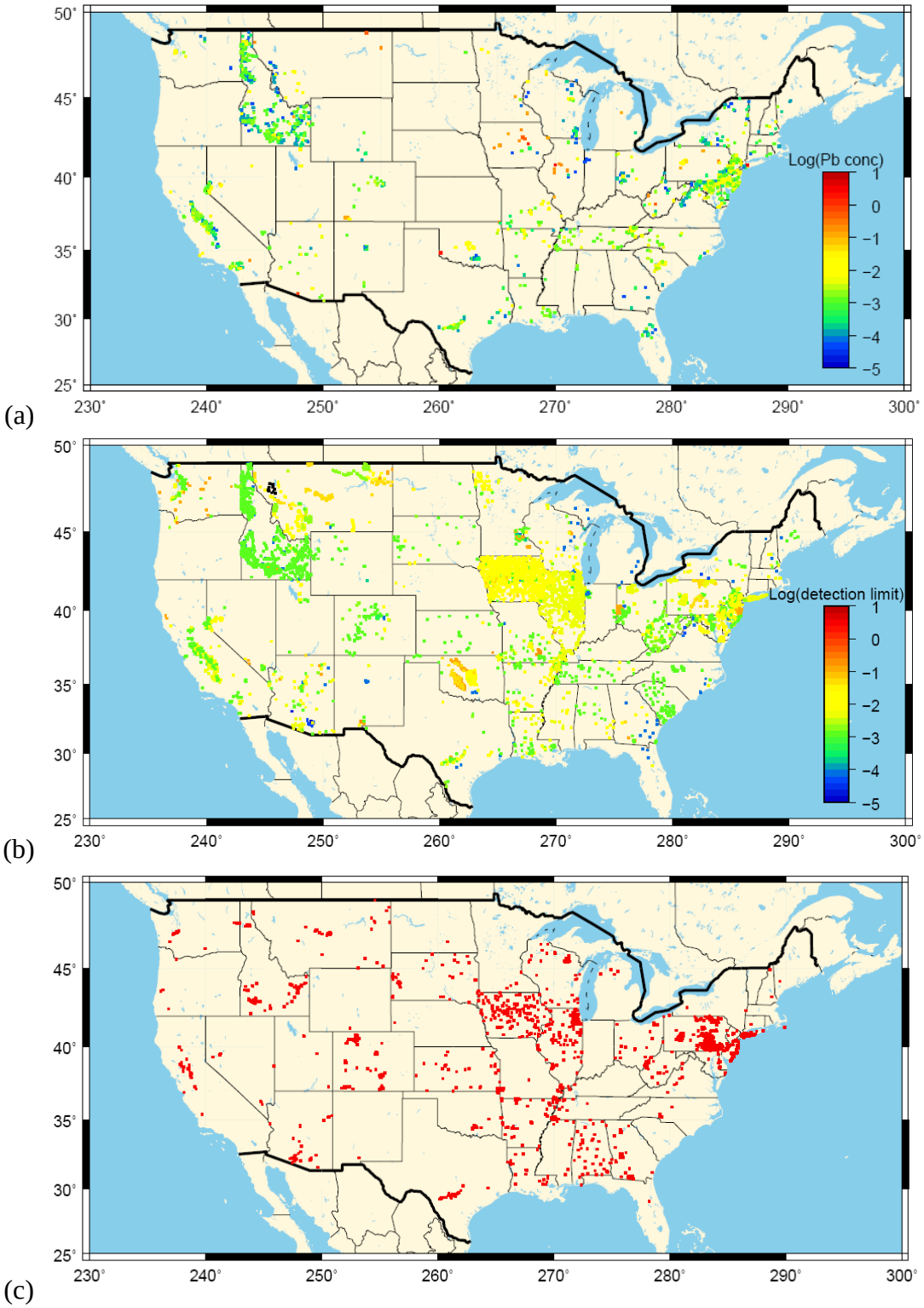

Fig. B1. Spatial distribution of (a) samples with measured aqueous concentration (Log mg/L) of lead, (b) samples with non-detects for lead with color scheme indicating the detection limit of the analytical method (in Log mg/L), and (c) samples with text stating "presence verified, but not quantified". The plots were drawn from more than 38,000 groundwater quality analyses downloaded from the National Water Information System Database (NWIS).

B2. Characterization of Analytical Artifacts in the Measurement of Concentrations of Hazardous Inorganic Constituents

Section 3.3.5 discusses the possibility and the implications of analytical artifacts introduced by the differing accuracy and sensitivity of analytical methods. The Cd concentrations in Figure 3.6(d) were mentioned there as an example where almost all analyses may have been affected. The figure shows essentially two sets of measurements, with each set starting an initially high frequency, apparently corresponding to the detection limit for some of the analyses, which then falls off with increasing concentration until a relatively low frequency is recorded. This is, of course, very different from a normal or possibly log-normal distribution of concentrations to be expected in natural groundwaters.

The analogy of the observations in Figure 3.6(d) with radioactive decay suggests a similar process involving Poisson statistics. This is illustrated by Figures B2(a) and B2(b), which display the normalized analytical frequency versus log concentration for two selected analytical methods (i.e., PLA11 with a detection limit of 0.001 mg/L and up, and PLM43 with a detection limit of 0.00002 mg/L and up, see Table A1). A linear regression of the plots indicates a very good correlation between frequency and concentration, with $R^2 = 0.98$ for both analytical methods. The normalized frequency of "non-detects" for each method is plotted as the negative value of the detection limit, and is included in the regression analysis.

The theoretical basis for these correlations has not been evaluated, but probably relates to contamination or unknown interferences in the analytical method, as replicate analyses for these methods do not show such large spurious variations. Clearly, further study of this phenomenon is warranted, especially in relation to the analytical sensitivity of the method and its suitability for detecting actual concentrations expected in a given ground water sample.

Similar evaluations of selected analytical methods for other elements yield similar correlations. For example, Figure B3 is a plot of the normalized analytical frequency versus linear concentration for Hg analyses using the CV013 analytical method with a detection limit no lower than 0.0001 mg/L, suggesting the majority of reported Hg analyses are also artifacts. After

discounting for potential artifacts, the remaining chemical analyses are of marginal utility in predicting thermodynamic controls for mercury concentrations in ground waters, and therefore a theoretical interpretation of mercury behavior may be the only recourse for predicting the response of dissolved mercury to elevated partial pressures of CO_2. Figures B4(a) and B4(b) show similar artifacts are operative for lead when less sensitive analytical methods are utilized.

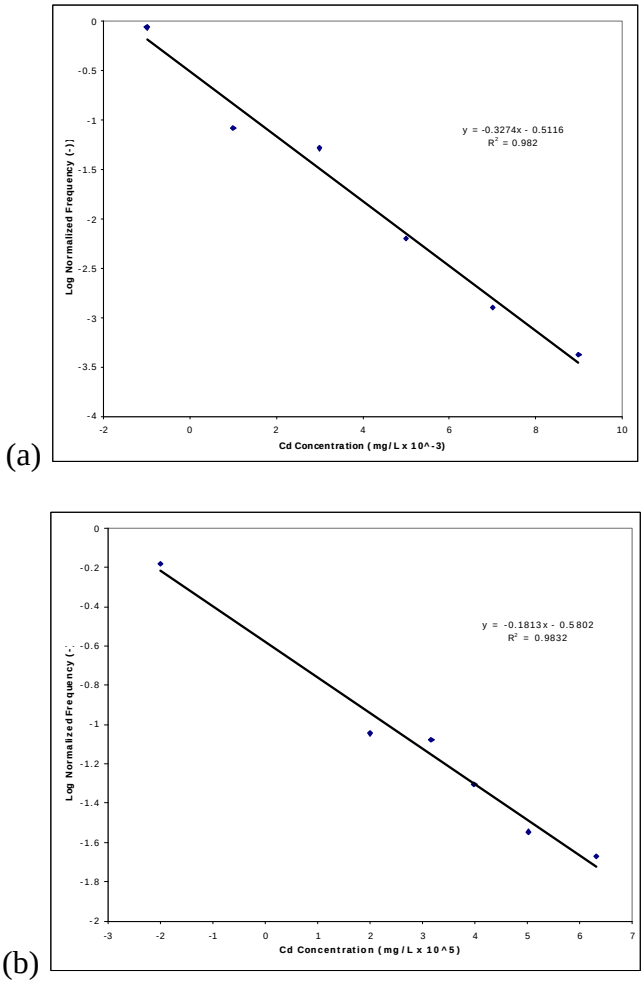

Fig. B2. Log normalized frequency of chemical analyses as a function of cadmium concentration in ground waters at and above the detection limit for the analytical method. (a) PLA11; (b) PLM43.

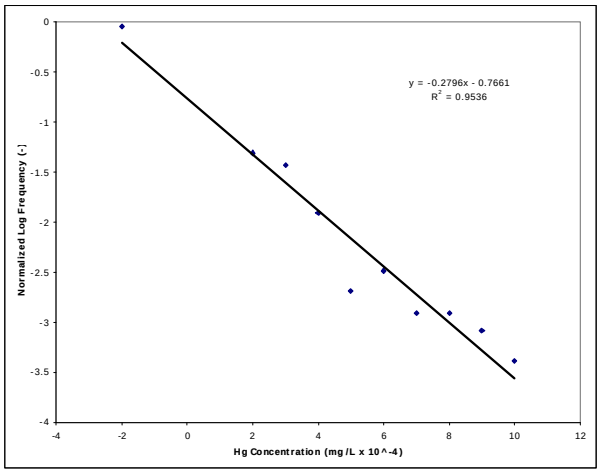

Fig. B3. Log normalized frequency of chemical analyses as a function of mercury concentration in ground waters at and above the detection limit for the CV013 analytical method.

(a)

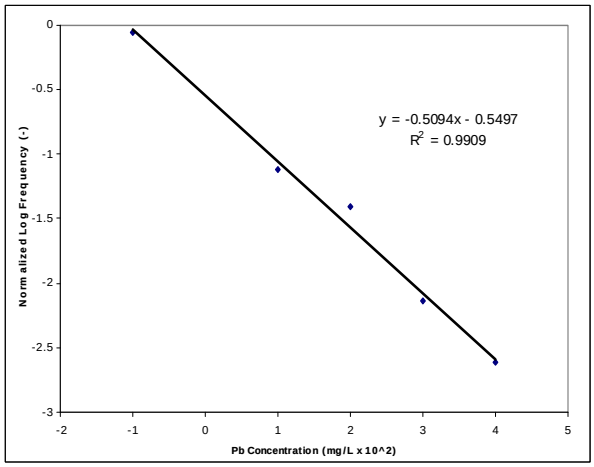

(b)

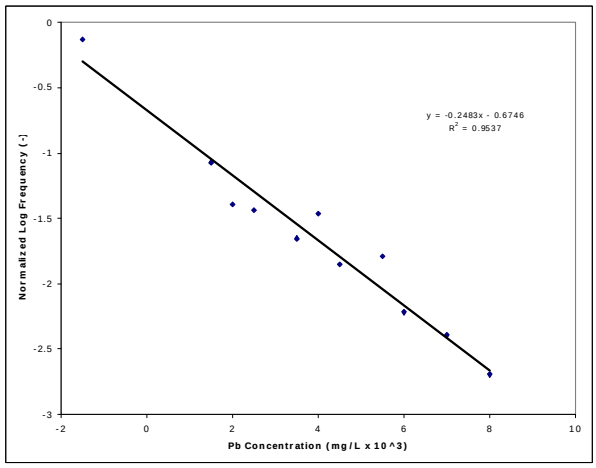

Fig. B4. Log normalized frequency of chemical analyses as a function of lead concentration in ground waters at and above the detection limit for the analytical method. (a) PLA11; (b) CX007.

Appendix C:
Thermodynamic Database Augmentation

C1. Introduction

A substantial augmentation of solubility products of solid phases and dissociation constants of aqueous species is required to adequately model the complex chemistry associated with the behavior of hazardous inorganic constituents in ground waters. The augmentation is not limited merely to those primary minerals and secondary alteration products where the hazardous constituent is an essential component; attention must also be paid to minerals that interact with the hazardous constituents through co-precipitation, ion exchange, and/or adsorption. Furthermore, the database used for EQ3/6 simulations, Data0.dat.YMP, suffers from obsolescence. The solubility products of many common rock-forming minerals listed in the database require revision to more accurately reflect advances since the original compilations used in the database were published.

Appendix C is subdivided into several sections dealing respectively with additional aqueous speciation and minerals for arsenic, lead, antimony and selenium. Corrections are also provided for Fe^{+2} and Fe^{+3} aqueous species, and an expanded database is provided for metastable iron oxides, oxy-hydroxides, and sulfides. Supplementary information for carbonates and chlorite is also included, because of their relevance in participating as pH or Eh buffers. The appendix concludes with a section in which data are presented on minerals that had to be included on a case-by-case basis in order to ensure that the geochemical model reflected reality.

C2. Arsenic

C2.1 Background

The presence of arsenic in groundwater has long been a serious problem in many parts of the world, particularly in the Ganges delta of Bangladesh (Smedley, 2003), where farmers draw drinking water from shallow aquifers that are subject to seasonal oxidation and mobilization of arsenate. In the United States, several areas are also characterized by elevated arsenic concentrations in ground waters, notably in northwestern Nevada, where the municipal water of

the city of Fallon has unacceptably high levels (Smedley, 2003) and the Rio Grande Rift of New Mexico (Bexfield and Plummer, 2003). The city of Albuquerque is forced to treat its water supplies to mitigate excessive concentrations of As. Other regions of the country, such as the Upper Michigan Peninsula and parts of Minnesota (Thornberg and Sahai 2004) and New Hampshire (Utsunomiya et al., 2003), are also affected by high As levels in groundwater. Increasing use of aquifer storage and recovery techniques (ASR) has also lead to arsenic contamination of the recovered water (Arthur et al., 2005). A significant proportion of the sampled more than 38,000 well water samples taken from the NWIS database already possess As levels exceeding current MCLs. The introduction of high pressure CO_2 into aquifers with such elevated ambient As concentrations could aggravate an already marginal water quality in some areas. Therefore, the evaluation of As chemistry in groundwaters is very important, and takes precedence over some other hazardous constituents in relation to the present problem.

The chemistry of As in surficial waters and shallow subsurface groundwaters is extraordinarily complex. As occurs naturally in at least five oxidation states (-3, 0, +2, +3 and +5). Both +3 and +5 states form hydroxy-anions in aqueous solution with varying degrees of protonation. Both are noted for reactions with Fe in both +2 and +3 states. As(V) adsorption onto hydrated ferric oxides (HFO) stabilizes the latter in a metastable or colloidal or nanoparticulate form, which can persist for tens to hundreds of years. In the presence of Ca^{+2}, Ca-As-Fe-OH macro complexes form in solution, which can aggregate to form glassy or amorphous minerals such as pitticite or yukonite. As an added complication, it is well known that the transformation of aqueous As(III) to As(V) and vice versa is sluggish (Cherry et al., 1979). Aqueous As concentrations in ground waters are therefore likely to be dictated not only by the formation of metastable phases and adsorption-stabilized colloids, but also by kinetically hindered redox transformations.

A substantial literature has evolved in which the thermodynamic and kinetic properties of As species have been studied and elucidated, mainly because of the interest in groundwater treatment, and the need to remediate contamination from current and former mining operations. The literature has been searched and thermodynamic data compiled (or in some cases estimated) for 24 aqueous species and complexes, and 15 minerals or potential stabilizing precipitates. Most of these data have been formatted for entry in the EQ3 Data0.dat and TOUGHREACT thermodynamic databases in the form of relevant dissociation constants or solubility products at

25°C. Additional calculations were also conducted using SUPCRT92 (Johnson et al., 1992) to generate solubility and dissociation constant data wherever feasible.

One aspect of As chemistry, which has not been adequately addressed in this report, concerns the substitution of As for S in pyrite. One of the principal causes of As contamination in aquifers occurs through the oxidation of arsenian pyrite. Reich and Becker (2006) have formulated a theoretical solid-solution model quantifying As substitution for S in both pyrite and marcasite. Time constraints prevented the incorporation of this model in the TOUGHREACT simulator. Instead, an empirical correction factor was applied to both arsenopyrite and gudmundite solubility products to account for their dilution from unit activity due to solid solution in pyrite. This was accomplished by reconciling field observations of both As and Sb concentrations in NWIS potable groundwater samples with thermodynamic predictions of their concentrations, as described in Section 3.4.

In the following two sections, methods are described for building an expanded internally consistent database of thermodynamic properties of aqueous As species and solid As phases, respectively, based on an earlier study by Nordstrom and Archer (2003).

C2.2 Aqueous Arsenic Species.

C2.2.1 Calculation of HKF Equation of State Parameters for Aqueous Arsenate and Arsenite Species

The thermodynamic properties of aqueous arsenic species as derived by Nordstrom and Archer (2003) were used as a point of departure. They are summarized in Table C1. Entropy, $\overline{S}^0_{P_r,T_r}$, of two species, $HAsO_3^{-2}$, and AsO_3^{-3}, needed to be estimated. This was accomplished through a correlation plot of the entropies of several oxyanion species as listed in Table C2, and illustrated in Figure C1.

Table C1. Thermodynamic properties of Arsenic Solid Phases and Aqueous Species (from Nordstrom and Archer, 2003)

Phase	$\Delta G^0_{f,P_r,T_r}$ cal mol^{-1}	$\Delta H^0_{f,P_r,T_r}$ cal mol^{-1}	$S^0_{P_r,T_r}$ cal mol^{-1} K^{-1}	$C^0_{P_r,T_r}$ cal mol^{-1} K^{-1}
As	0	0	8.516	5.839
S	0	0	7.600	5.402
O_2(g)	0	0	49.003	7.016
H_2(g)	0	0	31.208	6.889
H_2O(l)	-56687	-68315	16.709	17.995
As_2O_3(cub)	-137749	-157091	25.664	23.155
As_2O_3(mon)	-137794	-156709	27.096	23.179
As_2O_5	-185220	-219309	25.201	27.701
S_2(g)	18953	30681	54.510	7.761
AsS(a)	-7481	-7600	15.033	11.233
AsS(b)	-7385	-7409	15.177	11.233
As_2S_3(a)	-20292	-20507	39.149	38.958
As_2S_3(am)	-18356	-15989	47.801	
Phase	$\Delta \overline{G}^0_{f,P_r,T_r}$ cal mol^{-1}	$\Delta \overline{G}^0_{f,P_r,T_r}$ cal mol^{-1}	$\overline{S}^0_{P_r,T_r}$ cal mol^{-1} K^{-1}	$\overline{C}^0_{P_r,T_r}$ cal mol^{-1} K^{-1}
H_2S(aq)	-6661	-9610	28.920	39.914
HS^-(aq)	2880	-4216	15.010	-21.989
$As_3S_4(SH)_2^-$	-30019			
$AsS(OH)(SH)^-$	-58413			
H_3AsO_3(aq)	-152971	-177428	46.804	
$H_2AsO_3^{-1}$	-140454	-170827	26.957	
$HAsO_3^{-2}$	-121272		(-1.839)	
H_3AsO_4(aq)	-183258	-215930	43.755	
H_2AsO_4-	-180127	-217835	26.859	
$HAsO_4^{-2}$	-170586	-217115	-2.729	
AsO_4^{-3}	-154484	-212765	-42.139	
AsO_3^{-3}	-100813		(-46.715)	

Table C2. Standard Partial Molal Entropies, $\overline{S}^0_{P_r,T_r}$, of Selected Oxyanions

Charge	$\overline{S}^0_{P_r,T_r}$, cal mol^{-1} K^{-1}					
	AsO_4^{-3}	AsO_3^{-3}	PO_4^{-3}	PO_3^{-3}	SO_4^{-2}	CH_3COO^-
0	43.755	46.804		43.6		42.7
1	26.859	26.957	21.6	31.7	30	20.6
2	-2.729		-8	4	4.5	
3	-42.139		-53			

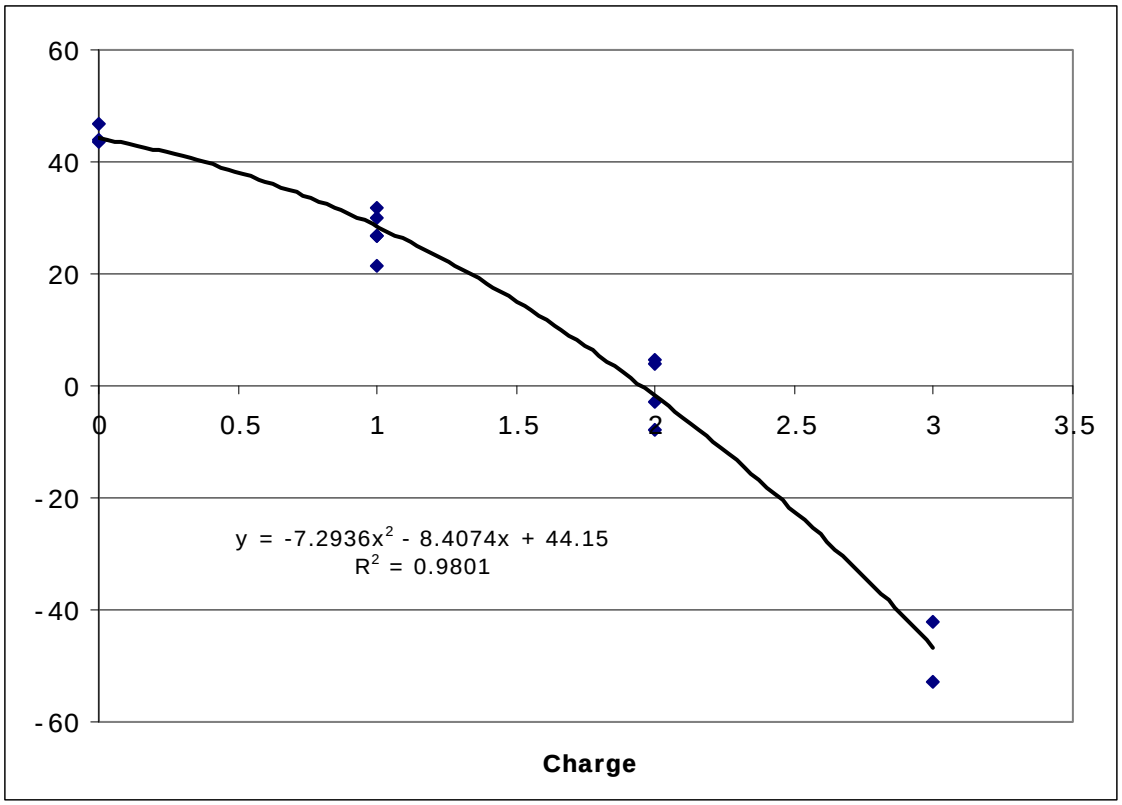

Fig. C1. Regression analysis of standard partial molal entropies, $\overline{S}^0_{P_r,T_r}$, of selected oxyanions as a function of charge.

A regression analysis through all data points yielded the equation listed in Figure C1, with a regression coefficient, R^2, = 0.9801. The calculated values of $\overline{S}^0_{P_r,T_r}$ at Z = -2 and -3 were used as estimates for $HAsO_3^{-2}$ and AsO_3^{-3}. The heat capacities, $\overline{C}^0_{P_r,T_r}$ of all species were then calculated using equations derived by Shock et al. (1997; Table 6), which are for hydrogen bearing anions

$$\overline{C}^0_{P_r,T_r} = 1.65\overline{S}^0_{P_r,T_r} - 46.8$$

and for hydrogen-free anions where $z_j = -3$

$$\overline{C}^0_{P_r,T_r} = 0.60\overline{S}^0_{P_r,T_r} - 92.8$$

Calculation of the HKF equation of state parameters, c_1, c_2 and the Born coefficient, ω_{P_r,T_r}, then follows with application of the following equations (Shock and Helgeson, 1988; Shock et al., 1989). For charged species, the Born coefficient can be calculated from:

$$\omega_{j,P_r,T_r} = \eta Z_j \left[\frac{\eta Z_j}{r_{e,j,P_r,T_r}} - \frac{1}{3.08} \right]$$

where $\eta = \frac{N^0 e^2}{2} = 1.66027 \times 10^5 \overset{0}{A}$ cal mol^{-1}, with N^0 Avogadro's number and e the absolute electronic charge with a value of $4.80298 \times 10^{-10} esu$. r_{e,j,P_r,T_r} is the effective electrostatic radius of the ion

$$r_{e,j,P_r,T_r} = \frac{Z_j^2 \left(\eta Y_{P_r,T_r} - 100 \right)}{\overline{S}^0_{P_r,T_r} - \alpha_z}$$

where Y_{P_r,T_r} has the value $-5.802 \times 10^{-5} K^{-1}$ and refers to the Born function

$$Y = \frac{1}{\varepsilon} \left(\frac{\partial \ln \varepsilon}{\partial T} \right)_P$$

and α_z is a charge dependent correlation parameter

$$\alpha_z = 71.5 \left| Z_j \right|$$

For neutral aqueous inorganic species, the effective Born coefficient is

$$\omega_e = -1514.4 \overline{S}^0_{P_r,T_r} + 0.34 \times 10^5$$

Calculation of c_1 proceeds through the following steps. The heat capacity of an ion is assumed to consist of two components, thus

$$\overline{C}^0_P = \Delta \overline{C}^0_{P,n} + \Delta \overline{C}^0_{P,s}$$

representing respectively the nonsolvation and solvation contributions. The Born coefficient can be used to calculate $\Delta \overline{C}^0_{P,s}$, thus

$$\Delta \overline{C}^0_{P_r,T_r,s} = \omega T X$$

where X is the standard partial molal heat capacity Born Function (Helgeson and Kirkham, 1974)

$$X = \frac{1}{\varepsilon}\left(\left(\frac{\partial^2 \ln\varepsilon}{\partial T^2}\right)_P - \left(\frac{\partial \ln\varepsilon}{\partial T}\right)_P^2\right)$$

which at P_r, T_r has the value of $3.09 K^{-2} \times 10^{-7}$.

$\Delta\overline{C}^0_{P,n}$ can then be obtained by difference. Furthermore, we have

$$\Delta\overline{C}^0_{P,n} = c_1 + c_2\left(\frac{1}{T-\theta}\right)^2$$

where $c_2 \times 10^{-4} = 0.2037\overline{P}^0_{P_r,T_r} - 3.0346$ and $\theta = 228K$.

The general form of the HKF equation of state is given by

$$\begin{aligned}\Delta\overline{G}^{\,o} = {} & \Delta\overline{G}^{\,o}_{f_{\mathrm{Pr},Tr}} - \overline{S}^{o}_{\mathrm{Pr},Tr}\left(T - T_r\right) - c_1\left(T\ln\left(\frac{T}{T_r}\right) - T + T_r\right) \\ & - c_2\left(\left[\left(\frac{1}{T-\theta}\right) - \left(\frac{1}{T_r-\theta}\right)\right]\left(\frac{\theta - T}{\theta}\right) - \frac{T}{\theta^2}\ln\left[\frac{T_r\left(T-\theta\right)}{T\left(T_r-\theta\right)}\right]\right) \\ & + a_1\left(P - P_r\right) + a_2\ln\left(\frac{\Psi + P}{\Psi + P_r}\right) + a_3\left(\frac{P - P_r}{T-\theta}\right) + a_4\left(\frac{1}{T-\theta}\right)\ln\left(\frac{\Psi + P}{\Psi + P_r}\right) \\ & + \omega_{\mathrm{Pr},Tr}\left[\frac{1}{\varepsilon} - \frac{1}{\varepsilon_{\mathrm{Pr}\,Tr}} + Y_{\mathrm{Pr},Tr}\left(T - T_r\right)\right] + k\left[\omega - \omega_{\mathrm{Pr},Tr}\right]\left(\frac{1}{\varepsilon} - 1\right);\end{aligned}$$

$$\overline{V}^{\,o} = a_1 + a_2\left(\frac{1}{\Psi + P}\right) + \left(a_3 + a_4\left(\frac{1}{\Psi + P}\right)\right)\left(\frac{1}{T-\theta}\right) - \omega Q + \left(\frac{1}{\varepsilon} - 1\right)\left(\frac{\partial\omega}{\partial P}\right)_T;$$

$$\begin{aligned}\overline{C}^{\,o}_P = {} & c_1 + \frac{c_2}{\left(T-\theta\right)^2} - \left(\frac{2T}{\left(T-\theta\right)^3}\right)\left(a_3\left(P - P_r\right) + a_4\ln\left(\frac{\Psi + P}{\Psi + P_r}\right)\right) \\ & + \omega T X + 2TY\left(\frac{\partial\omega}{\partial T}\right)_P - T\left(\frac{1}{\varepsilon} - 1\right)\left(\frac{\partial^2\omega}{\partial T^2}\right)\end{aligned}$$

where and $[k]$ is a switch function equal to 1 for charged species and 0 for neutral species (Sverjensky et al., 1997), and $[Q]$, $[Y]$, and $[X]$ are given by (Tanger and Helgeson, 1988)

$$Q \equiv -\left(\frac{\partial(1/\varepsilon)}{\partial P}\right)_T = \frac{1}{\varepsilon^2}\left(\frac{\partial \varepsilon}{\partial P}\right)_T;$$

$$Y \equiv -\left(\frac{\partial(1/\varepsilon)}{\partial T}\right)_P = \frac{1}{\varepsilon^2}\left(\frac{\partial \varepsilon}{\partial T}\right)_P;$$

$$X \equiv \left(\frac{\partial Y}{\partial T}\right)_P = \frac{1}{\varepsilon^2}\left(\left(\frac{\partial^2 \varepsilon}{\partial T^2}\right)_P - \frac{2}{\varepsilon}\left(\frac{\partial \varepsilon}{\partial T}\right)_P^2\right)$$

and can be computed from equations expressing the dielectric properties of water to 1000°C and 5 kbar (Johnson and Norton, 1992).

However, the parameters a_1, a_2, a_3 and a_4 relate only to corrections for pressure. Because potable ground waters are obtained from relatively shallow wells, correction of $\Delta\overline{G}^0_{f,j}$ for pressure would be trivial and almost certainly within the uncertainties associated with the derivations under discussion.

C2.2.2 Calculation of HKF Equation of State Parameters for Metal Complexes with Aqueous Arsenate and Arsenite Species

Langmuir et al. (2006) present estimated values of the association constants of a number of metal arsenate complexes. Those complexes relevant to the problem at hand are listed in Table C3.

Table C3. Association Constant and Gibbs Free Energy of Formation of Selected Arsenate Complexes (after Langmuir et al., 2006) and Derived HKF Equation of State Parameters

Complex	$\log K_{assoc}$ at 25°C	$\Delta\overline{G}^0_{f,P_r,T_r}$ cal mol-1	$\overline{S}^0_{P_r,T_r}$ cal mol^{-1} K^{-1}	$\overline{C}^0_{P_r,T_r}$ cal mol^{-1} K^{-1}	c_1 cal mol^{-1} K^{-1}	c_2 cal K mol^{-1} x 10^{-4}	ω_{P_r,T_r} cal mol^{-1} x 10^{-5}	Z
Arsenite Species								
$H_4AsO_3^+$	-0.29	-116510	-81.203					+1
H_3AsO_3(aq)		-152971	46.80	30.43	20.6012	3.1635	-0.3688	0
$H_2AsO_3^-$	-9.17	-140454	26.96	-2.32	15.9835	-3.5072	1.2132	-1
$HAsO_3^{-2}$	-23.27	-121272	-1.84	-49.83	7.0916	-13.1859	3.2706	-2
AsO_3^{-3}	-38.27	-100813	-46.71	-120.83	-13.3179	-27.6474	5.5714	-3
Arsenate Species								
H_3AsO_4(aq)		-183258	43.75	25.40	18.0776	2.1384	-0.3226	0
$H_2AsO_4^-$	-2.30	-180127	26.86	-2.48	15.9024	-3.5402	1.2146	-1
$HAsO_4^{-2}$	-9.29	-170590	-2.73	-51.30	6.3549	-13.4851	3.2840	-2
AsO_4^{-3}	-21.09	-154489	-42.14	-118.08	-12.3472	-27.0882	5.5021	-3
$MgH_2AsO_4^+$	-0.78	-290706	25.86	42.18	32.2896	5.5571	0.1524	1
$MgHAsO_4$(aq)	-6.43	-282997	-19.38	-6.64	8.1099	-4.3879	0.6336	0
$MgAsO_4^-$	-14.75	-271645	-74.45	-73.42	-11.5410	-17.9910	2.7487	-1
$CaH_2AsO_4^+$	-1.24	-313693	45.36	41.23	29.0125	5.3636	-0.1429	1
$CaHAsO_4$(aq)	-6.60	-306380	1.19	-7.59	4.6829	-4.5814	0.3220	0
$CaAsO_4$-	-14.87	-295096	-52.80	-74.37	-15.1173	-18.1845	2.4209	-1
$AlH_2AsO_4^{+2}$	0.77	-300826	-0.73	15.02	25.0924	0.0246	1.0989	2
$AlHAsO_4^+$	-2.00	-297046	-48.43	-33.80	-1.8770	-9.9204	1.2773	1
$AlAsO_4$(aq)	-6.99	-290238	-105.95	-100.58	-34.8667	-23.5235	1.9445	0
$MnHAsO_4$(aq)	-5.54	-230206	-1.66	-5.40	6.3638	-4.1353	0.3651	0
$MnAsO_4^-$	-14.96	-217353	-55.80	-72.18	-13.4157	-17.7384	2.4663	-1
$FeH_2AsO_4^+$	0.38	-205421	33.56	39.62	29.7151	5.0356	0.0358	1
$FeHAsO_4$(aq)	-5.75	-197057	-11.26	-9.20	5.4762	-4.9094	0.5105	0
$FeAsO_4^-$	-14.03	-185759	-65.90	-75.98	-14.2337	-18.5124	2.6193	-1
$FeH_2AsO_4^{+2}$	1.74	-200131	10.05	28.92	31.7358	2.8560	0.9358	2
$FeHAsO_4^+$	0.57	-198535	-37.03	-19.90	4.6789	-7.0890	1.1047	1
FeAsO4(aq)	-2.19	-194769	-93.93	-86.68	-28.3985	-20.6920	1.7624	0
$ZnHAsO_4$(aq)	-6.08	-210169	-12.21	-6.63	7.1149	-4.3859	0.5249	0
$CdHAsO_4$(aq)	-5.58	-194212	-2.93	-4.80	6.8921	-4.0131	0.3843	0
$PbH_2AsO_4^+$	-0.77	-187925	63.06	34.82	22.7867	4.0579	-0.4109	1
PbHAsO4(aq)	-6.25	-180447	19.86	19.86	19.8614	1.0112	0.0392	0

Using the information supplied by Nordstrom and Archer (2003), $\Delta\overline{G}^0_{f,j}$ can be calculated, as also listed in Table C3. A necessary requirement for calculating the HKF equation of state parameters is quantification of $\overline{S}^0_{P_r,T_r}$ and $\overline{C}^0_{P_r,T_r}$, neither of which have been measured or estimated. Calculation of $\overline{S}^0_{P_r,T_r}$ is facilitated by the observation by Sverjensky et al. (1997) that the standard partial molal entropies of association $\Delta\overline{S}^0_{assoc.,P_r,T_r}$ of metal sulfate complexes

$$M^{Z+2} + SO_4^{2-} = MSO_4^Z$$

of a given charge, Z, are essentially identical, as indicated in Figure C2.

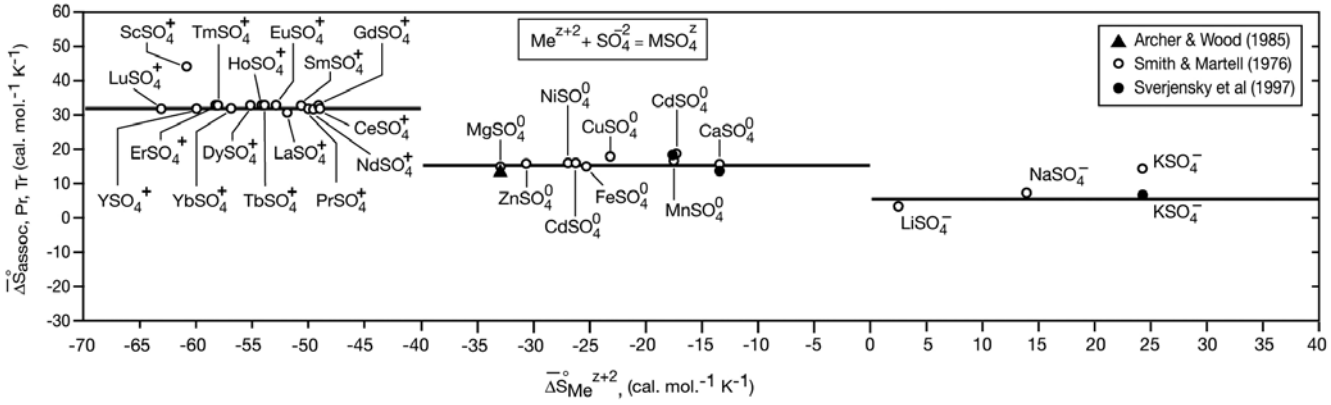

Fig. C2. Standard partial molal entropies of association $\Delta\overline{S}^0_{assoc.,P_r,T_r}$ of metal sulfate complexes (after Sverjensky et al., 1997)

These correlations were summarized by the authors in the form of the following equation:

$$\Delta\overline{S}^0_{assoc.,P_r,T_r,y=1} = \alpha_{Z,SO_4^{2-}}\,\overline{S}^0_{M^{Z+2}} + \beta_{Z,SO_4^{2-}}$$

where $\alpha_{Z,SO_4^{2-}} = -0.055Z + 0.055$ and $\beta_{Z,SO_4^{2-}} = 13.84Z + 18.16$.

Recognizing that the entropies of oxyanions of identical charge are nearly identical, as shown in Table C2 and Figure C1, above, the assumption was made that $\Delta\overline{S}^0_{assoc.,P_r,T_r}$ for metal arsenate complexes with charges equivalent to those of metal complexes would be equivalent. Thus, for

example, values of $\Delta\overline{S}^0_{assoc.,P_r,T_r}$ for $CaHAsO_4$(aq) are equivalent to $CaSO_4$(aq). The estimated values of $\overline{S}^0_{P_r,T_r}$ all metal complexes listed were calculated using the above equation, and are presented in Table C3.

The estimation of $\overline{C}^0_{P_r,T_r}$ for metal arsenate complexes could not be accomplished by reference to the existing papers describing parameter estimations for the HKF equation of state. The normal procedure is to use correlation plots relating $\overline{C}^0_{P_r,T_r}$ to $\overline{S}^0_{P_r,T_r}$ for given families of ionic or molecular species, e.g., Schock and Helgeson (1988, Eq. 91) and Shock et al. (1989, Eq. 24). However, in this case, no such correlation plots have been developed, and published plots are neither relevant nor adaptable for to arsenate complexes. Perusal of limited $\overline{C}^0_{P_r,T_r}$ data available for metal complexes of oxyanions presented in Sverjensky et al. (1997) indicates that the $\Delta\overline{C}^0_{P,assoc.,P_r,T_r}$ for these species are all of similar magnitude, i.e., circa 50 cal mol^{-1} K, suggesting the formation of outer sphere complexes, as proposed many years ago by Garrels and Christ (1965, Figure 4.4, p. 100). Table C4 presents the results of this analysis. Among those listed complexes is $MnSO_4$(aq). However, Sverjensky et al. (1997), referring to supporting literature, have asserted that the complexation of Fe^{+2} Mn^{+2} and Zn^{+2} involves the release of one or more molecules of water from the inner coordination sphere of central cations in such complexes, and indeed, this may be consistent with the elevated $\Delta\overline{C}^0_{P,assoc.,P_r,T_r}$ values for CH_3COO^- complexes of Fe^{+2} and Zn^{+2}. Compensating for one mol of water would result in a correction of –18.0 cal mol^{-1} K^{-1} to $\Delta\overline{C}^0_{assoc.,P_r,T_r}$ for CH_3COOFe^+ and CH_3COOZn^+ leading to equivalent values of 65 and 67.33 cal mol^{-1} K^{-1}, respectively, which is more in accord with $\Delta\overline{C}^0_{assoc.,P_r,T_r}$ for the oxyanion complexes listed in Table C4. Note, however, that $\Delta\overline{C}^0_{assoc.,P_r,T_r}$ for the reaction between CH3COOH(aq) and either Fe^{+2} or Zn^{+2} is also approximately 50 cal mol^{-1} K^{-1}. Bearing in mind the tentative nature of the analysis, we have made a provisional assumption that $\overline{C}^0_{P_r,T_r}$ for all metal arsenate complexes listed in Table C3 can be estimated assuming that $\Delta\overline{C}^0_{assoc.,P_r,T_r}$ = 50 cal mol^{-1} K^{-1} for all association reactions.

Table C4. A Comparison of Heat Capacities of Dissociation of selected Oxyanions

Reaction	Participating Species	$\overline{C}^0_{P_r,T_r}$	$\Delta\overline{C}^0_{assoc.,P_r,T_r}$
$K^+ + SO_4^{-2} = KSO_4^-$	K^+	-3.0	56.48
	SO_4^{-2}	-64.38	
	KSO_4^-	-10.9	
$K^+ + HSO_4^- = KHSO_4(aq)$	K^+	-3.0	49.42
	HSO_4^-	5.3	
	$KHSO_4(aq)$	57.72	
$Mn^{+2} + SO_4^{-2} = MnSO_4(aq)$	Mn^{+2}	-4.1	47.88
	SO_4^{-2}	-64.38	
	$MnSO_4(aq)$	-20.6	
$Ca^{+2} + CO_3^{-2} = CaCO_3(aq)$	Ca^{+2}	-7.53	47.43
	CO_3^{-2}	-69.5	
	$CaCO_3(aq)$	-29.6	
$Na^+ + HSiO_3^- = NaHSiO_3(aq)$	Na^+	9.06	36.55
	$HSiO_3^-$	-21	
	$NaHSiO_3(aq)$	24.61	
$Ca^{+2} + HSiO_3^- = CaHSiO_3^+$	Ca^{+2}	-7.63	61.5
	$HSiO_3^-$	-21	
	$CaHSiO_3^+$	32.87	
Average Value			49.9
$Fe^{+2} + CH_3COO^- = CH_3COOFe^+$	Fe^{+2}	-7.9	83.0
	CH_3COO^-	6.2	
	CH_3COOFe^+	81.3	
$Zn^{+2} + CH_3COO^- = CH_3COOZn^+$	Zn^{+2}	-5.33	85.33
	CH_3COO^-	6.2	
	CH_3COOZn^+	86.2	
$Fe^{+2} + CH_3COOH = CH_3COOFe^+ + H^+$	Fe^{+2}	-7.9	48.64
	CH_3COOH	40.56	
	CH_3COOFe^+	81.3	
$Zn^{+2} + CH_3COOH = CH_3COOZn^+ + H^+$	Zn^{+2}	-5.33	51.07
	CH_3COOH	40.56	
	CH_3COOFe^+	86.2	

Calculation of the HKF equation of state parameters, c_1, c_2 and the Born coefficient, ω_{P_r,T_r}, follows the procedures outlined above. The respective values are listed in Table C3.

C2.2.3 Derivation of Thermodynamic Properties of Arsenic Solid Phases and Minerals

The following two tables summarize information on arsenic solid phases. Table C5 gives the crystallographic information necessary to calculate molar volumes of the solid phases, which are used in thermodynamic calculations to correct for the effects of pressure, and Table C6 provides

thermodynamic data for the solid phases. This information, in conjunction with the corresponding aqueous basis species information, is used to calculate the solid phase solubility products.

The thermodynamic properties of some of the phases or minerals listed in Table C6 are incomplete. Information available in the literature may be sufficient to estimate preliminary values of $\Delta G^0_{P_r,T_r}$ for the minerals in question, but time constraints prevented further evaluation. In some cases, $\Delta G^0_{P_r,T_r}$ values were taken directly, or calculated from solubility product data reported in the literature, rather than by re-evaluating raw data and using revised thermodynamic data for aqueous species published by Nordstrom and Archer (2003) to recalculate solubility product and $\Delta G^0_{P_r,T_r}$ values. The tabulated data are not entirely consistent internally, and are therefore preliminary. However, the uncertainties introduced by taking this expedient approach are well within the uncertainties of the geochemical model developed in Section 3 of the report, and have no impact on the resulting findings and conclusions.

A very recent paper by Perfetti et al. (2008) gives revised thermodynamic data for arsenopyrite. In this paper, $\Delta G^0_{P_r,T_r}$ for arsenopyrite is given as –32,612 cal/mol, which differs by +1,231 cal/mol from the value reported in Table C6, which was cited from an earlier paper by Pokrovski et al. (2002). Using this revised value for the calculation of solubility products would decrease the extent of undersaturation of arsenopyrite reported in Section 3.4.5.2, Figure 3.34a, by approximately one unit in SI. This change would necessitate a smaller calibration correction (-1.8 vs. –3.0) to match the modeled As concentration in groundwaters in equilibrium with an arsenopyrite solid solution in pyrite, to that actually observed, as presented in Section 3.5.2, Table 3.13. This revised correction appears to be more realistic, although further corroborating evidence is needed.

Table C5. Crystallographic Properties of Arsenic Solid Phases

Name	Formula	Cell Constants							Space Group	Reference
		a_o (Å)	b_o (Å)	c_o (Å)	α	β	γ	Z		
Arsenolite	As_2O_3	11.07343	11.07343	11.07343	90	90	90	16	*Fd3m	Ballirano and Maras (2002)
Claudetite II	As_2O_3	7.99	4.645	9.115	90	78.3	90	4	P2_1/n	Pertlik (1975)
Arsenic	As	3.7597	3.7597	10.4412	90	90	120	6	R3m	Schiferl and Barrett (1969)
Arsenic Oxide	As_2O_5	8.64	8.45	4.62	90	90	90	4	$P2_12_12_1$	Hansen (1977)
Ferrarisite	$Ca_5(AsO_3OH)_2(AsO_4)_2.9H_2O$	8.294	6.722	11.198	106.16	92.94	99.2	1	P-1	Catti et al. (1980)
Guerinite	$Ca_5(AsO_3OH)_2(AsO_4)_2.9H_2O$	17.63	6.734	23.47	90	90.6	90	5	P2_1/n	Catti and Ferraris G (1974)
Haidingerite	$Ca(AsO_3OH).H_2O$	6.904	16.161	7.935	90	90	90	8	Pcnb	Ferraris et al. (1972)
Hornesite	$Mg_3(AsO_4)_2.8H_2O$	10.2573	13.4211	4.7526	90	105.076	90	2	C2/m	Rojo et al. (1996)
Johnbaumite	$Ca_5(AsO_4)_3(OH)$	9.70	-	6.93				2	P 6_3/m or $P6_3$	Dunn et al. (1980)
Johnbaumite-Pb	$Pb_5(AsO_4)_3(OH)$									
Mimetite	$Pb_5(AsO_4)_3(Cl)$	10.211	-	7.4185				2	P6_3/m	Yonshan et al. (1991)
Pyromorphite	$Pb_5(PO_4)_3(Cl)$	9.9764	-	7.3511				2	P6_3/m	Dai and Hughes (1989)
Orpiment	As_2S_3	11.475	9.577	4.256	90	90.68	90	4	P2_1/n	Mullen and Nowacki (1972)
Pharmacolite	$CaHAsO_4.2H_2O$	5.9745	15.434	6.2797	90	114.83	90	4	Ia	Ferraris et al. (1971)
Pharmacosiderite	$KFe_4(AsO_4)_3(OH)_4.6H_2O$	7.9816	7.9816	7.9816	90	90	90	2	P-43m	Buerger et al. (1967)
Picropharmacolite	$Ca4Mg(HAsO_4)_2(AsO_4)_2.11H_2O$	13.547	13.5	6.71	99.85	96.41	91.6	2	P-1	Cattiet al. (1981)
Pitticite	$Fe_2(AsO_4)(SO_4)(OH).6H_2O$									
Realgar	AsS	9.327	13.563	6.59	90	106.46	90	16	P2_1/n	Kyono et al. (2005)
Pararealgar	AsS	9.909	9.655	9.502	90	97.29	90	16	P2_1/c	Bonazzi et al. (1995)
Scorodite	$FeAsO_4.2H_2O$	8.942	10.075	10.339	90	90	90		Pbca	Xu et al. (2007)
Scorodite	$FeAsO_4.2H_2O$	10.325	8.953	10.038	90	90	90		Pbca	Kitahama et al. (1975)
Symplesite	$Fe_3(AsO_4)_2.8H_2O$	7.97	9.41	4.72	99.917	97.383	105.967	1	P-1	Wolfe (1940)
Talmessite	$Ca_2Mg(AsO_4)_2.2H_2O$	5.874	6.943	5.537	97.3	108.7	108.1	1	P-1	Catti M, et al. (1977)
Tooeleite	$Fe_6(AsO_3)_4(SO_4)(OH)_4.4H_2O$	8.9575	6.4238	9.7912	90	96.032	90	1	C2/m	Morin et al. (2007)
Weilite	$CaHAsO_4$	7.0591	6.8906	7.2006	97.43	103.55	87.75	4	P-1	Ferraris and Chiari (1970)
Yukonite	$Ca_7Fe_{11}(AsO_4)_9O_{10}.24H_2O$									
Arsenopyrite	FeAsS	5.744	5.675	5.785	90	112.28	90	4	P-1	Morimoto and Clark (19610

Table C6. Thermodynamic Properties of Arsenic Solid Phases

Mineral name	Formula	$\Delta G^0_{f,P_r,T_r}$ cal mol^{-1}	Ref	$\Delta H^0_{f,P_r,T_r}$ cal mol^{-1}	Ref	$S^0_{P_r,T_r}$ cal mol^{-1} K^{-1}	Ref	$V^0_{P_r,T_r}$ cm^3 mol^{-1}	Ref	$C^0_{P_r}$ cal mol^{-1} K^{-1}			Ref
										a	$b\times10^3$	$c\times10^{-5}$	
(C3RH2.25)	$Ca_3(AsO_4)_2.2.25H_2O$	-862066								88.361	3.2400	-4.68E+00	5
(C3RH3)	$Ca_3(AsO_4)_2.3H_2O$	-904227								96.911	3.2400	-4.68E+00	5
(C3RH3.67)	$Ca_3(AsO_4)_2.3.67H_2O$	-942878	2							104.549	3.2400	-4.68E+00	5
(C3RH4.25)	$Ca_3(AsO_4)_2.4.25H_2O$	-976338	2							111.161	3.2400	-4.68E+00	5
(C4RH5)	$Ca_4(OH)_2(AsO_4)_2.4H_2O$	-1176881	2							119.981	4.3200	-6.24E+00	5
(F2R1.5SH)	$Fe_4(AsO_4)_3(SO_4)(OH)$									106.309	31.0062	-5.92E+00	5
(FR1.5HX)	$Fe_2(HAsO_4)_3.xH2O$												
(FRX)	$Fe_2(AsO_4)x(HAsO_4)y$												
(R)	As_2O_5	-185220	1	-219309	1	25.201	1	50.781	7	27.701	0.000	0.000	4
Arsenic	As	0	1	0	1	8.516	1	13.049	8	5.137	2.602	-0.089	
Arsenopyrite	FeAsS	-33843	11			16.370	11	26.420	8	18.047	4.780	-7.543	
Arseniosiderite	$Ca_2Fe_3(AsO_4)_3O_2.3H_2O$	-887437				111.33	6	195.618	8	134.327	30.060	-8.450	5
Arsenolite	As_2O_3	-137749	1	-157091	1	25.664	1	50.724	8	8.37	48.6	0.000	4
Ca-arsenate	$Ca_3(AsO_4)_2.xH2O$	-887437				49.761		100.070	8	61.700	13.900	-15.010	
Claudetite	As_2O_3	-137794	1	-156709	1	27.096	1	47.257	8	23.197	9.326	-6.300	
Ferrarisite	$Ca_5(AsO_3OH)_2(AsO_4)_2.9H_2O$	-1866157	2			189.017	6	354.655	8	223.462	5.400	-7.800	5
Guerinite	$Ca_5(AsO_3OH)_2(AsO_4)_2.9H_2O$	-1864962	2			184.458	6	335.580	8	223.462	5.400	-7.800	5
Haidingerite	$Ca(AsO_3OH).H_2O$	-366396	2			35.591	6	66.991	8	40.476	1.080	-1.560	5
Hornesite	$Mg_3(AsO_4)_2.8H_2O$	-887437				114.241	6	190.194	8	149.441	5.220	-4.440	5
Johnbaumite	$Ca_5(AsO_4)_3(OH)$	-1216375	2			94.817	6	170.031		103.457	5.400	-7.800	5
Johnbaumite-Pb	$Pb_5(AsO_4)_3(OH)$	-635516	3			123.721	6	204.215		90.357	32.000	0.000	5
Mimetite	$Pb_5(AsO_4)_3(Cl)$	-630019	10	-713432	10	143.164	10	204.215	8	119.981	4.3200	-6.2400	5
Orpiment	As_2S_3	-20292	1	-20507	1	39.149	1	70.503	8	22.73	13.82	0.605	9
As_2S_3,am	As_2S_3	-18356	1	-15989	1	47.801	1	70.503		22.73	13.82	0.605	9
Pharmacolite	$CaHAsO_4.2H_2O$					43.177	6	79.363	8	51.876	1.080	-1.560	5
Pharmacosiderite	$KFe_4(AsO_4)_3(OH)_4.6H_2O$					162.563	6	306.084	8	184.967	42.605	-9.100	5
Picropharmacolite	$Ca4Mg(HAsO_4)_2(AsO_4)_2.11H_2O$					199.568	6	361.370	8	244.772	10.385	-7.720	5
Pitticite	$Fe_2(AsO_4)(SO_4)(OH).6H_2O$					103.29	6	100.070		123.518	12.406	-2.370	5
Realgar	AsS	-7481	1	-7600	1	15.033	1	29.743	8	12.94	-0.0133	1.396	9
Pararealgar	AsS	-7385	1	-7409	1	15.177	1	30.368	8	12.94	-0.0133	1.396	9
Scorodite	$FeAsO_4.2H_2O$	-306991				49.761		69.117	8	48.396	9.300	-1.780	
Scorodite,am	$FeAsO_4.2H_2O$	-303130				38.313	6	69.117		48.396	9.300	-1.780	5
Symplesite	$Fe_3(AsO_4)_2.8H_2O$	-872736				119.583	6	198.385	8	155.261	6.210	-2.250	5
Talmessite	$Ca_2Mg(AsO_4)_2.2H_2O$					70.333	6	120.084	8	84.021	3.900	-4.600	5
Tooeleite	$Fe_6(AsO_3)_4(SO_4)(OH)_4.4H_2O$					177.878	6	337.409	8	161.252	66.906	-9.470	5
Weillite	$CaHAsO_4$					27.344	6	51.858	8	29.076	1.080	-1.560	5
Yukonite	$Ca_7Fe_{11}(AsO_4)_9O_{10}.24H_2O$			-940771		515.389	6	100.070		609.140	109.860	-30.400	5

Notes: 1. Nordstrom and Archer (2003); 2. Bothe and Brown (1999); Lee and Nriagu (2007); 4. Kelley (1960); 5. Calculated using the summation of oxide components. This work; 6. Calculated using the procedure described by Holland (1989). This work; 7. Jansen (1977); 8. Calculated from cell parameter data. 9. Pokrovski et al. (1996); 10. Flis et al. (2007), $S^0_{P_r,T_r}$ recalculated using elemental data from NIST; 11. Pokrovski et al. (2002).

C3. Lead

C3.1 Introduction

Incorporation of a wider range of lead solid and aqueous species in the ongoing evaluation of groundwater analyses, and in model development, is important for two reasons. First, the ingress of oxygen into aquifers that were formerly reducing, and where lead was presumably immobilized as the sulfide, galena, could induce solubilization of lead exceeding MCLs, even more so than would be induced through pH lowering through the ingress of high-pressure CO_2. It is important to know whether the precipitation of secondary lead salts might restrain lead solubility under those conditions, especially with respect to those ground waters downloaded from the NWIS database, some of which exhibit lead concentrations that are supersaturated with respect to galena. Secondly, the addition of relevant aqueous lead complexes, especially those of carbonate, sulfide and selenide, will aid in a more precise calculations of lead concentrations in solutions saturated with respect to minerals containing lead as an essential component. These additional species might also affect the predicted sorption and ion exchange of lead on aquifer minerals, depending on the nature of the problem at hand. In this appendix, we present thermodynamic properties of lead minerals and other phases where lead is an essential component, and for all aqueous species except for lead sulfide and selenide complexes, which are discussed in Appendices D and E of this report.

C3.2 Aqueous Lead Species

An earlier unpublished compilation of internally consistent thermodynamic properties of a variety of lead carbonates, chlorides and sulfates, and a corresponding compilation relating to lead complexes in solution, was used to calculate their respective solubility products and dissociation constants in the Data0.dat database of EQ3 and the corresponding TOUGHREACT database. All respective constants were calculated using SUPCRT92, in which estimated HKF-equation-of-state parameters for the aqueous species were included. In addition to replacing seven extant aqueous species and eleven solid phases in the database, three additional aqueous species, and thirteen additional solid phases were incorporated. Table C7 lists the thermodynamic properties of aqueous lead species together with their calculated HKF-equation-of-state parameters.

C3.3 Lead Solid Phases and Minerals

The following two tables summarize information on lead solid phases. Table C8 gives the crystallographic information necessary to calculate molar volumes of minerals, which are used in thermodynamic calculations to correct for the effects of pressure, and Table C9 provides thermodynamic data for the solid phase. This information, in conjunction with the corresponding aqueous basis species information is used to calculate the solid phase solubility products. The listed solid phases also include those known to very insoluble. An example is the Pb phosphate, pyromorphite, $Pb_5(PO_4)_3(Cl)$, in the presence of which lead concentrations are known to be depressed to low levels. The application of phosphate compounds as a means of controlling Pb mobility in contaminated soils has been suggested. The corresponding lead arsenate, mimetite, $Pb_5(AsO_4)_3(Cl)$, is also known to be very insoluble, and it is possible that mimetite could limit the saturation concentration of both As and Pb in ground waters. Therefore this mineral is also included as well as the arsenic analogue of apatite, johnbaumite, $Pb_5(PO_4)_3(OH)$.

It should be noted that many of the data compiled in Tables C7, C8, and C9 were evaluated and reconciled over a decade ago. Time did permit only limited retrieval of new information published in the archival literature since that time. A casual perusal of the literature indicates that no substantive changes have occurred since the original work was compiled; rather, the data has been refined and augmented. Therefore, the application of more recent data, where available, would not change the findings of this report in any significant manner, and would be within the limits of geochemical model uncertainty. The advantage in using the current database is that it is internally consistent, and that the solubility product and dissociation constant data have been uniformly treated, as all calculations were performed using SUPCRT (Johnston et al., 1992). However, a complete review of the data in the light of more recent published data is definitely recommended.

C3.4 Acknowledgements

We would like to acknowledge the contributions of Mr. Motomi Oshika, a guest scientist at the Berkeley Lab during 1992-3, who assisted in the evaluation of the thermodynamic properties of lead minerals, under a FY 1992 allocation of Exploratory R&D Funds to one of the authors (John Apps) for the project “Synthesizing Optical $PbSO_4$ for Advanced Scintillation Applications”.

Table C7. Thermodynamic Properties of Lead Aqueous Species

Aqueous Species	$\Delta G^0_{f,P_r,T_r}$	$\Delta H^0_{f,P_r,T_r}$	$\overline{S}^o$	$\overline{C}p^{obf}$	$\overline{V}^{oCg}$	$a_1^{uaa} x10$	$a_2^{uaa} x10^{-2}$	$a_3 v.aa$	$a_4^{w.aa} 10^{-4}$	c_1^{baa}	$c_2^{waa} \times 10^{-4}$	$w^{az} \times 10^{-5}$	Charge
H^+	0	0	0	0	0	0	0	0	0	0	0	0	+1
HCO_3^-	-140282[l]	-164898[m]	23.53[m]	-8.46	24.6	7.5621	1.1505	1.2346	-2.8266	12.93965	-4.7579	1.2733	-1
CO_3^{-2}	-126191[m]	-161385[m]	-11.95[m]	-69.5[n]	-5.02	2.8524	-.39844	6.4142	-2.6143	-3.3206	-17.1917	3.3914	-2
Pb^{+2}	-5710[h]	220[e]	4.2[e]	-12.74	-15.6	-0.0051	-7.7939	8.8134	-2.4568	8.6624	-5.6216	1.0788	2
$Pb(OH)^+$	-52089	-57652[*]	21.34	4.54	7.029	2.804	-0.9348	6.1174	-2.7404	10.9315	-2.1098	0.2284	1
$Pb(OH)_2(aq)$	-95060	-111214[*]	41.57	33	48.127	8.4485	12.8476	.07206	-3.3101	22.8390	3.6875	-0.2895	0
$Pb(OH)_3^-$	-137641	-166209[*]	40.06	15.1792	40.06	7.5921	10.7680	1.4938	-3.2241	24.4800	0.0574	1.0223	-1
$PbCO_3(aq)$	-141819	-156632[*]	40.72	29	46.880	8.2735	12.3922	0.9392	-3.2913	20.6134	2.8727	-0.2767	0
$Pb(CO_3)_2^{-2}$	-272746	-301163[*]	70.01	-14.492	83.41	13.906	26.173	-4.5397	-3.8610	17.5025	-5.9866	2.1523	-2
$PbCl^+$	-39046	-43260[*]	28.0		3.400[*]	2.2870	-2.9703	8.5760	-2.6502	21.8	1.8542	0.16800	1
$PbCl_2$	-71190	-78281[*]	45.0		22.400[*]	4.7542	3.9456	3.9447	-2.9421	22.2616	3.2801	-0.2550	0
$PbCl_3^-$	-102147	-115066[*]	52.1		41.400[*]	7.7573	12.3640	-1.6927	-3.2901	39.698	5.521	0.9679	-1
$PbCl_4^{-2}$	-133254	-153342[*]	54.7		60.399[*]	10.7757	20.8252	-7.3588	-3.6399	57.0825	7.5985	2.2060	-2
Cl^-	-31379[h]	-39933[e]	13.56	-29.44[d]	17.79[d]	4.0320	4.8010	5.5630	-2.847	-4.40	-5.714	1.4560	-1
OH-	-3.7595[h]	-54977[e]	-2.56[e]	-32.79[d]	-4.18[d]	1.2527	0.0738	1.8423	-2.7821	4.15	-10.346	1.7246	-1
SO_4^{-2}	-177930[h]	-217400e	4.50[e]	-64.38[d]	13.88[d]	8.3014	-1.9846	-6.2122	-2.6970	1.64	-17.998	3.1463	-2
HSO_4^-	-180630[r]	-212500[r]	30.0[r]	5.3	35.2	6.9788	9.2590	2.1108	-3.1618	20.0961	-1.9550	1.1748	-1

Notes a: cal mol^{-1}; b: cal $mol^{-1}K^{-1}$; c:cm^3mol^{-1}; d: Tanger and Helgeson; e: CODATA(1978); *: supcrt; f: from electrolytes in Table 10 unless otherwise indicated; h: calculated from $\Delta\overline{H}^o_{SPT}$ and $\overline{S^O}$ shown using standard entropiues of the elements from CODATA (1978); g: From electrolytes in Table 9 unless otherwise indicated; l: Helgeson, Kirkham, and Flowers (1981); m: Berg and Vanderzee (1978); r: consistent with log KrPT, Δ HrPt AND Δ Srpt from dissociation reaction; u: Cal $Mol^{-1}xbar^{-1}$; v: cal K $mol^{-1}xbar^{-1}$; w: cal K mol^{-1}; z: from Table 1, 2, and 3; aa: calculated in a manner consistent with table 8 unless otherwise indicated

Table C8. Crystallographic Properties of Lead Solid Phases

Mineral Name	Formula	Unit	Cell Parameters						Z	Space Group	Reference
			a_o	b_o	c_o	α	β	γ	4		
Cotunnite	$PbCl_2$	Kx Å	7.67 7.68	9.15 9.17	4.5 4.51	90	90	90	4	Pnam	Palache et al. (1951)
Laurionite	PbOHCl	Å Kx	9.72 9.7	4.06 4.05	7.11 7.1	90	90	90		Pcmn	Palache et al. (1951)
	$3PbO.PbCl_2.nH_2O$	Å	9.57	-	-	90	90	90			
Lorettoite	$Pb_7O_6Cl_2$								4		Palache et al. (1951)
Mendipite	$Pb_3O_2Cl_2$	Kx Å	9.50 9.52	11.87 11.89	5.87 5.88	90	90	90	4	Pnma $P2_12_12_1$	Palache et al. (1951)
Paralaurionite	Pb(OH)Cl	Kx Å	10.77 10.79	3.97 3.98	7.18 7.19	90	117.22	13/60		$C2_1/m$	Palache et al. (1951)
Penfieldite	Pb_2OHCl_3	Å	11.28	x	48.65				4	P6/m	Cesbron and Schubnel (1968);
Fieldlerite	$Pb_3(OH)_2Cl_4$	Kx Å	16.59 16.62	8.00 8.02	7.19 7.20	90	102.20	90	4	$P2_1/a$	Palache et al. (1951)
Anglesite	$PbSO_4$	Kx Å	8.45 8.47	5.38 5.39	6.93 6.94	90	90	90	4	Pnma	Palache et al. (1951)
Lanarkite	$Pb_2(SO_4)O$	Kx Å	13.73 13.76	5.68 5.69	7.07 7.08	90	116.22	90	2	C_2/m	
Sulfate Dibasque (Second Source)	$2PbO.PbSO_4$	Å Å	7.814 8.06	5.803 5.79	8.035 7.17	90	102.64 103	90	2	$P2_1$ or $P2_1/m$	Boivin et al. (1968)
	$3PbO.PbSO_4$	Å	10.30	6.37	7.45	87.2	75.0	79.2	4	P1 or p1	
Lanarkite	$PbO.PbSO_4$	Å	13.751	5.6969	7.0699	–	115.82	-	2	P	
	$3PbO.PbSO_4.H_2O$	Å	10.30	6.37	7.45	87.2	75.0	79.2	4	P1 or p1	Boivin et al. (1968)
2nd Source	$4PbO.PbSO_4$	Å	11.5234 11.443	11.7138 11.666	7.3152 7.316	90 90	91.04 90.82	90 90		$P2_1/a$	Boivin et al. (1968)
Hydrocerussite											
Plumbonacrite											
Matlockite											
Lead											
Litharge											
Massicot											

Notes a. Palache et al. (1951); b. Did not calculate; c. Cesbron and Schubnel (1968); d. Boivin et al. (1968), Tridot et al. (1969); e. Kuzel (1973).

Table C9. Thermodynamic Properties of Lead Solid Phases

Mineral Name	Formula	G.F.W. g. .mol^{-1}	$\Delta G^0_{f,P_r,T_r}$ cal.mol^{-1}	Ref.	$\Delta H^0_{f,P_r,T_r}$ kcal.mol^{-1}	Ref.	$S^0_{P_r,T_r}$ cal.mol^{-1}.k^{-1}	Ref.	$V^0_{P_r,T_r}$ cm^3.mol^{-1}	Ref.	$C^0_{P_r}$ Coefficients, cal.mol^{-1}.k^{-1}			Ref.
											a	b x 10^3	c x 10^{-5}	
Lead	Pb	207.2	0.0		0.0		15.484		18.153		5.290 7.77	2.80 -0.72	0.23 0.00	
Litharge	PbO	223.199	-45244		-52440		16.214		23.983		10.385 10.794	4.77 4.0	-0.610 0.00	
Massicot	PbO	223.199	-44910	8,9,11	-51940		16.42		23.983	23	9.05	6.40	0.00	14
Lead Hydroxide	$Pb(OH)_2$	241.215	-108100	8,9,11,12	-123300	8,9,11	26.69	26	41.2	26	17.71	12.24	0.00	26
Cotunnite	$PbCl_2$	278.106	-75050		-85800	20	32.50		47.84		15.96	8.00	0.00	14
Anglesite	$PbSO_4$	303.258	-194353		-219870		35.51		47.95		10.96	31.0	4.2	
Cerussite	$PbCO_3$	267.209	-150370		-168000		31.3		40.747		12.39	28.60	0.00	
-	$(PbO)_2.Pb(OH)_2$	687.613					58.9	26	90.33	15	38.91	20.24	0.00	26
Matlockite	$PbO.PbCl_2$	501.305	-126557	26	-144700	8,9	47.93	26	68.89		26.56	12.0	0.00	26
Lorretoite	$Pb_7O_6Cl_2$													
Mendipite	$(PbO)_2.PbCl_2$	724.505	-176860	6	-199800	8,9	65.79		100.305		37.16	16.0	0.00	26
-	$(PbO)_3.PbCl_2$	947.704			-253400	8,9					47.76	20.0	0.00	26
Lanarkite	$PbO.PbSO_4$	526.457	-246700	8,9,12	-276658		53.374		75.1		21.778	33.87	3.473	3
-	$(PbO)_2.PbSO_4$	749.656	-294000	9	-328189		70.326		107.1	26	34.830	39.28	2.940	3
-	$PbO.(PbCO_3)_2$	757.618	-351600		-395342	26	74.097		79.469		35.165	61.970	-0.621	
Laurionite	PbClOH	259.660	-93470	9	-109402	26	28.83		42.26		16.835	10.12	0.00	26
Paralaurionite	PbOHCl	259.660	-92340		-108361	26	28.53	26	41.36	26	16.835	10.12	0.00	26
Penfieldite	Pb_2OHCl_3	537.766					61.22		89.71		32.795	18.12	0.00	26
Fieldlerite	$Pb_3(OH)_2Cl_4$	797.427					93.22	26	141.285	26	49.63	28.24	0.00	26
-	$(Pb(OH)_2)_3.PbCl_2$	1001.770									69.09	44.72	0.00	26
Hydrocerussite	$Pb(OH)_2.(PbCO_3)_2$	775.633	-408328		-456000	21	86.083		112.894		45.735	61.970	-0.621	
-	$(PbO)_3.PbSO_4$	990.871	-341200	8	-388800	8,9	81.4	8,9	139.7	26	42.74	43	4.2	26
Plumbonacrite	$Pb_{10}O(OH)_6(CO_3)_6$	2550.098	-1270767		-1448776	26	272.629		357.584		144.590	190.680	-2.448	

Notes 1. Solans-Huguet and Font-Altaba (1967); 2. Derriche and Perrot (1976); 3. Kellogg (1989). 4. Esdaile (1967). 5. Kellogg and Basu (1960) Abdul-Samad et al. (1982). 6. Humphreys et. al. (1980). 7. Loza et. al. (1984). 8. Wagman et al. (1968); 9. Wagman et. al. (1982); 10. Chase et. al. (1985); 11. Weast et al. (1984); 12. Dekock (1986). 14. Kelley (1960); 15. Tolkachev et. al. (1958). 16. Brasseur (1940); 17. Toptygina et. al. (1984). 18. Kuzel (1973) 19. Cesbron and Schubnel (1968). 20. Shelton (1970). 21. Ball and Casson (1977). 22. Taylor and Lopata (1984). 23. Hill (1985). 24. Howie and Moser (1968), density referred to Clark and Tyler (1939). 25. SUPCRT. 26. This work.

C4. Antimony and Selenium

C4.1 Aqueous Antimony and Selenium Species

Table C10 gives the thermodynamic properties for aqueous species of Sb(III). Sb(V) species, SbO_2^+ and $Sb(OH)_6^-$, were also included in the geochemical model using extant data in the EQ3 Data0.dat database. The relevant selenite and selenate complexes included in the model were also extant data in the EQ3 Data0.dat database. The properties of selenide species used or derived in this study are discussed in Appendix E.

C4.2 Antimony and Selenium Solid Phases and Minerals.

Trace concentrations of selenides of heavy metals can play an important role in defining the solubility of hazardous constituents selected for study in this report. In Table C11, the crystallographic properties of selected selenides and antimony minerals are summarized with the purpose of calculating their molar volumes, which are given, together with other thermodynamic properties in Table C12.

Table C10. Thermodynamic Properties of Antimony Aqueous Species

Aqueous Species	$\Delta\overline{G}^0_{f,P_r,T_r}$ cal mol^{-1}	$\overline{S}^0_{P_r,T_r}$ cal mol^{-1} K^{-1}	$\overline{C}^0_{P_r,T_r}$ cal mol^{-1} K^{-1}	$\overline{V}^0_{P_r,T_r}$ cm^3 mol^{-1}	a_1[d] x 10 cal mol^{-1} bar^{-1}	a_2[a] x 10^{-2} cal mol^{-1}	a_3[e] cal K mol^{-1} bar^{-1}	a_4[f] x 10^{-4} cal K mol^{-1}	c_1 cal mol^{-1} K^{-1}	c_2 x 10^{-4} cal K mol^{-1}	ω_{P_r,T_r} cal mol^{-1}
$Sb(OH)_3$(aq)	-154010	49.43	39.09	54	9.1415	14.5397	0.0630	-3.3801	28.6838	4.9284	-0.038
$Sb(OH)_4^{-1}$	-195038	42.28	22.96	44.58	8.1966	12.2325	0.9671	-3.2847	28.6515	1.6426	0.9815
$H_2Sb_2S_4$(aq)	-35488	69.36	71.3	70.7	11.4268	20.1196	-2.1236	-3.6107	47.5025	11.4892	-0.038
$HSb_2S_4^{-1}$	-28583	50.70	32.56	50.7	8.9913	14.1728	0.2068	-3.3649	33.0864	3.5984	0.8540
$Sb_2S_4^{-2}$	-15622	42.38	-30.48	44.66	8.7546	13.5948	0.4332	-3.3410	12.3553	-9.2424	2.6016

Note: Data after Akinfiniev et al. (1994) and Bessinger (2000)

Table C11. Crystallographic Properties of Antimony and Selenium Minerals

Name	Formula	Cell Constants							Space Group	Reference
		a_o (Å)	b_o (Å)	c_o (Å)	α	β	γ	Z		
Naumannite	Ag_2Se	4.333	7.062	7.764	90	90	90	4	*P2_12_12_1	Wiegers (1971)
Berzelianite	Cu_2Se	5.765	5.765	5.765	90	90	90	4	Fm3m	Heyding and Murray (1976)
Antimonselite	Sb_2Se_3	11.794	3.986	11.648	90	90	90	4	Pnma	Caracas and Gonze (2005)
Clausthalite	PbSe	6.1243	6.1243	6.1243	90	90	90	4	Fm3m	Wyckoff (1963)
Tiemannite	HgSe	6.084	6.084	6.084	90	90	90	4	F-43m	Earley (1950)
Ferroselite	$FeSe_2$	4.804	5.784	3.586	90	90	90	2	Pnnm	Pickardt et al. (1975)
Stibnite	Sb_2S_3	11.3107	3.8363	11.2285	90	90	90	4	Pnma	Bayliss and Nowacki (1972)
Antimony	Sb	4.50661	4.50661	4.50661	57.108	57.108	57.108	20	R-3m	Wyckoff (1963)
Senarmonite	Sb_2O_3	11.1519	11.1519	11.1519	90	90	90	16	Fd-3m	Svensson (1975)
Valentinite	Sb_2O_3	4.911	12.464	5.412	90	90	90	4	Pccn	Svensson (1974)
Berthierite	$FeSb_2S_4$	11.401	14.148	3.758	90	90	90	4	Pnam	Lemoine et al. (1991)
Gudmundite	FeSbS	6.02	5.93	6.02	90	67.87	90	4	P1_1/c	Buerger (1939)
Kermesite	Sb_2S_2O	8.147	10.709	5.785	102.78	110.63	101.00	4	P-1	Bonazzi et al. (1987)

Table C12. Thermodynamic Properties of Selenides and Antimony Minerals

Mineral name	Formula	$\Delta G^0_{f,P_r,T_r}$ cal mol^{-1}	Ref	$\Delta H^0_{f,P_r,T_r}$ cal mol^{-1}	Ref	$S^0_{P_r,T_r}$ cal mol^{-1} K^{-1}	Ref	$V^0_{P_r,T_r}$ cm^3 mol^{-1}	Ref	$C^0_{P_r}$ cal mol^{-1} K^{-1}			Ref
										a	$b\times10^3$	$c\times10^{-5}$	
Naumannite	Ag_2Se	-11998		-10397		35.813		35.768		19.479	-	-	
Berzelianite	Cu_2Se	-17089		-15607		30.914		28.846		19.460	-	-	
Cadmoselite	CdSe	-33830		-34600		19.900		33.727		11.190	2.23	-	3
Clausthalite	PbSe	-23566		-24092		23.827		34.583		11.29	2.39	-	3
Tiemannite	HgSe	-9130		-10397		23.995		33.905		11.70	3.70	-	3
Ferroselite	$FeSe_2$	-19598		-21511		13.011		30.003		16.871	-	-	
Kullerudite	$NiSe_2$	-25096		-26052		24.138		32.206		18.028	-	-	
Antimony	Sb	0.		0.		10.773		18.188	6	2.490	5.930	1.880	
Senarmonite	Sb_2O_3	-151400				27.370		52.220	6	22.530	12.030	-3.179	
Valentinite	Sb_2O_3	-149600				29.430		49.874	6	24.840	10.300	-3.197	
Stibnite	Sb_2S_3	-35846				43.499		73.352	6	28.750	3.927	-1.264	
Antimonselite	Sb_2Se_3	-30019		-30497		48.911		82.441	6	28.38	5.00	-	3
Gudmundite	FeSbS	-109433	5	-109060	5	106.000	5	29.971	6	126	-	-	5
Berthierite	$FeSb_2S_4$	-61176				58.560		91.261	6	46.590	0.2630	-3.860	
Kermesite	Sb_2S_2O		8		8		8	66.282	6				

Notes 1. Zotov et al. (2003); 2. Xiong (2003); 3. Mills (1974); 4. Robie (1967); 5. Williams Jones and Normand (1997); 6. Calculated from cell parameters. See text; 7. Bonazzi et al. (1987); 8. Thermodynamic properties for kermesite require calculation based on data reported by Williams Jones and Normand (1997), which was in turn based on earlier work by Babcan (1976) and used in this study to calculate Log K(kermesite) directly.

C5. Iron

C5.1 Revision of Fe^{2+} and Fe^{3+}

Uncertainties relating to the thermodynamic properties of the ferrous and ferric ions in aqueous solution have bedeviled precise modeling of geochemical systems involving these species for some time, e.g. see Nordstrom (1984) and Reardon and Beckie (1987). Recent work on the solubility of siderite (Preis and Gamsjager, 2002) provides support for the validity of the properties of Fe^{2+} in the survey by Parker and Khodakovskii (1995). We therefore incorporated revised properties of Fe^{2+} and Fe^{3+} in SUPCRT92 and recalculated the solubility products of all participating minerals whose thermodynamic properties were derived from calorimetry. These included chlorite, daphnite, pyrite, goethite and hematite, as well as appropriate corrections to the solubility products of siderite and ankerite.

Calculations for generating the HKF EoS parameters for Fe^{2+} and Fe^{3+} were conducted with the aid of an Excel spreadsheet. In order to independently check the correctness of the transcribed equations, calculations were repeated for both species using the $\overline{C}^0_{P_r,T_r}$ and $\overline{S}^0_{P_r,T_r}$ cited by Shock et al. (1997). The derived values for the Born coefficient, ω_{P_r,T_r}, and c_1, which depends on the value of , did not match closely with those cited by Shock et al. (1997). Agreement was obtained only if r_{e,j,P_r,T_r} for each species was assumed to have a discrete value of 2.64 and 3.56 $\overset{o}{A}$, respectively. Furthermore, instead of using

$$\alpha_z = 71.5|Z_j|,$$

the original intercepts were used for the regressed data for $\Delta\overline{S}^o_{n,j} - Z_j\Delta\overline{S}^o_{s,H^{+abs}}$ (cal mol^{-1} K^{-1}) for aqueous species with Z_j = 1, 2 or 3 against $Z_j^2/r_{e,j}$ ($\overset{o}{A}$), where α_z = 72, 141 and 211 cal mol^{-1} K^{-1}, respectively. After appropriate substitution, close agreement was obtained, as shown in Table C13.

Table C13. Comparison of HKF EoS Parameters for Fe^{2+} and Fe^{3+}

Parameter	Shock et al. (1997)		This Work	
	Fe^{2+}	Fe^{3+}	Fe^{2+}	Fe^{3+}
c_1, cal mol^{-1} K^{-1}	14.7860	19.0459	14.7863	19.0462
c_2, cal K mol^{-1} x 10^{-4}	-4.6437	-6.8233	-4.6438	-6.8234
ω_{P_r,T_r}, cal mol^{-1} x 10^{-5}	1.4382	2.5812	1.4382	2.5812

In the present study, the calculated values for r_{e,j,P_r,T_r} given in Shock and Helgeson (1988) were used in the calculation of ω_{P_r,T_r} and c1. The a1 through a4 HKF equation of state parameters for Fe2+ and Fe3+ (Shock et al., 1997) were retained. The thermodynamic properties for both species are summarized in Table C14.

Table C14. Thermodynamic Parameters for Fe^{2+} and Fe^{3+}

Parameter	Fe^{2+}	Fe^{3+}
$\Delta\overline{G}^0_{f,P_r,T_r}$, cal mol^{-1}	-21637	-3891
$\Delta\overline{H}^0_{f,P_r,T_r}$, cal mol^{-1}	-21511	-11711
$S^0_{P_r,T_r}$, cal mol^{-1} K^{-1}	-24.283	-66.539
$\overline{C}^0_{P_r,T_r}$, cal mol^{-1} K^{-1}	-7.37	-18.85
$\overline{V}^o$, cm^3 mol^{-1}	-22.2	-37.0
a_1, cal mol^{-1}xbar^{-1}	-0.7867	-2.4256
a_2, cal mol^{-1}	-9.6869	-13.6961
a_3, cal K mol^{-1}xbar^{-1}	9.5479	11.1141
a_4, cal K mol^{-1}	-2.3780	-2.2127
c_1, cal mol^{-1} K^{-1}	15.2738	20.0173
c_2, cal K mol^{-1} x 10^{-4}	-4.5359	-6.8743
ω_{P_r,T_r}, cal mol^{-1} x 10^{-5}	1.4574	2.6358

C5.2 Iron Minerals

Iron minerals are a particularly important factor in modeling the behavior of hazardous constituents in shallow groundwaters. Not only do they participate in buffering the redox potential of the system, but also by virtue of their adsorptive properties and their commonly very large specific surface areas (i.e., very fine crystallinity), they can be a significant reservoir of adsorbed hazardous constituents. Iron minerals of interest to the problem at hand consist of three broad classes: (1) Ferric/ferrous oxides and oxy-hydroxides, (2) silicates containing ferrous iron, particularly phyllites, and (3) sulfides. The recent literature was reviewed, and crystallographic

and thermodynamic data compiled, for a number of pertinent minerals, and the resulting information is summarized in Tables C15 and C16.

Because the point of zero charge (PZC) of ferric oxides/hydroxides lies in the pH range of circa 8.5, these minerals are generally positively charged over the pH range of the majority of shallow potable groundwaters, and would remain so upon intrusion of high-pressure CO_2. The net positive charge attracts and adsorbs anionic species from solution. They are therefore likely to adsorb oxy-anionic species of As(III), As(V), Sb(III), Sb(V) and Se(II), Se(IV) and Se(VI). Other potential adsorbents include negatively charged sulfide and selenide complexes of heavy metals (Appendix D and Appendix E), although it is quite likely that sulfide and selenide species could be destabilized through oxidation of S(-II) and Se(-II) to higher oxidation states, depending on the overall equilibrium state.

Two of the minerals listed are of particular interest: ferrihydrite and green rust. Ferrihydrite, a nanocrystalline or amorphous hydroxide, traditionally given the formula, $Fe(OH)_3$, is commonly used in laboratory studies to quantify adsorption of charged or molecular species from solution, e.g., see the classic text on surface complexation modeling by Dzomback and Morel (1990). Until very recently, the structure of ferrihydrite was unknown. Indeed, it was commonly believed that ferrihydrite might consist of two separate phases (on the basis of X-ray diffraction studies) and thus referred to as "2-line" and "6-line" ferrihydrite. All this changed in 2007, when Michel and his co-workers (Michel et al., 2007a, 2007b; Penn, 2007), using advanced X-ray diffraction techniques and sophisticated methods of interpretation, were able to resolve the structure unambiguously as being isostructural with akdalaite, $Al_{10}O_{14}(OH)_2$, more commonly known as tohdite (Shpanov et al., 1970; Tilley and Eggleton, 1994). With ferrihydrite now known to possess the stoichiometry, $Al_{10}O_{14}(OH)_2$, calorimetric data for a series of ferrihydrites with differing specific surface areas and quantities of adsorbed water, (Majzlan et al., 2004) could be re-evaluated, and the enthalpy of formation, $\Delta H^0_{f,P_r,T_r}$, for coarsely crystalline ferrihydrite calculated. Figure C3 shows a plot of measured $\Delta H^0_{f,P_r,T_r}$, vs. excess water, extrapolated to zero excess water, the value at the intersection of the regression trendline with the y-axis being $\Delta H^0_{f,P_r,T_r}$ reported in Table C16.

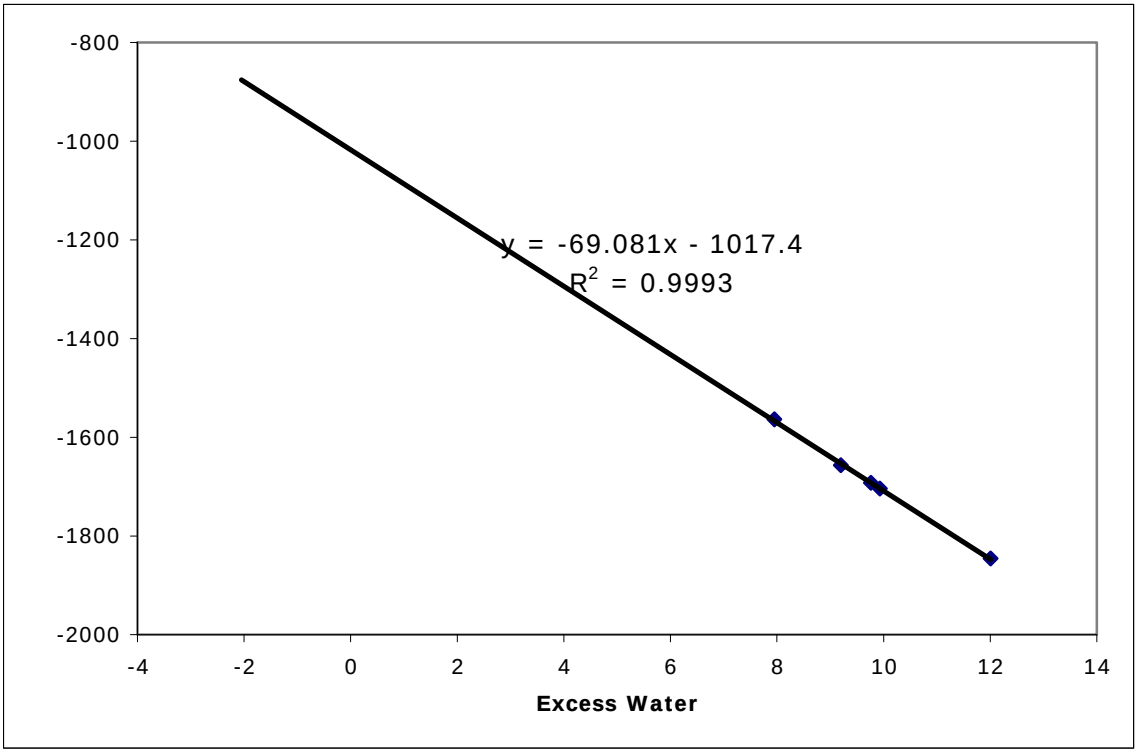

Fig. C3. Correlation of calorimetrically determined enthalpy of formation of ferrihydrite samples in relation to their content of excess water. Data from Majzlan et al. (2004)

Green rust is a mineral consisting of stacked layers separated by coordinated water molecules of Fe(II) tri-octahedral sheets, one of the basic building blocks of phyllosilicates or clay minerals. The octahedral sheet can be either of the gibbsite type, $Al_2(OH)_6$, or of the brucite type $Mg_3(OH)_6$, representing di- and tri-octahedral sheets, respectively. Partial *in situ* oxidation of the Fe(II) to Fe(III) in a tri-octahedral sheet causes the octahedral sheet to develop a net positive charge, which is satisfied through the uptake of anionic species in the inter-layer sites. The charge-balancing anion is commonly SO4-2, but any of the oxy-anionic species of As(III), As(V), Sb(III), Sb(V), Se(II), Se(IV) and Se(VI), as well as HCO3- or CO3-2 can also occupy sites. Because of their structural similarity to clays, such phases are sometimes referred to as "anionic" clays in distinction to regular "cationic" clays. In Tables C15 and C16, the properties of a typical idealized anionic clay, green rust, is given, where the stoichiometry of the waters of hydration were adjusted to fully saturate the interlayer positions.

Table C15. Crystallographic Properties of Iron Minerals, excluding those containing Arsenic

Name	Formula	Cell Constants							Space Group	Reference
		a_o (Å)	b_o (Å)	c_o (Å)	α	β	γ	Z		
Goethite	FeO(OH)	4.5979	9.9510	3.0178	90	90	90	4	Pbnm	Yang et al. (2006)
Lepidocrocite	FeO(OH)	12.4	3.87	3.06	90	90	90	4	Bbmm	Wyckoff (1963)
Hematite2	Fe_2O_3	5.038		13.772				6	R-3c	Blake et al. (1966)
Maghemite	Fe_2O_3	8.33			90	90	90	12	Fd3m	Pecharroman et al. (1995)
E-Fe_2O_3	Fe_2O_3	5.095	8.789	9.437	90	90	90	8	$Pna2_1$	Tronc et al. (1998)
Marcasite	FeS_2	4.4446	5.4246	3.3864	90	90	90	2	Pnnm	Rieder et al. (2007)
Pyrite	FeS_2	5.4166			90	90	90	4	Pa3	Bayliss (1977)
Ferrihydrite	$Fe_{10}O_{14}(OH)_2$	~5.95		~9.06	90	90	90	1	$P6_3mc$	Michel et al. (2007)
Mackinawite	FeS	3.6735		5.0328	90	90	90	2	P4/nmm	Lennie et al. (1995)
Greigite	Fe_3S_4	9.876			90	90	90	8	Fd3m	Skinner et al. (1964)
Schwertmannite	$Fe(III)_{16}O_{16}(OH)_{12}(SO_4)_2$	10.66(4)		6.04(1)	90	90	90	1	P4/m (?)	Bigham et al. (1994)
Green Rust	$Fe(II)_4Fe(III)_2(OH)(SO_4).8H_2O$	5.524		11.011				0.5	$P\bar{3}m1$	Simon et al. (2003)

Table C16. Thermodynamic Properties of Iron Phases (Excluding those containing Arsenic and Carbon)

Mineral name	Formula	$\Delta G^0_{f,P_r,T_r}$ cal mol^{-1}	Ref	$\Delta H^0_{f,P_r,T_r}$ cal mol^{-1}	Ref	$S^0_{P_r,T_r}$ cal mol^{-1} K^{-1}	Ref	$V^0_{P_r,T_r}$ cm^3 mol^{-1}	Ref	$C^0_{P_r}$ cal mol^{-1} K^{-1}			Ref
										a	$b\times10^3$	$c\times10^{-5}$	
Goethite	FeO(OH)	-117065	5			14.269	4	19.866	9	0.289	55.736	0.750	4
Lepidocrocite	FeO(OH)	-114747	5			15.559	4	22.108	10	14.283	14.465	-1.847	4
Hematite	Fe_2O_3	178155	20	-197720		20.940	20	30.384	11	23.490	18.600	-3.550	20
Maghemite	Fe_2O_3	-173972	5			22.228	4	29.007	12	25.526	15.557	-4.508	4
E-Fe_2O_3	Fe_2O_3	-171558	6	-190727	6	22.228	6	31.811	13	25.526	15.557	-4.508	21
Marcasite	FeS_2	-37859	23	-40511	23	12.882	23	24.584	26	17.880	1.320	-3.050	25
Pyrite	FeS_2	-38293	20	-41000	20	12.650	20	23.926	14	17.880	1.320	-3.050	20
Ferrihydrite	$Fe_{10}O_{14}(OH)_2$	-799730	6,7	-1017400		101.800	3	167.280	15	124.560	93.000	-17.800	2
Mackinawite	FeS	-22300	22	-21900	24	15.4	24	20.450	16	12.000	-	-	24
FeS,am	FeS	-21300	22	-20900	24	15.4	24			12.000	-	-	24
Greigite	Fe_3S_4	-69400	22	-70300	24	47.1	24	72.511	17	42.000	-	-	24
Schwertmannite	$Fe(III)_{16}O_{16}(OH)_{12}(SO_4)_2.12H_2O$	-2661124	6,8	-		254.950	3	413.335	18	395.855	136.399	-26.000	2
Green Rust	$Fe(II)_4Fe(III)_2(OH)(SO_4).8H_2O$	-1330280	1	-		192.870	3	350.466	19	220.065	20.6806	-5.370	2

Notes 1. Hansen et al. (1994), modified to account for $8H_2O$ of water; 2. Calculated using the summation of oxide components; 3. Calculated using the procedure described by Holland (1989). This work. 4. Majzlan et al. (2003a); 5. Majzlan et al. (2003b); 6. Majzlan et al. (2004); 7. Data reinterpreted. See text; 8. Modified to account for $12H_2O$ of water; 9. Yang et al. (2006); 10. Wyckoff (1963); 11. Blake et al. (1966); 12. Pecharroman et al. (1995); 13. Tronc et al. (1998); 14. Bayliss (1977); 15. Michel et al. (2007); 16. Lennie et al. (1995); 17. Skinner et al. (1964); 18. Bigham et al. (1994); 19. Simon et al. (2003); 20. As reported by Helgeson et al. (1978); 21. Assumed the same as for maghemite, in conformity with assumption for $S^0_{P_r,T_r}$ by Majzlan et al. (2004); 22. Berner (1967); 23. Robie and Hemingway (1995); 24. Estimates provided by Anderko and Shuler (1998); 25. Assumed to be equivalent to pyrite; 26. Rieder et al. (2007)

C6. Carbonates

An essential requirement for reactive transport simulations involving CO_2 sequestration is the need for accurate thermodynamic data of participating carbonate phases. Recent studies have revealed respectively the possible existence of substantial errors in the Gibbs free energy of formation of magnesite and dolomite (Rock et al., 2001). Furthermore, the experimental consistency of siderite solubility data (Preis and Gamsjager, 2002) has been recently established, and by inference, validated the thermodynamic data for ferrous and ferric ions recommended by Parker and Khodakovskii (1995). These modifications also require a redetermination of the thermodynamic properties of the ankerite solid solution utilized in earlier work (Xu et al., 2003).

The thermodynamic properties of dolomite and magnesite were calculated, using the Gibbs free energy values determined by Rock et al. (2001), together with the respective entropies provided by Robie and Hemingway (1995). These, together with entropy data for end-member ankerite, $CaFe(CO3)_2$, from Holland and Powell (1998), and the properties of siderite from Preis and Gamsjager (2002) as well as calcite from the SUPCRT92 database, were used to calculate the properties of end-member ankerite and the ankerite ideal binary solid solution with the limiting composition: $CaMg_{0.3}Fe_{0.7}CO_3)_2$, using the lattice energy calculations reported by Chai and Navrotsky (1996). The thermodynamic data for carbonates, either calculated as described above or utilized in the present study, are summarized in Table C17.

Table C17. Thermodynamic Properties of Selected Carbonate Minerals

Mineral name	Formula	$\Delta G^0_{f,P_r,T_r}$ cal mol^{-1}	Ref	$\Delta H^0_{f,P_r,T_r}$ cal mol^{-1}	Ref	$S^0_{P_r,T_r}$ cal mol^{-1} K^{-1}	Ref	$V^0_{P_r,T_r}$ cm^3 mol^{-1}	Ref	$C^0_{P_r}$ cal mol^{-1} K^{-1}			Ref
										a	$b\times10^3$	$c\times10^{-5}$	
Calcite	$CaCO_3$	-269880	1,2	-288552	1,2	22.150	1	36.934	1	24.980	5.240	-6.200	1
Magnesite	$MgCO_3$	-240791	4	-260816	6	15.557	3	28.018	1	19.731	12.539	-4.748	1
Siderite	$FeCO_3$	-162261	5	-179732	5	22.818	5	29.378	1	11.630	26.800	0.000	1
Dolomite	$CaMg(CO_3)_2$	-513341	4	-552250	6	37.089	3	64.365	1	41.557	23.952	-9.884	1
Ankerite	$Ca(Mg_{0.3}Fe_{0.7})(CO_3)_2$	-457553	6	-494243	6	43.627	6	65.594	6	46.070	18.011	-10.437	6

Notes 1. Helgeson et al. (1978); 2. Helgeson (1990), Gibbs free energies calculated from solubility data reported by Plummer and Busenberg (1982) [Enthalpies adjusted for the correction in the Gibbs free energy]; 3. Robie and Hemingway (1995); 4. Rock et al. (2001); 5. Preis and Gamsjager (2002); 6. This work. See text.

C7. Chlorite

In prior simulations (Xu et al., 2002), chlorite was represented as a 1:1 mixture of clinochlore and daphnite. The solubility products used were those derived originally from the thermodynamic evaluation of phase equilibria by Helgeson et al. (1987). More recent and comprehensive evaluations, e.g., those conducted by Holland and Powell (1998), indicate that a revision in the solubility products of clinochlore and daphnite is called for. Although clinochlore and daphnite are only minor components in most sedimentary arenaceous rocks, a revision is justified because they compete with secondary carbonates for magnesium and ferrous iron, and they can buffer the redox potential when coexisting with pyrite.

The calculated thermodynamic properties for clinochlore and daphnite were taken from Holland and Powell (1998). The thermodynamic properties of chlorite, $Mg_{2.5}Fe_{2.5}Al_2[Si_3O_{10}](OH)_8$, were calculated assuming ideal solid solution between the end members. These properties were entered into the SUPCRT92 database, and the chlorite solubility products were calculated. The thermodynamic data used in the current study are given in Table C18.

Table C18. Thermodynamic Parameters for Chlorite Minerals

Parameter	Units	Clinochlore $Mg_5Al_2[Si_3O_{10}](OH)_8$	Ref.	Daphnite $Fe_5Al_2[Si_3O_{10}](OH)_8$	Ref.	Chlorite $Mg_{2.5}Fe_{2.5}Al_2[Si_3O_{10}](OH)_8$	Ref.
$\Delta G^0_{f,P_r,T_r}$	cal mol^{-1}	-1975051	4	-1562107	4	-1768992	4
$\Delta H^0_{f,P_r,T_r}$	cal mol^{-1}	-2134288	1	-1709845	1	-1922066	4
$S^0_{P_r,T_r}$,	cal mol^{-1} K^{-1}	98.112	1	130.258	1	115.562	4
$V^0_{P_r,T_r}$,	cm^3 mol^{-1}	207.110	1	213.420	1	210.260	4
$C^0_{P_r}$ Coefficients							
a	cal mol^{-1} K^{-1}	166.500	2	176.210	2	171.355	3
$b\times10^3$		42.100	2	43.760	2	42.930	3
$c\times10^{-5}$		-37.470	2	-33.820	2	-35.645	3

Notes 1. Holland and Powell (1998); 2. Helgeson et al. (1978); 3. Interpolated between clinochlore and daphnite; 4. This work.

C8. Miscellaneous

The mineral hemimorphite proved to be an important thermodynamic control on the concentration of dissolved zinc in oxidized groundwaters, and might also control in part the

concentration in reducing groundwaters containing sphalerite. Thermodynamic data are extremely limited, essentially confined to preliminary study by McPhail et al. (2006), who measured the solubility at 50 and 80ºC and computed the solubility product at the same temperatures. In Figure C4, a linear extrapolation of Log K(hemimorphite) is made as a function of reciprocal temperature to 25ºC. The resulting value, Log K = 23.981, incorporated in the EQ3/6 and TOUGHREACT thermodynamic databases.

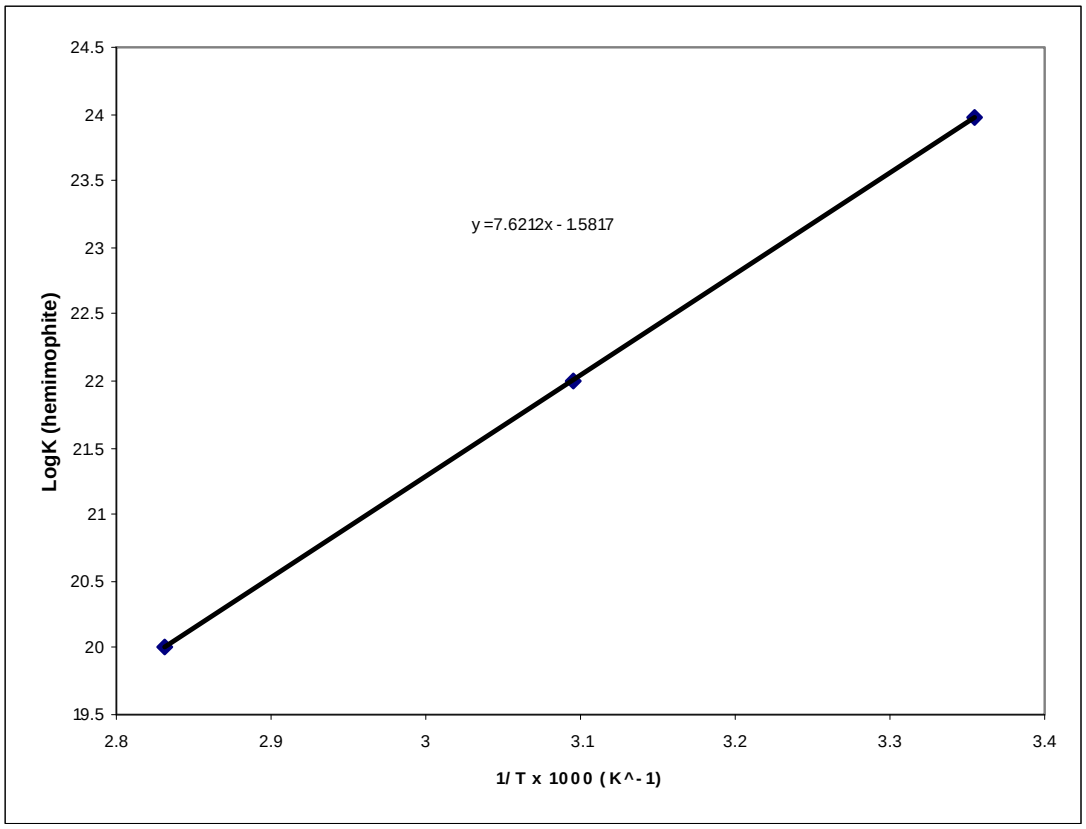

Fig. C4. A linear extrapolation of the solubility product of hemimorphite to 25ºC with reciprocal temperature, 1/K. Data from McPhail et al. (2006).

Appendix D:
Solubilities of Sulfides of Cadmium, Mercury, Lead and Zinc at 25°C

D1. Background

The present study requires the calculation of the solubilities of minerals containing hazardous inorganic constituents as essential components under conditions that might occur in shallow potable water aquifers. The majority of the more than 38,000 groundwaters downloaded from the NWIS database and evaluated during the course of the present investigation appear to be reducing, and it is probable that pyrite or some other iron sulfide is present. Under such conditions, log P_{H2S} (bar) ranges from approximately –8 to –10, and among the minerals potentially controlling the solubility of Zn, Cd, Hg and Pb in solution are the corresponding sulfides sphalerite, greenockite, cinnabar and galena. The divalent cations of these four elements can also complex with sulfide species (HS^- and H_2S) and selenide species (HSe^- and H_2Se) in solution, potentially enhancing both sulfide and selenide mineral solubilities.

Among the sulfide and presumably selenide complexes in solution at equilibrium with the respective sulfides and selenide minerals are a series of neutral species of undefined stoichiometry, but circumstantial evidence suggests that they may be oligomers possessing formulas Me_xS_x, where x = 1,2,3,4… Experimental evidence also suggests that these species are predominant under equilibrium conditions with the metal sulfide mineral, and thus must be taken into account if thermochemical data pertaining to sulfide mineral equilibria with respect to the aqueous phase are to be reconciled and mineral sulfide equilibria are to be modeled realistically. For this reason, both the identities of sulfide complexes of the cations of and their respective dissociation constants needed to be incorporated in the thermodynamic databases of both EQ3/6 and TOUGHREACT codes. Without such data, simulations of reactive chemical transport of these metals in the presence of elevated P_{CO2} would not be representative.

In this appendix, we review the issues concerning identification of the relevant sulfide complexes, and how their dissociation constants, K_{diss}, relate to the solubility products, K_s, of the

corresponding sulfide minerals, using galena (PbS) as an example. In the companion Appendix E, we review issues relating to the corresponding selenide complexes. Then, on the basis of a literature review, we choose and describe internally consistent data sets of sulfide and selenide species dissociation constants and associated solubility products for incorporation in the EQ3/6 and TOUGHREACT databases.

The procedure followed was first to generate a correlation plot for Log $K(MeS)_s$ and Log $K(MeS)_{aq}$ for sulfide species (Me = metal). A correlation plot was also generated comparing solid phase sulfide and selenide species, together with Hg sulfide and selenide species (Appendix E). The latter plot then allowed prediction of unknown neutral and charged selenide complexes of the relevant heavy metals based upon the identities and literature values of aqueous sulfide complexes of Cd, Hg Pb and Zn, and neutral sulfide complexes estimated from the first correlation plot. The resulting data were then incorporated in the EQ3/6 database and EQ3 run using a representative groundwater composition, based on the distribution of heavy metal concentrations observed in NWIS groundwaters, taking into account possible analytical artifacts. Alternative hypotheses were tested until a satisfactory reconciliation of all parameters was achieved, and the calculated saturation indices for those heavy metal sulfides and selenides expected to be present, based on observed modes of occurrence, fell close to 0, i.e., within ± 2 units. The interdependence of all parameters tightly restricted the ranges over which each parameter could be varied independently. Therefore, although the results presented in this appendix and the following Appendix E leave room for refinement, it is expected that such refinements would not alter substantially the findings presented in this report.

D2. Issues

In both the EQ3/6 and TOUGHREACT codes, mineral solubility is defined in terms of a dissolution equation relating the mineral to the "basis" species in solution, e.g., for galena, the reaction is:

$$PbS + H^+ = Pb^{+2} + HS^- \qquad (D1)$$

where Pb^{+2} and HS^- are the basis species in this case, and the solubility product is defined as

$$K_s = \frac{[Pb^{+2}][HS^-]}{[PbS][H^+]} \quad \text{(D2)}$$

with [ ] denoting thermodynamic activities. The activity of the solid phase is unity for a pure substance. In addition, knowledge of the potential complexes of the basis species in solution is required. In the example given, these complexes modify the total aqueous concentrations of both Pb^{+2} and HS^-. Elsewhere in this report (Section 3.5), we show that apart from sulfide and selenide complexes, other significant aqueous species affecting the saturation concentration of Pb in shallow potable aquifers include $PbCO_3(aq)$, $PbOH^+$, $Pb(CO_3)_2^{-2}$ and $PbCl^+$ in addition to Pb^{+2}. The corresponding dissociation constants for these complexes are also defined in terms of the basis species. At higher sulfide concentrations, not normally encountered in potable water aquifers, significant quantities of sulfide complexes with Pb^{+2} might also form, e.g., $Pb(HS)_2(aq)$ and $Pb(HS)_3^-$, as shown by Hemley (1953) and Giordano and Barnes (1979). It is under such conditions that experiments are sometimes conducted, either to measure mineral sulfide solubilities, or to characterize the dissociation constants of relevant sulfide complexes in solution, where the saturated mineral is used as a thermodynamic control.

The solubility product, defined by Eqn. (D2) can also be calculated from independent knowledge of the Gibbs free energies, $\Delta G^0_{f,P_r,T_r}$, of the participating species, just as the measured solubility can be used to calculate $\Delta G^0_{f,P_r,T_r}$ of the solid phase. $\Delta G^0_{f,P_r,T_r}$ of the solid phase or mineral can be obtained from calorimetric, thermo- or electro-chemical, or phase equilibrium studies. For example, $\Delta G^0_{f,P_r,T_r}$(galena) has been determined from electrochemical (galvanic cell) measurements (Kiukkola and Wagner, 1957), thermochemical measurements (Stubbles and Birchenall, 1959), and by high-temperature oxide-melt solution calorimetry (Deore and Navrotsky, 2006). In Table D1, the solubility products of four sulfide phases are cross-compared with the corresponding values of $\Delta G^0_{f,P_r,T_r}$ derived from various property measurements.

Table D1. Gibbs Free Energy of Formation and Solubility Products of Selected Trace Metal Sulfides

Source	Notes	ZnS (sphalerite)		CdS (greenockite)		HgS (cinnabar)		PbS (galena)	
		$\Delta G^0_{f,P_r,T_r}$ kcal mol^{-1}	$\log K_s$ at 25°C	$\Delta G^0_{f,P_r,T_r}$ kcal mol^{-1}	$\log K_s$ at 25°C	$\Delta G^0_{f,P_r,T_r}$ kcal mol^{-1}	$\log K_s$ at 25°C	$\Delta G^0_{f,P_r,T_r}$ kcal mol^{-1}	$\log K_s$ at 25°C
Robie and Hemingway (1995)		**-47.71±0.36**	-11.27±0.26	**-34.92±0.31**	-14.09±0.23	**-9.73±0.65**	-38.08±0.48	**-23.14±0.48**	-14.87±0.35
Deore and Navrotsky (2006)		**-48.29±0.96**	-11.69±0.70	**-34.73±0.99**	-13.95±0.73			**-23.09±1.04**	-14.84±0.76
Dyrssen and Kremling (1990)		-47.25±0.93 -44.55±0.44	**-10.93±0.68** **-8.95±0.32** (wurtzite)	-33.97±0.93	**-13.39±0.68**	-10.85±0.55 -11.67±0.55	**-38.9±0.4** (black) **-39.5±0.4** (red)	-21.91±0.78	**-13.97±0.57**
Daskalakis and Helz (1993)		-48.005	**-11.482**						
Shea and Helz (1989)								-20.29	**-12.78**
Daskalakis and Helz (1992)				-33.93±0.35	**-13.36±0.26**				
Paquette and Helz (1995)						-7.85	**-36.7**		

Notes:

1. Bold face values are given or derived directly from the source reference.
2. $\log K_s$ is in reference to the dissolution reaction: MS(s) + H^+ = M^{+2} + HS^-. Where M is Zn, Cd, Hg or Pb.
3. $\Delta G^0_{f,P_r,T_r}$ values referenced to Deore and Navrotsky (2006) were calculated from $\Delta H^0_{f,P_r,T_r}$ assuming that $T\Delta S^0_{f,P_r}$ corresponds to that assumed by Robie and Hemingway (1995)
4. Uncertainties in derived values are calculated assuming no uncertainty in values of the aqueous species, and are therefore minimum values.
5. $\Delta G^0_{f,P_r,T_r}$ values given by Robie and Hemingway (1995) are from Schaefer and Gokcen (1982) for sphalerite; Adami and King (1964) for greenockite; Pankratz and King (1987) for cinnabar; Stubbles and Birchenall (1959) and Kiukkola and Wagner (1957) for galena.

Most $\Delta G^0_{f,P_r,T_r}$ values calculated from solubility measurements in Table D1 are less negative than those determined using other methods. However, the thermochemical determinations summarized by Robie and Hemingway (1995) agree with the calorimetric determinations by Deore and Navrotsky (2006) within experimental error. Thus, it appears that solubility measurements may not adequately describe the speciation or thermodynamic behavior of the system. Tossell (1999), in his paper advocating *ab initio* quantum mechanical methods to calculate the stabilities of Hg complexes in solution, summarized the serious limitations of corresponding experimental methods:

(1) "The speciation models are often ambiguous, with different researchers obtaining apparently different sets of species and formation constants."
(2) "… chemical components[,] whose activities or concentrations cannot be varied experimentally[,] are indeterminable, e.g., the participation of water in such species cannot be determined in aqueous solution. Spectral studies could, in principle, determine which species were present, as well as their concentrations if relative spectral intensities for the different species could be assessed. However, in many cases the species concentrations are so low that no usable spectra can be obtained."

Tossell, in particular, singled out Hg sulfide speciation as a case in point, but such problems also extend to the other metal sulfide species considered in this appendix. In a more recent review, Rickard and Luther (2006) reiterate the limitations of current experimental methods, noting that "One of the astonishing things the uninitiated reader will discover… is the large number of sulfide complexes that have been proposed and even modeled with little or no evidence to support their existence in the first place." Given the current uncertainties in the literature, it is prudent to regard the following analysis with caution, even though the results presented are sufficiently robust to allow their use in the evaluation of thermodynamic controls on heavy metal solubilities in potable groundwaters.

Explanations for the mismatch between the calculated and measured aqueous solubilities of chalcogenides in general has been accommodated by postulating equilibrium with a neutral species in solution, possessing the same stoichiometry as that of the solid phase, thus:

$$MeS(s) = MeS(aq) \qquad (D3)$$

where [MeS(aq)]/[MeS(s)] = K_{int}, the intrinsic solubility product (Dyrssen, 1985, 1988; Dyrssen and Wedborg, 1989, 1991; Benoit et al., 1999; Rickard, 2006). The precise nature of the complex is unknown. Dyrssen and Wedborg (1991) argue convincingly that it could not be a monomer. They point out that HgS(aq) is equivalent to the hydrated species, Hg(OH)(SH)(aq), and one cannot be distinguished from the other using conventional speciation studies (Tossell, 1999; *vide supra*), i.e.,

$$HgS(aq) + H_2O = Hg(OH)(SH)(aq);\ \text{Log K is undetermined.} \quad \text{(D4)}$$

Although the two stoichiometries cannot be distinguished in solubility studies, it is reasonable to assume that the complex is composed of $(OH)^-$ and SH^- rather than S^{-2} and H_2O. Dyrssen and Wedborg (1991) showed, using correspondence plots for Hg stability constants, and theory relating to calculation of mixed ligand complexes (Anfalt et al., 1968), that the calculated dissociation constant for the latter species is

$$Hg(OH)(SH)(aq) + H^+ = HgSH^+ + H_2O;\ \text{Log K} = +3.4. \quad \text{(D5)}$$

This dissociation constant is comparable with those of other hydrolytic reactions, e.g.,

$$Hg(OH)2(aq) + H^+ = HgOH^+ + H_2O;\ \text{Log K} = +2.6 \quad \text{(D6)}$$

$$HgCl(OH)(aq) + H^+ = HgCl^+ + H_2O;\ \text{Log K} = +3.1 \quad \text{(D7)}$$

However, the measured dissociation constant for

$$HgS(aq) + H^+ = HgSH^+;\ \text{Log K} \approx -8.9 \quad \text{(D8)}$$

differs by approximately 12 log units. Similar incompatibilities were also recognized in computing the intrinsic solubility products for ZnS and CdS, based respectively on the work by Gubeli and Ste-Marie (1967) and by Ste-Marie et al. (1964).

More recently, Rickard (2006), in studying the solubility of mackinawite (FeS), also identified and determined experimentally the intrinsic solubility product for this mineral

$$FeS(\text{mackinawite}) = FeS(aq) \quad \text{(D9)}$$

He concluded that the FeS(aq) complex was an oligomer, citing earlier electrochemical studies by Buffle et al. (1988) and Theberge and Luther (1997) of FeS(aq) in equilibrium with amorphous FeS. The exact stoichiometry of FeS(aq) is uncertain. Theberge and Luther (1997) concluded that polymerization occurred as a two-step process, in which the octahedrally coordinated hex-aquo Fe^{+2} ion reacted with HS^-, thus,

$$Fe(H_2O)_6^{+2} + HS^- = Fe(H_2O)_5(HS)^+ + H_2O \quad \text{(D10)}$$

followed by polymerization to form a trimer

$$3Fe(H_2O)_5(HS)^+ + 3HS^- = Fe_3S_3(H_2O)_6(aq) + 3H_2S + 9H_2O \quad \text{(D11)}$$

Implicit in this reaction is a transformation from octahedral to tetrahedral coordination in the ferrous ion, and formation of a closed six-member ring representing a basic building block in both cubic FeS and in mackinawite (where Fe(II) is tetrahedrally coordinated in both). However, it should be noted that the probability of the simultaneous reaction of six aqueous entities is extremely unlikely. Therefore Eqn. D11 must be considered merely a summary reaction that incorporates a series of intermediate steps, including the formation of a precursor dimer, and that it is probable that equilibria between the postulated trimer and its precursors is established at saturation with respect to the solid phase.

A further comparison can be made with sulfide complexes of As and Sb, which form ionizing oligomeric complexes $H_3As_3S_6(aq)$ and $H_2Sb_2S_4(aq)$, respectively. These complexes apparently form to the exclusion of simpler monomeric species. Although both As and Sb are present in these complexes in the (III) state, a parallelism with the formation of postulated analogous oligomers with divalent (II) metals is suggested by the limited experimental evidence regarding the formation of $Fe_3S_3(H_2O)_6(aq)$.

Similar arguments could be advanced in defining polymer formation with respect to Zn and Cd sulfide complexes, where both Zn and Cd are tetrahedrally coordinated in both isostructural polymorphs, i.e., cubic sphalerite and hawleyite, and hexagonal wurtzite and greenockite, respectively. Hg(II) is tetrahedrally coordinated in cubic met cinnabar, but in cinnabar it is octahedrally coordinated. A similar coordination change is also noted in the sulfides of manganese (MnS). For example, in alabandite, Mn is octahedrally coordinated, whereas in

ramsbergite, it is tetrahedrally coordinated in an anti-wurtzite structure. Thus, it is unclear whether Hg(II) aqueous sulfide complexes are octahedrally or tetrahedrally coordinated. Because metacinnabar is less stable than cinnabar, it is more likely that Hg(II) is octahedrally coordinated in sulfide complexes. With octahedral coordination, as also occurs with respect to Pb in galena, it would be logical to infer that the aqueous complexes are dimers, $Me_2S_2(H_2O)_x(aq)$, or tetramers, $Me_4S_4(H_2O)_y(aq)$ (where Me is either Hg or Pb), forming single or double four-member rings respectively. However, Rozen et al. (2003), on the basis of mass spectrometry of freeze dried aqueous samples, indicated that the species had the formula Pb_3S_3.

D3. Estimation of the Dissociation Constants of Neutral Sulfide Complexes

If a comparison is made between the sulfide solubility products and the dissociation constants of the neutral oligomeric sulfide complexes for the four metals for which data are available (Fe(II), Zn(II), Cd(II) and Hg(II)), conventionally written as

$$MeS(s) + H^+ = Me^{+2} + HS^- \quad (D12)$$

and

$$1/x[Me_xS_x(aq) + xH^+ = xMe^{+2} + xHS^-]$$

i.e.,

$$MeS(aq) + H^+ = Me^{+2} + HS^- \quad (D13)$$

where x is probably 2, 3 or 4 (depending on the nature of the metal ligand), a surprisingly good correlation between the two is obtained, as shown by regression trendline (a) in Figure D1.

Table D2. A Comparison between the Solubility Product of a Sulfide Mineral, and the Apparent Dissociation Constant of the Corresponding Neutral Species in Solution at 25°C

Mineral	**Composition**	**Log K $(MeS)_s$**	**Source**	**Log K $(MeS_{)aq}$**	**Source**
Mackinawite	FeS	-3.50	1	+2.20	1
Sphalerite	ZnS	-11.27	2	-5.63	3
Greenockite	CdS	-14.09	2	-7.24	3
Cinnabar	HgS	-38.08	2	-28.08	4
Galena	PbS	-14.87	2	-8.06	5

Notes:

1. Rickard (2006)
2. Derived from thermochemical data provided by Robie and Hemingway (1995)
3. Dyrssen and Wedborg (1991) from data reported by Gubeli and Ste-Marie (1967) and Ste-Marie et al. (1964)
4. Dyrssen and Wedborg (1989)
5. This work.

However, despite the impressive correlation between Log $K(MeS)_s$ and Log $K(MeS)_{aq}$, incorporation of the dissociation constants of neutral sulfide and corresponding selenide complexes in the database did not satisfactorily resolve the unrealistic predictions of sulfide and selenide mineral saturation indices in NWIS potable waters.

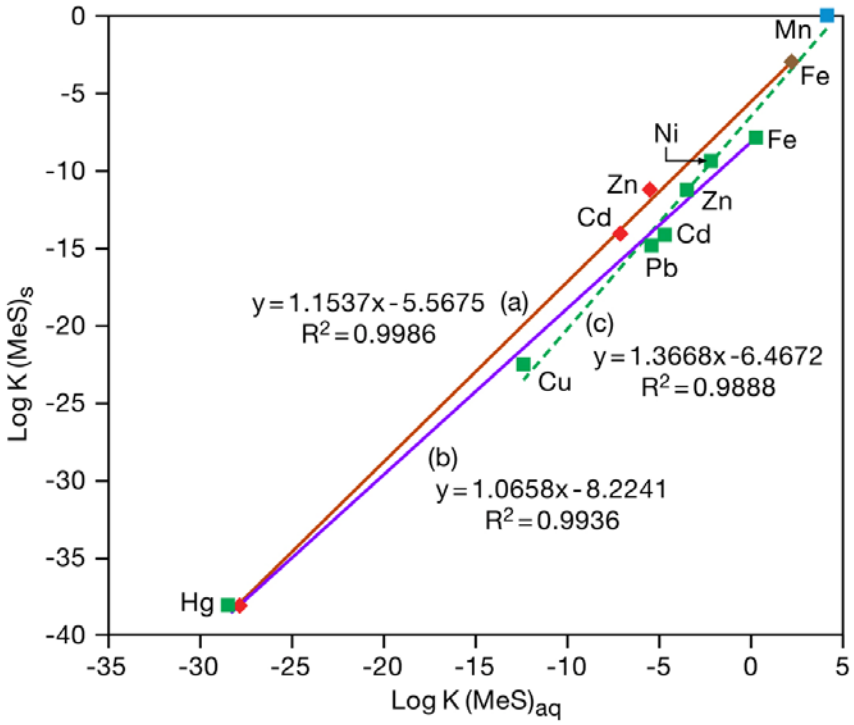

Fig. D1. Correlation between the solubility product of a sulfide mineral, and the apparent dissociation constant of the corresponding neutral species in solution at 25°C.

An alternative approach at estimating the correlation between the solid and aqueous sulfides and selenide species was then examined. Dyrssen (1988), citing earlier work (Dyrssen, 1985), attempted to correlate the stability constants for sulfide complexes of a range of heavy and transition metals with the corresponding aqueous extraction constants, K_{ex}, for dithizone dissolved in carbon tetrachloride:

$$Me^{n+} + n\ H_2Dz(org) = Me(Hdz)_n(org) + n\ H^+ \qquad (D14)$$

He used studies by Ste-Marie et al. (1964) and Gubeli and Ste-Marie (1967) on Cd and Zn sulfide complexes, respectively, to calibrate the correlation equation:

$$\log K(MeS)_{aq} = -0.95 \log K_{ex} - A \qquad (D15)$$

where $\log K(MeS)_{aq}$ represents Eq. (D13), and $A = 3.02$. Table D3 summarizes the respective parameters cited in Dyrssen (1988, 1989) together with other data used in the current analysis. When the data given in Table D3 are plotted, both Pb and Zn deviated significantly from the

observed trend, although the data for Cd and Hg yielded satisfactory results for both sulfides and selenides (greenockite and cadmoselite, and cinnabar and tiemannite, respectively). Arbitrary revisions of the values of $\log K(MeS)_{aq}$ to –5.5 and –3.5 for Pb and Zn, respectively, not only achieved better coherence with $\log K(MeS)_{aq}$ values for other metals, but also yielded satisfactory saturation indices for galena, clausthalite, and sphalerite for the representative NWIS potable waters. The resulting regression trendline (b) is shown in Figure D1. For the purposes of this study, the $\log K(MeS)_{aq}$ values for Cd, Pb and Zn summarized in Table D3 with the noted corrections for Pb and Zn are provisionally accepted for use in the databases for EQ3/6 and TOUGHREACT, and applied for the prediction of neutral selenide complexes of Cd, Pb and Zn. With respect to Hg, the value for $\log K(MeS)_{aq}$ is chosen that was used in the construction of regression trendline (a) in Figure D1. This value is based on the intrinsic solubility product for HgS estimated by Dyrssen and Wedborg (1991), $\log K_{\text{int}} - 10$. This value gave somewhat better agreement with postulated saturation with respect to cinnabar in NWIS potable waters.

Table D3. Estimated Values of Neutral Sulfide Stability Constants, $K(MeS)_{aq}$, based on the Corresponding Dithizone Extraction Constants, K_{ex}, compared with Sulfide Solubility Products, $K(MeS)_S$

Metal	$\log K_{ex}$ [1]	$\log K(MeS)_{aq}$ [4]	$K(MeS)_S$
Mn(II)	-5.4	+2.1	-0.02
Fe(II)	-3.4	+0.2	-7.90[3]
Ni(II)	-0.8	-2.3	-9.50[3]
Cu(II)	10.0	-12.5	-22.50[3]
Zn(II)	2.0	-4.9[2]	-11.27
Cd(II)	1.9	-4.8	-14.09
Hg(II)	26.8	-28.5	-38.08
Pb(II)	0.4	-3.4[2]	-14.87

Notes:

1. As cited by Dyrssen (1988) from Irving (1977)
2. Adjusted to -3.5, -5.5 respectively for Zn and Pb. See text.
3. Values cited by Dyrssen (1989). All other values for Log K(MeS), as given in Table D1.
4. As cited by Dyrssen (1989)

Despite the satisfactory agreement achieved through the correlation of $\log K(MeS)_{aq}$ with $\log K_{ex}$ proposed and used by Dyrssen in several of his papers, agreement is poor with respect to FeS from the more recent work of Rickard (2006). Furthermore, if $\log K(MeS)_{aq}$ for Mn is correlated with $\log K(MeS)_s$ using $\Delta G^0_{f,P_r,T_r}$ by Robie and Hemingway (1995), correlation of Mn(II) with

the rest of the data set is also poor. Arbitrary correction of $\log K(MnS)_{aq}$ to account for the relative difference between $\log K_{ex}$ for Fe(II) and Mn(II) does, however, restore a more restricted correlation, if the outlier for Hg is excluded and the values obtained by Rickard (2006) replace those given by Dyrssen (1989), as indicated for regression trendline (c) in Figure D1. Clearly, such speculations do little to improve the rigor of the analysis and are included merely to suggest further lines of inquiry.

In the following paragraphs, we briefly describe the data sets for sulfide complexes of Zn, Cd, Hg and Pb with reference to the compilations in Tables D1 and D2, and to selected speciation models for each metal in the published literature.

D4. Greenockite (CdS)

The data for $\Delta G^0_{f,P_r,T_r}$ for greenockite indicates ≈ 1.00 kcal/mol discrepancy between those values obtained by calorimetry or thermochemical measurements, and those derived from solubility measurements. Davies-Colley et al. (1985), in comparing measured Cd^{+2} concentrations in relatively high $p(HS^-)$ anaerobic estuarine sediments with those based on the assumed presence of greenockite precipitate, found that greenockite solubility was exceeded by about one log unit. The basis for their calculations was $\Delta G^0_{f,P_r,T_r}$(greenockite) = -34.8 kcal/mol from an earlier publication by Robie et al (1978), which is similar to that given by Robie and Hemingway (1995). The sulfide speciation used in their calculations also differs from that given by Daskalakis and Helz (1992). Davies-Colley et al. (1985) attribute the discrepancy to the possible presence of polysulfide complexes, or that the solubility-controlling sulfide was a poorly ordered CdS phase. Given the inherent uncertainties in the interpretation of field data, and lack of knowledge as to the nature of immobile Cd^{+2} in the sediments, i.e., whether as a discrete solid phase, or in solid solution with sphalerite, or whether adsorbed on thiol groups on organic material, it is perhaps surprising that such good agreement was obtained. Table D4 presents the internally consistent data set for Cd sulfide complexes from the study by Daskalakis and Helz (1993). The Log K value for the dissociation of CdS(aq) is derived from data presented by Dyrssen and Wedborg (1991) as summarized in Table D4, and the solubility product is based on thermochemical data given by Robie and Hemingway (1995).

Table D4. Complexes of HS- with Cd+2 after data by Daskalakis and Helz (1993), CdS(aq) after Dyrssen and Wedborg (1991) and Greenockite Solubility Product derived from Thermochemical Data given by Robie and Hemingway (1995), all at 25°C

Reaction	Log K
$Cd(HS)_3^- = Cd^{+2} + 3\ HS^-$	-16.44
$Cd(HS)_4^{-2} = Cd^{+2} + 4\ HS^-$	-17.89
$Cd(OH)_2(HS)^- + 2\ H^+ = Cd^{+2} + 3\ HS^- + 2\ H_2O$	+2.47
$CdS(aq) + H^+ = Cd^{+2} + HS^-$	-4.8
$CdS(greenockite) + H^+ = Cd^{+2} + HS^-$	-14.09

D5. Cinnabar (HgS)

Discrepancies in derived values of $\Delta G^0_{f,P_r,T_r}$(cinnabar) are substantial, ranging over almost 4 kcal/mol, and the corresponding values of log K_s show a range of approximately 3 units (Table D1). The uncertainty is aggravated by questions concerning the identification of Hg sulfide species in solution and the magnitudes of their dissociation constants, *c.f.* Tossell (1999). We have identified and calculated the relevant dissociation constants using the results presented by Schwarzenbach and Widmer (1963) and modified by Paquette and Helz (1997) on the solubility of red cinnabar in buffered 0.7 M KCl solution at 25°C. In order to retrieve the dissociation constants from their data, a solubility product for cinnabar must be assumed, and the first dissociation constant for H_2S(aq) specified. The solubility product derived from $\Delta G^0_{f,P_r,T_r}$(cinnabar), given by Robie and Hemingway (1995) (Log K = -38.08), and the dissociation constant for H_2S(aq) specified by Bessinger (2000) (Log K = -6.980) were used in the calculation. Corrections to zero ionic strength standard state conditions were not applied, as activity coefficient corrections are self compensating for two of the three species, and correction for the third would not be very accurate given the limited amount of available data. Results of the calculations are presented in Table D5.

Table D5. Complexes of HS- with Hg+2 after data by Schwartzenbach and Widmer (1963) and modified by Paquette and Helz (1997), HgS(aq) after Dyrssen and Wedborg (1989) and Cinnabar Solubility Product derived from Thermochemical Data given by Robie and Hemingway (1995), all at 25°C

Reaction	**Log K**
$Hg(HS)_2(aq) = Hg^{+2} + 2\ HS^-$	-39.65
$HgS(HS)^- + H^+ = Hg^{+2} + 2\ HS^-$	-32.67
$HgS_2^{-2} + 2\ H^+ = Hg^{+2} + 2\ HS^-$	-23.91
$HgS(aq) + H^+ = Hg^{+2} + HS^-$	-28.08
$HgS(cinnabar) + H^+ = Hg^{+2} + HS^-$	-38.08

Incorporation of the neutral HgS(aq) complex in the analysis is essential, as use of the cited solubility product for cinnabar and the dissociation constants of the Hg sulfide aqueous species alone would predict unrealistically low Hg concentrations in groundwaters. This difficulty was also recognized by Benoit et al. (1999), who incorporated HgS(aq) in their study of dissolved mercury behavior in sediments from the Florida Everglades and the Patuxent River Estuary of Maryland. Our value for Log K = -28.08 can be compared with their value of –26.5 and their assumed Log solubility product of cinnabar of –37.0 instead of –38.08 used here. Correction for the higher solubility product would yield a value of –27.6, which is in substantial agreement with our own value for this parameter.

It should be noted that Benoit et al. (1999) did not assume that dissolved mercury had at any time equilibrated with cinnabar as a discrete solid phase in the sediments under study. Rather, they considered cinnabar as a potential solid solution component in a matrix of iron monosulfide or pyrite. Their treatment was analogous to their assumption that Hg^{+2} complexes with a "solid solution" of thiol groups on organic material. However, although saturation with respect to cinnabar was never observed, their model predicted quite well the variability of Hg concentration in sediment pore waters with dissolved sulfide concentration, and was independently correlated with expected methyl mercury speciation. Their model could therefore be considered a reasonable paradigm for testing the correlation of aqueous Hg concentrations with cinnabar saturation, even extrapolated to the much lower dissolved sulfide concentrations expected in potable groundwaters.

D6. Galena (PbS)

Issues relating to the solubility of galena in groundwaters are discussed at somewhat greater length than in previous sections for other sulfide minerals, because of its relevance in this project. Reported values for the solubility product of galena (PbS), as defined by the dissolution equation

$$PbS + H^{+} = Pb^{+2} + HS^{-} \qquad (D16)$$

vary over two orders of magnitude, as shown in Table D1. The value utilized by Wang and Jaffe (2004) in their simulations of galena dissolution in shallow potable water aquifers was taken from a database compiled for the MINTEQ code (Felmy et al., 1984; Hydrogeologic and Allison Geoscience Consultants, 1999), but also used by the PHREEQ-C code (Parkhurst and Appelo, 1999). This database (minteq.v4.dat 85 2005-02-02 16:13:00Z dlpark), gives a $\log K_s$ value of -13.97 at 25°C for the above reaction. The source of this value can be traced to Dyrssen and Kremling (1990), who in a study of trace metal behavior in anoxic Baltic waters attempted to derive Log K_s values for a number of metal sulfides. The values presented are based on the product of two reaction constants, K_1, and K_{sO}, representing respectively the reactions:

$$H^{+} + S^{2-} = HS^{-} \qquad (D17)$$

and

$$M_aS_b(s) = aM^{n+} + bS^{2-} \qquad (D18)$$

where M represents the metal with charge +2 (n=2, a=b=1) or +1 (n=1, a=2, b=1). Because of the high degree of uncertainty in K_2 (published values of $\log K_1$ vary between 12 and 18.51±0.56), the authors utilized published values of K_{sO} together with corresponding values for K_1 from the original sources to calculate the product (K_1 K_{sO}) for the reaction:

$$M_aS_b(s) + bH^{+} = aM^{n+} + bHS^{-} \qquad (D19)$$

which for galena is represented by the reaction described in Eq. (D1).

The PHREEQ-C code is also capable of using another database used by the WATEQ code (wateq4f.dat 431 2005-08-23 17:29:36Z dlpark). This database gives a $\log K_s = -12.780$ at 25°C for the reaction in Eq. (D1), which is 1.2 log units higher than the value cited by Dyrssen and Kremling (1990). The cited value is a correction by Shea and Helz (1989) for Pb complexation by chloride ion based on results from an earlier experimental study by Uhler and Helz (1984). The latter investigators enhanced the solubility of galena through Pb^{+2} complexing with ethylene diamine acetic acid (EDTA) in a solution of disodium EDTA and 0.1 M NaCl. The technique overcomes a serious difficulty in analyzing solution compositions where one or more of the principal chemical components are at or below the detection limits of available analytical methods, yet introduces additional complexity and uncertainty associated with the thermodynamic parameters needed to interpret the behavior of the chelating agents used in the study. The technique is also dependent on knowledge of the identities and thermodynamic properties of lead sulfide complexes in solution. Finally, derivation of K_s depends on appropriate ionic strength corrections to permit extrapolation to standard state conditions. Despite much progress in making such corrections, current techniques still leave room for improvement.

The EQ3/6 code (Wolery et al., 1992) used in this study utilizes another thermodynamic database data0.ymp.R4 (downloaded N.S. 3/3/05 DTN: SN0410T0510404.002), which was qualified for use under the Yucca Mountain Project and supported by the U.S. Department of Energy. The database gives a $\log K_s = -14.8544$ at 25°C for the reaction in Eq. (1), which is 0.95 log units lower than the value cited by Dyrssen and Kremling (1990). This value was calculated from the thermodynamic properties for galena reported in Helgeson et al. (1978), who in turn cited Mills (1974). The reported value for $\Delta G^0_{f,P_r,T_r}$, -23.12 kcal/mol, is close to the -23.14 kcal/mol reported by Robie and Hemingway (1995), which is in turn based on thermochemical measurements by Stubbles and Birchenall (1959). Stubbles and Birchenall (1959) conducted thermochemical measurements on lead/lead sulfide equilibria between 585 and 920ºC, necessitating a substantial extrapolation to the 25ºC reference temperature. Uhler and Helz (1984), in referring to the same work, note further that, apart from the magnitude of the extrapolation, additional uncertainties arise from phase changes in both elemental lead and sulfur between 585 and 25ºC, contributing

to an overall uncertainty in excess of 2 kcal/mol in $\Delta G^0_{f,P_r,T_r}$(galena), or > ±1.5 units in $LogK_s$. However, this uncertainty is much larger than that estimated by Robie and Hemingway (1995) for the same data (Table D1).

Barrett and Anderson (1982, 1988) measured the solubility of both galena and sphalerite (ZnS) at temperatures between ≈25 and 95ºC in sodium chloride brines ranging between 3 and 5 M. These investigators then independently calculated the solubilities of galena and sphalerite to 300ºC in sodium chloride brines between 1 and 5 M at pH = 4 and $m_{s(r)} = 0.001$. They also compared their measured solubilities with the independently calculated values, and obtained a reasonable match (calculated values were between 0.3 and 0.7 log units too low). Their calculations were based on $logK_s$(galena) cited in Bowers et al. (1985), which appears to have been derived from the sources cited by Helgeson et al. (1976). The calculations took into account Pb chloride complexing quantified by Seward (1984) and Ruaya and Seward (1986), and activity coefficient (γ_i) corrections were based on the b-dot method described by Helgeson (1969). Barrett and Anderson (1988) contrasted their results using the $logK_s$(galena) cited in Bowers et al. (1985) with those obtained by Uhler and Helz (1984), noting the almost two order of magnitude discrepancy, and pointing out that using the latter would result in calculated solubilities much greater than their measured values. However, they also note that their own experimental measurements are subject to errors arising from inadequate corrections for liquid junction potentials in their measurements of pH. Furthermore, their calculated solubilities are subject to the same uncertainties associated with corrections for chloride and sulfide complexing by Pb^{+2}. Inadequate corrections for activity coefficients of the ionic species in high-ionic strength sodium chloride brines are also of concern to the derived results of Uhler and Helz (1984), as noted above.

In conclusion, the discrepancies between K_s(galena) derived from solubility measurements and those based on thermochemical measurements are so significant that meaningful predictions of galena solubility in shallow potable groundwaters at ambient temperatures are not possible unless the conflict is resolved. This conflict appears to be caused by failure to account for the presence of the oligomeric complex PbS(aq), by analogy with the resolved discrepancies between measured and calculated sphalerite, greenockite and cinnabar solubilities, given in the preceding sections. We therefore adopted the strategy described in the introduction of this

Appendix, i.e., Log K_s(galena) would be based on thermochemical data, and the dissociation constant of PbS(aq) would be estimated based on the regression analysis between Log $K(MeS)_s$ and $\log K(MeS)_{aq}$ illustrated in Figure D1. The value chosen for Log (PbS)aq, -5.5, is consistent, within the overall uncertainty of the analysis, with independent measurements by Rozan et al. (2003), who give a value for $LogK_{THERM} = 16.83 \pm 0.33$ for PbS(aq), 36.38±0.47 for Pb_2S_2(aq), 62.49±0.61 for Pb_3S_3, and 135.6±0.8 for Pb_6S_6, respectively, for the reaction

$$xPb^{+2} + xS^{-2} = Pb_xS_x(aq) \qquad (D20)$$

Normalizing these $LogK_{THERM}$ values to unit stoichiometry, as well as recasting the reaction in terms of HS^- and as a dissociation yields $LogK(PbS)(aq)$ = +0.31, -1.67, -4.46 and -6.08, respectively. Bearing in mind that Rozan et al. (2003), on the basis of mass spectrometry determinations of freeze-dried samples, found that the species Pb_3S_3(aq) appeared to predominate, it can be seen that there is reasonable agreement between the normalized log K value for that species, -4.46, and the value of –5.5 provisionally accepted for the average of all oligomeric PbS(aq) species. Note, however, that the foregoing calculation assumed $LogK_{THERM} = 16.83 \pm 0.33$ for the reaction

$$S^{-2} + H^+ = HS^- \qquad (D21)$$

Values ranging from 18.51 ± 0.56 (Schoonen and Barnes, 1988) to ≈ 14.0 have been reported in the literature (Dyrssen, 1989). Therefore the uncertainties in the derived values for $LogK(PbS)(aq)$ from Rozan et al. (2003) are substantial.

The dissociation constants for other Pb sulfide species in solution are derived from the association constants reported by Giordano and Barnes (1979) at 30°C, which are essentially identical to earlier work by Hemley (1953) at 25°C, and were treated analogously to those for Hg sulfide complexes using solubility products derived from $\Delta G^0_{f,P_r,T_r}$ (galena), given by Robie and Hemingway (1995) (Log K = -14.870), and the dissociation constant for H_2S(aq) specified by Bessinger (2000) (Log K = -6.98). The relevant data are given in Table D6.

Table D6. Complexes of HS- with Pb^{+2} after data by Giordano and Barnes (1979), PbS(aq) computed in this Appendix, and Galena Solubility Product derived from Thermochemical Data given by Robie and Hemingway (1995), all at 25°C

Reaction	Log K
$Pb(HS)_2(aq) = Pb^{+2} + 2\ HS^-$	-14.058
$Pb(HS)_3^- = Pb^{+2} + 3\ HS^-$	-15.258
$PbS(aq) + H^+ = Pb^{+2} + HS^-$	-5.5
$PbS(galena) + H^+ = Pb^{+2} + HS^-$	-14.870

D7. Sphalerite (ZnS)

Excellent agreement is obtained for the calculated values of $\Delta G^0_{f,P_r,T_r}$ for sphalerite derived from the data by Daskalakis and Helz (1993), Deore and Navrotsky (2006), and Schaefer and Gokcen (1982). The value of $\Delta G^0_{f,P_r,T_r}$ derived from data by Dyrssen and Kremling (1990) is somewhat higher, but otherwise in reasonable agreement. Barrett and Anderson (1988), using a value of Log K_s for sphalerite of –11.40, found that the measured solubility at 25°C was 0.4 log units higher in 3 *M* NaCl brine, i.e., Log Ks ≈ –11.00, consistent with that of –10.93 reported by Dyrssen and Kremling (1990). Bearing in mind that Barrett and Anderson's measured solubility measurements are difficult to interpret, as noted further in Section D5 of this appendix, the consistency of their results with other solubility measurements, and with thermochemical determinations of $\Delta G^0_{f,P_r,T_r}$ suggests that reasonable confidence can be attached to the internally consistent dataset for sulfide speciation and log K_s for sphalerite, obtained by Daskalakis and Helz (1992), and presented in Table D7, below. An uncertainty of about ± 1 log unit is expected in predictions of sphalerite saturation indices. The Log K value for the dissociation of ZnS(aq) is derived from data presented by Dyrssen and Wedborg (1991) as summarized in Table D7, and the solubility product is based on thermochemical data given by Robie and Hemingway (1995).

Table D7. Complexes of HS- with Zn+2 after data by Daskalakis and Helz (1992), ZnS(aq) after Dyrssen and Wedborg (1991) and Sphalerite Solubility Product derived from Thermochemical Data given by Robie and Hemingway (1995), all at 25°C

Reaction	Log K
$Zn(HS)_4^{-2} = Zn^{+2} + 4\ HS-$	-14.640
$ZnS(HS)^- + H^+ = Zn^{+2} + 2\ HS^-$	-6.842
$ZnS(HS)_2^{-2} + H^+ = Zn^{+2} + 3\ HS^-$	-6.152
$ZnS(aq) + H^+ = Zn^{+2} + HS^-$	-3.5
$ZnS(sphalerite) + H^+ = Zn^{+2} + HS$	-11.27

D8. Recommendations for Further Refinement of Thermodynamic Data Pertinent to Sulfide and Selenide Solubilities

A pragmatic approach was taken in the foregoing analysis to reconcile thermochemical data for solid sulfide and selenide minerals with measured aqueous solubilities, and further reconcile field measurements of heavy metal concentrations in potable groundwaters with postulated saturation indices for the sulfide and selenide minerals. For reasons of time, an in-depth analysis was not conducted.

In their review of metal sulfide complexes and clusters, Rickard and Luther (2006) cite studies suggesting the existence of several other charged and uncharged oligomeric metal clusters of Fe, Cu, Zn, Cd, Ag, Au, Pb and Hg. Supporting evidence is for the most part equivocal, and further definitive studies are needed to resolve current ambiguities regarding cluster stoichiometries and stabilities. The same authors also cite recent work by Zhang and Millero (1994), Al-Farawati and van den Berg (1999), and Rozan et al. (2003) all of whom used various voltammetric techniques to identify sulfide speciation in marine waters for a range of elements, including those of interest in this report. Unfortunately, time did not permit evaluation of their findings in relation to the work presented here. However, some preliminary checks indicate consistency with the results presented in this appendix. Further analysis of the data presented in these and other papers cited by Rickard and Luther (2006), as well as the work of ongoing investigations must be conducted as part of a broader strategy to refine the geochemical model for potable waters.

The following are aspects of the problem that were insufficiently addressed.

(1) The aqueous species MeS(aq) represents a distribution of oligomeric complexes, which would vary depending on both intensive and extensive variables in the system. Molecular dynamic modeling and/or spectroscopic studies will be required to establish the identities of species and their thermodynamic relations. Recent studies of sulfide complexation in marine waters using voltammetric methods (*vide supra*) must be reviewed and compared with earlier work cited in this appendix and account taken of oligomeric species where their thermodynamic properties have been quantified.

(2) Experimental measurements of sulfide and selenide mineral solubilities were conducted in a variety of supporting electrolytes. Ionic strength corrections to the activities of species were not uniformly treated or evaluated.

(3) Corrections to mineral solubilities by assuming the presence of neutral sulfide complexes were made without a re-evaluation of the raw data. Consequently, corrections to the distributions between species such as MeS(aq) and species such as $Me(HS)_2(aq)$ were accounted for in a consistent manner.

(4) Improved correlation plots between sulfide and selenide species might be achieved by consideration of experimental work on selenide complexes of Mn and Ag by Mehra and Gubeli (1970a and 1970c).

(5) Changes in the distributions of sulfide and selenide minerals as a function of heavy metal abundances and redox potential in natural systems should be examined further to establish the phase relations of selenide minerals in relation to corresponding sulfide minerals in potable water aquifers.

(6) In making tests of the validity of calculated saturation indices of sulfides and selenides in potable groundwaters, the effect of temperature was ignored. Potable groundwater temperatures could range down to as low as 5ºC, which could shift the calculated saturation index by as much as one log unit. In situ temperatures of the studied NWIS potable waters should be retrieved and temperature corrections made for the dissociation constants of all participating aqueous species and all participating mineral solubility products.

(7) The stability constants of mixed sulfide/selenide complexes should be estimated and incorporated in the thermodynamic database used in the evaluation of saturation indices of sulfide and selenide minerals in potable groundwaters.

Appendix E:
Dissociation Constants for Selenides of Arsenic, Cadmium, Mercury, Lead and Antimony

E1. Background

During the course of the current investigation, it became apparent that the concentrations of several hazardous inorganic constituents in groundwaters could be controlled by their selenides, rather than their corresponding sulfides. This supposition is reinforced by field evidence for the existence of clausthalite (PbSe) occurring in over 50% of coals in the Appalachian Basin and 10% outside the Basin (Finkelman, 1981), and the occasional occurrence of tiemannite (HgSe) in coal (Tewalt et al., 2001). Furthermore, both cadmoselite (CdSe) and antimonselite (Sb_2Se_3) have been observed in sedimentary formations under conditions that might suggest their presence in potable groundwater aquifers.

Preliminary calculations of the saturation indices for metal (Me) selenides, using solubility products based on thermodynamic data in reported in the published literature, for the reaction:

$$Me_aSe_b(s) + bH^+ = aMe^{n+} + bHSe^- \qquad (E1)$$

also indicated that all of the cited selenides would be extremely supersaturated in those groundwaters from the NWIS database reporting Se together with Cd, Hg, Pb or Sb. In fact, the calculated saturation indices were so unrealistically high (≈ +5 to +10), that it was clear that that the thermodynamic database used in the EQ3/6 code for the evaluation was seriously deficient and failed to represent the behavior of selenide mineral solubilities. this deficiency would compromise the objective of the study to correctly identify and quantify the thermodynamic controls governing the concentrations of the cited constituents in potable groundwaters.

An obvious omission in the Data0.dat database were the selenide complex dissociation constants corresponding to those of sulfide complexes with As^{+3}, Cd^{+2}, Hg^{+2}, Pb^{+2}, Sb^{+3}, Zn^{+2} and Fe^{+2}, which were incorporated on the basis of a review of their dissociation constants given in Appendix D. A perusal of the literature lead to the discovery of two reviews regarding the solubilities of selenium phases and selenium speciation in solution, Cowan (1988) and Seby et al.

(2001). Both reviews cited the same sources regarding selenide complexation with metal ions, which were limited to studies by Mehra and Gubeli (1970a,b, 1971) concerning Ag, Mn and Hg selenide complexation. No other studies relating to selenide complexation with metals in aqueous solution appear to have been published since date of the latest review. Only the information by Mehra and Gubeli (1971) concerning Hg selenide complexing is relevant to the current study. In the following paragraphs, we discuss how the available data were adapted to account for selenide complexation with As^{+3}, Cd^{+2}, Hg^{+2}, Pb^{+3}, Sb^{+3}, Zn^{+2} and Fe^{+2}.

E2. Hg Selenide Complexes in Aqueous Solution

Mehra and Gubeli (1971) independently determined the Log solubility product of HgSe, according to the reaction

$$HgSe(s) = Hg^{+2} + Se^{-2} \quad \text{(E2)}$$

to be –56.6±0.2. Assuming Log K for the reaction

$$HSe- = H^{+} + Se^{-2} \quad \text{(E3)}$$

is –14.0±1.0 (Seby et al., 2001), it follows that Log K(tiemannite) for the reaction

$$HgSe(s) + H^{+} = Hg^{+2} + HSe^{-} \quad \text{(E4)}$$

is –42.6. This value is comparable with the value, -43.27, calculated from thermochemical data reported by Vaughan and Craig (1978), and the same as that reported by Mills (1974), which has been incorporated in the EQ3/6 Data0.dat, V4.2.YMP, and accepted in this report.

The data presented by Mehra and Gubeli (1971) also allows calculation of the intrinsic solubility of HgS (tiemannite) under acid conditions (i.e., at pH < 3.8), as their measurements were conducted in 1 Normal $NaClO_4$ solution assumed to be in equilibrium with solid HgSe. Assuming the reaction

$$HgSe(s) = HgSe(aq) \quad \text{(E5)}$$

is in equilibrium with a total log concentration of Hg = -7.83, as reported by Mehra and Gubeli (1971), then $LogK_{\text{int}} = -7.83$. Given that Log K(tiemannite) for the reaction (E2) is –43.27, the dissociation constant for the reaction

$$HgSe(aq) + H^{+} = Hg^{+2} + HSe^{-} \qquad (E6)$$

is $LogKHgSe(aq) = -35.43$.

Instead of postulating the existence of HgSe(aq) as a proxy for oligomeric species in solution, Mehra and Gubeli (1971) assumed the existence of a complex of the form Hg(HSe)(OH)(aq), which, through subtraction of one H_2O, assumes the same form as HgSe(aq). The two species are therefore equivalent, and it would be impossible to discriminate between the two on the basis of the experimental results alone.

Mehra and Gubeli (1971) also postulated the existence of two other species in solution, $Hg(HSe)_2(OH)^-$ and $Hg(HSe)_2(OH)_2^{-2}$, which are equivalent to $HgSe(HSe)^-$ and $HgSe_2^{-2}$, respectively.

Association constants for each were defined thus:

$$\beta_{21} = \frac{\left[Hg(HSe)_2(OH)^{-}\right]}{\left[Hg^{+2}\right]\left[HSe^{-}\right]^2\left[OH^{-}\right]} = \frac{\left[Hg_{complex}\right]K_2^2}{K_{sp} \bullet K_W\left[H^{+}\right]\left[Se^{-2}\right]} \qquad (E7)$$

where $Log\beta_{21} = 52.8 \pm 0.3$, and

$$\beta_{22} = \frac{\left[Hg(HSe)_2(OH)_2^{-2}\right]}{\left[Hg^{+2}\right]\left[HSe^{-}\right]^2\left[OH^{-}\right]^2} = \frac{\left[Hg_{tot}\right]K_2^2}{K_{sp} \bullet K_W{}^2\left[Se^{-2}\right]} \qquad (E8)$$

where $Log\beta_{22} = 61.0 \pm 0.3$. The value of the second ionization constant, $LogK_2 = -11.6$, had been determined earlier by Mehra and Gubeli (1970a). $LogK_{sp} = 56.6 \pm 0.2$ is the solubility product of HgSe, tacitly assumed to be tiemannite. It was also calculated from the value reported for the reaction

$$HgSe = Hg^{+2} + Se^{-2} \qquad (E9)$$

Log K_w is the dissociation constant for water, which was not specified. The log K_2 value is inconsistent with that recommended by Seby et al. (2001) (log K_2 = -14.0 ±1.0), the elevated value being possibly caused by inadvertent contamination by polyselenides generated through oxidation of HSe^- by traces of oxygen (Wood, 1958), even though the study was conducted under an inert atmosphere of nitrogen. Because a 1 M $NaClO_4$ solution was used as the supporting electrolyte, a more realistic value for log K_W is –13.7, a value used by Dyrssen (1988) in correcting for the ionic strength of seawater. Finally, $LogK_{sp}$ differs from that calculated from thermochemical data by approximately 0.7 log unit, which might be due to a finer crystallinity of the material used in their solubility determinations. Because this discrepancy is within the overall uncertainty of the calculations, no correction was applied to account for this difference. Application of appropriate corrections yields revised values for the dissociation constants, which are presented in Table E1.

Table E1. Dissociation Constants of Complexes of HSe- with Hg+2 and the Tiemannite Solubility Product in 1 M NaClO4 Solution at 25ºC (after data by Mehra and Gubeli, 1971).

Reaction	**Log K**
$HgSe(aq) + H^+ = Hg^{+2} + HSe^-$	-35.43
$HgSe(HSe)^- + H^+ = Hg^{+2} + 2\ HSe^-$	-39.10
$HgSe_2^{-2} + 2\ H^+ = Hg^{+2} + 2\ HSe^-$	-28.80
$HgSe(s) + H^+ = Hg^{+2} + HSe^-$	-43.27

Corrections were inconsistently applied to the reported dissociation constants for $HgSe(HSe)^-$ and $HgSe_2^{-2}$. The corrected value for Log K($HgSe(HSe)^-$) should have been –34.30. However, had this value been used instead of that cited in Table E1, the calculated Log K values of selenide complexes given in this appendix would have differed very little from those actually calculated and used in subsequent calculations in this report. With respect specifically to Hg selenide complexation, the differences are also inconsequential, and well within the overall uncertainty of the model results, as the $HgSe(HSe)^-$ species is always less than 10^{-6} % of the total Hg in groundwaters. It should also be noted that the corrections are preliminary, and that a more careful re-evaluation of the findings by Mehra and Gubeli (1971) is required. Furthermore, it is very probable that both $HgSe(HSe)^-$ and $HgSe_2^{-2}$ species are oligomeric, and this should also be taken into account in re-interpreting the data.

E3. Estimated Dissociation Constants of Selenide Complexes of As^{+3}, Cd^{+2}, Pb^{+3}, Sb^{+3}, Zn^{+2} and Fe^{+2} in Aqueous Solution

In the absence of any information pertaining to selenide complexes for Cd^{+2}, Pb^{+3}, Sb^{+3}, Zn^{+2} and Fe^{+2}, values of their dissociation constants were estimated from those of the corresponding sulfide complexes using a linear correlation equation in which were plotted solubility product pairs for metal sulfide and selenide minerals, offset values of the dissociation constant pairs for $H_2S(aq)$ and $H_2Se(aq)$, and HS^- and HSe^-, respectively, and dissociation constants for Hg sulfide and selenide aqueous complex pairs. The respective sulfide and selenide solubility products are calculated from thermochemical, electrochemical or calorimetric data, but not solubility measurements. The data used in this plot and the sources of information are given in Table E2. Note that metacinnabar and marcasite solubility products are used in place of those for cinnabar and pyrite, respectively, in order to compare sulfide and selenide minerals with identical crystal structures.

The initial regression was conducted on all species together, correcting $H_2Se(aq)$ and HSe^- species values by an identical amount sufficient to bring them into colinearity with the trend of the solid phases. The aqueous species were then restored to the original values, and then the value for the dissociation constant for HSe^- adjusted to ensure that the slopes of the two lines were identical. This entailed adjustment from Log $K(HSe^-) = -14.0 \pm 1.0$ to -14.67, which is well within the uncertainty of value assigned by (Seby et al., 2001). The reason for the offset is not known, but might be ascribed to the effects of solvation and electrostriction in the aqueous phase acting on these molecular and ionic species, e.g., see Shock and Helgeson (1988). The analysis and interpretation is quite speculative, and may be modified upon more comprehensive review.

Table E2. Log K Values of Sulfide and Selenide Aqueous Complex and Mineral Pairs used to generate a Correlation Plot to Estimate the Dissociation Constants of Unknown Metal Selenide Complexes and Effective Solubility Products of Metal Selenides

Sulfide			Selenide		
Species	**Log K**	**Source**	**Species**	**Log K**	**Source**
Aqueous					
HS^-	-16.52	1	HSe^-	-14.67	4
H_2S(aq)	-6.99	2	H_2Se(aq)	-3.81	5
HgS(aq)	-28.08	3	HgSe(aq)	-35.43	4
$HgS(HS)^-$	-32.67	3	$HgSe(HSe)^-$	-39.10	4
HgS_2^{-2}	-23.91	3	$HgSe_2^{-2}$	-28.80	4
Mineral					
CdS (greenockite)	-14.09	6	Cadmoselite	-18.89	7
Meta-cinnabar	-37.78	6	Tiemannite	-43.27	7
Galena	-14.87	6	Clausthalite	-20.78	7
Marcasite	-49.87	7	Ferroselite	-55.45	7

Notes:

1. Dyrssen (1988); 2. Bessinger (2000); 3. Paquette and Helz (1997); 4. this appendix; 5. Seby et al. (2001); 6. Appendix D; 7. EQ3/6 Data0.ymp.R4 database (see Appendix D)

The data summarized in Table E2 and results from the regression analysis are shown in Figure E1. The linear regression of the data is good ($R^2 = 0.993$). The regression equation was used to estimate the dissociation constants for the corresponding selenide analogues of sulfide complexes of As(III), Cd(II), Pb(II), Sb(III), Zn(II) and Fe(II), which are presented in Table E3. These estimated values were incorporated in the thermodynamic databases of EQ3/6 and TOUGHREACT, and used to calculate saturation indices of selenide minerals in those NWIS groundwaters that were analyzed for Se.

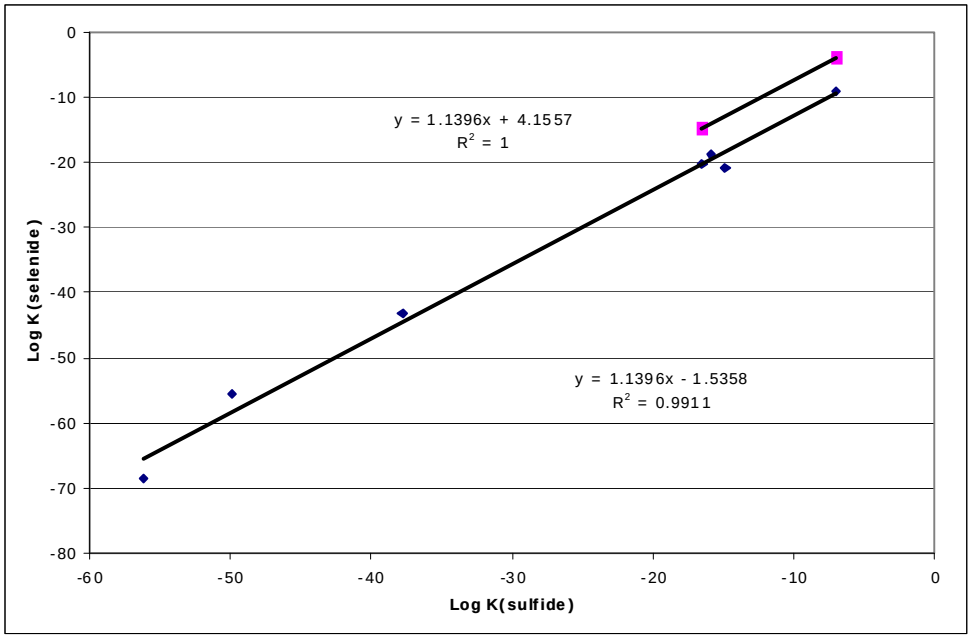

Fig. E1. Linear regression of dissociation constants of Hg sulfide and selenide complex pairs, and solubility product pairs for metal selenides and sulfides. "aq." refers to aqueous species.

Table E3. Estimated Log K Values of Selenide Aqueous Complexes of As+3, Cd+2, Pb+3, Sb+3, Zn+2 and Fe+

Reaction	**Log K**
Arsenic	
$H_3As_3Se_6(aq) + 1.5O_2(g) + 9H_2O = 3H_2AsO_4^- + 6HSe^- + 9H^+$	-23.96
$H_2As_3Se_6^- + 1.5O_2(g) + 9H_2O = 3H_2AsO_4^- + 6HSe^- + 8H^+$	-19.63
$HAs_3Se_6^{-2} + 1.5O_2(g) + 9H_2O = 3H_2AsO_4^- + 6HSe^- + 7H^+$	-10.64
$AsSe(OH)(SeH)^- + 0.5O_2(g) + 2H_2O = H_2AsO_4^- + 2HSe^- + 2H^+$	-6.91
Cadmium	
$CdSe(aq) + H^+ = Cd^{+2} + HSe$	-10.24
$Cd(HSe)_3^- = Cd^{+2} + 3HSe^-$	-23.47
$Cd(HSe)_4^{-2} = Cd^{+2} + 4HSe^-$	-25.12
$Cd(OH)_2(HSe)^- + 2H^+ = Cd^{+2} + 3HSe^- + 2H_2O$	-1.98
Lead	
$PbSe(aq) + H^+ = Pb^{+2} + HSe^-$	-11.04
$Pb(HSe)_2(aq) = Pb^{+2} + 2HSe^-$	-20.76
$Pb(HSe)_3^- = Pb^{+2} + 3HSe^-$	-22.15
Antimony	
$H_2Sb_2Se_4(aq) + 6H_2O = 2Sb(OH)_3 + 4HSe^- + 4H^+$	-70.63
$HSb_2Se_4^- + 6H_2O = 2Sb(OH)_3 + 4HSe^- + 3H^+$	-64.88
$Sb_2Se_4^{-2} + 6H_2O = 2Sb(OH)_3 + 4HSe^- + 2H^+$	-54.08
Zinc	
$ZnSe(aq) + H^+ = Pb^{+2} + HSe^-$	-8.76
$Zn(HSe)_4^{-2} = Zn^{+2} + 4HSe^-$	-21.42
$ZnSe(HSe)^- + H^+ = Zn^{+2} + 2HSe^-$	-12.56
$ZnSe(HSe)_2^{-2} + H^+ = Zn^{+2} + 3HSe^-$	-11.78
Iron	
$FeSe(aq) + H^+ = Fe^{+2} + HSe^-$	-2.28

Appendix F:
Improved Adsorption Models in TOUGHREACT

F1. Introduction

Many minerals such as metal oxides, hydroxides and layered silicates (Al_2O_3, TiO_2, FeOOH, SiO_2, kaolinite, etc.) exhibit electrically charged surfaces in the presence of natural waters. These surfaces contain ionizable functional groups (e.g., silanol groups in hydrated silica, Si-OH) being responsible for chemical reactions at the surface. Adsorption via surface complexation has been widely studied (Dzombak and Morel, 1990; Lutzenkirchen, 2006) and is a key process with respect to the fate and transport of heavy metals (e.g., Bradl, 2004) or other hazardous constituents such as arsenic (Goldberg, 2002; Goldberg et al., 2005; Manning and Goldberg, 1997). We have therefore incorporated into TOUGHREACT a model considering adsorption via surface complexation, using different surface complexation models such as the non-electrostatic model, the double layer model, and the constant capacity model (Dzombak and Morel, 1990). The surface complexation models implemented in TOUGHREACT were verified by comparison with other codes such as PHREEQC (Parkhurst and Appelo, 1999) and CRUNCH (Steefel, 2001). This Appendix includes two main parts. In the first part, we described the mathematical formulation and numerical implementation of surface complexation adopted in TOUGHREACT, while in the second part, we review the surface complexation reactions and their thermodynamic data used in the reactive transport simulations conducted in Section 4.

F2. Surface Complexation Models

F2.1 Surface Electric Potential Model

The sorption of solutes on solid surfaces can be described as a chemical reaction between the aqueous species and the specific surface sites (surface complexation). These surface reactions include proton exchange, cation binding and anion binding via ligand exchange at surface

hydroxil sites (represented here as XOH to avoid confusion with other chemical species). For example, the sorption of a metal could be represented as:

$$XOH + M^{z+} = XOM^{z+-1} + H^{+} \quad \text{(F1)}$$

At equilibrium, the sorption reactions can be described by the mass law equation:

$$K_{app} = \frac{\left[XOM^{z_+^{-1}} \right] a_{H^+}}{\left[XOM \right] a_{M^{z+}}} \quad \text{(F2)}$$

where K^{app} is referred to as the apparent equilibrium constant, because it includes surface charge effects and hence is dependent on the extent of surface ionization (Dzombak and Morel, 1990), *a* is the thermodynamic activity of the aqueous species, and the terms in brackets represent the concentration of surface complexes (mol/kg).

In aqueous complexation reactions, the electric charge is assumed to be homogeneously distributed in the solution. However, surface reactions take place on a fixed charged surface which creates an electrostatic field. An additional energetic term accounting for the work needed for the aqueous species to travel across the surface electric field is required:

$$\Delta G_{ads} = \Delta G_{intr} + \Delta G_{coul} = \Delta G_{intr} + (\Delta G_{\psi=0} - \Delta G_{\psi=\psi_0}) = \Delta G_{intr} - zF\psi_0 \quad \text{(F3)}$$

where ΔG_{ads} is the free enthalpy change of the overall adsorption reaction, ΔG_{intr} and ΔG_{coul} are the free enthalpy change due to chemical bonding and to the electrostatic work, respectively, z is the charge of the surface species, F the Faraday's constant (96485 C/mol), and ψ_0 is the mean surface potential (V). Since

$$\Delta G = -RT\ln K \,, \quad \text{(F4)}$$

Equation (F3) can be rewritten as:

$$K_{app} = K_{int}\, e^{\frac{zF\psi_0}{RT}} \,, \quad \text{(F5)}$$

where R is the gas constant (8.314 J/mol/K), T is the absolute temperature (K), and K_{int} is the intrinsic equilibrium constant which does not depend on the surface charge.

F2.2 Diffuse Layer Model

The diffuse layer model has been described in great detail by Dzombak and Morel (1990) and was applied to adsorption of metals on iron oxide surfaces. In the diffuse layer model, the solid-water interface is composed of two layers: a layer of surface-bound complexes and a diffuse layer of counter ions in solution. The surface charge is calculated from the total surface species adsorbed on the layer:

$$\sigma_p = \frac{F}{A}\sum_{k=1}^{N_s} z_k y_k \tag{F6}$$

According to the Gouy-Chapman theory, the surface charge density σ_p (c/m^2) is related to the potential at the surface (volt) by:

$$\sigma_d = (8RT\varepsilon\varepsilon_0 I\times 10^3)^{1/2}\sinh(zF\psi_0/2RT), \tag{F7}$$

where R is the molar gas constant (8.314 J mol^{-1} K^{-1}), T is the absolute temperature (K), ε is the relative dielectric constant of water (ε = 78.5 at 25 ^{o}C), ε_0 is the permittivity of free space (8.854×10^{-12} C V^{-1} m^{-1} or 8.854×10^{-12} C^2 J^{-1} m^{-1}), and c is the molar electrolyte concentration (M). Equation (F7) is only valid for a symmetrical electrolyte (Z=ionic charge).

It is common to use the linearized version of Equation (F7) for low values of the potential:

$$\sigma_p = \varepsilon\varepsilon_0\kappa\psi_0, \tag{F8}$$

where $1/\kappa$ (m) is the double-layer thickness defined as:

$$\frac{1}{\kappa} = \left(\frac{\varepsilon\varepsilon_0 RT}{2F^2\cdot 1000I}\right)^{1/2} \tag{F9}$$

Equations (F7) can be simplified by rewritten $(8RT\varepsilon\varepsilon_0 I\times10^3)^{1/2}$ for 25 ^{o}C :

$$\sigma_p = 0.1174 I^{1/2}\sinh(zF\psi_d/2RT) \tag{F10}$$

Therefore, in the diffuse-layer model, the value of the capacitance C relating the surface charge and the potential can be calculated based on theoretical considerations (Equation (F8)) instead of being an experimental fitting parameter.

F2.3 Constant Capacitance Model

Similar to the diffused-layer, the constant capacitance model is based on the assumption that all the species are adsorbed in the same layer and a diffuse layer of counterions constitutes the transition to homogenous solution. However, differently from the diffuse-layer model, the relationship between the surface charge and the potential is assumed to be linear:

$$\sigma = C\psi \tag{F11}$$

where C is a constant value to be obtained from fitting experimental data.

F2.4 Mathematical Formulation of Adsorption Reactions

Lets us consider the following surface desorption reaction:

$$XOM^{z_+-1} = XOH + M^{z_+} - H^+$$

with the equilibrium constant of the reaction given as:

$$K_{\text{int}} = \frac{[XOH]a_M}{[XOM]a_{H^+}} e^{\left(\frac{-zF\psi_0}{RT}\right)} \tag{F12}$$

Usually, the neutral surface complex XOH is included in the N_C aqueous primary species. The new unknown is the potential term

$$\tilde{\psi} = \frac{-F\psi_0}{RT} \tag{F13}$$

The concentration of a surface complex, y_j, (mol/m^3), can be expressed in terms of the concentration of the primary species and the potential term:

$$y_j = K_j^{-1} \prod_{i=1}^{N_C} c_i^{\nu_{ji}^y} \gamma_i^{\nu_{ji}^y} e^{z_j \tilde{\psi}} \qquad j = 1 \ldots N_Y \tag{F14}$$

where K_j is the intrinsic equilibrium constant of the desorption reaction.

In order to solve for the potential term, an additional equilibrium equation is needed. For the double diffuse layer model, we obtain Equation (F15), if the Guy-Chapman double-layer theory is used to relate surface charge and the potential (Equation (F7)). If the linearized Equation (F8) is used, we obtain Equation (F16). If a constant capacity model is used, we obtain Equation (F17).

$$(8RT\varepsilon\varepsilon_0 I \times 10^3)^{1/2} \sinh(-\tilde{\psi}/2) - \frac{F}{A} \sum_{k=1}^{N_s} z_k y_k = 0 \tag{F15}$$

$$\frac{F^2}{A\varepsilon\varepsilon_0 \kappa RT} \sum_{k=1}^{N_s} z_k y_k + \tilde{\psi} = 0 \tag{F16}$$

$$\frac{F^2}{ACRT} \sum_{k=1}^{N_s} z_k y_k + \tilde{\psi} = 0 \tag{F17}$$

F2.5 Implementation in TOUGHREACT

When surface complexation is considered, the total concentration of the primary species j at time zero (initial conditions) is assumed to be known, given by:

$$T_j^0 = \; c_j^0 + \sum_{k=1}^{N_x} \nu_{kj} c_k^0 + \sum_{m=1}^{N_p} \nu_{mj} c_m^0 + \sum_{n=1}^{N_q} \nu_{nj} c_n^0 + \sum_{s=1}^{N_s} \nu_{sj} c_s^0 \qquad j = 1 \ldots N_C \tag{F18}$$

where superscript 0 represents time zero; c denotes concentration; subscripts j, k, m, n and s are the indices of the primary species, aqueous complexes, minerals at equilibrium, minerals under kinetic constraints, and surface complexes, respectively; N_c, N_x, N_p, N_q and N_s are the number of corresponding species and minerals; and ν_{kj}, ν_{mj}, ν_{nj} and ν_{sj} are stoichiometric coefficients of the primary species in the aqueous complexes, equilibrium, kinetic minerals, and surface complexes, respectively.

After a time step Δt, the total concentration of primary species j (T_j) is given by

$$T_j = c_j + \sum_{k=1}^{N_x} \nu_{kj} c_k + \sum_{m=1}^{N_p} \nu_{mj} c_m + \sum_{n=1}^{N_q} \nu_{nj} \left(c_n^0 - r_n \Delta t \right) + \sum_{s=1}^{N_s} \nu_{sj} c_s \qquad j = 1...N_C \tag{F19}$$

where r_n is the kinetic rate of mineral dissolution (negative for precipitation, units used here are mole per kilogram of water per time), for which a general multi-mechanism rate law can be used (Xu et al., 2006). T_j^0 and T_j are related through generation of j among primary species as follows

$$T_j - T_j^0 = \sum_{l=1}^{N_a} \nu_{lj} r_l \Delta t \qquad \mathrm{j} = 1,...\mathrm{N_C} \tag{F20}$$

where l is the aqueous kinetic reaction (including biodegradation) index, N_a is total number of kinetic reactions among primary species, and r_l is the kinetic rate which is in terms of one mole of product species.

By substituting Equations (F18) and (F19) into Equation (F20), and denoting residuals as F_j^c (which are zero in the limit of convergence), we have

$$\begin{aligned} F_j^c \;=\; & (c_j - c_j^0) && \text{Primary species} \\ & + \sum_{k=1}^{N_x} \nu_{kj} (c_k - c_k^0) && \text{equilibrium aqueous complexes} \\ & + \sum_{m=1}^{N_p} \nu_{mj} (c_m - c_m^0) && \text{equilibrium minerals} \\ & - \sum_{n=1}^{N_q} \nu_{nj} r_n \Delta t && \text{kinetic minerals} \\ & - \sum_{l=1}^{N_a} \nu_{lj} r_l \Delta t && \text{kinetics among primary species} \\ & + \sum_{s=1}^{N_s} \nu_{sj} (c_s - c_s^0) && \text{surface complexes} \\ = \quad & 0 \qquad j = 1...N_C \end{aligned} \tag{F21}$$

According to mass-action equations, the concentrations of aqueous complexes c_k can be expressed as functions of concentrations of the primary species c_j. Kinetic rates r_n and r_l are functions of c_j. The expression for r_n is given in Xu et al. (2006), and r_l will be presented later.

No explicit expressions relate equilibrium mineral concentrations c_m to c_j. Therefore, N_P additional mass-action equations (one per mineral) are needed. Surface complexes are expressed as the product of primary species and an additional potential term $\tilde{\psi}$. Additional equilibrium equations (Equation (F16) or (F17) depending on the surface complexation model) have to be solved together with Equation (F21) and the N_p mass-action equations for equilibrium minerals.

The final Jacobian matrix has $Nc+Np+N_{\psi}$ rows and $Nc+Np+N_{\psi}$ columns, as follows:

$$\begin{array}{c|ccc} & Nc & Np & N\psi \\ Nc & \dfrac{\partial F_j^c}{\partial c_i} & \dfrac{\partial F_j^c}{\partial p_i} & \dfrac{\partial F_j^c}{\partial \tilde{\psi}} \\ Np & \dfrac{\partial F_j^p}{\partial c_i} & \dfrac{\partial F_j^p}{\partial p_i} & \dfrac{\partial F_j^p}{\partial \tilde{\psi}} \\ N\psi & \dfrac{\partial F^{\tilde{\psi}}}{\partial c_i} & \dfrac{\partial F^{\tilde{\psi}}}{\partial p_i} & \dfrac{\partial F^{\tilde{\psi}}}{\partial \tilde{\psi}} \end{array} \tag{F22}$$

$$J^{cc} = \frac{\partial F_j^c}{\partial c_i} = \delta_{ji} + \sum_{k=1}^{N_x} \nu_{kj}\nu_{ik}\frac{c_k}{c_i} + \sum_{n=1}^{Nq} \nu_{nj}\nu_{in}\frac{k_n A_n \Omega_n}{c_i} + \sum_{s=1}^{Ns} \nu_{sj}\nu_{is}\frac{c_s}{c_i} \tag{F23}$$

$$J^{c\tilde{\psi}} = \frac{\partial F_j^c}{\partial \tilde{\psi}} = \sum_{s=1}^{Ns} \nu_{sj} z_s c_s \tag{F24}$$

$$J^{\tilde{\psi}c} = \frac{\partial F^{\tilde{\psi}}}{\partial c_i} = -\sum_{s=1}^{N_s} z_s \nu_{is}\frac{c_s}{c_i} \tag{F25}$$

or

$$J^{\tilde{\psi}c} = \frac{\partial F^{\tilde{\psi}}}{\partial c_i} = \frac{F^2}{A\varepsilon\varepsilon_0\kappa RT}\sum_{s=1}^{N_s} z_s \nu_{is}\frac{c_s}{c_i} \tag{F26}$$

or

$$J^{\tilde{\psi}c} = \frac{\partial F^{\tilde{\psi}}}{\partial c_i} = \frac{F^2}{ACRT}\sum_{s=1}^{N_s} z_s \nu_{is}\frac{c_s}{c_i} \tag{F27}$$

$$J^{\tilde{\psi}\tilde{\psi}} = \frac{\partial F^{\tilde{\psi}}}{\partial \tilde{\psi}} = -\tfrac{1}{2}(8RT\varepsilon\varepsilon_0 I\times 10^3)^{1/2}\cosh(-\tilde{\psi}/2) - \frac{F}{A}\sum_{k=1}^{N_s} z_k z_k y_k \tag{F28}$$

or

$$J^{\tilde{\psi}\tilde{\psi}} = \frac{\partial F^{\tilde{\psi}}}{\partial \tilde{\psi}} = \frac{F^2}{A\varepsilon\varepsilon_0 \kappa RT} \sum_{s=1}^{N_s} z_s z_s c_s + 1 \tag{F29}$$

or

$$J^{\tilde{\psi}\tilde{\psi}} = \frac{\partial F^{\tilde{\psi}}}{\partial \tilde{\psi}} = \frac{F^2}{ACRT} \sum_{s=1}^{N_s} z_s z_s c_s + 1 \tag{F30}$$

F2.6 Verification in Comparison with Other Codes

The surface complexation calculation by TOUGHREACT has been verified against other codes such as PHREEQC (Parkhurst and Appelo, 1999) and CRUNCH (Steefel, 2001). The example of zinc sorption at low site density presented by Dzombak and Morel (1990) has been used by PHREEQC and CRUNCH to verify their surface complexation calculation. Zinc sorption on hydrous ferric oxide is simulated assuming two types of sites, weak and strong. Protons and zinc ions compete for the two types of binding sites, and equilibrium is described by mass-action equations. The double layer model is used to calculate the speciation of Zn^{2+} in aqueous and surface complexes. The example considers the variation in sorption of zinc on hydrous ferric oxides as a function of pH for low zinc concentration (10^{-7} M) and high zinc concentrations (10^{-4} M) in 0.1 M sodium nitrate electrolyte.

Figure F1 shows the calculation results of Dzombak and Morel (1990). Table 1 compares the calculated equilibrium speciation of Zn^{2+} calculated by TOUGHREACT and CRUNCH. Both simulators arrive at almost identical results. Figures F2 shows the calculated equilibrium speciation of Zn^{2+} as a function of pH calculated by TOUGHREACT.

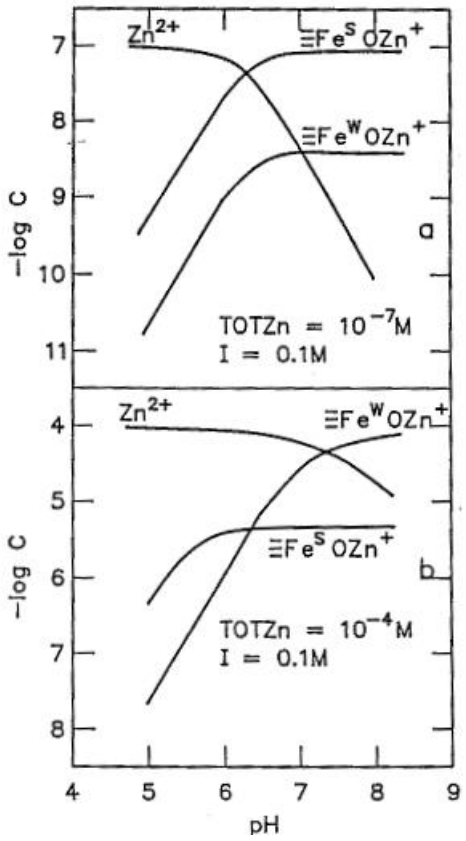

Fig. F1. Calculated equilibrium speciation as a function of pH for zinc in a 90-mg/L HFO suspension: The top figure shows results for Total Zn=10^{-7} M, I = 0.1 M; the bottom figure shows results for Total Zn = 10^{-4} M, I = 0.1 M (Dzombak and Morel, 1990).

Table F1. Calculated equilibrium speciation for zinc by TOUGHREACT and by CRUNCH

pH	Zn^{2+}		$Fe^{s}OZn^{+}$		$Fe^{w}OZn^{+}$	
	TOUGHREACT	CRUNCH	TOUGHREACT	CRUNCH	TOUGHREACT	CRUNCH
5	9.94E-08	9.94E-08	5.51E-10	6.03E-10	2.31E-11	2.52E-11
6	6.48E-08	6.28E-08	3.38E-08	3.57E-08	1.43E-09	1.51E-09
7	2.60E-09	2.61E-09	9.34E-08	9.34E-08	3.99E-09	3.99E-09
8.062	1.40E-10	1.38E-10	9.58E-08	9.58E-08	4.09E-09	4.09E-09

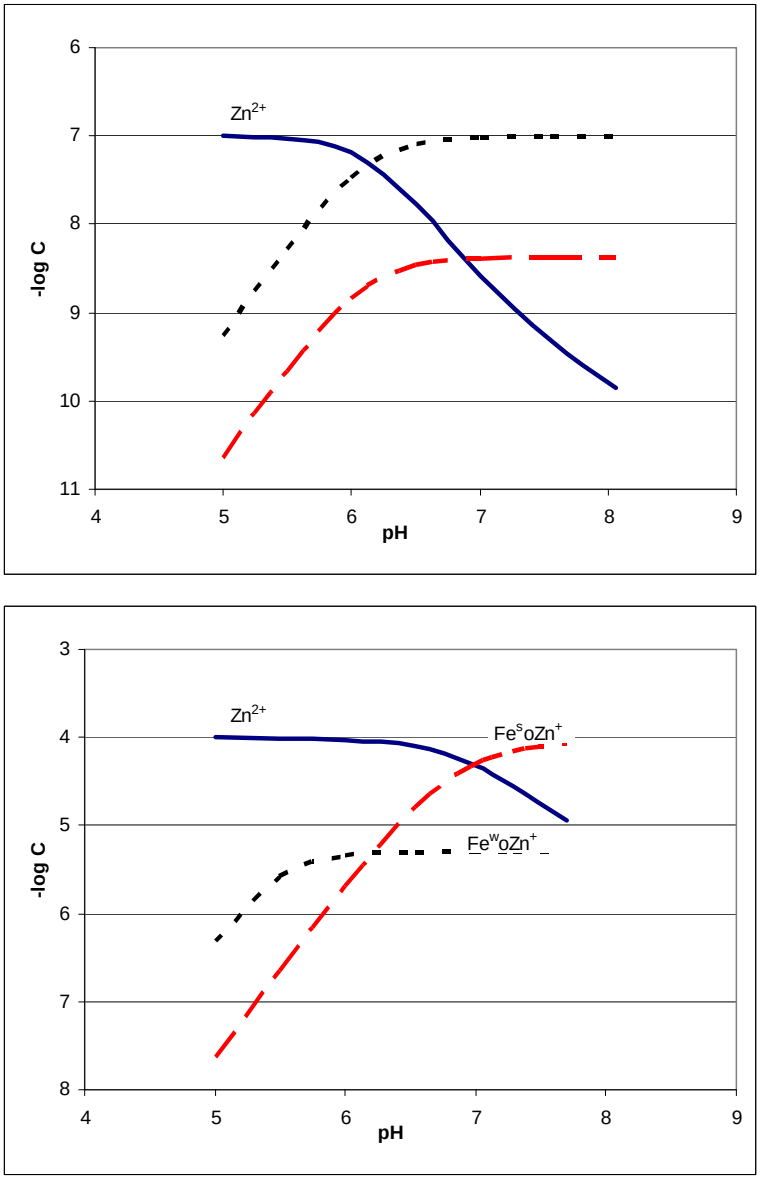

Fig. F2. Calculated equilibrium speciation as a function of pH for zinc. The top figure shows results for Total Zn=10^{-4} M, I = 0.1 M; the bottom figure shows results for Total Zn=10^{-7} M, I = 0.1 M.

F3. Surface Complexation Reactions and Parameters Used in Section 4

The adsorption of heavy metal (and arsenic) ions on minerals is influenced by a variety of factors, the most important being pH, type and speciation of metal ion involved, as well as heavy metal competition (Bradl, 2004). In this study, we consider goethite, illite, kaolinite, and smectite as principal adsorbents, mainly because these minerals have strong adsorption capacity, and we focus on lead and arsenic as relevant hazardous constituents**.** A literature analysis was conducted to determine the relevant surface complexation reactions and their thermodynamic constants for these cations and minerals, as summarized below.

Adsorption of Pb(II) on goethite was investigated under varying conditions. Kovacevic et al. (2000) experimentally studied the adsorption of lead species on goethite. Experiments were carried out for total Pb species concentrations of 2.5×10^{-4} mol/L, ph of 3–6, and ionic strength of 2×10^{-3} mol/L. The calculated surface complexation constant (logK) is -0.9 for a reaction expressed in the following form:

$$SOPb^{+} + H^{+} \rightleftharpoons Pb^{+2} + SOH \qquad \text{(F31)}$$

where *S* indicates surface, and $SOPb^{+}$ and SOH are surface complexes.

Muller and Sigg (1991) investigated the adsorption of Pb(II) on goethite in dilute (i.e., 2.41×10^{-7} mol/L) Pb (II) solutions over a pH range 6.6–8.2. Their published surface complexation constant (logK) is 0.52 for the monodentate surface complex (Equation F31) and 6.27 for the bidentate surface complex. Published surface complexation constants by Muller and Sigg (1991) are adopted in our simulations here, since they were obtained under conditions similar to the simulation setup in terms of Pb(II) concentration and pH. Since PbCO3(aq) is used as the primary species in our simulation instead of Pb(II), the reaction described in Equation (F31) occurs together with the following reaction between PbCO3(aq) and Pb(II):

$$Pb^{+2} + HCO_3^{-} \rightleftharpoons H^{+} + PbCO_3(aq) \qquad \log K = -3.06 \qquad \text{(F32)}$$

Note that the log*K* value of Equation (F32) was taken from the EQ3/6 V7.2b data base (Wolery, 1993).

Combining Equations (F31) and (F32), we obtain the surface complexation reaction shown in Table F2, where log*K* is -2.56. Note that the surface complex is expressed as Goe_OPb^{+} instead of $SOPb^{+}$, in order to distinguish it from other surface complexes of Pb(II).

Hizal and Apak (2006) studied lead(II) adsorption individually on kaolinite-based clay minerals. They performed experiments on three samples and calculated surface complexation constants and site densities. In our study, the surface complexation constant is taken to be the average of the value for these three samples, which is -1.87 for Equation (F31). Combining Equations (F31) and (F32), the log*K* value is -4.95.

Using batch adsorption experiments, Gu and Evans (2007) investigated the adsorption of Pb(II) onto illite as a function of pH and ionic strength. (Surface complexation of Pb on illite in a 0.01 mol/L $NaNO_3$ electrolyte is considered in our model because the majority of the potable groundwaters recorded in the NWIS database (USGS, 2008) have an ionic strength around 0.01M.) The investigators provided surface complexation constants for complexes on both edge and basal sites. Here, we refer to these as constants for strong sites ($Ill^{s}\_OPb^{+}$) and weak sites ($Ill^{w}\_OPb^{+}$), respectively (see Table F2).

Bradbury and Baeyens (2005) summarized surface complexation constants on smectite for more than ten metals. They presented linear free energy relationships (LFER) for strong and weak sites. The LFER correlated the surface complexation constants with aqueous complexation constants of the corresponding aqueous complexes. The calculated surface complexation constants for Pb(II) on montmorillonite, a member of the smectite group, for strong and weak sites using the LFERs (see Table 6 in Bradbury and Baeyens, (2005) are adopted in our simulation (see Table F2).

All the surface complexation reactions for lead used in the present simulation are listed in Table F2, while Table F3 summarizes these reactions using Pb^{+2} as primary species.

Adsorption of arsenite species on minerals can be described by three surface complexation reactions:

$$SH_2AsO_3 + H_2O \rightleftharpoons SOH + H_3AsO_3 \qquad \text{(F33)}$$

$$SHAsO_3^- + H_2O + H^+ \rightleftharpoons SOH + H_3AsO_3 \quad \text{(F34)}$$

$$SHAsO_3^{-2} + H_2O + 2H^+ \rightleftharpoons SOH + H_3AsO_3 \quad \text{(F35)}$$

where *S* denotes the surface of any mineral.

Surface complexation constants (see Table F3) for adsorption of arsenite on goethite are taken from Dixit and Hering (2003) by combining two reactions:

$$Goe\_OH_2AsO_3 + H_2O \rightleftharpoons Goe\_OH + AsO_3^{-3} + 3H^+ \qquad \log K = -39.93 \quad \text{(F36)}$$

$$AsO_3^{-3} + 3H^+ \rightleftharpoons H_3AsO_3 \qquad \log K = 34.74 \quad \text{(F37)}$$

Goldberg (2002) published the surface complexation constants (log*K*) for Equations (F36) and (37), which are -4.68 and 2.27, respectively. These constants are similar to those reported by Dixit and Hering (2003).

Goldberg (2002) also presented the surface complexation constants for the adsorption of arsenite on illite, kaolinite, and smectite. However, Manning and Goldberg (1997) gave a more complete description for adsorption of arsenite on these three minerals. In our study, we use the published surface complexation constants for Equations (F33), (F34) and (F35) from Manning and Goldberg (1997) (see Table F4). Table F4 summarizes the surface complexation reactions of As used in Section 4.

Specific surface area and site density are the other two important parameters affecting adsorption. Table F5 summarizes some published values for specific surface area and site density, while Table F6 lists those values used in the base model.

Table F2. Surface complexation of Pb on different minerals using PbCO3(aq) as primary species

Adsorbent	Surface Complexes	Reactions	Log k_{int}	Reference
goethite	Goe_OPb+	Goe _OPb^{+} + HCO_3^{-} ⇌ Goe_OH + $PbCO_3$(aq)	-2.56	(Muller and Sigg, 1991)
goethite	(Goe _O)$_2$Pb	(Goe _O)$_2$Pb + H^{+} + HCO_3^{-} ⇌ 2Goe_OH + $PbCO_3$(aq)	3.18	
kaolinite	Kao_OPb+	Kao_OPb^{+} + HCO3^{-} ⇌ Kao_OH + PbCO3(aq)	-4.95	(Hizal and Apak, 2006)
illite	Ill^{s}_OPb+	Ill^{s}_OPb^{+} + HCO3^{-} ⇌ Ill^{s}_OH + PbCO3(aq)	-4.43	(Gu and Evans, 2007)
illite	Ill^{w}_OPb+	Ill^{w}_OPb^{+} + HCO3^{-} ⇌ Ill^{w}_OH + PbCO3(aq)	0.78	
smectite	Sme^{s}_OPb+	Sme^{s}_OPb^{+} + HCO3^{-} ⇌ Sme^{s}_OH + PbCO3(aq)	-4.18	(Bradbury and Baeyens, 2005)
smectite	Sme^{w}_OPb+	Sme^{w}_OPb^{+} + HCO3^{-} ⇌ Sme^{w}_OH + PbCO3(aq)	-1.78	
glauconite	Gla_OPb^{+}	Gla_OPb^{+} + HCO_3^{-} ⇌ Gla _OH + $PbCO_3$(aq)	-6.4	(Smith et al., 1996)

Table F3. Surface complexation of Pb on different minerals using Pb^{+2} as primary species.

Adsorbent	Surface Complexes	Reactions	Log k_{int}	Reference
goethite	Goe_OPb+	Goe _OPb^{+} + H^{+} ⇌ Goe_OH + Pb^{+2}	0.5	(Muller and Sigg, 1991)
goethite	(Goe _O)$_2$Pb	(Goe _O)$_2$Pb+2H^{+} ⇌ 2Goe_OH + Pb^{+2}	6.24	
kaolinite	Kao_OPb+	Kao_OPb^{+} + H^{+} ⇌ Kao_OH + Pb^{+2}	-1.89	(Hizal and Apak, 2006)
illite	Ill^{s}_OPb+	Ill^{s}_OPb^{+} + H^{+} ⇌ Ill^{s}_OH + Pb^{+2}	-1.37	(Gu and Evans, 2007)
illite	Ill^{w}_OPb+	Illw_OPb^{+} + H^{+} ⇌ Illw_OH + Pb^{+2}	3.84	
smectite	Sme^{s}_OPb+	Sme^{s}_OPb^{+} + H^{+} ⇌ Sme^{s}_OH + Pb^{+2}	-1.12	(Bradbury and Baeyens, 2005)
smectite	Sme^{w}_OPb+	Sme^{w}_OPb^{+} + H^{+} ⇌ Sme^{w}_OH + Pb^{+2}	1.28	
glauconite	Gla_OPb^{+}	Gla_OPb^{+} + H^{+} ⇌ Gla _OH + Pb^{+2}	-3.34	(Smith et al., 1996)

Table F4. Surface complexation of H_3AsO_3 on different minerals

Adsorbent	Surface Complexes	Reactions	Log k_{int}	Reference
goethite	Goe $\_H_2AsO_3$	Goe $\_H_2AsO_3 + H_2O \rightleftharpoons$ Goe $\_OH + H_3AsO_3$	-5.19	(Dixit and Hering, 2003)
goethite	Goe $\_HAsO_3^-$	Goe $\_HAsO_3^- + H_2O + H^+ \rightleftharpoons$ Goe_OH + H_3AsO_3	2.34	
kaolinite	Kao_H_2AsO_3	Kao $\_H_2AsO_3 + H_2O \rightleftharpoons$ Kao $\_OH + H_3AsO_3$	-8.23	(Manning and Goldberg, 1997)
kaolinite	Kao $\_HAsO_3^-$	Kao_$HAsO_3^- + H_2O + H^+ \rightleftharpoons$ Kao $\_OH$ + H_3AsO_3	0.664	
kaolinite	Kao $\_OAsO_3^{2-}$	Kao_$AsO_3^{2-} + H_2O + 2H^+ \rightleftharpoons$ Kao $\_OH$ + H_3AsO_3	13.67	
illite	Ill_H_2AsO_3	Ill $\_H_2AsO_3 + H_2O \rightleftharpoons$ Ill_$OH + H_3AsO_3$	-9.07	(Manning and Goldberg, 1997)
illite	Ill $\_HAsO_3^-$	Ill $\_HAsO_3^- + H_2O + H^+ \rightleftharpoons$ Ill $\_OH + H_3AsO_3$	-3.000	
illite	Ill_AsO_3^{2-}	Ill_$AsO_3^{2-} + H_2O + 2H^+ \rightleftharpoons$ Ill_$OH + H_3AsO_3$	10.3	
smectite	Sme $\_H_2AsO_3$	Sme $\_H_2AsO_3 + H_2O \rightleftharpoons$ Sme $\_OH + H_3AsO_3$	-8.89	(Manning and Goldberg, 1997)
smectite	Sme $\_HAsO_3^-$	Sme $\_HAsO_3^- + H_2O + H^+ \rightleftharpoons$ Sme $\_OH$ + H_3AsO_3	4.650	
smectite	Sme $\_AsO_3^{2-}$	Sme $\_AsO_3^{2-} + H_2O + 2H^+ \rightleftharpoons$ Sme $\_OH$ + H_3AsO_3	13.700	
albite~low	Alb $\_OH_2AsO_3$	Alb $\_H_2AsO_3 + H_2O \rightleftharpoons$ Alb $\_OH + H_3AsO_3$	-7.58	(Manning and Goldberg, 1997)
albite~low	Alb $\_OHAsO_3^-$	Alb $\_OHAsO_3^- + H_2O + H^+ \rightleftharpoons$ Alb $\_OH$ + H_3AsO_3	2.43	
albite~low	Alb $\_OAsO_3^{2-}$	Alb $\_OAsO_3^{2-} + H_2O + 2H^+ \rightleftharpoons$ Alb $\_OH$ + H_3AsO_3	14.8	

Table F5. Summary of published specific surface area and site densities

Absorbent	Specific surface area (m^2/g)	Site density (mol/m^2)		Reference
		Strong site	Weak site	
hematite	5.4	0.00219	0.219	Dzombak and morel (1990)
goethite	54	3.32e-6		Dixit and Hering (2003)
goethite	14.7	1.76e-6	3.22e-6	Muller and Sigg (1991)
kaolinite	19.53	1.02 e-8		Hizal and Apak (2006)
kaolinite	14.73	2.2e-6	3.0e-6	Lackovic, et al. (2003)
kaolinite	9.1	2.68e-7		Manning and Goldberg (1997)
illite	66.8	1.3e-6	2.27e-6	Gu and Evans (2007)
illite	123	2e-7	6e-7	Lackovic, et al. (2003)
illite	24.2	4.79e-8		Manning and Goldberg (1997)
Na-smectite	56.38	4.77e-8	9.54e-7	Bradbury and Baeyens (2005)
smectite	18.6	1.1e-6		Manning and Goldberg (1997)
albite~low	5.9	2.9e-5		Manning and Goldberg (1997)
glauconite	48.7	1.6e-6		Smith et al. (1996)

Table F6. Specific surface area and site densities used in the base model

Absorbent	Specific surface area (m^2/g)	Site density (mol/m^2)		Reference
		Strong site	Weak site	
goethite	14.7	1.76e-6	3.22e-6	Muller and Sigg, (1991)
kaolinite	14.73	2.2e-6	3.0e-6	Lackovic et al. (2003)
illite	66.8	1.3e-6	2.27e-6	Gu and Evans (2007)
Na-smectite	56.38	4.77e-8	9.54e-7	Bradbury and Baeyens (2005)